Micromechanical Aspects of Aging in Granular Soils

Nestor R. Suarez

Dissertation submitted to the faculty of the Virginia Polytechnic Institute and State University in partial fulfillment of the requirements for the degree of

Doctor in Philosophy
in
Civil and Environmental Engineering

Thomas L. Brandon, Chair
James K. Mitchell, Co-Chair
George M. Filz
Russell A. Green

September 3, 2012
Blacksburg, VA

Keywords: aging, creep, sand, acoustic emissions, computed tomography, discrete element method, rate process theory

Micromechanical Aspects of Aging in Granular Soils

by Nestor R. Suarez

Dr. Thomas L. Brandon, Dr. James K. Mitchell
Charles E. Via, Jr. Department of Civil and Environmental Engineering

ABSTRACT

Granular soils exhibit a generally beneficial change in engineering properties with time after deposition or densification, during a process commonly known as aging. Soil properties reported to change during aging include the small strain modulus and stiffness, penetration resistance, liquefaction resistance, and pile setup. Different hypotheses have been proposed to explain the occurrence of aging in granular soils, including cementation induced by dissolution of silica and precipitation at the particle contacts, cementation due to microbiological activity, internal stress redistribution caused by particle crushing, and buckling of the load chains due to particle slippage. New evidence points out that internal and time-dependent changes in the soil structure caused by particle slippage and rearrangement as the source of the time-dependent variations in soil properties.

This investigation is focused on the study of aging at the particle scale to determine its main driving mechanism and define the factors which affect it. Results from an extensive laboratory testing program and computer simulations based on the discrete element method provide insight into the causes of aging and its effects on the macroscopic properties of sands based on the analysis of the interaction between sand grains.

DEDICATION

This work is dedicated to my wife and my parents, for their unconditional support during all these years. Esto nunca habría sido posible sin ustedes…

ACKNOWLEDGEMENTS

First and foremost I would like to express my most sincere gratitude to my advisors, Prof. James K. Mitchell and Prof. Thomas L. Brandon, for their unwavering support, extraordinary patience, and invaluable guidance. I consider myself very fortunate of having the opportunity to work with and learn from them during the last five years.

I am indebted to my committee members, Dr. George M. Filz and Dr. Russell A. Green, for providing their valuable insight and suggestions, and generously offering their time and assistance.

Special thanks to Dr. Joseph E. Dove. I greatly appreciate all the help he provided during this research, in particular while preparing and developing the DEM models.

I would also like to acknowledge Dr. Linbing Wang for allowing me to use the X-Ray CT scanner in his laboratory, and Dr. Cristian Druta, who kindly offered his time and expertise during the laboratory testing program.

I also thank all the great friends I made during my time at Virginia Tech. In particular, Alfredo, Ivka, and their lovely daughters, who made me feel as part of their family since the first day I arrived in Blacksburg; and Ashly and Celso, for their invaluable friendship.

Lastly, I want to thank my family, who have always given me their unconditional love; and my wife, who has always been there for me, during good and bad times.

Table of Contents

List of Figures

List of Tables

Chapter 1

Introduction

1.1 Background

Laboratory and field studies show that engineering properties of many freshly deposited or disturbed granular materials change over time, under constant effective stress, and with little or no change in void ratio. Soil properties reported to change during this process, commonly known as aging, include small strain modulus and stiffness (Baxter and Mitchell 2004; Daramola 1980; Howie et al. 2002), soil compressibility (Daramola 1980), penetration resistance (Dowding and Hryciw 1986; Mitchell and Solymar 1984; Schmertmann 1991), liquefaction resistance (Arango et al. 2000; Leon et al. 2006; Andrus et al. 2009; Hayati and Andrus 2009); and pile setup (driven piles) (Chow et al. 1998; Jardine et al. 2006). Aging has not yet been routinely incorporated into geotechnical engineering practice quantitatively due to the lack of reliable methods

for predicting its effects on soil properties. To development such tools it is important to determine why and how do soil properties change during aging.

Mitchell and Solymar (1984) detected aging following densification of the 70 m thick layer of deposits of alluvial uniform clean sand forming the foundation of the Jebba Dam hydroelectric development in Nigeria. They noted a decrease in the penetration resistance of the soil immediately after explosive compaction, even though soil densification was evident. This was followed by a time-dependent increase in the penetration resistance observed during a period of months after the densification. These findings led Mitchell and Solymar (1984) to hypothesize that the rupture of cementing bonds in the soils was the cause of the initial decease in the penetration resistance, while the following time-dependent increase was caused by their reformation due the precipitation of silica, previously in solution, at the particle contacts.

Schmertmann (1991) found a time-dependent increase in the cone penetration resistance of a 10 m thick layer of silty sand following deep dynamic compaction (DDC). The time-dependent increase in the penetration resistance was greater for higher levels of soil disturbance, connected to the number of 105 ft drops of a 33 ton weight. Schmertmann (1991) suggested that these changes were caused by time-dependent particle rearrangement and reorientation during drained secondary compression, resulting in load chain buckling and stress redistribution in the soil structure. This hypothesis is also supported by Mesri (1990) and Bowman and Soga (2003).

Other hypotheses proposed to explain the occurrence of aging in granular soils include factors such as particle cementation due to microbiological activity, as observed in recent studies under laboratory controlled conditions (DeJong et al. 2006), and particle

crushing during secondary compression (Lade et al. 2010), which would cause changes in the load carrying configuration of the soil structure.

1.2 Motivation

Time-dependent changes in the properties of freshly deposited and densified granular soils have been evidenced in the field and the laboratory for over 30 years, but the driving mechanism responsible for aging remains unclear. Recent evidence points towards mechanical processes such as particle rearrangement and internal stress redistribution in the soil structure as the main cause of aging (Mitchell 2008). However, the processes involved in the soil aging mechanism have not yet been studied, and the compositional or environmental factors which may control its effects on the properties of granular soils have not yet been identified. Without a clear understanding of why and how does aging occur in granular soils, it is unlikely that it could be reliably incorporated into geotechnical engineering practice.

Previous investigators have considered the possibility of simulating creep in clay (Kuhn 1987) and granular soils using the discrete element method (DEM), a computational tool which allows estimating the macroscopic properties of a granular assembly by studying the particle interactions. This research will focus on the study of aging in granular materials following a similar approach, but using 3D assemblies of irregular particles formed by clumps of spheres, and with the incorporation of a newly developed contact model which incorporates rate process theory with the Hertz-Mindlin contact mechanism, allowing the simulation of time-dependent particle interactions using DEM.

1.3 Research Objective

This research focuses on the determination and quantification of the time-related changes in the properties granular materials occurring during aging. The purpose of the research includes the determination of the driving mechanism responsible for aging, and the development of tools to study its effect on the properties of the soil. The research proposes studying aging from the micro- to the macro-scale, by analyzing the processes at the particle level occurring within a granular sample and studying their effect on the properties of the material. Three main questions will be addressed: (1) Why do properties of granular materials change with time during aging, (3) Which properties are affected?, and (3) What are the magnitude and the rate of these changes?

A literature review was conducted to find soil properties which have been reported to change during aging, estimate the magnitude of the respective changes, and find the different hypotheses proposed to explain the occurrence of aging in granular soil. Based on this information, a series of laboratory tests were prepared to study changes in the characteristics of granular materials at the micro- (particle-level) and macro-scales. Processes occurring at the particle-level, including crushing and particle movements, were studied using laboratory experiments which included the analysis of the Acoustic Emissions (AEs) produced during aging, and the direct observation of changes in the internal structure of the soil using X-Ray Computed Tomography (CT). Aging was also studied during one-dimensional and triaxial compression, by measuring time-dependent changes in the axial and volumetric strains of granular samples formed by particles of different angularity and strength. Computer models were developed using DEM, including a new contact model developed to simulate time-dependent particle

interactions. Lastly, results from computer simulations were analyzed and the applicability of the models was assessed.

1.4 Research Outline

This thesis is organized into six chapters.

Chapter 2 presents a review on aging. It includes a discussion of the different hypotheses formulated to explain the occurrence of aging in granular materials, as well as reported variations of the engineering properties of granular soils in the field and the laboratory. Other time-dependent properties of granular materials, including creep and rate effects, will be also discussed.

Chapter 3 summarizes the micro-scale laboratory tests conducted to study changes occurring in specimens of sand and other granular materials during aging. The chapter introduces basic concepts of X-ray Computed Tomography, which was used to detect particle movements and rotations during creep inside a granular specimen without causing any disturbance to the experiments.

Chapter 4 summarizes the macro-scale laboratory experiments conducted to study changes in macroscopic properties of granular specimens due to aging. Creep was studied during one-dimensional compression (constant vertical stress and restrained lateral deformation) and triaxial compression (constant major vertical and horizontal stresses). Changes to the internal structure of the samples during aging were evaluated using acoustic emission (AE) techniques.

Chapter 5 introduces the principles of DEM. This chapter will discuss the applicability and limitations of this methodology in geotechnical engineering practice.

Chapter 6 presents the methodology used to model creep and other time processes using DEM. The chapter discusses the development of a new contact model, based on the rate process theory, to simulate time-dependent particle interactions. The chapter also includes a brief description of rate process theory, which has been used previously in geotechnical engineering to describe the deformation during creep in clays.

Chapter 7 includes the analysis of results from DEM simulations. It will describe in detail the DEM models used, from the creation of the particle arrangements to the parameter selection and the simulation characteristics. It will include results from both 2D and 3D simulations, comparing the results with tests conducted in the laboratory. The effect of environmental factors, such as the level of stress anisotropy or the magnitude of the confining stress, as well as compositional factors, including particle angularity initial void ratio, on the aging mechanism will be studied and discussed.

Chapter 8 summarizes the major findings of this investigation and presents recommendations for future research.

Chapter 2

Aging of Granular Soils

2.1 Introduction

Engineering properties of granular soils have been observed to change with time after deposition of densification, during a process known as aging. During aging, properties such as the penetration resistance may as much as double in magnitude measured just after disturbance or deposition. The magnitude of other soil properties, such as the small strain shear modulus or the liquefaction resistance, may also show substantial changes with time during aging.

This chapter discusses the main characteristics of aging, as described by previous investigators, and summarizes some of their main findings. A brief overview of sand aging effects on different soil properties is also provided. Additionally, various hypotheses formulated to account for the occurrence of aging in granular soils will be presented and discussed.

2.2 Aging Effects on Granular Soils

The magnitude of various soil properties have been reported to change with time during aging. These include the penetration resistance measured using SPT and CPT, liquefaction resistance, soil stiffness and strength, and capacity of driven and jacked piles. A summary of some of the most representative case studies illustrating these effects is now presented.

2.2.1 Penetration Resistance

Changes in the penetration resistance of granular soils are often observed using field measurements and laboratory tests. This section will describe the conditions under which aging have been evidenced, as well as the main characteristics of the aging effects as reported by different investigators.

2.2.1.1 Field Measurements

Mitchell and Solymar (1984) reported time-dependent changes in the penetration resistance of a deposit of alluvial clean sand following densification by explosive compaction and vibrocompaction. The loose alluvial deposits, formed by medium to coarse sub-rounded to round silica sand, were the foundation of the Jebba Dam, a 42 m high earth and rockfill dam on the Niger River in Nigeria. Mitchell and Solymar (1984) noticed that the penetration resistance of the sand deposits decreased immediately following explosive compaction, even though densification was evidenced by significant soil subsidence. This behavior, which they called *sensitivity*, is shown in Fig. 2-1, which includes the recorded magnitudes of penetration resistance from 3 cone penetration tests (CPT) located 1.5 m away horizontally from the blasting tube insertion point.

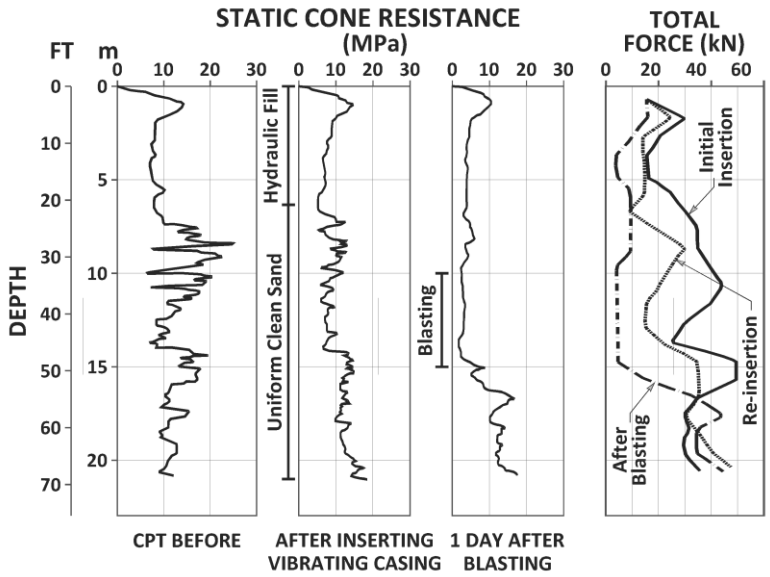

Fig. 2-1. Effect of sand disturbance on resistance to penetration (redrawn from Mitchell and Solymar, 1984).

Subsequent cone penetration tests showed an increase in the magnitude of the CPT resistance over a period of months after densification by blasting or vibrocompaction, as shown in Fig. 2-2. Increases in the penetration resistance were also observed after deposition of a 10 m thick hydraulic fill which was used as a construction platform in the river.

Skempton (1986) also noticed that time affected the magnitude of the penetration resistance of granular soils, although he considered much larger time periods (more than 100 years). According to his findings, the ratio of the SPT N-value normalized to an effective overburden pressure of 1 atm and the soil's relative density squared ($(N_1)_{60}/D_r^2$) changed from around 35 for laboratory tests on samples aged for about 10^{-2} years to 40 for recent fills (aged for 10 years) and 55 for natural deposits (aged for over 100 years).

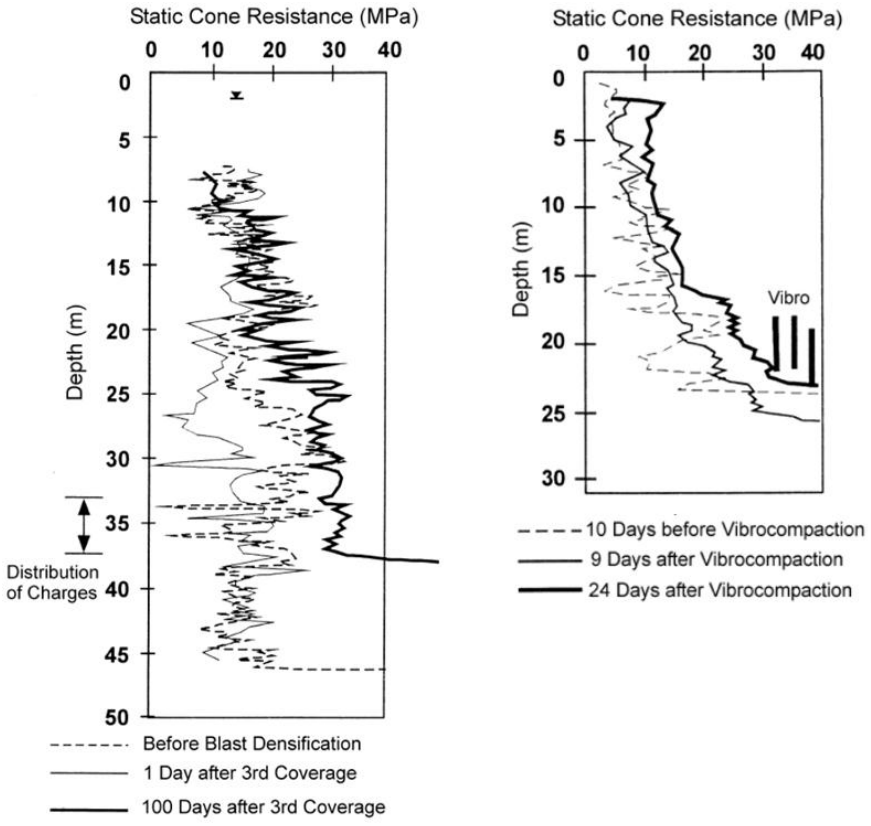

(a) (b)

Fig. 2-2. Effect of time on the cone penetration resistance of sand after (a) explosive compaction and (b) vibrocompaction. Jebba dam site, Nigeria (Mitchell 2008).

Dumas and Beaton (1986) reported aging effects after deep dynamic compaction (DDC) of a clean sand fill at the Pointe Noire deep sea harbor in Quebec. After the application of 330 t-m/m^2 of compactive energy, a 6 to 17 m thick layer of loosely deposited medium to coarse clean sand showed an immediate increase in the magnitude of CPT resistance (q_c). The penetration resistance of the soil continued to increase, and showed a significant change 8 days after compaction. Fig. 2-3 shows the reported magnitudes of q_c previous to, immediately after, and 8 days after DDC.

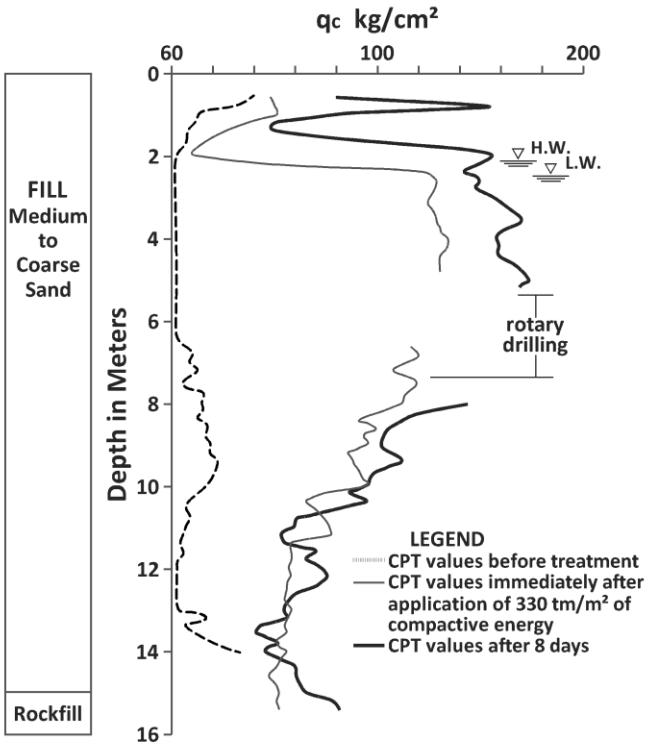

Fig. 2-3. Changes in penetration resistance with time at the Pointe Noire deep sea harbor, Quebec (redrawn from Dumas and Beaton, 1986).

Changes in the cone penetration resistance of a 10 m thick layer of silty sand in Jacksonville, Florida, after densification by deep dynamic compaction were reported by Schmertmann (1991). Fig. 2-4 shows the magnitude of this change in the form of a normalized increase, calculated as the ratio of q_c at any given time and its corresponding value just after compaction using a 33 ton weight dropped 105 ft. According to Fig. 2-4, not only did the value of penetration resistance increase with time, but the magnitude of this change seemed to depend on the number of drops used during DDC.

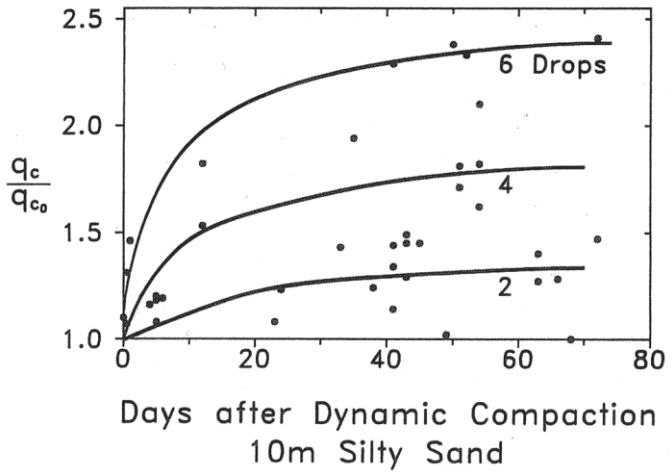

Fig. 2-4. Increase in cone penetration resistance of a 10 m thick layer of silty sand in Jacksonville, Florida (Schmertmann 1991).

Jefferies and Rogers (1993) reported increases in cone penetration resistance in the Molikpaq sand core hydraulic fill after explosive densification. The Molikpaq is a mobile caisson approximately 100 m wide, with a 70 m by 70 center core, used for offshore hydrocarbon drilling. Its center was filled with hydraulically-placed sand to provide resistance to the lateral forces produced by moving ice in the Artic. The Molikpaq was deployed at four sites: Tarsiut P-45, Amauligak I-65, Isserk I-15, and Amauligak F-24. Initial results reported by Jefferies et al. (1988) at the Tarsiut P-45 site, where the hydraulically-placed clean sand was not densified after placement, did not evidence any apparent aging effect. The magnitudes of cone penetration resistance measured for Tarsiut P-45 were constant for over ten months after deposition. Nonetheless, the results from the Amauligak F-24 site did show significant time-dependent changes in penetration resistance. The sand used for the hydraulic fill for the Amauligak F-24 came from the same borrow source as Tarsiut P-45, and was placed using the same process (Jefferies and Rogers 1993). However, blasting was used for Amauligak F-24 to compact the granular fill, providing an additional protection against

cyclic ice loading expected at the site. Densification of the fill was attested by settlements of around 1 m after blasting. The cone penetration resistance of the Molikpaq sand core increased with time after blast densification. Fig. 2-5 shows this variation for the initial 16 days. Jefferies and Rogers (1993) reported that the CPT resistance continued increasing for several weeks at a decreasing rate, following a similar trend to that reported by Schmertmann (1991).

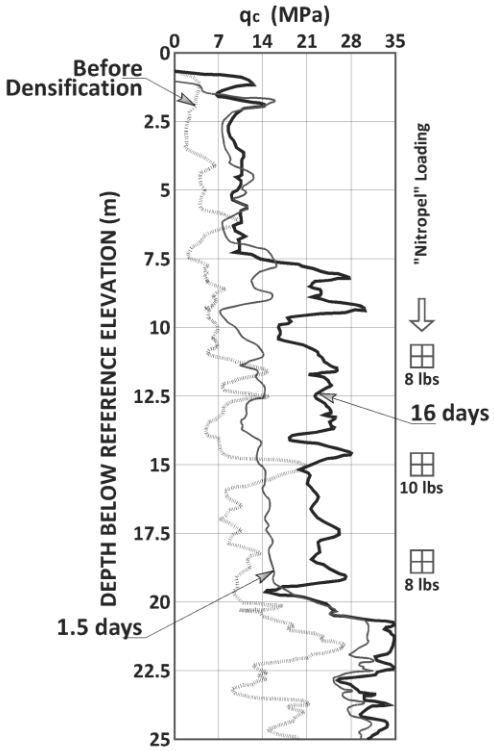

Fig. 2-5. Cone penetration resistance of the Molikpaq sand core previous, 1.5 days after, and 16 days after blast densification (redrawn from Rogers et al., 1990).

Charlie et al. (1992) studied the aging effects after explosive compaction of a 1.5 m thick layer of poorly graded medium fine sand overlaying a 3.6 m thick layer of dense to very dense (D_r from 70% to 85%) poorly graded gravely sand. Blasting produced very little densification (approximately 1 cm of settlement). Charlie et al. (1992) observed that the CPT resistance of the soil decreased immediately following blasting, showing

reductions in both the measured tip resistance and sleeve friction. After 18 weeks, the value of tip resistance increased approximately 13% relative to the magnitude recorded one week after blasting, while the sleeve friction decreased about 40% relative to its value after one week. Charlie et al. (1992) relates the decrease in sleeve friction to a possible reduction in the horizontal stress in the soil.

Changes in the magnitude of cone penetration resistance of fine sand and silty sand hydraulic fill after blasting densification were reported by Ashford et al. (2004). For this project, soil liquefaction was produced using two sets of blasts, each with a total of sixteen 0.5 kg charges, producing settlements of up to 10 cm. Ashford et al. (2004) reported a decrease in the cone penetration resistance two days after the second blast. However, measurements taken 42 days after a third blast, which followed approximately the same pattern of the second blast, the cone penetration resistance at depths ranging from 2 m to 5 m had increased by approximately twice the pre-blast value and 2.5 times above the value two days following blasting (Ashford et al. 2004).

The previous examples correspond to cases where increases in the penetration resistance of granular soils have been reported. However, there are also reports where no significant changes were observed. Human (1992) reported no significant change with time in the magnitude of cone penetration resistance of a 4 m thick fine silty sand fill in Alameda, CA, following the 1989 Loma Prieta Earthquake. In this study, results from cone penetration tests conducted 4, 14, 30, 65, and 317 days after the earthquake were compared with values recorded previous to 1989. The results did not indicate any consistent change in the penetration resistance of the soil, even though liquefaction was evidenced by sand boils observed above the sand fill. Other examples, cited by Mitchell

(2008), include the investigation conducted by Gohl et al. (1994) on blast densification in British Columbia. Gohl et al. (1994) did not observe any consistent change in the penetration resistance of a layer of loose sand overlaid by 2 to 3 meters of random fill, during 450 days following blast-induced liquefaction. Similar results were obtained by Liao and Mayne (2005) after blast-induced liquefaction of clean quartz sand at two sites in the New Madrid Seismic Zone. Liao and Mayne (2005) observed a decrease of about 10% in the magnitude of cone penetration resistance following blast-induced liquefaction, with no significant increase over the following 8 months.

2.2.1.2 Laboratory Penetration Resistance

Changes in the penetration resistance of granular materials have been also observed under laboratory control conditions. Dowding and Hryciw (1986) studied the effects of blast densification on saturated sand using laboratory tests. The material for these tests was Evanston Beach sand, a poorly graded silica sand with a coefficient of uniformity (C_u) of 1.50. The sand was placed into 107 cm diameter and 102 cm high cylindrical tanks, and liquefied by pumping water upwards to obtain an initial relative density of about 50%. Multiple explosive charges in the center of the tank, set off with a delay of up to 50 ms, were used for blast densification, resulting in values of relative density ranging from 60% to 78% after blasting. The penetration resistance was measured using mini-cone tests 10, 20, 30, and 40 cm away horizontally from the blasting point. Changes in point resistance measured 1, 5, and 15 days after blasting are shown in Fig. 2-6. The results show that the penetration resistance increased with time, even if blast densification was not applied, with the increases being greater close to the center of the tank, where the explosives where located. The tests also showed that the penetration

resistance measured close to the center of the tank 1 day after blasting, was lower or equal to the values recorded previous to blasting. This behavior is similar to that described by Mitchell and Solymar (1984).

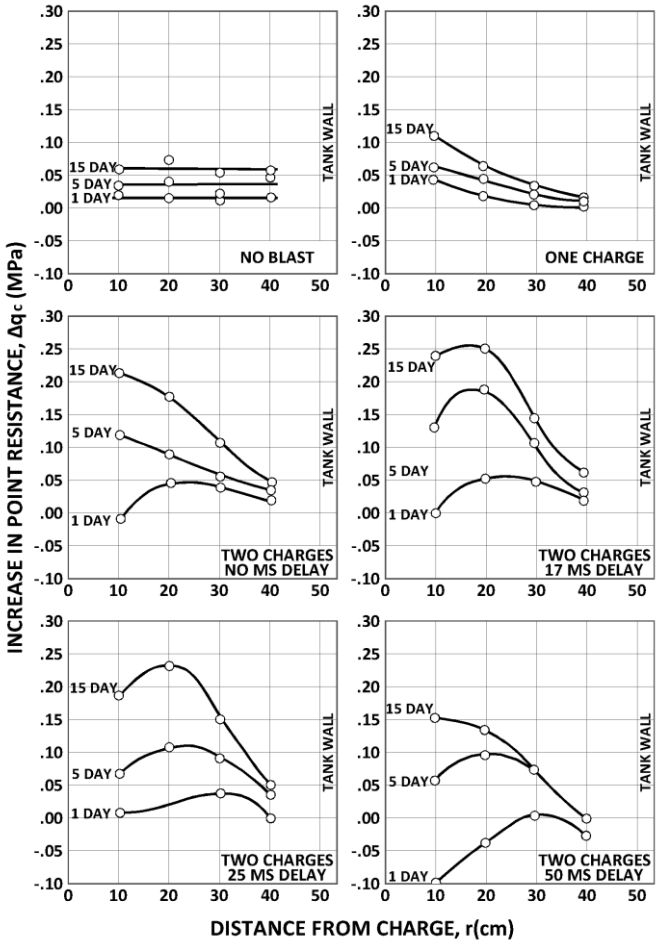

Fig. 2-6. Change in penetration resistance of Evanston Beach sand with time after blast densification (redrawn from Dowding and Hryciw, 1986).

Joshi et al. (1995) studied the changes in the penetration resistance of local river sand (poorly graded, angular), and Beaufort Sea sand (poorly graded, rounded) under one-dimensional compression. Sands were allowed to age under a constant vertical stress of 100 kPa for a period of up to 2 years. Three different pore fluids were used: (1) air, (2) distilled water, and (3) simulated sea water. The penetration resistance was measured using a 10 mm diameter penetration probe. Fig. 2-7, which shoes the variation in

penetration resistance with respect to time of aging for Beaufort Sea sand submerged in sea water, is a typical example of the results obtained. All the tests showed increases in the penetration resistance with time during aging. Greater aging effects were measured for samples submerged in sea water, followed by those submerged in distilled water and in dry state (in that order).

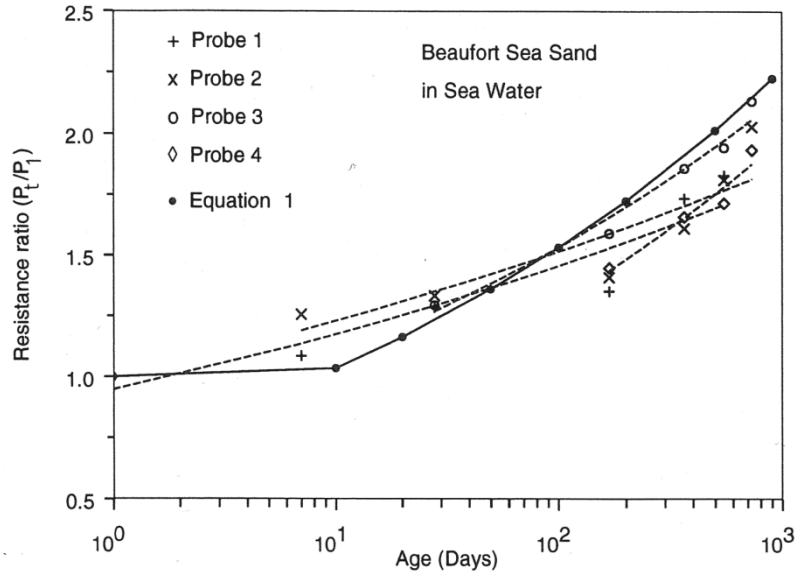

Fig. 2-7. Change in penetration resistance with time of Beaufort Sea sand submerged in sea water. The magnitude of penetration resistance (P_t) is normalized with respect to the magnitude recorded after 1 day of aging (P_1) (Joshi et al. 1995).

2.2.2 Small Strain Modulus and Stiffness

Aging effects on the small strain modulus of granular soils have been reported for over 40 years. Most of these studies are related to laboratory investigations, with only few cases being reported in the field. A summary of some of the most representative is presented next.

2.2.2.1 Field Studies

One of the few reported field cases were time-dependent changes in the stiffness of the soil have been observed comes from an investigation done by Troncoso and Garces

(2000). Troncoso and Garces (2000) measured the shear modulus of the soil at four abandoned tailing dams in Chile, named Veta del Agua, La Cocinera, Cauquenes, and Barahona, using in-situ downhole wave propagation tests. The tailings consisted primarily of low plasticity silts, and their properties are given in Table 2-1. Fig. 2-8 shows the variation of shear modulus normalized by the vertical effective stress (G_n), with respect to the age of the tailings. The results show that the time of aging has a significant effect on the small strain stiffness of the material.

Table 2-1. Properties of fine tailings (Troncoso and Garcés 2000).

Property	Veta del Agua	La Cocinera	Cauquenes	Barahona
Fines content [%]	60-95	58-99	50-95	57-90
Liquid Limit	23	26	29	41
Plasticity Index	2	4	6	14
Specific Gravity	2.80	3.42	2.78	2.80
USCS Classification	ML	ML	ML	ML

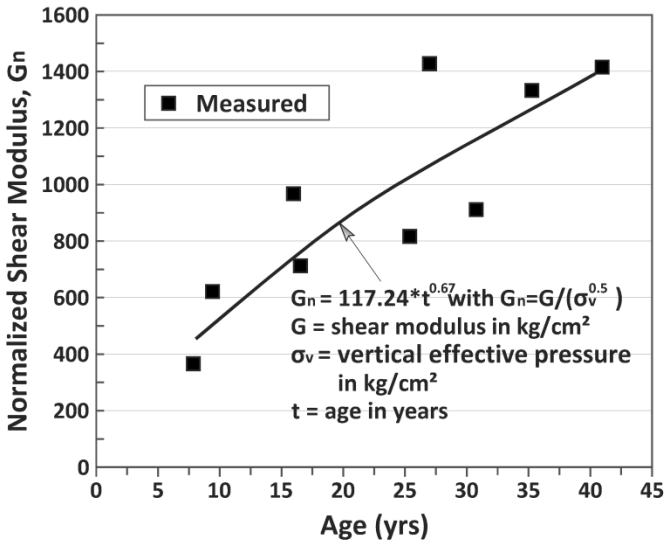

Fig. 2-8. Normalized shear modulus as function of age for tailings (redrawn from Troncoso and Garces, 2000).

2.2.2.2 Laboratory Studies

One of the first investigations that showed changes in the small strain modulus of sands during aging was done by Afifi and Richart (1973). Based on resonant column tests, they observed that the low amplitude dynamic shear modulus of sands increased over time under constant confining pressure. Similar results were reported by Anderson and Stokoe (1978), who approximated this behavior to that described by Eqs. 1 and 2, where the value of small strain shear modulus at a time t (G_t) can be extrapolated based on normalized change in small strain shear modulus with time (N_G), and ΔG, the change in small strain shear modulus between a reference time after the completion of the primary consolidation (G_{1000}), taken as 1000 minutes (t_{1000}), and any other time thereafter (t_2).

$$N_G = \frac{\Delta G}{G_{1000} * \log(t_2 / t_{1000})} \quad (1)$$

$$G_t = G_{1000}\left(1 + N_G \log\left(\frac{t}{t_{1000}}\right)\right) \quad (2)$$

The value of the parameter N_G represents the rate of increase in the magnitude of small strain shear modulus per logarithmic cycle of time, with greater values of N_G representing greater increments in shear modulus. Values of N_G reported by Jamiolkowski and Manassero (1995) for several sands and clays are shown in Table 2-2.

Changes with time in the stiffness of granular materials were also observed by Daramola (1980) during triaxial tests on samples of Ham River sand isotropically consolidated under 400 kPa for up to 152 days. Results from these tests are shown in Fig. 2-9. Aging caused a change of about 50% in the value of the secant Young's modulus at 1% strain, but did not have any conclusive effect on the strength of the material, as illustrated by similar values of maximum stress ratio (σ_1'/σ_3') in Fig. 2-9. These results

contrast with those obtained by Human (1992), who did not find any significant change in the stress-strain characteristics of dense (D_r=78%) samples of Crystal silica sand aged under an isotropic consolidation stress of 150 kPa for up to 28 days.

Table 2-2. Values of N_G for sands and clays (Jamiolkowski and Manassero 1995).

Soil	d_{50} [mm]	PI [%]	N_G [%]	Notes
Ticino sand	0.54		1.2	Predominantly silica
Hokksund sand	0.45		1.1	Predominantly silica
Messina sand and gravel	2.10		2.2 to 3.5	Predominantly silica
Messina sandy gravel	4.00		2.2 to 3.5	Predominantly silica
Glauconite sand	0.22		3.9	50% Quartz, 50% Glauconite
Quiou sand	0.71		5.3	Carbonatic
Kenya sand	0.13		12	Carbonatic
Pisa clay		23-46	13 to 19	
Avezzano silty clay		10-30	7 to 11	
Taranto clay		35-40	16	

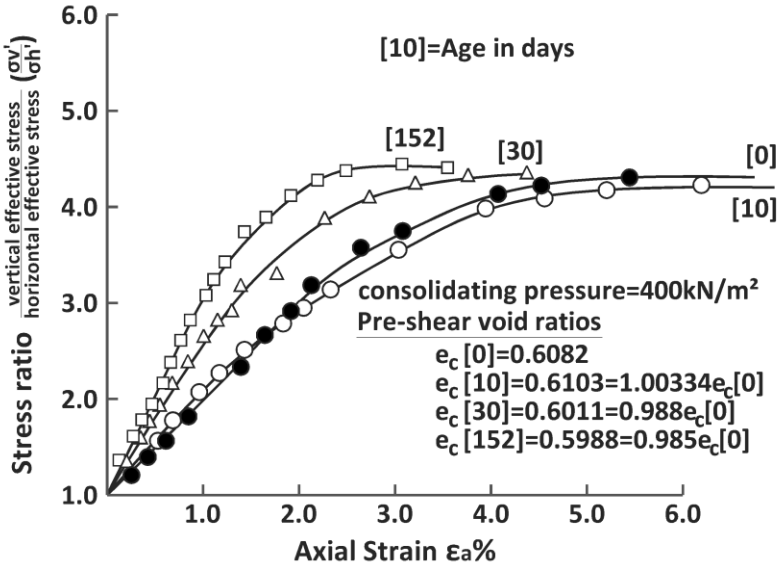

Fig. 2-9. Effect of age of consolidation on the stress-strain characteristics of Ham River sand (redrawn from Daramola, 1980).

Howie at al. (2002) studied the effects of aging on granular soils by means of triaxial tests on samples of loose Fraser River sand, a uniform (C_u=1.9) fine clean sand. Samples of sand were allowed to age for time periods ranging from 1 to 10,000 minutes, under a constant horizontal confining stress (σ_3') of 100 kPa at different stress ratios (1.0,

2.0, and 2.8). Some of the results are shown in Table 2-3. The tests showed increases in shear modulus calculated based on the magnitude of secant modulus (E), which agreed with the behavior described by Anderson and Stokoe (1978) (shown in Eqs. 1 and 2), with a linear increase in the value G with respect to the logarithm of time. The magnitude of this increase, represented by the value of the parameter N_G, was greater for larger values of stress ratio during aging and looser samples. The value of N_G depended on the axial strain at which the secant modulus was calculated. Greater values of strain resulted in smaller magnitudes of N_G, as can be seen in Table 2-3 for the values calculated using the secant modulus at 0.02% and 0.1% strain. This seems to indicate that the aging effects disappear or are diminished at high strains. The value of the parameter N_G was also affected by the reference time (t_p) selected, with N_G increasing with decreasing t_p. Previous investigators assumed a value t_p of 1000 min for the calculation of N_G; e.g., Anderson and Stokoe (1978), Jamiolkowski and Manassero (1995).

Table 2-3. Values of N_G for loose Fraser River sand (Howie et al. 2002).

Stress ratio during aging	***G* at 1 min [MPa]**	***E* at 1000 min [MPa]**	**N_G [%]**	
			t_p=1 min	**t_p=1000 min**
G from $E_{0.02\%}$				
1.0	23	32	21	1
2.0	10	28	92	2
2.8	5.5	27	148	3
G from $E_{0.1\%}$				
1.0	14	18	10	<0.5
2.0	7	11	25	1
2.8	4	9	50	1.2

Baxter and Mitchell (2004) studied the effects of aging on samples of poorly graded fine subangular sand (Evanston Beach sand) and poorly graded rounded fine to medium sand (Density sand) under one-dimensional compression. Samples of sand were prepared in fixed ring consolidometers and allowed to age for up to 118 days under a

constant vertical stress of 100 kPa. Aging was studied under numerous conditions, including different initial sample relative densities (40% to 80%), temperatures (25 to 40ºC), and pore fluids (air, distilled water, CO_2 saturated water, ethylene glycol). During the tests, parameters such as the small strain shear modulus, electrical conductivity, pore fluid chemistry, and mini-cone penetration resistance, were measured and calculated at different times. Values of the parameter N_G calculated based on those results are shown in Table 2-4. The majority of the tests showed an increase in the value of small strain shear modulus with time during aging. Mini-cone tests failed to detect any significant change in the magnitude of penetration resistance.

Table 2-4. Values of N_G for Evanston Beach sand and Density sand allowed to age under oedometric conditions (Baxter and Mitchell 2004).

Temperature [ºC]	**Initial D_r [%]**	**N_G [%]**			
		Distilled Water	**Ethylene Glycol**	**CO_2 sat. Water**	**Dry**
Evanston Beach sand					
25	40	1.7	0.5	1.8	-
40	80	2.8	0.8	2.8	0.5
25	40	1.6	0.1	-	-
40	80	4.0	1.3	-	-
Density sand					
25	40	-0.6	0.8	-0.7	0
40	80	0.3	0.8	0.3	2.2
25	40	-0.1	-0.7	-	-
40	80	1.0	0.1	-	-

Wang and Tsui (2009) studied the changes with time in small strain shear modulus of samples of Ottawa sand (round, poorly graded) and Toyoura sand (angular, poorly graded) aged under an isotropic confining stress ranging from 35 kPa to 100 kPa for up to 7 days. An energy-injecting virtual mass resonant column system was used to measure dynamic properties of the soil samples, including the small strain shear modulus and the damping ratio. The influence of factors such as the initial packing density of the

samples, magnitude of confining stress, and fines content was evaluated. A typical set of the results obtained by Wang and Tsui (2009) is shown in Fig. 2-10, corresponding to dense (D_r=76.8%) Toyoura sand. Values of the parameter N_G, calculated using a reference time (t_p) equal to 1000 min, are shown in Table 2-5. Table 2-5 also shows the normalized change in small strain shear modulus ($\Delta G_{7d}/G_i$) and damping ratio ($\Delta D_{7d}/D_i$) after 7 days of aging. The results indicate that the small strain shear modulus increased and the damping ratio decreased with time during aging for all the tests. The increase with time in small strain shear modulus was greater in loose than in dense samples for a confining pressure of 35 kPa. However, the opposite occurred if a greater confining stress (100 kPa) was applied during aging. In addition, Wang and Tsui (2009) found that shearing to large strains gradually diminished the effects of aging on the damping ratio and small strain shear modulus.

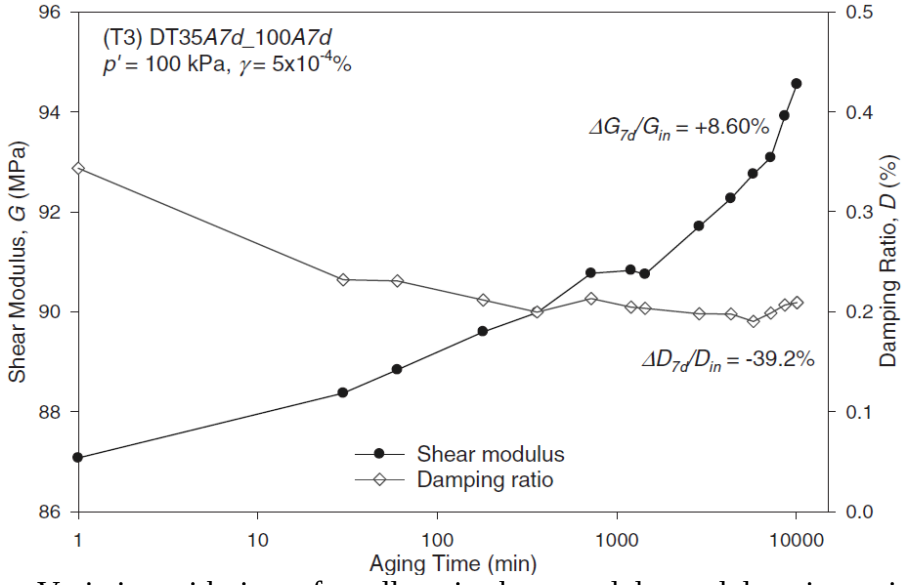

Fig. 2-10. Variation with time of small strain shear modulus and damping ratio in dense Toyoura sand under isotropic confining stress of 100 kPa (Wang and Tsui 2009).

Table 2-5. Change in small strain dynamic properties of Ottawa sand and Toyoura sand allowed to age under isotropic confinement for up to 7 days (Wang and Tsui 2009).

Sand Tested	Aging at 35 kPa			Aging at 100 kPa		
	$\Delta G_{7d}/G_i$ [%]	$\Delta D_{7d}/D_i$ [%]	N_G [%]	$\Delta G_{7d}/G_i$ [%]	$\Delta D_{7d}/D_i$ [%]	N_G [%]
Dense Ottawa	5.5	-6.0	2.3	3.6	-8.7	1.0
Loose Ottawa	6.0	-7.7	3.2	2.4	-16.9	1.1
Dense Toyoura	3.9	-17.2	-0.3	8.6	-39.2	4.4
Loose Toyoura	7.1	-23.1	1.9	4.8	-17.8	1.3

2.2.3 Shear Strength

Reports of aging effects on the static shear strength of granular soils are rare. Al-Sanad and Ismael (1996) examined the time-dependent strength gain of sand using direct shear tests. They used a fine to medium well graded silty sand, formed mainly by quartz, with calcium carbonates, calcium magnesium carbonates, and gypsum representing approximately 20% of the total composition. Samples were prepared at a relative density of 60%, and allowed to age for up to 6 months under a very low vertical stress (2 kPa) at 25ºC. The normal stress used during the direct shear tests ranged from 40 to 120 kPa. Results from these tests are shown in Fig. 2-11. The results show an increase in the shear strength of the sand with time during aging. The angle of internal friction (ϕ) increased from 36º to 38.7º in 6 months, which is equivalent to an increase of about 10% in the value of $\tan(\phi)$. These results contrast with those obtained by Daramola (1980), who found no discernible change in shear strength on samples of Ham River sand isotropically consolidated under 400 kPa for up to 152 days (see Section 2.2.2.2).

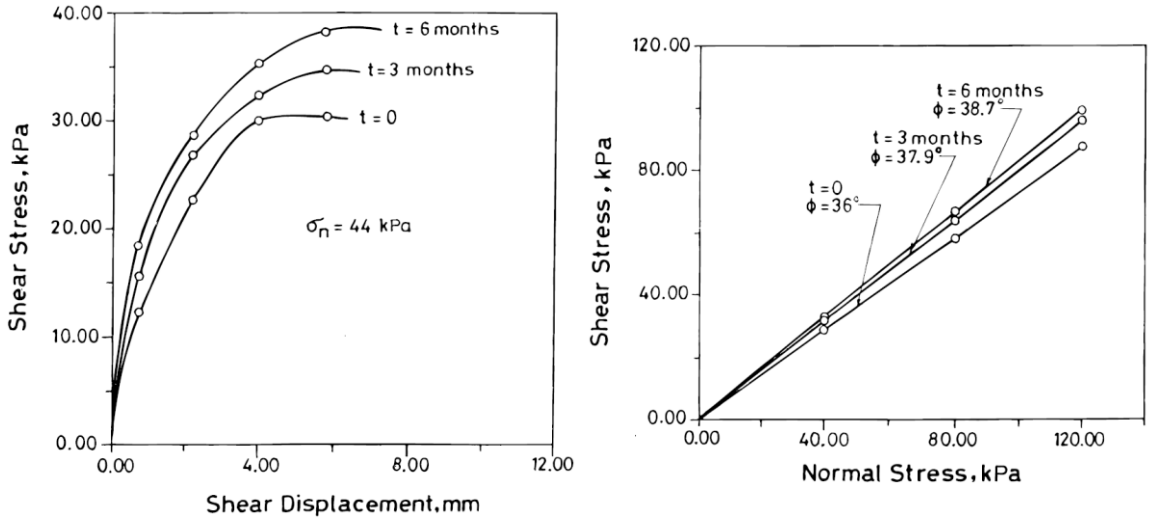

(a) (b)

Fig. 2-11. (a) Shear stress versus displacement and (b) failure envelopes for aged samples of sand (Al-Sanad and Ismael 1996).

2.2.4 Liquefaction Resistance

Most of the studies regarding aging effects on the liquefaction resistance of soils consider changes occurred during time periods orders of magnitude greater than those considered in this study; i.e. thousands of years (*geological times*) rather than a few months to years (*engineering times*). Early reports go back to Seed (1979) (cited by Mitchell, 2008), who presented the data in Fig. 2-12, showing the change in cyclic strength shear modulus with respect to time after deposition. Arango et al. (2000) complemented this data with reports from Skempton (1986) and Kulhawy and Mayne (1990), and historic records of the cyclic shear strength of Miocene-age clayey sands from the Charleston area, in South Carolina. Their results are shown in Fig. 2-13. This figure shows the relationship between the strength gain factor, which represents the gain in cyclic shear strength relative to unaged material, and the age of the deposits.

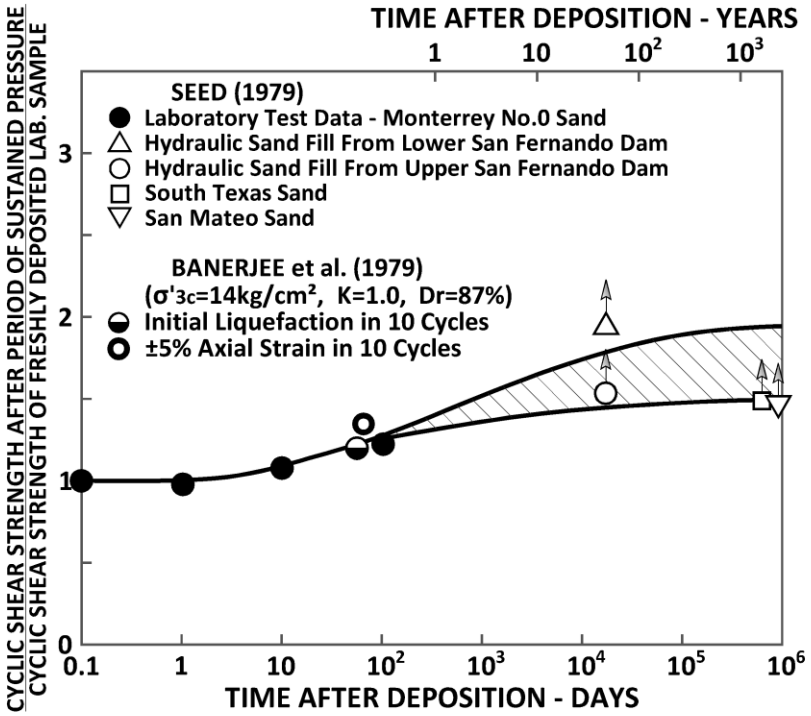

Fig. 2-12. Change in cyclic strength shear modulus with time under confinement (adapted from Seed, 1979, by Mitchell, 2008).

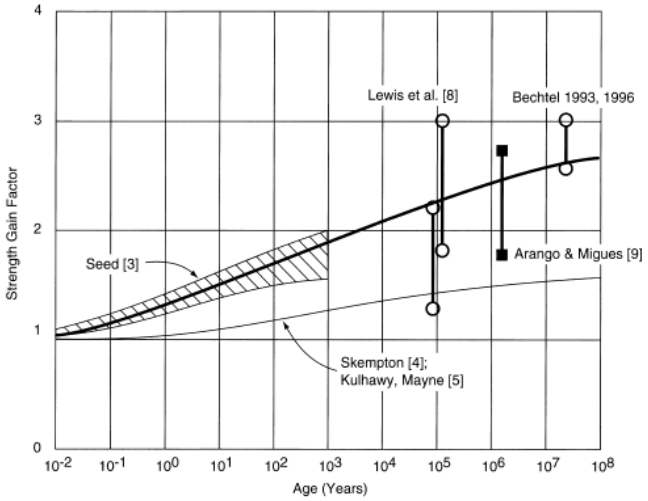

Fig. 2-13. Field cyclic strength of aged sand deposits (Arango et al. 2000).

Leon et al. (2006) studied the effects of aging on the liquefaction resistance of old (older than Holocene) sand deposits. They compared the liquefaction resistance of deposits in the South Carolina Coastal Plain (SCCP) older than 100,000 years, with the empirical correlations commonly used to assess the liquefaction resistance of sand

deposits based on in-situ indices; i.e., $(N_1)_{60}$, q_c, or V_s. Their results indicated that sand deposits in SCCP had 60% more resistance to liquefaction than indicated by the existing liquefaction resistance correlations, which are regularly derived from young Holocene sand deposits.

Recently, Andrus et al. (2009) and Hayati and Andrus (2009) studied the effects of aging on the liquefaction resistance of sands using correlations based on data collected from over 30 sites. They found that the cyclic resistance ratio (CRR) of sands increases by a factor of about 0.12 per log-cycle of time in reference to values measured after 2 days of age. This factor increases to about 0.13 if a reference time of 23 years is used.

2.2.5 Pile Setup

Changes with time in the pile capacity of driven and jacked piles have been reported by numerous investigators (Chow et al. 1998; Jardine et al. 2006; Bowman and Soga 2005). A dataset of the variations in shaft (Q_s) and total (Q_t) pile capacity collected by Chow et al. (1998) is shown in Fig. 2-14. The dataset shows significant variability in reported changes of pile capacity over time. Nonetheless, similar changes in the magnitudes of Q_s and Q_t seem to indicate that most of the increase in pile capacity is caused by a corresponding increase in shaft capacity. Data reported by Chow et al. (1998) shows an increase in pile capacity of around 50% per logarithmic cycle of time.

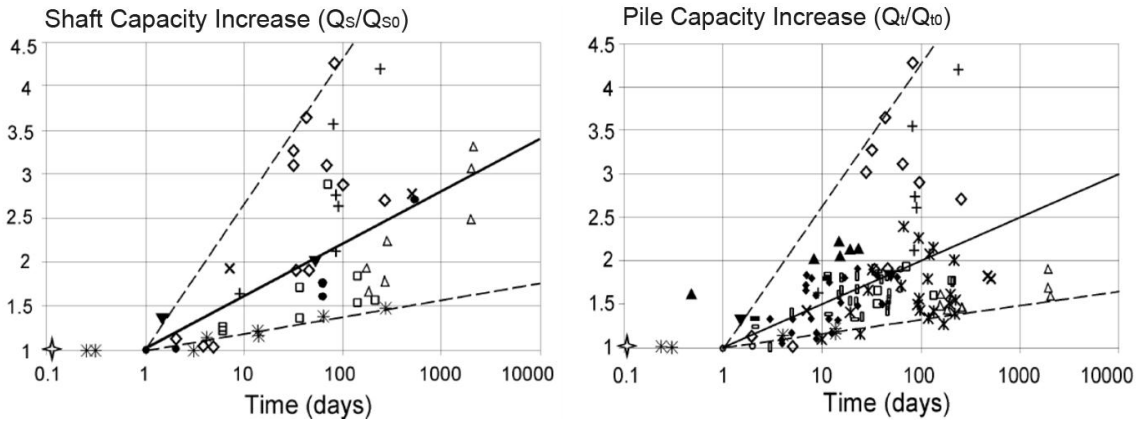

(a) (b)

Fig. 2-14. Increase in shaft (a) and total (b) pile capacity with time (Chow et al. 1998).

Interesting behaviors have been evidenced during the aging process of driven and jacked piles. Jardine et al. (2006) studied the changes in pile capacity of steel pipe piles driven on dense sand at Dunkirk, France. They observed that aged piles showed a brittle response after failure, where retests performed soon after unloading from previous tests failed to achieve the same capacities. This brittle behavior agrees with observations by Howie et al. (2002) and Wang and Tsui (2009), which indicate a rapid decay in the effects of aging when the soil is subjected to high strains. According to Bowman and Soga (2005), pile setup has been reported in strong silica sand but not in weak calcareous sand, which appears to indicate the particle strength can significantly affect the effects of aging in granular soils.

2.3 Driving Mechanism

Several hypotheses have been proposed to explain the occurrence of aging in granular soils. These include: (1) chemical processes involving cementation due to the dissolutions and precipitation of silica and other materials at the particle contacts, (2) micro-biological activity, (3) mechanical processes including particle rearrangement and

internal stress redistribution in the soil structure, and (4) a combination of the above. Mitchell (2008) did a state-of-the-art review of aging in granular soils, which provides a comprehensive summary of some of the main findings in this area. Some of the main characteristics of aging in sands include:

- Natural deposits may exhibit sensitivity, observed as a loss in strength immediately following a disturbance, even if the soil has been densified by the disturbance. The strength of the soil often recovers during the following weeks to months.
- Excess pore water pressure is dissipated rapidly after the disturbance and does not play an important role in the aging process.
- Aging has been reported to affect the magnitude of penetration resistance, small strain shear modulus and stiffness, shear strength, liquefaction resistance, and pile capacity (driven piles). The magnitude and the rate of these changes have great variability.
- Aging has been reported for dry and saturated conditions, with the effects being greater for saturated soils.
- Ground surface settlements during aging are very small and often undetectable.
- In some cases the penetration resistance of sand has not been observed to change with time after densification.
- The increase in the pile capacity of driven piles reported during aging is caused primarily by a corresponding increase in shaft capacity, with little variations in tip resistance.

The author considers that the driving mechanism of aging should be compatible with the following behaviors, in addition to those previously mentioned:

- The rate of change in soil properties during aging increases with increasing magnitudes of stress level (SL) acting during aging.
- The aging effects on the sand disappear or are significantly diminished under high strains.

Some of the hypotheses proposed to explain the occurrence of aging in granular materials are summarized next.

2.3.1 Chemical Processes

The changes in the penetration resistance of deposits of alluvial uniform clean sand observed during aging after explosive compaction and vibrocompaction at the Jebba Dam project in Nigeria, led Mitchell and Solymar (1984) to propose that the rupture and subsequent reconstruction of cementing bonds formed due to precipitation of silica gel at the particle contacts was the main driving mechanism of aging. This theory would help to explain the occurrence of *sensitivity*, as the sudden and disturbance produced during blasting would immediately destroy the cementing bonds found in the natural deposit.

The hypothesis proposed by Mitchell and Solymar (1984) was supported by reports from other investigators, such as Denisov and Reltov (1961) (cited by Mitchell and Solymar, 1984). Denisov and Reltov (1961) found that the force required to dislodge a grain of quartz sand from a quartz plate on which it rests, increases with the time of contact between particle and plate. A schematic view of the vibrating plate experiment used to measure the change in the plate-particle adhesion force over time is shown in Fig. 2-15, along with some of their results. According to their finding, for a test in air, the

force required to separate particle and plate doubled over the first 20 hours after the particle was placed on the plate. If, after that period, the two elements were submerged in water for 14 days, the force increased by a factor of about 3 (see Fig. 2-15).

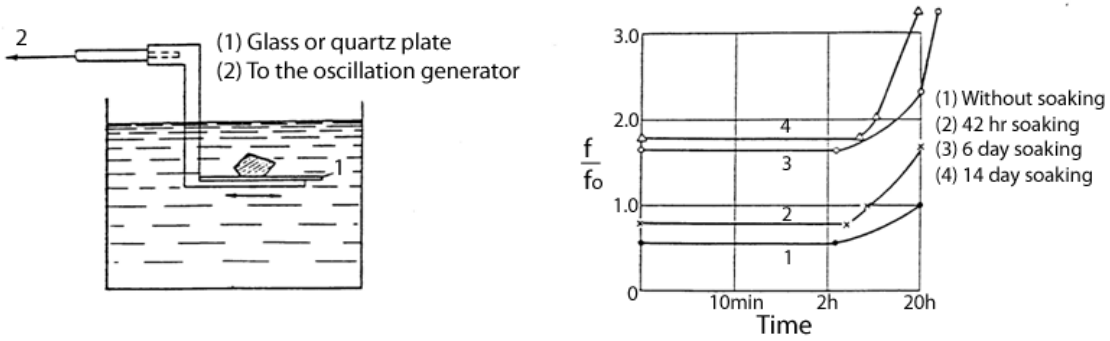

Fig. 2-15. (a) Schematic view of the vibrating plate experiments run by Denisov and Reltov (1961) and (b) results showing the change with time in adhesive force (f) between the particle and the plate (Denisov and Reltov 1961).

Denisov and Reltov (1961) proposed that this behavior was likely caused by the disruption of the silicate particle surface, due to hydrolysis, forming silica gel which adhered in thin layers to the surface of the particle, producing cementation derived from crystal overgrowth caused by pressure solution and the compressive stresses. According to Mitchell (2008), a possible problem with this hypothesis arises from the fact that pressure dissolution is unlikely in the conditions encountered for cases where aging has been commonly reported; e.g., temperatures from 0ºC to 30ºC and effective stresses less than 200 kPa.

Particle cementation due to precipitation of silica and other materials at the particle contacts was reported by Joshi, el al. (1995). Their laboratory tests, described in Section 2.2.1.2, showed that the rate of increase in penetration resistance was greater for samples of sand submerged in simulated sea water than for samples submerged in distilled water or dry samples (in that order). Scanning electron micrographs of sand samples submerged in both distilled and sea water, detected the formation of cementing

bonds at the grain contacts and interspaces. Larger quantities of precipitates were found in sands submerged in sea water. The chemical analysis of the precipitates using a Kevex Micro X-700 energy dispersive x-ray analyzer showed that the precipitates were formed by calcium and possibly silica in samples of river sand in distilled water, and sodium, silica, calcium, and chlorine in samples of river sand in sea water.

Baxter and Mitchell (2004) did mineralogical studies of the sand and pore fluid before and after aging on the tests described in Section 2.2.2.2. Results from inductively coupled plasma analyses of the pore fluid indicated significant dissolution of calcium and silica during aging, with larger amounts of ions in solution detected for the Evanston Beach sand, which contained dolomite. The largest increase in dissolved Ca^{2+} and HCO^{-} was observed in samples of Evanston Beach sand submerged in CO_2 saturated water. However, the analysis did not show a corresponding increase in in the concentration of dissolved silica for these samples. The concentration of SiO_2 in solution after aging ranged from 12 to 25 ppm for samples aged at 25ºC, and from 24 to 34 ppm for samples aged at 40ºC. Considering that the solubility of SiO_2 at 25ºC is 11 ppm and at 40ºC is 16 ppm (Rimstidt 1997) (cited by Baxter and Mitchell, 2004), precipitation of silica would have been expected. However, scanning electron micrographs of aged samples did not detect any precipitates.

Predicted variations in the dissolution rates of quartz with respect to pH and NaCl concentration is shown in Fig. 2-16 (Dove and Elston 1992). According to Dove and Elston (1992), the dissolution rates of quartz at 25ºC range from 10^{-13} mol m^{-2} s^{-1} at pH 2 in 0.0001 m NaCl, to 10^{-10} mol m^{-2} s^{-1} at pH 13 in 0.2 m NaCl. Mitchell (2008) used the upper bound limit (10^{-10} mol m^{-2} s^{-1}), and estimated that quartz dissolution in a fine sand

under ideal conditions (high pH and ionic content in pore fluid), would be in the order of $5 \cdot 10^{-5}$ kg per kg of sand per year. This led Mitchell (2008) to conclude that, even if this material precipitated immediately at the particle contacts, it was unlikely that it could produce enough cementation to account for a significant strength gain during *engineering times* (months to years after a disturbance).

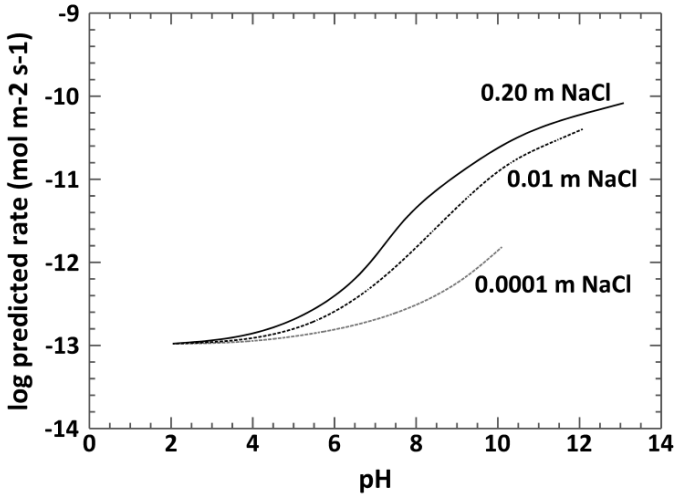

Fig. 2-16. Predicted dissolution rates of quartz at 25ºC as a function of pH (redrawn from Dove and Elston, 1992).

Cementation due to precipitation of materials such as AlOOH, $Al(OH)_3$, FeOOH, $Fe(OH)_3$, and aluminum silicates could account for increases in the strength of the soil during aging. However, this type of cementation is mostly a characteristic of evaporite deposits, where cyclic periods of wetting and drying and high concentrations of alumina and/or iron facilitate the formation and precipitation of such materials. Deposition of calcium carbonates forming cementing bonds, as observed by Joshi et al. (1995), are perhaps more common, but would not be strong enough to account for the changes in soil properties observed during aging.

Mesri (1990) considered that hypotheses involving chemical cementation, where the particles are assumed to remain stationary so that cementing bonds are formed at their

contacts, would preclude the existence of uncemented sand deposits. In addition, this theory fails to explain the occurrence of aging in dry environments, as has been reported by Dowding and Hryciw (1986), Joshi et al. (1995), and Baxter and Mitchell (2004).

2.3.2 Micro-biological Processes

Micro-biological activity can have a significant effect on properties of the soil, including changes to its strength and deformability. Stocks-Fischer et al. (1999) found that treatments with *Bacillus pasteurii*, an alkalophilic microorganism commonly found in nature, increased significantly the rates of precipitation of calcite in the soil. DeJong et al. (2006) studied the effects of microbial induced calcite cementation with *Bacillus pasteurii* on the properties of sands. Triaxial tests on loose (D_r=35%) and dense (D_r=70%) samples of Ottawa 50-70 sand (d_{50}=0.12 mm, C_u=1.6) treated with this bacteria showed significant increases over time in axial capacity under monotonic shearing conditions. The treated specimens showed increased initial shear stiffness and higher elastic capacity. The value of shear wave velocity (V_s) measured using bender elements also evidenced a significant increase over time. The rates of variation of V_s were similar to those observed for samples of sand artificially cemented using gypsum. The rates of change in the magnitude of V_s were low during the initial stages of the test, increased gradually towards mid-test, and later decreased approaching zero. The results obtained from treating the samples with bacteria were highly dependent on the pH, oxygen supply, metabolic status, concentration of microbes, and availability of nutrients.

It is widely recognized that microbial activity can result in significant changes in the properties of granular soils over time (Stocks-Fischer et al. 1999; DeJong et al. 2006; Mitchell and Santamarina 2005). Nevertheless, multiple conditions are required in order

for these changes to be relevant for engineering purposes. These include the presence of large amounts of bacteria in an adequate environment with the appropriate acidity conditions, and constant access to abundant nutrients and energy. As these conditions are not necessarily found in the environments where aging has been reported, it is unlikely that micro-biological activity alone could account for the reported changes in the engineering properties during aging.

2.3.3 Mechanical Processes

Following the initial hypotheses that attributed the changes in soil properties during aging to chemical processes involving particle cementation, Mesri et al. (1990) and Schmertmann (1991) proposed an alternative explanation involving grain slippage and increased particle interlocking as the main driving mechanism of aging.

Mesri et al. (1990) studied reported changes in the shear modulus and penetrations resistance of soils, and related these changes to the time-dependent rearrangement of particles, which results in macro-interlocking of sand grains and micro-interlocking of grain surface roughness. Based on the study of previous reports on aging and new tests conducted to evaluate the behavior during compression of saturated poorly graded fine silica sand (Lake Michigan sand), Mesri et al. (1990) concluded that the variations in the properties of granular soils reported during aging cannot be explained solely by the densification occurred during secondary compression, as its magnitude is too small to account for such changes. They proposed the relationship shown in Eq. 3 to estimate the cone penetration resistance at a time t (q_t), based on its value at a reference time t_R ($(q_c)_R$), the compression index (C_C), the secondary compression index (C_α), and the densification in excess of the compression under static loading, represented by the

parameter C_D. The value of C_D ranges between 3 and 20 and depend on the type of densification used.

$$\frac{q_c}{(q_c)_R} = \left(\frac{t}{t_R}\right)^{\frac{C_D C_\alpha}{C_C}} \tag{3}$$

Schmertmann (1964) (cited by Schmertmann, 1991) developed a modified triaxial test, named the IDS test, which allows to determine the contributions from the frictional strength, referred as tan(ϕ''), and from the curvature effects, cementation and cohesion (referred as *c*''), to the total mobilized shear strength. Results from IDS tests on samples of extruded kaolinite are shown in Fig. 2-17. Schmertmann (1991) found that the effect of aging on the stress-strain characteristic of kaolinite was primarily the result of an increase in the mobilized friction with time during aging. Fig. 2-17 shows that, for the case of kaolinite, the cohesive component (*c*'') remains the same or even decreases as a result of aging, while the friction component (tan ϕ'') increases significantly over time.

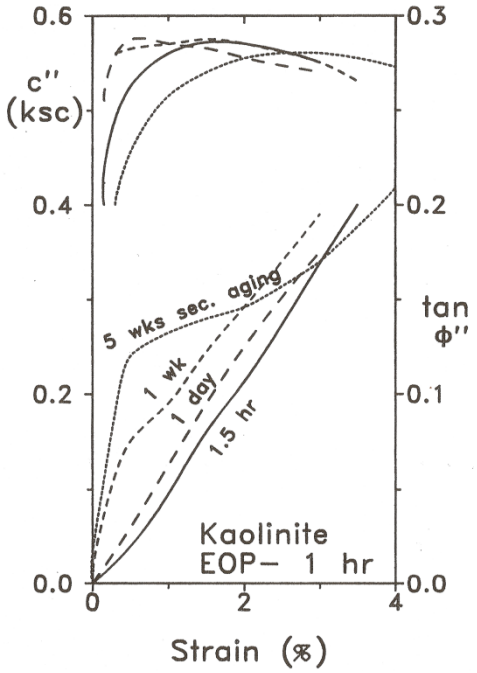

Fig. 2-17. Comparative IDS-tests *c*'' and tan(ϕ'') component after aging for up to 5 weeks (Schmertmann 1991).

Schmertmann (1991) proposed that the changes in the properties of soils during aging were primarily caused by particle slippage driven by the in-situ effective stresses, resulting in increased particle interlocking and changes in the internal stress distribution.

According to the driving mechanism proposed by Mesri et al. (1990) and Schmertmann (1991), aging would result in increases in the macroscopic frictional resistance and the resistance to deformation. In addition, grain interlocking would increase the tendency of the soil towards volumetric dilation during shear. Changes in the volumetric strain characteristics of sands after aging were reported by Daramola (1980). Details of his investigation were described in Section 2.2.2. Daramola (1980) found that longer periods of aging resulted in a greater tendency towards volumetric dilation. Changes in the volumetric strain during shear of samples of Ham River sand aged up to 152 days under an isotropic stress of 400 kPa are shown in Fig. 2-18.

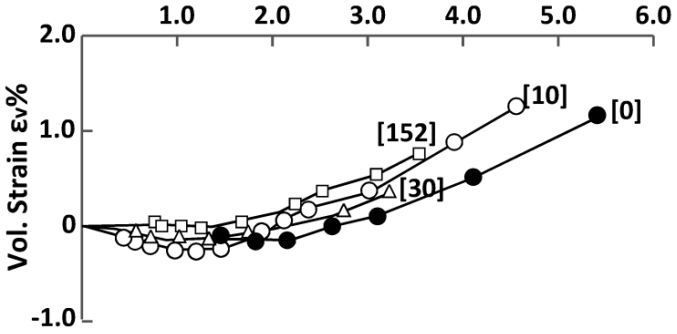

Fig. 2-18. Effect of age of consolidation on the volumetric strain-axial strain characteristics of Ham River sand (redrawn from Daramola, 1980).

Bowman and Soga (2003) studied the changes in the soil fabric of dense (Dr≈74%) samples of Leighton Buzzard sand (d_{10}=0.120 mm, d_{50}=0.148 mm) under one-dimensional compression. Samples of sand were loaded for up to 4 months under a vertical stress of 500 kPa. Changes in the soil fabric were evaluated using optical micro-structural analysis of cross-sections of the samples obtained using resin impregnation.

Based on the image processing of the cross-sections obtained, Bowman and Soga (2003) observed that, once the load was applied, the particles tried to align with their long-axes more perpendicular to the applied load. However, as time passed, the particles started rotating away from this initial orientation. In addition, the particles, which were initially uniformly distributed in space, started forming clusters as aging progressed. These observation led Bowman and Soga (2003) to propose that aging in granular materials is driven by the buckling of strong load chains in the soil structure, producing zones of greater interlock. This ultimately results in a soil structure formed by areas of relatively large voids besides areas of tightly packed particles, which have a greater resistance to load application.

Chow et al. (1998) analyzed previous case studies and new static and dynamic load tests on open-ended small diameter (0.324 m) intensively instrumented piles. They suggested that the time-dependent gain in pile capacity commonly observed in driven piles is caused by an increase in radial stress due to the breakdown during creep of arching stresses formed during pile driving, which limit the radial stress acting on the pile after installation. This aging mechanism is compatible with findings which show that the increase in the pile capacity overtime is mostly the result of increases in the magnitude of shaft capacity, with little changes in tip resistance (Chow et al. 1998). A similar mechanism was proposed by Bowman and Soga (2005), where the increase in shaft capacity in driven piles is caused by the time-dependent increase in the horizontal stress due to creep on the surrounding sand under the high stress ratios imposed by the installation of the pile. During creep, the sand grains rearrange to redistribute the loads, and the soil tends to show a more dilative behavior. As the pile imposes a kinematic

restraint, this tendency towards volumetric expansion is translated into a time-dependent increase in the radial stresses acting on the pile.

More recently, Lade et al. (2010) have suggested an alternative hypothesis, which links aging in granular soils with grain crushing occurring over time. According to Lade et al. (2010), the strength of sand particles is strongly dependent on time, where sand grains subjected to a constant stress over long periods of time may fail under a load significantly lower than its ultimate short-term strength, a behavior they called *static fatigue*. This delayed grain fracturing causes changes in the stress distribution of the soil fabric, which ultimately produce the changes in macroscopic properties observed during aging. Lade et al. (2010) explains this behavior using Fig. 2-19, which illustrates the effect of particle crushing on the internal stress distribution of a granular assembly. This figure shows that if a particle breaks during a creep tests (as shown in Fig. 2-19 (c)), the particle structure reaccommodates to support the vertical stress, thus resulting in changes in the internal load distribution and a small vertical deformation. During a stress relaxation test, where vertical deformation is not permitted, particle breakage causes a reduction in the capacity of the assembly to support load, thus resulting in a decrease in the vertical stress. Even though grain crushing may play a significant role in the time-dependent behavior of sands under high stresses, this hypothesis does not fully explain the occurrence of aging that have reported under low confinement stresses, where particle crushing effects are not expected; e.g., Dowding and Hryciw (1986) (σ_v'<20 kPa), Wang and Tsui (2009) (σ_{3con}=35 kPa).

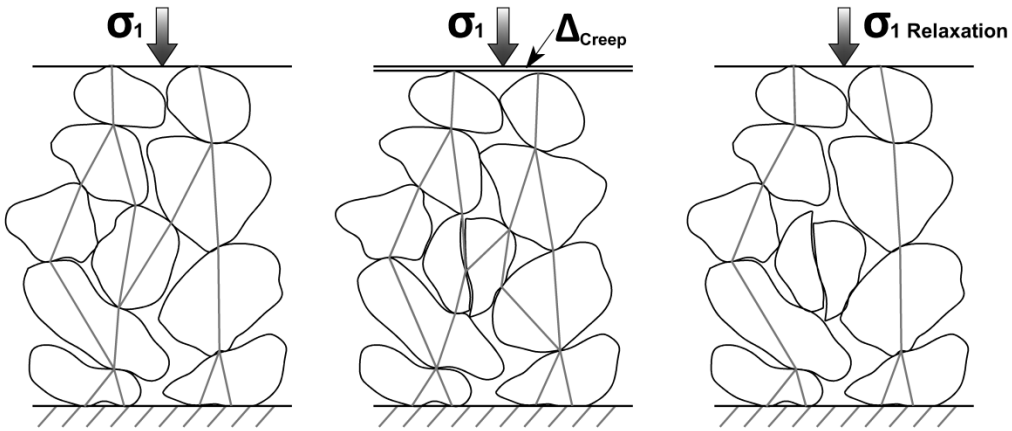

Fig. 2-19. (a) Initial force chains in particle structure and effects of particle breakage on (b) creep tests and (c) stress relaxation tests (redrawn from Lade et al., 2010).

2.4 Rate and Magnitude of Change in Soil Properties during Aging

Section 2.2 discussed numerous examples on the effects of aging in the engineering properties of granular soils, including the penetration resistance, small strain modulus and stiffness, shear strength, liquefaction resistance, and pile setup. The following section studies the magnitude of these changes, comparing results reported by different investigators, and providing available relationships used for their estimation.

A summary of the rate and magnitude of change in properties of sand during aging from numerous sources is shown in Table 2-6, which includes the corresponding references, predictive equations, and a brief explanation for each case. Reported and measured changes in engineering properties of sands during aging are also shown in Fig. 2-20. Aging effects shown in Fig. 2-20 are normalized with respect to their corresponding magnitude measured just after deposition or densification. Fig. 2-20 shows that properties such as the pile capacity of driven piles (as reported by Chow et al., 1998) or the

penetration resistance (as reported by Joshi at al., 1995), may as much as double during the first year after deposition or densification. The figure also shows that there is significant variation among values reported from different authors, although many of them correspond to magnitudes of different soil properties. To account for this factor, data from Fig. 2-20 was separated according to the property represented, and was used to develop Fig. 2-21 to Fig. 2-25.

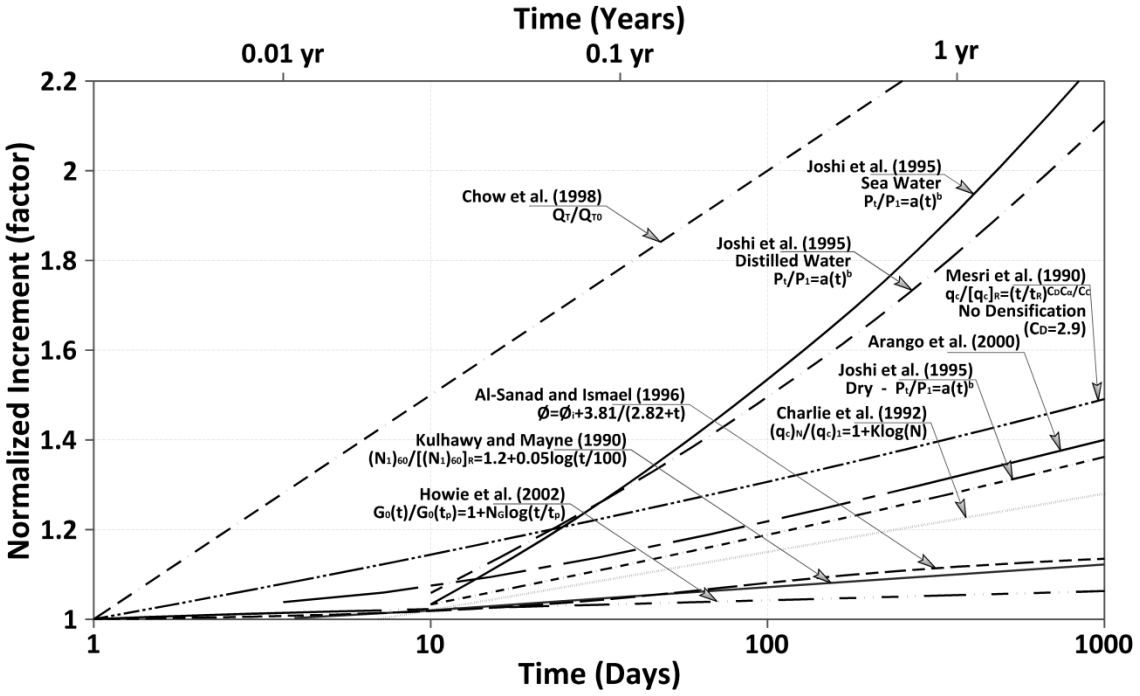

Fig. 2-20. Measured and predicted rates of change in engineering properties of granular soils during aging.

Fig. 2-21 shows the reported variations in the shear modulus of granular materials during aging. Greater increases were reported by Jamiolkowski and Manassero (1995), who found values of N_G ranging from 1.1% to 12%, with the upper limit corresponding to carbonate sands. Jamiolkowski and Manassero (1995) reported values of N_G for clean silica sand ranging between 1.1% and 3.5%. Values of N_G from Human (1992), Baxter and Mitchell (2004), and Howie at al. (2002), are also in that same range.

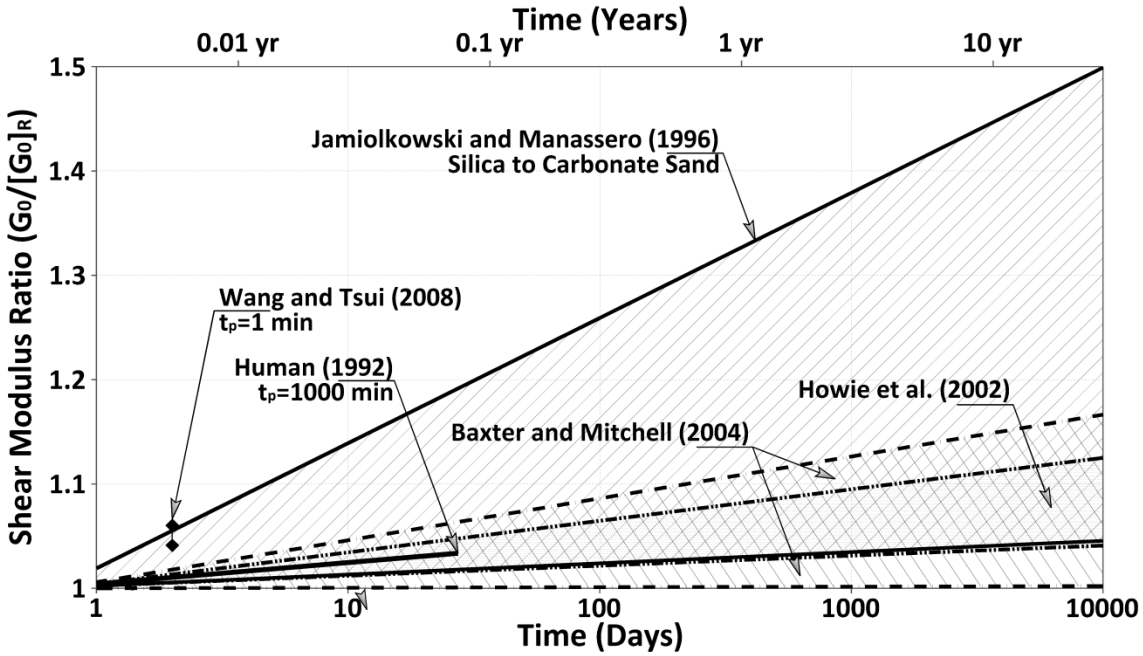

Fig. 2-21. Change in the shear modulus of sand with respect to time during aging.

Results from cone penetration tests have provided the majority of the data that show the beneficial effect of aging in granular soils. Some examples are included in Fig. 2-22, along with predicted values, such as those obtained by using Eq. 3 (Mesri et al. 1990). Significant variability can be observed in the data from Fig. 2-22. This variability could be related to factors such as the type of pore fluid, as shown by results from Joshi et al. (1995) for samples of sand aged in air, distilled water, and sea water, or the type of disturbance previous to aging; e.g., explosive compaction, vibrocompaction, deposition.

Table 2-6. Information on rate and magnitude of change in aging effects on sand properties (Mitchell 2008).

Property	Reference	Type of Data	Predictive Equation	Comments
Initial Shear Modulus (G)	Anderson and Stokoe, 1978; Mesri et al., 1990; Jamiolkowski and Manassero, 1995	Resonant Column	$G_t = G_{1000}\left(1 + N_G \log\left(\frac{t}{t_{1000}}\right)\right)$	N_G often ranges from 0 to 5%
	Human 1992	Laboratory triaxial tests		G is calculated based on V_s measured using bender elements
	Troncoso and Garces, 2000	Downhole shear wave velocity	$G_n = 117.24 \cdot t^{0.67}$	Detail are shown in Fig. 2-8
	Howie et al., 2002	Triaxial tests after consol. at different stress ratios		G is calculated based on E measured at low strains
	Baxter and Mitchell, 2004	Aging in fixed ring consolidometer		G is calculated based on V_s measured using bender elements
CPT Resistance (q_c)	Dumas and Beaton, 1986	Field CPT		Data for only one value of time
	Mesri et al., 1990	Laboratory compression tests. Analysis of data from other investigators	$\frac{q_c}{(q_c)_R} = \left(\frac{t}{t_R}\right)^{C_D C_\alpha / C_C}$	See Section 2.3.3 for details
	Schmertmann, 1991	CPT tests following DDC		q_c/q_{c0} calculated based on the data from Fig. 2-4
	Charlie et al., 1992	Field data from several sources	$\frac{(q_c)_N}{(q_c)_1} = 1 + K \cdot \log(N)$	N is the time in weeks, and K ranges from 0 to 1 and depends on the soil type, densification method, and temperature
	Joshi et al., 1995	Small diameter penetrometer in laboratory samples	$P_t / P_1 = a(t)^b$	Equation used to fit data from laboratory tests
SPT Resistance (N)	Kulhawy and Mayne, 1990	Laboratory tests and field data from several sources	$(N_1)_{60} = D_r^2 C_A C_P C_{OCR}$ $C_A = 1.2 + 0.05\log(t/100)$	C_p=60+25log(d_{50}), C_{OCR}=$(OCR)^{0.18}$ t is the time in years. d_{50} in mm
	Al-Sanad and Ismael, 1996	SPT test on calcareous sand		
Static Shear Strength	Al-Sanad and Ismael, 1996	Direct shear tests	$\phi = \phi_i + 3.81 \cdot t/(2.82 + t)$	t is the time in months
Cyclic Shear Strength	Seed, 1979	Cyclic loading after different periods of confinement		From Fig. 2-12
	Arango et al., 2000	Cyclic loading on samples of clayey sand		Complemented data from Seed (1979). From Fig. 2-13
Pile Capacity	Chow et al., 1998	Pile load tests	Linear increase of 50% per log-cycle of time	

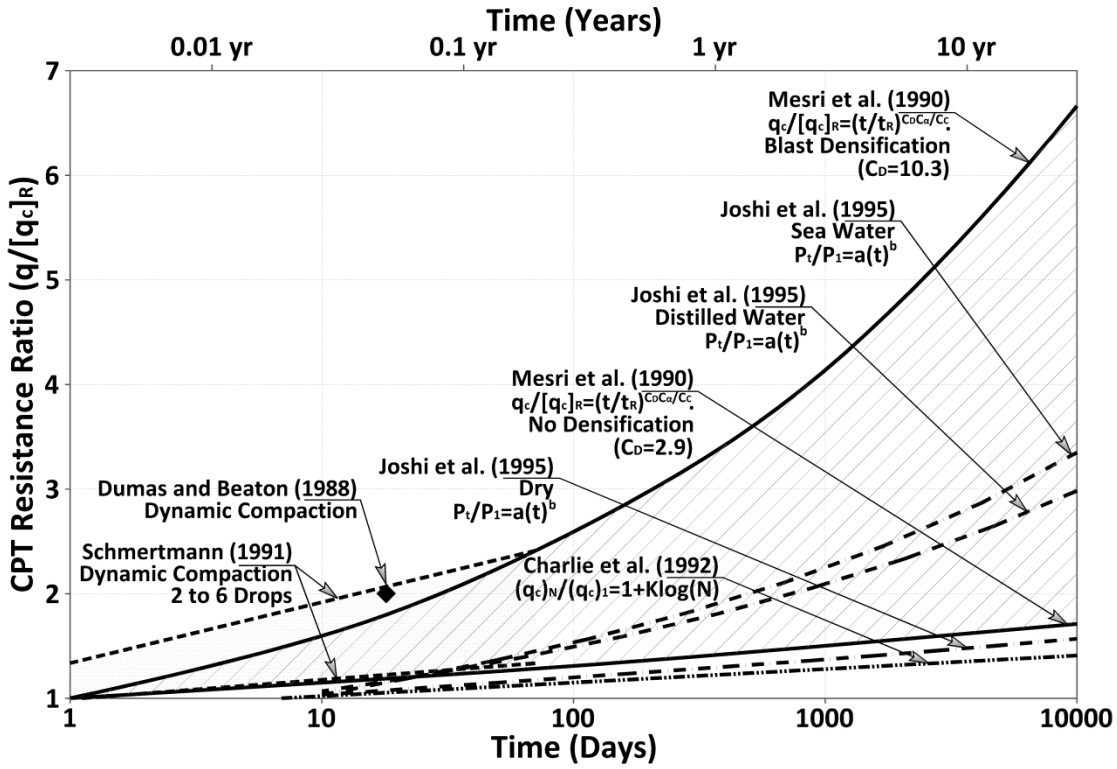

Fig. 2-22. Change in CPT resistance of sand with respect to time during aging.

Estimations made using the equation developed by Mesri at al. (1990), show that the rate of change in penetration resistance can be significantly affected by the type of disturbance, which affects potential for particle rearrangement and stress redistribution during aging, and is represented by the parameter C_D in Eq. 3. Fig. 2-22 shows that this parameter, that according to Mesri et al. (1990) can range from about 3 for no densification previous to aging, to around 10 for blast densification, has a significant effect on the estimated changes in penetration resistance. However, for their investigation, Mesri et al. (1990) back calculated the magnitude of C_D using data from previous case studies. Methods to predict the value of C_D *a priori* do not appear to be available.

Another factor which may affect the rate of change in soil properties during aging is the temperature. Charlie et al. (1992) suggested that the rate of change in cone

penetration resistance, expressed by the parameter K in Eq. 4, where N is the time of aging in weeks, and $(q_c)_1$ is the CPT resistance at a reference time of 1 week, increases for higher temperature. Jefferies and Rogers (1993) provided a correction to the data reported by Charlie et al. (1992). The revised data, along with a possible trend suggested by Jefferies and Rogers (1993) is shown in Fig. 2-23. Even though these examples would suggest that the temperature has an effect on the rate of change in the engineering properties of sands during aging, more data is needed to arrive to a conclusive result. The possibly of temperature affecting the aging effects on granular materials will be analyzed in following sections of this dissertation.

$$\frac{(q_c)_N}{(q_c)_1} = 1 + K\log(N) \tag{4}$$

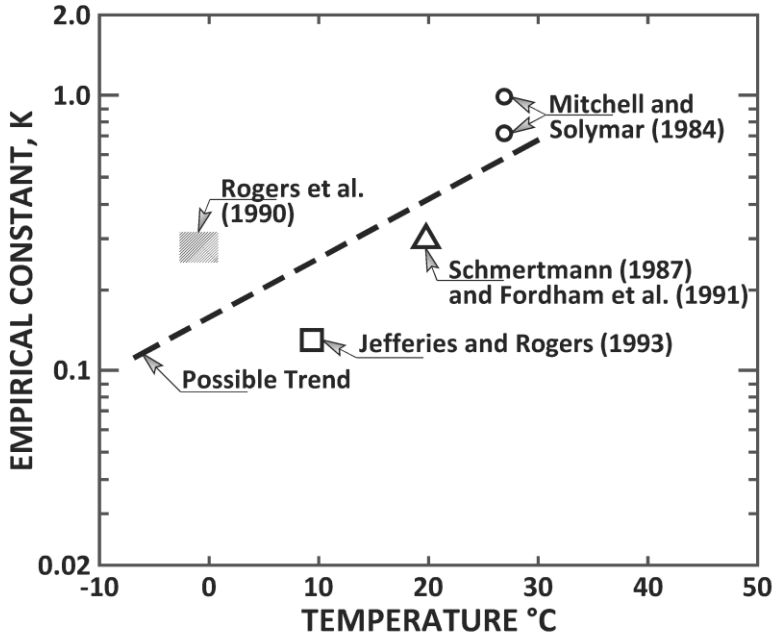

Fig. 2-23. Revised rate of increase of normalized tip resistance (K) versus temperature (redrawn from Jefferies and Rogers, 1993).

Only limited information is available on changes in the magnitude of SPT resistance with time during aging. Data shown in Fig. 2-24 comes from reports by Al-

Sanad and Ismael (1996), and Kulhawy and Mayne (1990). As mentioned by Mitchell (2008), data from Al-Sanad and Ismael (1996) were measured from deposits of carbonate sand which can show greater increases in penetration resistance than silica sand, while data from Kulhawy and Mayne (1990) come from a broad approximation based on scattered data corresponding to times of aging significantly greater (>50 years) than those considered in this study.

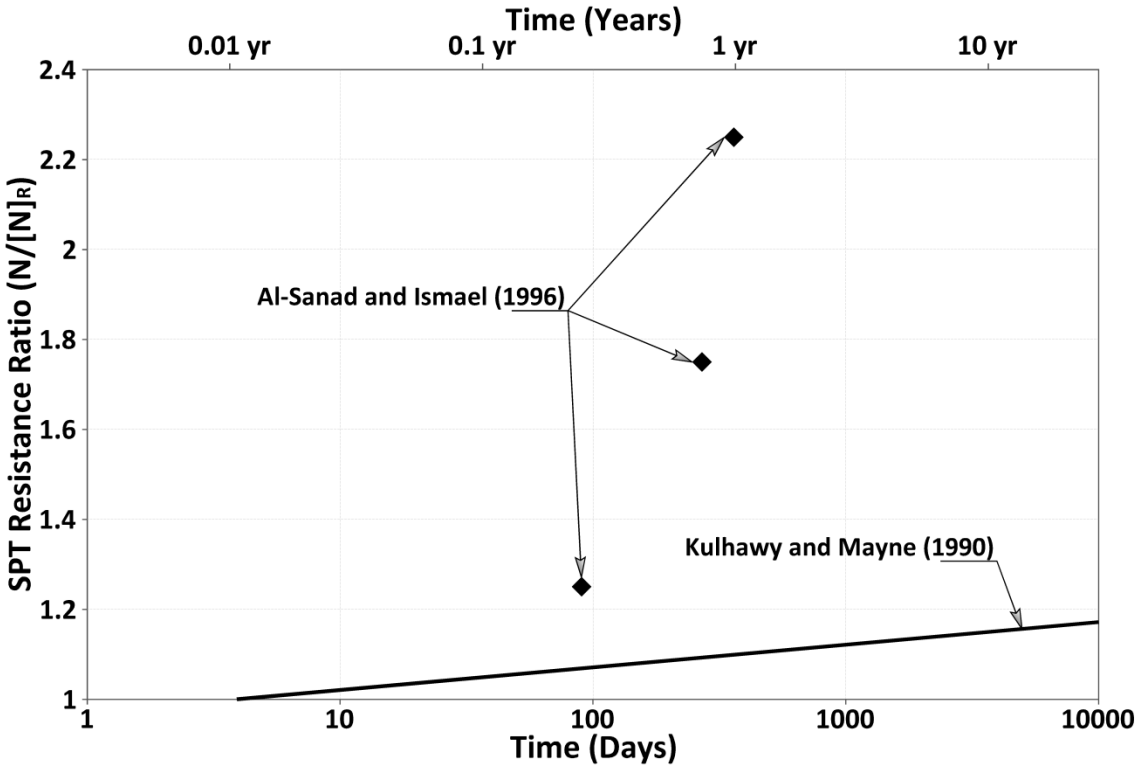

Fig. 2-24. Change in SPT resistance of sand with respect to time during aging.

Changes in the static and cyclic strength of sands are shown in Fig. 2-25. Only data reported by Al-Sanad and Ismael (1996) have shown an increase in the static resistance of samples of sand. These data disagree with findings from other investigators, such as Daramola (1980), who found no conclusive change in the shear strength of samples of Han River sand aged up to 152 days, despite the fact that a significant increase in stiffness was observed. Changes in the ultimate strength of sands during aging

are not often expected, as it corresponds to an end-point soil property measured at high strains. Data from numerous investigators, e.g., Wang and Tsui (2009) and Howie et al. (2002), have shown that aging effects are significantly diminished or can be completely eliminated as the sand is deformed. This may be due to remolding occurring during shear, which alters the aged structure of the soil, thus eliminating its effects on the macroscopic properties. As the static shear strength is measured at high strain, while the cyclic shear strains is measured using consecutive small strain cycles, one would expect that aging would significantly affect the magnitude of the latter while having little to no effect on the former.

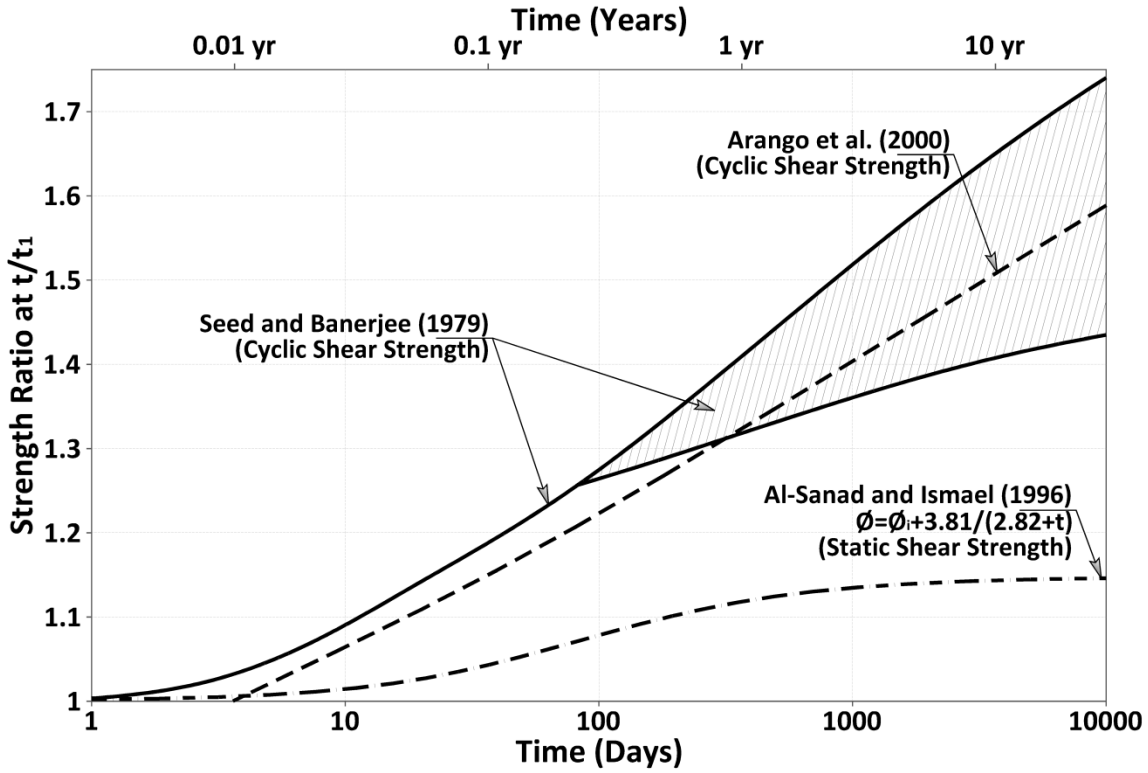

Fig. 2-25. Change in cyclic and static strength of sand with respect to time during aging.

2.5 Conclusions

Changes in the engineering properties of granular soil following deposition of densification have been reported for over 30 years. These changes are generally beneficial and occur with little to no change in void ratio. Examples of aging effects on the properties of granular materials reported by numerous investigators have been presented in this section. Different hypothesis formulated to explain how and why aging occurs in sands have been discussed. Some of the main conclusions are:

- Aging can produce changes in the magnitude of soil properties such as the SPT and CPT penetration resistance, small strain shear modulus, shear strength, liquefaction resistance, and pile capacity of driven and jacked piles. These changes cannot be explained solely by the densification occurring during secondary compression.
- Aging is likely caused by small particle movements and rotations occurring with time under the new in-situ stress conditions following deposition or densification. Rearrangement during aging produce increased macro-interlocking of particles, resulting in the formation of a stiffer and more resistant soil fabric.
- Soil sensitivity, represented by a decrease in the penetration resistance of granular soils immediately following disturbance and/or densification, has been evidenced when blast densification is used. The decrease in penetration resistance can be related to the destruction of the aged structure of the soil, which is stiffer and stronger than that of freshly redeposited material. A possible reduction in effective confinement due to loosening and the presence of blast gases could also contribute to the decrease in penetration resistance after explosive compaction.

- Chemical dissolution and precipitation of silica and other materials, such as aluminum oxide hydroxide, aluminum hydroxide, iron oxide hydroxide, iron hydroxide, aluminum silicates, or calcium carbonate, can play an important role during aging, but only under certain and specific conditions; e.g., large concentration of ions in the pore fluid, soil is exposed to cyclic periods of wetting and drying.
- The rate of chemical cementation can be increased significantly by treatment with bacteria such as the Bacillus pasterii. Micro-biological induced cementation is highly dependent on factors including the pH, oxygen supply, metabolic status, the concentration of microbes, and availability of nutrients.
- Engineering properties of granular soils, such as CPT resistance, may as much as double during the first year following densification. The small strain shear modulus of clean silica sand increases about 1% to 3% per log-cycle time. The small strain shear modulus of carbonate sands can increase at rates of up to 13% per log-cycle of time.
- Aging effects are significantly diminished if the material is deformed.
- Changes in soil properties seem to occur more rapidly at higher temperatures.

Significant evidence points towards physical-mechanical processes as the main driving mechanism of aging in sand. This dissertation will study aging as a mechanical processes resulting from interactions between the particles in the soil structure. Factors which influence these processes will be studied and quantified, in an effort to aid in the development of methods for predicting the magnitude and rate of change in the properties of the soil during aging of granular materials.

Chapter 3

Micro-scale Laboratory Experiments

3.1 Introduction

Aging processes in granular soils were studied by conducting an extensive laboratory testing program, including micro- and macro-scale experiments to detect changes in the internal structure and the macroscopic properties of sands during aging. The main purpose of the laboratory testing program was to provide a base for comparison and calibration of DEM models.

Micro-scale laboratory experiments presented in this chapter study changes occurring within granular specimens during creep. Different theories have been postulated to account for aging in granular soils and explain why macroscopic properties of sands change with time after deposition or densification. The most tenable theory relates aging with changes in the internal structure of the soil caused by particle rearrangement over time. Micro-scale laboratory tests conducted during this investigation

intend to detect if soil grains continue moving during creep and aging, and quantify the magnitude of the particle movements and rotations, helping to validate or refute this theory as a feasible driving mechanism for aging. The magnitude of the particle movements and rotations will be compared with values obtained from DEM creep simulations in following chapters.

Changes in micro-scale characteristics of sands during creep and aging were studied by conducting one dimensional compression tests on samples of reconstituted sand. X-ray Computed Tomography (CT) was implemented to study the changes in the internal structure of the granular soils occurring over time. Initially developed for medical purposes, X-ray CT has been implemented in a wide range of industrial applications, including the study of the internal composition of alloys (Latière and Mazerolle 1987), rocks (Raynaud et al. 1989), and granular soils (Desrues et al. 1996).

During this investigation, X-ray CT was used to detect particle movements and rotations in granular samples subjected to constant vertical effective stress and restrained lateral deformation. The main advantage of the X-ray CT is its capability to determine internal characteristics of the specimen without disturbing the sample. This is particularly useful for the analyses conducted in this research, since it allows studying internal changes in specimen over time during aging without affecting the experiment.

X-ray CT uses radiation generated by a micro-focus source which penetrates the sample. A flat panel detector, located opposite to the source, measures X-Ray patterns passing through the specimen. A schematic of the system is shown in Fig. 3-1. The X-ray images acquired, called *views*, are often shown in gray-scale and represent the geometry and composition of the sample.

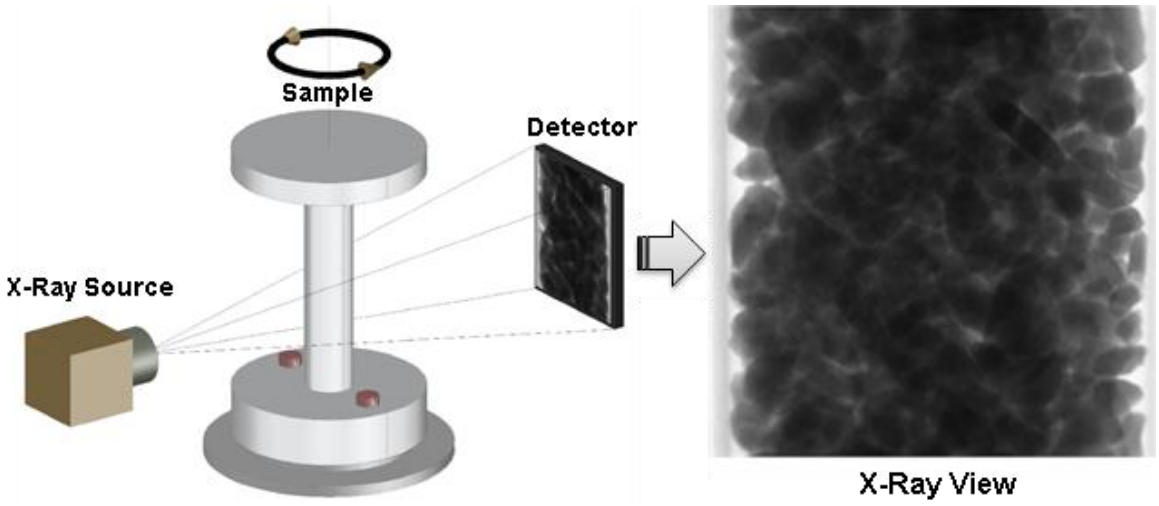

Fig. 3-1. Schematic of an X-ray CT scanner.

It is important to understand the concepts and principles of X-Ray CT before interpreting results from the experiments. A brief description of the theoretical background of X-ray CT is presented next.

3.2 Theoretical Background

3.2.1 Interaction of X-Ray Radiation with Matter

This section introduces a brief description of the interaction of x-rays with the soil while they travel through the specimen. A detailed explanation can be found in Latière and Mazerolle (1987) and Ketcham and Carlson (2001).

When an X-ray photon travels through a sample, it interacts with the atoms of its constitutive materials. Once the X-ray photon encounters the electron cloud covering the nucleus of an atom, it can either be absorbed or scattered. True absorption of X-ray emissions accounts for the greatest part of the X-Ray attenuation (Latière and Mazerolle 1987). During true absorption, energy from the X-ray photon is transformed into the

energy required to break the bond between the electron and the nucleus, and additional kinetic energy used by the electron to escape from the atom.

If true absorption does not occur, the X-ray photon can also be scattered by the interactions with electrons, transferring part of its energy and momentum. According to Latière and Mazerolle (1987), the amount of scattering with respect of the level of true absorption depends on the density of the element, represented by its atomic number (Z), and the wavelength of the photon. It is commonly considered insignificant for elements heavier than iron (Z>26) and wavelengths greater than 0.5 Å. Soils are often formed by elements including silicon (Z=14), oxygen (Z=8), magnesium (Z=12), aluminum (Z=13), calcium (Z=20), and iron (Z=26), so scattering can become important depending on the wavelengths used and the compositional characteristics of the material.

The magnitude of the X-ray attenuation is also affected by the degree of crystallinity of the material. Perfect crystals, with parallel crystallites, cause only little reflection and attenuation of X-ray beams, while disoriented crystallites cause significant attenuation of a wide range of wavelengths (Latière and Mazerolle 1987). The attenuation of the X-ray emissions is therefore greater for thicker samples, formed by denser materials, heavy elements, and amorphous crystals.

According to Ketcham and Carlson (2001), low energy X-rays show with more detail variations in material composition than high energy emissions. Fig. 3-2 shows the variations of the attenuation ($\mu\rho$) with respect to the energy of the incident beam for typical geotechnical minerals. Note that the attenuation of quartz and orthoclase is different at low energies due to the presence of potassium (Z=19) (Ketcham and Carlson 2001). At high energies, the attenuation of both minerals becomes very similar. Calcite,

which has high concentrations of calcium (Z=20) and is more dense than orthoclase and quartz, gives a higher attenuation over a wider range of X-ray energies. X-ray CT should therefore differentiate calcite from orthoclase and quartz at a wide range of energies. However, low energy X-rays are required to discern between quartz and orthoclase. The equipment used for this investigation has a maximum X-ray energy output of 50 kV, and should therefore allow differentiating between these minerals.

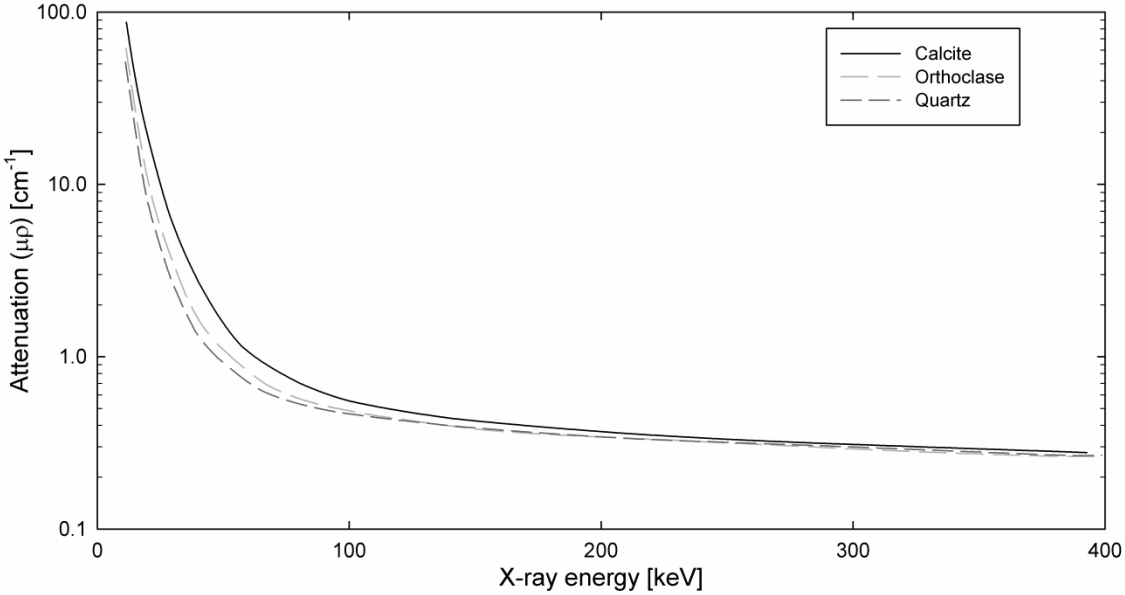

Fig. 3-2. Variation in X-ray attenuation of typical geotechnical minerals with respect to the X-ray energy (modified from Ketcham and Carlson, 2001).

3.2.2 Equipment

An X-ray CT scanning system requires three main components: (1) an X-ray source, (2) a specimen being examined, and (3) detectors which measure the intensity of the X-ray beams after passing through the specimen. The intensities measured by the detectors at a given time are called a *view*. The view represents the level of attenuation of the X-rays after passing through the specimen, which is closely related to the specimen's density and composition. A typical example for coarse sand was shown in Fig. 3-1, where denser and thicker sections of the sample were represented by darker colors.

Characteristics of the X-ray radiation emitted by the source controls the effectiveness of a CT system in a particular task. Higher energy X-rays penetrate the sample more effectively than low energy beams, but are less susceptible to changes in material density (Ketcham and Carlson 2001). High intensity X-rays reduce the amount of noise in the views acquired, but require larger focal spots, which may reduce the resolution of the X-ray views.

The main factor which differentiates X-ray CT scanners in medical and industrial application is the type of X-ray emissions used. For medical applications, CT scanners use limited doses of low energy X-rays (<125 keV) to minimize the exposure of the patient to radiation. Low energy X-ray sources are often grouped with large, high efficiency detectors to improve the quality of the results. The limitations encountered in medical applications are not relevant in industrial systems. Consequently, longer times of exposure and higher intensities can be used. Industrial CT systems often have smaller detectors which provide higher resolutions (Ketcham and Carlson 2001).

A Skyscan 1174 compact micro-CT was used for the experiments conducted in this investigation. The apparatus is shown in Fig. 3-3. This X-ray CT scanner uses a 20 to 50 kV X-ray source (target material: tungsten) with a maximum output of 40W, emitting beams of wavelengths ranging from 0.25 to 0.6 Å. The system has a 1.3 megapixel X-ray camera, which gives a resolution as small as 6 μm. Times of exposure of up to 5 s were used for the experiments.

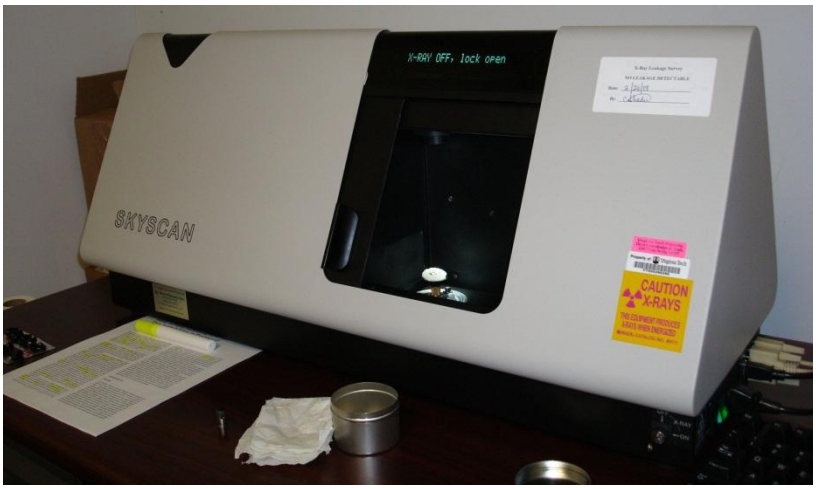

Fig. 3-3. Skyscan 1174 compact micro-CT.

During CT scanning, numerous views of a specimen, acquired at different orientations, are used to mathematically reconstruct two-dimensional images representing horizontal cross-sections of the specimen at different elevations. These cross-sections are called *slices*. The views are often acquired by rotating the sample using constant rotation intervals. In medical CT scanners, the X-ray source and detectors rotate instead of the specimen. Fig. 3-4 shows slices reconstructed from multiple X-ray views. For this investigation, up to 720 views were acquired for each sample over 360° of rotation, using intervals ranging from 0.5° to 4°.

Slices are calculated by first passing the information in each view though a filter, and superimposing them over a square grid at an angle equal to the angle of acquisition (Ketcham and Carlson 2001). Data from the views are transformed into *CT numbers* in the horizontal grid, which are often represented using grayscale colors.

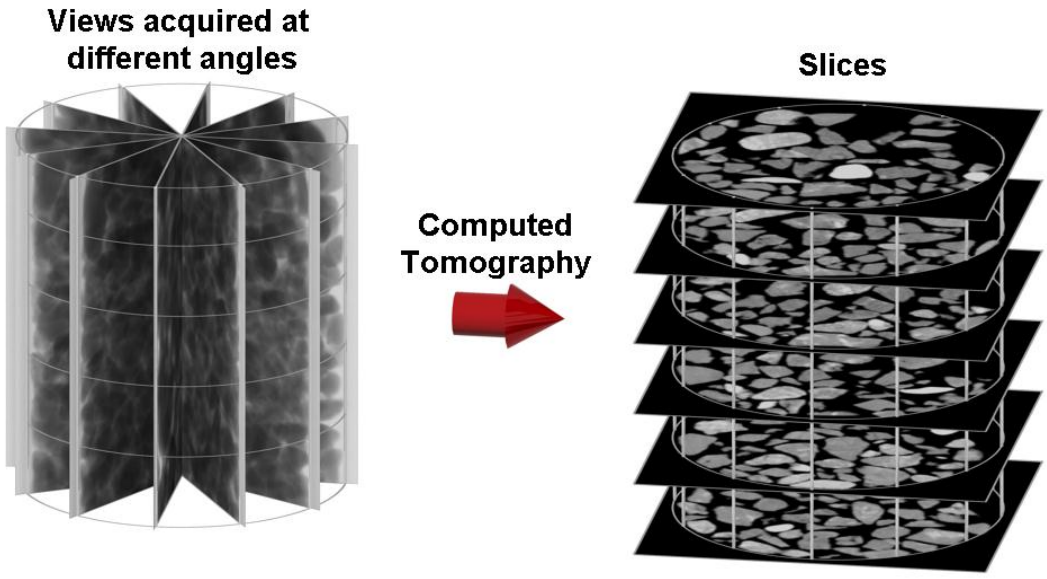

Fig. 3-4. Reconstruction of slices based on X-ray views.

Three dimensional representations of CT results are commonly obtained by using *isocontouring*, where a three-dimensional mesh is created joining points of equal CT number in the slices. The CT number is selected such that it defines the limits of the materials being studied. The mesh generated allows visualizing any distinct material within the sample from any orientation in three dimensions. Fig. 3-5 shows the three-dimensional reconstruction of a section of a cylindrical sample formed by Duralum DW, an industrial abrasive composed primarily by aluminum oxide (Al_2O_3).

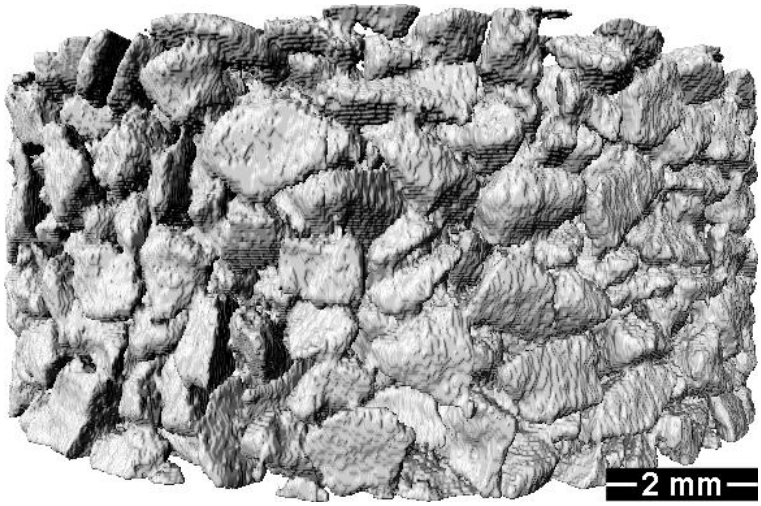

Fig. 3-5. Three-dimensional reconstruction of sample of Duralum GW.

3.3 Materials

Samples of reconstituted sand were formed by air-pluviation into a 4 cm tall by 1 cm diameter cylindrical acrylic container, shown in Fig. 3-6. The dimensions of the container were selected to reduce the attenuation of X-ray emissions and increase the quality of the acquired X-ray views. Larger diameter samples were also tested, however X-ray emission from the CT equipment were not strong enough to penetrate the specimens. The container was made of acrylic to keep additional attenuation to a minimum and allow significant contrast between the container and the sample. Once samples were prepared, the acrylic container was securely attached to the rotating platform inside the X-ray CT.

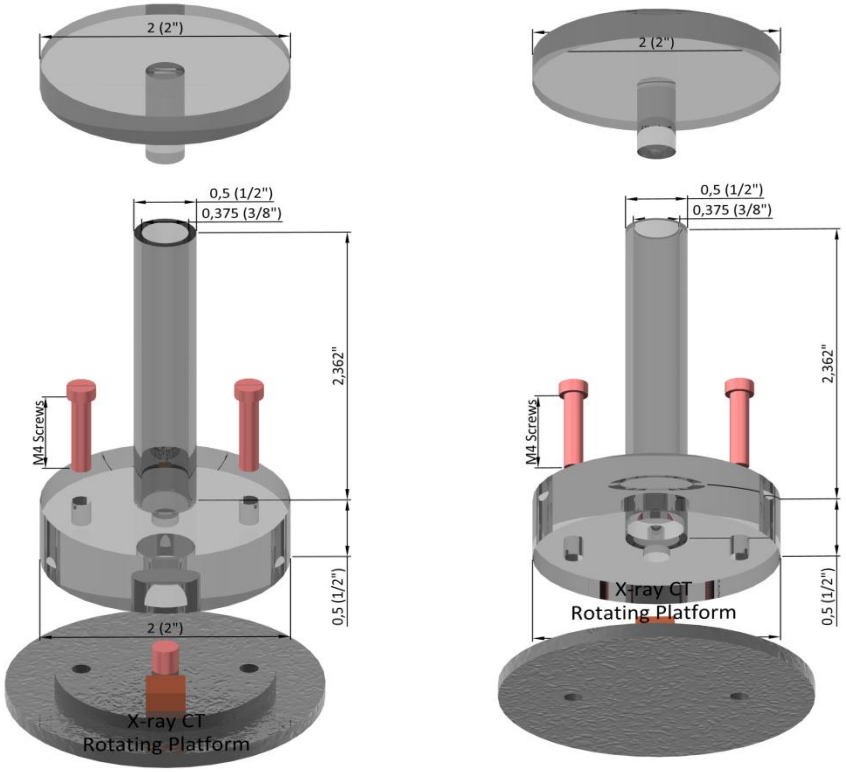

Fig. 3-6. Three-dimensional representation of the container used during X-ray CT scanning with approximate dimensions.

Five types of sand with different particle sizes and compositions were tested: (1) coarse, heterogeneous, poorly graded, sub-angular to angular river sand; (2) fine, poorly graded, sub-angular to angular micaceous sand, (3) fine, poorly graded, rounded silica sand; (4) medium, heterogeneous, poorly graded, sub-angular to angular river sand, and (5) medium, poorly graded, rounded silica sand (Ottawa sand). Some characteristics are given in Table 3-1. Grain size distribution curves and photos of the different sands used for this investigation are shown in Fig. 3-7 and Fig. 3-8.

Table 3-1. Characteristics of sands used for X-ray CT analysis.

Name	C_u	C_c	d_{50} **[mm]**
(1) Coarse river sand	1.97	0.87	1.64
(2) Fine micaceous sand	2.65	1.32	0.37
(3) Fine silica sand	1.93	0.88	0.13
(4) Medium river sand	1.65	1.19	0.49
(5) Ottawa sand	1.30	0.95	0.53

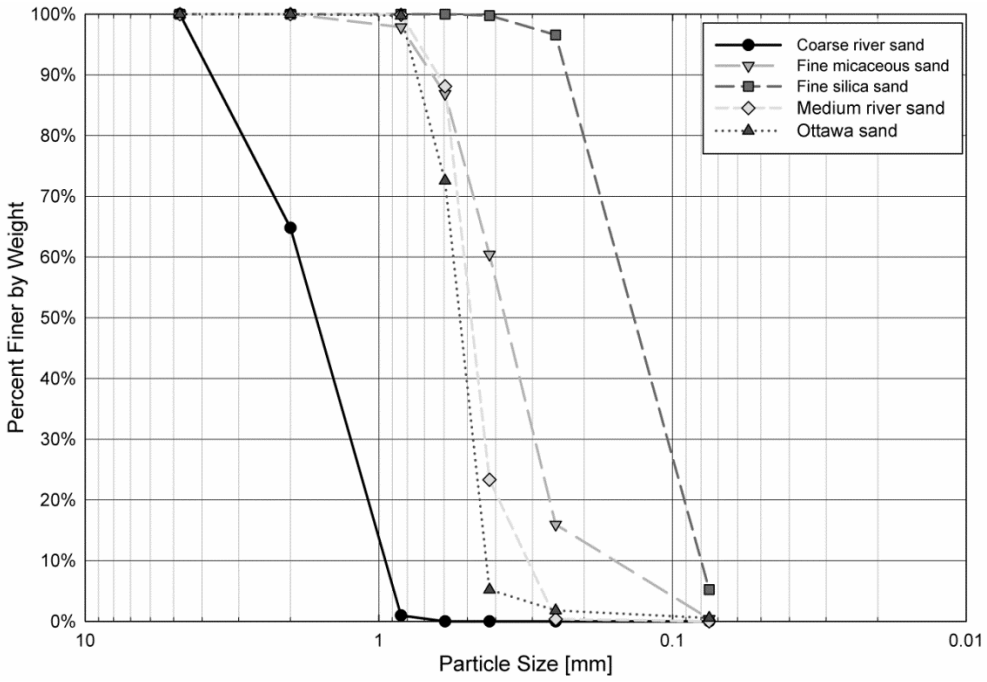

Fig. 3-7. Gradation of sands used for X-ray CT analysis.

(1) Coarse river sand

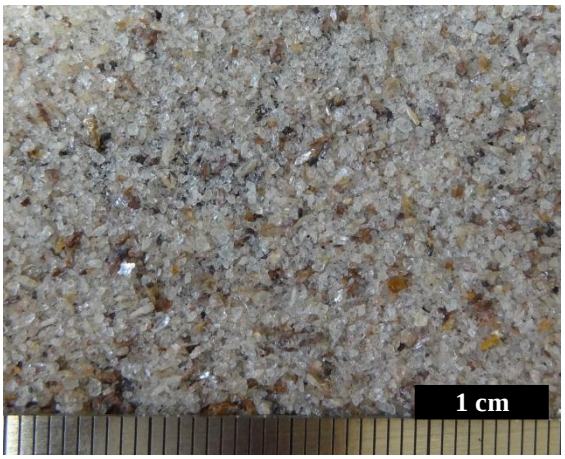

(2) Fine micaceous sand

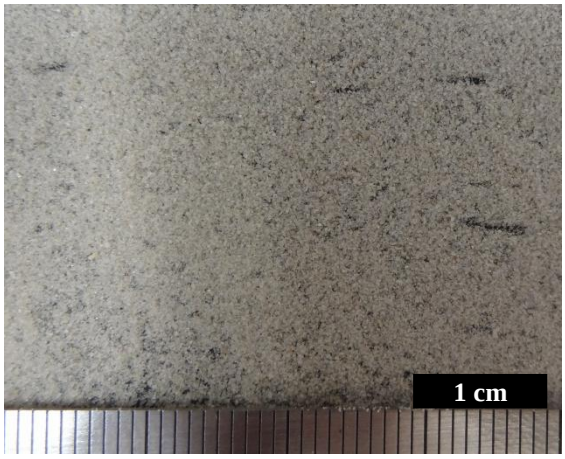

(3) Fine silica sand

(4) Medium river sand

(5) Ottawa sand

Fig. 3-8. Sands used during X-ray CT analysis.

The first step of the micro-scale laboratory investigation involved selecting the material that gave the best quality reconstructions during X-ray CT. Samples formed by

the 5 different sands described previously were prepared, and the container was then attached to the rotating platform inside the X-ray CT scanner. A total of 90 views were acquired at 2° intervals over 180° rotation for each sample. The X-ray energy was set at 50 kV, and the source current was kept at 0.8 mA. This setup corresponds to the highest energy emissions supported by the equipment. The time of exposure was set between 1.5 and 2.4 s. Typical examples of X-ray views and reconstructed slices for each of the materials used are shown in Fig. 3-9.

To detect small particle movements occurring during aging and creep using X-ray CT, the quality of the reconstructed slices must be enough to clearly define the boundary of each particle in each slice. That was not the case for the reconstructed slices of samples formed by fine micaceous sand (type 2) and fine silica sand (type 3), where the particles cannot be delimited with certainty. The quality of the reconstruction improved for medium river sand (type 4) and Ottawa sand (type 5), which are composed of coarser grains. However, the quality of the slices obtained for these types of sand is still not enough to detect small particle movements during aging and creep. Coarse River sand (type 1) was finally selected for the analysis of aging during one-dimensional compression using X-ray CT.

	X-ray View	Reconstructed Slice
(1) Coarse river sand	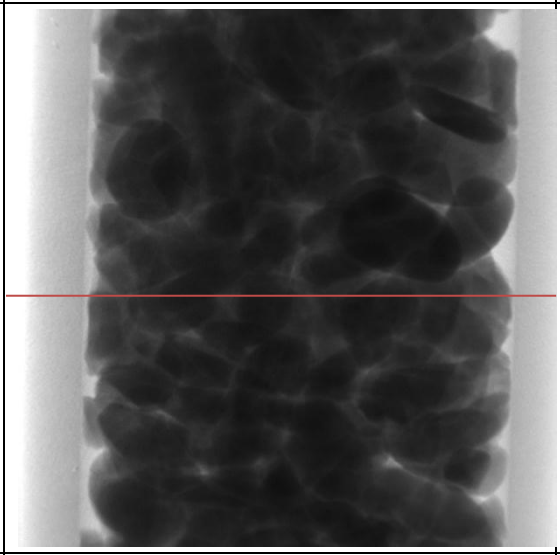	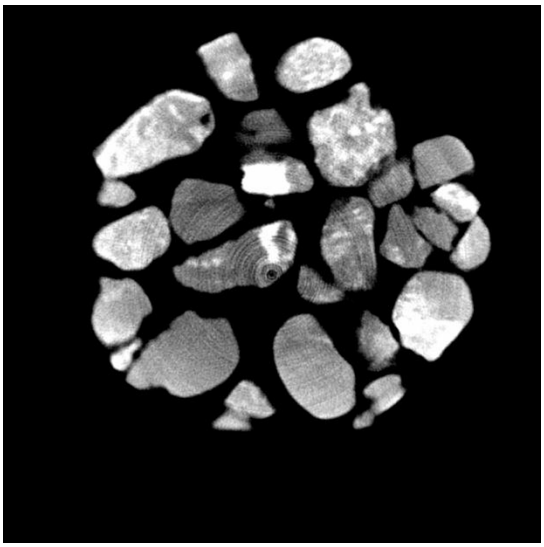
(2) Fine micaceous sand		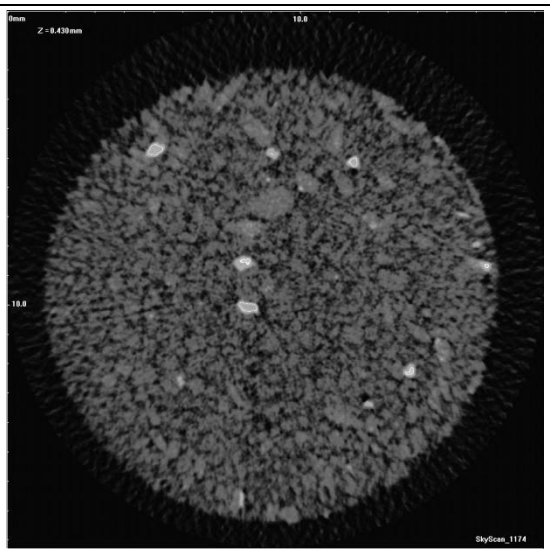
(3) Fine silica sand		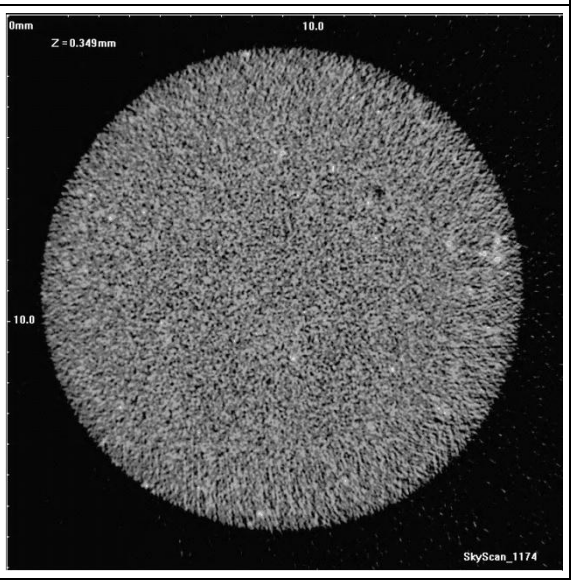

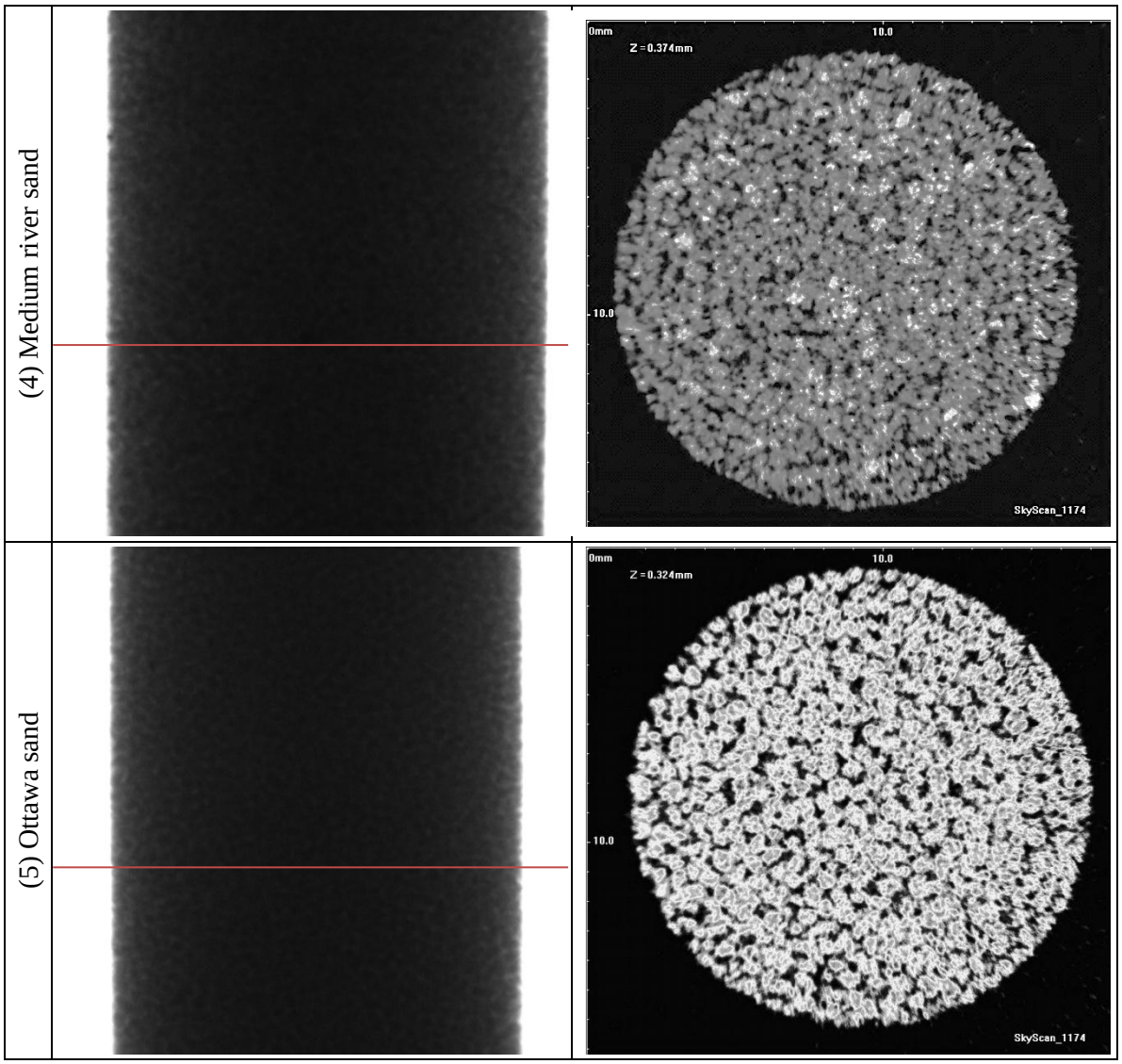

Fig. 3-9. Typical X-ray views and reconstructed slices of the five different sands. The red line over the X-ray view indicates the approximate location of the slice.

3.4 Test Setup

The samples used for the study of creep and aging during one-dimensional compression were prepared following the same procedure described in Section 3.3. A total of 720 views were acquired at 0.5° intervals over 360° rotation every time the specimen was scanned. The X-ray source was set at 50 kV and 0.8 mA. Image magnification was selected to fit the diameter of the specimen (1 cm) with the width of

the X-ray view, resulting in a resolution of approximately 11.97 μm per pixel. Times of exposure ranging from 1.9 to 4.5 s were considered. Best quality reconstructions were obtained using a time of exposure 2.1 s, which was finally selected for the experiments.

After placing and attaching the specimen inside the scanner, a weight of 500 g was placed over the sample, resulting in a vertical stress of about 62 kPa. A dead weight greater than 500 g could not be used due to the risk of damaging the equipment. Fig. 3-10 shows a picture of the sample inside the X-ray CT scanner. The sample was allowed to creep under the constant vertical stress for up to 7 days. The three-dimensional location of the particles during that period was studied by scanning the specimen once every day.

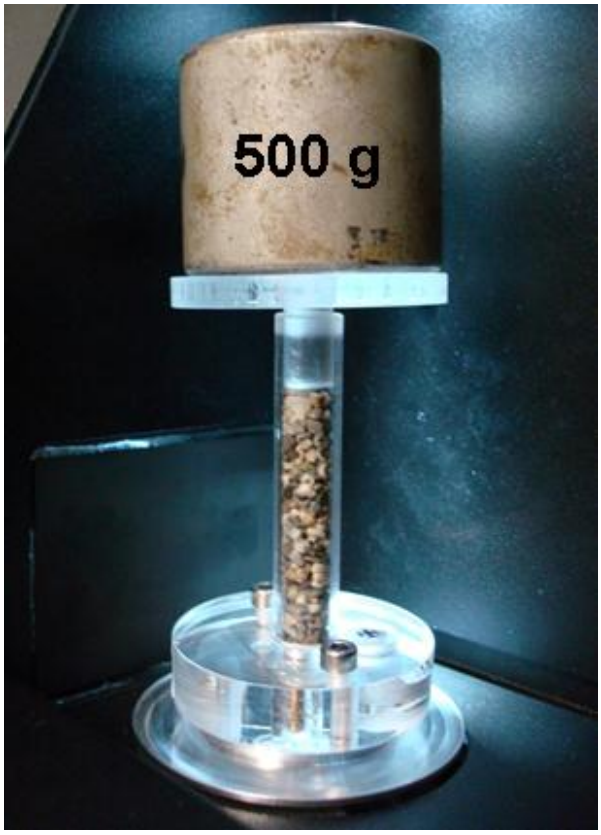

Fig. 3-10. Specimen inside the X-ray CT scanner.

3.5 Calculations

Results from X-ray CT are often shown as slices, which represent cross-sectional images of the specimen at different elevations. In order to detect particle movements based on the slices, it is necessary to process and analyze the images. That is done using the following procedure:

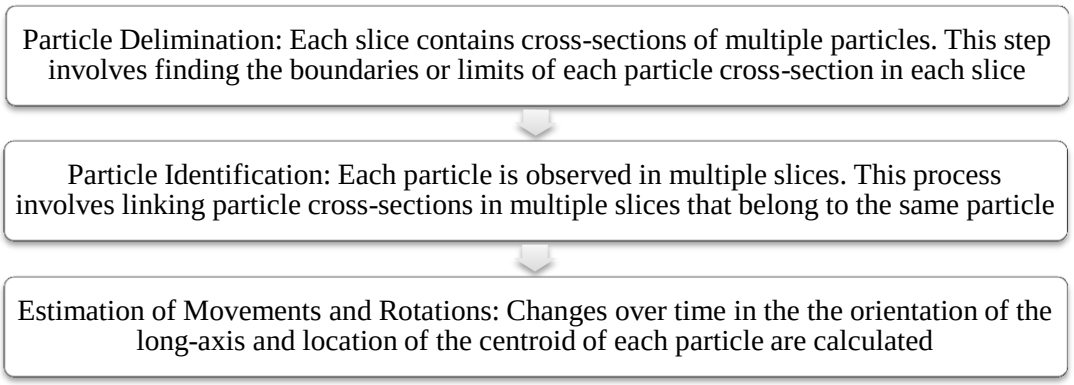

Each of the calculation steps is described next.

3.5.1 Particle Delimitation

Before particles can be identified and delimited, it is necessary to post-process the reconstructed slices to increase the contrast between particles and voids, and separate particles which may appear combined in the slices due to surrounding noise. That is done by passing each slice through a series of enhancement and morphological filters, which modifies the CT number of each pixel in the slice based on the values of the pixels around them. The application filters help separate particles based on their color, intensity, and shape, reducing image imperfections such as noise. Some of the filters used include:

- Erode filter: Erodes the edges of the particles in the slice.
- Open filter: Smooths the contours of the particles and separates narrowly connected objects.

- Gauss filter: Eliminates high frequency information and softens sharp edges. In the slices, sharp edges are often formed when the cross-sections of two particles are joined due to the surrounding noise.
- Flatten filter: Evens out the background variation. This filter eliminates the noise in the background by deleting small pixels that may have the same intensity as the particles.
- Sobel filter: Increases the intensity of the edges of the particles in the slice.

Once the slices were post-processed, the particles in each slice were delimited using an image processing software software. Besides defining the limits of each particle, this software also estimates the approximate area, the location of the centroid, and the orientation and length of the major and minor axes of the cross-section of the particles. A typical example of a slice before and after post-processing is shown in Fig. 3-11. The limits of the particles' cross-sections in the slice are shown in red.

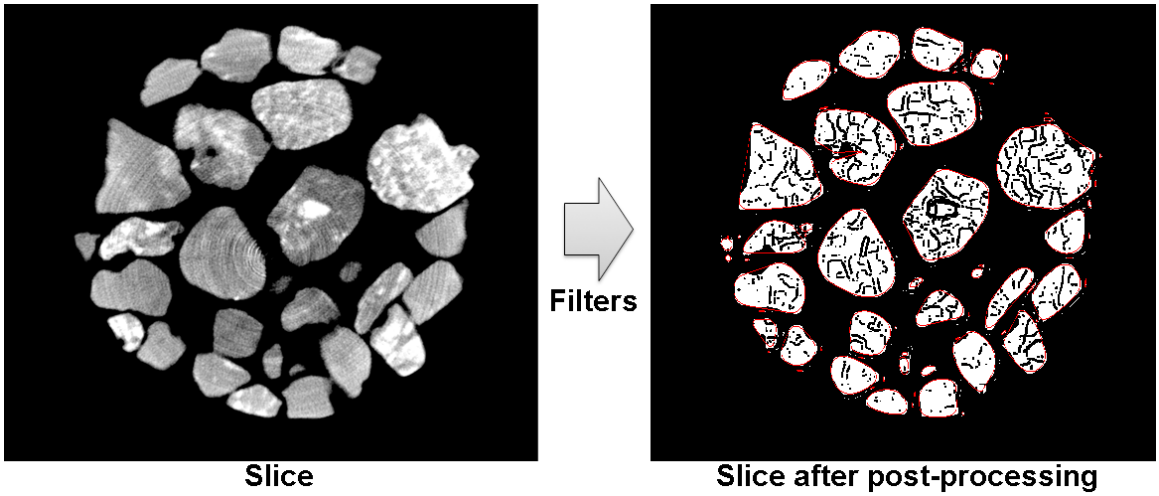

Fig. 3-11. Post-processing of the slices and particle delimitation.

3.5.2 Particle Identification

Once particles are delimited and two-dimensional properties (e.g.; location of the centroid, orientation of the minor and major axes, area) are calculated using an image processing software, the cross-sections in the different slices need to be grouped according to the particle they represent. Fu (2005) performed this task by calculating a parameter named *SI*, which was related to the distance between two cross-sections in adjacent slices. The magnitude of *SI* of two cross-sections, *i* in slice z and *j* in the slice z+1, is calculated as:

$$SI(i,j) = \left|x_{i,z} - x_{j,z+1}\right| + \left|y_{i,z} - y_{j,z+1}\right| \tag{5}$$

where *x* and *y* are the two-dimensional coordinates of their centroids. Cross-sections *i* and *j* were linked to the same particle if their respective value of *SI* was less than for any other pair formed by *i*. This can also be expressed as $SI=SI_{min}$, with SI_{min} given by:

$$SI_{\min}(i) = \min(SI(i,j)) = \min\left(\left|x_{i,z} - x_{j,z+1}\right| + \left|y_{i,z} - y_{j,z+1}\right|\right) \tag{6}$$
$$j = 1,2,\cdots m$$

where *m* is the number of particle cross-sections in slice z+1.

A similar procedure was used for this investigation, but the two-dimensional distance between cross-section centroids (*S*) was used instead of *SI*. The magnitudes of *S* and S_{min} can be expressed as:

$$S(i,j) = \sqrt{\left(x_{i,z} - x_{j,z+1}\right)^2 + \left(y_{i,z} - y_{j,z+1}\right)^2} \tag{7}$$

$$S_{\min}(i) = \min(S(i,j)) = \min\left(\sqrt{\left(x_{i,z} - x_{j,z+1}\right)^2 + \left(y_{i,z} - y_{j,z+1}\right)^2}\right) \tag{8}$$
$$j = 1,2,\cdots m$$

Besides the previous condition ($S=S_{min}$), which will be referred as *condition 1*, additional factors were considered for particle identification. These include:

- Condition 2 – Centroid Location: Two cross-sections, *i* and *j*, in adjacent slices were considered to belong to the same particle only if the centroid of *j* in slice z+1 lies within the area of *i* when projected onto slice z. This eliminates the possibility of linking the cross-section of two different particles, one disappearing and the other appearing in slice z+1, as long as one particle does not lie on top of the other. An example is shown in Fig. 3-12 for two spheres. Even if $S=S_{min}$ for *i* and *j*, as the centroid of *j* is not inside the limits of cross-section *i*, the two cross-sections will be linked to different particles.
- Condition 3 - Area Tendency: If the area of the cross-section in slice z-1 is greater than in slice z, and the area of the cross-section in slice z+2 is greater than in slice z+1 ($Area_{z-1}>Area_z$ and $Area_{z+1}<Area_{z+2}$), the cross-sections in z+1 and z+2, and in z-1 and z will be linked to different particles. This eliminates the possibility of linking cross-sections that belong to two different particles which are located one on top of the other. An example is shown in Fig. 3-13 for two spheres. Even if conditions 1 and 2 are met for cross-sections *h*, *i*, *j*, and *k*, since $Area_h>Area_i$ and $Area_j<Area_k$, cross-section *j* and *k*, will be linked to a different particle than *h* and *i*. Because this consideration requires the analysis of 4 contiguous cross-sections, its implementation takes place after conditions 1 and 2 have been used to identify particles in all the reconstructed slices.

The application of the three conditions previously described allows linking cross-sections in each slice according to the particle they belong to. The next step of the analysis is to detect and estimate particle movements and rotations occurring over time in the specimen.

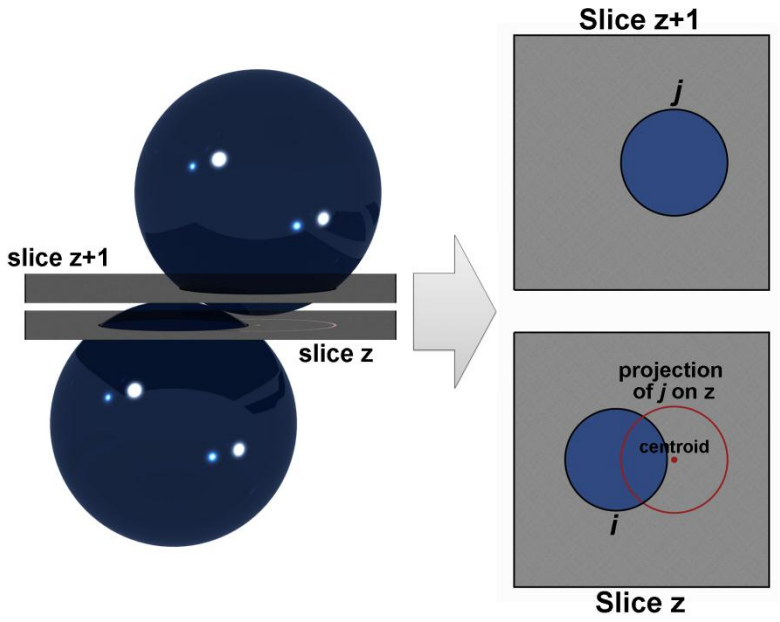

Fig. 3-12. Particle identification – condition 2 (location of the centroid).

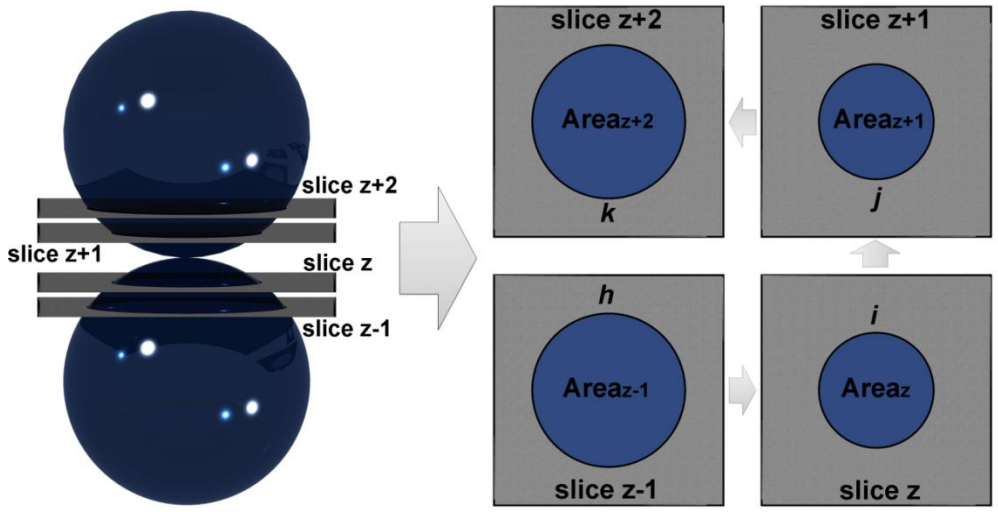

Fig. 3-13. Particle identification – condition 3 (area tendency).

3.5.3 Estimation of Particle Movements and Rotations

Once the cross-sections of the particles are identified in each slice, the orientation of the long-axis and the location of the centroid of each particle can be calculated. For this research, the orientation of the long-axis of each particle was estimated using the following procedure:

- The cross-section of the particle in a slice was approximated to an equivalent ellipse, with the same area, first and second degree moments. The orientation and magnitude of the major and minor axes of the equivalent ellipse are calculated using an image processing software.
- Particle cross-sections are replaced by the respective equivalent ellipses. The vertical distance between adjacent ellipses is equal to the separation between slices (Δz). For the X-ray CT analysis of samples of coarse river sand, this distance is equal to 11.97 μm.
- The equivalent ellipses are subdivided into a user-defined number of segments. Using more segments increases the precision of the calculation, but also requires longer times for computation. A total of 36 segments per ellipse were used for this study.
- The distance (D) between each segment in each ellipse is calculated geometrically using Eq. 9, where x_i, x_j, y_i, and y_j are the coordinates in the x and y direction of two segments i and j, and n is the number of slices that separate the ellipses containing the segments being considered (i.e., if i belong to slice z and j belongs to slice z+2, n=2).
- The long-axis of the particle is delimited by the two segments farthest apart, and its length is equal to D. The inclination of the long-axis of the particle with respect to the vertical axis (θ) is calculated using Eq. 10.

$$D = \sqrt{\left(x_i - x_j\right)^2 + \left(y_i - y_j\right)^2 + \left(n \cdot \Delta z\right)^2} \tag{9}$$

$$\theta = \mathrm{a\,tan}\left(\frac{\sqrt{\left(x_i - x_j\right)^2 + \left(y_i - y_j\right)^2}}{n \cdot \Delta z}\right) \tag{10}$$

Each of the calculation steps used to estimate the length and orientation of the long-axis of the particles is illustrated in Fig. 3-14. The calculation procedure was programmed using macros for Microsoft Excel.

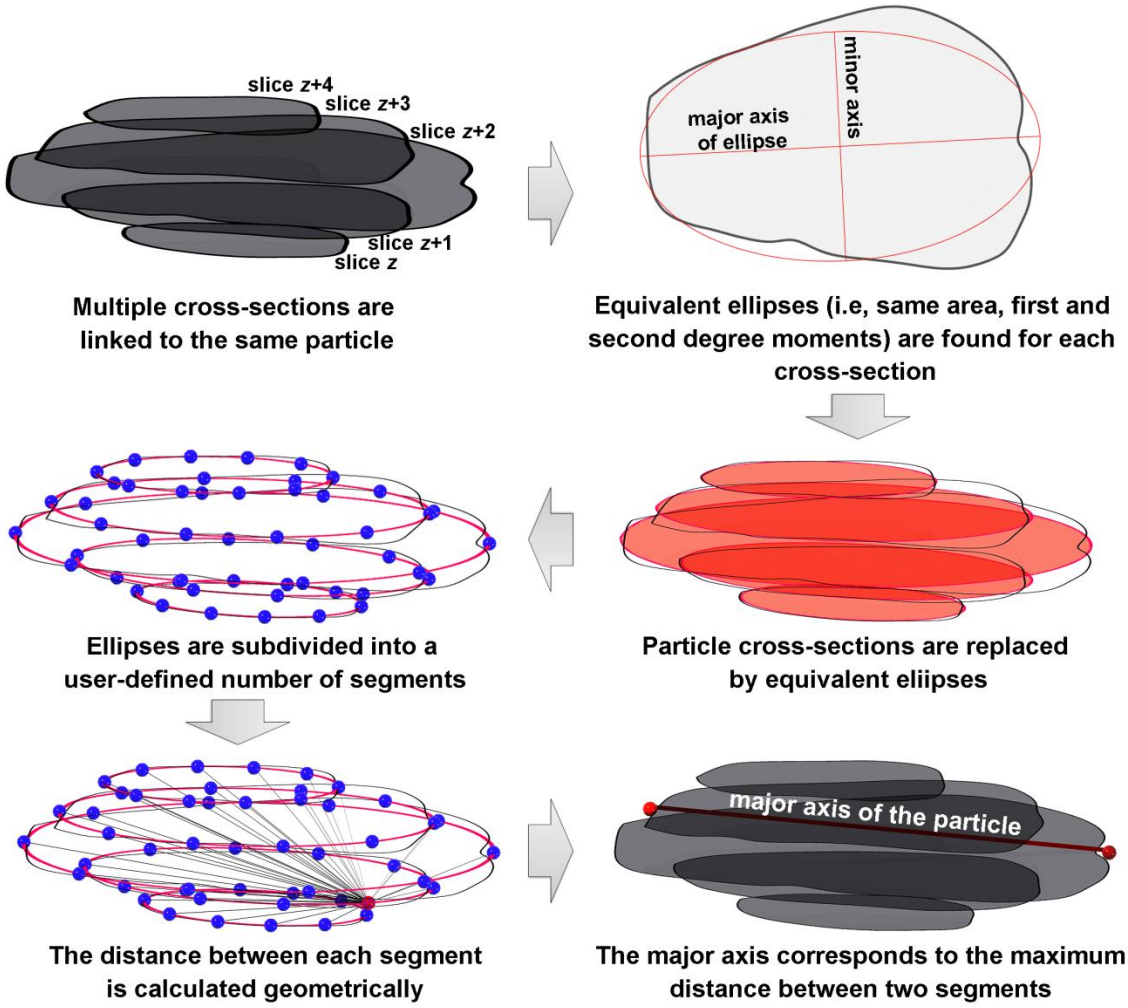

Fig. 3-14. Procedure for the calculation of the major axis of the particles.

Detection and quantification of particle movements and rotations require comparing the location of the centroids and the orientation of the long-axes of the particles on slices obtained at different times during the experiment. Therefore, it is necessary to identify the particles in different sets of views, where a *set of views* defines the group of X-ray images obtained by scanning the sample at one particular moment in time.

The particles in the specimen were identified in different sets of views by comparing their location, orientation, volume, and long-axis length. If two particles detected in two different sets of views correspond to the same particle in the specimen, their long-axis length and volume should be equal. However, it is expected that the filters applied to the slices during particle identification may have a small effect on the volume and long-axis length calculated for each particle from each set of views. A difference of 5% was allowed between the volumes and long-axis lengths calculated for the same particle from different sets of views.

Particle locations were also considered during this process to prevent linking grains in different sets with similar volumes and long-axis lengths but very different positions. Characteristics of a particle *i* in the reference set of views were compared with the properties the *n* closest particles in the other sets, named the comparison sets. The value of *n* was taken as 10. Particles were compared from the closest to the furthest apart. The decision tree used to identify particles in different sets of X-ray views is summarized next:

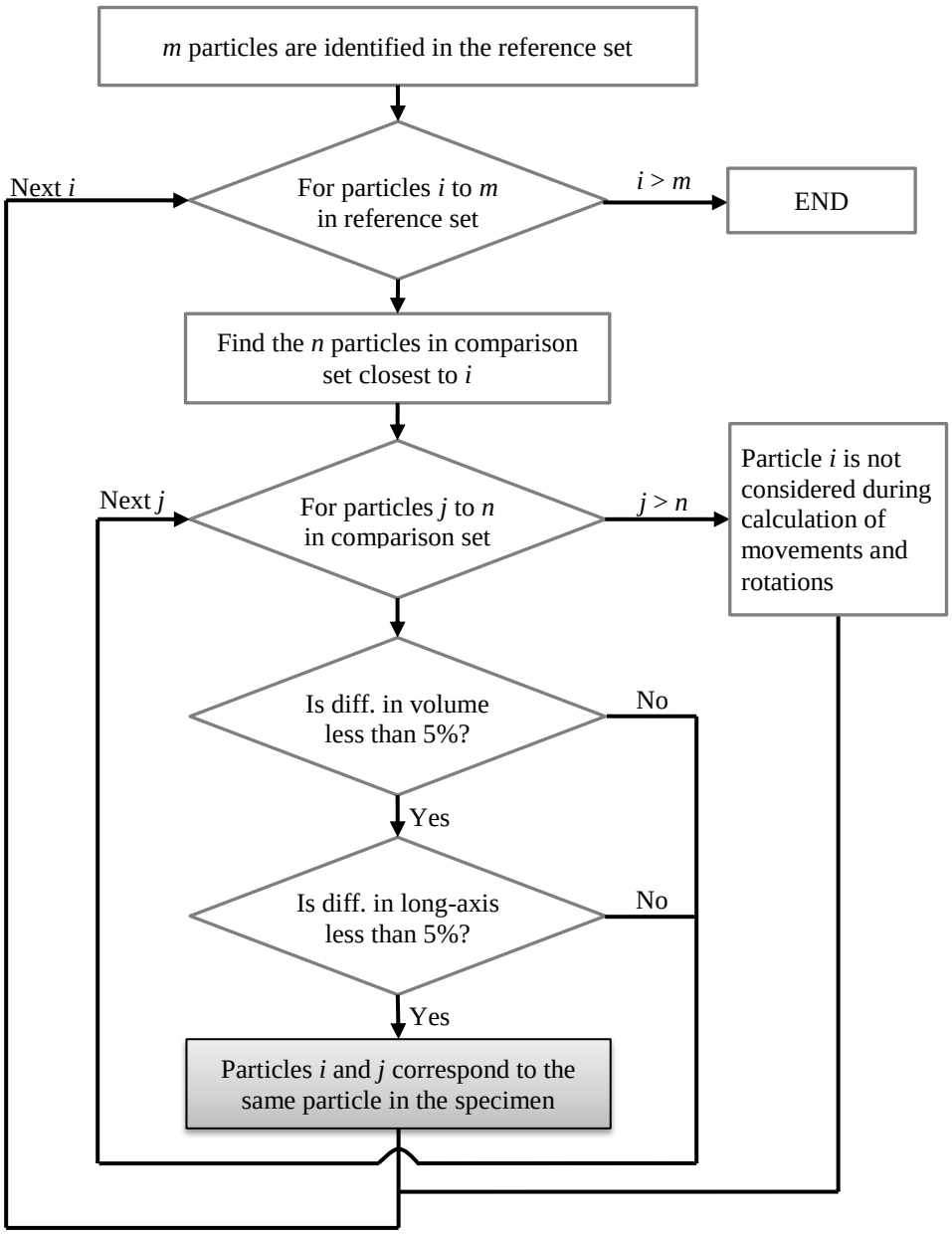

Fig. 3-15. Decision tree used for the identification of particles in different sets of views.

3.6 Analysis of Results

Changes in the internal structure of reconstituted coarse river sand were studied during one-dimensional compression under a constant vertical stress of 62kPa for up to 7 days. Two different factors were considered: (1) particle rotations, which are estimated

using Eq. 10; and (2) particle movements, calculated based on the change in position of the centroid of the particles.

Specimens were prepared in a 1 cm diameter acrylic cylinder. To improve the quality of the CT reconstruction, the equipment magnification was set so that the diameter of the specimen fitted approximately the width of the X-ray view, as shown in Fig. 3-16. For coarse river sand, the equipment setup gave a resolution of 11.97 μm per pixel. The views obtained from X-ray CT have 1024 by 1024 pixels, or 12.26 by 12.26 mm.

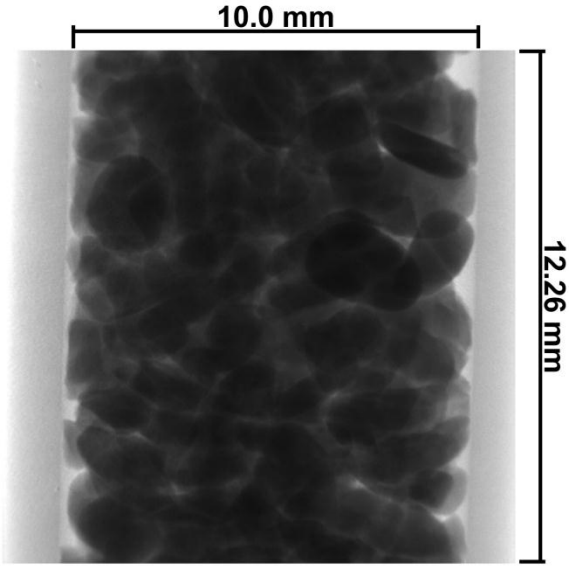

Fig. 3-16. Dimensions of the specimen considered in one X-ray view.

A total of 1020 slices 11.97 μm apart were generated using 720 views acquired at 0.5° rotation intervals. That means that a particle with a minimum diameter of 1 mm would be observed in at least 84 contiguous slices. About 150 particles were identified in the 12.26 mm high section of the specimen. Only particles observed in more than 60 (minor diameter of about 72 mm) slices were considered for the subsequent analyses.

3.6.1 Particle Rotations

Particle rotations are defined as the change in inclination of the long-axis of the particles (θ). Particle rotations over time during one-dimensional compression were calculated using the procedure described in Section 3.5.3.

The frequency distribution of the particle long-axis orientation just after, 1 day, and 6 days after the application of the load is given in Fig. 3-17. The rose diagram for 6 days of creep shows that the orientation of the long-axis of the particles tends to move away from the horizontal and become more homogeneously distributed over time during creep. A similar behavior was observed by Bowman and Soga (2003) on samples of dense ($D_r \approx 74\%$) Leighton Buzzard sand aged under one-dimensional conditions for up to 4 months. Details of the experiments conducted by Bowman and Soga (2003) were discussed in Section 2.3.3.

Fu (2005) calculated the displacement of individual particles during confined compression test of coarse limestone aggregate (d_{max}=12.7 mm and d_{min}=9.51 mm) by manually identifying each of the particles in every set of views. That was possible due to the small number of particles (about 30) and slices (around 70). The large number of particles (over 150) within the section of the specimen studied in this investigation makes it difficult to manually calculate the rotations and displacements for individual particles. Thus, identification of particles in different sets of views was done automatically using the procedure described in Section 3.5.3. Particle rotations are calculated with respect to particle orientations for the first set of views, just after the application of the vertical load. A summary of the results is given in Table 3-2.

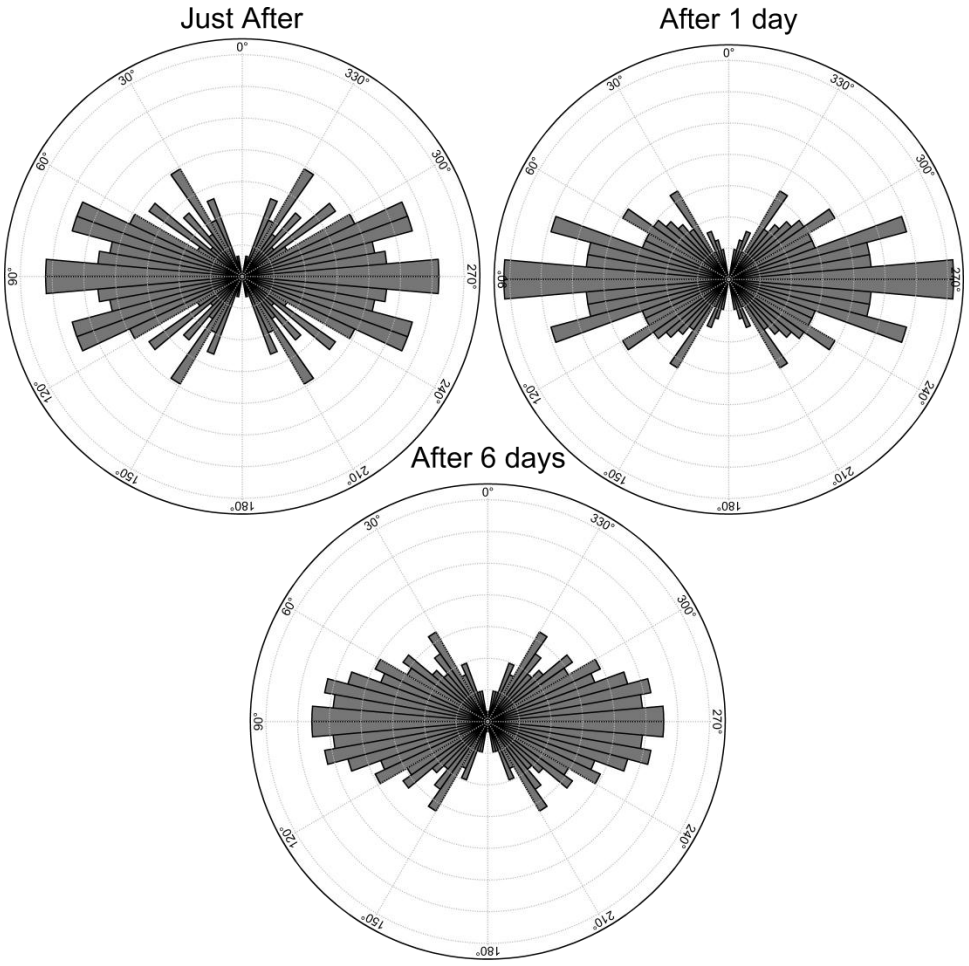

Fig. 3-17. Frequency distribution of particle orientation just after, 1 day, and 6 days after the application of the load.

Table 3-2. Particle rotations during one-dimensional compression and constant vertical stress.

Time of creep [days]	**Mean [deg]**	**Standard Deviation [deg]**	**Maximum [deg]**
1	3.31	5.42	46.81
6	4.59	8.19	54.23

The spatial distribution of the magnitudes of particle rotation can be obtained by projecting the corresponding values over the x-z, y-z, and x-y planes using the coordinates of the centroid of each particle. The orientation of the x, y, and z axes is shown in Fig. 3-18. The spatial distribution of particle rotations in the x-z, y-z, and x-y planes after 1 day and 6 days of creep is shown in Fig. 3-19 and in Fig. 3-20.

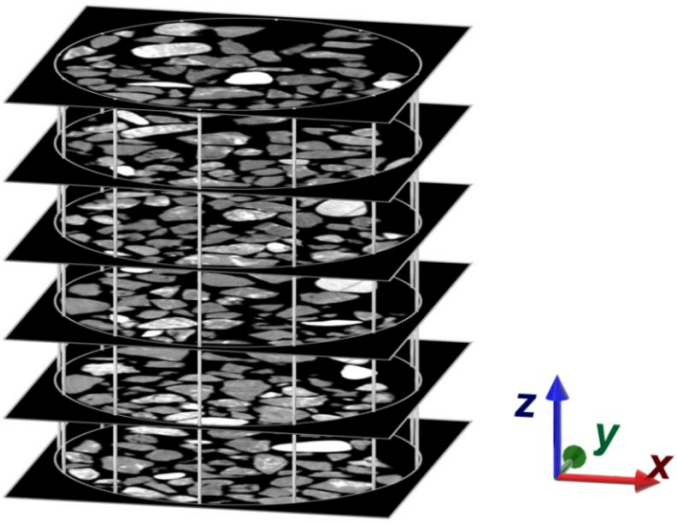

Fig. 3-18. Orientation of x, y, and z axes.

Fig. 3-19 and in Fig. 3-20 show that most particles in the specimen rotated less than 5° after 6 days of creep. Only few particles in the specimen rotated more than 20°. The magnitude of the particle rotations appear to increase over time. The frequency distribution of particle rotations after 1 day and 6 days of creep are shown in Fig. 3-21. Note that over 40% of the particles rotated less than 1° after 1 day of creep.

Particle rotated and moved during one-dimensional compression and constant vertical stress. The magnitude of the particle rotations increased over time during creep, and showed a significant change from 1 day to 6 days after the application of the vertical load. Some of the particles in the specimen showed a significant change in the inclination of their long-axis, being as high as 45° after 1 day of creep.

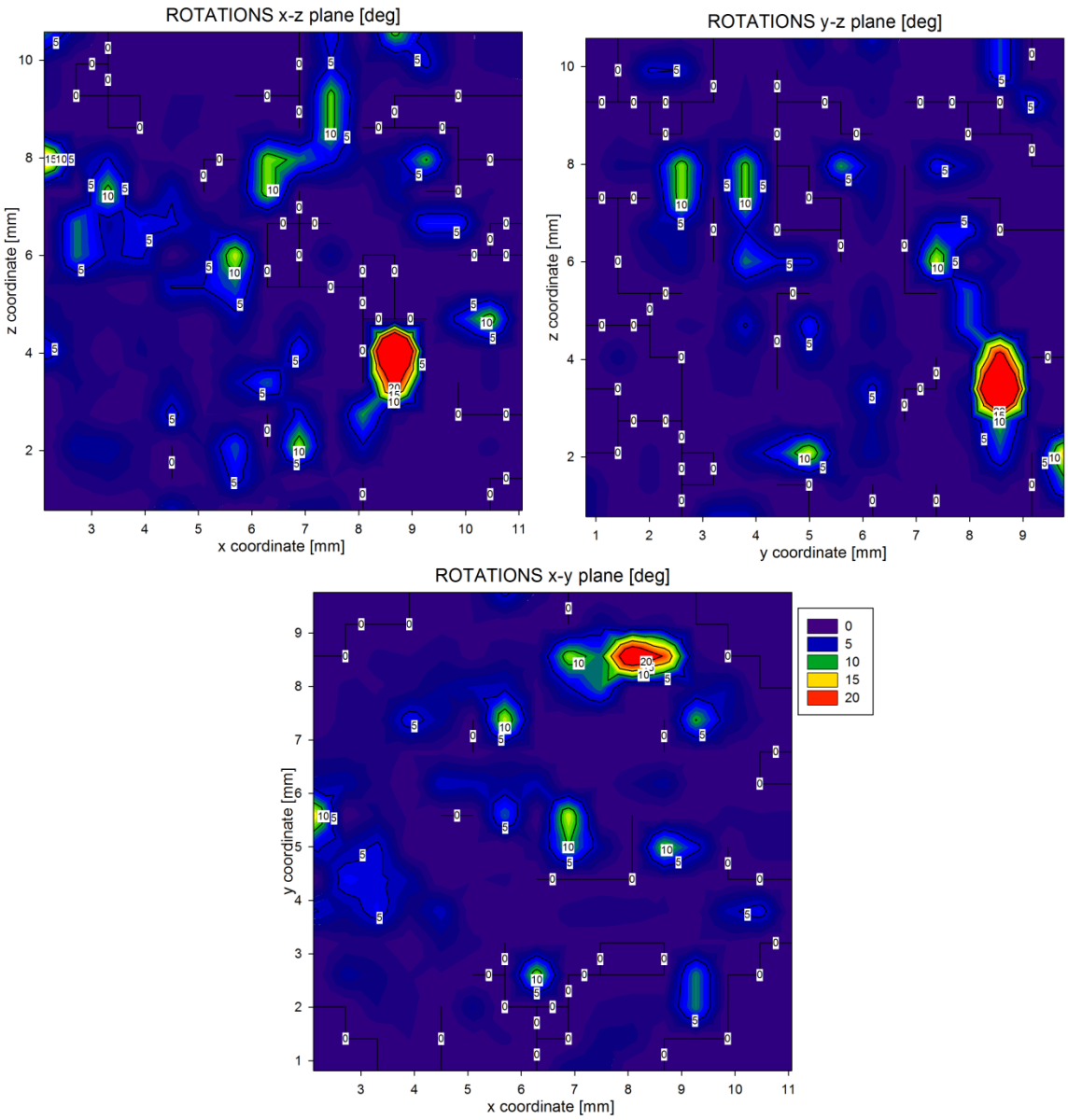

Fig. 3-19. Spatial distribution of particle long axis rotation after 1 day of creep (degrees).

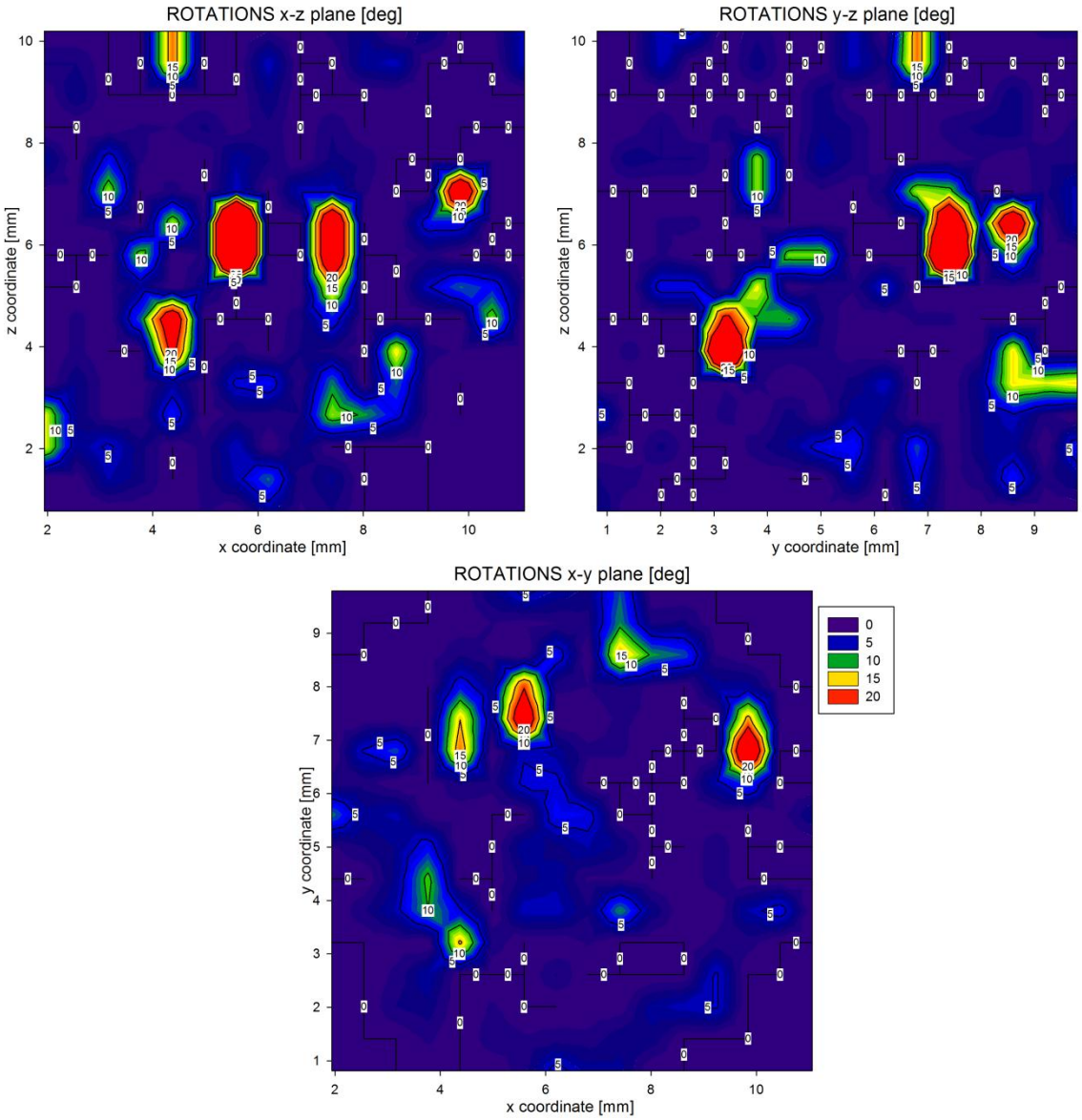

Fig. 3-20. Spatial distribution of particle long axis rotation after 6 days of creep (degrees).

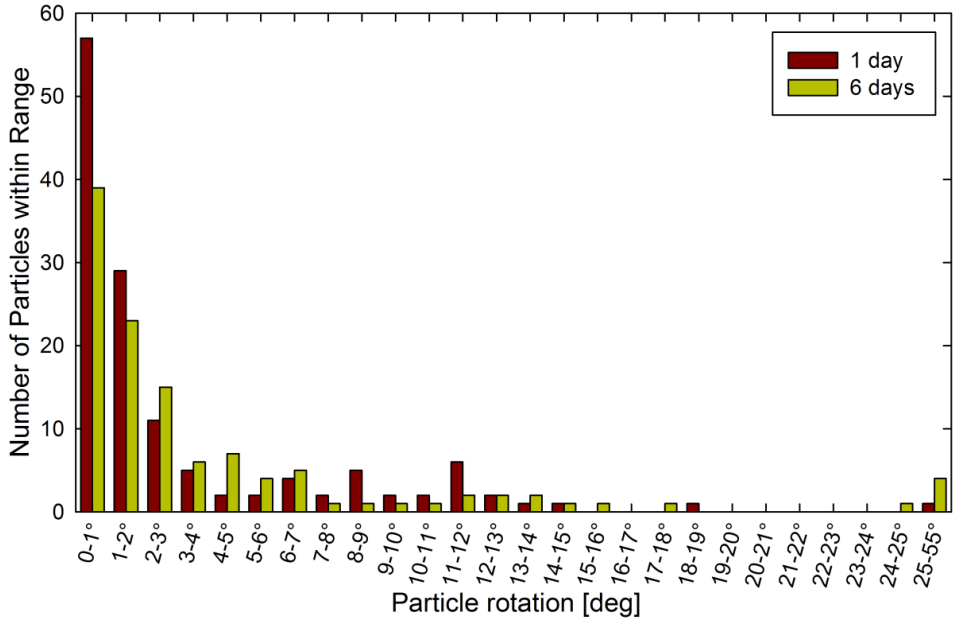

Fig. 3-21. Frequency distribution of particle rotations after 1 day and 6 days of creep.

3.6.2 Particle Displacements

Particle displacements, as indicated by the movement of the particle centroids, were initially identified by visually inspecting 3D reconstructions of the specimen. The comparison of particle locations at different times during the experiment provides a general idea of the magnitude of the particle movements. Fig. 3-22 shows the 3D reconstruction of a section of the specimen just after, 1 day, and 6 days after the application of the vertical stress, seen from 4 different orientations 90° apart.

Particle displacements were not detected by visually inspecting the reconstructed specimens shown in Fig. 3-22, indicating that particles movement must be of small magnitude. Three-dimensional reconstructions just before, 1 day, and 6 days after the application of the vertical stress are practically identical. To identify displacements that may not be detectable by visual inspection, a similar approach to that used for the calculation of particle rotations was implemented to estimate and quantify the movements of the individual particles.

	Just after Load Application	After 1 day of creep	After 6 days of creep
0° Rotation	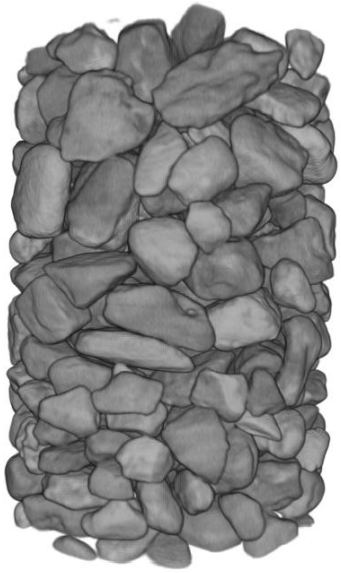	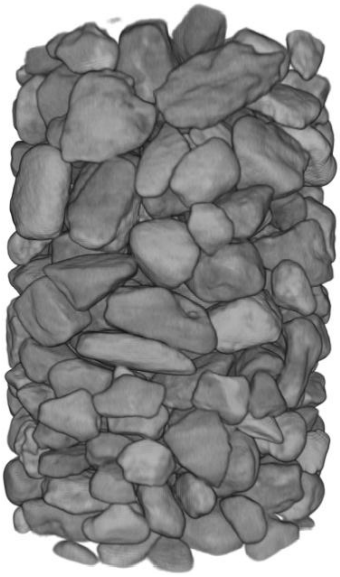	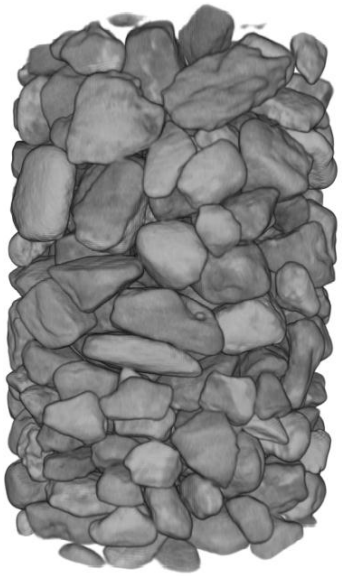
90° Rotation	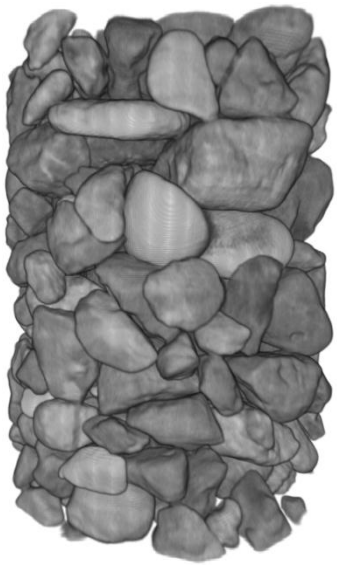	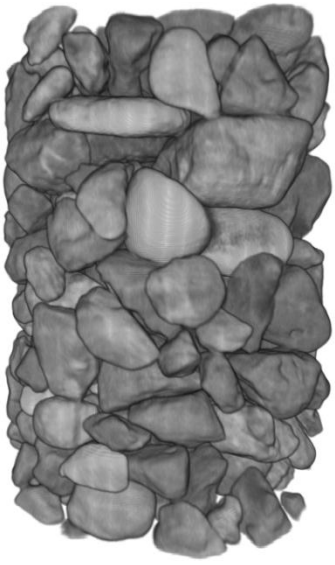	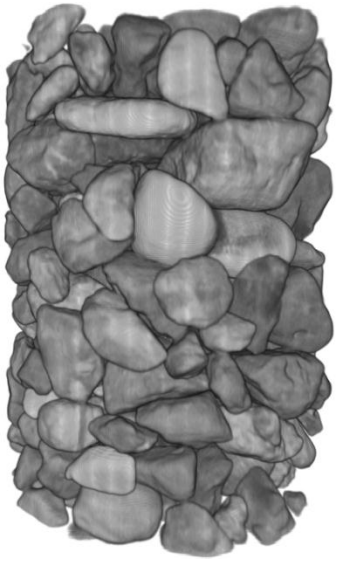

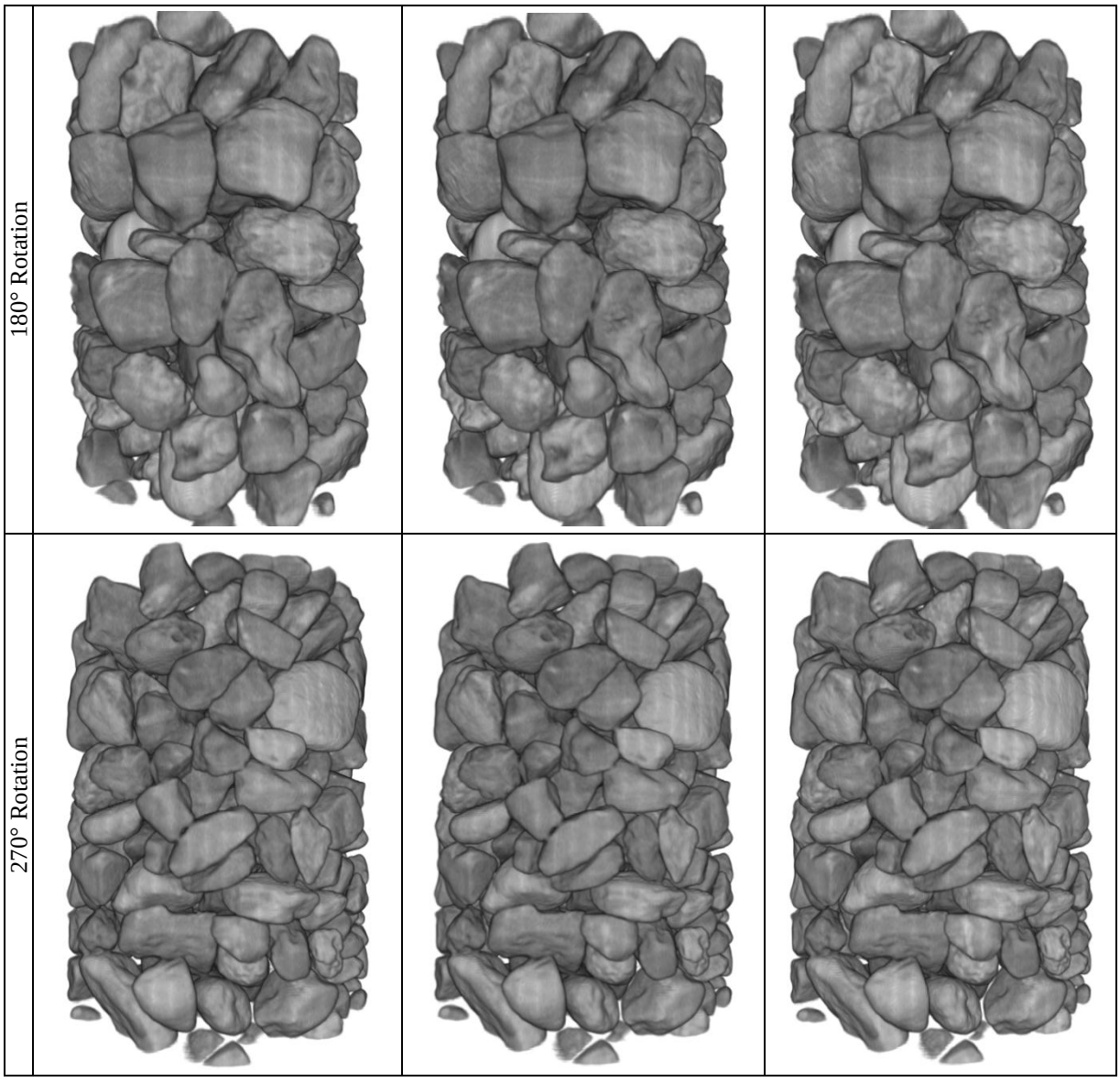

Fig. 3-22. Three-dimensional reconstruction of a section of the specimen just after, 1day, and 6 days after the application of the load.

Particles in the specimen were identified in sets of views acquired just after, 1 day, and 6 days after the application of the vertical stress. Particle displacements were then calculated as the movement of the centroid of each particle with respect to their location just after the application of the load. The x, y, and z coordinates of the centroid of each particle are calculated using Eqs. 11, 12, and 13; where *m* is the number of slices which include a given particle in one set of views. A summary of the results is presented in Table 3-2.

$$x = \frac{\sum_{j=1}^{m} A_j \Delta z \cdot x_j}{\sum_{j=1}^{m} A_j \Delta z} \tag{11}$$

$$y = \frac{\sum_{j=1}^{m} A_j \Delta z \cdot y_j}{\sum_{j=1}^{m} A_j \Delta z} \tag{12}$$

$$z = \frac{\sum_{j=1}^{m} A_j \Delta z \cdot z_j}{\sum_{j=1}^{m} A_j \Delta z} \tag{13}$$

Table 3-3. Particle displacements during one-dimensional compression and constant vertical stress.

Time of creep [days]	**Mean [mm]**	**Standard Deviation [mm]**	**Maximum [mm]**
1	0.0477	0.0260	0.1421
6	0.1269	0.0955	0.9445

The spatial distribution of particle displacements with respect to their location just after the application of the load is shown in Fig. 3-23 for 1 day of creep and in Fig. 3-24 for 6 days of creep. Fig. 3-23 and Fig. 3-24 show a clear increase in the magnitude of the displacement over time during creep. Only few particles show a displacement greater than 0.05 mm after 1 day of creep. However, after 6 days of creep, various sectors

of the specimen have particles which have moved over 0.1 mm. That can also be observed in Fig. 3-25, which gives the frequency distribution of the particle displacements 1 day and 6 days after the application of the load.

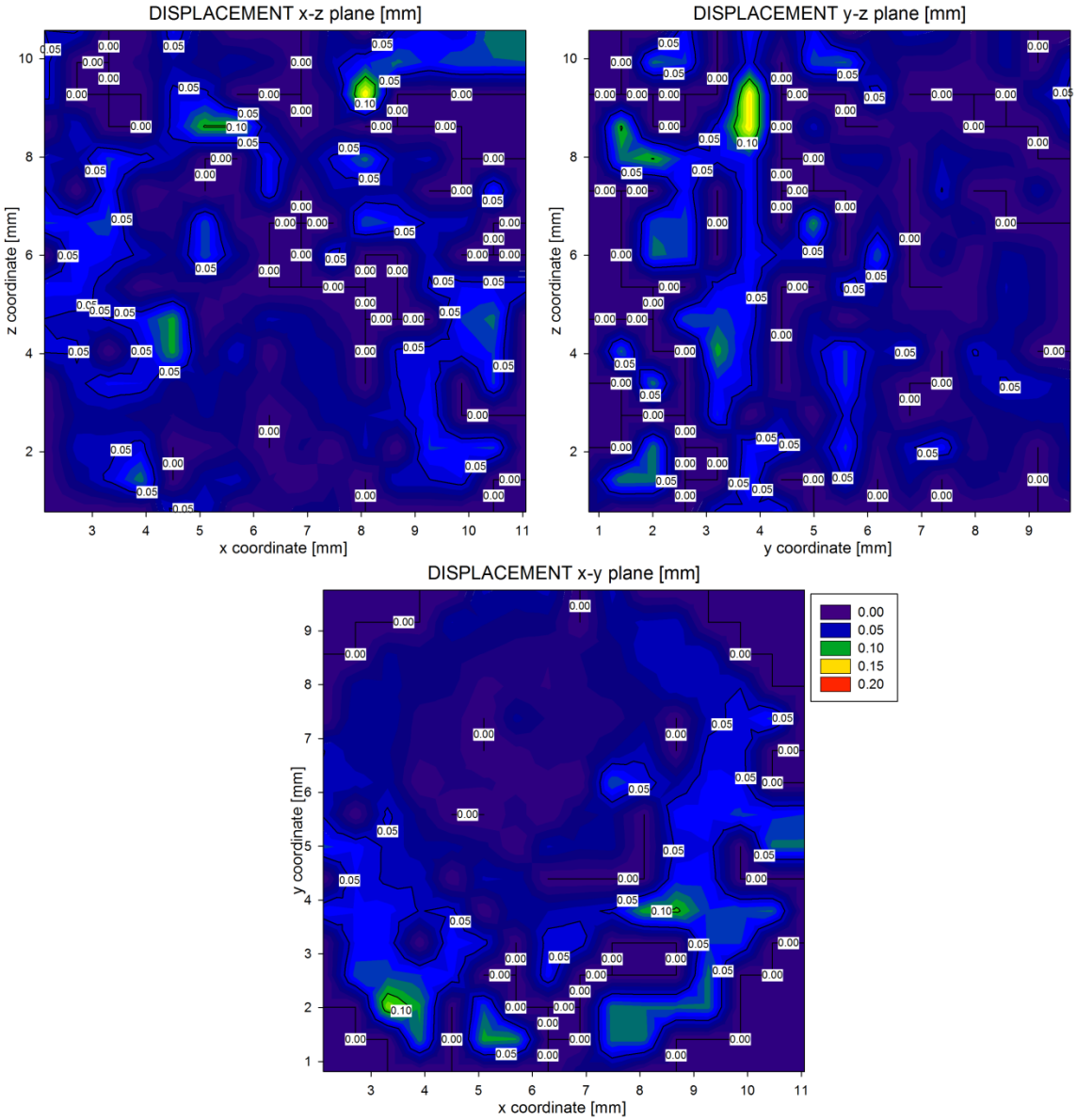

Fig. 3-23. Spatial distribution of particle displacements in the x-z, y-z, and x-y planes after 1 day of creep (in mm).

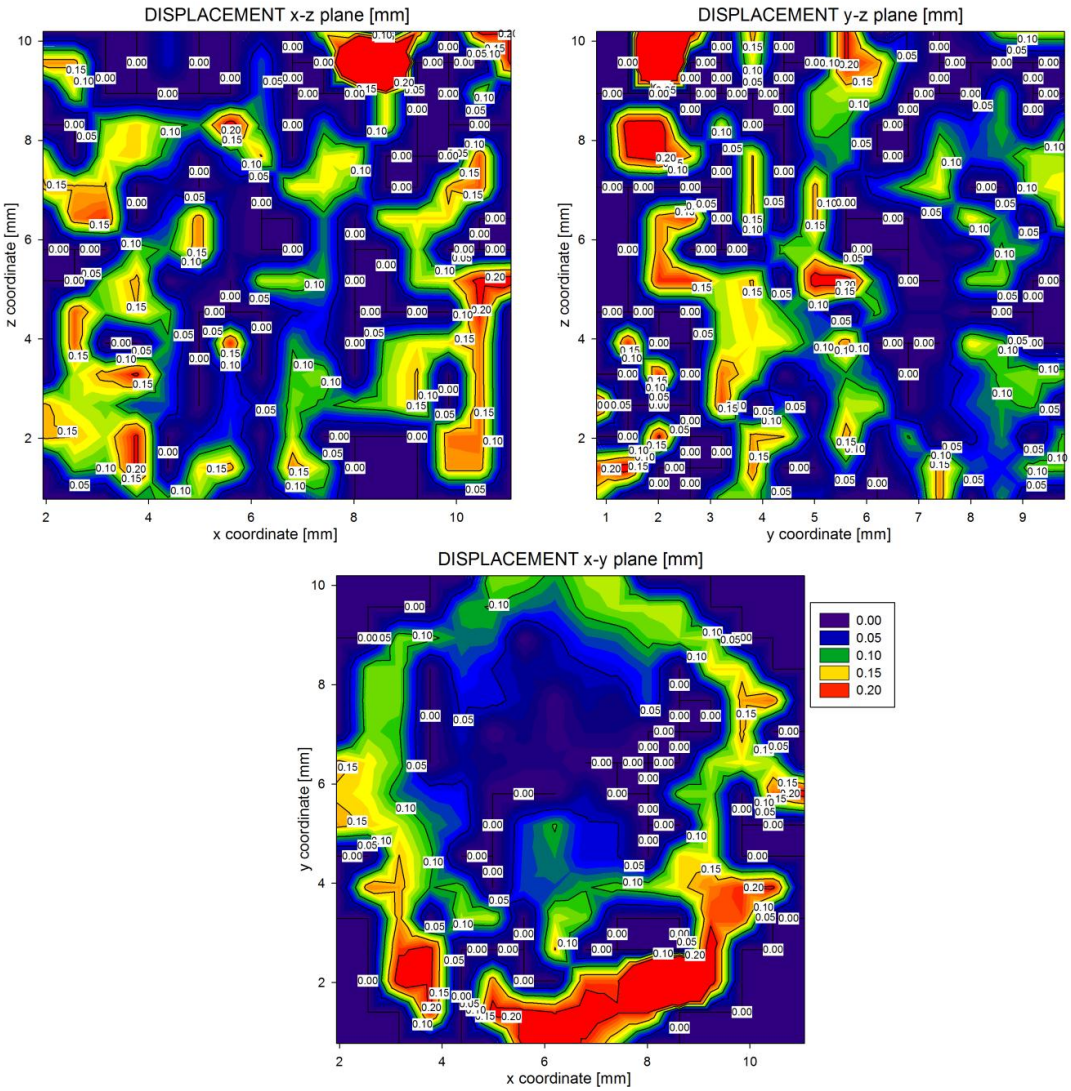

Fig. 3-24. Spatial distribution of particle displacements in the x-z, y-z, and x-y planes after 6 days of creep (in mm).

According to Fig. 3-25, more than 50% of the particles had a displacement of less than 0.05 mm during the first day of creep. Particles continued moving during the experiment. After 6 days of creep, over 60% of the particles had a displacement greater than 0.1 mm. The spatial distribution shows that particle displacements appear to occur in clumps throughout the extent of the specimen. Clumps of high particle displacement were often surrounded by areas of little particle movement.

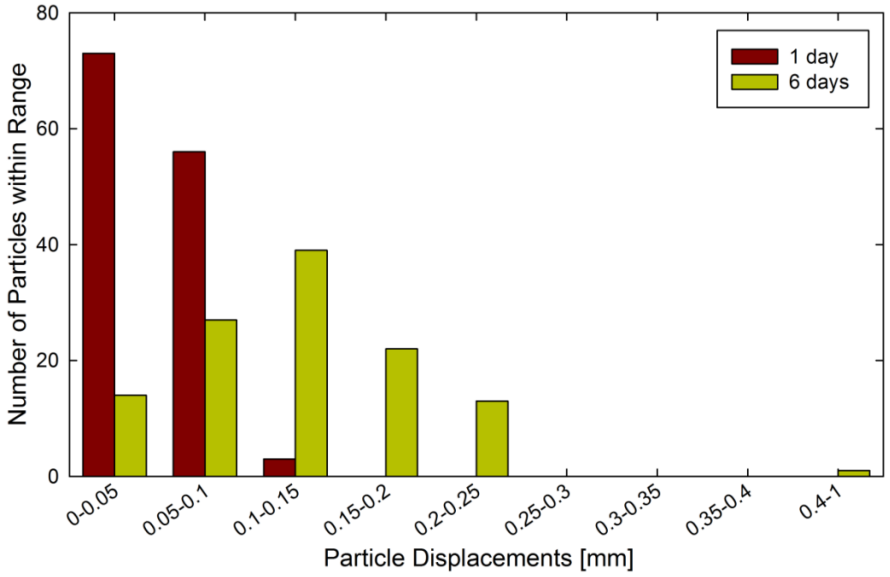

Fig. 3-25. Particle displacements distribution with respect to magnitude.

3.7 X-Ray CT of Abrasives of Heterogeneous Composition

In addition to the materials described in Section 3.3, the effectiveness of X-ray CT to study the changes in the internal structure of samples formed by industrial abrasives of heterogeneous chemical composition was also analyzed. The main purpose of these tests was to study the possibility of using materials formed by heavier elements as an alternative to allow the analysis of creep and aging in samples formed by finer particles.

According to Ketcham and Carlson (2001), true X-ray absorption is proportional to Z^4, while scattering is proportional only to Z. Consequentially, the presence of small concentrations of heavy elements, as in the abrasives used for this analysis, should help reduce the amount of noise in the reconstituted slices. Presence of heavier elements increases significantly the level of true X-ray absorption while causing only small changes in to the magnitude of the scattering. Because the ratio of the energy attenuated due to absorption with respect to the energy scattered increases with increasing Z, the

level of noise in the reconstructed slices should decrease along with the magnitude of *Z*. The increase in attenuation with increasing element mass can be compensated by increasing the time of exposure when the acquiring the views.

Abrasives were supplied by Washington Mills (www.washingtonmills.com). A brief description of the materials used is presented in Table 3-4. The gradation of all the different abrasives was very similar. Washington Mills refers to this particular gradation as *grain size 36*, which defines materials with a maximum particle size of 0.841 mm and less than 3% by weight finer than 0.354 mm. A typical gradation for the material is presented in Fig. 3-26. Photos of the different abrasives are shown in Fig. 3-27.

Table 3-4. Description of abrasives used for X-ray CT analysis.

Name	**Description**	G_s	**Chemical Composition**
Carborex	Black, semi-friable, medium density, silicon carbide abrasive used for grinding low tensile strength, ductile, non-ferrous metals	3.20	SiC 97.8% SiO_2 0.6% Si 0.8% Fe 0.2% Al 0.3% C 0.3%
NZ Plus	Hard, very tough abrasive formed by fusing zircon sand and alumina. Often used for grinding mild stainless and high alloy steel	4.60	Al_2O_3 60% ZrO_2 39% TiO_2 0.15% SiO_2 0.35% Fe_2O_3 0.15% Na_2O 0.03% CaO 0.09% MgO 0.02% Y_2O_3 0.8%
Duralum ATZ	Dense, fused alumina – zirconia abrasive	4.50	AlO_3 60% ZrO_2 39% TiO_2 0.3% Y_2O_3 0.7%
Duralum GW	Blocky, medium density, fused brown aluminum oxide abrasive	3.92	AlO_3 96.2% TiO_2 2.7% SiO_2 0.67% Fe_2O_3 0.11%

The time of exposure used during X-ray CT of industrial abrasives ranged from 4 to 5 s. The X-ray CT scanner was configured to produce the maximum tolerable energy X-ray emissions; i.e. 50 kV and 800 μA. Typical examples of acquired X-ray views and reconstructed slices are shown in Fig. 3-28.

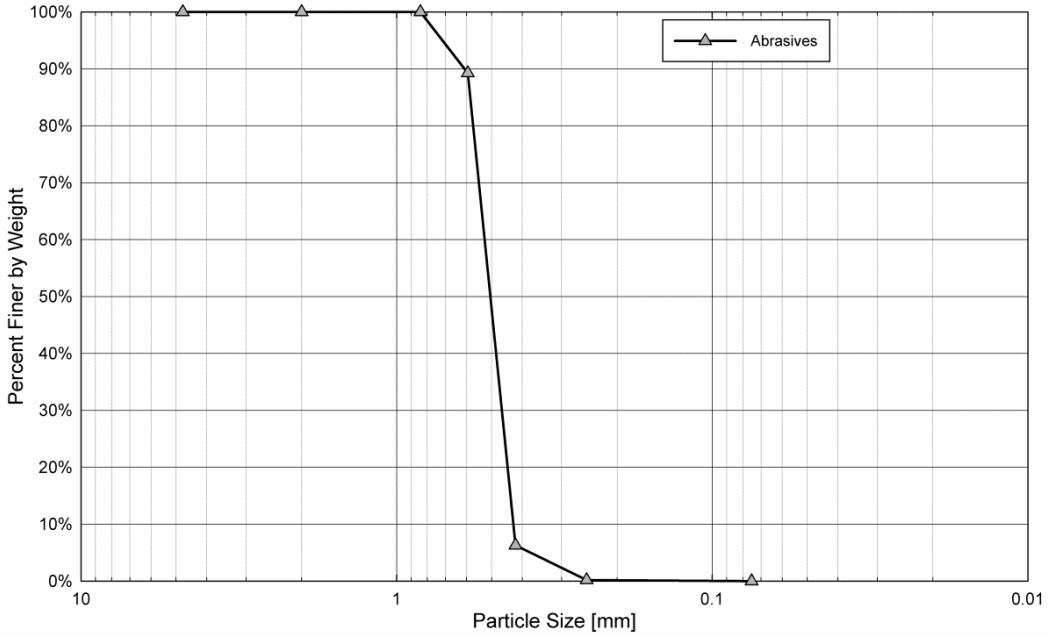

Fig. 3-26. Typical gradation of abrasives used for X-ray CT.

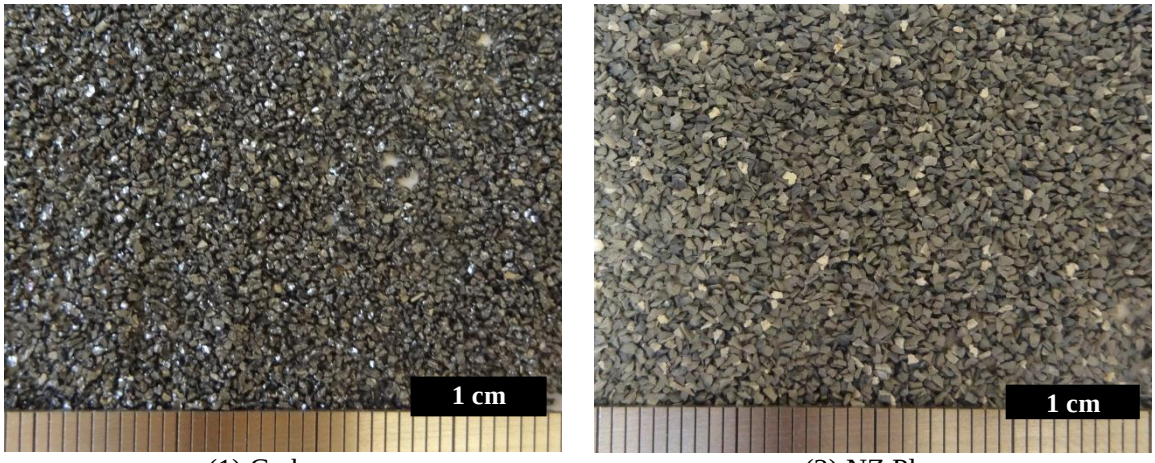

(1) Carborex (2) NZ Plus

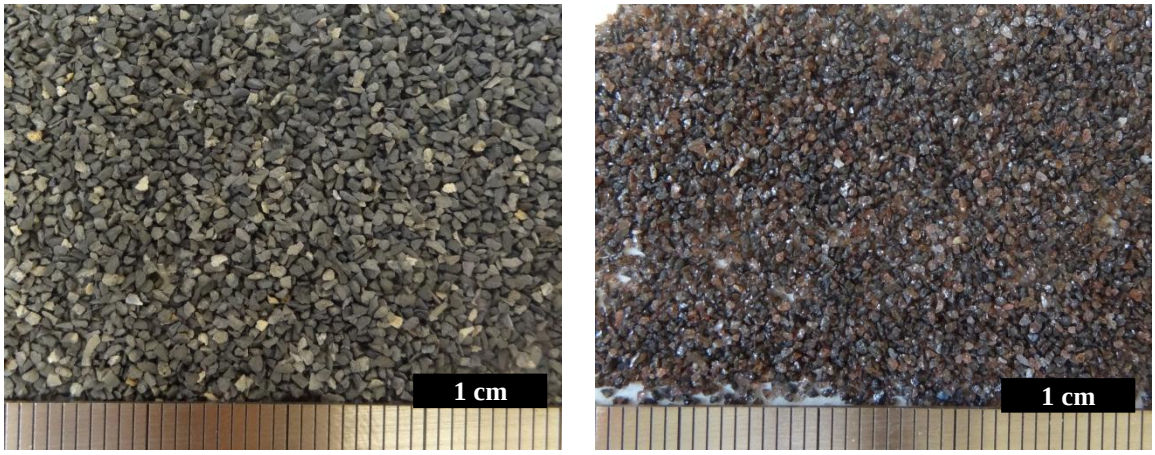

(3) Duralum ATZ (4) Duralum GW

Fig. 3-27. Abrasives used for X-ray CT.

	X-ray View	Typical Slice
Carborex	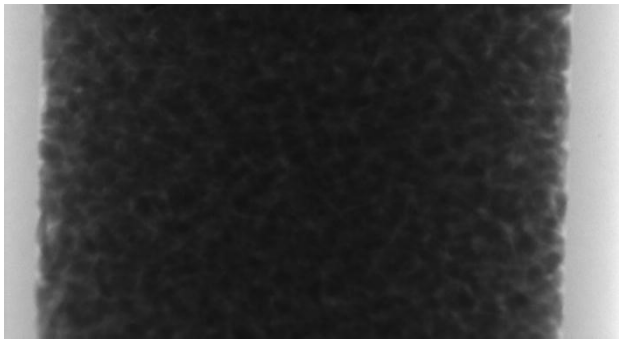	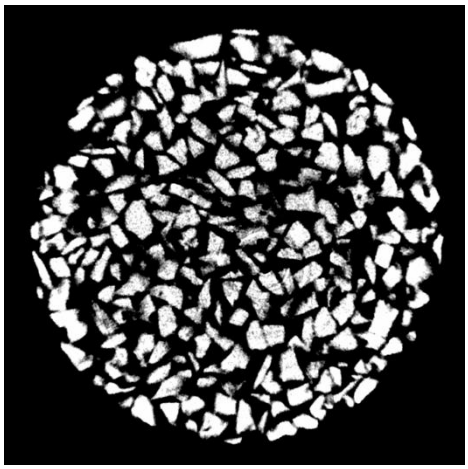
NZ Plus		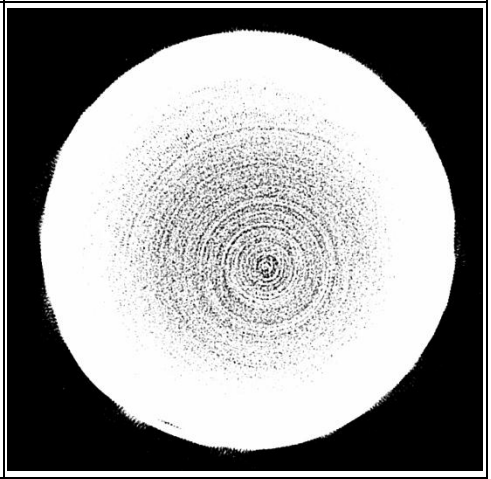
Duralum ATZ	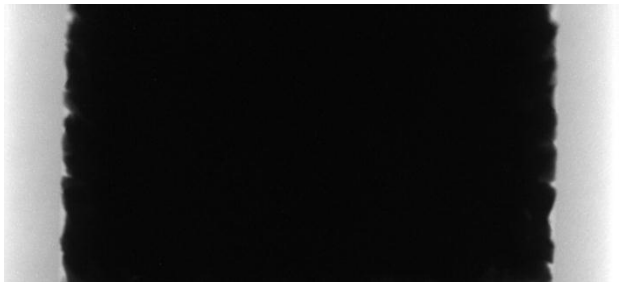	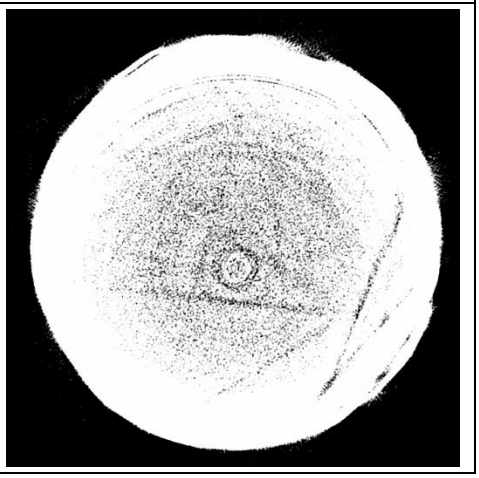

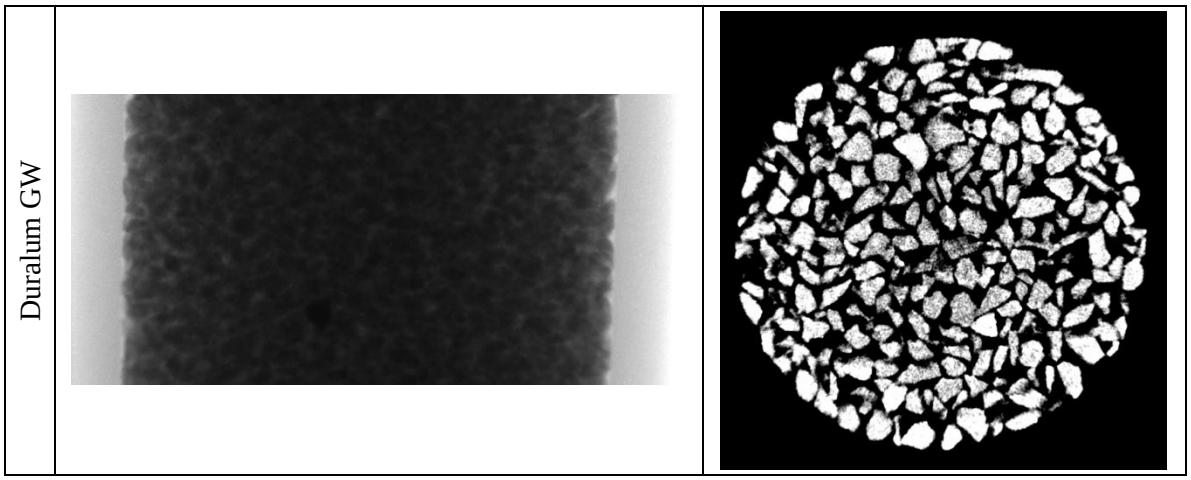

Fig. 3-28. Typical X-ray views and reconstructed slices of the abrasives used during X-ray CT.

Results from X-ray CT indicate that X-ray emissions produced by the Skyscan 1174 compact micro-CT were not able to penetrate samples of NZ Plus and Duralum ATZ. The high X-ray attenuation evidenced by those materials is likely caused by the elevated concentrations of Zirconium (Z=40). Even though increasing the time of exposure could have improved the quality of the slices for NZ Plus and Duralum ATZ, times of exposure higher than 5 s were not used due to the risk of overheating the X-ray source.

CT reconstructions of Duralum GW and Carborex showed only small amounts of noise. The quality of the slices was significantly better than for medium river sand and Ottawa sand (see Fig. 3-9), which have a similar gradation. The improvement in the quality of the slices was likely caused by the presence of small quantities of heavy elements such as iron (Z=26) and titanium (Z=22).

Changes in the structure of samples formed by Duralum GW during one-dimensional compression and a constant vertical stress of 62 kPa were studied using X-ray CT. Samples of Duralum GW were formed following the same procedure used for

samples of sand, which was described in Section 3.4. The specimen was allowed to creep under the constant vertical stress for up to 4 days.

3D reconstructions of the specimen just after, 1 day, and 4 days after the application of the load are shown in Fig. 3-29. Particle displacements during creep are difficult to identify during visual inspection of the three-dimensional reconstructions, which look practically identical.

It was shown that using materials which have small concentrations of heavy elements reduces the amount of noise in the reconstructed slices and allows studying of samples formed by smaller particles. However, characteristics and behaviors of specimens formed by such type of materials may differ considerably from natural sands. Consequentially, results from creep and aging studies conducted on that type of materials may not be necessarily applicable to describe behaviors of real soils.

	Just after Load Application	After 1 day of creep	After 4 days of creep
0° Rotation	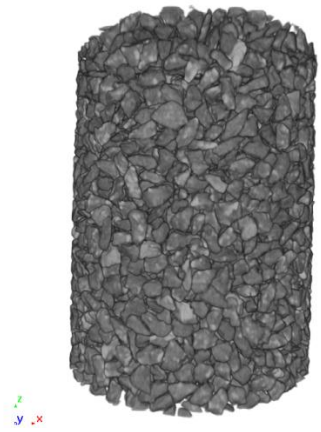		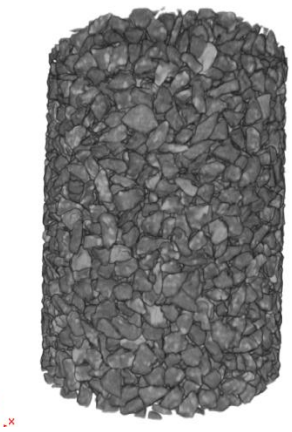
90° Rotation	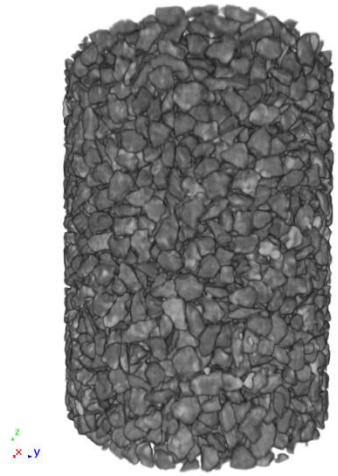	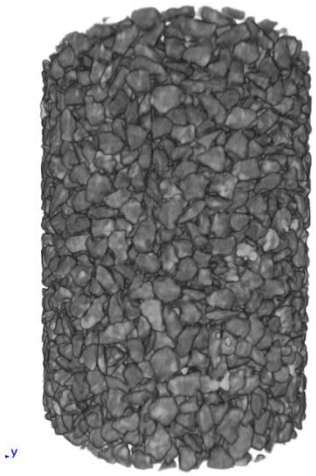	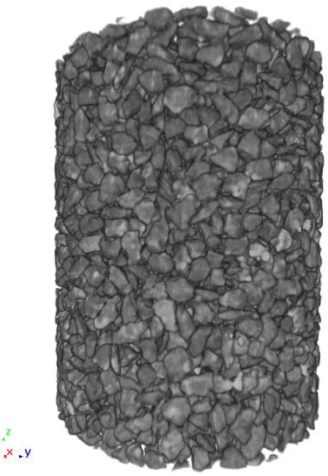
180° Rotation			

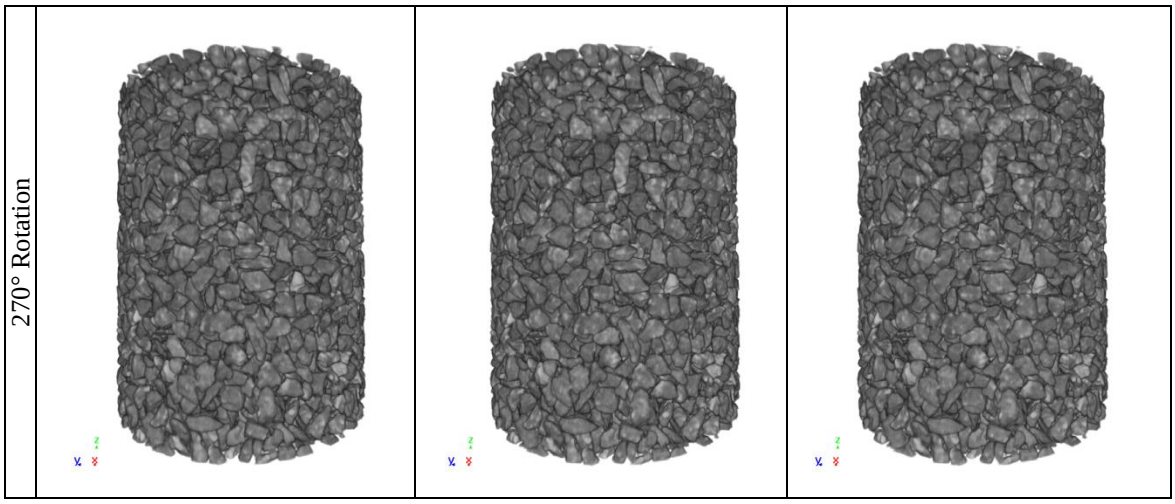

Fig. 3-29. Three-dimensional reconstruction of a section of the sample of Duralum GW abrasive just after, 1day, and 6 days after the application of the load.

3.8 Conclusions

X-ray CT was used to detect particle movements and rotations occurring in samples of reconstituted sand during one-dimensional compression and constant vertical stress. A methodology to detect movements of individual particles was developed and implemented. Some of the main conclusions are:

- Small particle movements and rotations were detected during aging under constant vertical stress and restrained lateral deformation. Their magnitude was too small to be identified by visual inspection.
- Particles rotate during creep, and the inclination of their long-axes becomes more homogeneously distributed as time progresses.
- Particle rotations during aging were very small. Most particles rotated less than 2 degress during the first day of aging. Particles seem to remain moving over time during creep.
- Particle movements during creep were very small. Over 55% of the particles moved less than 0.05 mm during the first day of creep. Particles continued

moving over time, and after 6 days of creep only 12% of the particles had moved less than 0.05 mm. Only one particle moved more than 0.25 mm after 6 days of creep.

- Particle movements seem to occur in clumps throughout the extent of the specimen. Clumps of large particle movement were often surrounded by areas of small displacements.
- Various factors may influence the results of the CT scans. The ratio of the diameter of the specimen container to the diameter of the sand grains is smaller than desired to prevent boundary effects. Also, the load applied (62 kPa) is modest compared to *in situ* vertical stresses for documented field cases of time-dependent property changes.
- Small concentrations of heavy metals such as iron (Z=26) and titanium (Z=22) help to reduce the noise from the reconstituted slices and allow studying granular materials formed by smaller particles using X-ray CT. However, the behavior of samples formed by materials with that type of chemical composition (e.g., Duralum GW, Carborex) may differ considerably from that of natural sands.
- It was shown that particles continue moving and rotating with time during creep. The magnitude of these movements and rotations, although small, lead towards a more homogeneous soil structure, which was evidenced by more evenly distributed long axis orientation. It is still not clear if this internal restructuration of granular materials can account for a significant change in macroscopic properties (that will be evaluated using DEM simulations), but it does point towards physical process as the main driving mechanism of aging in sands.

Chapter 4

Macro-scale Laboratory Experiments

4.1 Introduction

This chapter provides a general description of the methodologies used for macroscopic soil testing to study aging and creep on granular specimens, and a discussion of some of the main findings obtained from the experiments conducted.

Macro-scale laboratory tests were conducted to study changes in the engineering properties of granular materials during aging. Results from laboratory tests will be used to calibrate and validate results obtained from DEM simulations. Macro-scale laboratory experiments include one-dimensional compression tests in fixed ring consolidometers, and creep tests run using triaxial tests. Granular materials with different particle shapes, sizes, strengths, and compositions were tested during the macro-scale laboratory experiments to study the effect that those factors can have on creep and aging processes occurring over time in granular soils.

Acoustic emissions (AEs) produced during creep were recorded using a piezoelectric sensor. AEs have been previously used in geotechnical engineering for the characterization of granular soils and the estimation of properties such as the preconsolidation pressure (Koerner et al. 1976; Koerner et al. 1984; Fernandes et al. 2010). For this investigation, the amount and magnitude of the recorded AEs may provide a qualitative and quantitative estimation of particle rearrangement and changes in the internal structure of the soil occurring during aging.

This chapter also includes a brief theoretical background on acoustic emissions, presenting cases where AE techniques have been implemented in geotechnical practice. A comprehensive explanation of the theory of AEs techniques and their application in engineering practice can also be found in Hardy (2003) and Baranov et al. (2007).

4.2 Acoustic Emissions

4.2.1 Theoretical Background

Acoustic emissions are mechanical elastic waves produced during the rearrangement of the internal structure of a material (Baranov et al. 2007). Most solids produce low-level seismic emissions or AEs when they are stressed or deformed. The amount of AEs emitted is often correlated to the stability of material or structure, where more AEs are emitted as the material becomes more unstable (Obert 1977).

There are several acoustic techniques used to study geotechnical materials. The two most commonly implemented are the sonic technique and the AE technique, which are illustrated in Fig. 4-1. Sonic techniques use a transmitter transducer to generate mechanical signals, which are monitored and recorded by a receiver transducer. Material

characteristics are estimated based on the properties of the acquired signals, and the analysis of alterations experienced by the original signal while traveling through the material. A typical example of sonic techniques is the resonant column method, used to estimate soil properties including the shear modulus and the shear damping (Drnevich et al. 1978).

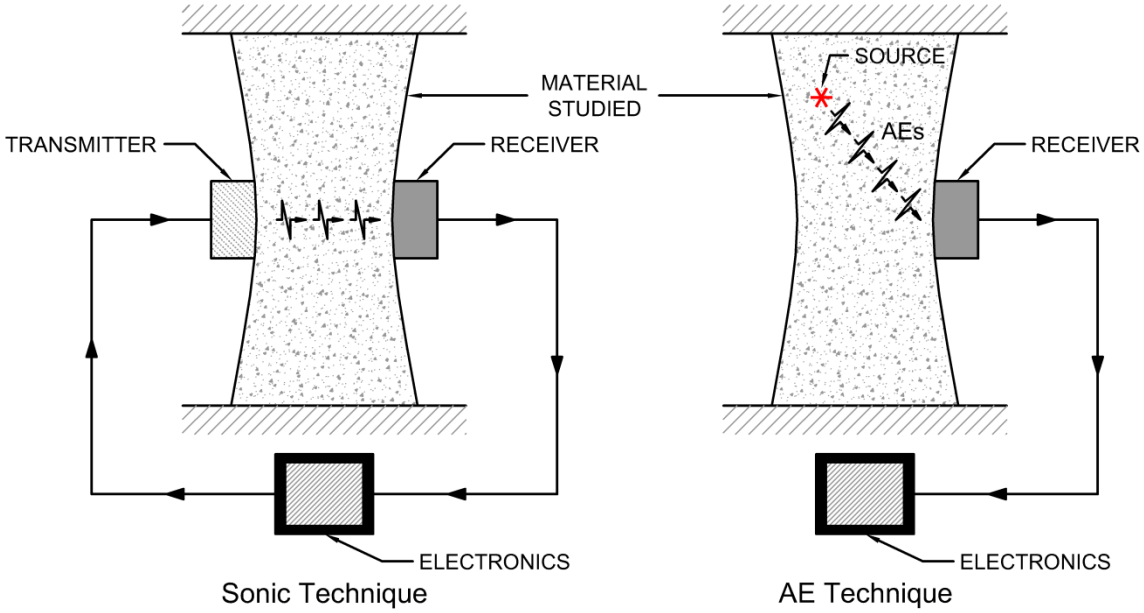

Fig. 4-1. Two acoustic techniques used to study geotechnical materials (modified from Hardy, 2003).

Opposite to sonic techniques, AE techniques do not use transmitter transducers. Instead, AE techniques use one or several receiver transducers to detect acoustic signals which are emitted by the material.

According to Baranov et al. (2007), sources of acoustic emissions in metals include processes occurring during plastic deformation such as grain-boundary slip and twinning. An extended list of possible sources of AEs in metals is presented in Table 4-1. The origin of AEs in geologic materials is not quite clear, but they appear to be related to the release of strain energy caused by dislocations, grain boundary movements, and crack growth (Hardy 2003). For the current investigation, AEs are expected to be primarily

related to particle crushing and inter-particle frictional sliding. The specific source of the AEs is difficult to determine.

Table 4-1. Sources of AEs in metals (Baranov et al. 2007).

AE Source Type	Examples
Mechanisms inducing plastic deformation	• Migration of dislocations • Grain boundary slip • Twinning
Mechanisms related to phase transformation and phase transitions	• Polymorphic transformations • Phase transitions in magnetics and superconductors • Magnetomechanical phenomena
Mechanisms relating to damage	• Microdefects • Growth of cracks • Corrosion damage

AE events contain a wide range of frequencies. According to Hardy (2003), the frequency content of recorded AEs depends primarily on two factors: (1) the characteristics of their source, and (2) the distance between the source and the receiver transducer. AE attenuation is frequency dependent, being greater at higher frequencies, so the frequency spectrum of an AE event changes as it travels through the material. AEs recorded under laboratory controlled conditions often have higher frequency contents than in field studies because the receiver transducer can be placed closer the source, thus reducing the amount of attenuation.

Koerner (1976) suggested that the predominant AE frequency of granular soils ranged between 0.5 and 8 kHz. Hardy (2003) compiled some of the frequency ranges studied during previous AE investigations, which are shown in Fig. 4-2. The identification of the AE frequency range of the event under consideration is important when selecting the AE sensor. For the investigation described in this dissertation, AEs were acquired using a Mouser AB2072S sensor, formed by a flat, circular piezoceramic element with a resonant frequency of 7200 Hz.

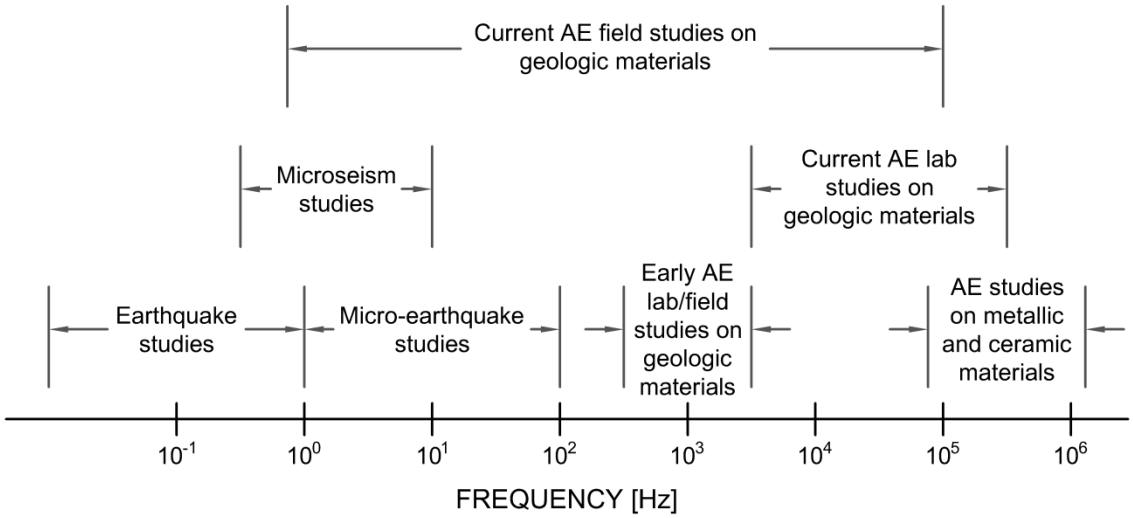

Fig. 4-2. Frequency ranges studied in previous AE investigations (redrawn from Hardy, 2003).

In addition to the frequency content, other characteristics of AE events are often analyzed. These include:

- Amplitude (A): Peak value of an event.
- Total number of pulses: Total number of events observed during a specific time interval.
- AE activity: Total number of pulses per unit time.
- AE count (C): Number of AE signals with amplitude higher than a preset value. The threshold value is often selected based on the energy of the background noise.
- Count rate ($\dot{N}$): Number of AE signals with amplitude higher than a preset value per unit time.
- Amplitude distribution: Number of pulses with amplitudes within small magnitude intervals (dA).

Baranov et al. (2007) related characteristics of AE events recorded in metals to the properties of their source. A list indicating the informative content of some main characteristics of recorded AE events is presented in Table 4-2. It should be noted that

properties of AEs are often affected by numerous factors when travelling through a media. It was previously discussed that attenuation can have considerable effect on the frequency content of AE events. Other properties such as the amplitude also depend on factors, such as the magnitude of the confining stress or the stiffness of the material. Baranov et al. (2007) summarized some of the main factors which increase the amplitude of AE pulses produced during friction sliding. These include: high surface roughness, high hardness, anisotropy of the surface, inhomogeneity of surface properties, coarse grains, low toughness, defects in the surface layer, low temperature, high sliding velocity, heavy loads, dry friction, failure due to micro-cutting (rather than plastic deformation of asperities), and presence of surfactants. Properties such as the AE count and the Count Rate can also be dependent on the gradation of the material and the shape of the grains (Koerner et al. 1976). The existence of numerous factors which influence the properties of recorded AE events makes the identification of their source mechanish difficult.

Table 4-2. Informative content of characteristics of AEs in metals (modified from Baranov et al., 2007).

AE Characteristics	Informative Content
Frequency spectrum	Nature of AE source
Amplitude	Energy of AE source
Amplitude distribution	Type of defects and failure mode (i.e., ductile or brittle failure)
Count rate	Rate of defect growth

4.2.2 Literature Review

Acoustic emissions are produced when materials are subjected to stress or deformation. AEs have been studied since the early 30s and 40s, and were initially

associated to the mechanical stability of rocks, being used to assess the stability of rock tunnels. Obert and Duvall (1942) (cited by Obert, 1977) found that the AE activity increased as the rock material or structure became less stable.

Further development on AE analysis was done by Kaiser (1953) (cited by Koerner, 1984), who noted a relationship between the AE activity and the loading history of metals. He concluded that AEs were primarily emitted after previously applied stresses were exceeded, a behavior commonly referred as the *Kaiser effect*.

Koerner et al. (1976) used a piezoelectric sensor to detect AEs produced during drained triaxial compression of sand drain soil (subangular), Ottawa sand (rounded), concrete sand (angular), and beach sand (sub-rounded). A pickup accelerometer ½" long with a ¾" diameter embedded in the sample was used to detect AEs emitted by the soil. The accelerometer was connected to an amplifier and an electronic counter. Variations in the AE count with respect to time, axial strain, and vertical effective stress were studied for each material. Two different conditions were studied: (1) creep under isotropic confining stress of 5, 10 and 20 psi; and (2) drained triaxial compression. Some of their main conclusions were:

- The predominant AE frequency of granular soils ranged between 500 and 8000 Hz, with the magnitude being affected by the confining pressure.
- Angular particles produce more AEs than rounded ones. Additionally, during creep, samples formed of angular particle emit AEs for longer time periods than samples formed of rounded particles.
- Well graded soils emit more AEs than poorly graded soils.
- Particle size does not have a significant effect on AEs.

Hardy (2003) made an extensive compilation of some of the major historical developments associated with the implementation of AE techniques in geotechnical practice. According to Hardy, early studies of AEs in geotechnical engineering were mainly focused on the stability of underground excavations, driven by the difficulties experienced in mining at increasing depths. The application of AE techniques to predict rock bursts was of particular interest. Since then, most advances have focused on areas such as monitoring slope stability, location of rock bursts, and mine safety (Hardy 2003).

AE analysis is often used to monitor and predict catastrophic events such as slope failure and rock fracture. AE methodologies are rarely implemented in practice to estimate engineering properties of soils. Koerner et al. (1984) used AE analysis to determine the preconsolidation pressure of granular soils based on the Kaiser effect. They conducted one-dimensional consolidation experiments using an oedometer and a pneumatic loading system. AEs were detected and recorded using an Acoustic Emission Technology 204GR single channel system. Five cohesionless soils with a range of particle sizes (d_{10} from 0.0033 to 0.38 mm) and shapes (rounded to angular) were tested. The results indicated that the analysis of recorded AEs could predict reasonably well (within 5%) the preconsolidation pressure of granular soils.

Fernandes et al. (2010) studied AEs emitted during one-dimensional compression of granular soils. They used a hardened steel oedometer to conduct constant rate of deformation one-dimensional compression experiments. Three soils were tested: (1) Ottawa sand (d_{min}=0.6 mm, d_{max}=0.85 mm); (2) heterogeneous, subangular, natural beach sand from northern California formed by quartz and feldspar grains (d_{min}=0.85 mm and

d_{max}=2 mm), and (3) homogeneous carbon chips (d_{min}=0.85 mm, d_{max}=2 mm). AEs were recorded using a circular bender transducer with a free resonant frequency of 7.2 kHz.

Fig. 4-3 shows the variation of the vertical stress (σ), relative breakage (B_r), AE normalized amplitude (A/Amax), and AE count (C) during constant rate of strain ($\dot{\varepsilon}$ =0.05 mm/s) compression tests on Ottawa sand and natural beach sand. The threshold value for the calculation of the AE count was set slightly higher than the normalized signal amplitude measured before the start of the test. The relative breakage, or Hardin's breakage factor (B_r), represents the level of particle crushing at a specific stress. It was determined using additional experiments on identical specimens loaded to vertical stresses less or equal to the to σ_{max} from the AE experiments. The value of B_r was calculated by sieving and comparing the gradation of the material before and after the test. Details on the calculation of B_r can be found in Hardin (1985).

Fernandes et al. (2010) noted that the variation of AE count over time kept "certain parallelism" with the magnitude of the vertical stress during the evolution of the experiments. However, a clear correlation between C and σ could not be derived. Perhaps more relevant for the current investigation is the fact that pronounced AE activity was recorded by Fernandes et al. (2010) at levels of vertical stress corresponding to low values of $B_{r,}$ and were therefore accompanied by minimal particle breakage. That appears to indicate that most AE activity must have been related to particle slippage rather than particle crushing. Additionally, Fernandes et al. (2010) observed that strong-grain soils, such as Ottawa sand, produce higher amplitude AEs than weak-grain soils. Low amplitude AEs can be easily overwhelmed by background noise.

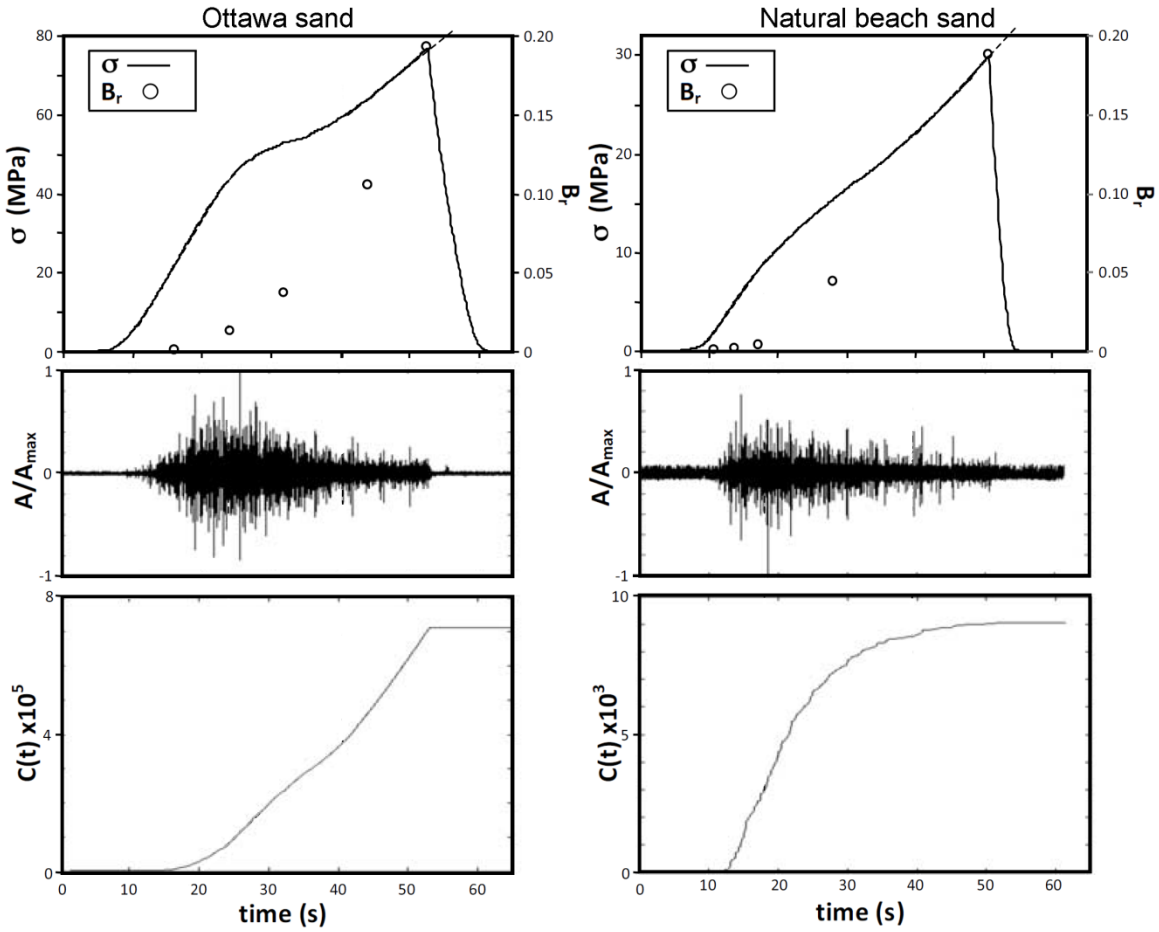

Fig. 4-3. Evolution of vertical stress (σ), relative breakage (B_r), normalized AE amplitude (A/A_{max}), and AE count (C) for Ottawa sand and natural beach sand during one-dimensional compression tests (modified from Fernandes et al., 2010).

AE techniques focus on the study of elastic energy suddenly liberated during the rearrangement of the internal structure of a material. The release of elastic energy is often related to the growth of defects or changes in the internal stress state of the specimen (Baranov et al. 2007). The detection of AEs is therefore useful to study the stress state and damage of materials. Currently, AE techniques are most commonly used for monitoring the stability of underground structures including mines, tunnels, and radioactive waste repositories; and surface structures such as slopes, foundations, dams, and bridge abutments (Hardy 2003).

4.3 Creep during One-Dimensional Compression

Changes in the macroscopic properties and the internal structure of specimens of sand occurring during drained creep were studied during one-dimensional compression tests using a consolidometer. Vertical stresses were applied in two ways: (1) using dead loads, and (2) using automated load actuators. Aging effects, as indicated by changes in the properties of the specimen after creep, were evaluated after periods of creep that ranged from 30 minutes up to 1 day.

4.3.1 Equipment

Two types of equipment were used to apply the vertical stress during one-dimensional compression tests:

- Vertical stress applied using dead loads with a table top consolidation apparatus (ELE 25-0402) with a maximum load capacity of 16000 N (maximum vertical stress of about 5150 kPa on a 63.5 mm diameter sample).
- Vertical stress applied using an automated actuator (Geotac Geojac) with 1.5 in maximum stroke and 2000 lb (8900 N) maximum load capacity (maximum vertical stress of about 2800 kPa on a 63.5 mm diameter sample).

Specimens were prepared by air-pluviation into 2.5 in diameter fixed ring consolidometers. The specimens were then vibrated until the desired initial void ratio was achieved.

AEs were recorded using a Mouser AB2072S sensor connected to the audio input of a personal computer with a 1/8” monaural plug. The sensor was attached to the loading

cap of the consolidometer using conductive epoxy, as recommended by Hardy (2003). The equipment setup is shown in Fig. 4-4.

Fernandes et al. (2010) and Koerner et al. (1984) attached the receiver transducer to the bottom of the fixed ring consolidometer, with Koerner et al. using in addition a 1.14 mm diameter wave guide (i.e., a metallic element used to transfer waves to a receiver) penetrating 6.35 mm inside the sample. For this investigation, attaching the sensor to the metallic loading cap was judged to provide an adequate media for the propagation of AEs from their source to the receiver. Attaching the sensor to the loading cap does not require any special modification to the equipment, resulting in an easy, fast, and practical equipment setup. Furthermore, the loading cap is placed in direct contact with the sample, so acoustic waves do not travel through the porous stones or any other heterogeneous material (besides the specimen itself) before reaching the receiver, thus reducing AE attenuation. Post-processing of acoustic data was done using Matlab and Excel.

(a) (b)

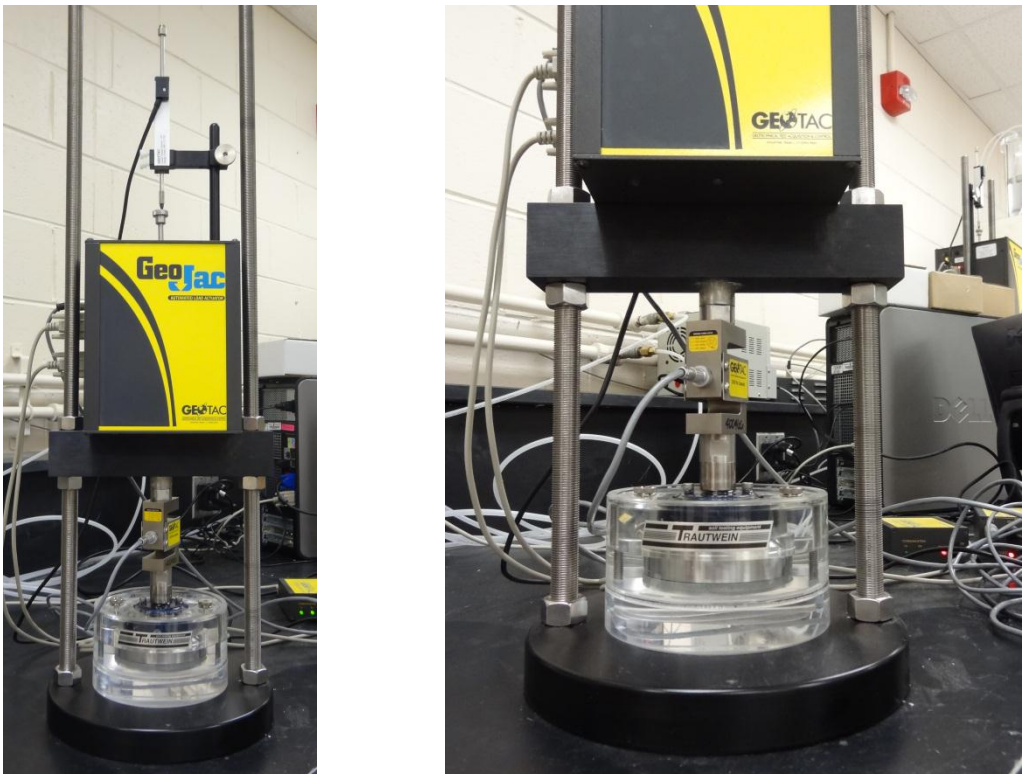

(c) (d)

Fig. 4-4. Setup for one-dimensional compression experiments: (a) loading cap with attached AE sensor, (b) table top consolidation apparatus, (c) automated consolidation equipment, (d) automated consolidation equipment (detail).

4.3.2 Materials

4.3.2.1 General Description

Experiments were conducted using three different granular materials, with different particle shapes and compositions: (1) medium, angular, poorly graded, quartz sand (Silica sand); (2) medium, sub-angular to angular, poorly graded, quartz sand from Berkeley Springs, WV, used in filtering applications (filter sand); and (3) uniform, spherical glass ballotini (glass beads). Some material properties are presented in Table

4-3. The grain size distribution and photos of the material are shown in Fig. 4-5 and Fig. 4-6.

Table 4-3. Properties of materials used for one-dimensional compression tests.

Material	C_u	C_c	d_{50} [mm]
Silica sand	1.59	0.94	0.64
Filter sand	2.03	1.05	0.61
Glass beads	1.23	0.98	0.73

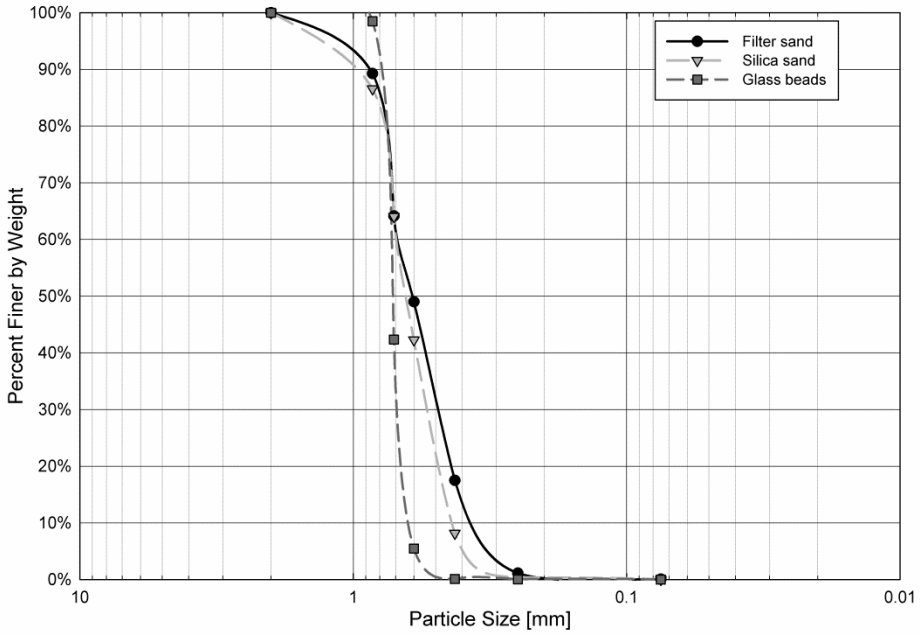

Fig. 4-5. Grain size distribution of materials used during one-dimensional compression tests.

(1) Silica sand

(2) Filter sand

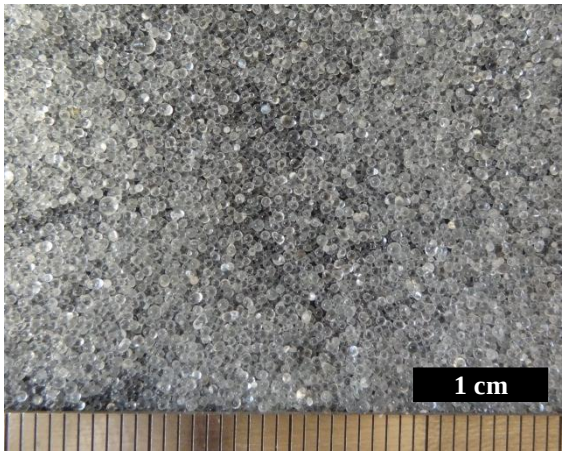

(3) glass beads

Fig. 4-6. Photos of materials used during one-dimensional compression tests.

4.3.2.2 Maximum and Minimum Void Ratio

The maximum (e_{max}) and minimum (e_{min}) void ratios for each material were determined following the specifications ASTM D4253-06 and ASTM D4254-06. Results are summarized in Table 4-4, Table 4-5, and Table 4-6. The values of e_{min} for Silica sand and filter sand were obtained using the wet method, while values for glass beads were determined using the dry method. The wet method was also used for the determination of e_{min} for glass beads, but the material tended to flow through the opening formed between the mold and the surcharge base plate, locking the plate and inhibiting the compaction of the material. Values of e_{min} calculated using the wet method were greater than the values obtained by the dry method.

Table 4-4. Maximum and minimum void ratio of Silica sand (wet method).

	e_{max}	e_{min}	$\gamma_{dry\ min}$ [gf/cm3]	$\gamma_{dry\ max}$ [gf/cm3]
	0.82	0.55	1.45	1.71
	0.81	0.56	1.46	1.70
	0.81	0.55	1.46	1.71
Average=	**0.81**	**0.55**	**1.46**	**1.71**

Table 4-5. Maximum and minimum void ratio of filter sand (wet method).

	e_{max}	e_{min}	$\gamma_{dry\ min}$ [gf/cm3]	$\gamma_{dry\ max}$ [gf/cm3]
	0.88	0.70	1.41	1.56
	0.91	0.68	1.39	1.57
	0.92	0.70	1.38	1.56
Average=	**0.90**	**0.69**	**1.39**	**1.56**

Table 4-6. Maximum and minimum void ratio of glass beads (dry method).

	e_{max}	e_{min}	$\gamma_{dry\ min}$ [gf/cm3]	$\gamma_{dry\ max}$ [gf/cm3]
	0.66	0.52	1.51	1.65
	0.64	0.56	1.52	1.60
	0.68	0.56	1.49	1.60
	0.67		1.50	
Average=	**0.66**	**0.55**	**1.51**	**1.62**

The effect of the specimen's initial density on the aging mechanism in granular soils was evaluated by conducting creep experiments on samples reconstituted to different void ratios. Samples of Silica sand and filter sand with relative densities (D_r) of 30% (loose) and 80% (dense) were used in the experiments. Samples formed of glass beads were prepared to a relative density of about 40%. Only one value of relative density was studied for glass beads because of the small difference between e_{max} and e_{min}.

4.3.2.3 Sphericity

Images of the material were acquired using a digital microscope with a magnification of up to 100x. Images with 20x and 40x magnification are shown in Fig. 4-7. The sphericity of the grains was estimated by calculating the ratio of the maximum (D_{max}) to minimum (D_{min}) diameters, which were measured from the microscope images.

A typical example for Silica sand is shown in Fig. 4-8. Approximately 60 grains were measured for each material. Results are presented in Table 4-7.

Table 4-7. Material sphericity.

Material	**Maximum** D_{max}/D_{min}	**Minimum** D_{max}/D_{min}	**Mean** D_{max}/D_{min}	**Standard Dev.** D_{max}/D_{min}
Silica sand	2.61	1.00	1.45	0.34
Filter sand	2.00	1.01	1.40	0.25
Glass beads	1.95	1.00	1.09	0.17

Grains of filter sand are slightly more spherical than those of Silica sand. Also, glass bead particles are not completely spherical, and in some cases the ratio of the maximum to minimum diameter of the particles can be close to 2.0. High values of D_{max}/D_{min} seem to be related to joined grains. Values included in Table 4-7 will be used in the following chapters to generate DEM arrangements formed by particles with shapes similar to the grains of these materials.

4.3.2.4 Grain Strength

The strength of the grains was evaluated using a simple crushing test, where individual soil particles were placed over a metallic disk and crushed using force applied by a steel piston. A schematic diagram of the equipment is shown in Fig. 4-9. The vertical load was applied using a lever arm connected to the piston.

	20x Magnification	40x Magnification

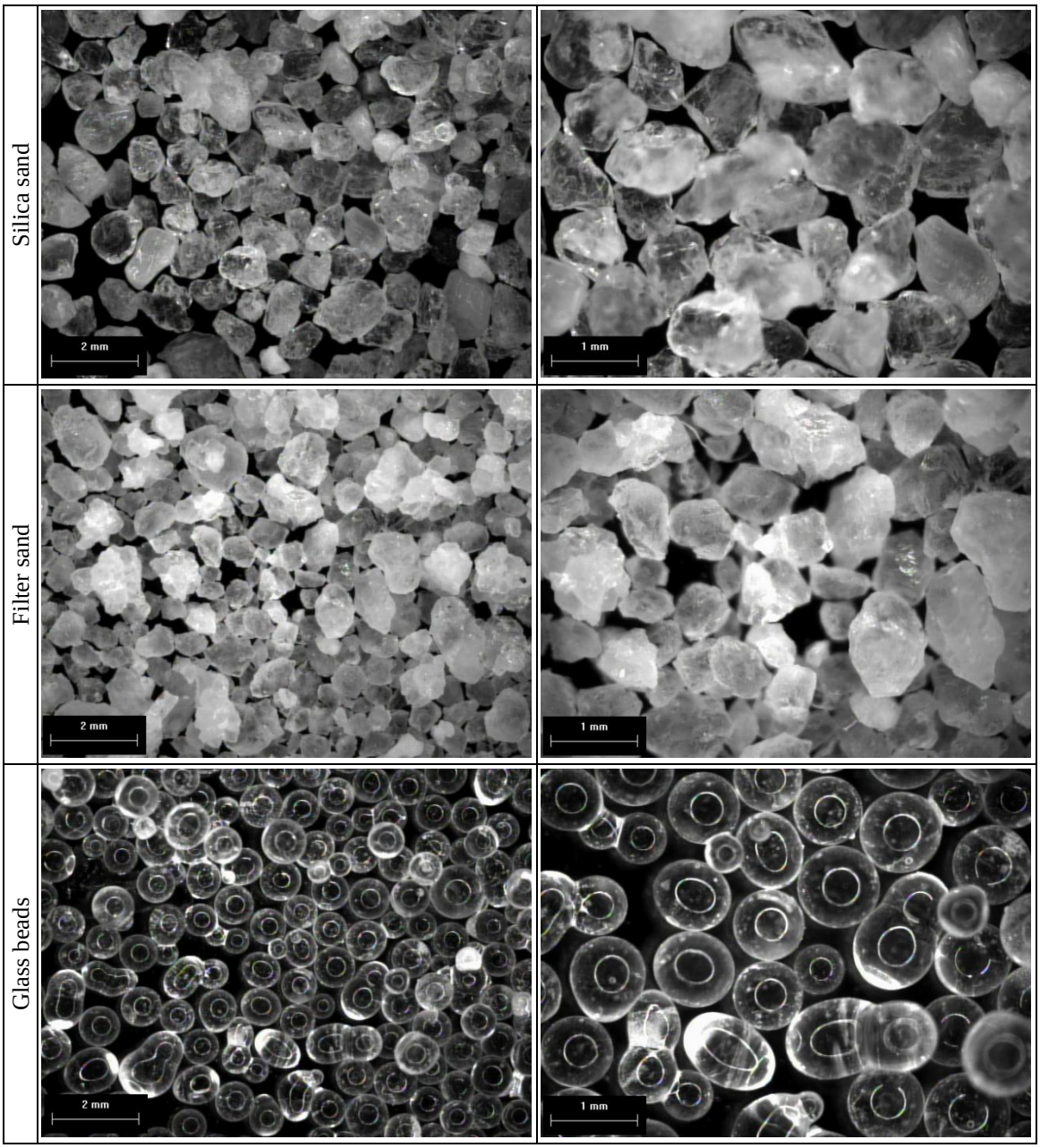

Fig. 4-7. Microscope images of materials used for one-dimensional compression tests.

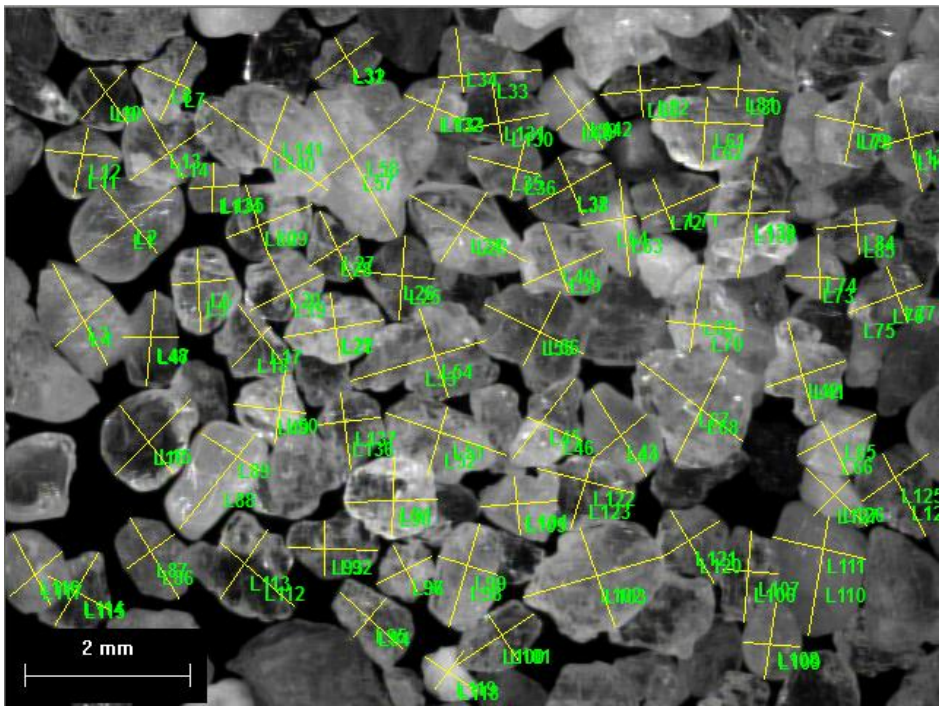

Fig. 4-8. Microscope image at 20x magnification of Silica sand showing the maximum and minimum diameters measured for each grain.

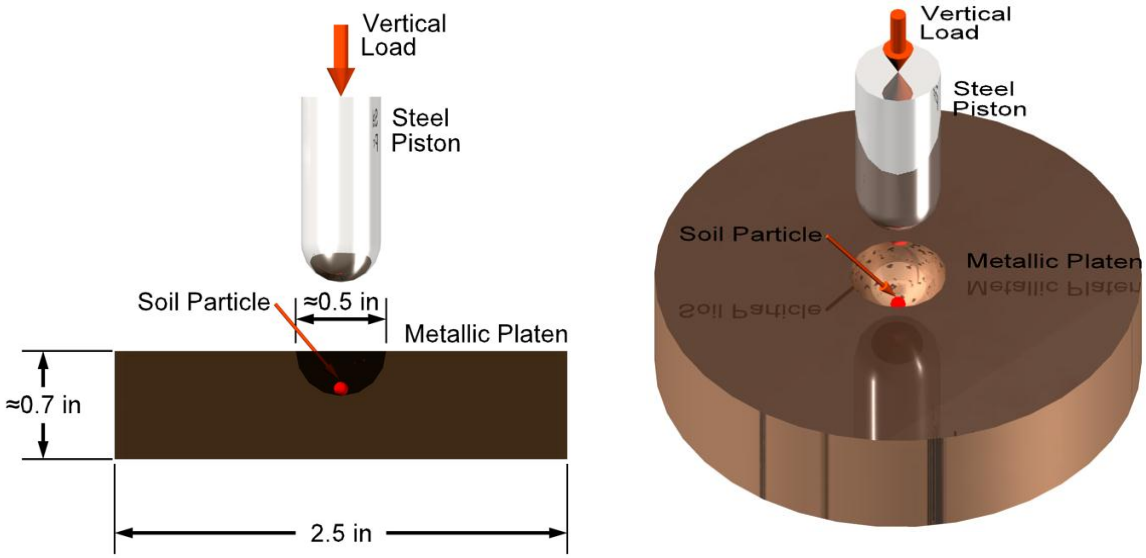

Fig. 4-9. Schematic of the equipment used for particle crushing.

The load was gradually increased by filling a container with water connected to the lever arm until failure, which was defined as a sudden and large increase in axial deformation with no change in vertical load, was reached.

Crushing tests were conducted on grains of Silica sand and glass beads. Results from these tests showing the vertical deformation-vertical load relationships are presented in Fig. 4-10 and Fig. 4-11. The crushing load determined for each of the tests is shown in Fig. 4-12.

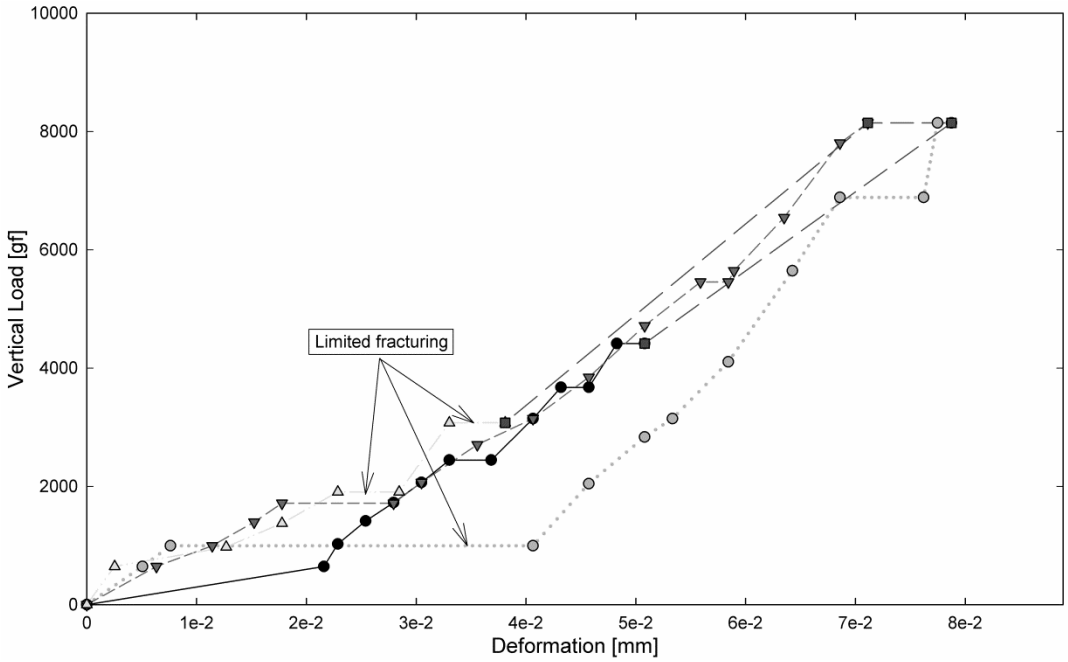

Fig. 4-10. Vertical load-vertical deformation relationship for Silica sand.

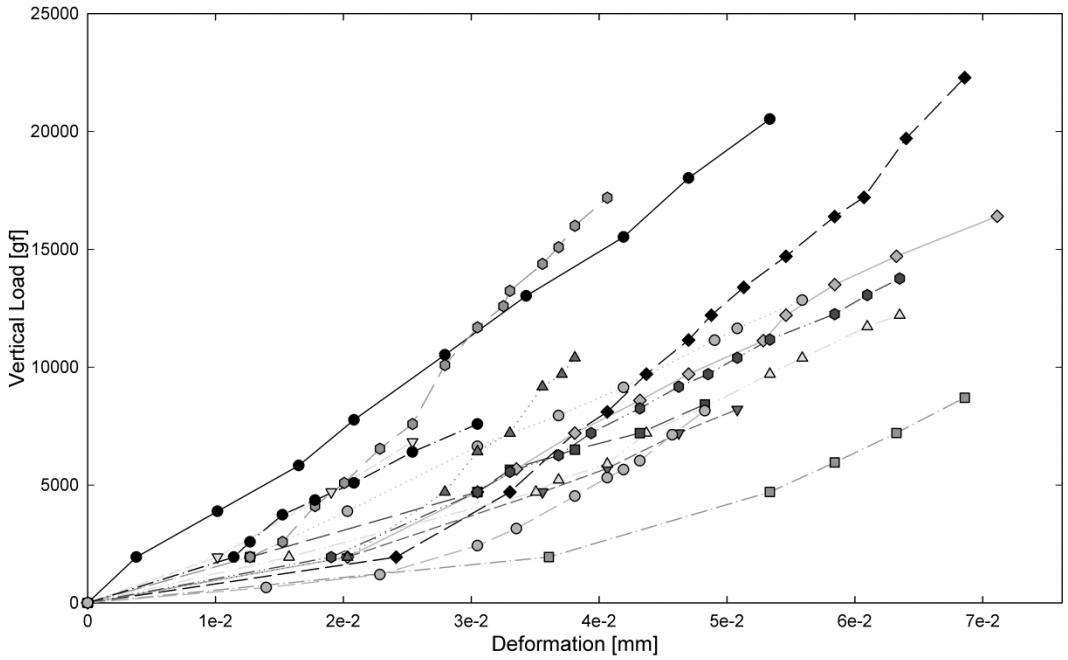

Fig. 4-11. Vertical load-vertical deformation relationship for glass beads.

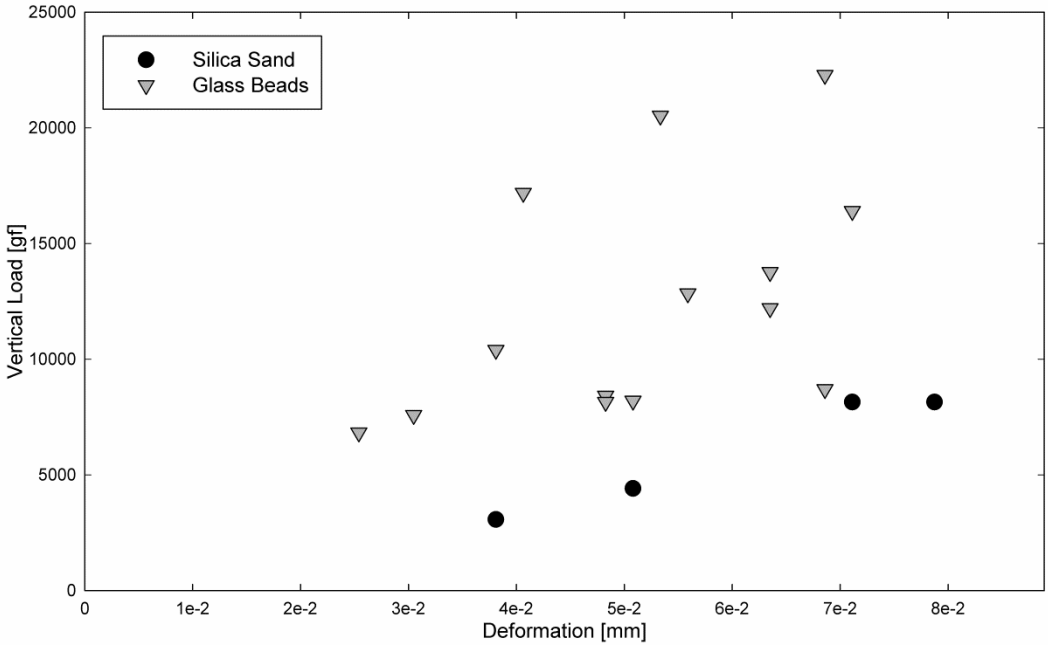

Fig. 4-12. Crushing load for grains of Silica sand and glass beads.

According to the results, glass beads have higher strength and show smoother load-deformation curves than Silica sand grains. Glass beads fail suddenly, turning into fine powder. Grains of Silica sand show limited fracturing before ultimate failure, resulting in saw tooth-like load-deformation curves.

The information obtained from crushing experiments on Silica sand and glass beads will be used in following chapters to generate DEM arrangements formed by particles that resemble these materials.

4.3.3 Test Setup

The specimens and the equipment used for one-dimensional compression experiments conducted for this research were prepared according to the following procedure:

- Specimens were prepared by air-pluviation of air-dried material into a 2.5 in diameter fixed ring consolidometer.

- The specimen was vibrated until the desired initial relative density was achieved.
- The consolidometer was placed on the consolidation apparatus. The loading cap with the attached AE receiver transducer is placed on top of the specimen.
- An initial vertical stress of 170 kPa is applied, and the sample was allowed to creep for 30 min. AEs were captured by the receiver transducer and recorded in a personal computer.
- After finalizing the creep stage, the vertical stress was doubled and the specimen was allowed to creep again for 30 min. The process was repeated until a vertical stress of 1360 kPa is reached.
- The same process was followed for samples prepared to the same initial void ratio, but allowing longer periods of creep after the application of each load. Creep periods of 30 min, 3 hours, and 1 day were used.

4.4 Creep during Triaxial Compression

During triaxial compression experiments, creep and aging in granular materials are evaluated by allowing the sample to creep under constant anisotropic confining stresses under drained conditions. Aging effects on the macroscopic properties of the specimen (e.g., stiffness, strength) are evaluated by continued shearing of the specimen after the creep stage is completed.

4.4.1 Equipment

An automated Geotac Sigma 1 load frame (Trautwein Soil Testing Equipment Company) with a maximum load capacity of 5000 lb was used for these experiments. Additional equipment included two Digiflow automated flow pumps with a maximum

capacity of 300 psi, used to control the confining stress and back pressure. Deviator loads were measured using an external 500 lb load cell. Temperature of the pore fluid was measured and the ambient temperature was controlled during the experiments.

AEs were recorded using a Mouser AB2072S sensor, with a resonant frequency of 7200Hz, connected to a personal computer. The setup was similar to that used for AE acquisition during one-dimensional compression, as described in Section 4.3.1. The installation of the AE receiver transducer for triaxial experiments presented a particular challenge. If the transducer needs to be installed directly on the specimen, special modifications to the equipment are required to pass the electrical connections from interior of the pressurized jacket to the external recording equipment. Additionally, special and expensive high-pressure liquid-tight AE receiver transducers are required. Details on equipment modifications used for the direct installation of receiver transducers for AE analysis during triaxial experiments can be found in Khair (1972) and Byerlee and Lockner (1977).

Receiver transducers can also be installed outside the confining jacket, therefore measuring emitted AEs indirectly. However, indirect mounting techniques introduce some difficulties to the AE analysis. Because indirect mounting increases the distance between the source of the emissions and the receiver, the recorded sound wave can be affected by the reflection of the primary emission on the boundaries of the loading system (Hardy 2003). If the rate of events is low, the reflected waves can be either manually or systematically eliminated from the recorded data. However, for high rate events, this process becomes very difficult. It is expected that reducing the distance from the receiver

to the source, and selecting an acoustic path of low heterogeneity will help reduce the effect of reflected waves on the recorded events.

Three different alternatives were considered for the installation of the AE receiver transducer during this investigation, as shown in Fig. 4-13. The receiver transducer was finally attached to the metallic bottom plate of the triaxial cell (Alternative 1 in Fig. 4-13) using conductive epoxy. The bottom plate was selected because it offers a more direct acoustic path between the source of the AEs and the receiver transducer, and provides also a flat surface that facilitates the installation of the sensor and allows full contact with the receiver. One of the main drawbacks of this setup is the obstacle imposed by the acrylic lower loading platens. The low stiffness of the acrylic compared to the metallic bottom plate causes dissipation and reflection of incoming AEs. Even though this effect may influence the recorded acoustic signal, overcoming that impediment is very complex and would require additional modifications to the equipment. The receiver was finally installed on the bottom plate to reduce the complexity of the experimental setup, which is shown in Fig. 4-14.

4.4.2 Materials

The same materials described in Section 4.3.2 were used for the creep experiments during triaxial compression. Samples of Silica sand and filter sand were reconstituted to approximately 30% (loose) and 80% (dense) relative density, and samples of glass beads were prepared to a relative density of close to 40%.

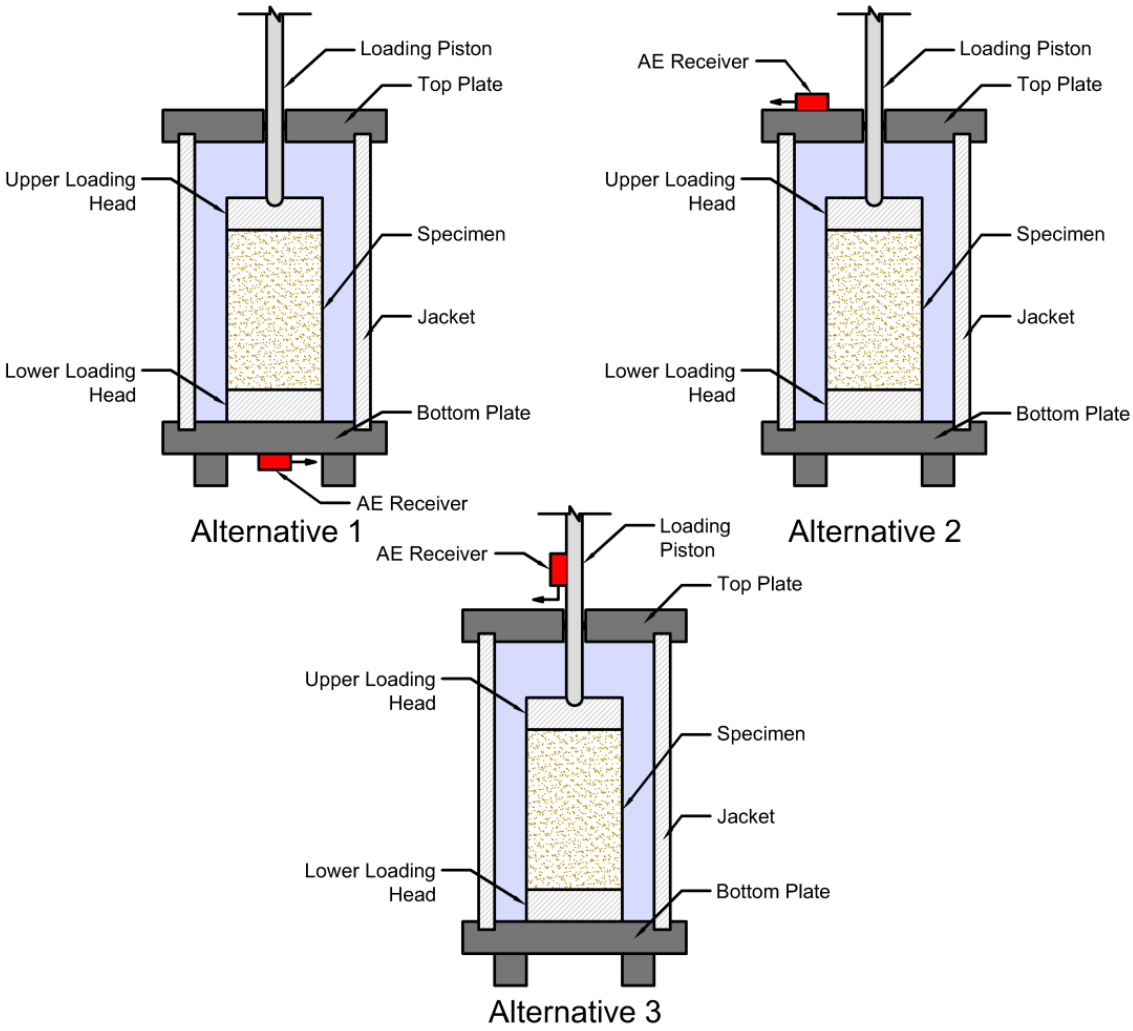

Fig. 4-13. Schematic of the locations for the installation of the AE receiver transducer considered for this investigation (not to scale).

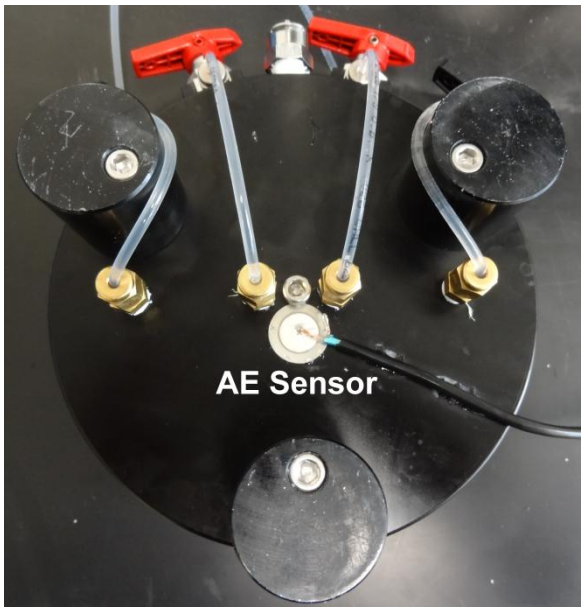

(a)

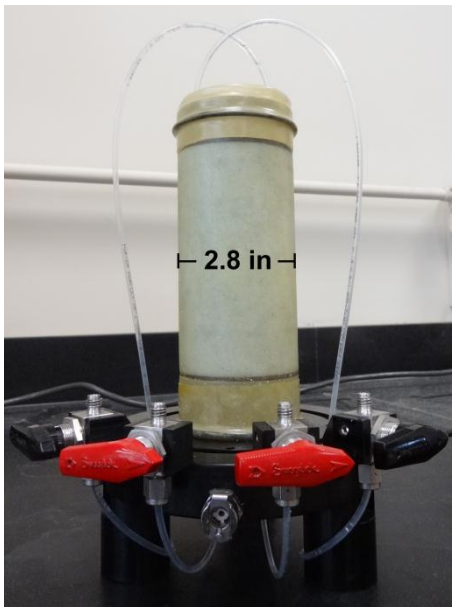

(b)

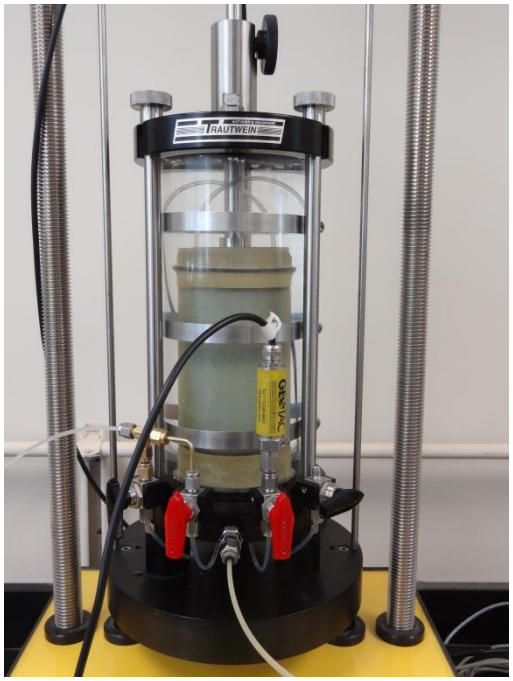

(c)

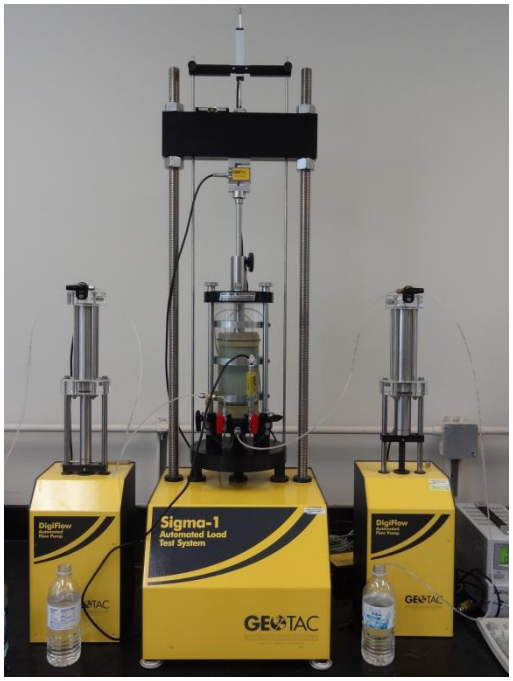

(d)

Fig. 4-14. Setup for triaxial compression experiments: (a) bottom plate of triaxial cell with attached AE sensor, (b) 2.8 in diameter sample, (c) mounted triaxial cell, (d) load frame and flow pumps.

4.4.3 Test Setup

The initial step of the experiment involves preparing 2.8” diameter samples using the Modified Moist Tamping (MMT) method (Bradshaw 2006), based on the

undercompaction approach developed by Ladd (1978). A magnitude of 1% under-compaction was selected for this study. Samples were prepared in 6 layers. Specimens of Silica sand and filter sand were compacted moist (water content of 5%), and glass beads were compacted dry. Once the specimen was prepared, the sample was mounted on the equipment and tested. The experimental procedure used is summarized below:

- The triaxial cell was assembled and a small seating pressure was applied.
- Back pressure of 50 psi was applied to saturate the specimen. A small confining pressure ($\sigma'_3 \approx 5$ psi, $\sigma_3 \approx 55$ psi) is applied during the saturation stage.
- An effective isotropic confining stress of 10 psi ($\sigma_3 \approx 60$ psi) is applied to the specimen.
- Following consolidation, the deviator stress (σ_d) was increased at a constant strain rate of 0.02% min^{-1} until a stress level (SL= $\sigma_d/\sigma_{d\,max}$) of about 25% is reached.
- The specimen was allowed to creep during 3 hours under constant vertical and horizontal confining stresses (SL=25%).
- After 3 hours, the deviator stress was increased up to a stress level of about 50%, and the specimen was allowed to creep again for an additional 3 hours under constant confining stresses.
- The same process was repeated for a stress level of about 75%.
- After the last creep stage (SL≈75%) the sample was sheared until failure at a constant strain rate of 0.02% min^{-1}.

Creep periods of 3 hours were used based on recommendations by Kuwano and Jardine (2002) to lessen the effect of temperature changes in the results. Long-term creep

strains in sand are small and the measured deformations are easily influenced by minute fluctuations in temperature, making the results unreliable.

The same process was followed to test samples with the same initial void ratio, but not allowing the specimen to creep during the experiment (i.e., regular drained triaxial compression tests at an axial strain rate of 0.02% min^{-1}). These experiments provide a reference to estimate the effect of creep and aging on macroscopic properties of the specimens such as the secant modulus, strength, and dilatancy.

4.5 Analysis of Results

4.5.1 Creep and Aging during One-Dimensional Compression

4.5.1.1 Macroscopic Stress and Strain

Results from one-dimensional compression tests showing the variation in void ratio with respect to the vertical stress for loose ($D_r \approx 30\%$) and dense ($D_r \approx 80\%$) samples of Silica sand are shown in Fig. 4-15 and Fig. 4-16. The figures include results from experiments where samples were allowed to creep for periods of 30, 180, and 1440 min after the application of each load. The results shown in this and the following sections take into account the deflection of the equipment, which is subtracted from the measured strains.

The figures show that the change in void ratio after the application of the vertical stress is very small, as is expected for samples of sand. The magnitude of that change is in many cases smaller than the deviation of the specimen's initial void ratio from the desired value (i.e., e=0.73 for loose and e=0.60 for dense samples). Some deviation from

the required initial void ratio is expected due to the small thickness of the samples (approximately 1.0 in thick); e.g., a change of 0.1 mm in specimen thickness results in a deviation of about 0.1 in the initial void ratio of the sample.

The information in Fig. 4-15 and Fig. 4-16 can also be expressed as a variation in axial strain ($\Delta\varepsilon_a$) with respect to the change in vertical stress ($\Delta\sigma_v$), as shown in Fig. 4-17 and Fig. 4-18. Note that specimens allowed to age for periods of 30, 180, and 1440 min exhibit similar $\Delta\varepsilon_a$ versus $\Delta\sigma_v$ relationships.

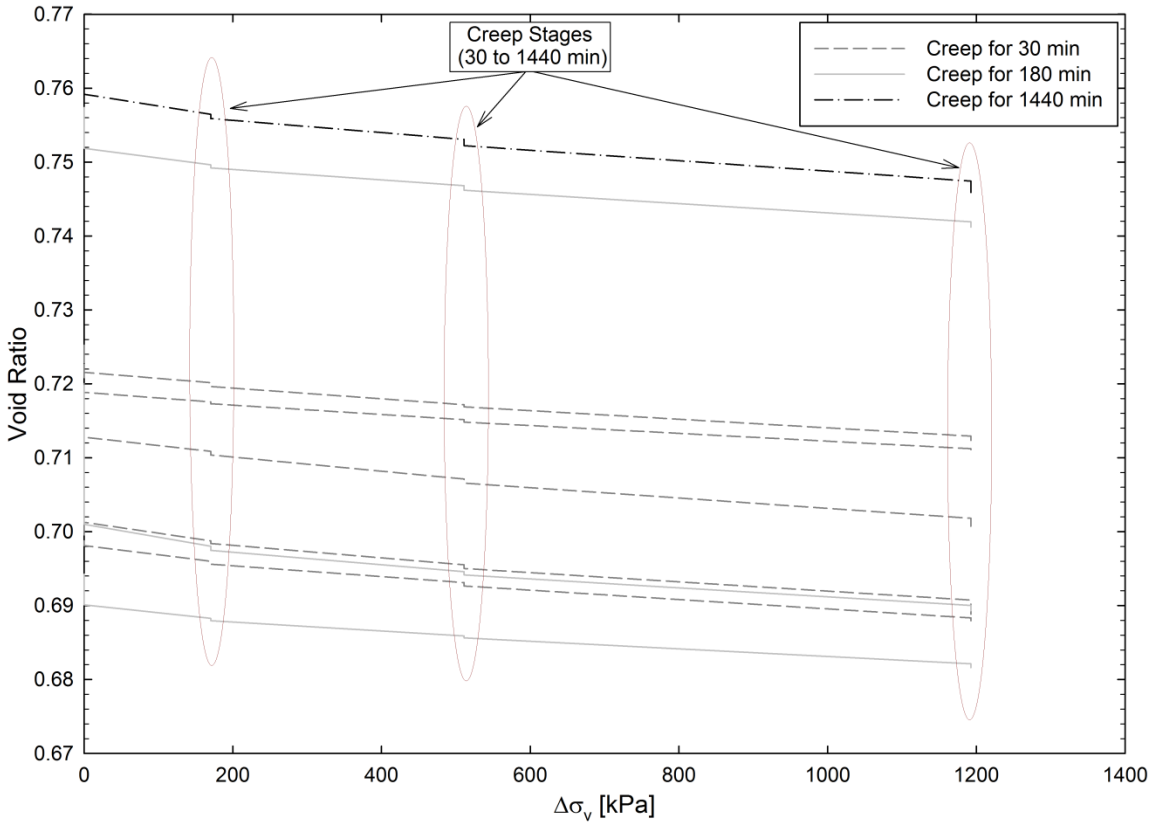

Fig. 4-15. Change in void ratio versus vertical stress for loose Silica sand. Specimens aged for 30, 180, and 1440 min.

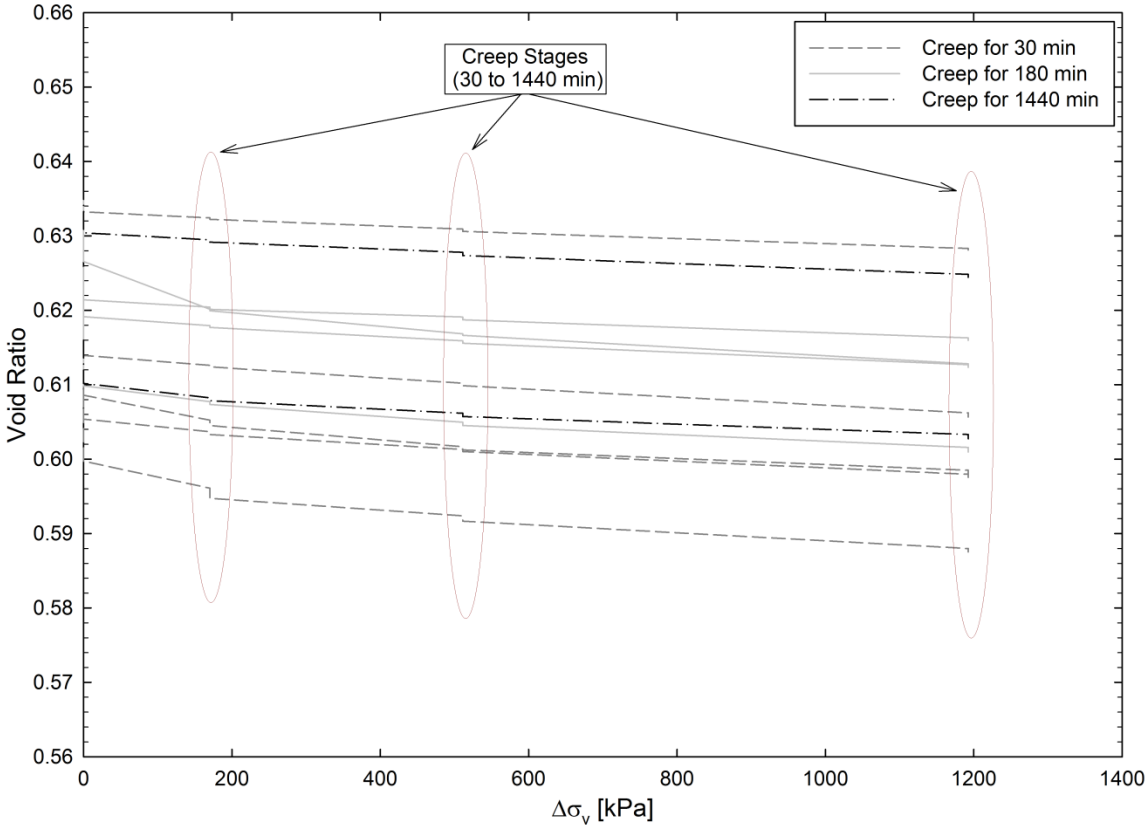

Fig. 4-16. Change in void ratio versus vertical stress for dense Silica sand. Specimens aged for 30, 180, and 1440 min.

The effect of the length of the creep period on the stress-deformation characteristics of the material can also be evaluated by calculating the constrained modulus (*M*) using the following equation:

$$M = \frac{\Delta\sigma_v}{\Delta\varepsilon_a} \tag{14}$$

where $\Delta\sigma_v$ is equal to 170, 340, or 680 kPa according to the load step considered, and $\Delta\varepsilon_a$ is the deformation recorded after the application of each load. Values of *M* determined for loose and dense specimens of Silica sand are shown in Fig. 4-19 and Fig. 4-20. The figures show the mean and standard deviation (error bars) calculated for specimens allowed to creep for the same periods of time.

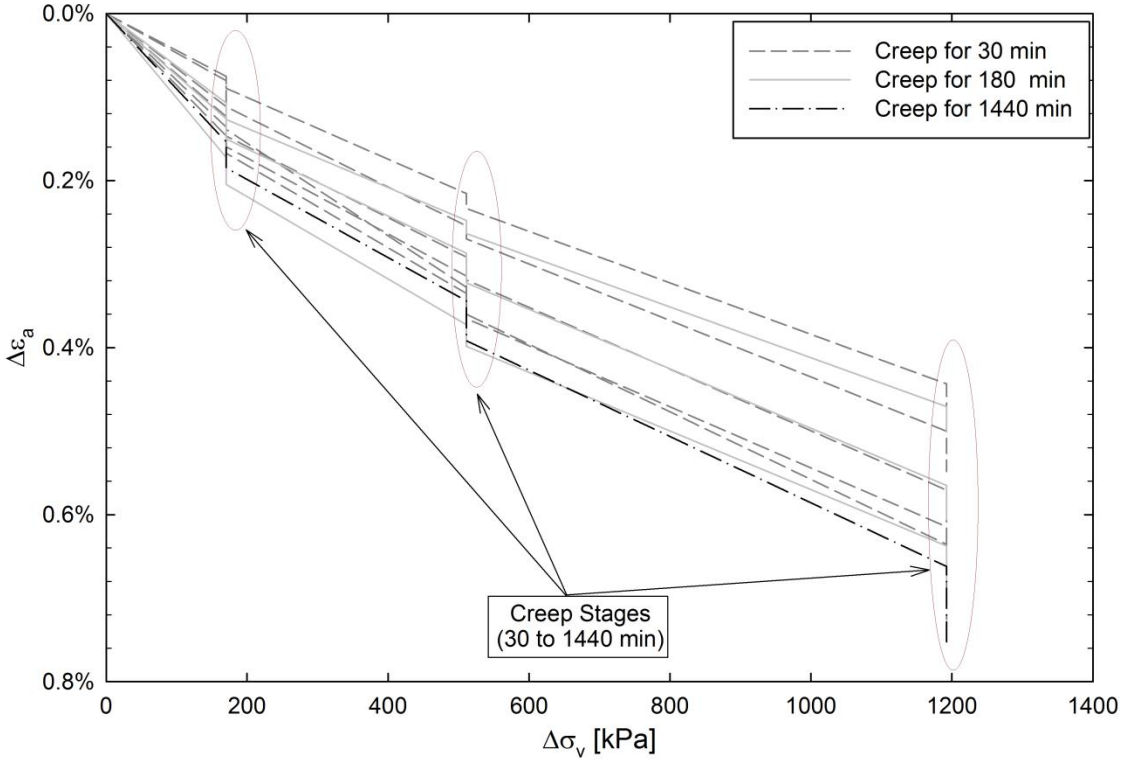

Fig. 4-17. Change in axial strain versus change vertical stress for loose Silica sand.

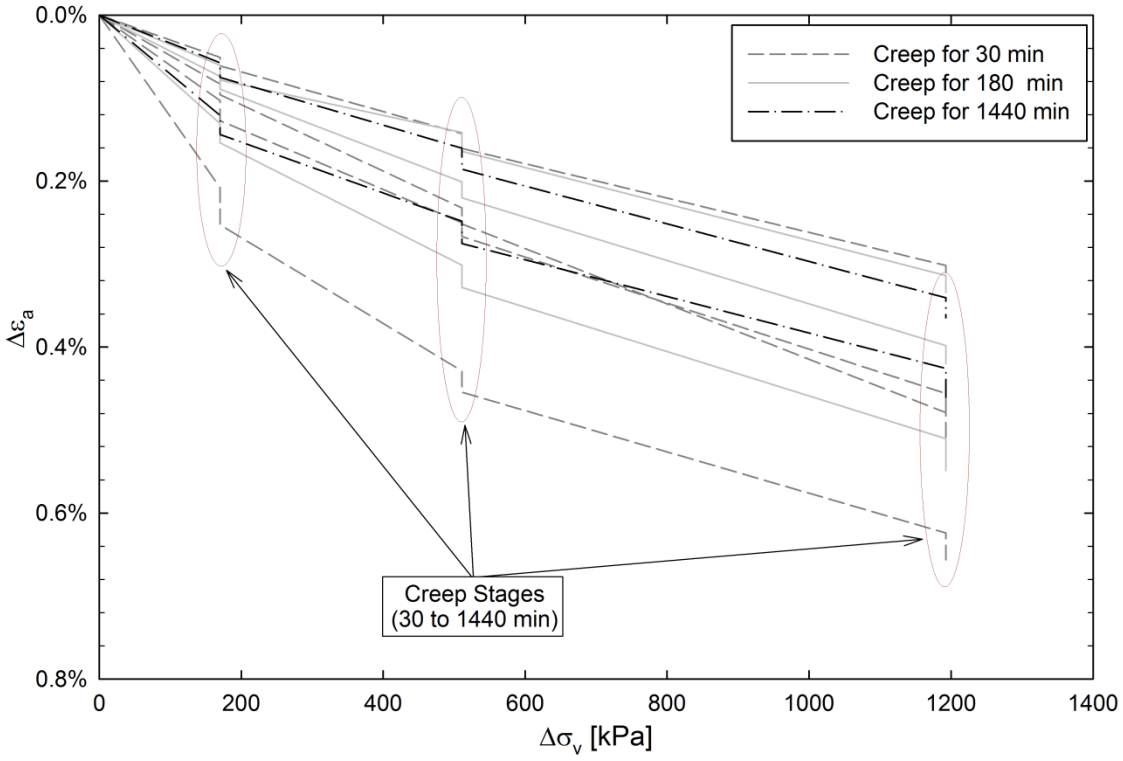

Fig. 4-18. Change in axial strain versus change vertical stress for dense Silica sand.

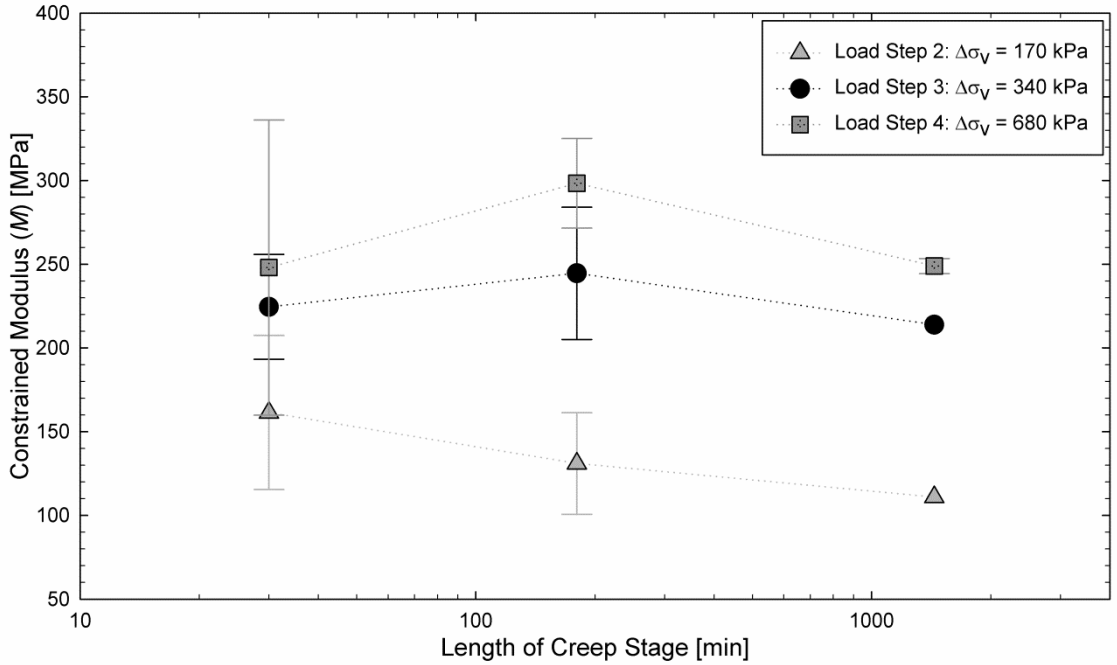

Fig. 4-19. Constrained modulus (*M*) of loose Silica sand.

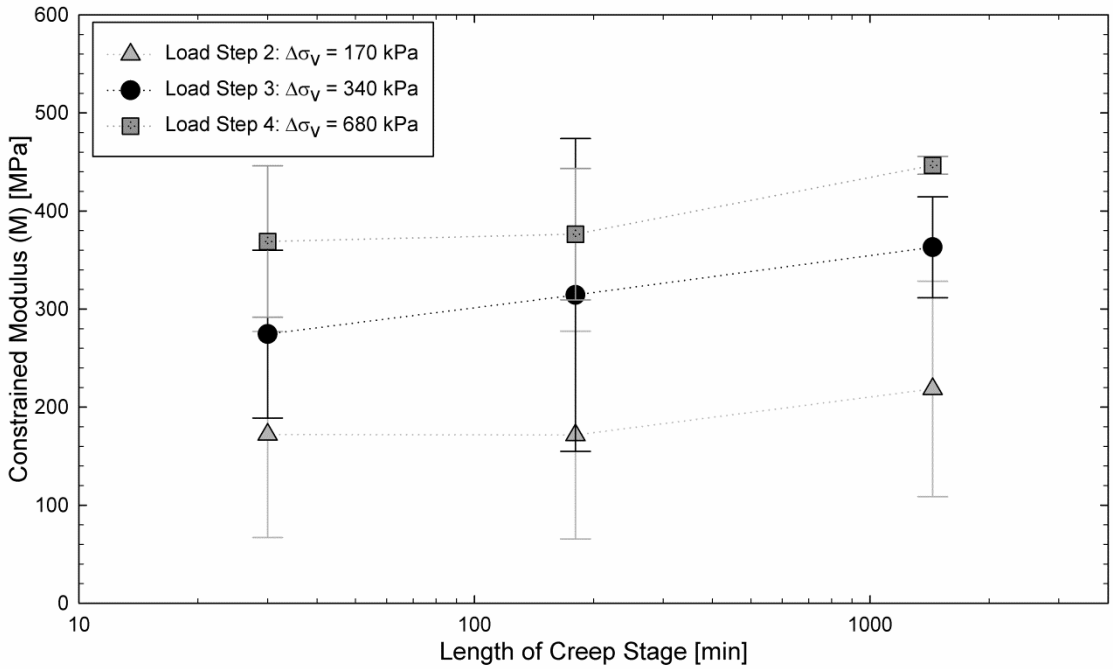

Fig. 4-20. Constrained modulus (*M*) of dense Silica sand.

The results show greater magnitudes of *M* for dense samples under greater vertical stresses, as was expected. The length of the creep stage before the application of each load does not affect the magnitude of the *M*. Only dense samples seem to show a

small increase in the magnitude of *M* for greater times of creep. However, the magnitude of that change is well within the data dispersion.

The variation of the axial strain with time during creep for specimens of loose and dense Silica sand is shown in Fig. 4-21 to Fig. 4-24.

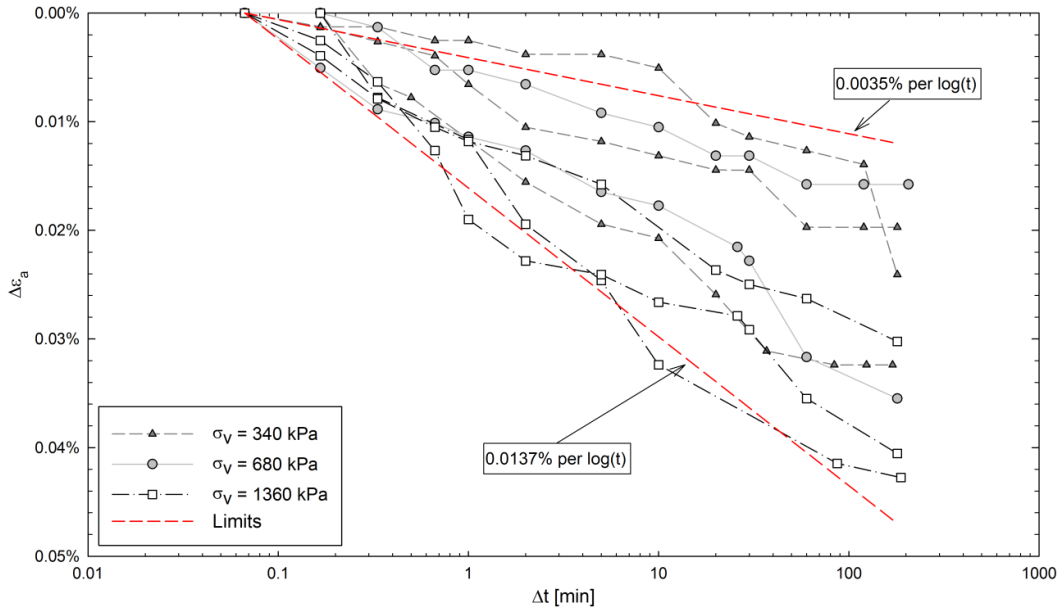

Fig. 4-21. Change in axial strain with time during creep for loose Silica sand. Specimens aged for 180 min.

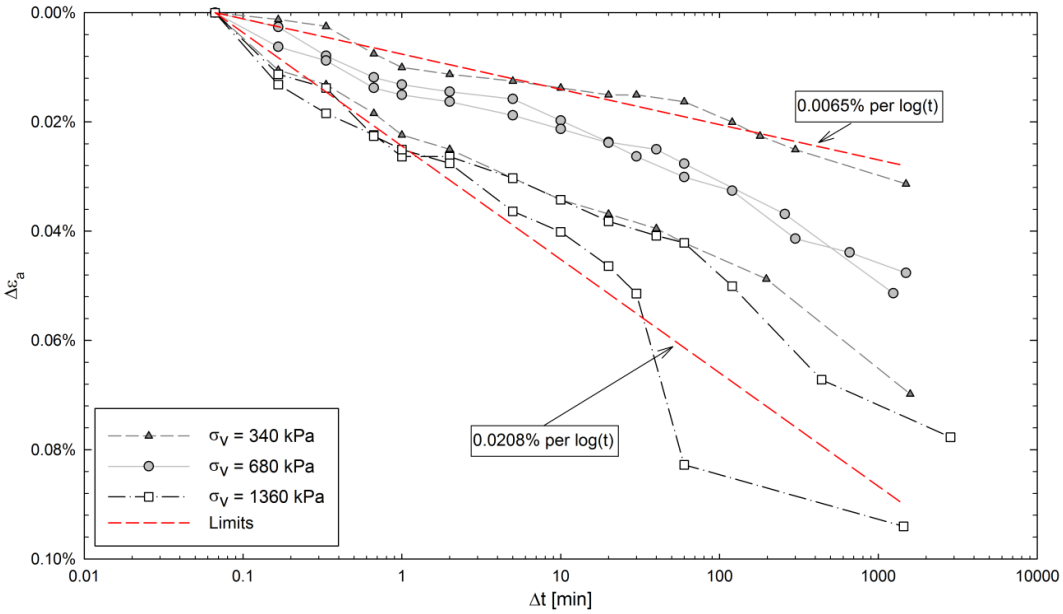

Fig. 4-22. Change in axial strain with time during creep for loose Silica sand. Specimens aged for 1440 min.

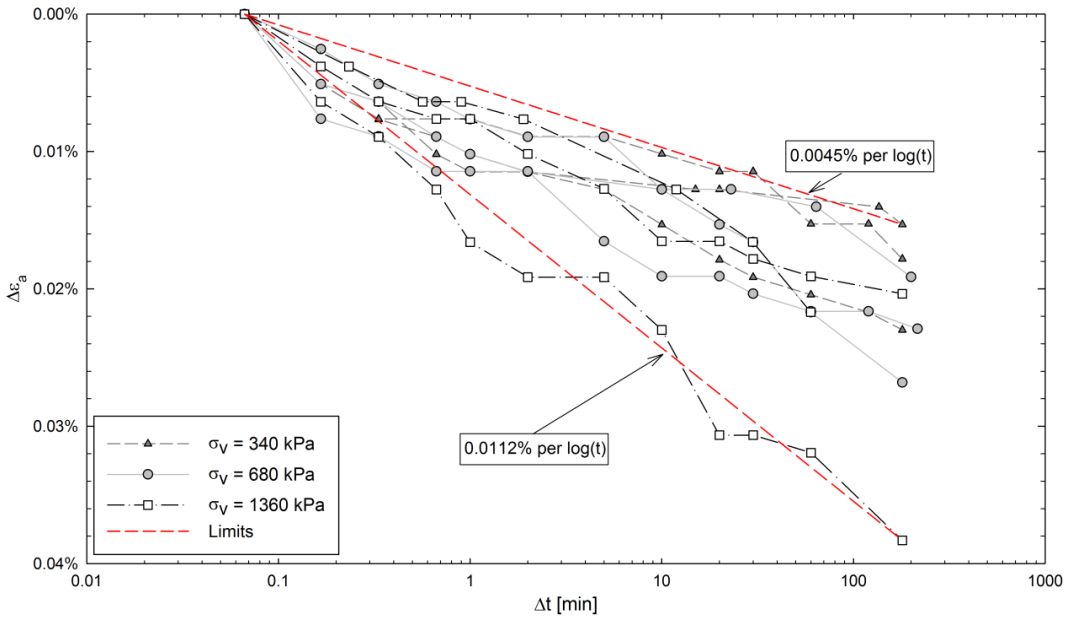

Fig. 4-23. Change in axial strain with time during creep for dense Silica sand. Specimens aged for 180 min.

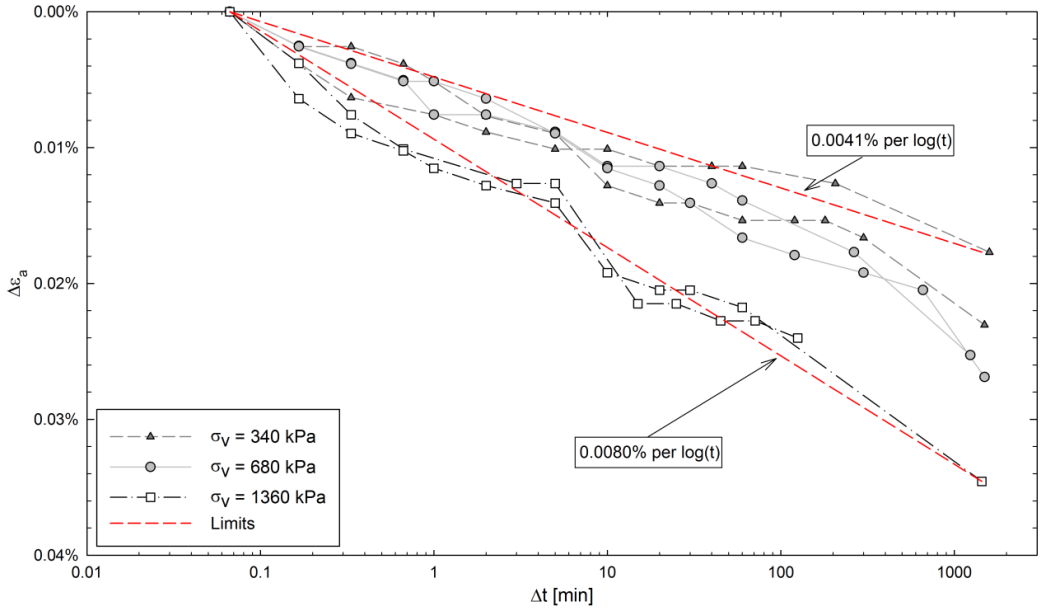

Fig. 4-24. Change in axial strain with time during creep for dense Silica sand. Specimens aged for 1440 min.

Some behavioral trends exhibited by the materials during creep, which can be gleaned from the previous figures, are summarized below:

- The length of the creep stage before the application of each load step does not seem to affect the creep rate.

- The change in axial strain during creep follows an approximately linear relationship with respect to the logarithm of time; i.e. the magnitude of C_α remains constant over time. The rate of change ranged from about 0.0035% to 0.0208% per log-cycle of time for specimens of loose silica sand, and from 0.0041% to 0.0112% per log-cycle of time for dense Silica sand.
- The creep rate is greater for loose samples than dense samples.
- The creep rate of change in axial strain during creep appears to be greater at higher magnitudes of vertical stress.

One-dimensional compression experiments were also conducted on samples of glass beads prepared to a relative density of about 40% (e≈0.62). Results showing the change in void ratio and axial strains with respect to the change in vertical stress are shown in Fig. 4-25 and Fig. 4-26.

Axial strains measured for glass beads ranged from about 0.4% to 0.7% after the application of the last load (σ_v=1360 kPa). These are of similar magnitude to the deformations measured for loose Silica sand (e≈0.73) and smaller than those measured for dense Silica sand (e≈0.6). The change in void ratio due to the application of the vertical stress was often less than the deviation in the target initial void ratio. This error could easily affect the results from the experiments, particularly due to the small deformation measured during the tests. It is recommended that other methodologies be developed or bigger samples are used in future research to achieve more accurate values of initial void ratio during sample preparation.

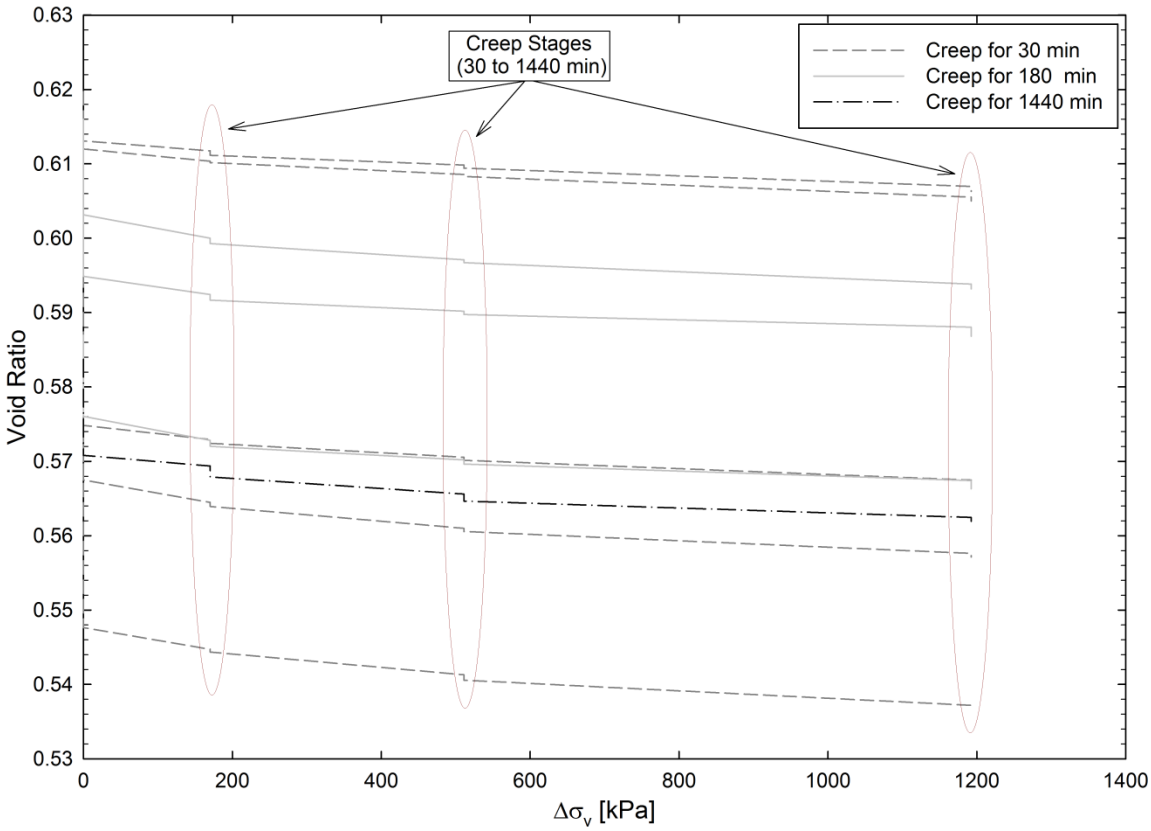

Fig. 4-25. Change in void ratio versus vertical stress for glass beads. Specimens aged for 30, 180, and 1440 min.

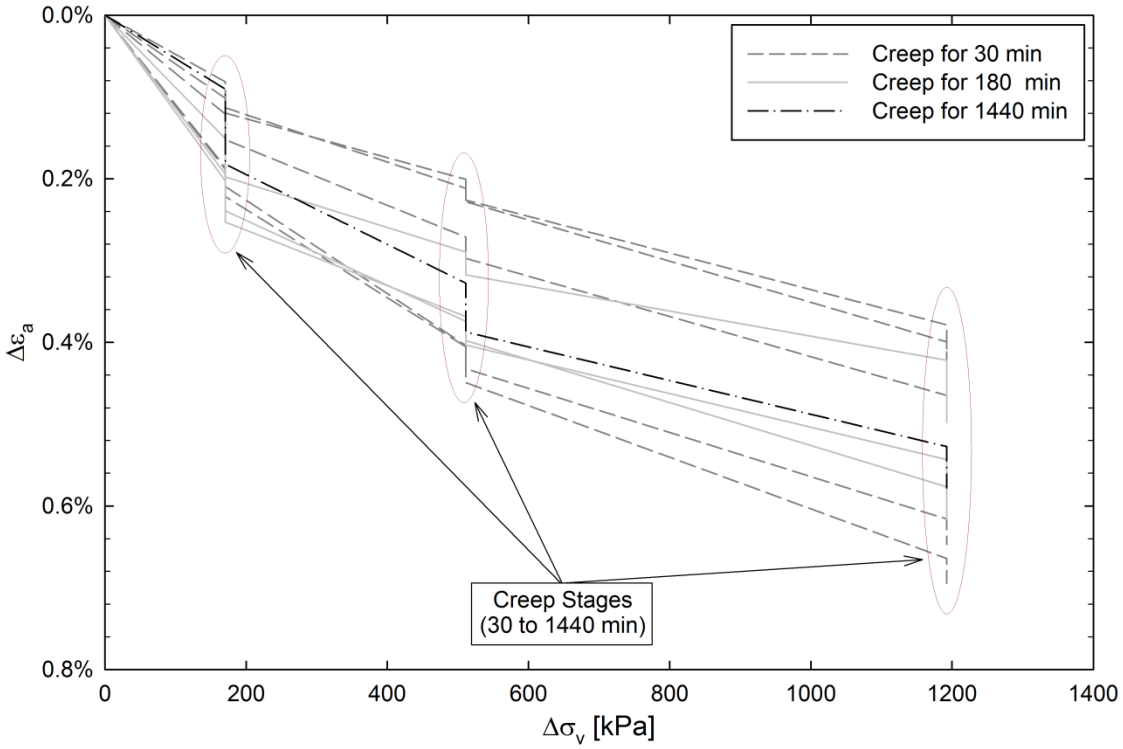

Fig. 4-26. Change in axial strain versus change vertical stress for glass beads.

The average magnitude of constrained modulus and the standard deviation (shown as error bars) determined for test specimens of glass beads allowed to creep for the same time periods are shown in Fig. 4-27. The constrained modulus of specimens of glass beads is smaller than *M* determined for Silica sand (dense and loose) at low vertical stresses, but it becomes greater as the stresses increase. This behavior could be caused by the greater strength of glass beads in comparison with Silica sand grains, which would reduce the effect of particle crushing under high vertical stresses. The time of creep before the application of the load does not seem to have an effect on the magnitude of *M*.

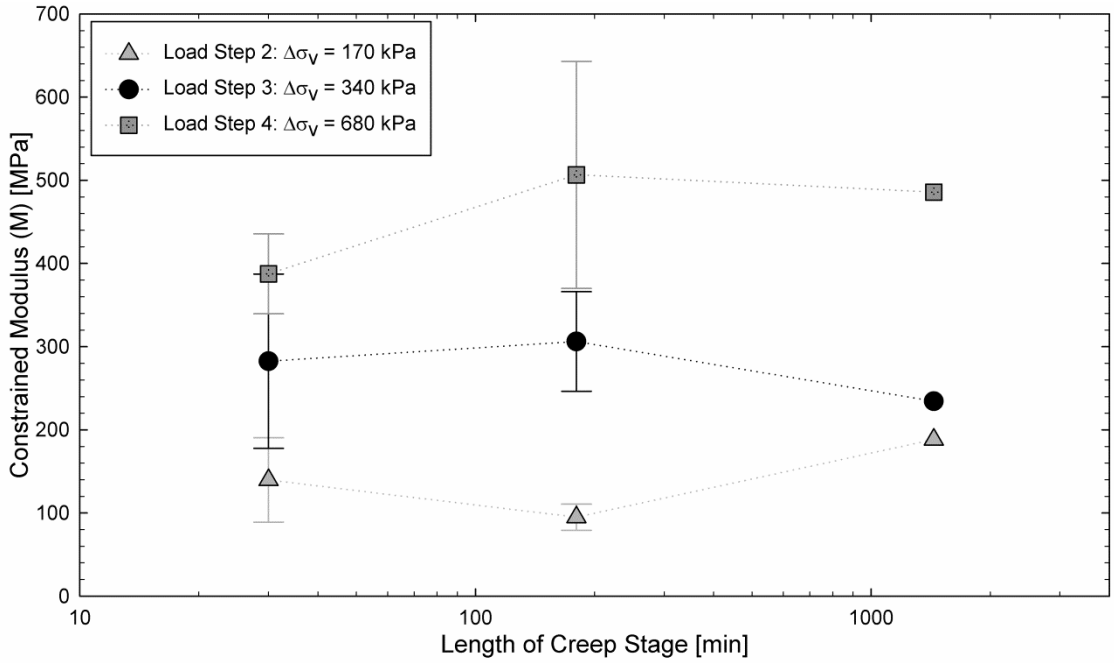

Fig. 4-27. Constrained modulus (*M*) of glass beads.

The change in axial strain with time during creep measured for specimens of glass beads allowed to creep for 180 and 1440 minutes is shown in Fig. 4-28 and Fig. 4-29. The figures show a similar behavior to that observed for Silica sand, with an approximately linear variation in axial strain with respect to the logarithm of time. The rate of change in axial strain ranged from about 0.0081% to 0.0231% per log-cycle of time (higher than for Silica sand) both loose and dense, and does not seem to be affected by the length of the creep stage allowed for the specimen.

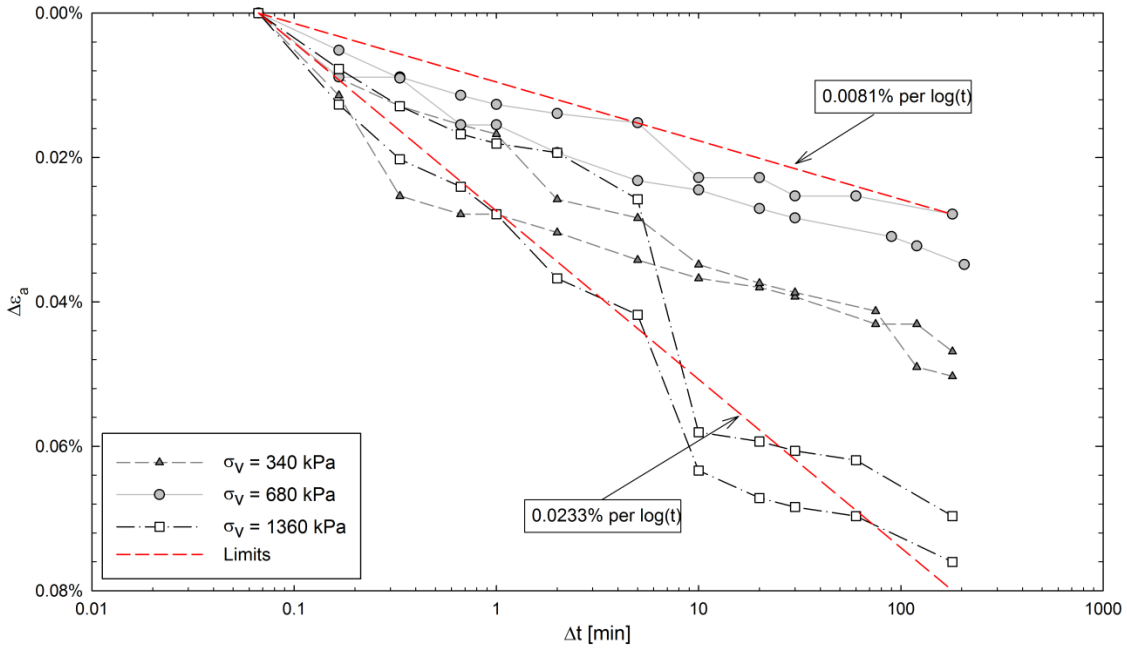

Fig. 4-28. Change in axial strain over time during creep for glass beads. Specimens aged for 180 min.

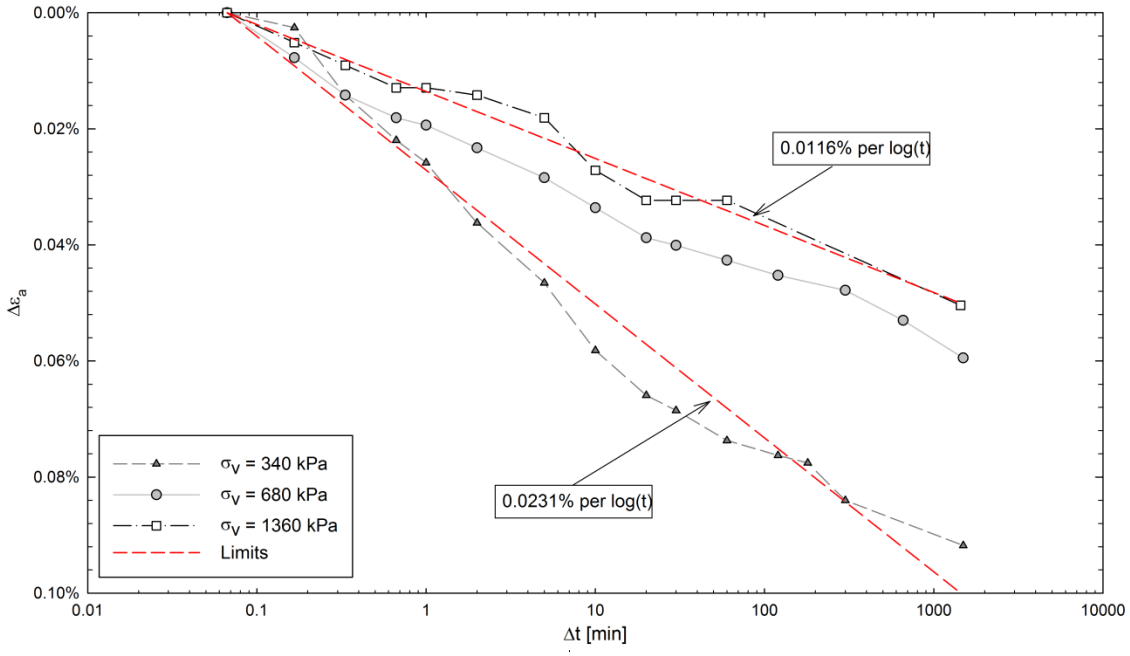

Fig. 4-29. Change in axial strain over time during creep for glass beads. Specimens aged for 1440 min.

Creep tests were also conducted using an automated Geotac Geojac actuator, which applies and controls the required vertical load by continuously calculating the specimen stiffness and adjusting the specimen deformation. The process is relatively

simple and allows automating a major part of the experiment. However, the load applied by the actuator is not as constant as dead weight apparatuses. Regularly, these cyclic deviations in the vertical stress are neglected. However, because the axial strain during creep of sands is very small (often less than 0.1% after 1 day), small changes in the applied vertical stress can have a significant effect on the experimental results.

The change in axial strain with time during creep of dense Silica sand measured during one-dimensional compression tests conducted using automated equipment is shown in Fig. 4-30 and Fig. 4-31. Note that the change in axial strain shows an erratic behavior, compression and dilating cyclically over time. It seems clear that the automated equipment cannot apply loads that are constant enough for small-strain creep tests. Results obtained for specimens formed by glass beads exhibited a similar behavior.

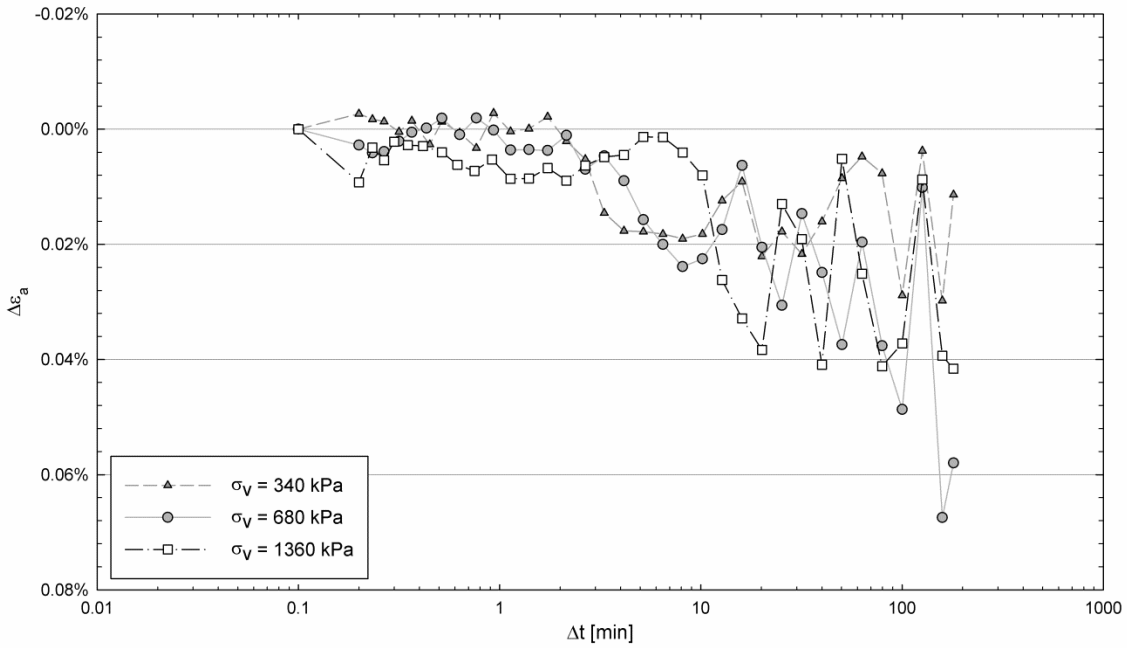

Fig. 4-30. Change in axial strain over time during creep for dense Silica sand. Specimens aged for 180 min. Results obtained using automated equipment.

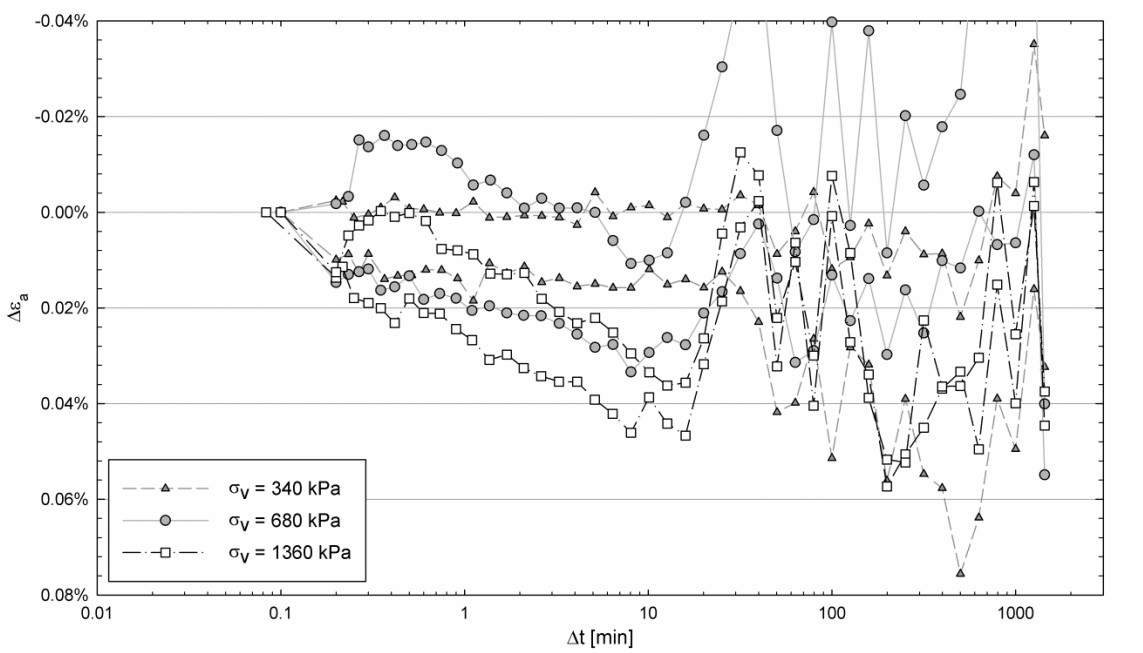

Fig. 4-31. Change in axial strain over time during creep for dense Silica sand. Specimens aged for 1440 min. Results obtained using automated equipment.

The results shown in the previous figures indicate that experiments conducted using the manual equipment, which maintains the load constant over time, provide a better description of creep deformations in granular materials. Results acquired using the automated equipment were discarded.

4.5.1.2 AEs during Creep

AEs were recorded during the one-dimensional compression experiments using the equipment described in Section 4.3.1. AEs were only recorded and analyzed during the experiments conducted using the manual equipment.

Acoustic signals recorded during one-dimensional compression of dense Silica sand (D_r=85%), loose Silica sand (D_r=46%) and glass beads (D_r=52%) are shown in Fig. 4-32 to Fig. 4-34. The figures show the amplitude of the acoustic wave (A) normalized with respect to the maximum amplitude recorded during each test (A_{max}). The application

of the load can be easily identified in the signal as a sudden increase in the amount of AEs recorded. After the application of each load, the AE activity decreases over time during creep.

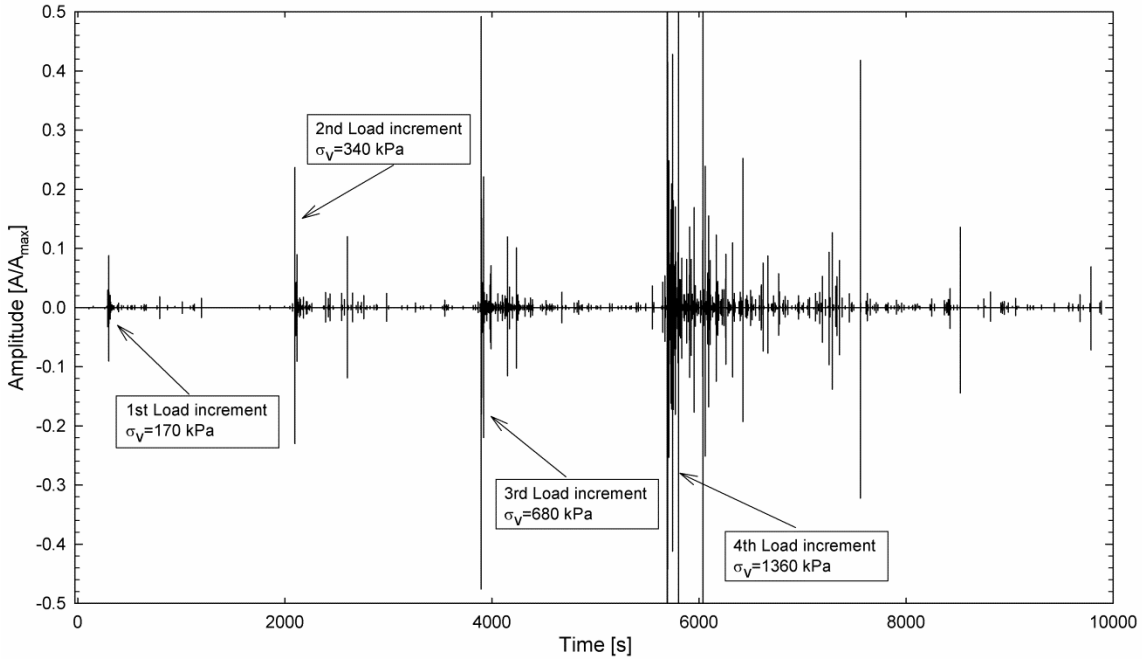

Fig. 4-32. Acoustic signal recorded during one-dimensional compression of dense Silica sand (D_r=85%). Specimen allowed to creep for 30 min after the application of each load.

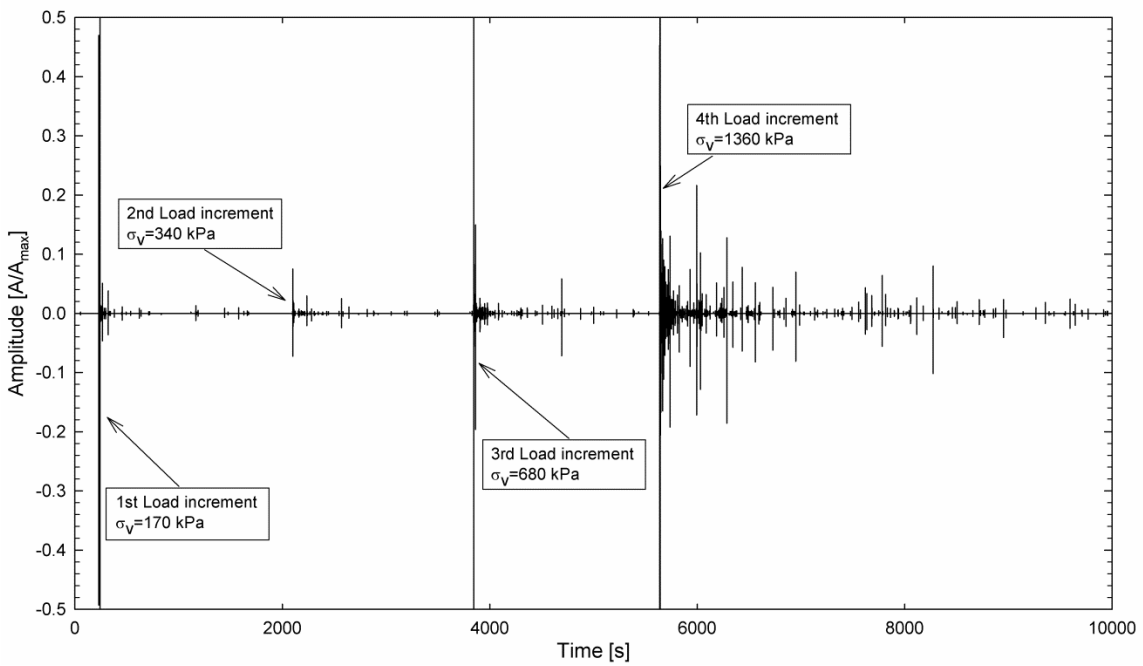

Fig. 4-33 Acoustic signal recorded during one-dimensional compression of loose Silica sand (D_r=46%). Specimen allowed to creep for 30 min after the application of each load.

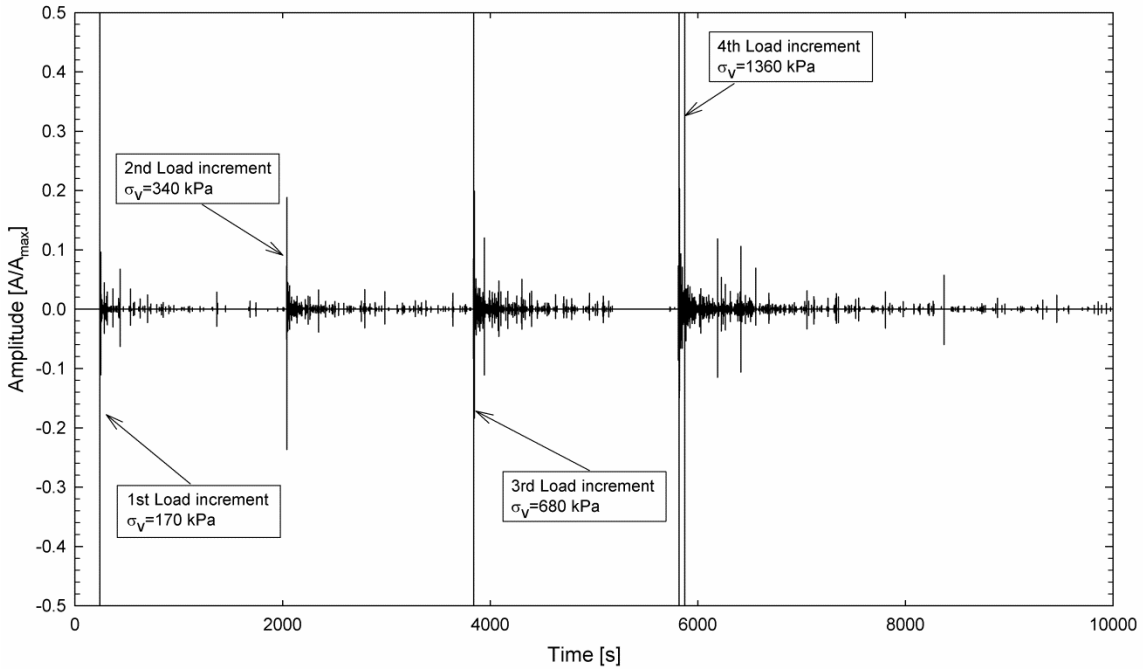

Fig. 4-34 Acoustic signal recorded during one-dimensional compression of glass beads (D_r=52%). Specimen allowed to creep for 30 min after the application of each load.

It is typical during AE characterization to use the AE count (C) to quantitatively describe the phenomenon under study (Fernandes et al. 2010). The AE count represents the number of times the amplitude (A) of the acoustic wave surpasses a preset threshold. The magnitude of that threshold is often selected based on the characteristics of the background noise, which in this case was recorded previous to starting each test. A normalized threshold (A/A_{max}) of 2.1E-3 was used for this analysis. This magnitude, which is slightly higher than the normalized signal amplitude measured before loading, was selected was based on the AE count calculated for about 5 min of background noise (a maximum AE count of 20 events was permitted). The same threshold value was used for all the calculations because the characteristics of the background noise recorded during all the experiments were practically identical.

The variation of the AE count with time during one-dimensional compression of dense Silica sand, determined using a threshold value of 2.1E-3, is shown Fig. 4-35. Note that the AE count versus time and the axial strain versus time relationship have similar shapes. Additionally, even though deformations measured during creep were very small (i.e., less than 0.03% after 30 minutes of creep), the AE count continued to increase noticeably over time. The rate of increase of the AE count with time during the creep stages decreases over time, but up to 10000 AEs were measured during 30 minutes of creep. The change in AE count and axial strain with time during each of the three 30 min creep stages (σ_{v1}=340 kPa, σ_{v2}=680 kPa, and σ_{v3}=1360 kPa) is shown in Fig. 4-36.

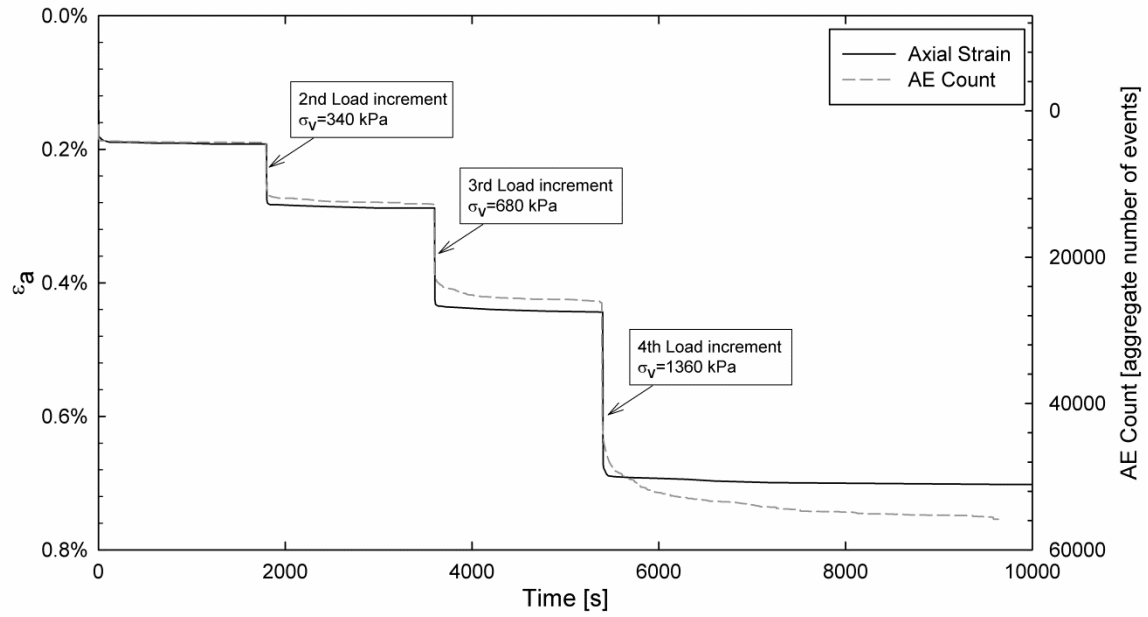

Fig. 4-35. Variation in vertical strain and AE count with time during one-dimensional compression of dense Silica sand.

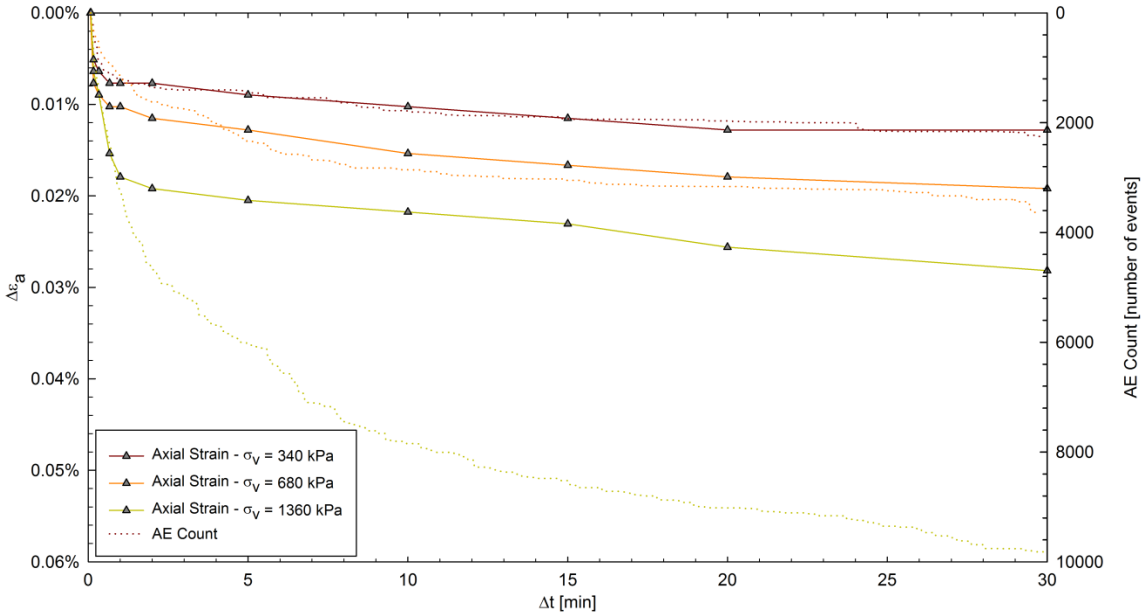

Fig. 4-36. Variation in vertical strain and AE count with time during creep for dense Silica sand.

Fig. 4-36 shows that about 2000 AE events and a vertical strain of approximately 0.01% were measured after 30 minutes of creep under a vertical stress of 340 kPa. The axial strain and the AE count during creep increased for greater magnitudes of σ_v. About 10000 AEs and a vertical strain of 0.025% were measured during creep under a vertical

stress of 1360 kPa. A similar behavior is also observed during one-dimensional compression experiments on glass beads, as shown in Fig. 4-37.

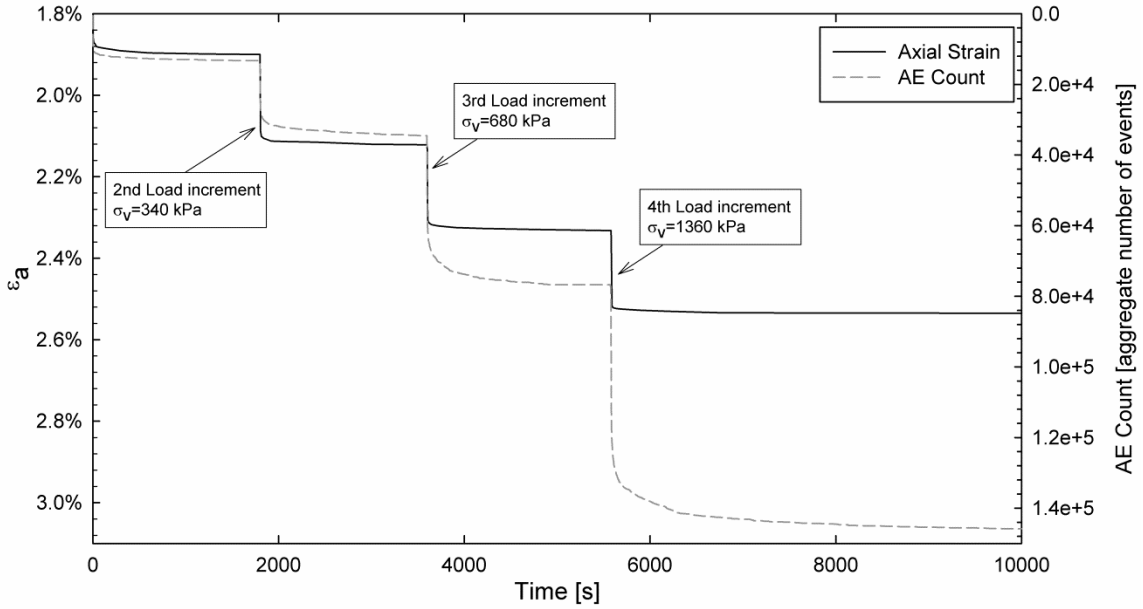

Fig. 4-37. Variation in vertical strain and AE count with time during one-dimensional compression of glass beads.

Based on the results presented previously it can be observed that: (1) the magnitude of the vertical stress during creep has a significant effect on the AE count measured during creep, and (2) the specimen continues emitting AEs during creep even though only minimal vertical deformations are measured.

The first observation could be explained by either an increase in AE events caused by more particle breakage at higher vertical stresses, or by the increase in the amplitude of frictional AEs caused by higher normal forces acting between the particles. Baranov et al. (2007) indicate that increasing the force acting between sliding objects causes also an increase in the amplitude of the frictional AEs emitted. If the amplitude of the AEs increases, it is likely that pulses which could be hidden by background noise during creep under low vertical stresses would be detected as the applied stresses and the AE amplitude increase, thus resulting in higher values of AE count.

To determine if particle crushing could account for the increase in AE count observed at high vertical stresses, sieve tests were conducted after the one-dimensional compression experiments. The grain size distribution curves for specimens of dense Silica sand, loose Silica sand and glass beads after one-dimensional compression are shown in Fig. 4-38, Fig. 4-39, and Fig. 4-40. The figures also include the original material gradation, determined based on four sieve tests for each material. The average, maximum, and minimum original material gradations are presented.

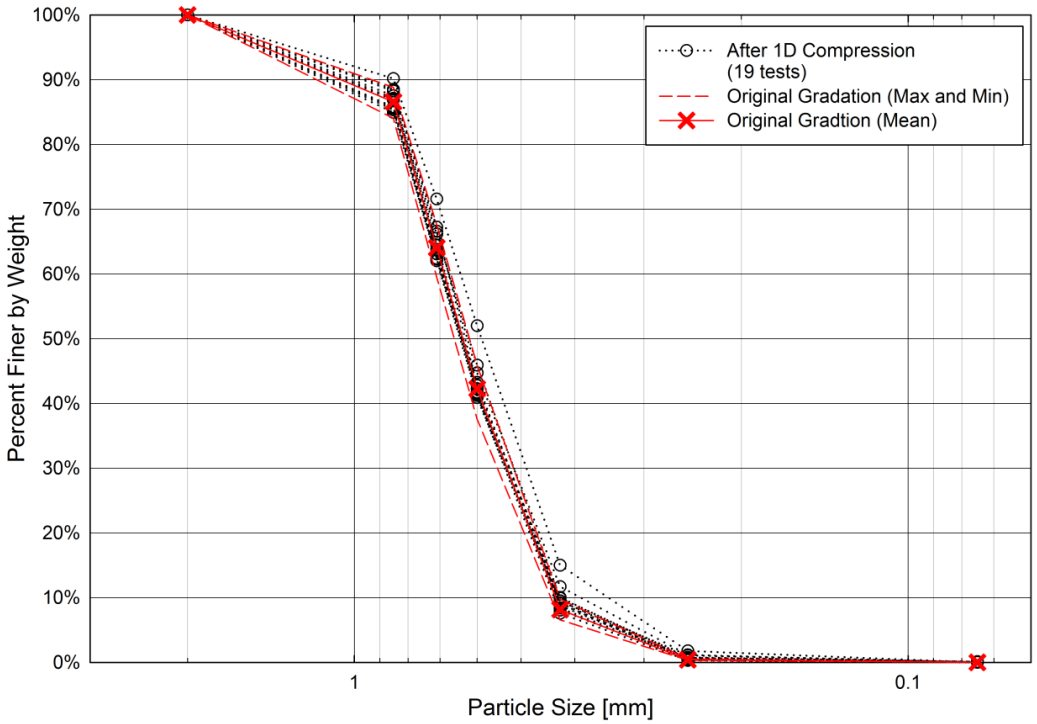

Fig. 4-38. Grain size distribution of dense Silica sand before and after one-dimensional compression experiments (19 tests).

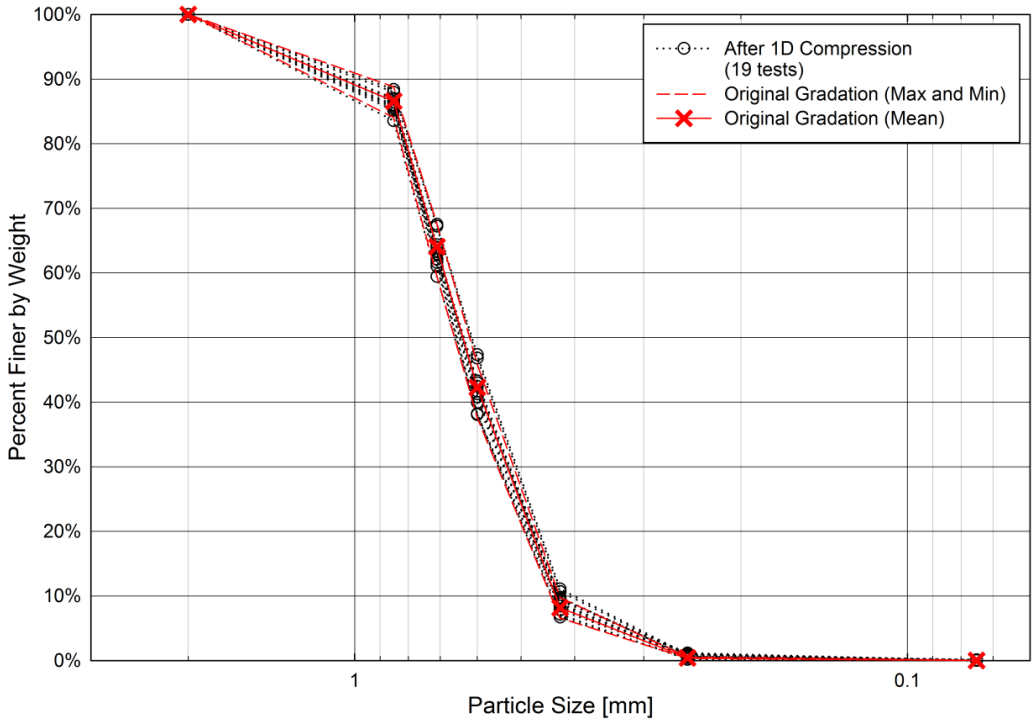

Fig. 4-39. Grain size distribution of loose Silica sand before and after one-dimensional compression experiments (19 tests).

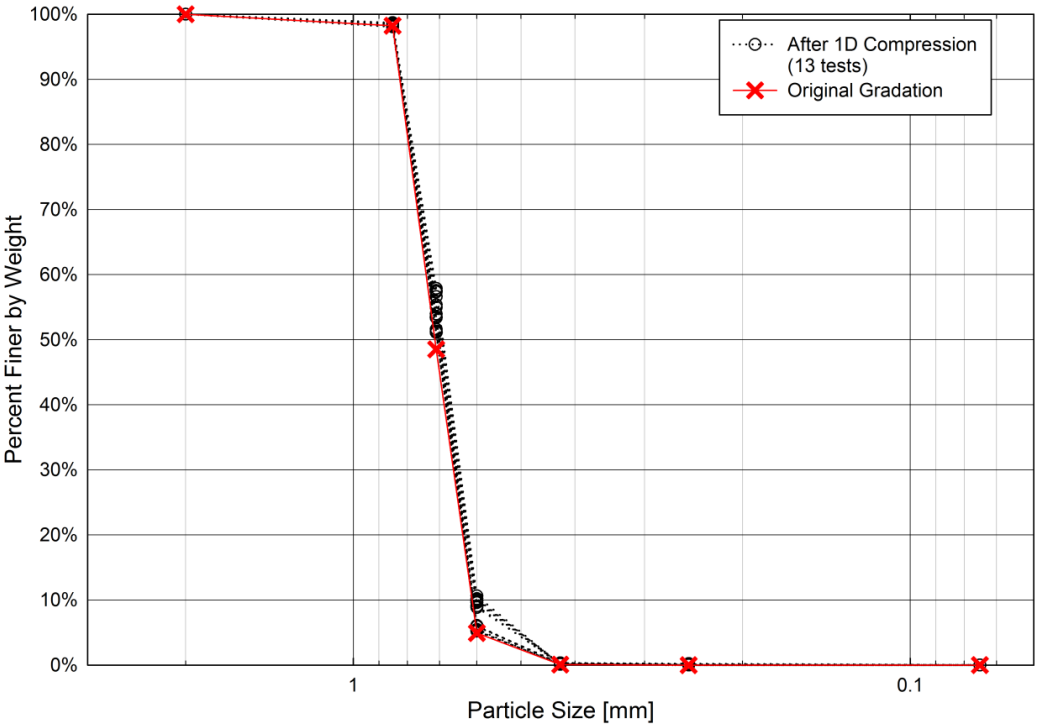

Fig. 4-40. Grain size distribution of glass beads before and after one-dimensional compression experiments (13 tests).

It is clear that only small changes in the gradation of the material are observed after the one-dimensional compression experiments. These changes were quantified using Hardin's breakage factor, B_r. Details of the calculation of B_r can be found in Hardin (1985). The magnitude of the B_r ranged from about 0 to 4.5% for dense Silica sand, 0 to 2.1% for loose Silica sand, and 0.2% to 1.5% for glass beads, which denote minimal particle breakage (Fernandes et al. 2010). The increase in AE count is therefore more likely related to an increase in particle contact force rather than to particle crushing.

It was mentioned that the AE count continued to increase during creep, and it was associated with small vertical strains (<0.03%). Because particle crushing is not expected to be important under the magnitudes of vertical stress used during the experiments (<1360 kPa), AEs appear to be mainly related to friction during particle movement. Therefore, the increase in AE count indicates that particles continue moving during creep, and those movements are reflected in minimal macroscopic deformations.

The frequency content of the acoustic signal recorded during each of the three creep stages (σ_v=340 kPa, σ_v=680 kPa, and σ_v=1360 kPa) was obtained using a fast Fourier transform with a length of 65536 points. The same process was used to obtain the frequency content of the background noise, which was later subtracted from the data determined for each creep stage. Results showing the frequency content of the acoustic signals recorded for dense Silica sand, loose Silica sand, and glass beads are shown in Fig. 4-41. Peak amplitudes are observed at frequencies of about 3.7, 10.7, and 18.6 kHz for dense Silica sand; 2.9, 4.9, 10.7, and 20 kHz for loose Silica sand; and 4.0, 8.7, 12.0, 16.4, and 10.8 kHz for glass beads. The amplitude at each peak frequency tends to increase as the vertical stress applied during creep increases. The change in amplitude

seems to be more significant at high frequencies for Silica sand (>8.4 Hz) and at low frequencies for glass beads (<4KHz). Characteristics such as the predominant frequency of AEs recorded during the experiments may provide an indication of their source. However, that type of analysis is out of the scope of this study.

4.5.2 Creep and Aging during Triaxial Compression

4.5.2.1 Macroscopic Stress and Strain

Results of triaxial compression experiments conducted on specimens of dense filter sand are shown in Fig. 4-42. The figure shows the change in principal stress ratio (*PSR*) and volumetric strain (determined based on the change in pore fluid volume) during triaxial compression of two test specimens of loose filter sand prepared to approximately the same initial relative density (D_{r1}=25%, D_{r2}=28%). One of the specimens, which will called the *reference sample*, was sheared drained at a constant strain rate of 0.02% min^{-1}. For the second specimen, called the *creep sample*, shearing was stopped and the specimen was allowed to creep for 3 hours at stress levels of about 25%, 50%, and 75%. After each of these *creep stages*, shearing continued until the next stress level was reached, and a new creep stage was initiated. The start and end of each of the three creep stages is indicated by dotted red lines in Fig. 4-42.

It is observed in Fig. 4-42 that creep causes an increase in the dilatancy of the specimen during shear. The creep sample also had a slightly higher value of maximum principal stress ratio (PSR_{max}=4.7, ϕ=40.5°) than the reference sample (PSR_{max}=4.5, ϕ=39.5°). Changes in axial strain and volumetric strain occurring during creep are shown in more detail in Fig. 4-43, which includes only axial deformations of up to 0.7%.

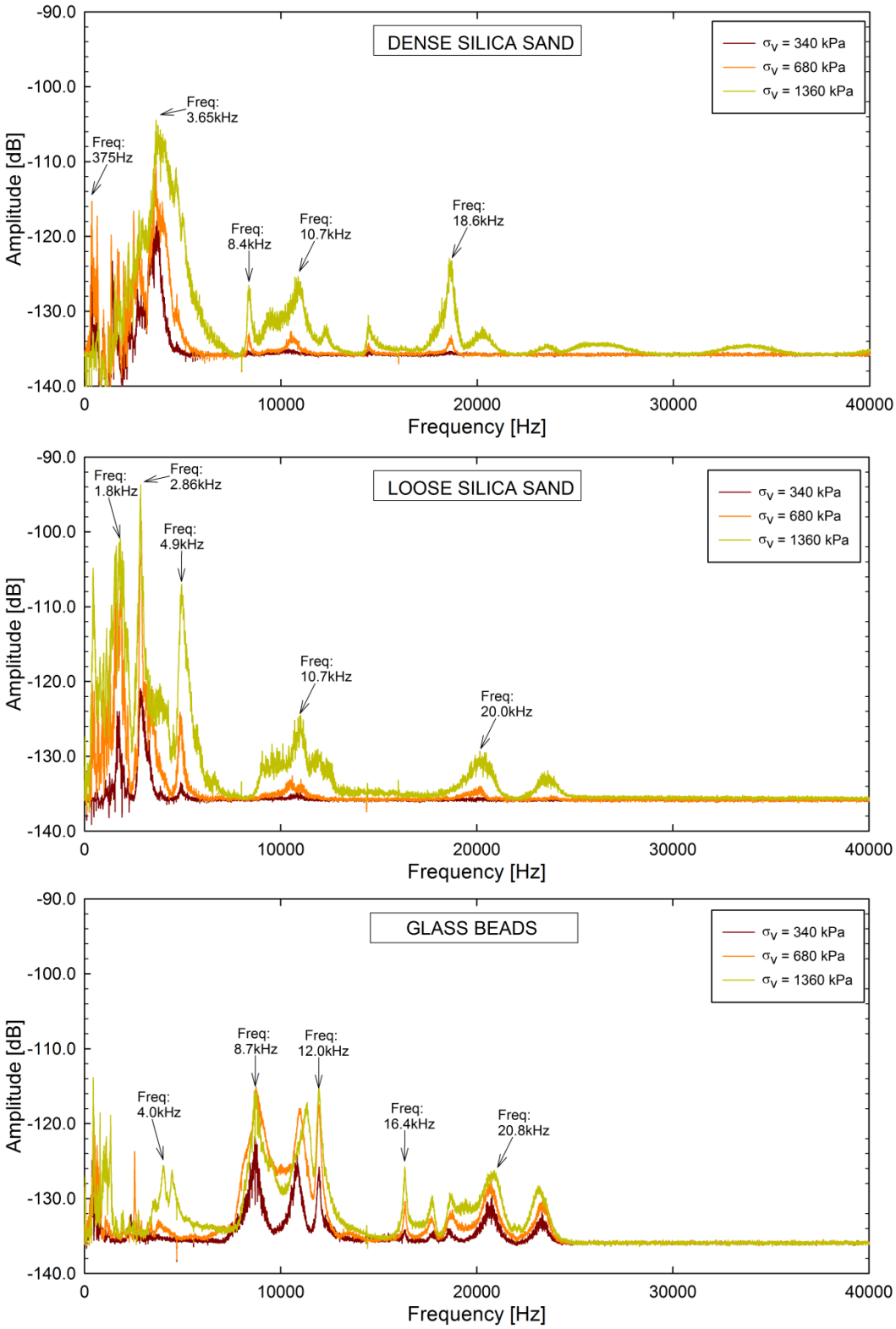

Fig. 4-41. Frequency content of acoustic signal recorded during creep of dense Silica sand, loose Silica sand, and glass beads.

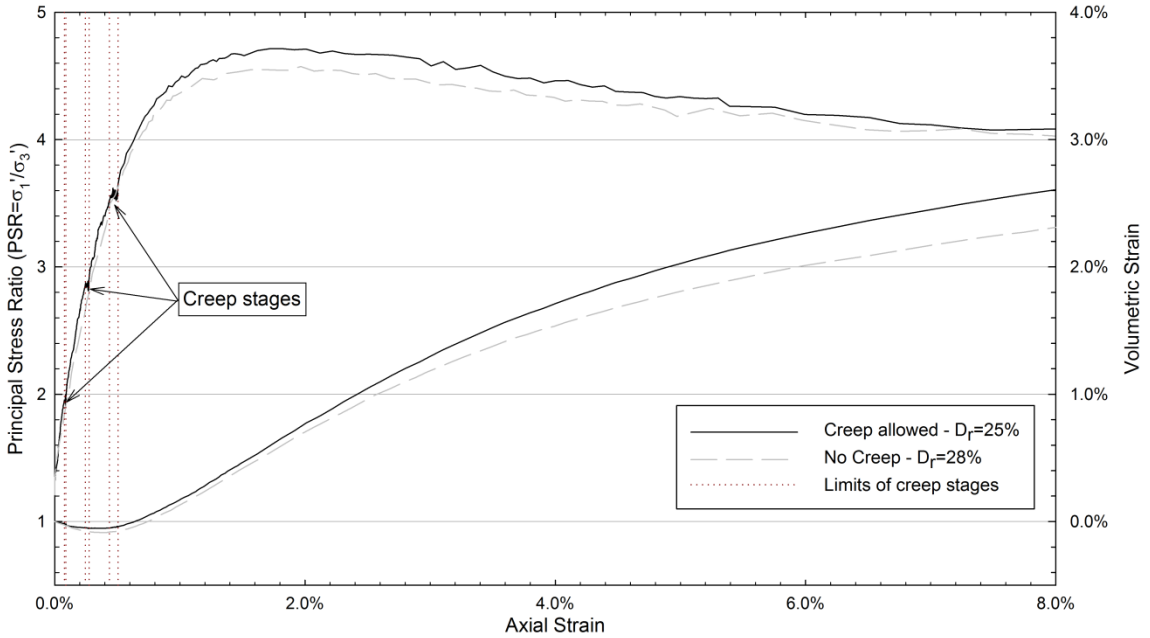

Fig. 4-42. Change in principal stress ratio and volumetric strain with axial strain during triaxial compression. Specimens of loose filter sand with and without creep.

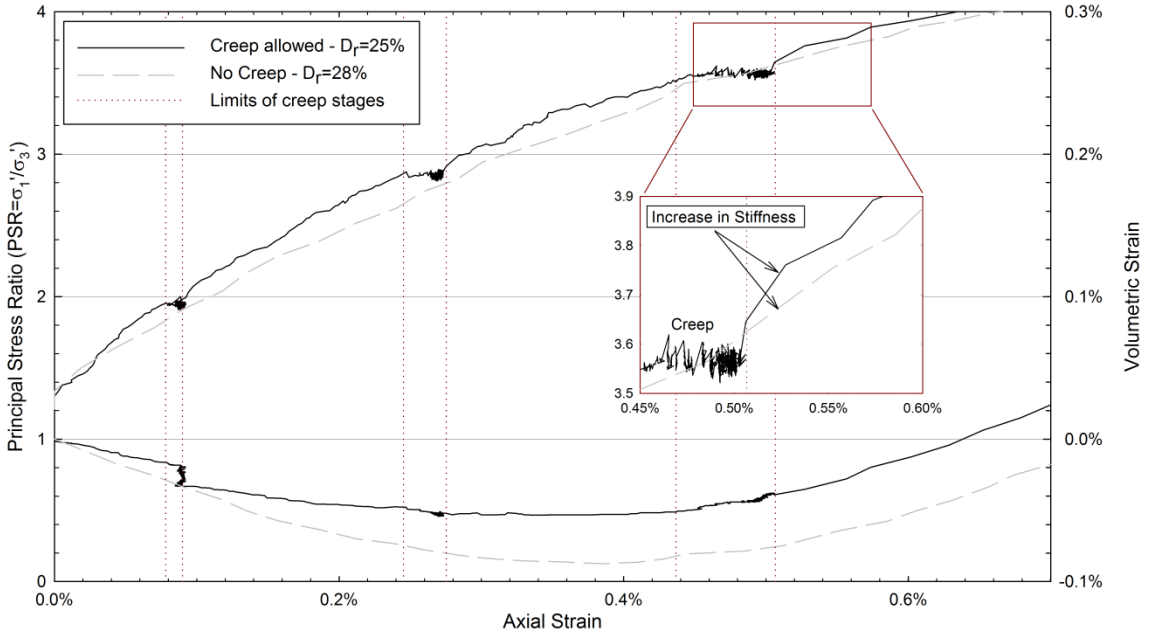

Fig. 4-43. Change in principal stress ratio and volumetric strain with axial strain during triaxial compression – initial 0.7% axial strain. Specimens of loose filter sand with and without creep.

The figure shows that, once shear starts after creep, the stiffness of the sample increases momentarily. The increase in stiffness is lost as the sample deforms. Additionally, the volumetric strain – axial strain relationship during creep of the creep

sample follows the same trend shown by the reference sample during shear at the same value of strain; i.e. if the creep stage starts at a magnitude of strain at which the reference sample is compressing, the creep sample will tend to compress during creep, or it will dilate if the reference sample was dilating. The change in volumetric strain with time during the creep for loose filter sand is shown in Fig. 4-44.

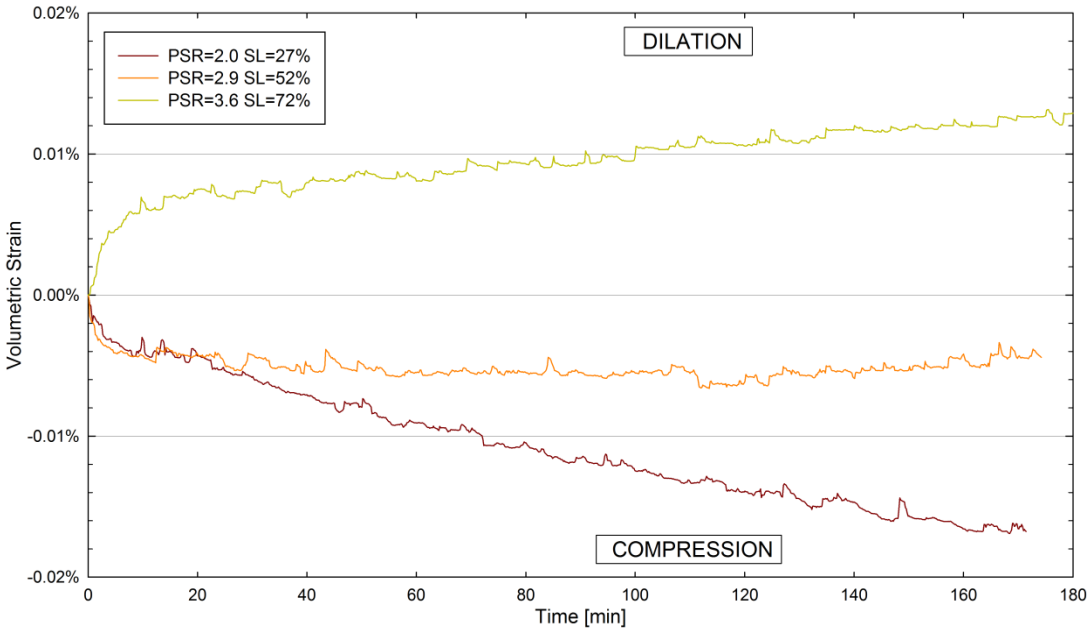

Fig. 4-44. Change in volumetric strain during creep for loose filter sand.

The figure shows that the sample compresses during creep at low stress levels (where the reference sample is also compressing), and tends to dilate as the stress level during creep increases. Similar observations were made Murayama et al. (1984) and Mejia (1988), who noted that dense sand under high deviator stress dilates during drained creep. Bowman and Soga (2003) also observed that some dense granular samples compress and then dilate with time during drained creep, a behavior that was exhibited by the filter sand at a stress level of around 52%. Note that a stress level of about 52% corresponds to a point where the volumetric strain – axial strain relationship of the

reference sample became almost horizontal (i.e., the transition from compressive behavior to dilative behavior).

The change in axial strain with time during creep is shown in Fig. 4-45. The change in axial strain measured during the creep experiments is not smooth, and could be the result of continuous adjustments of the actuators for the application of the deviator and confining stresses. Similar to the results presented in Section 4.5.1 for one-dimensional creep experiments conducted using automatic equipment, results from triaxial compression tests presented in this section were obtained using actuators for the applications of the respective loads. Load actuators do not apply a constant stress, but they continuously readjust the specimen's deformation and estimate the specimen's stiffness to reach the desired load. Inevitably, the applied load continuously overshoots and undershoots by a small amount the targeted force. Generally that deviation is small in comparison with the stresses and strains for conventional triaxial testing, so it can be neglected. However, in the current research studies the magnitudes of strain are only of the order of hundredths of a percent, so small deviations in load and deformation due to the actuator can have a significant effect on the results of the experiments. In the case of Fig. 4-45, this results in an irregular variation in axial strain over time during creep. The application of a constant deviator stress by means of dead loads rather than load actuators is recommended for future research.

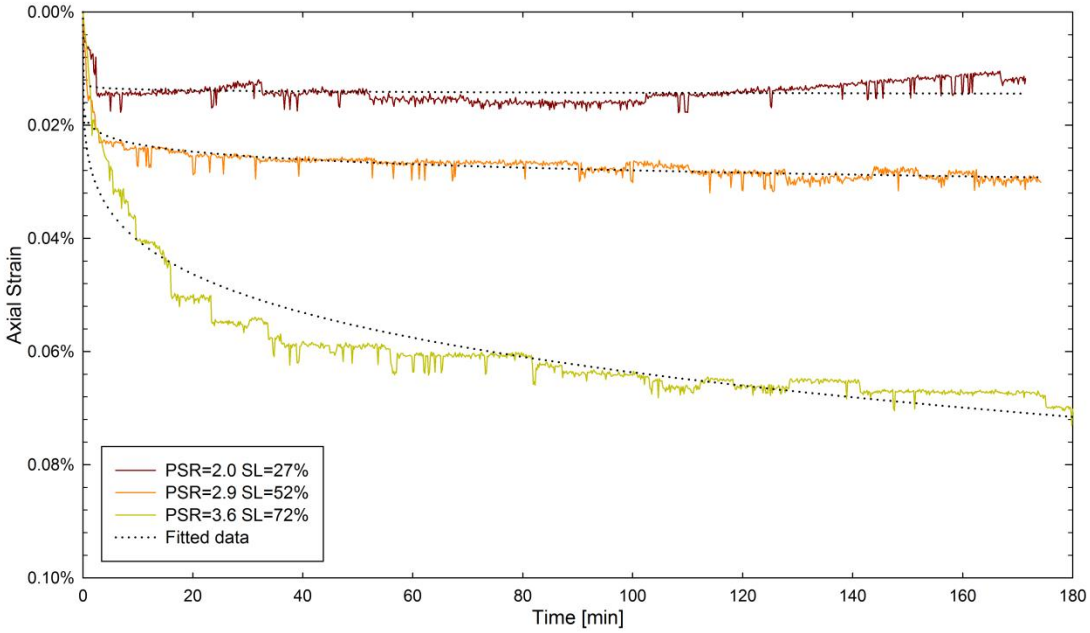

Fig. 4-45. Change in axial strain during creep for loose filter sand.

According to Mitchell and Soga (2005), the strain rate ($\dot{\varepsilon}$) behavior during creep of a wide variety of soils can be described using the relationship:

$$\dot{\varepsilon} = Ae^{\alpha D}\left(\frac{t_1}{t}\right)^m \tag{15}$$

where D is the stress intensity, often taken as the deviator stress, t represents the time of creep, t_1 is a reference time, and the parameters A, α, and m, are characteristics of a given soil and can be found based on results from creep experiments conducted on identical specimens using different stress intensities. The value of m is estimated as the slope for a plot of log strain rate versus log time, and the magnitudes of α and A are obtained from the slope and intercept at a unit time in a plot of log strain rate versus stress intensity for different values of time.

The estimation of the values of the parameters A, α, and m, for the granular soils used in this study is not straightforward due to the constant fluctuation in axial strain caused by the load actuator, which has a significant effect on the magnitude of axial

strain rate measured during the creep stages. The values of strain rate calculated based on the data shown in Fig. 4-45 ranged approximately from -0.01% min^{-1} (extension) to 0.025% min^{-1} (compression). Therefore, errors in the magnitude of $\dot{\varepsilon}$ caused by the load actuator hinders the use of plots involving the axial strain rate to calculate *A*, α, and *m*.

To account for the continuous strain readjustment induced by the load actuator, the data shown in Fig. 4-45 was fitted using a relationship derived from Eq. 19. The following relationship is obtained by integrating Eq. 19 with respect to time:

$$\int \dot{\varepsilon} dt = \int A e^{\alpha D} \left(\frac{t_1}{t} \right)^m dt$$

$$\varepsilon = A e^{\alpha D} t_1^m \frac{t^{1-m}}{1-m} + C \qquad (16)$$

where *C* is a constant. If the start of the creep stage (t=0) is taken as the reference strain (ε_0), the change in axial strain occurring during creep can be expressed as:

$$\Delta\varepsilon = A e^{\alpha D} t_1^m \frac{t^{1-m}}{1-m} - \varepsilon_0 \qquad (17)$$

The values of *A*, α, and *m* were determined for each of the stress levels and creep stages by fitting Eq. 21 to the axial strain versus time relationships shown in Fig. 4-45 using least squares. Even though the parameters *A*, α, and *m* are characteristic for each soil, a different set of values was determined for each creep stage, and were later compared, to avoid introducing a prescribed behavior to the fitted data; e.g., parallel log strain rate versus log time and log strain rate versus stress intensity curves. The values of the parameters *A*, α, and *m* estimated for loose filter sand are shown in Table 4-8. Fitted axial strain versus time curves are shown in Fig. 4-45. Note that Eq. 21 describes the creep behavior of the specimen quite well.

Table 4-8. Values of A, α, and m for triaxial compression experiments on loose filter sand.

Stress Level	***m***	***A***	***α*** **[1/psi]**
27%	0.98104248	1.47E-05	8.62E-02
52%	0.92184893	3.65E-05	8.62E-02
72%	0.8020093	4.56E-05	8.62E-02

The change in axial strain rate with time during creep estimated using the parameters A, α, and m is shown in Fig. 4-46. The log strain rate versus log time curves during creep under stress levels at approximately parallel, a behavior which is often observed in a wide variety of soils (Mitchell and Soga 2005).

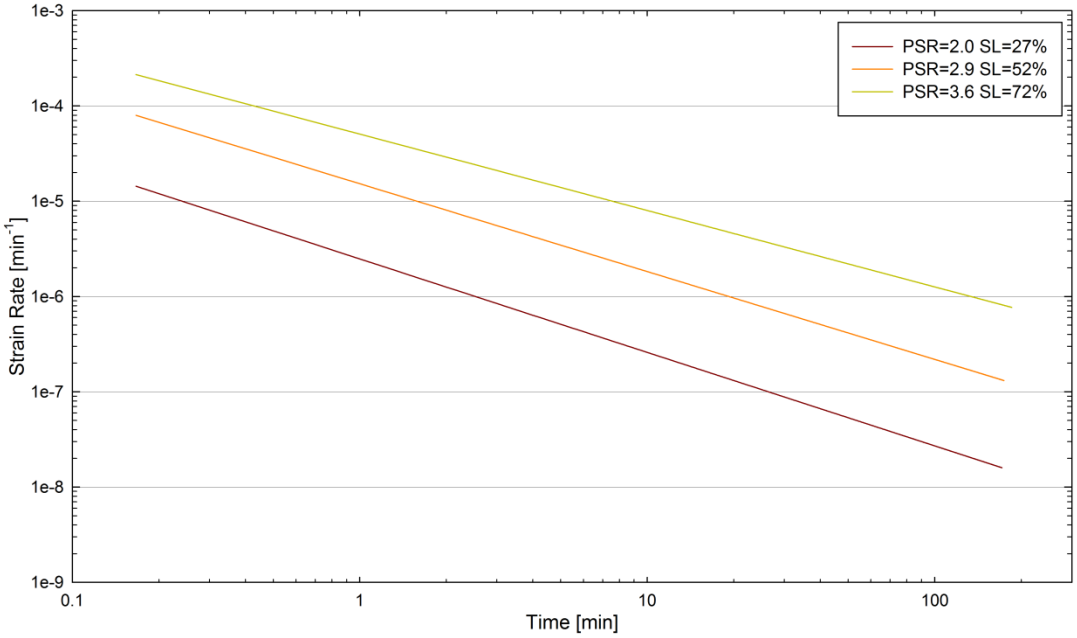

Fig. 4-46. Axial strain rate during creep for loose filter sand.

The change in principal stress ratio and volumetric strain during triaxial compression of two specimens of dense filter sand (D_{r1}=80%, D_{r2}=88%) is shown in Fig. 4-47. Fig. 4-48 shows the results in detail up to an axial deformation of 0.8%. The test results show a similar behavior to that observed in samples of loose filter sand, with a

momentary increase in stiffness following each of the creep stages which disappears as the specimen is deformed.

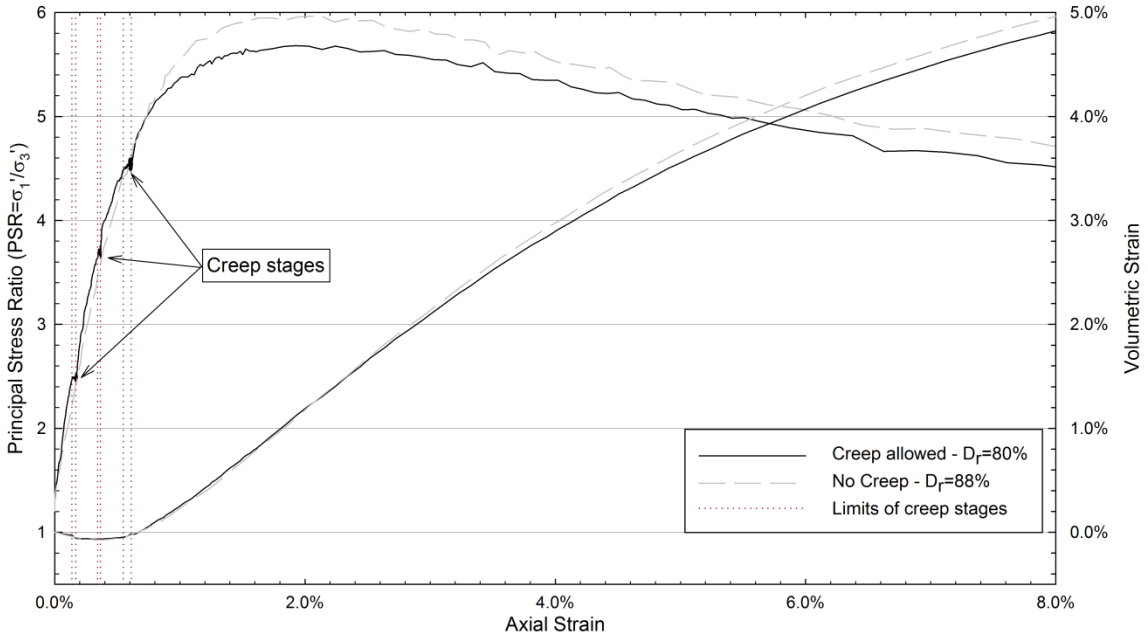

Fig. 4-47. Change in principal stress ratio and volumetric strain with axial strain during triaxial compression. Specimens of dense filter sand with and without creep.

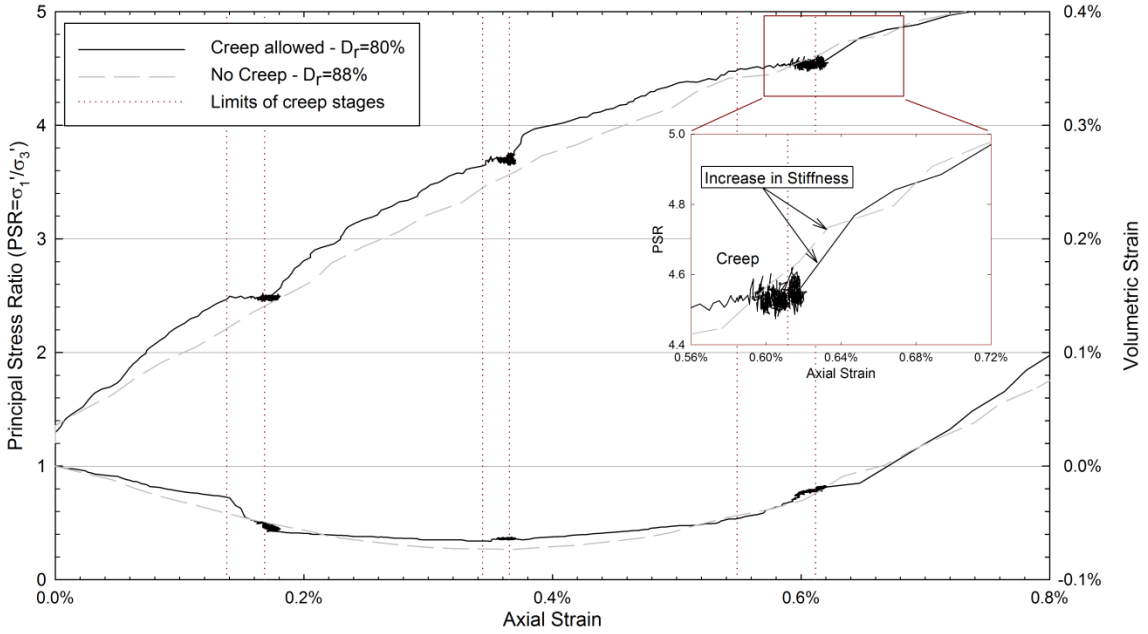

Fig. 4-48 Change in principal stress ratio and volumetric strain with axial strain during triaxial compression – initial 0.8% axial strain. Specimens of loose filter sand with and without creep.

The volumetric strain during creep follows the same tendency exhibited by the reference sample at the same axial deformation during shear. The change in volumetric strain with time during creep under stress levels of 30%, 54%, and 71% is shown in Fig. 4-49. The specimen compresses during creep under low stress levels (SL=30%), has almost no change in volume during the second creep stage (SL=54%), and dilates as the stress level during creep increases (SL=71%).

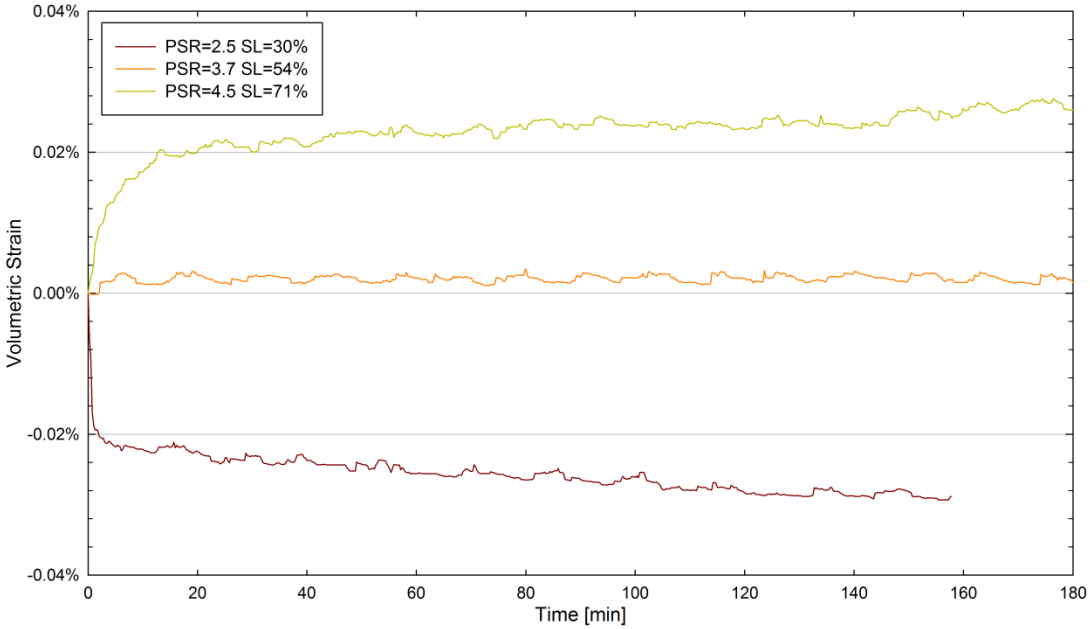

Fig. 4-49. Change in volumetric strain during creep for dense filter sand.

Fig. 4-47 shows that the reference sample (with no creep) was marginally stronger (PSR_{max}=5.95, ϕ=45.4°) than the creep sample (PSR_{max}=5.68, ϕ=44.5°). Both specimens had an almost identical axial strain – volumetric strain relationship up to about 3% axial deformation, and the reference specimen dilated more at higher strains. This behavior could be related to differences in the initial void ratio of the samples: e=0.715 for the reference samples and e=0.731 for the creep sample.

Similar experiments were conducted on samples of glass beads, and loose and dense Silica sand. The measured variation in principal stress ratio and volumetric strain with respect to axial strain is shown in Fig. 4-50, Fig. 4-51, and Fig. 4-52. Certain behavioral trends are observed in the results, including:

- The change in volumetric strain during the creep stage follows the tendency exhibited by the reference sample during shear at the same axial strain in all the materials.
- For specimens of glass beads and dense Silica sand, the strength of the reference and creep samples were approximately equal. The effect of creep on the strength of loose Silica sand could not be verified because the test was terminated before failure was reached.
- The creep sample was more dilative than the reference sample for all the materials tested with the exception of dense filter sand. The higher initial relative density of the reference sample of dense filter sand could account for that atypical behavior.
- The stiffness of the material increases after the creep stage. That momentary increase in stiffness disappears as the sample continues to deform during shear.

It is evident that creep causes an increase in the stiffness of the material on reloading, but this increase is lost after additional strain. To quantify that increase, the secant modulus of the material immediately following each of the creep stages was determined and compared with the secant modulus of the reference sample at the same stress level. The change in the magnitude of secant modulus at 0.005% strain after additional loading ($E_{0.005\%\text{-creep}}/E_{0.005\%\text{-reference}}$) for each of the materials tested, measured after each creep stage, is shown in Fig. 4-53. Positive values in Fig. 4-53 mean that the

stiffness of the material increased during creep as compared with the stiffness determined for the reference sample.

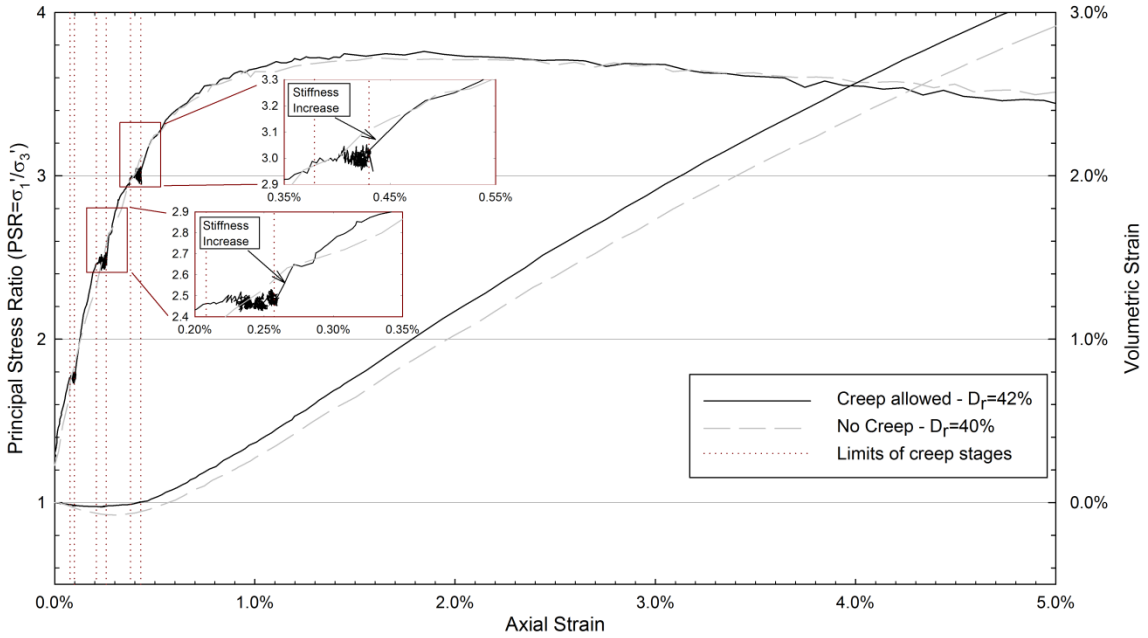

Fig. 4-50. Change in principal stress ratio and volumetric strain with axial strain during triaxial compression. Specimens of glass beads with and without creep.

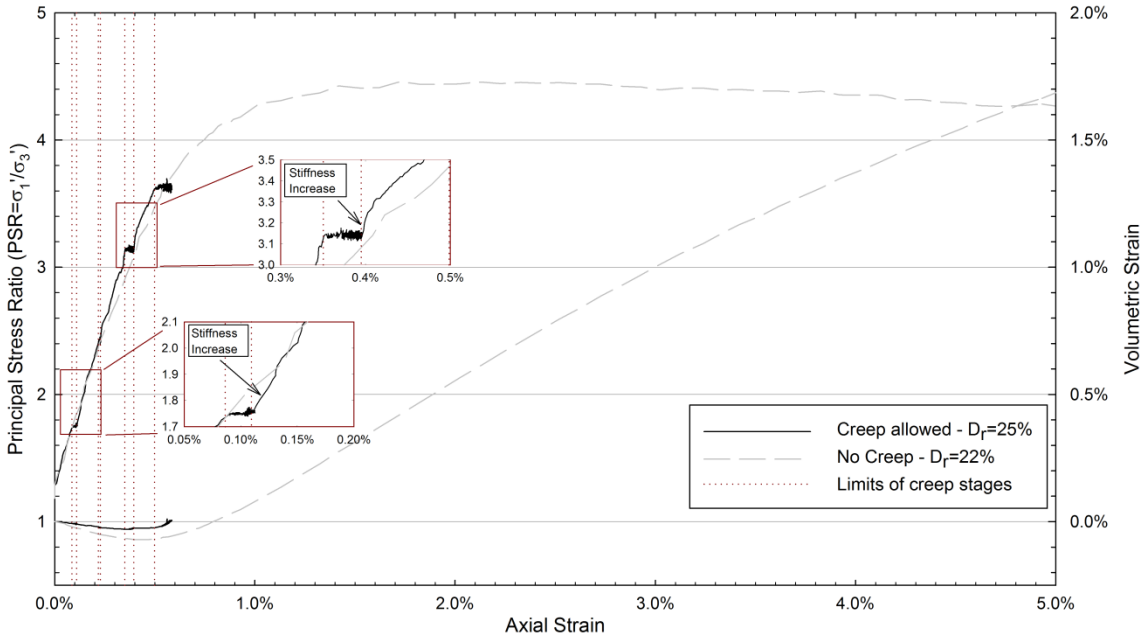

Fig. 4-51. Change in principal stress ratio and volumetric strain with axial strain during triaxial compression. Specimens of loose Silica sand with and without creep.

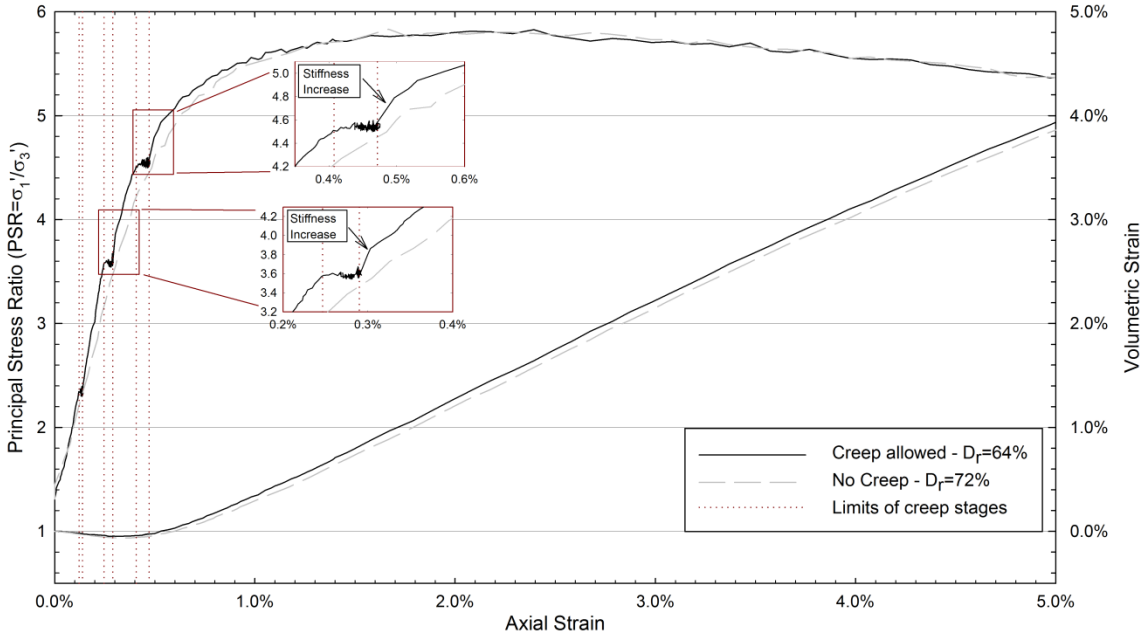

Fig. 4-52. Change in principal stress ratio and volumetric strain with axial strain during triaxial compression. Specimens of dense Silica sand with and without creep.

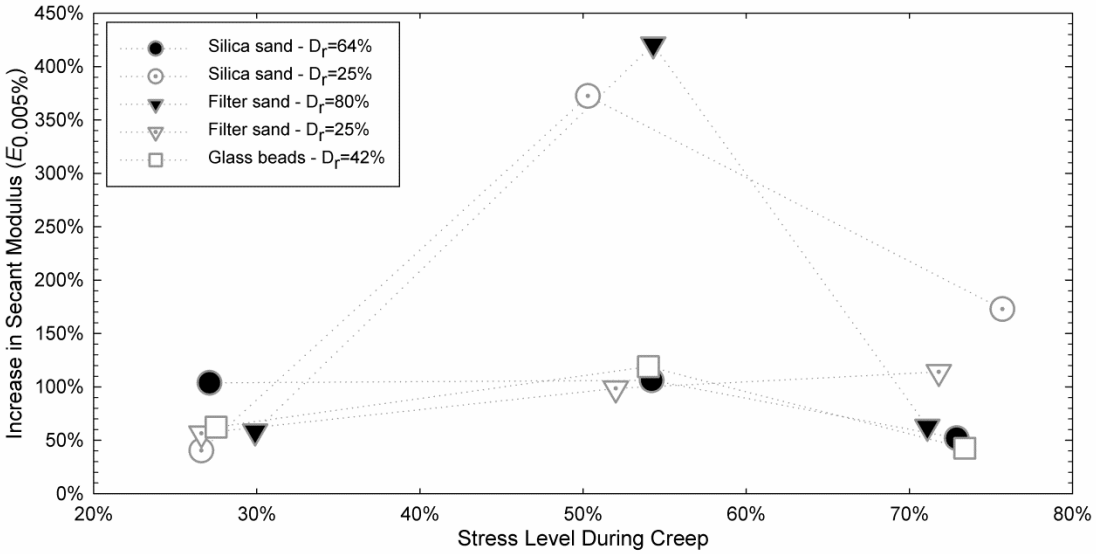

Fig. 4-53. Change in the secant modulus ($E_{0.005\%}$) of the material after creep.

According to the results presented in Fig. 4-53 it is evident that the material stiffens during aging. The secant modulus of the soil increased at least 40% after 3 hours of creep, and the magnitude of the change in $E_{0.005\%}$ seems larger if creep occurs under an intermediate stress level (SL≈50% for this study). However, the data shows a lot of scatter and a clear trend cannot be deduced.

Changes in axial strain with time during creep under constant confining stress measured during each experiment were fitted to curves described by Eq. 21 to estimate the magnitude of the parameters *A*, α, and *m*. An example showing the change in axial strain during creep and fitted curves, represented by dotted lines, of dense Silica sand is shown in Fig. 4-54. Values of the parameter *m*, which represents the rate of decrease in axial strain rate over time during creep, determined for the test soils are shown in Fig. 4-55. Magnitudes of *m* determined from the creep experiments range from about 0.72 to 0.98, with lower values often observed for rounded particles (glass beads) and higher deviator stresses. Mejia et al. (1988) reported a value of *m* of approximately 0.9 for Tailings sand, while Murayama et al. (1984) reported a value of about 1.0 for Toyoura sand. The values shown in Fig. 4-55 will be compared to results from DEM creep simulation in Chapter 7.

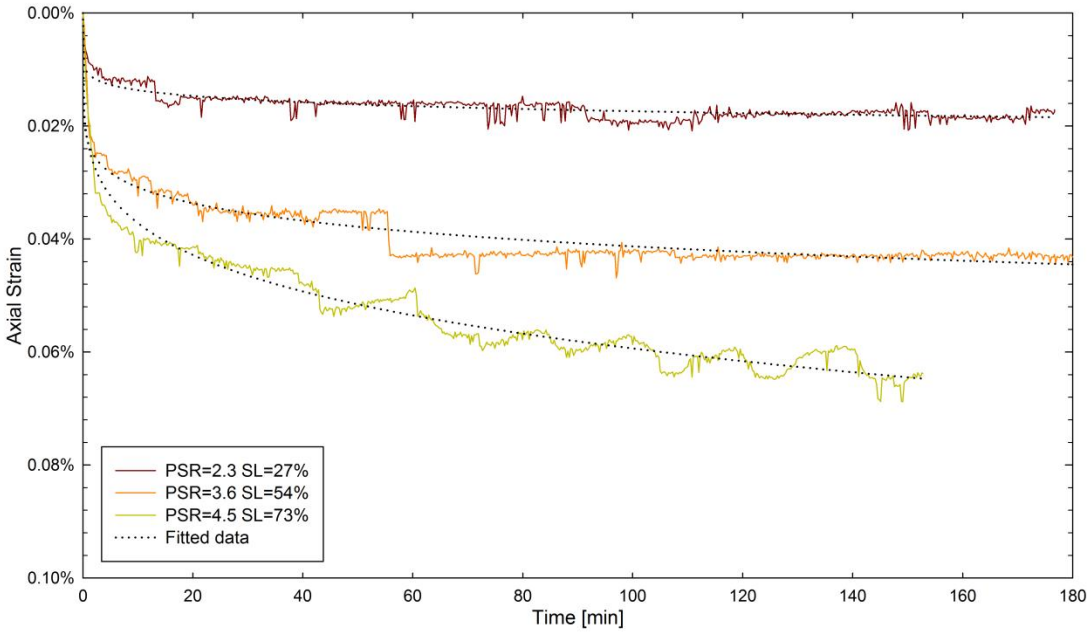

Fig. 4-54. Change in axial strain during creep for dense Silica sand.

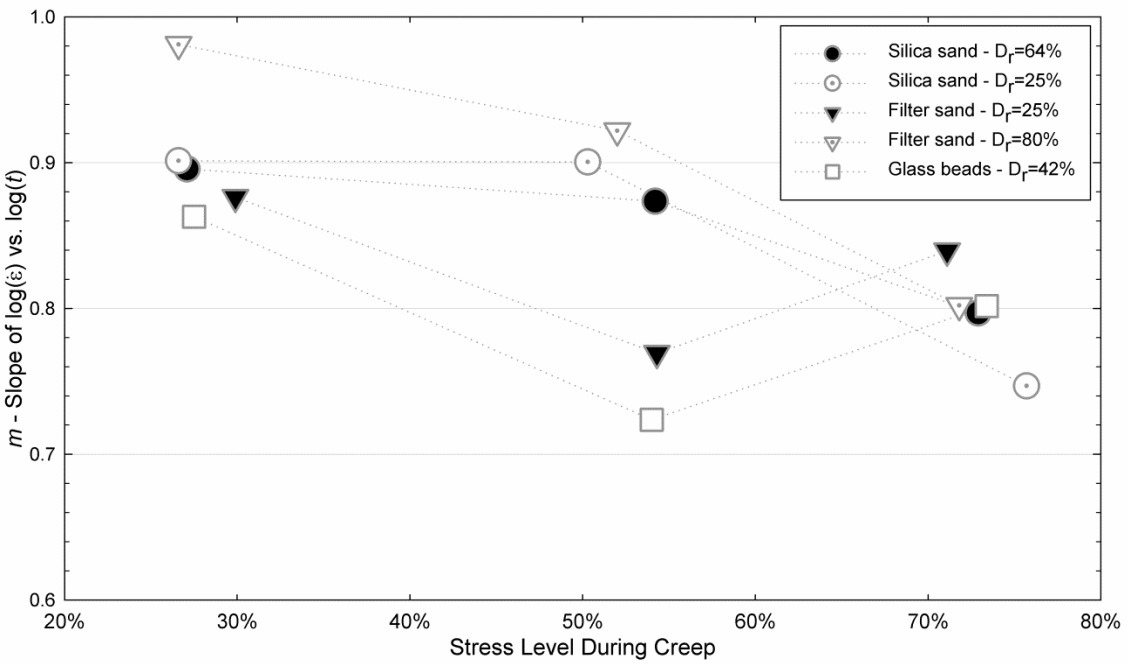

Fig. 4-55. Values of the parameter *m* determined for the granular materials.

4.5.2.2 AEs during Creep

AEs were recorded during triaxial compression experiments conducted using an effective consolidation stress (σ'_3) of 30 psi (207 kPa). High magnitudes of stress increase the amplitude of AEs emitted, facilitating their detection using the external receiver described in Section 4.4.1. Particle crushing is still expected to play a minor role in the AEs produced, because the magnitude of the applied stresses are still lower than those used during the one-dimensional compression tests presented in Section 4.5.1.

Results from triaxial compression tests on dense Silica sand, loose Silica sand, and glass beads are shown in Fig. 4-56, Fig. 4-57, and Fig. 4-58.

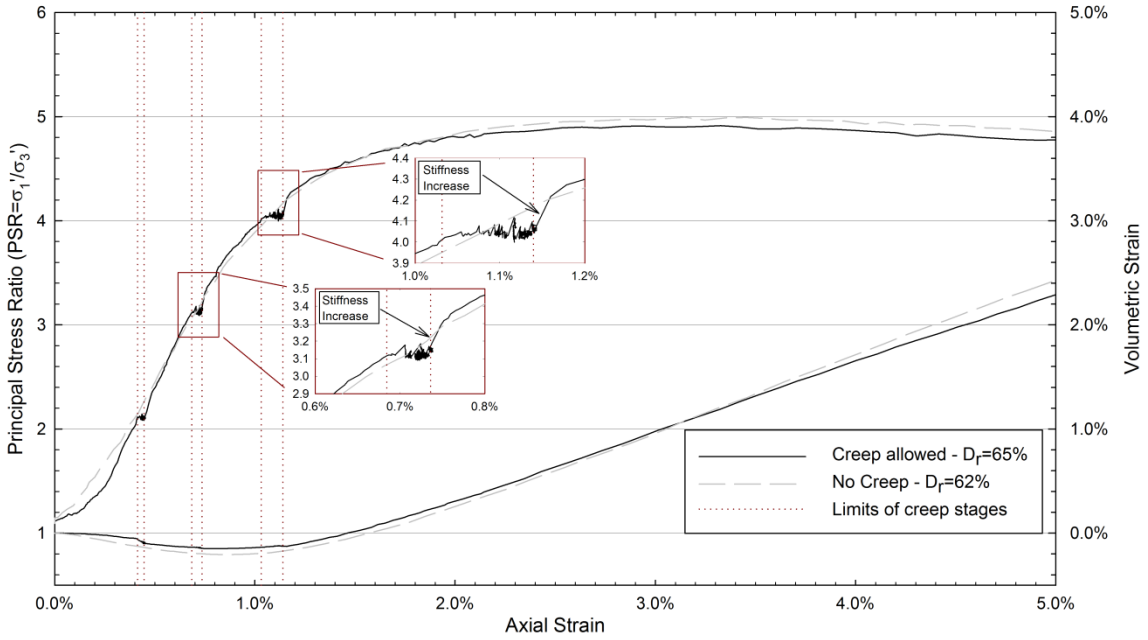

Fig. 4-56. Change in principal stress ratio and volumetric strain with axial strain during triaxial compression of dense Silica sand. Consolidation stress (σ'_3) of 30 psi.

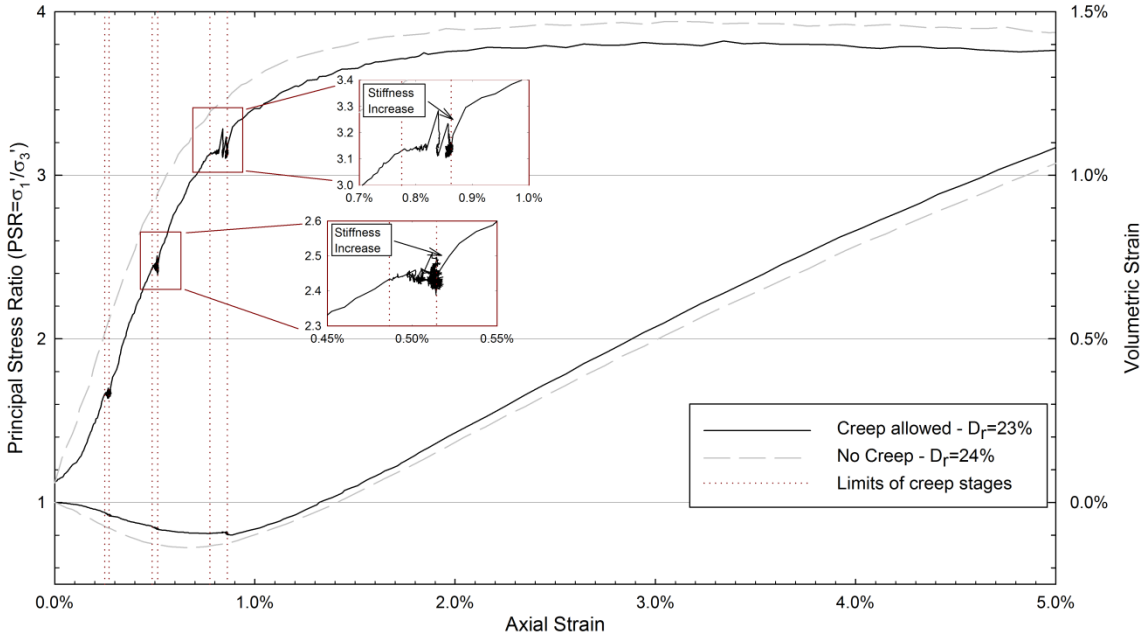

Fig. 4-57. Change in principal stress ratio and volumetric strain with axial strain during triaxial compression of loose Silica sand. Consolidation stress (σ'_3) of 30 psi.

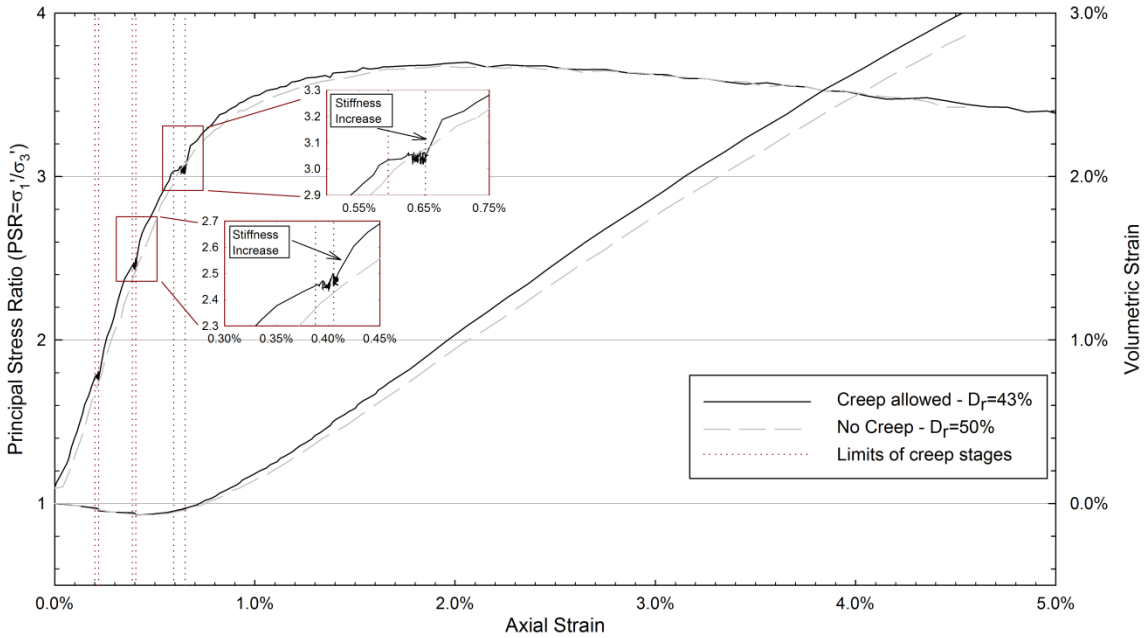

Fig. 4-58. Change in principal stress ratio and volumetric strain with axial strain during triaxial compression of glass beads. Consolidation stress (σ'_3) of 30 psi.

Stress-strain relationships from triaxial compression experiments conducted using a value of σ'_3 of 30 psi show similar characteristics to the tests described in Section 4.5.2.1 (σ'_3=10 psi). After each 3 hour creep stage, the specimen exhibited a momentary increase in stiffness, which disappeared as the specimen was deformed further. Additionally, specimens allowed to creep during the experiment exhibited a greater tendency towards dilation during shear.

The acoustic signals recorded during each of the tests are shown in Fig. 4-59, Fig. 4-60, and Fig. 4-61.

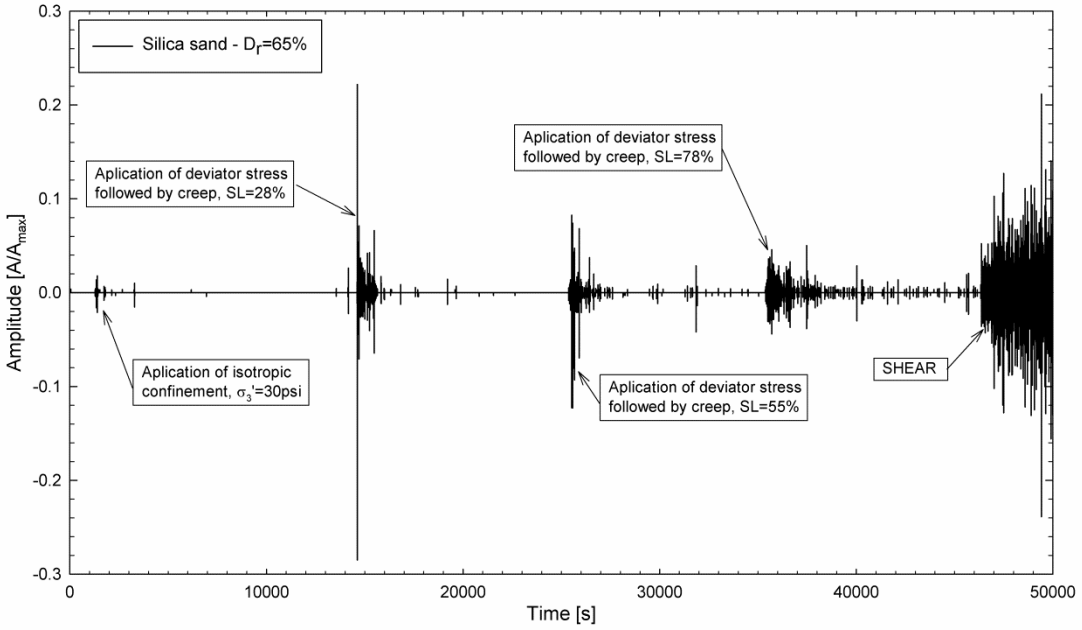

Fig. 4-59. Acoustic signal recorded during triaxial compression of dense Silica sand.

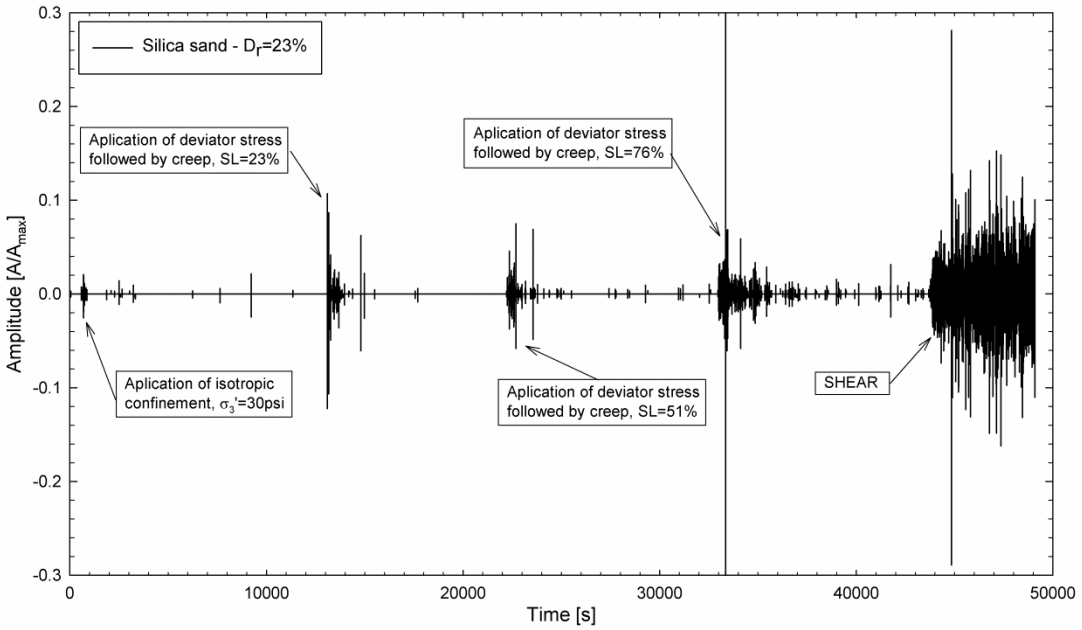

Fig. 4-60. Acoustic signal recorded during triaxial compression of loose Silica sand.

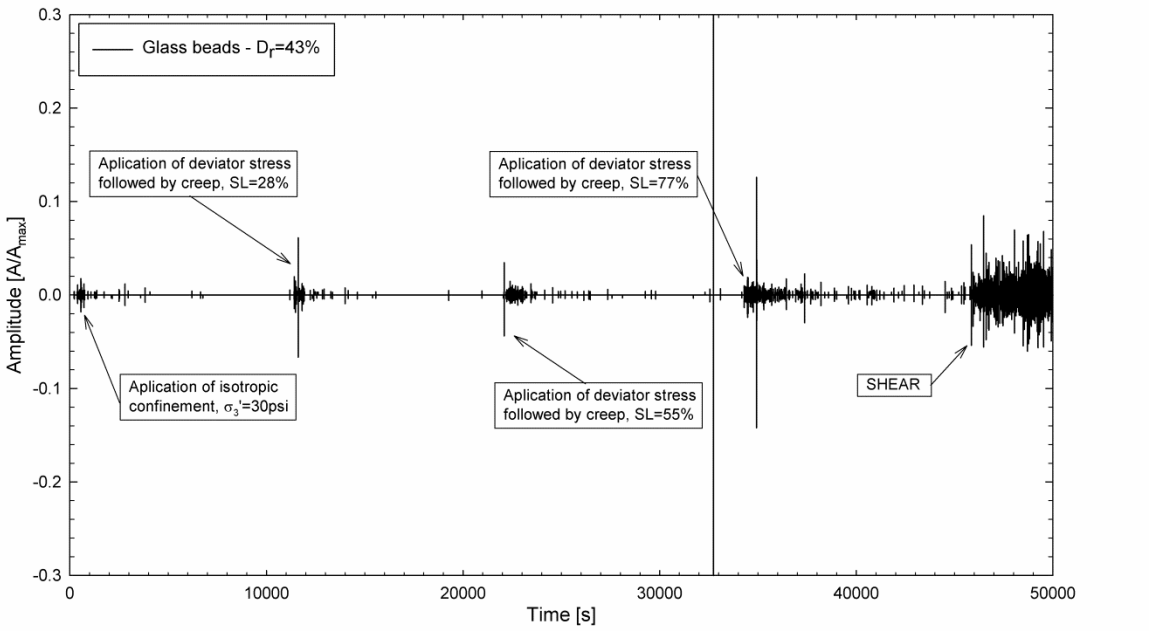

Fig. 4-61. Acoustic signal recorded during triaxial compression of glass beads.

The information from the previous figures was processed to calculate the respective AE count for each test, using the procedure used for one-dimensional compression experiments, described in Section 4.5.1.2, and a threshold value of 2.1E-3. The change in AE count during the triaxial compression experiments is shown in Fig. 4-62, Fig. 4-63, and Fig. 4-64. Characteristics of the acoustic signal recorded during the experiments, and observed in the previous figures, include:

- Similar to one-dimensional compression experiments, in the triaxial compression tests, the AE count continues to increase during creep. The AE count versus axial strain relationship follows a similar slope during creep to that shown during the application of the deviator stress before the start of the creep stage.
- The AE count versus axial strain relationship becomes more horizontal just after the start of shear following creep. After some deformation, the curve retakes its initial slope. That occurs after about the same deformation required for the momentary stiffness increase to disappear.

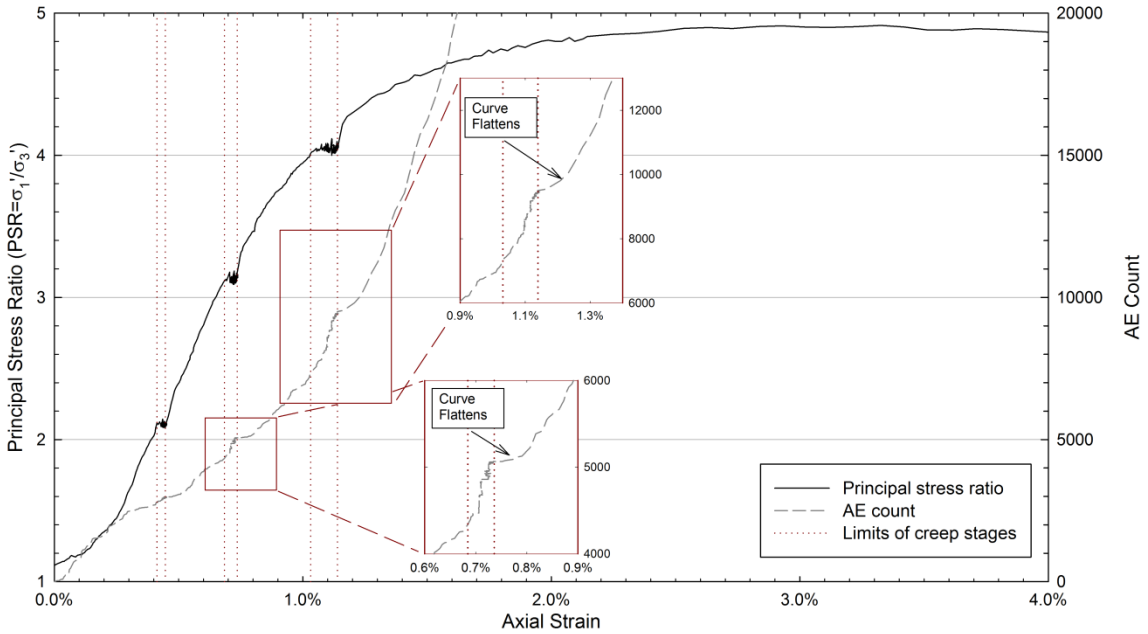

Fig. 4-62. Change in principal stress ratio and AE count with axial strain during triaxial compression of dense Silica sand (σ'_3=30 psi).

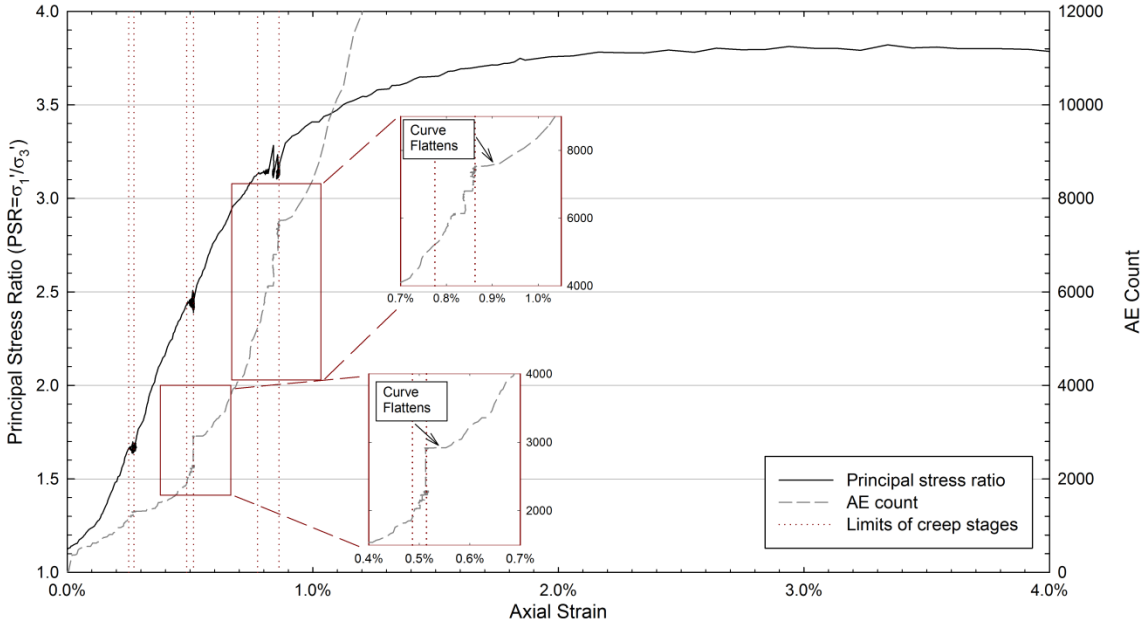

Fig. 4-63. Change in principal stress ratio and AE count with axial strain during triaxial compression of loose Silica sand (σ'_3=30 psi).

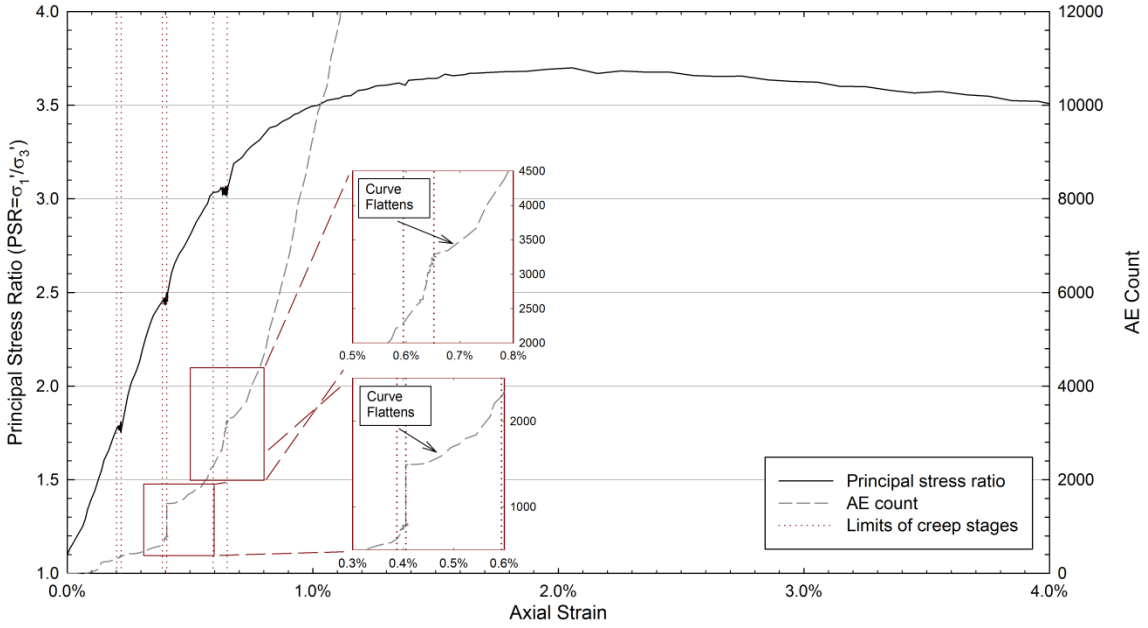

Fig. 4-64. Change in principal stress ratio and AE count with axial strain during triaxial compression of glass beads (σ'_3=30 psi).

The analysis of AEs recorded during creep indicates that particles continue moving during the creep. Following creep, the rate of increase in AE count with respect to axial deformation becomes more horizontal, and increases as the specimen deforms. Because AEs have been linked to rearrangement of the internal structure of the material (Baranov et al. 2007), low rates of increase in AE count with respect to axial deformation would be related to less *internal remolding* during deformation, represented by fewer particle movements and less production of AEs.

The variation of axial strain and AE count with time during the test conducted on dense Silica sand (D_r=65%) is shown in Fig. 4-65. The figure shows that the AE count continues to increase over time during creep, even though only small axial deformations are measured (i.e., axial strains measured after three hours of creep were less than 0.1%).

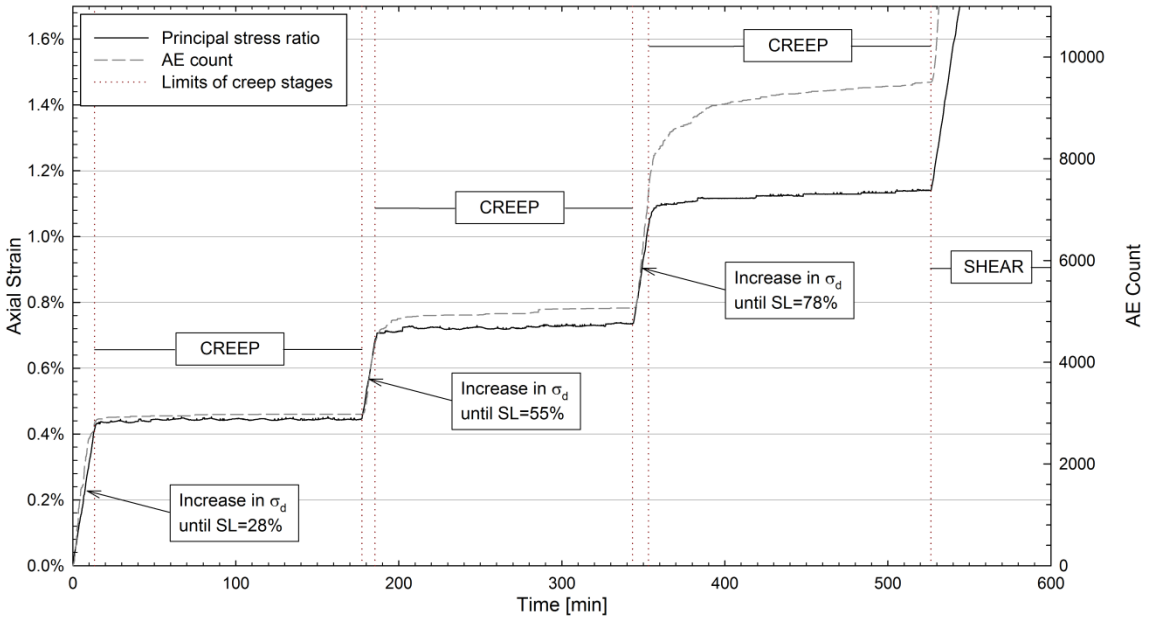

Fig. 4-65. Change in axial strain and AE count with respect to time during triaxial compression experiments on dense Silica sand.

According to Obert (1977) higher AE activity is linked to a more unstable material. Consequently, results from AE analysis indicate that particles continue rearranging during creep, and that this rearrangement leads to a more stable internal structure that is reflected in a decrease in the AE activity over time. When the specimen is sheared again after creep, it exhibits an immediate increase in stiffness which disappears as deformation increases. That increase in stiffness occurs along with a reduction in the rate of change in AE count with respect to axial strain. It appears that the internal equilibrium achieved during the creep accounts for the observed change in macroscopic stiffness. The gain in stiffness during creep disappears at about the same strain at which the AE count - to axial strain relationship reaches a slope similar to that observed previous to the creep stage. At that point, remolding due to shear has destroyed the stable structure achieved during creep, which will be called the *aged soil structure*. Internal processes occurring during creep which ultimately produce this aged soil

structure, as well as resulting changes in macroscopic properties of the material, will be studied in the following chapters using the Discrete Element Method.

4.6 Conclusions

This chapter presented the results from creep experiments conducted during one-dimensional and triaxial compression of filter sand, Silica sand, and glass beads. Some of the main conclusions are:

- The analysis of AEs shows that particles in the specimen continue rearranging during creep.
- Particle movements occurring during creep are reflected only by minor specimen deformations.
- Specimens of granular materials allowed to creep during triaxial compression tend to compress or dilate depending on the magnitude of stress level applied. The change in volumetric strain during creep follows the same trend shown by an identical specimen being sheared without creep and at the same stress level.
- Results from laboratory creep experiments agree with the stress-strain-time relationship proposed by Mitchell and Soga (2005) and shown in Eq. 15.
- Creep produces an increase in the macroscopic stiffness of the material. This increase in stiffness disappears as the sample deforms during further shear.
- Specimens allowed to creep during triaxial compression exhibit a greater tendency towards dilation than samples where no creep is allowed.
- The analysis of AEs emitted during creep under constant vertical and horizontal confining stresses show that the AE count continues to increase but the AE

activity decreases over time. That indicates that particle movements during creep produce a more stable soil structure, which appears to be also responsible for the momentary increase in stiffness observed after creep.

- It is recommended that creep studies in sands should implement dead weight loading as opposed to servo-controlled loading to assure that the applied stresses are kept constant during the tests.

The creep experiments presented in this chapter demonstrate that granular materials continue to change during creep. AE analysis during creep under oedometric and constant stress conditions show that particles in the specimens continue moving over time, even though only small macroscopic strains can be measured. Particle movements during creep cause the soil structure to become more stable, thus resulting in greater macroscopic stiffnesses. The effect of creep on the stiffness of the material disappears as the sample deforms. The values of the Hardin's breakage factor (B_r) determined after the tests show that particle breakage/crushing was not important during creep. These observations agree with behavioral characteristics of aged sands, and point towards physical processes involving particle reorientation and soil restructuration as the main driving mechanism of aging in granular materials.

Small variations during the specimen preparation for one-dimensional compression, and introduced by the load adjustments from the application mechanism (actuators) for triaxial compression, makes it difficult to assess the influence of factors such as the initial void ratio or the particle shape on aging and creep processes observed during this laboratory study.

Stress-strain characteristics observed and measured during the tests will be used for comparison with results obtained from DEM simulations in following chapters. Properties such as the grain sphericity and strength will be used to generate DEM assemblies that resemble the materials used for these laboratory experiments.

Chapter 5

The Discrete Element Method

5.1 Introduction

New evidence indicates that internal and time-dependent changes in the soil structure caused by particle slippage and rearrangement are the main driving mechanism causing sand aging effects. Considering that the proposed mechanism is controlled primarily by physical processes at the particle-level, the implementation of the Discrete Element Method (DEM) should be useful for studying aging in granular materials, as it allows studying processes from the micro-scale (particle level) to macro-scale.

The Discrete Element Method, initially developed by Cundall et al. (1979), is a numerical tool which allows modeling the macroscopic response of granular materials by simulating its micro-scale behavior under the effect of a disturbance. DEM models granular materials as composed of multiple discrete and rigid particles. The macroscopic

response of the material is estimated by tracking the movement of each of the particles and determining the forces that act between them.

The application of DEM to solve geotechnical engineering problems is not straight forward. Calculating the movement of each individual particle and the forces acting between them is very computationally demanding, especially considering the great number of particles required to model granular soils. To reduce the amount of calculations performed, and decrease the execution time, DEM models assume that the particles' response remains constant during a certain time period. In this way, particle interactions, including contact forces and particle accelerations, are only calculated at discrete moments in time.

The time period which separates each calculation cycle is called the time step (Δt). Large values of time step help reduce the execution time, but may also result in the calculation of unrealistic particle indentations and erratic internal forces. In order to avoid this, DEM simulations often require scaling some of the simulation parameters. Even though this technique has become common practice in DEM applications, it can significantly alter the simulation, producing meaningless results. This does not mean that DEM cannot be used to study soil behaviors such as aging, but rather that it should be used carefully with understanding of its limitations.

This chapter will introduce the DEM's theoretical background. DEM simulations will be studied using simple geometries (2D assemblies) and shearing conditions (biaxial compression). Even though this investigation will use DEM simulations in three dimensions using complex particle geometries, the particle configuration described in this

chapter provides a reasonable starting point to understand the applicability of DEM models in geotechnical engineering problems.

5.2 Theoretical Background

Since its initial development DEM has been used in a wide variety of fields, including pharmaceutics, rock mechanics, chemical engineering, and civil engineering. Applications range from simulations of simple geotechnical tests (Antony et al. 2005), to models of asphalt mixtures (Dai and You 2007), granular flow on hoppers and belt conveyers (Vu-Quoc et al. 2000; Li et al. 2004), tumbling mills (McBride et al. 2004), and many others.

Due to its capacity to simulate the macro-scale behavior of granular materials based on micro-scale properties of their particles, DEM has been used in geotechnical engineering to study the behavior of soils. It offers the opportunity to study the internal behavior of a particle assemblage; e.g., formation of load chains, particle movements, development of shear bands; and the associated effect on the macro-scale properties of the soil. Some examples of DEM applications in geotechnical engineering include the simulation of samples under direct shear (Bharadwaj et al. 2008), simple shear (Thornton and Zhang 2006), triaxial and biaxial shear (Ng 2009), and cyclic loading (Sitharam 2003).

DEM is based on two main concepts: (1) particle dynamics, analyzed using Newton's second law of motion; and (2) particle interaction, simulated by the implementation of a Contact Mechanism (CM). Even though DEM seems simple in concept, it requires multiple assumptions, along with the scaling and manipulation of

certain parameters, to have any practicality. Difficulties can arise, as some of these parameters can have a significant effect in the simulations if they are not controlled correctly. Special attention is needed in order to identify these parameters, define reasonable values, and determine their effect in the results obtained using DEM simulations.

5.2.1 Calculations

DEM simulations are based on the estimation of the particle interactions and the calculation of the corresponding particle movements. There are many DEM computer codes available, and all rely on a simple cyclic calculation process to perform the simulations: (1) normal and tangential particle indentations are calculated geometrically based on particle positions and radial velocities; (2) normal and tangential inter-particle forces are found using particle indentations and the implementation of a contact mechanism; (3) the total force and moment acting on each particle are used to calculate new particle accelerations; (4) new particle velocities and positions are found based on the particle accelerations and the magnitude of time step selected.

Open source and non-commercial DEM software packages used in geotechnical applications include BALL (Cundall and Strack 1979), TRUBAL (Strack and Cundall 1984), OVAL (Kuhn 1999), ELLIPSE2 (Ng 1994), ELLIPSE3D (Lin and Ng 1997), and DISC (Sitharam 2003). Commercial DEM packages include PFC2D and PFC3D, developed by Itasca Consulting Group Inc., and EDEM, developed by DEM Solutions.

Differences between DEM software packages are mainly related to the contact detection algorithm, macroscopic stress and strain determination, default boundary conditions, available contact mechanisms, and the incorporation of simulation parameters

such as viscosity. While the contact detection mechanism influences primarily the calculation efficiency and execution time, other conditions, such as the process used for macroscopic stress and strain determination, may have a significant effect on the results of DEM simulations.

5.2.1.1 Particle Interactions

The first step in a DEM calculation cycle is the determination of particle positions and indentations. Particles are assumed rigid in DEM, and grain indentations are estimated based on the overlapping between particles. The calculation of the normal particle indentation is simple: assuming two particles *a* and *b*, the normal particle indentation U_n, shown in Fig. 5-1, can be expressed by Eq. 18, where r_a and r_b, and $\mathbf{x}_a$ and $\mathbf{x}_a$, represent the radii and positions of particles *a* and *b*. A middle point in the particle indentation, called $\mathbf{x}_c$, is calculated using Eq. 19. Sub-indices 1 and 2 indicate the vector components in directions x_1 and x_2.

$$U_n = (r_a + r_b) - |\mathbf{x}_b - \mathbf{x}_a| \tag{18}$$

$$\mathbf{x}_c = \mathbf{x}_a + \left(r_a - \frac{U_n}{2} \right) \frac{\mathbf{x}_b - \mathbf{x}_a}{|\mathbf{x}_b - \mathbf{x}_a|} \tag{19}$$

$$|\mathbf{x}_b - \mathbf{x}_a| = \sqrt{(x_{b,1} - x_{a,1})(x_{b,2} - x_{a,2})} \tag{20}$$

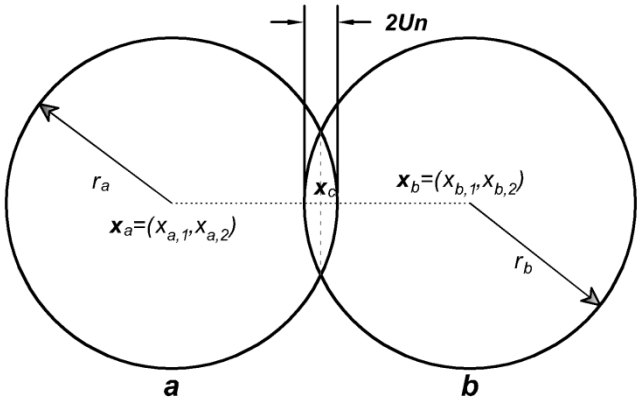

Fig. 5-1. Nomenclature for particle indentation.

The particle indentation in the tangential direction is calculated following a different procedure, based on the relative particle translational and angular velocities. The calculation is done incrementally, assuming that the tangential forces and indentations are equal to zero for the initial step of the simulation, and subsequently adding their corresponding value for each time step.

The relative tangential velocity (V_t) of two particles in contact (*a* and *b*) is found using Eq. 21, where $\dot{\mathbf{x}}$ and $\mathbf{w}$ are the translational and angular velocities of the particle. For a 2D problem, $\mathbf{w}$ denotes the angular velocity in the direction x_3. The parameter $\hat{\mathbf{t}}$ represents a unit vector in the direction tangent to the particle contact, as shown in Fig. 5-2. The magnitudes of $\hat{\mathbf{t}}$ in the directions x_1 and x_2 are calculated using Eq. 23.

$$V_t = (\dot{\mathbf{x}}_b - \dot{\mathbf{x}}_a) \cdot \hat{\mathbf{t}} - \mathbf{w}_b |\mathbf{x}_c - \mathbf{x}_b| - \mathbf{w}_a |\mathbf{x}_c - \mathbf{x}_a| \tag{21}$$

$$\hat{\mathbf{n}} = \frac{\mathbf{x}_b - \mathbf{x}_a}{|\mathbf{x}_b - \mathbf{x}_a|} \tag{22}$$

$$\hat{\mathbf{t}} = (-n_2, n_1) \tag{23}$$

The increment in tangential indentation (ΔU_t) during a time step can be calculated using Eq. 24 and the value of V_t,.

$$\Delta U_t = \Delta t * V_t \tag{24}$$

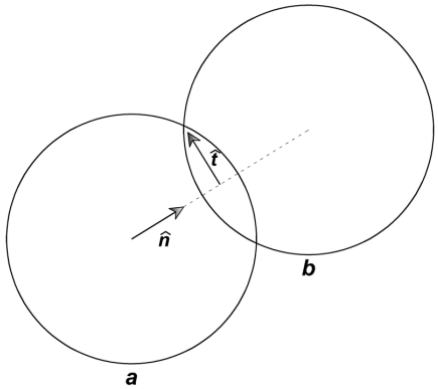

Fig. 5-2. Normal ($\hat{\mathbf{n}}$) and tangential ($\hat{\mathbf{t}}$) unit vectors.

The normal (f_n) and tangential (f_t) components of the contact force are calculated based on the normal and tangential particle indentations. In DEM, the normal contact

force (f_n) is found using the normal particle stiffness (K_n), which relates the total normal particle indentation to the total normal contact force, as shown by Eq. 25. The fact that f_n can be calculated based solely in the current assemblage configuration, makes the code less susceptible to numerical drift (Itasca Consulting Group Inc. 2008). The tangential force is calculated accumulatively, using a secant particle tangential stiffness (k_t) relating the change in tangential indentation (ΔU_t) to the variation in the tangential force (Δf_t). This relationship is shown in Eq. 26. The total tangential force (f_t) is the addition of the total contact tangential force for the previous time step and the variation in tangential force calculated for the current step (Δf_t). The difference in the calculation processes used for finding f_n and f_t is particularly important for cases where the value of secant modulus changes along with the level of indentation, such as the Hertz-Mindlin CM described below.

$$f_n = U_n K_n \tag{25}$$

$$\Delta f_t = -\Delta U_t k_t \tag{26}$$

The contribution from the contact force to the forces on particles *a* and *b* ($\mathbf{f}_a$ and $\mathbf{f}_b$) are calculated using Eqs. 27 and 28. Likewise, the contribution from the contact force to the moment acting on particles *a* and *b* ($\mathbf{M}_a$ and $\mathbf{M}_b$) are calculated using Eqs. 29 and 30. The total forces and moments acting on a particle are calculated by adding the force and moment contributions from each one of the contacts formed by the given particle.

$$\mathbf{f}_a = -\left(f_n \hat{\mathbf{n}} + f_t \hat{\mathbf{t}}\right) \tag{27}$$

$$\mathbf{f}_b = \left(f_n \hat{\mathbf{n}} + f_t \hat{\mathbf{t}}\right) \tag{28}$$

$$\mathbf{M}_a = \mathbf{f}_a \times \left(\mathbf{x}_c - \mathbf{x}_a\right) \tag{29}$$

$$\mathbf{M}_b = \mathbf{f}_b \times \left(\mathbf{x}_c - \mathbf{x}_b\right) \tag{30}$$

5.2.1.2 Contact Mechanisms

Contact forces are estimated by the implementation of a contact mechanism (CM), which models particle interactions using mathematical relationships. Contact mechanisms used in DEM regularly include: (1) elastic properties of the rigid particles relating normal and tangential particle indentations to normal and tangential forces; (2) a shear failure criterion, commonly represented by a frictional slider and/or cohesive bonds, to limit the maximum attainable tangential force at a contact; and (3) a viscous dashpot, which helps to dissipate excess energy in the system, and can have a significant effect on the properties of the assembly, particularly when modeling time-dependent processes such as strain rate effects and creep. Fig. 5-3 shows the graphical interpretation of the normal and tangential particle indentation, and their relation with f_n and f_t.

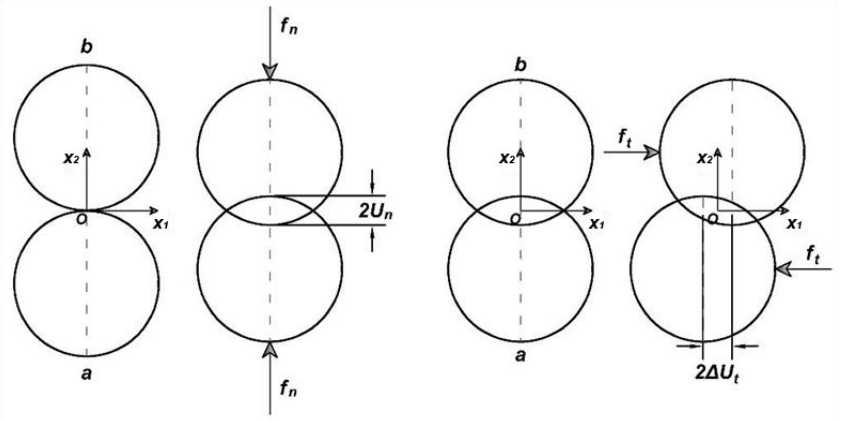

Fig. 5-3. Normal (U_n) and tangential (U_t) indentations between two 2D particles with acting normal and tangential forces f_n and f_t.

Two contact mechanisms are commonly used in DEM models of granular soils: (1) the linear elastic CM, and (2) the Hertz-Mindlin CM. The main difference between these two methods is in the assumptions used for the calculation of the normal and tangential contact stiffnesses.

Linear Elastic Contact Mechanism

The linear elastic CM is perhaps the most simple and least computationally demanding contact mechanism used in DEM. For this CM, normal particle interactions are modeled using a linear-elastic spring. The normal (K_n) and tangential (k_t) contact stiffnesses are calculated based on the stiffness of the two particles in contact, using Eqs. 31 and 32. A viscous dashpot is commonly added parallel to the elastic spring to dissipate excess kinetic energy.

$$K_n = \frac{k_{n,a} k_{n,b}}{k_{n,a} + k_{n,b}} \tag{31}$$

$$k_t = \frac{k_{t,a} k_{t,b}}{k_{t,a} + k_{t,b}} \tag{32}$$

Tangential particle interactions are modeled using a similar approach, but with the addition of a frictional slider in series with the linear spring. The frictional slider incorporates the Mohr-Coulomb failure mechanism, controlling the maximum attainable tangential force at the contacts, and the related macro-scale strength of the material. Fig. 5-4 shows a diagram of the linear elastic CM regularly used to model (a) normal and (b) tangential particle interactions. In granular assemblies, the normal and tangential contact forces contribute to support the deviatory stress. While the contribution from the normal component is considerably higher, particle sliding, resulting from the inter-particle tangential forces and controlled by the contact failure mechanism, has a significant effect on the macroscopic strength of the assembly.

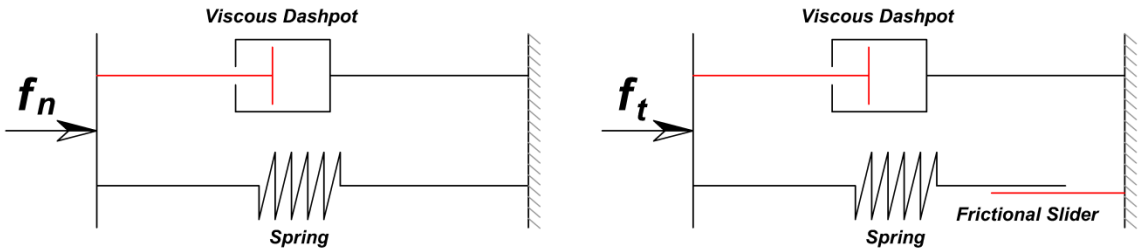

(a) (b)

Fig. 5-4. Linear elastic contact model for: (a) normal and (b) tangential particle interactions.

The linear elastic CM requires fewer and simpler calculations than the Hertz-Mindlin CM. Therefore, models using the linear elastic CM often require shorter execution times. Since one of the principal disadvantages of DEM is the long time required to run simple simulations, the implementation of the linear elastic CM has become very common in DEM practice. Some examples of investigation where the linear elastic CM have been used include simulations of clay creep (Kuhn and Mitchell 1993), aging in sand (Wang et al. 2008), biaxial shear in sand (Huang et al. 2008), cyclic loading of granular materials (Sitharam 2003), liquefaction simulations (Dinesh et al. 2004), deep penetration in granular materials (Jiang et al. 2006), and grain crushing (Lobo-Guerrero and Vallejo 2005).

Hertz-Mindlin Contact Mechanism

The Hertz-Mindlin contact mechanism allows calculating non-linear particle interactions. This model assumes that the particles are homogeneous, isotropic, and elastic. In an unstressed state, two particles in contact share common tangent (x_1) and normal (x_2) planes passing through the point of contact, named *O* in Fig. 5-3. Once a normal force is applied, the particles deform and the area of contact increases. This is illustrated in Fig. 5-5.

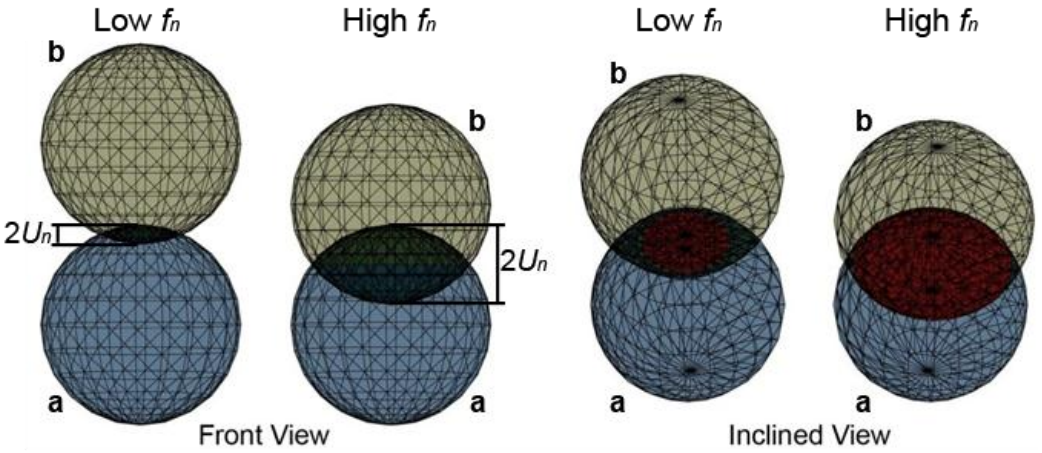

Fig. 5-5. Indentation (U_n) and area of contact between two spheres as f_n increases (area of contact is shown in red).

According to Hertz's theory (Mindlin 1949), the boundary of the area of contact is an ellipse, and the magnitude and orientation of the principal axis, as well as the distribution of the normal stress (σ) over the surface, can be calculated using mathematical relationships. The problem can be simplified by analyzing spheres, in which case the normal force can be determined using Eqs. 33 to 35 (Thornton and Randall 1988), where E is the Young's modulus of a particle, v is the Poisson's ratio, and r is the radius.

$$f_n = \frac{4}{3} E_{ab} r_{ab}^{\frac{1}{2}} U_n^{\frac{3}{2}} \tag{33}$$

$$\frac{1}{E_{ab}} = \frac{1-v_a^2}{E_a} + \frac{1-v_b^2}{E_b} \tag{34}$$

$$\frac{1}{r_{ab}} = \frac{1}{r_a} + \frac{1}{r_b} \tag{35}$$

The derivation of these relationships neglects the energy dissipated from the system through sound waves and the possibility of exceeding the elastic limit, which may result in permanent plastic deformation of the particles. These factors can be important under certain conditions, including large confining stresses and cyclic shear, and may invalidate the model under particular circumstances (Duran 2000). However, their

inclusion in the model increases the complexity and the amount of calculations during already computationally demanding DEM simulations.

Mindlin (1949) derived a formulation for the particle interaction in the tangential direction based on the tangential and torsional compliance of the two bodies in contact. For spheres, the incremental tangential displacement can be found based on the normal and tangential forces, the elastic constants, Coulomb's failure characteristics, and the geometry of the particles (Mindlin and Deresiewicz 1953).

According to Mindlin's contact model, under a constant normal force f_n, two spheres have a planar circular contact area with a radius a. The application of a tangential force (f_t) generates tangential traction (τ) on the contact surface. The tangential traction does not affect the distribution of the normal stress (σ) on the contact surface (Mindlin and Deresiewicz 1953). The resultant tangential stress is parallel to the direction of the applied force and axially symmetric in magnitude, forming concentric circular contours of constant tangential traction. If slip does not occur, its magnitude rises from half the average at the center to infinity at the edges (Mindlin 1949).

As the tangential traction cannot exceed the product of the coefficient of friction (μ) and the normal stress, slip occurs in the section of the area of contact surface with higher tangential stresses; i.e., outer ring. The area of slip forms an annulus with an external radius equal to the radius of the contact surface (a), internal radius c, and traction τ equal to $\mu\sigma$. The tangential component of displacement is constant in the adhered surface, where slip has not occurred (Mindlin and Deresiewicz 1953). Fig. 5-6 shows a diagram of the distribution of the tangential traction over the contact surface. The variation in the magnitude of τ with respected to the distance from the center of the

contact area is given by curve *B*-*A*-*a*. In this figure, ρ is distance from the center of the contact area, *a* is the radius of the contact surface, and *c* the internal radius of the annulus of slip. Once point *A* (ρ=*c*) is reached, the magnitude of the tangential traction equals $\mu\sigma$. The decrease in the magnitude of τ after *A* is caused by the reduction of the normal stress away from the center of contact.

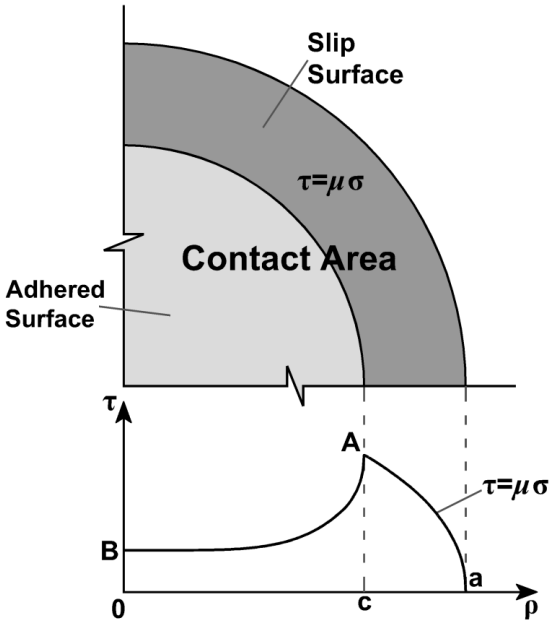

Fig. 5-6. Distribution of the tangential traction (τ) in the area of contact between two spheres.

If the magnitude of the tangential force reaches μf_n, as indicated by point *F* in Fig. 5-7, the adhered surface is reduced to zero, slippage starts to take place over the entire contact surface, and the displacement becomes indeterminate. This condition was named *sliding* by Mindlin and Deresiewicz (1953).

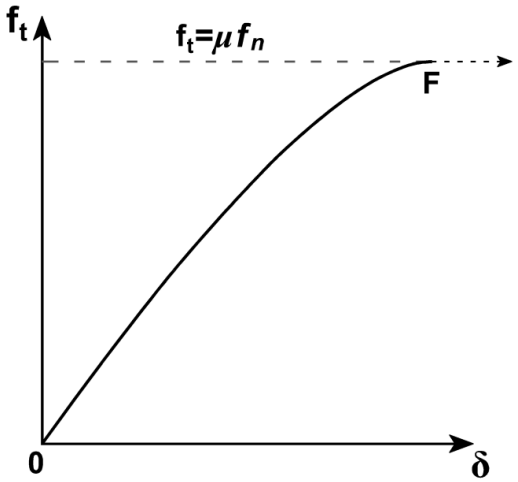

Fig. 5-7. Relation between tangential force (f_t) and tangential displacement (δ) according to Mindlin's contact theory.

If the magnitude of the tangential force is reduced, slip in the opposite direction (*counter-slip*) occurs at a distance *a* away from the center, and penetrates radially inwards until $\rho=b$, as shown in Fig. 5-8. The magnitude of *b* depends on the level of load reversal. Fig. 5-8 shows the distribution of the tangential traction over the contact surface and its variation with respect to ρ for load reversal conditions (f_t is reduced). Curve *B-A-a* represents the initial traction distribution under the application of a tangential force *T*, where $0<T<\mu f_n$. The hatched area shows the counter-slip surface generated by a reduction in the tangential force from *T* to *T*'. Since the magnitude of the tangential traction in the counter-lip surface is $-\mu\sigma$, a unit increase in the counter-slip surface causes a change of $-2\mu\sigma$ in the tangential traction. The change in tangential traction caused by the counter-slip is shown by the curve *B'-A'-a* in Fig. 5-8. The total traction distribution is calculated as the sum of the initial traction (curve *B-A-a*) and the change in τ (curve *B'-A'-a*), shown as curve *F-E-D-a* in Fig. 5-8.

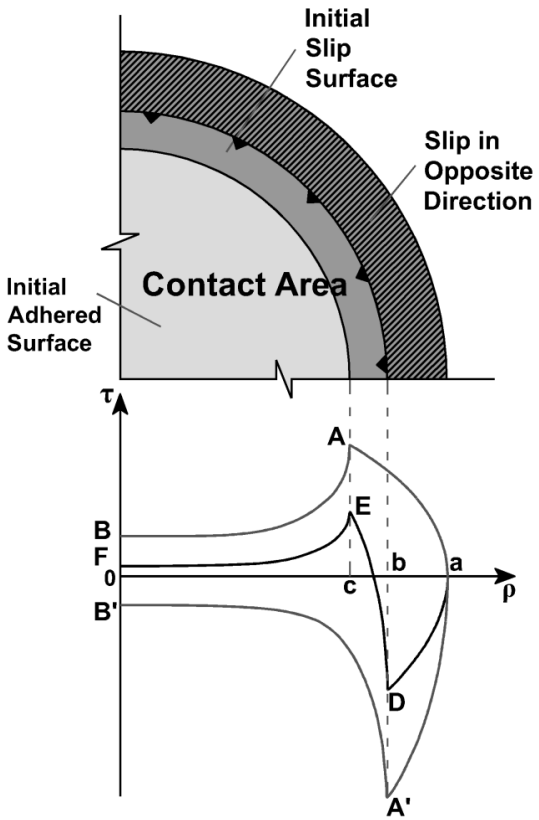

Fig. 5-8. Distribution of tangential traction (τ) on the contact surface for load reversal (reduction in the magnitude of f_t).

Once f_t reaches a value of $-T$, the counter-slip annulus penetrates to the depth of the initial slip ($b=a$). The resulting distribution of the tangential traction over the contact surface is equal to the distribution produced by the initial tangential force (T), shown as curve *B-A-a* in Fig. 5-8, but in the opposite direction.

The tangential force-displacement relationship after the load-unload cycle, according to Mindlin and Deresiewicz (1953), is shown in Fig. 5-9. Mindlin's contact theory calculates a plastic deformation, shown as *0-R* in Fig. 5-9, caused by a reduction in the magnitude of f_t from T back to 0. Fig. 5-9 also shows that the tangential displacement for $f_t=-T$ is equal the displacement calculated for $f_t=-T$, but in the opposite direction. Mindlin's theory predicts an identical force-displacement relationship for a change in tangential force from $-T$ to T, than from T to $-T$, thus resulting in the load-unload-reload

curve shown in Fig. 5-10. The magnitudes of the displacements *0-R* and *0-U* in Fig. 5-10 are equal.

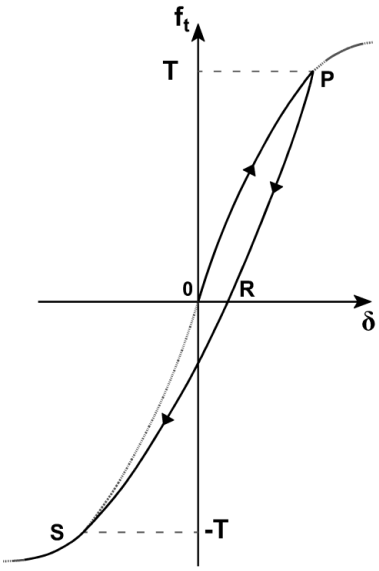

Fig. 5-9. Tangential force-displacement relationship for load-unload cycle according to Mindlin's contact theory.

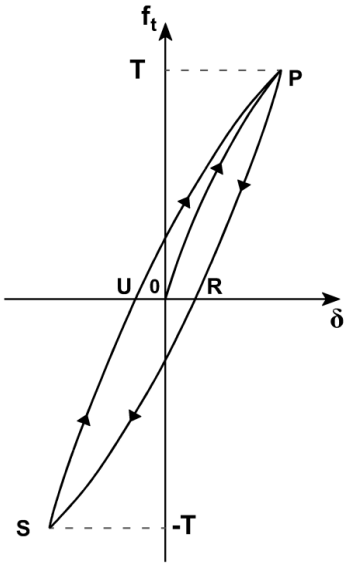

Fig. 5-10. Tangential force-displacement relationship for load-unload-reload cycle according to Mindlin's contact theory.

Thornton and Randall (1988) developed a method to incorporate the Hertz-Mindlin contact theory in DEM analysis, where the tangential particle stiffness and the macroscopic sample properties are stress-history dependent. Some simplifications to the

original Hertz-Mindlin CM are commonly used in DEM software such as PCF2D and PFC3D (Itasca Consulting Group Inc. 2008). In these software packages the tangential contact stiffness is calculated using Eq. 36, where G_{ab} and v_{ab} are the average shear modulus and Poisson's ratio of particles *a* and *b*.

$$k_t = \left[\frac{2\left(3G_{ab}^2 r_{ab}\left(1-v_{ab}\right)\right)^{\frac{1}{3}}}{2-v_{ab}} \right] f_n^{\frac{1}{3}} \tag{36}$$

$$r_{ab} = 2\frac{r_a r_b}{r_a + r_b} \tag{37}$$

While the linear elastic CM requires values of material stiffness in units of force per unit length, the Hertz-Mindlin CM allows using material properties with real physical units; e.g., Young's modulus and shear modulus in units of stress per unit strain. The implementation of the Hertz-Mindlin CM reduces the number of approximations required to run DEM simulations and gives better accuracy to DEM models, especially if the macro-scale sample stiffness or the strain at failure are important for the studies. Nevertheless, using the Hertz-Mindlin CM increases significantly the execution time. The Hertz-Mindlin contact mechanism has been used in various applications, including the study of biaxial compression (Thornton and Zhang 2006), direct shear (Wang et al. 2007), granular flow (Vu-Quoc et al. 2000), and the formation of sand piles (Li et al. 2005).

5.2.1.3 Particle Dynamics

This step of the DEM calculation cycle involves the determination of the particle motions based on the forces and moments acting on each particle. Particle dynamics are modeled by solving Newton's second law of motion. Based on the particle's mass (*m*) and the net total force acting on the particle (**F**), the particle acceleration ($\ddot{\mathbf{x}}$) can be

calculated using Eq. 38. Sub-indices i-1, i, and i+1, represent the values for the previous, current, and following time step.

$$\ddot{\mathbf{x}}_i = \frac{\mathbf{F}_i}{m} \tag{38}$$

Because DEM assumes that a particle's acceleration is constant during discrete time periods, called time steps (Δt), the particle's translational velocity ($\dot{\mathbf{x}}$) can be determined using Eq. 39 if the acceleration of gravity ($\mathbf{g}$) is considered, or Eq. 40 if gravity is neglected.

$$\dot{\mathbf{x}}_i = \dot{\mathbf{x}}_{i-1} + \left(\ddot{\mathbf{x}}_i \Delta t + \mathbf{g}\right) \tag{39}$$

$$\dot{\mathbf{x}}_i = \dot{\mathbf{x}}_{i-1} + \ddot{\mathbf{x}}_i \Delta t \tag{40}$$

The particle's angular velocity ($\mathbf{w}$) is calculated using the angular acceleration ($\dot{\mathbf{w}}$), which depends on the net moment ($\mathbf{M}$) and the inertia (I) of the particle, as shown in Eqs. 41 and 42.

$$\dot{\mathbf{w}}_i = \frac{\mathbf{M}_i}{I} \tag{41}$$

$$\mathbf{w}_i = \mathbf{w}_{i-1} + \dot{\mathbf{w}}_i \Delta t \tag{42}$$

Once the particle's translational and angular velocities are calculated, particle positions for the following time step ($\mathbf{x}_{i+1}$) are determined by calculating the particle's displacement ($\Delta\mathbf{x}_i$) using Eq. 43, and adding this displacement to the current particle position ($\mathbf{x}_i$). The particle's velocity is assumed constant during the time step.

$$\Delta\mathbf{x}_i = \dot{\mathbf{x}}\Delta t \tag{43}$$

$$\mathbf{x}_{i+1} = \mathbf{x}_i + \Delta\mathbf{x}_i \tag{44}$$

The same calculations are used for each particle in the assembly. Once all new particle positions are determined, new indentations for the following time step are determined.

5.2.2 Boundary Types

DEM models the movements and interactions of particles within a granular material, produced by the propagation of a disturbance. This disturbance generally originates at the boundaries of the assembly. Different boundary types can be used in DEM simulations. These range from simple rigid walls to more complex periodic boundaries. The ideal boundary type, as well as the method used to control the stress or strain at the boundaries, depends on the type of simulation and the conditions of the problem.

5.2.2.1 Rigid Walls

Rigid wall boundaries are commonly used in DEM simulations. The limits of the assembly are formed by non-deformable walls moving under a controlled velocity. Even though the displacements and forces at the boundaries can be controlled using rigid walls, only the displacements are defined directly. Boundary forces need to be controlled by continually and iteratively adjusting the boundary displacements in a servo-mechanical process (Kuhn 1987; Itasca Consulting Group Inc. 2008). Boundary forces for rigid walls are estimated as the sum of all contact forces formed by the wall. Stresses are calculated by dividing these forces by the area of the wall.

Strain boundary controls are specified by adjusting the wall velocity, such that it matches the required strain rate. For stress boundary controls, a servo-mechanism is used to estimate the wall movement necessary to achieve the desired boundary force for the following time step.

5.2.2.2 Particle boundary

Rigid walls can be replaced by strings of particles which act as the boundary of the assembly. This is usually done by initially running the model using rigid walls, detecting and fixing the particles in contact with the boundary, and later removing the rigid boundaries. Either the velocities or the forces on the boundary particles can be controlled.

For velocity-controlled boundaries, all the contact forces are calculated following the regular procedure, but the accelerations are only assigned to the internal particles of the arrangement. The total force at the boundary is calculated as the sum of the *out-of-balance* forces of the boundary particles. The o*ut-of-balance* force or net total force, shown as **F** in Fig. 5-11, is defined as the particle force which is not at equilibrium and which causes the particle to move.

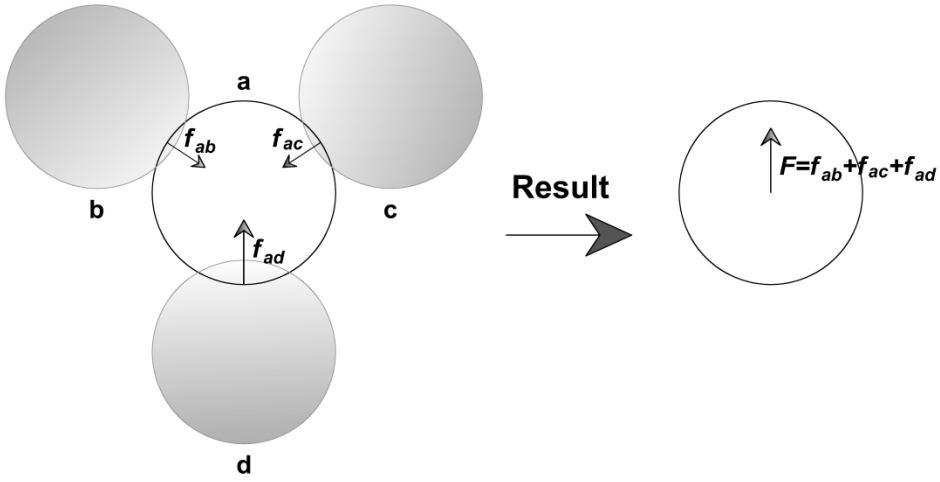

Fig. 5-11. Out-of-balance force (**F**) of particle *a.*

Boundary forces can be controlled directly on the boundary particles, and do not require the implementation of a servo-mechanism. Nevertheless, small perturbations can bring some of the boundary particles to conditions where their body forces are

insufficient to maintain equilibrium. A stabilizing algorithm is often used to help solve this problem (Itasca Consulting Group Inc. 2008).

5.2.2.3 Periodic Boundaries

In a periodic or repeating boundary the particles are contained within repeating parallelogram shaped cells. Particles within a reference cell are replicated to periodically fill up the system. During this process, the original and replicated particles are controlled such that they behave as one single particle, with the same force and velocity. The diagram in Fig. 5-12 shows a system with periodic boundaries. In this figure, three particles, named *a*, *b*, and *c*, are located within the reference cell, which is represented by continuous black lines. The periodic boundary replicates the particles onto the repeating cells, represented by dotted lines in Fig. 5-12. Each replicated particle (*a'*, *b'*, and *c'*) has the same force and velocity as the original particle. Particles located over the cell boundary, such as particle *b* in Fig. 5-12, are replicated on the opposite side of the cell, and may interact with particles located within the assembly. That is the case of particles *b'* and *c* in Fig. 5-12.

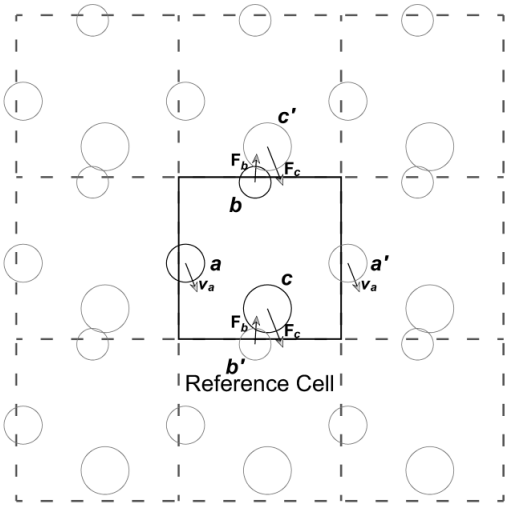

Fig. 5-12. Particle assembly with periodic boundaries.

The implementation of periodic boundaries removes unwanted edge effects that are often problematic when rigid walls are used. Additionally, the periodic boundaries allow the representation of larger assemblies using fewer particles (Kuhn 1987). Fig. 5-13 shows that DEM simulations of a small particle assembly (shown in black) can represent larger particle arrangements (shown in gray) if periodic boundaries are used.

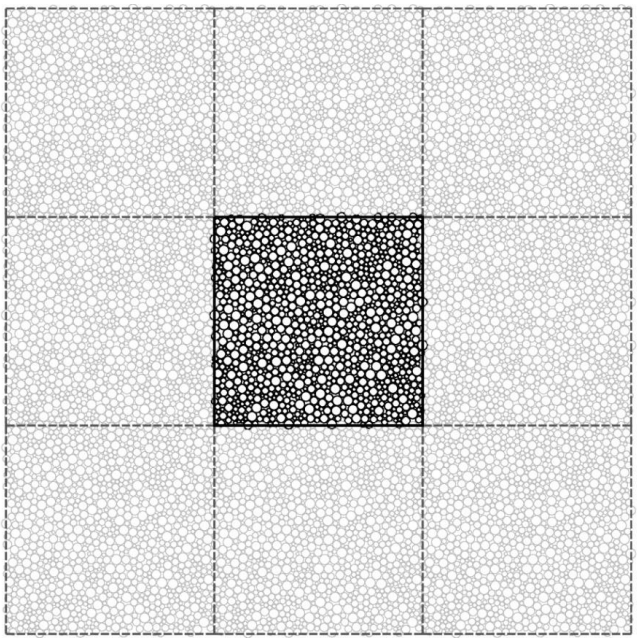

Fig. 5-13. Particle assembly used for DEM simulations (shown in black), and assembly represented by the periodic boundaries (shown in gray).

The average stress ($\bar{\sigma}$) within a granular assembly of volume *V*, that has *M* contacts, is calculated using Eq. 45, where *f* is contact force, and *l* is the distance between the particles in contact (Kuhn 1987). For periodic boundaries, the average stress is often assumed to be equal to the external macroscopic stress.

$$\bar{\sigma}_{ij} = -\frac{1}{V}\sum_{m=1}^{M} f_i l_j \qquad (45)$$

5.3 Required Input Parameters

DEM simulations require input parameters which are mainly related to micromechanical properties of the constitutive material of the particles. Table 5-1 contains a list of some of the parameters needed for DEM analysis. Although some of these parameters are simple to determine, others cannot be measured or assumed with certainty. It has become common practice in DEM studies to perform inverse modeling or calibrations to determine the values of unknown micromechanical properties of the material by matching DEM simulations with real test results (Itasca Consulting Group Inc. 2008; Fu et al. 2008). A better approach would be to define the parameters based on physical properties and then compare the results of the simulations with actual measured results (Class A prediction).

Table 5-1. Parameters and properties analyzed in this study.

Parameters and Properties for DEM Simulations
Time step (Δt)
Stiffness (K)
Density and Mass (ρ and m)
Viscosity and Damping
Friction Coefficient (μ)
Strain Rate ($\dot{\varepsilon}$)

A 2D particle arrangement formed by 4900 disks with radii ranging from 0.15 cm to 0.25 cm was used to evaluate the effects of variations in the values of the properties and parameters in Table 5-1. The particle assembly is shown in Fig. 5-14. Although this investigation will use 3D assemblies formed by particles of complex geometries, the particle assembly shown in Fig. 5-14 provides a simple starting point to study the applicability of DEM for solving geotechnical problems.

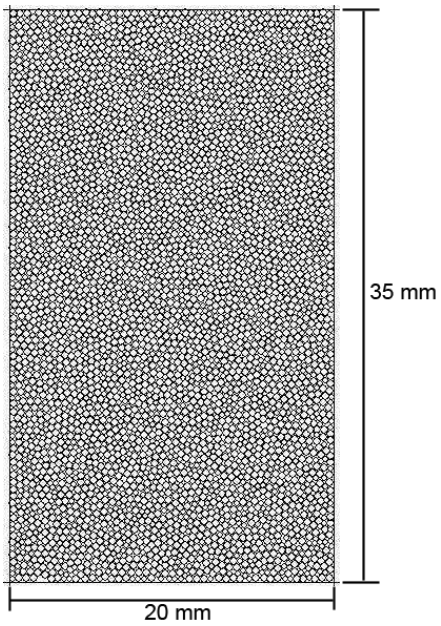

Fig. 5-14. Particle assembly used for biaxial simulations.

DEM simulations were run using two different computer codes: (1) PFC2D by Itasca Consulting Group Inc. (2008), and (2) OVAL, an open source DEM code developed by Mathew Kuhn at the University of Portland (1999). The assembly was initially generated using PFC and used in both codes.

5.3.1 Time Step

One of the major drawbacks of DEM analysis is the lengthy execution times. Simple lower-order time integration schemes such as the explicit central difference scheme used by PFC and OVAL help reduce the complexity of the calculations, and have shown to be reliable in terms of accuracy and computer efficiency as long as an appropriate value of time step is used. Different investigators have used time steps that range over several orders of magnitude, some examples are shown in Table 5-2. This illustrates the difficulty when selecting an adequate magnitude of Δt.

Table 5-2. Values of time step used in DEM geotechnical applications.

Time Step [s]	Application	Source
0.45E-3	Cyclic behavior of granular materials	Sitharam (2003)
1.318E-4	Creep modeling in excavation analysis	Feng et al. (2003)
2.0E-8 to 2.0E-7	High rate shear of a granular material	Schwarz et al. (1998)
2.86E-6	Punch indentation in a granular media	Muthuswamy et al. (2005)
3.98E-5 to 2.14E-5	Formation of "sandpiles"	Li et al. (2005)
1.0E-6	Biaxial test on granular assembly	Wang and Zhou (2008)
5.0E-5	Shear banding in interface shear tests	Wang et al. (2007)
2.12E-2	Triaxial compression of ellipsoidal particles	Ng (2006)

Choosing the largest possible value of time step reduces the execution time of DEM simulations. However, values of Δt that are too large cause errors in the simulation due to the occurrence of instability conditions. The value of time step at which instability occurs is called the critical time step (Δt_c). Once the magnitude of Δt_c is reached, small increases in the magnitude of time step result in deviations from physical reality. The magnitude of Δt_c is often controlled by the smallest particle of the arrangement, thus limiting the particle size range that can be used in DEM simulations.

DEM biaxial compression test simulations were conducted on the assembly shown in Fig. 5-14 to study the influence of the magnitude of Δt on the results of DEM simulations. Material properties of the particles are those of silica sand and are shown in Table 5-3. The value of density was scaled to 8 Mg/m^3 to obtain a reasonable critical time step, calculated as 4.266E-7 s in PFC. For the same conditions, OVAL recommended a time step lower than 1.02E-5 s. During the biaxial test, an isotropic confining stress of 100 kPa was applied to the sample. The sample was then sheared at a constant vertical

rate of strain of 2% s^{-1}. The value of strain rate was selected to assure a reasonable execution time.

Table 5-3. Particle properties for DEM biaxial tests.

Property	**Value**
Shear Modulus (G)	30 GPa
Poisson Ratio (v)	0.18
Friction Coefficient (μ)	0.4
Viscosity (α)	0.223
Strain Rate during Shear ($\dot{\varepsilon}$)	2%/s

The variation of the principal stress ratio ($PSR=\sigma'_1/\sigma'_3$) and volumetric strain as a function of the vertical strain during shear is shown in Fig. 5-15. High values of Δt result in unstable solutions, as is seen in the PFC results for time steps greater than 1.0E-6 s. Variations in Δt show a lesser effect on the results from OVAL simulations. The difference between the results obtained from the two DEM codes can be related to variations in the boundary types (periodic for OVAL and rigid walls for PFC), the stress calculation methods (wall stress for PFC and average internal stress for OVAL), the servo-mechanical processes for stress control, or other internal calculation procedures. The implementation of equal boundary types in the DEM simulations run using PFC and OVAL was not possible due to difficulties encountered when using periodic boundaries in PFC (which defaults to rigid walls) and rigid wall boundaries in OVAL (which defaults to periodic) under the conditions of the problem. Details on each boundary type were discussed in Section 5.2.2.

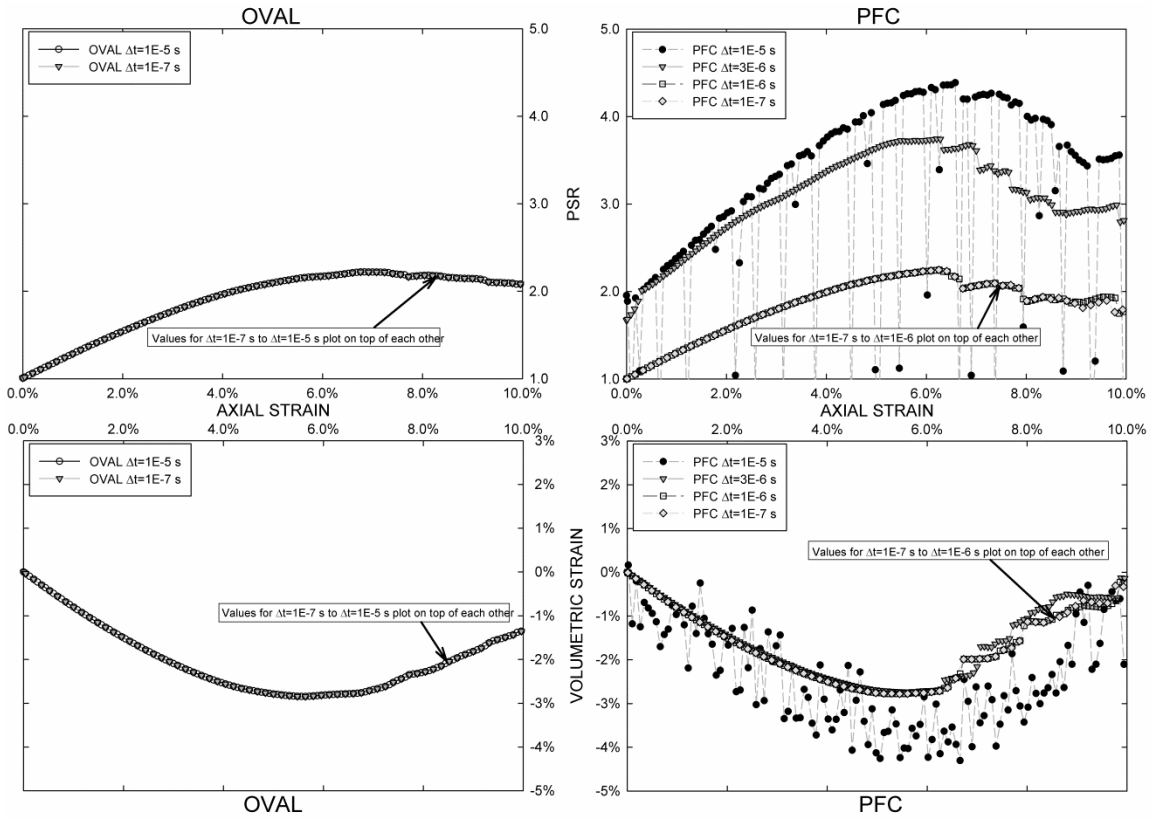

Fig. 5-15. Principal stress ratio and volumetric strain versus axial strain during shear for different values of time step. Results of OVAL and PFC2D simulations.

The magnitude of time step is very important for the practical application of the model. For the DEM simulations conducted, the execution time using an Intel Core 2 2.4GHz processor ranged from around 100 min for high values of Δt (1.0E-5 s) to over a 100,000 min for a time step of 1.0E-7 s.

The behavior observed in Fig. 5-15, with large variations in the magnitude of *PSR* for high values of time step, can be studied using fewer particles. A DEM model formed by two particles compressed by rigid walls was developed for this purpose. The particle assembly is shown in Fig. 5-16. One of the advantages of using this model is that the system can be solved exactly using the static solution, or approximately using DEM.

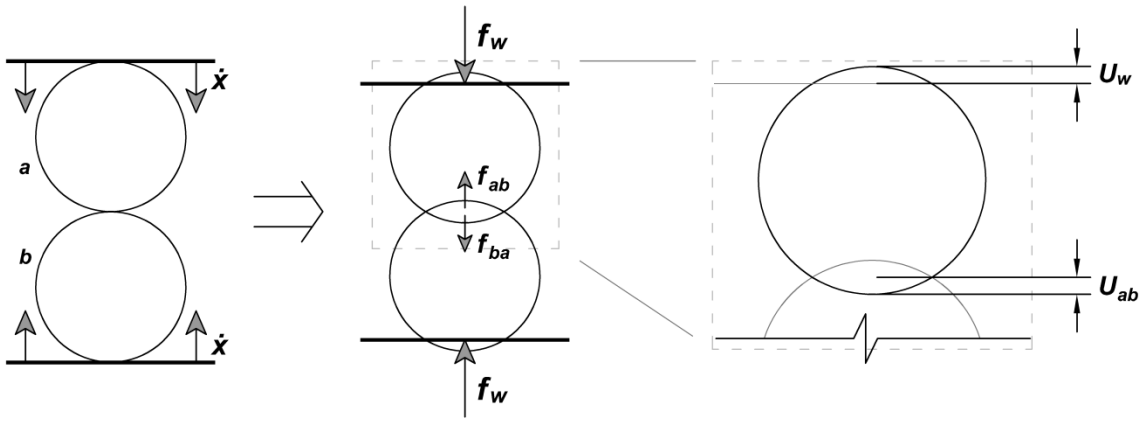

Fig. 5-16. Assembly formed by two particles being compressed by rigid walls with velocity equal to *v*.

Assuming a Hertzian contact model to simulate the particle's vertical compression, the static solution of the system can be determined using Eqs. 46 to 49, where f_w is the force applied by the wall, f_{ab} is the force between particles *a* and *b*, and U_w and U_{ab} are the indentations between particle *a* and the wall and between the two particles. These parameters are illustrated in Fig. 5-16.

$$f_w = f_{ab} \tag{46}$$

$$f_{ab} = \frac{2}{3}\frac{G\sqrt{2r}}{1-\nu}U_{ab}^{\frac{3}{2}} \tag{47}$$

$$f_w = \frac{2}{3}\frac{G\sqrt{2r}}{1-\nu}U_w^{\frac{3}{2}} \tag{48}$$

$$U_w = U_{ab} \tag{49}$$

The particles are 2 mm diameter spheres, with a shear modulus (G) of 30 GPa, Poisson's ratio (ν) equal to 0.18, and density of 2.4 Mg/m^3. A constant strain rate of 2% per minute ($\dot{x}$=7.0E-7 m/s) was applied to the walls during the simulation. The change in the wall force (f_w) with respect to vertical deformation during the particle compression, calculated using the static solution of the system, is shown in Fig. 5-17. DEM results obtained using values of time step ranging from 5.0E-7 s to 2.0E-6 s are shown in Fig. 5-18.

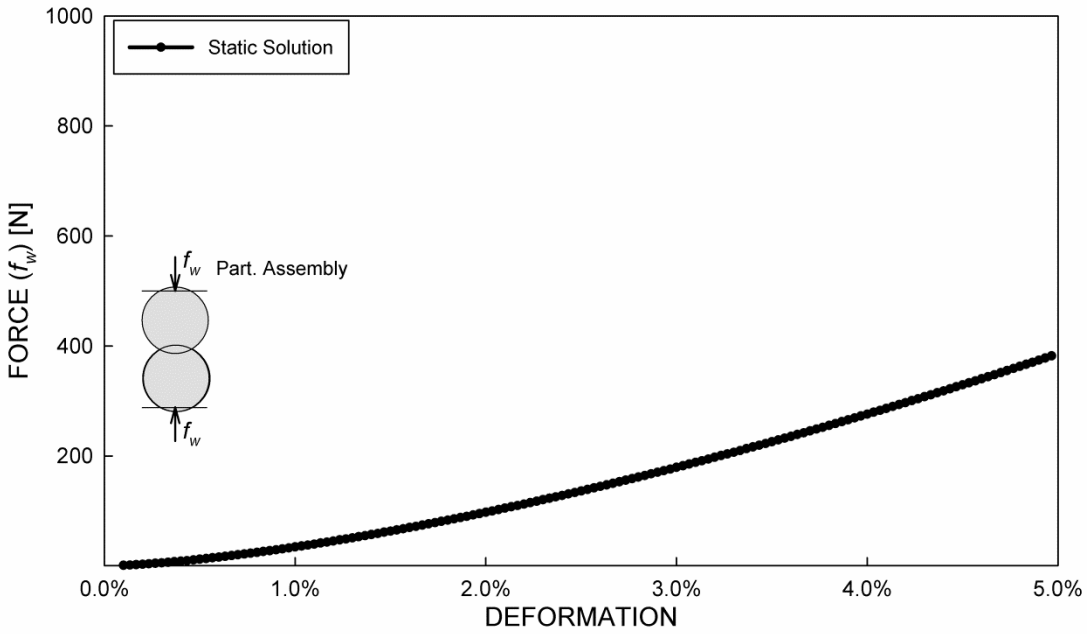

Fig. 5-17. Variation of the applied force (f_w) with respect to deformation for different values of Δt (static solution of the system).

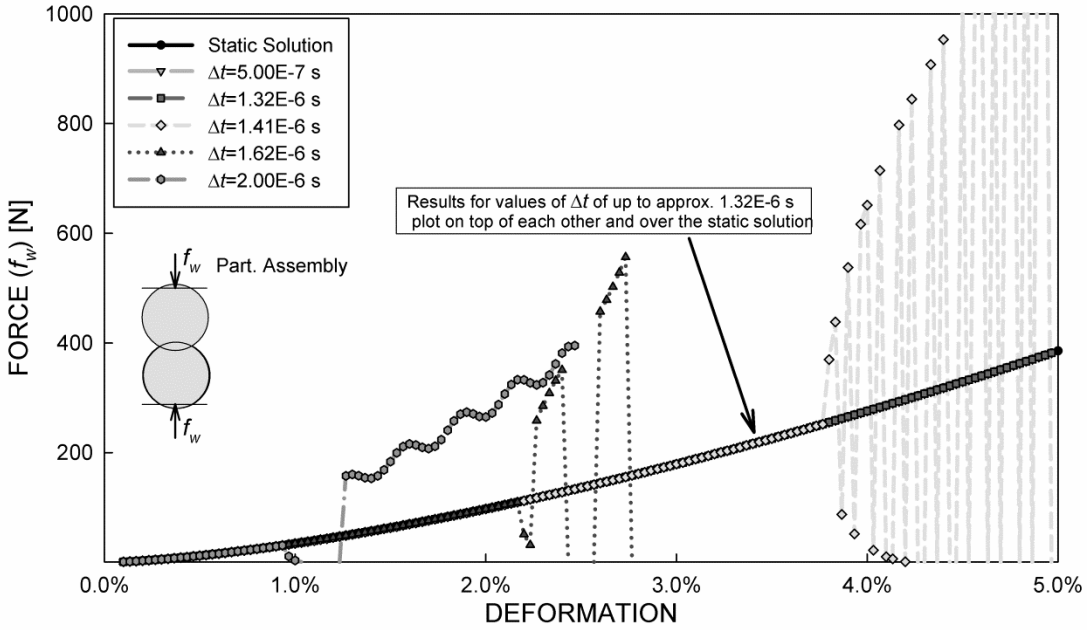

Fig. 5-18. Variation of the applied force (f_w) with respect to deformation for different values of Δt (results from DEM simulations).

DEM simulation becomes unstable for values of time step greater than 1.32E-6 s. The simulation becomes unstable sooner and at lower strains as the magnitude of Δt increases. Using an average stiffness (k) of 1.66E6 N/m, estimated based on a linear

regression of the values shown in Fig. 5-17, and a particle mass (m) of 10 mg, the critical time step for the particle assembly (Δt_c=1.32E-6 s) can be expressed as $0.5\sqrt{m/k}$.

Fig. 5-19 shows the position and the forces (f_w and f_{ab}) acting on particle *a* during the simulation run with Δt=1.41E-6 s, at strains ranging from 4.17% to 4.27% (t=125 to 128 s). During that period, the magnitude of f_w changed from 0 to 845 N, while the out-of-balance force (f_w+f_{ab}) changed from -795 to 866 N. The drastic changes are caused by the vibration of the particles, which also produced the sudden changes in the value of f_w observed in Fig. 5-18.

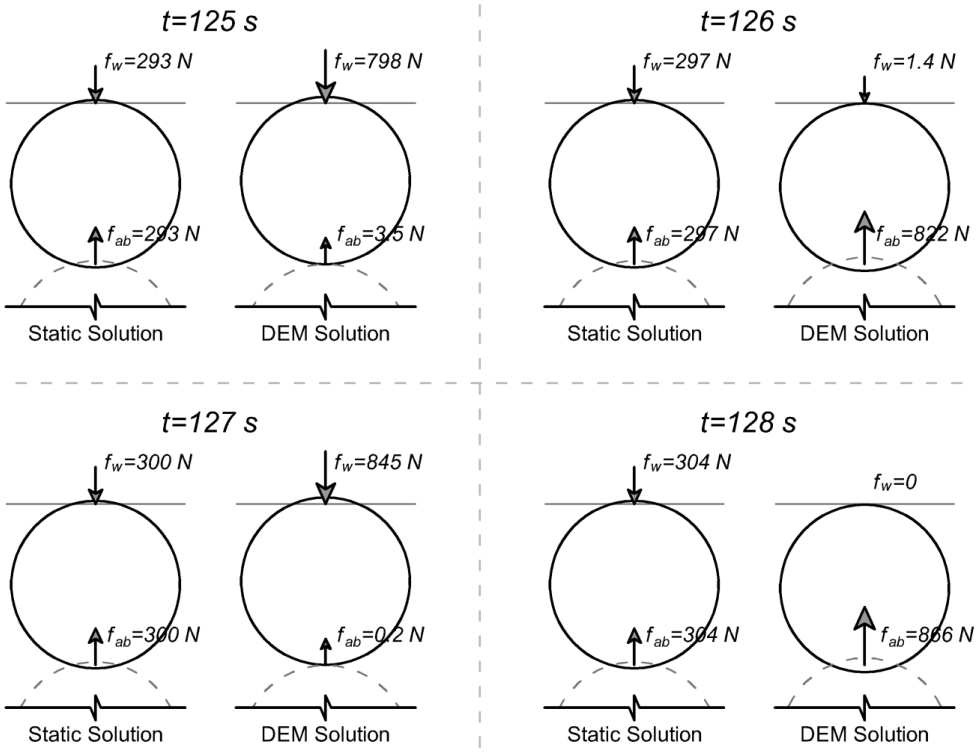

Fig. 5-19. Evolution of the DEM simulation from t=125 s to t=128 s (Δt=1.41E-6 s).

DEM fails to predict the macroscopic response of a granular assembly if the value of time step is larger than Δt_c, even for simple assemblies such as that shown in Fig. 5-16. A precise calculation of Δt_c is critical for any DEM analysis.

The value of critical time step is often expressed as a fraction of the natural frequency of an equivalent mass-spring system (Malone and Xu, 2008), and is commonly expressed as $\sqrt{m/k}$ multiplied by a factor. Variables m and k are the mass and the stiffness of a particle. Values of this factor reported in the literature differ considerably and may depend on the contact model used or other simulation parameters, such as viscosity. Values of this factor suggested by different investigators are shown in Table 5-4.

Table 5-4. Suggested values of time step.

Recommended Value of Δt	**Reference**	**Comments**
$2\sqrt{m/k}$	Cundall and Strack (1979)	
$0.8\sqrt{m/k}$ for linear elastic CM $0.25\sqrt{m/k}$ for Hertz-Mindlin CM	Itasca Consulting Group Inc. (2008)	
$0.2\sqrt{m/k}$ to $2\sqrt{m/k}$	Malone and Xu (2008)	Derived for analysis of granular flows on mills and hoppers
$0.17\sqrt{m/k}$ for 3D simulations $0.3\sqrt{m/k}$ for 2D simulations	O'Sullivan and Bray (2004)	
$1.57\sqrt{m/k}$	Cambou et al. (2009)	Recommend the final decision be made based on numerical experiments
$0.05\sqrt{m/k}$	Ng (2006)	Found Δt_c to be close to $0.2\sqrt{m/k}$

Li (2005) estimated the value of Δt_c for the Hertz-Mindlin CM based on the velocity of propagation of a Rayleigh wave through the particles. Previous work in this area was done by Johnson (1987). They recommended using Eq. 50 to calculate Δt_c, where λ is a parameter obtained from Eq. 51. For the particle assembly shown in Fig. 5-14, the application of Eqs. 50 and 51 give an estimated magnitude of Δt_c of 1.0E-6 s.

$$\Delta t_c = \frac{\pi r}{\lambda}\sqrt{\frac{\rho}{G}} \tag{50}$$

$$\left(2-\lambda^2\right)^4 = 16\left(1-\lambda^2\right)\left[1-\lambda^2\frac{1-2\nu}{2(1-\nu)}\right] \tag{51}$$

According to O'Sullivan and Bray (2004), the magnitude of the critical time step also depends on factors such as the packing configuration and the number of contacts per particle. Therefore, the determination of a maximum critical time step depends greatly on the type of simulation. In practice, the time step selected is ultimately based on the judgment of the analyst.

Increasing the magnitude of time step produces oscillatory movement in the particles. The oscillation frequency decreases and its amplitude increases for increasing values of time step. High frequency/low amplitude vibrations produced by small changes in Δt can be ignored or artificially damped in *pseudo-static* DEM applications, where the out-of-balance particle forces are very small, the arrangement is assumed to advance from one equilibrium or close-to-equilibrium condition to the next, and the true dynamic response of the assembly is ignored. This is not necessarily desirable if rate-dependent processes are being considered, as the time-dependent response of the arrangement is important. Large changes in Δt generate large amplitude oscillations and unrealistic particle indentation which may affect any type of model. Additionally, as DEM simulations using explicit time integration schemes suffer from the lack of good mathematical properties, such as a convergence theorem or bounds estimates (Cambou et al., 2009), the validity of the solution cannot be verified.

5.3.2 Mass and Density

The magnitude of the critical time step depends on the values of particle mass and stiffness. It has become common practice in DEM simulations to use mass and density

scaling to increase the value of Δt_c. This is especially common in geotechnical applications, where the size and corresponding mass of the particles are small, resulting in low values of critical time step.

Both of the DEM codes used in this study include automatic density scaling methods to increase Δt_c. PFC incorporates two different types of density scaling: (1) differential and (2) uniform (Itasca Consulting Group Inc. 2008); while OVAL only allows uniform density scaling.

Differential density scaling introduces an additional inertial mass to each particle. The magnitude is calculated to achieve a critical time step of 1. This procedure gives each particle a fictitious and variable value of density. As stated by Itasca C.G. (2008), this procedure can only be used when the time scale is not of concern and if the solution is not path dependent. These conditions are not frequently applicable in geotechnical applications.

Uniform density scaling allows the user to homogeneously scale the density of the particle material to achieve a desired value of critical time step. This method does not improve the calculation efficiency, but it allows the implementation of higher values of Δt, reducing the execution time (Itasca Consulting Group Inc. 2008). However, as will be later discussed, any change in the magnitude of particle density may have a considerable effect on the results of DEM simulations.

The influence of the magnitude of particle density (ρ) on the results of DEM simulations was studied using the particle assembly shown in Fig. 5-14. Simulations of a biaxial test were conducted using values of particle density ranging from 80 kg/m^3 to 8.0E10 kg/m^3. The variation in *PSR* and volumetric strain during shear is shown in Fig.

5-20. Values of density higher than 8.0E7 kg/m^3 for PFC and 8.0E5 kg/m^3 for OVAL caused high inertial forces, which produced significant deviations in the results.

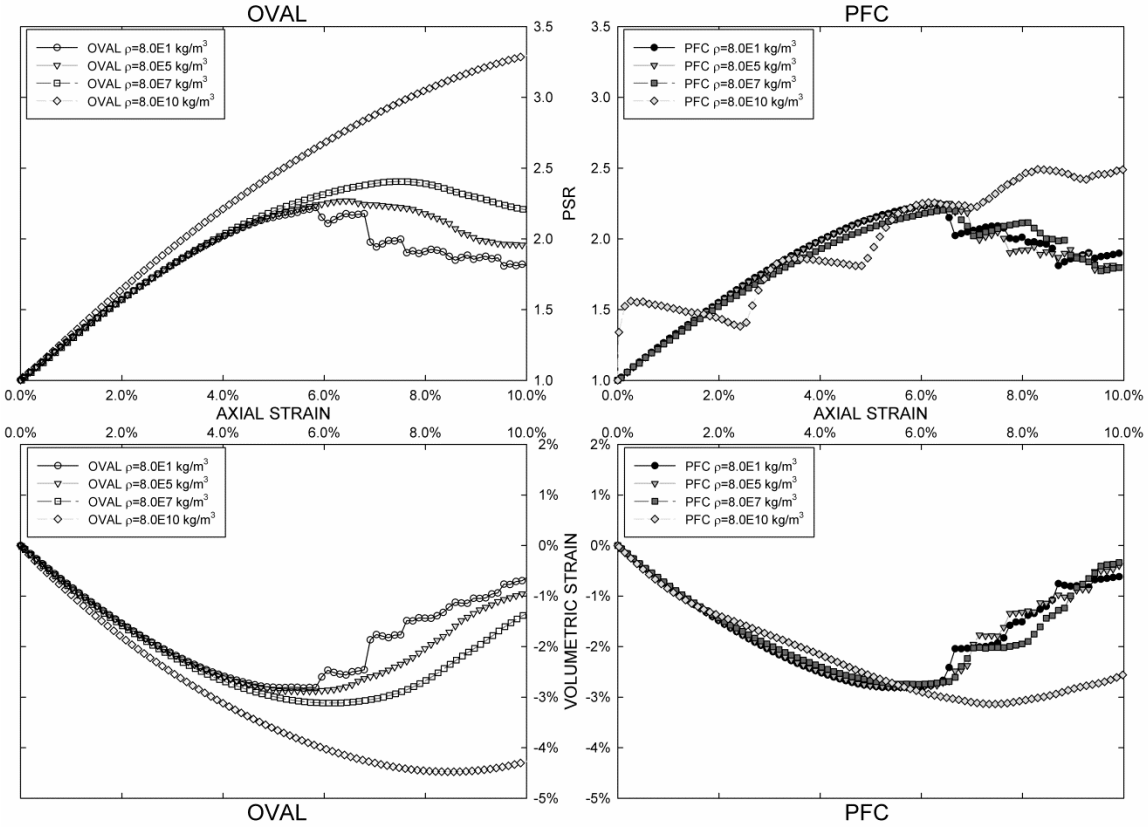

Fig. 5-20. Principal stress ratio and volumetric strain versus axial strain during shear for different values of particle density. Results of OVAL and PFC2D simulations.

Ng (2006) found that if the out-of-balance particle forces were kept within a certain threshold, changes in the particle density did not have a significant effect on DEM simulations. Ng (2006) reduced the magnitude of the out-of-balance forces during DEM simulations by stopping the test and allowing the assembly to rest and reach internal equilibrium every time that a certain limit was exceeded. This procedure neglects the true dynamic response of the assembly, as it artificially and arbitrarily modifies the magnitude of the forces that cause particle movements.

The deviations observed in Fig. 5-20 can be studied using the particle arrangement shown in Fig. 5-16. For these simulations, a time step of 5.0E-7 s was selected, and the particle density was changed from 24 kg/m^3 to 2.4E23 kg/m^3. The variation of the applied force (f_w) with respect to axial deformation is shown for a density range of 206 kg/m^3 to 2400 kg/m^3 in Fig. 5-21, and of 2400 kg/m^3 to 2.4E23 kg/m^3 in Fig. 5-22.

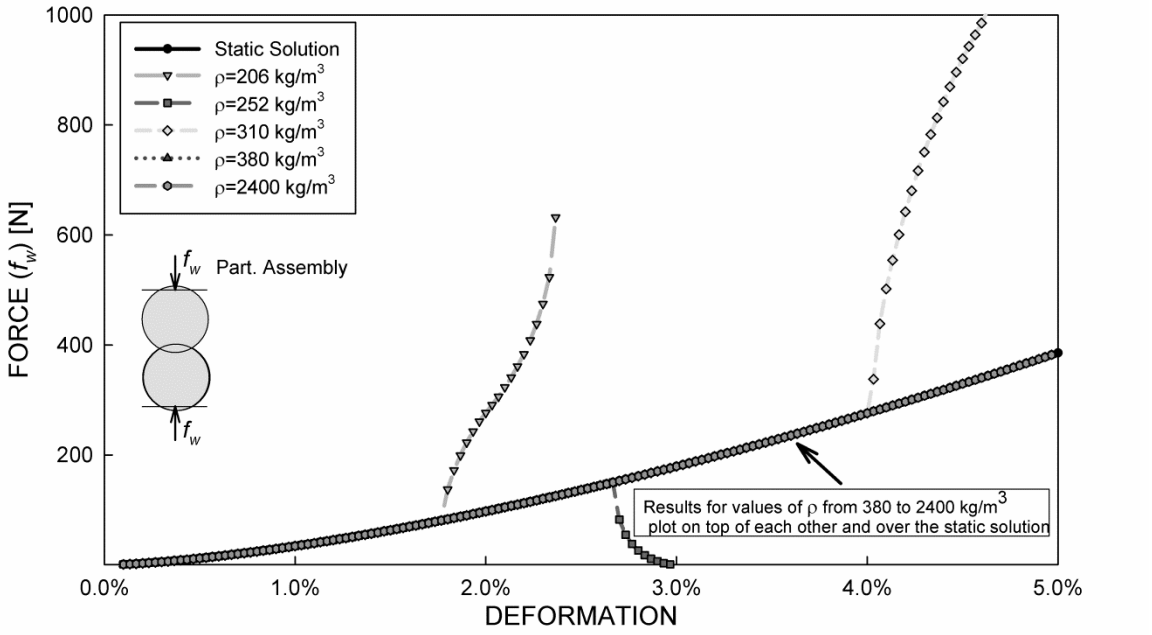

Fig. 5-21. Variation of the applied force (f_w) with respect to deformation for different values of ρ (206 kg/m^3 to 2400 kg/m^3).

Increasing or decreasing the magnitude of particle density can cause errors in the results from DEM simulations, represented in Fig. 5-21 and Fig. 5-22 by deviations from the static solution of the system. For the DEM model studied, values of particle density lower than 380 kg/m^3 or higher than 2.4E15 kg/m^3 produced significant errors in the results. Even though that seem like a large range of values, magnitudes of particle density outside those limits are often used in DEM simulations; e.g., Ng (2006) Kosoglu (2011).

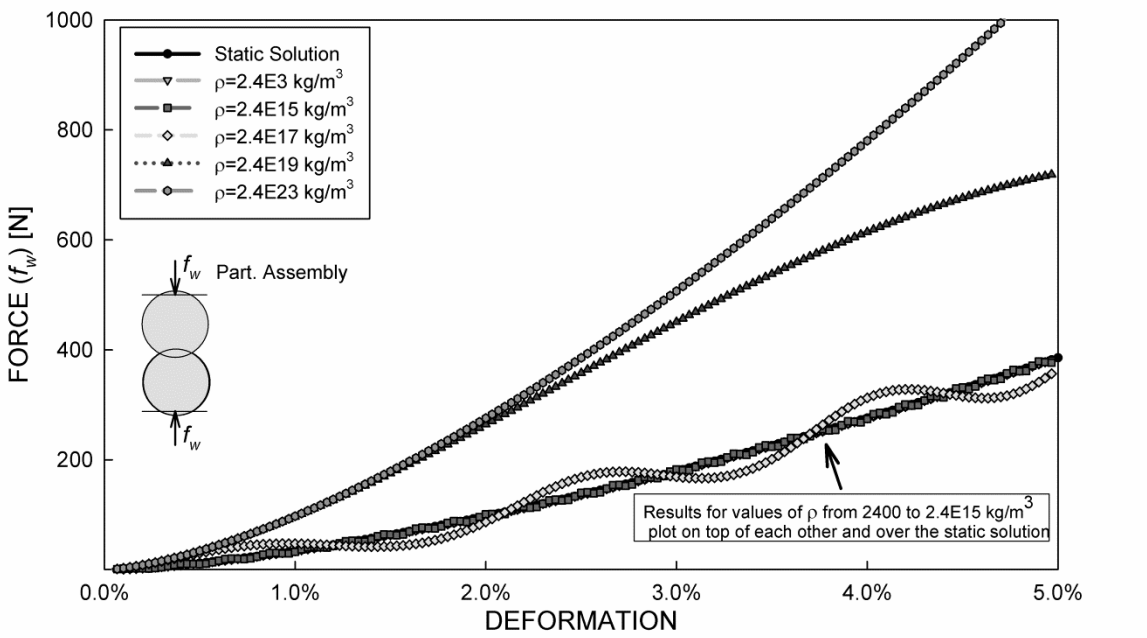

Fig. 5-22. Variation of the applied force (f_w) with respect to deformation for different values of ρ (2400 kg/m^3 to 2.4E23 kg/m^3).

The main cause of the errors produced by decreasing the value of particle density is illustrated in Fig. 5-23. If a force f_w is applied to particle *a*, the particle's displacement during the cycle, named x_a, will depend on the particle's acceleration ($\ddot{x}_a$) produced by that force. A reduction in the value of ρ causes a decrease of m_f in the value of particle mass, and an increase in the particle's acceleration from $\ddot{x}_a$ to $\ddot{x}_a[m_a/(m_a-m_f)]$, where m_a is the particle's mass before the change in density. Therefore, the magnitude of the particle's displacement for the cycle (x) increases as the particle density decreases, resulting in a behavior similar to that described for an increase in time step in Section 5.3.1.

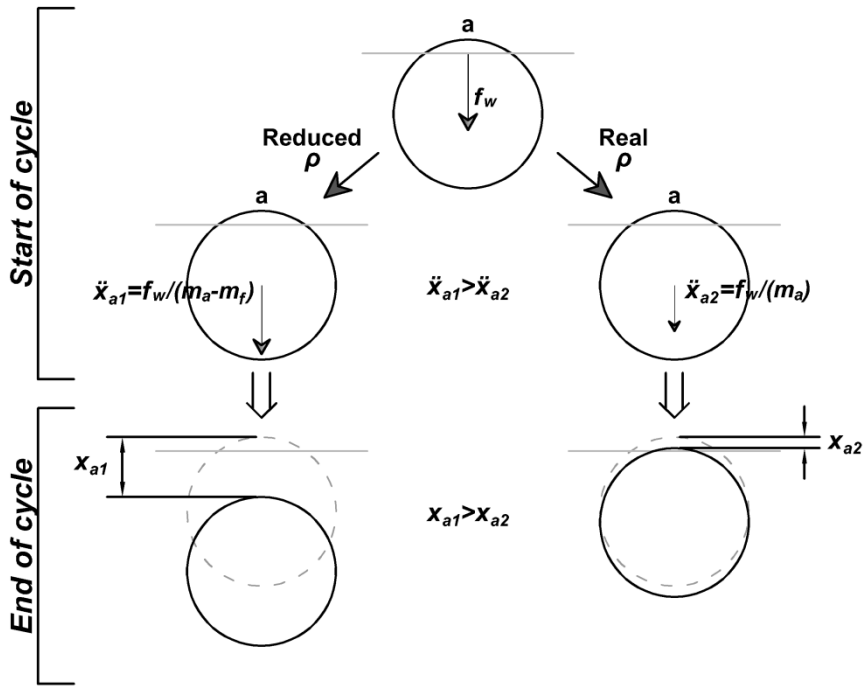

Fig. 5-23. Effect of reducing the magnitude of ρ during the iteration process in DEM simulation.

This explains the sudden changes in the magnitude of f_w shown in Fig. 5-21. Fig. 5-24 shows the position and the forces (f_w and f_{ab}) acting on particle *a* during the simulation with ρ=111 kg/m^3, at strains ranging from 1.8% to 2.4% (t=55 to 73 s). During that period, the magnitudes of the force applied by the rigid wall (f_w) and the out-of-balance force (f_w+f_{ab}) oscillated between 0 and 409 N. The sudden changes are generated by the large particle displacements calculated for each time step due to the low value of particle density, which causes the particle to vibrate. The magnitude of the oscillatory movement increased over time until the particles were ejected from the assembly at t=73 s.

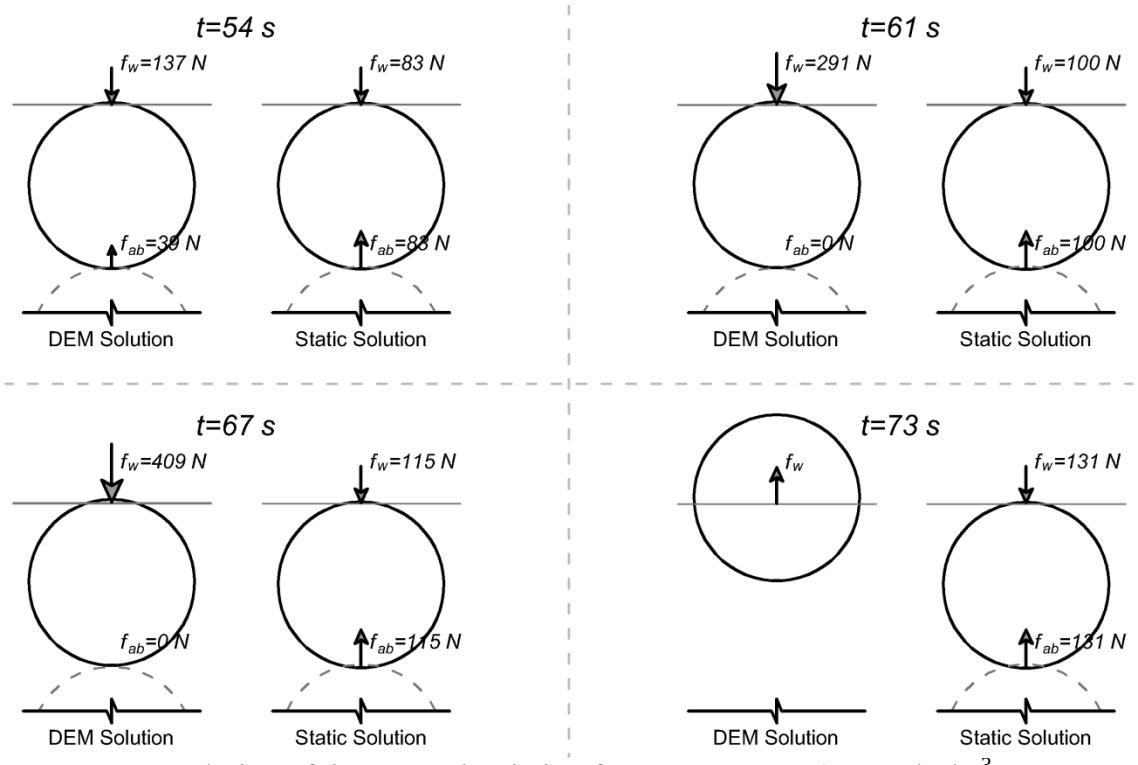

Fig. 5-24. Evolution of the DEM simulation from 54 s to 73 s (ρ=111 kg/m^3).

If the material density is increased, a fictitious inertial force (f_f) opposing the movements is added to the particles. Problems in the simulation arise when the magnitude of f_f starts controlling the dynamic response of the particles, as occurs for values of density higher than 2.4E15 kg/m^3 in Fig. 5-22.

DEM fails to represent the behavior of granular assemblies if the value of particle density is either too large or too small. DEM simulations gave incorrect results even using simple assemblies such as that shown in Fig. 5-16, if the value of particle density was lower than 380 kg/m^3 or higher than 2.4E15 kg/m^3.

An additional DEM biaxial test was conducted on the on the particle assembly shown in Fig. 5-13 using real particle properties and shear conditions (ρ=2400 kg/m^3, $\dot{\varepsilon}$ = 2% min^{-1}). Even for the simple particle configuration, the DEM simulation took over 50 days for completion (10% vertical strain) using an Intel Quad Core 2.4GHz processor.

Although this demonstrates that density scaling or other techniques to increase the value of Δt_c sufficiently to reduce the execution time are necessary, the magnitudes of these increases in any specific case are not readily apparent.

If not carefully controlled, the inertial forces produced by the density increase may cause instability in the simulation. Increasing the magnitude of the density may also produce a significant deviation from the true dynamic behavior of the assembly, which is regularly neglected during pseudo-static simulations.

It is common to check that parameters such as the *out-of-balance force ratio*, which is the ratio of the average out-of-balance particle forces to the average contact forces, are kept within a certain threshold to assure pseudo-static conditions. PFC recommends a value of out-of-balance force ratio lower than 1% (Itasca Consulting Group Inc., 2008) as a near-equilibrium criterion. O'Sullivan and Bray (2004) recommend monitoring the energy balance of the system to detect potential numerical instabilities, which are reflected in a sudden release of energy in the particle arrangement. The unbalanced energy is then kept within a certain threshold, which is selected by the analyst. These types of indicators are mainly applicable to DEM models where a steady-state solution is desired and true dynamic properties of the assembly are ignored.

5.3.3 Stiffness

The estimation of the particle stiffness (k) is complex when the linear elastic CM is implemented, because it requires the stiffness to be incorporated in terms of force per unit length of indentation. Reported values of linear elastic particle stiffness for DEM geotechnical applications show great variability, ranging from 1.0E5 N/m to 2.0E9 N/m, as shown by the examples in Table 5-5. The wide range in stiffness values makes it

difficult to assume a representative value. The actual value depends on factors such as the material composition, the particle size, or the level of deformation.

Table 5-5. Values of stiffness for the linear elastic CM used in DEM geotechnical applications.

Stiffness [N/m]	**Application**	**Reference**
1.2E5	Creep in clays	Kuhn and Mitchell (1993)
5.0E7	Biaxial compression of cemented sand	Wang and Leung (2008)
1.0E9	Biaxial compression of sands	Huang et al. (2008)
1.0E5	Undrained cyclic triaxial	Dinesh et al. (2004)
1.5E9-2.5E9	Undrained cyclic biaxial test in sand	Sitharam (2003)
1.5E9	Deep penetration in granular materials	Jiang et al. (2006)
1.0E8	Particle crushing during direct shear	Lobo-Guerrero and Vallejo (2005)
5.0E7	Contact creep in sands	Wang et al. (2008)
1.0E6	Creep in granular materials	Kwok (2008)

A DEM biaxial test was conducted on the assembly shown in Fig. 5-14 using the linear elastic CM. Three different values for the linear particle stiffness were used: 1.0E7 N/m, 1E8 N/m, and 1E9 N/m. The same magnitudes were used for the normal and tangential components (K_n=k_t). A time step of 1.0E-6 s was selected for simulation. Results from the biaxial test simulations are shown in Fig. 5-25.

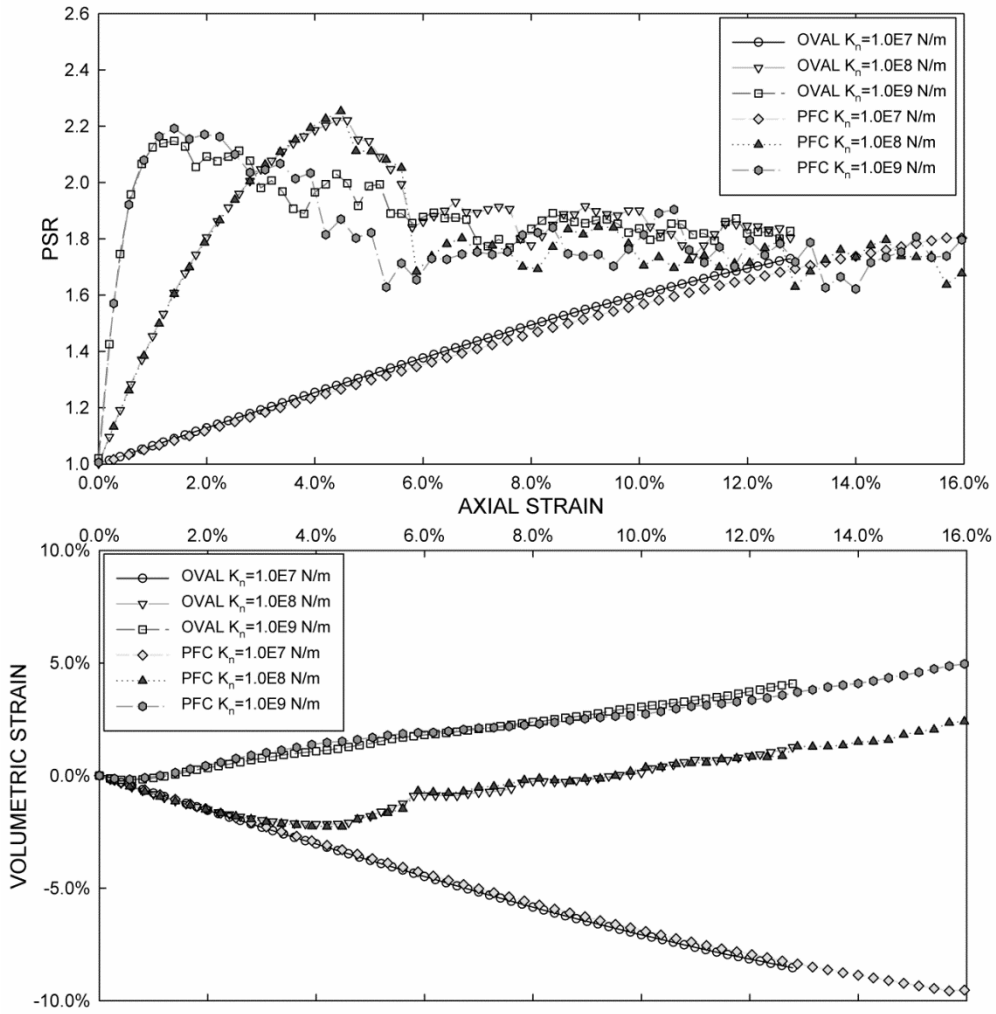

Fig. 5-25. Principal stress ratio and volumetric strain versus axial strain during shear for different values of shear modulus. Results of OVAL and PFC2D simulations.

Variations in the magnitude of *k* had a considerable effect on the macroscopic stiffness, dilatancy, and strain to failure. The macroscopic stiffness and dilatancy of the assembly increase, while the strain to failure decreases with increasing magnitude of *k*. This is consistent with expected behavior. Additionally, the results obtained using OVAL and PFC2D are in good agreement.

Values of particle stiffness based on laboratory data are scarce. Nakata et al. (1999) performed single-particle crushing tests on the component minerals of Aio sand. Typical results for tests on Quartz and Orthoclase are shown in Fig. 5-26. Quartz

exhibited an almost linear elastic behavior, while orthoclase showed a saw-tooth curve caused by limited fracturing occurring before final failure. A value of stiffness of 2.2E6 N/m for Quartz can be estimated based on the results shown in Fig. 5-26. This value only applies to particles with sizes close to those used in the crushing tests: diameter ranging from 0.85 mm to 2 mm.

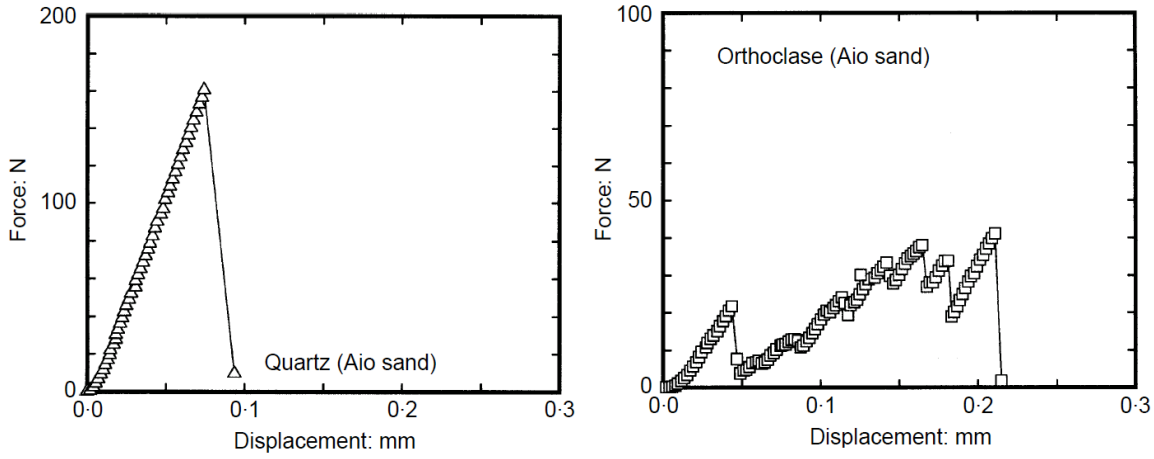

(a) (b)

Fig. 5-26. Particle crushing load-displacement relationship for minerals of Aio sand: (a) quartz, and (b) orthoclase; (Nakata et al. 1999).

Similar tests were conducted by Cavarretta et al. (2010) on glass ballotini and Leighton Buzzard sand. Typical results from compression tests are shown in Fig. 5-27. They noticed an initial soft response under loading with a transition to a stiffer behavior. The displacement to this transition, which they named δ_p, was related to the initial plastic deformation caused by damages to the asperities. This stage was followed by elastic displacement, which was in good agreement with a Hertzian model with a value of shear modulus of 29 GPa.

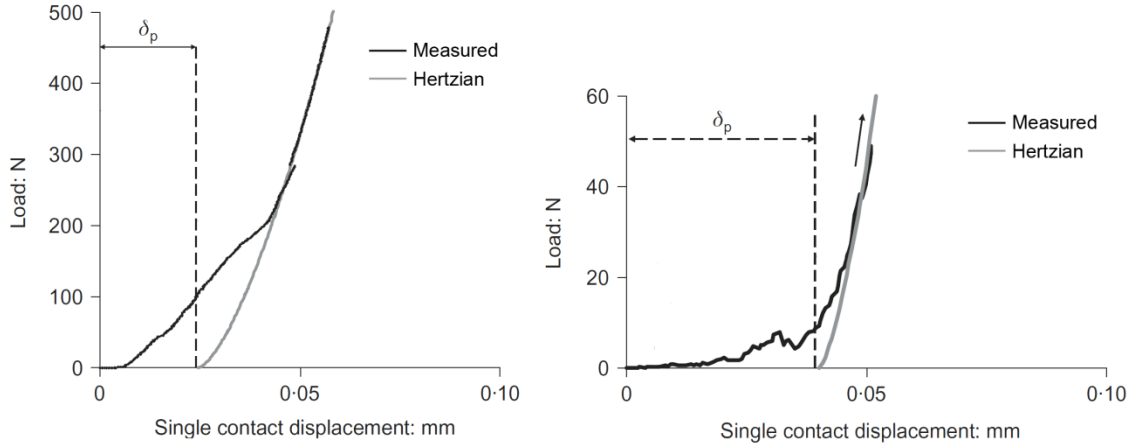

(a) (b)

Fig. 5-27. Typical compression test data for: (a) glass ballotini (diameter=2.49 mm), (b) Leighton Buzzard sand (diameter=1.67 mm). (Cavarretta et al. 2010).

Malone (2008) presented Eq. 52 to estimate the value of k based on the impact velocity ($\dot{x}_o$) between particles and the resulting particle indentation ($U_{\dot{x}o}$).

$$k = \frac{m\dot{x}_o^2}{U_{\dot{x}o}^2} \tag{52}$$

Vinogradov (2004) developed a similar formulation to estimate the normal particle stiffness for a linear elastic CM used for dynamic DEM simulations. The results are shown in Eqs.53 and 54. For these relationships, as well as for Eq. 52, the calculation of k requires the estimation of the maximum expected collision velocity. This can be simply estimated for granular flows, but for geotechnical applications, where particle velocities are small and cannot be accurately determined, the calculation of an approximate value for $\dot{x}_o$ and k is complex and uncertain.

$$K_n = \frac{4\sqrt{2}Er^{\frac{1}{2}}U_{\dot{x}o}^2}{15(1-\nu)^2} \tag{53}$$

$$U_{\dot{x}o} = \left(\frac{15\sqrt{2}m\dot{x}_o^2(1-\nu)^2}{8E\sqrt{r}}\right)^{\frac{2}{5}} \tag{54}$$

As variations in the particle stiffness can have a significant effect on DEM simulation results, the application of stiffness reduction to increase the critical time step and reduce execution time is not recommended in geotechnical applications where the macroscopic strength, stiffness, volume change, and strain to failure of the assembly are important.

5.3.4 Viscosity and Damping

Particle damping is commonly added to DEM models to dissipate excessive kinetic energy during simulation. Even though energy supplied to the system is normally dissipated through friction, particle damping helps in reaching a steady-state solution faster, being useful if pseudo-static conditions are desired. Additionally, as viscous effects introduce a time- and velocity-dependent force into the system, the magnitude is especially meaningful when analyzing conditions such as particle flow, strain rate effects, or creep, where the dynamic behavior or time-dependent response of the assembly is important in the analysis.

DEM codes incorporate viscous effects in two ways: (1) as an additional force applied directly to the particles (local damping), and (2) as viscous forces applied at the particle contacts (contact viscosity).

In PFC, the viscous force is determined as a fraction of the out-of-balance force of the particle, acting in the opposite direction of the particle velocity ($\dot{x}$). The magnitude of the viscous force (f^v) depends on the magnitude of the net total particle force (f) and the value of the local damping constant (α). This relationship is shown in Eq. 55. For small values of damping, the parameter α can be expressed as $D\pi$ where D is a fraction of the critical damping ($2\sqrt{km}$) (Itasca Consulting Group Inc. 2008)

$$f^{v} = -\alpha f \tag{55}$$

In OVAL, the viscous forces are directly related to the particle velocity ($\dot{x}$), as stated by the following equation:

$$f^{v} = -D\left(2\sqrt{km}\right)\dot{x} \tag{56}$$

PFC and OVAL apply contact viscosity using a similar procedure, where contact viscous forces in the normal and tangential directions (f_n^v and f_t^v) are proportional to the normal and tangential relative particle velocities ($\dot{x}_n$ and $\dot{x}_t$). This is shown in Eqs. 57 and 58, where the parameter β, called the coefficient of contact viscosity, represents the level of damping of the system.

$$f_n^{v} = -\beta_n\left(2\sqrt{K_n m}\right)\dot{x}_n \tag{57}$$

$$f_t^{v} = -\beta_t\left(2\sqrt{k_t m}\right)\dot{x}_t \tag{58}$$

Examples of magnitudes of viscosity used in DEM for a variety of applications are included in Table 5-6.

Table 5-6. Values of viscosity used in various DEM applications. Viscosity parameters are for use in Eqs. 55 to 58.

Viscosity	**Application**	**Reference**
β_n=0.2, β_t=0.1	Granular flow in tumbling mills	McBride at al. (2004)
α=4.0, β=0.01	Undrained cyclic biaxial test in sand	Sitharam (2003)
α=0.7	Biaxial compression in sands	Huang et al. (2008)
β_n=0.8, β_t=0.1	Settlement due to vibration in granular materials	Karrech et al. (2008)
β_n=1, β_t=1	Interface shear test	Wang et al (2007)
α=0.0133	Triaxial compression of ellipsoids	Ng (2006)

The influence of the magnitude of the local and contact viscosity on results from DEM simulations was evaluated using the 2D particle assembly shown in Fig. 5-13. The values of the local damping constant (α) were changed from 0 to 100, and the values of

the coefficient of contact viscosity (β) were changed from 0 to 1. Results from DEM biaxial test simulations run using PFC and OVAL are shown in Fig. 5-28 and Fig. 5-29.

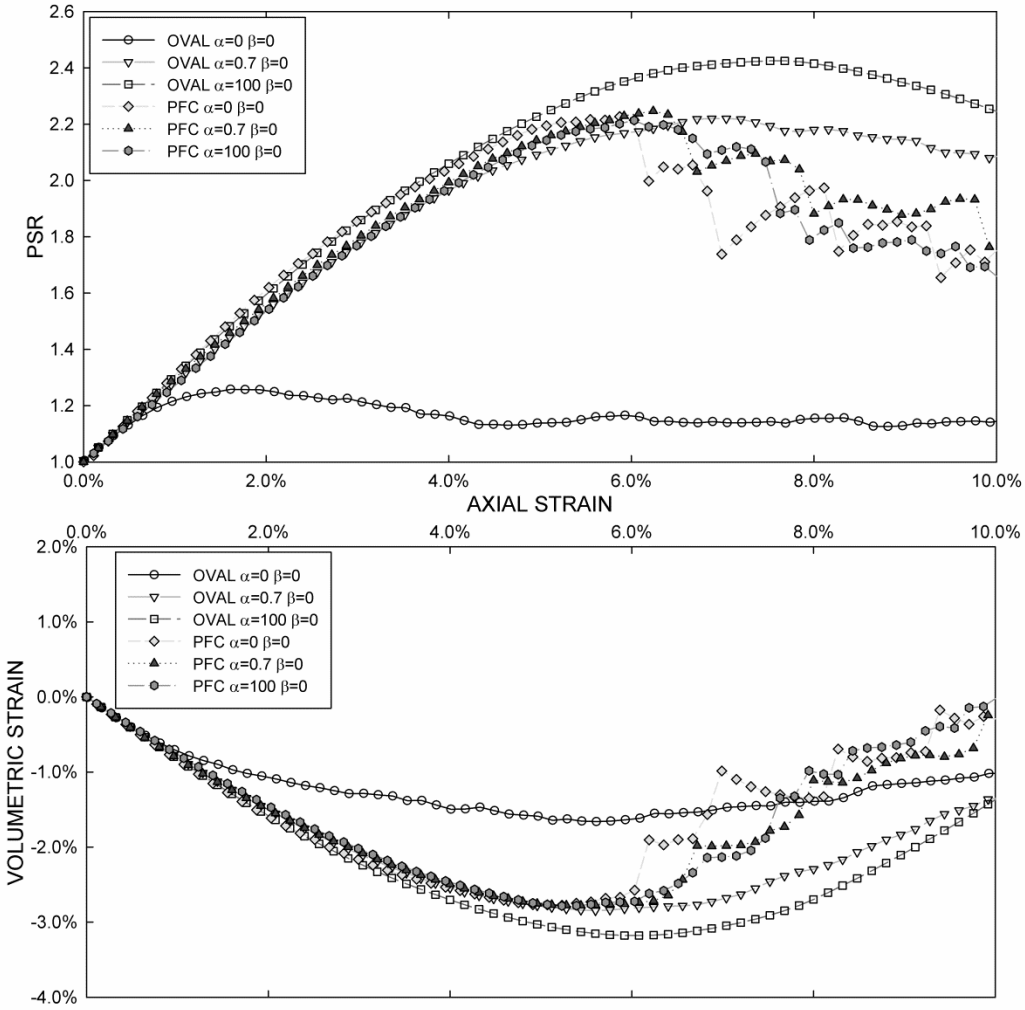

Fig. 5-28. Principal stress ratio and volumetric strain versus axial strain during shear for different values of local damping constant (α). Results of OVAL and PFC2D simulations.

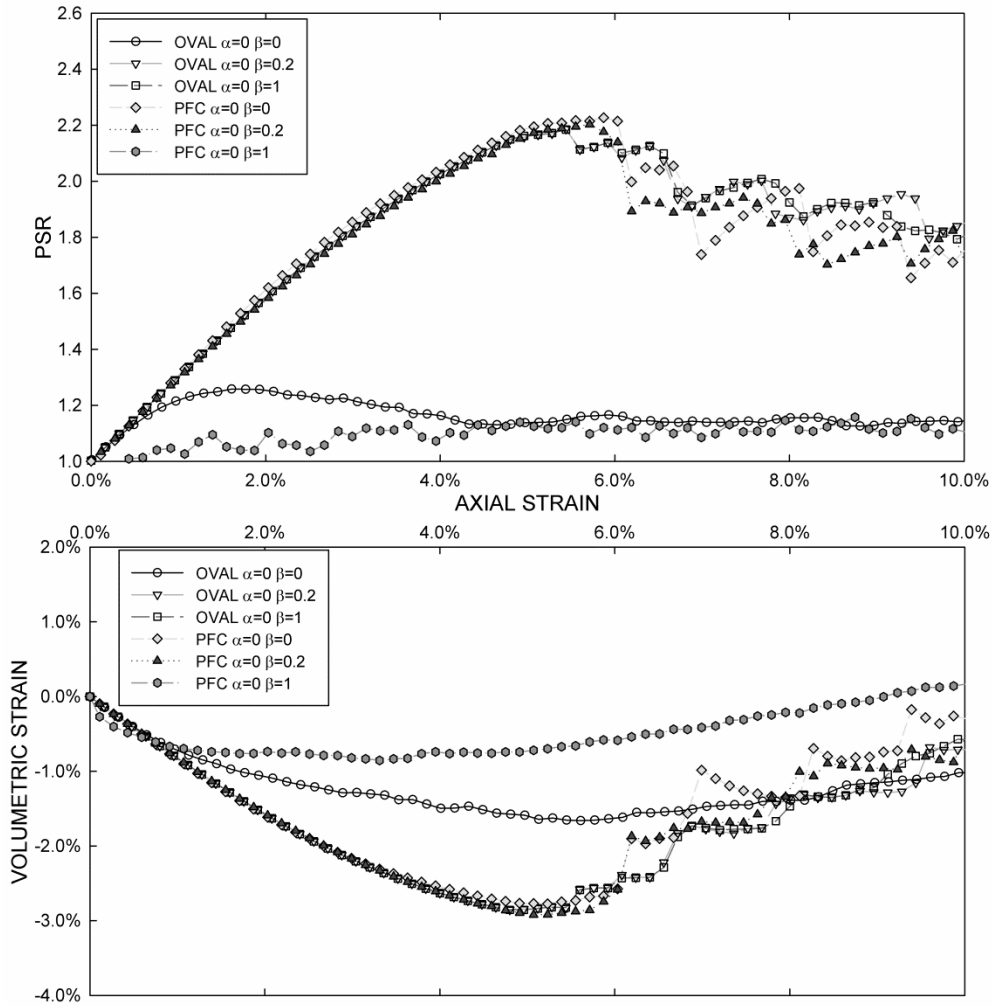

Fig. 5-29. Principal stress ratio and volumetric strain versus axial strain during shear for different values of coefficient of contact viscosity (β). Results of OVAL and PFC2D simulations.

Variations in the magnitude of α did not have a significant effect in the simulations performed using PFC. On the other hand, results from OVAL are greatly influenced by the magnitude of local damping constant. This disparity between the codes can be related to the different procedures used to incorporate viscous forces in the simulation. The magnitude of the coefficient of contact viscosity has a considerable effect in both OVAL and PFC simulations. For β equal to 1, PFC calculates high particle out-of-balance forces and unstable solutions. A similar behavior is observed in OVAL for values of β greater than 5.

Ng (2006) reported a similar behavior for DEM simulations of triaxial tests on granular assemblies formed by ellipsoidal particles. Changes in the value of local damping constant from 1.332E-3 to 1.332E-1 during DEM simulations run using ELLIPSE3H, caused significant changes in the macroscopic stress-strain characteristics of the assembly. The shear strength of the assembly, represented by the value of *PSR*, increased with increasing values of α. Ng (2006) observed that if the out-of-balance forces were kept within a certain threshold, which he selected arbitrarily, the effect of α on the macroscopic properties of the assembly was negligible. The magnitudes of the particle out-of-balance forces were reduced during the simulations by stopping the compression and allowing the assembly to rest and reach internal equilibrium every time that a certain value was exceeded. This procedure is only applicable when the dynamic response of the assembly is not important for the analysis. Any rate-dependent property of the assembly is ignored if this type of methodology is applied.

In pseudo-static simulations, where the true dynamic behavior of the assembly is not important, the magnitude of the viscosity is not a major concern. PFC uses a default value of α equal to 0.7, and assigns zero damping at the contacts (β=0). However, if time-dependent and dynamic effects are being considered, the magnitude of damping, in particular the level of contact viscosity, plays an important role in the simulation.

The determination of the value of β for DEM models is not straightforward, as it does not directly relate to any specific measureable material property. The magnitude of the coefficient of contact viscosity is commonly related to dynamic properties of the particles such as the coefficient of restitution (e). Malone and Xu (2008) expressed the value of β using Eq. 59. Such relationships only supply a rough estimate of the value of β,

as properties like the coefficient of restitution are affected by factors such as the magnitude of the impact velocity.

$$\beta = \frac{2\ln(e)\sqrt{mk}}{\sqrt{\ln(e)^2 + \pi^2}} \tag{59}$$

In geotechnical applications, the magnitude of viscosity has been related to time-dependent particle interactions at the contacts. Wang et al. (2008) studied the effect of variations in the magnitude of contact viscosity in the internal stress rearrangement of the particle assembly, linking it to the time-dependent changes in macroscopic properties observed in sands during aging. Kuhn and Mitchell (1993) developed a relationship for a sinh-type dashpot to model creep in clays, where the value of viscosity depended on the ratio of horizontal to vertical contact forces.

Even though the magnitude of the local damping and the contact viscosity can significantly affect the results from DEM, a method to determine or estimate their magnitude for geotechnical applications is still unclear.

5.3.5 Friction Coefficient

The macroscopic friction angle (ϕ) of a soil includes the contribution from sliding resistance of particles within the sample, as well as additional components related to the resistance to volume change, internal grain rearrangement, and particle crushing. DEM requires the use of a true particle friction coefficient (μ), related only to the resistance to sliding between two particles in contact. Using this particle-scale property, DEM estimates the macro-scale strength of a particle assembly. Contributions from the resistance to volume change and particle rearrangement are generated during simulation as a result of particle interactions.

The magnitude of the true friction angle (ϕ_μ), which is equal to the arctangent of the particle friction coefficient, is mostly a function of the compositional and structural properties of the mineral forming the particles. Values of true friction angle usually range between 21º and 31º for quartz, 28º and 38º for feldspar, and 7º to 28º for sheet minerals such as biotite and muscovite (Mitchell and Soga 2005). Some examples are shown in Table 5-7.

Examples of values of friction coefficient used in DEM for various geotechnical applications are shown in Table 5-8. Most DEM studies included in Table 5-8 assumed a magnitude of true friction coefficient (μ) close to 0.5. This value of μ, corresponding to a friction angle (ϕ_μ) of 26º, is reasonable for wet and dry quartz.

2D DEM biaxial tests were performed on the particle assembly shown in Fig. 5-13. The value of friction coefficient was changed from 0 to 0.9. Results from the simulations, including the variation of the principal stress ratio and the volumetric strain during shear, are shown in Fig. 5-30.

Changes in the magnitude of the friction coefficient have a significant effect on the ultimate strength and the strain to failure of the particle arrangement, where both properties increase with increasing μ. Higher values of friction coefficient result in higher tendency towards volumetric dilation. These relationships agree with behavioral characteristics of granular materials. Small deviations are observed between the results from OVAL and PFC2D, especially at higher strains.

Table 5-7. Values of friction angle (ϕ_μ) between mineral surfaces (Mitchell and Soga 2005).

Mineral	Type of Test	Condition	ϕ_μ (°)	Comments	Reference
Quartz	Block over particle set in mortar	Dry	6	Dried over $CaCl_2$ before testing	Tschebotarioff and Welch (1948)
		Moist	24.5		
		Water saturated	24.5		
Quartz	Three fixed particles over block	Water saturated	21.7	Normal load per particle from 1 to 100 g	Hafiz (1950)
Quartz	Block on block	Dry	7.4	Polished surfaces	Horn and Deere (1962)
		Water saturated	24.2		
Quartz	Particles on polished block	Water saturated	22-31	ϕ decreasing with increasing particle size	Rowe (1962)
Quartz	Block on block	Variable	0-45	Depends on roughness and cleanliness	Bromwell (1966)
Quartz	Particle-particle	Saturated	26	Single-point contact	Procter and Barton (1974)
	Particle-plane	Saturated	22.2		
	Particle-plane	Dry	17.4		
Feldspar	Block on block	Dry	6.8	Polished surfaces	Horn and Deere (1962)
		Water Saturated	37.6		
Feldspar	Free particle on flat surface	Water saturated	37	25-500 sieve	Lee (1966)
Feldspar	Particle-plane	Saturated	28.9	Single-point contact	Procter and Barton (1974)
Calcite	Block on block	Dry	8.0	Polished surfaces	Horn and Deere (1962)
		Water Saturated	34.2		
Muscovite	Along cleavage faces	Dry	23.3	Oven dry	Horn and Deere (1962)
		Dry	16.7	Air equilibrated	
		Saturated	13.0		
Phlogopite	Along cleavage faces	Dry	17.2	Oven dry	Horn and Deere (1962)
		Dry	14.0	Air equilibrated	
		Saturated	8.5		
Biotite	Along cleavage faces	Dry	17.2	Oven dry	Horn and Deere (1962)
		Dry	14.6	Air equilibrated	
		Saturated	7.4		
Chloride	Along cleavage faces	Dry	27.9	Oven dry	Horn and Deere (1962)
		Dry	19.3	Air equilibrated	
		Saturated	12.4		

Table 5-8. Values of friction coefficient used in various DEM applications.

Friction Coefficient	Application	Reference
0.5	Undrained cyclic biaxial test in sand	Sitharam (2003)
0.577	Drained triaxial test of Labenne sand	Belheine et al. (2009)
0.5	Cyclic undrained triaxial of granular material	Dinesh et al. (2004)
0.24	Direct shear test on glass beads	Bharadwaj et al. (2008)
0.8	Settlement of granular assembly (diorite) subjected to vibration	Karrech el al. (2008)
0.7	Direct shear test on granular material	Lobo-Guerrero and Vallejo (2005)
0.3	Biaxial test on sand to study aging effects	Wang et al. (Wang et al. 2008)
0.55	Triaxial tests on artificially cemented sand	Wang and Leung (2008)

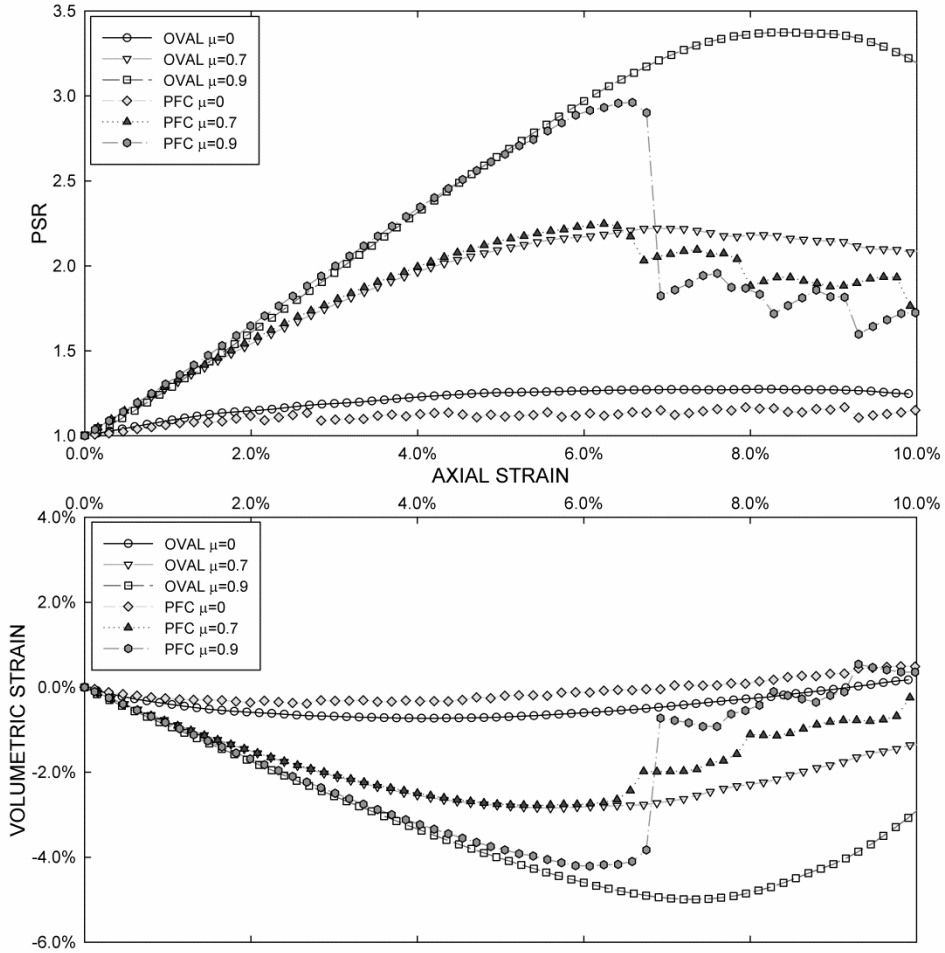

Fig. 5-30. Principal stress ratio and volumetric strain versus axial strain during shear for different values of friction coefficient. Results of simulations using OVAL and PFC2D.

DEM biaxial simulations yielded low values of PSR, corresponding to macroscopic friction angles (ϕ) of 33º, 25º, and 7º. Not only are the values of macroscopic strength low for a sand-like material, but two of them were less than the values for true friction angle (ϕ_μ) used for simulation (42º, 21.8, and 0º). Low values of shear strength obtained from DEM simulations are normally attributed to the lack of grain interlocking resulting from the simple geometries used for DEM analysis (Oda et al. 1997; Tordesillas 2007; Wang et al. 2007).

This issue can be addressed by the incorporation of rolling resistance. However, as the magnitude of rolling resistance cannot be estimated directly from any physical property of the material, incorporating it eliminates the possibility of a Class A prediction. A different alternative includes the implementation of particle clumping to form grains of complex geometries. Although this alternative incorporates the interlocking effect directly, it produces an additional level of complexity to the already computationally demanding DEM calculation process.

5.3.6 Strain rate

Changes in value of strain rate ($\dot{\varepsilon}$) are known to have a significant effect on the macroscopic properties of granular materials, as well as clays. An example of strain rate effects on the stress-strain characteristics of air-dried dense Houston Sand during drained triaxial compression is shown in Fig. 5-31 (Pham Van Bang et al. 2007). Bang et al. (2007) observed that the relationship between the deviator stress (q) and the axial strain (ε_1) from tests conducted at different strain rates ($\dot{\varepsilon}$ =0.06% /min to 0.6% /min) were very similar, but sudden variations in the magnitude of strain rate caused temporary changes in the shear resistance of the sample.

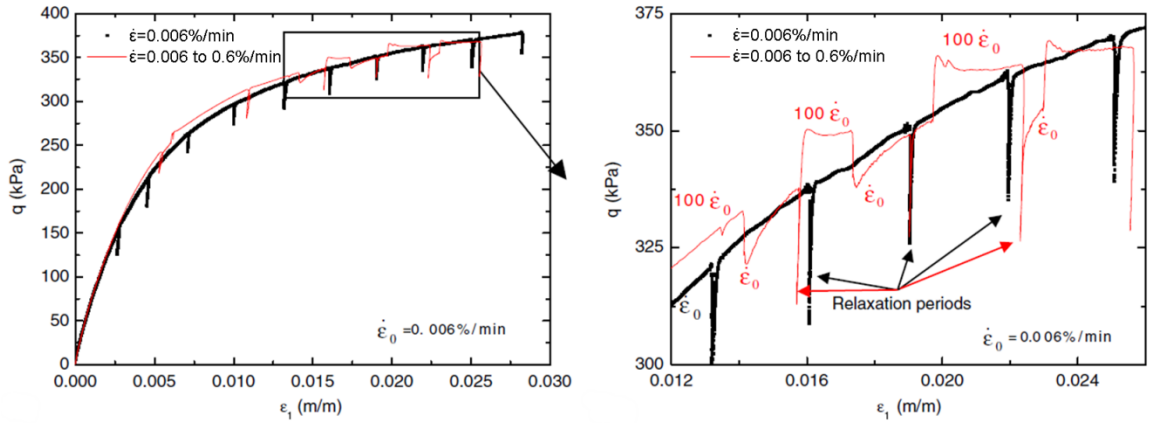

Fig. 5-31. Drained triaxial tests on air-dried dense Houston Sand showing effects of a constant and stepwise change in strain rate (Pham Van Bang et al. 2007).

A similar behavior was reported by Matsushita et al. (1999) during drained plane-strain compression and triaxial compression tests of Houston and Toyoura sand. Fig. 5-32 shows that stress ratio-shear strain relationships for tests run using constant strain rates ranging from 0.125 to 0.00125% min^{-1} were very similar. However, changes in value of $\dot{\varepsilon}$ during the test caused the shear stress to temporarily overshoot or undershoot the value recorded for *constant strain rate* tests.

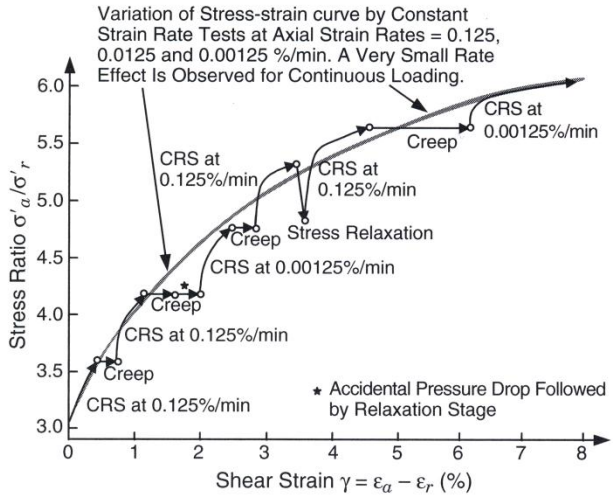

Fig. 5-32. Creep and stress relaxation on Houston Sand (Matsushita et al. 1999, after Mitchell and Soga 2005).

The value of $\dot{\varepsilon}$ has an effect on the stress-strain characteristics of granular materials. However, a common strategy to reduce execution time of DEM simulations is

to artificially increase the value of strain rate to values not normally found in geotechnical engineering applications; e.g., Wang and Zhou (2008), Bharadwaj et al. (2008), Kwok (2008). Increments in strain rate are used in pseudo-static simulations when the time scale is not of concern, and viscous and strain-rate effects can be ignored. Uncontrolled increments in strain rate generate unrealistic inertial forces. Assessing if these forces have affected the simulation results is difficult.

Values of strain rate used in some DEM geotechnical applications are shown in Table 5-9. Values used in DEM simulations often exceed by several orders of magnitude those commonly realized in laboratory or field situations.

Table 5-9. Values of strain rate and displacement rate used in various DEM applications.

Displacement Rate or Strain Rate	**Application**	**Reference**
0.01 m/s	Direct shear test on granular assembly	Bharadwaj et al. (2008)
0.01 min^{-1}	Biaxial compression tests	Jiang et al. (2006)
100 s^{-1}	Creep in clays – Biaxial tests	Kuhn (1987)
0.3 m/s	Biaxial test on granular assembly	Wang and Zhou (2008)
0.05 s^{-1}	Soil Creep – Triaxial tests	Kwok (2008)
1E-6 s^{-1}	Triaxial compression of ellipsoidal particles	Ng (2006)

The influence of the magnitude of strain rate on DEM simulations was evaluated using the particle assembly shown in Fig. 5-13. The magnitude of strain rate was changed from 0.033% s^{-1} (2% min^{-1}) to 200% s^{-1}. Results from biaxial test simulations showing the variation of the principal stress ratio and the volumetric strain during shear, are given in Fig. 5-33.

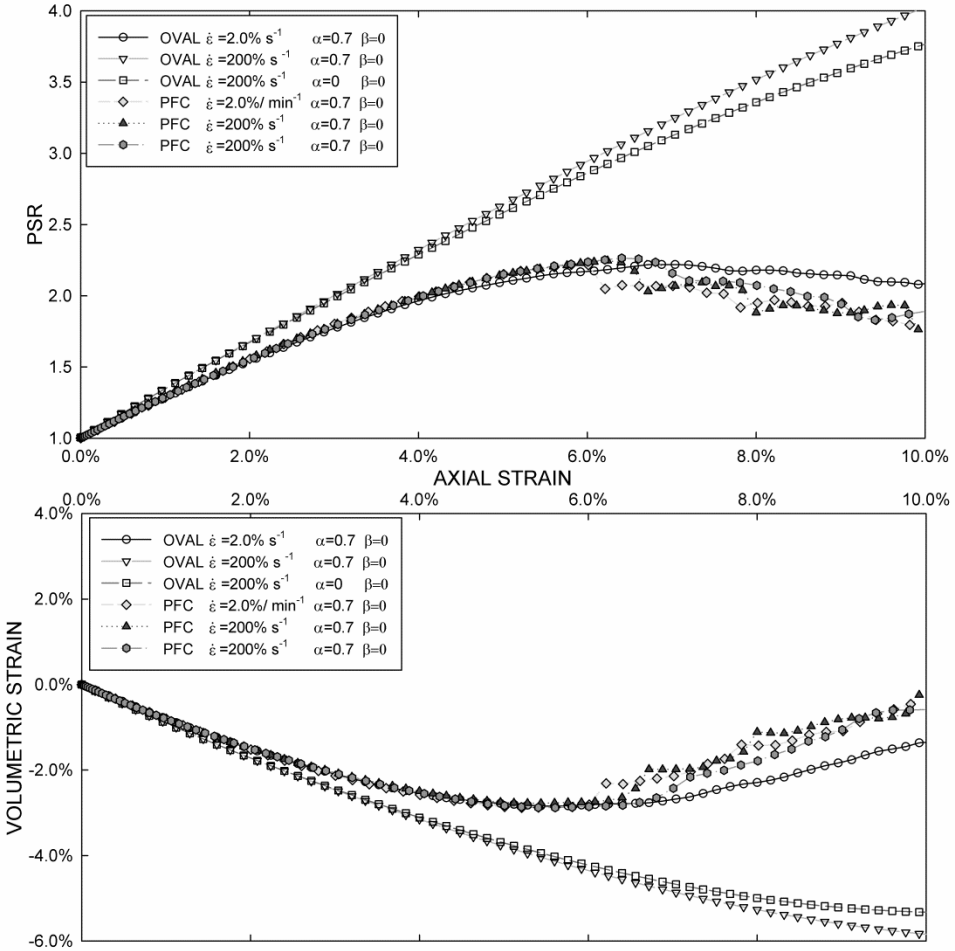

Fig. 5-33. Principal stress ratio versus axial strain during shear for different values of axial strain rate. Results of simulations using OVAL and PFC2D.

While PFC simulations do not show any significant strain rate effect, the *PSR*-axial strain plots obtained using OVAL show an increase in the shear resistance and dilatancy of the assembly for high values of $\dot{\varepsilon}$, even without viscous effects (α=β=0). Differences in the boundary types and the internal calculation processes of the two computer codes may account for the discrepancies observed in the results.

The effect of changes in the magnitude of strain rate on the results from DEM simulations can be studied using the particle assembly shown in Fig. 5-16 and described in Section 5.3.1. Calculations were performed for values of strain rate ranging from 2.0E-

3 to 2.0E5 min^{-1}. The variation of the force applied by the walls (f_w) with deformation is shown in Fig. 5-34.

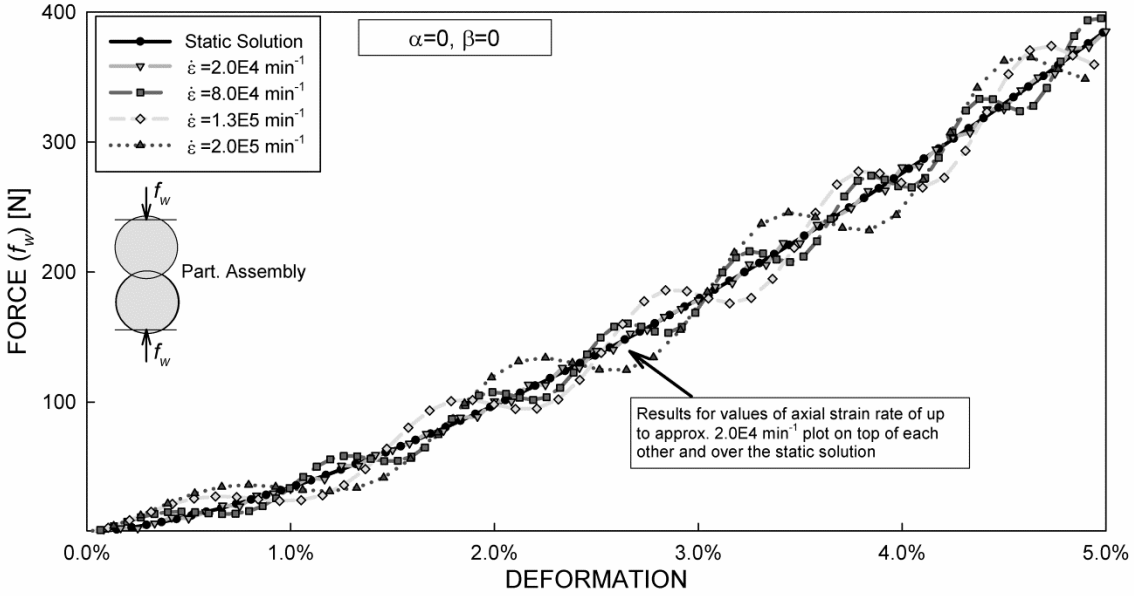

Fig. 5-34. Variation of the force applied by the walls (f_w) with deformation for different values of strain rate and α=β=0.

Increasing the magnitude of strain rate up to 2.0E4 min^{-1} does not produce any significant deviation from the static solution of the system. Further increments in the strain rate cause cyclic deviations from the static solution, which increase in magnitude for higher values of $\dot{\varepsilon}$.

Results shown in Fig. 5-34 correspond to particle interactions without viscous effects (α=β=0). If the value of viscosity is increased, the strain-rate effects become more important. This is shown in Fig. 5-35 for α=0.9. The change in viscosity causes larger deviations from the static solution of the system, as compared with Fig. 5-34. The effects of changes in viscosity on DEM simulations are also greater at higher strain rates.

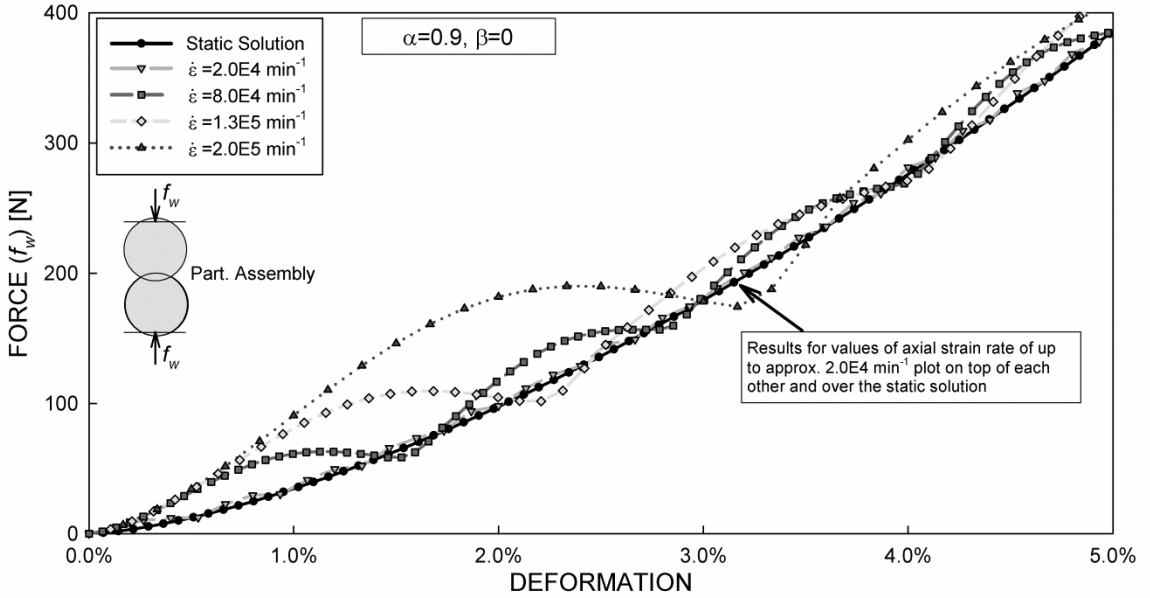

Fig. 5-35. Variation of the force applied by the walls (f_w) with deformation for different values of strain rate and α=0.9 and β=0.

Even though the simulation was done using a two-particle assembly, the same behavior is valid for complex particle arrangements. Therefore, the combination of the magnitude of viscosity and strain rate plays an important role when analyzing behaviors such as those observed previously. Viscous and rate-dependent effects are commonly neglected in DEM practice. However, the incorporation of these time-dependent effects into DEM simulations can be important in many geotechnical applications.

5.4 Application of DEM in Regular Assemblies

The applicability of DEM was studied using assemblies of regularly packed particles. The macroscopic behavior of that type of particle arrangements was studied by Rowe (1962). He conducted biaxial and triaxial compression tests on samples formed by regular packs of uniform rods and spheres. He found that the macroscopic response of the assembly, including its strength, dilatancy, and location of the slip plane, could be estimated using mathematical relationships based on the angle of friction between the

particle surfaces (ϕ_μ), the geometry of the packing, and the degree of energy loss during remolding.

The implementation of Rowe's findings allows evaluating the precision of results obtained using DEM. The analysis of results from DEM simulations of biaxial and triaxial tests using assemblies formed by regularly packed particles is presented next.

5.4.1 Two-Dimensional Particle Assemblies

Based on the static stability and the geometrical characteristics of a particle assembly, Rowe (1962) found that the principal stress ratio (σ_1'/ σ_2') of a particle assembly formed by uniform rods in a parallel stack can be calculated using Eq. 60, where α is the angle of the particle interlocking with respect to the orientation of the minor principal stress, and β is the angle at which the particles slide with respect to the orientation of the major principal stress. Both angles are geometrical characteristics of the assembly, and are shown in Fig. 5-36.

$$\frac{\sigma_1'}{\sigma_2'} = \tan(\alpha)\tan(\phi_\mu + \beta) \tag{60}$$

Rowe (1962) also conducted laboratory biaxial compression experiments of samples formed by regularly packed 0.16 in diameter steel rods. Results from these tests are shown in Fig. 5-37. Fig. 5-37 also includes the theoretical stress-strain relationship calculated using Eq. 60 for the conditions of the test (α=60° and ϕ_μ=10°).

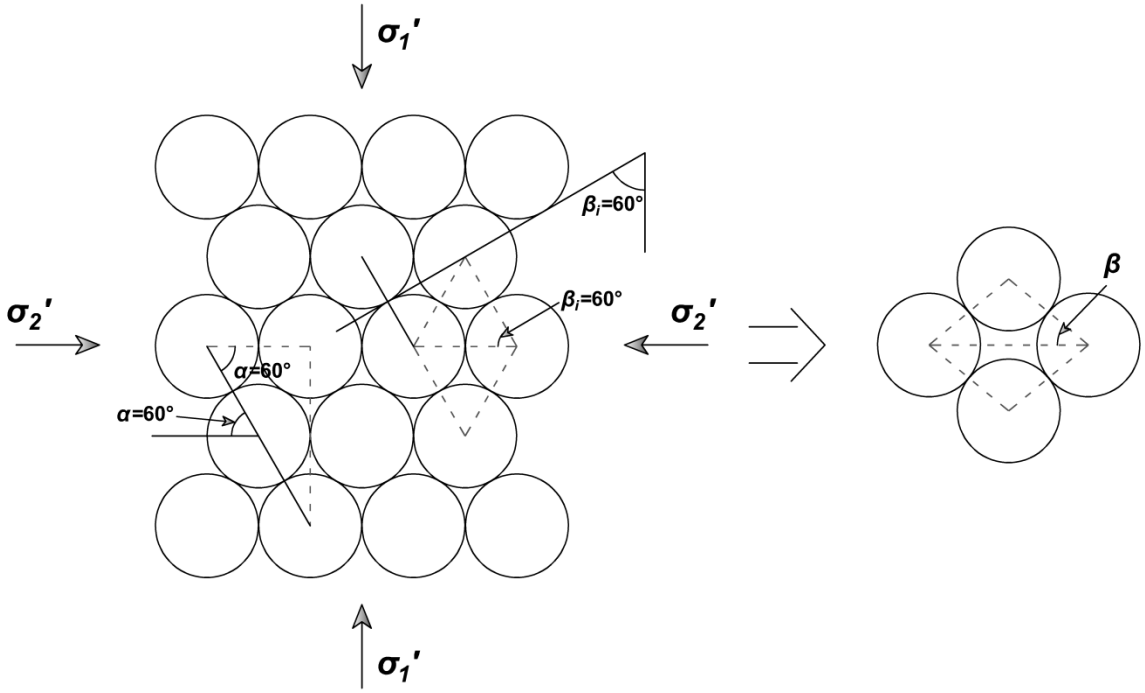

Fig. 5-36. Uniforms rods in a parallel stack (modified from Rowe, 1962).

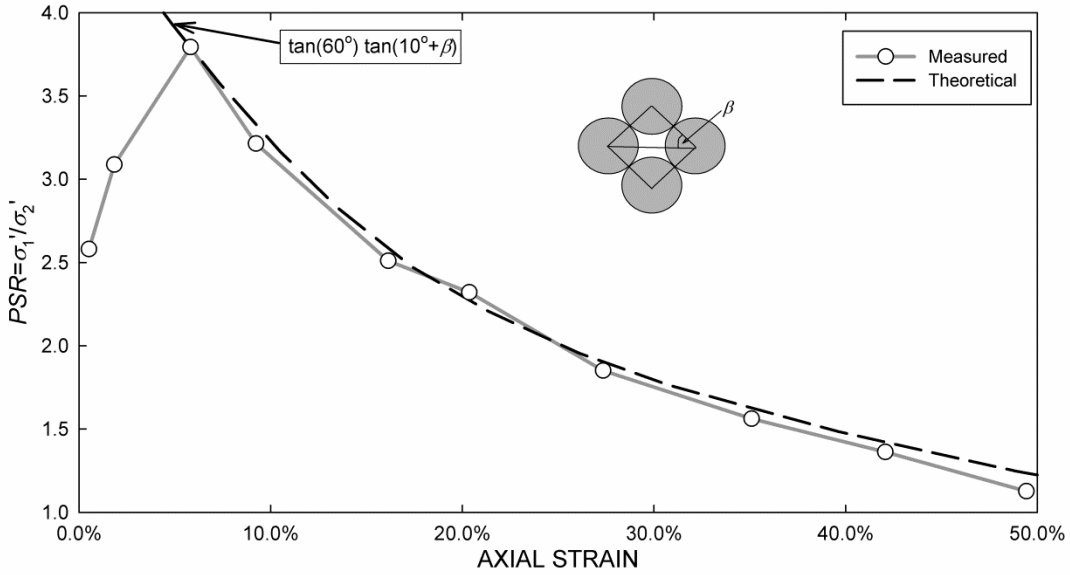

Fig. 5-37. Change in Principal Stress Ratio with respect to axial strain during biaxial compression of uniform steel rods (diameter=0.16 in).

DEM simulations were conducted using the particle assembly shown in Fig. 5-38. The assembly is formed by 5000 disks with 0.16 in diameter. The particles are stacked following the same pattern used by Rowe (1962), resulting in an assembly that is 13.88 in high and 8.08 in wide. Particle properties are those of steel, with a shear modulus equal to

80 GPa, and density of 7.8 Mg/m^3. The assembly was sheared at a constant rate of vertical strain of 0.07 s^{-1}. A value of time step of 5.0E-7 s was selected. Results from DEM simulations of drained biaxial compression tests using magnitudes of confining stress (σ'_2) ranging from 200 to 1000 kPa, are shown in Fig. 5-39.

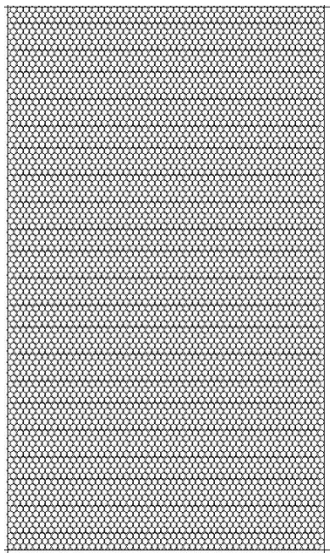

Fig. 5-38. DEM particle assembly formed by disks in a parallel stack.

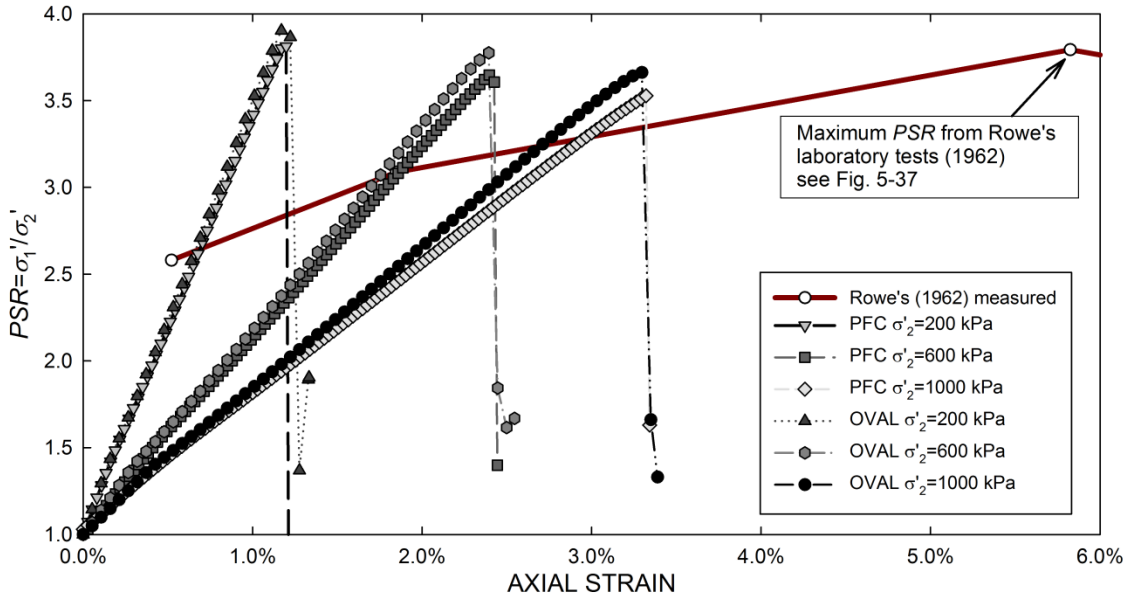

Fig. 5-39. Variation of the Principal Stress Ratio with axial strain during biaxial compression.

Results from PFC and OVAL are in good agreement. However, DEM failed to predict the stress-strain characteristics of the assembly. Fig. 5-39 shows that the values of strain at failure from DEM simulations are significantly less than those measured for assemblies of steel rods. Additionally, while laboratory experiments show a smooth decrease in the value *PSR* after failure, DEM simulations result in a drastic and sudden decrease in principal stress ratio once failure occurs.

The macroscopic strength of the particle assembly estimated using DEM is very close to that measured by Rowe (1962). DEM estimates a value of macroscopic friction angle ranging between 33.9° and 36.3°, while Rowe (1962) measured a value of ϕ of about 35.6°.

Differences in the strain at failure estimated with DEM and measured by Rowe (1962) can be related to unrealistic particle indentations calculated during DEM simulations, which assumes that the particles are rigid and estimates the contact forces based on the magnitude of the overlap between the particles. Fig. 5-40 shows the location of the failure surface after biaxial compression. The inclination of the failure surface obtained from DEM simulations (approximately 60°) is very similar to the inclination measured in laboratory tests and estimated by Rowe (1962) using mathematical relationships.

5.4.2 Three-Dimensional Particle Assemblies

Rowe (1962) studied the macroscopic response of assemblies formed by regularly packed uniform steel spheres during triaxial compression. Two different packing configurations were considered: (1) octahedral and (2) tetrahedral.

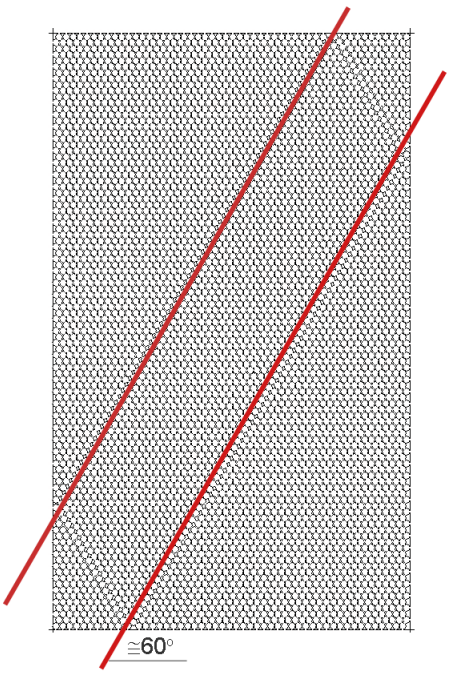

Fig. 5-40. Location of the failure surface after biaxial compression of particle assembly formed by uniform disks in a parallel stack.

5.4.2.1 Octahedral Packing

Using a similar procedure to that implemented for uniforms rods in a parallel stack, described in Section 5.4.1, Rowe (1962) found that the macroscopic strength during triaxial compression of an arrangement of spheres in an octahedral packing could be expressed as Eq. 61. The relationship assumes that the intermediate and minor principal stresses remain equal during the test ($\sigma'_2 = \sigma'_3$). The angles α and β are geometrical properties of the assembly. Fig. 5-41 shows the magnitude of these angles in an octahedral particle arrangement.

$$\frac{\sigma_1'}{\sigma_3'} = \tan(\alpha)\tan(\phi_\mu + \beta) \qquad (61)$$

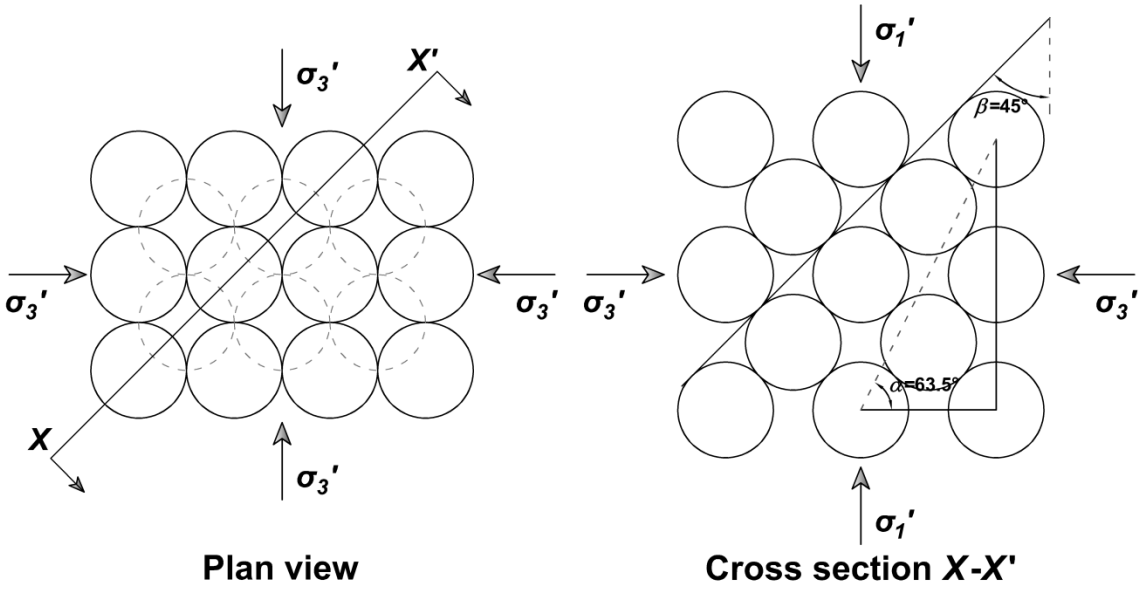

Fig. 5-41. Octahedral packing of spheres.

Drained triaxial compression experiments using samples formed by 0.25 in diameter steel spheres packed in an octahedral arrangement yielded a macroscopic friction angle of 24.7° (Rowe 1962). Using Eq. 61 with α=63.5°, β=45°, and ϕ_μ=7° (friction angle between steel spheres), the theoretical friction angle is calculated as 26°. A value of 45° was selected for β because it corresponds to its maximum magnitude and the largest value of *PSR*. The value of β decreases from its initial value (45°) as the sample is sheared, causing a decrease in the magnitude of principal stress ratio.

DEM simulations were run using OVAL on a particle assembly formed by 0.25 in diameter spheres packed in an octahedral configuration, similar to that used for the laboratory experiments conducted by Rowe (1962). The particle assembly is shown in Fig. 5-42. Particle properties are those of steel, with a shear modulus equal to 80 GPa, and friction coefficient of 0.12 (ϕ_μ=7°). A time step of 0.01 s was used for the simulation. The assembly was sheared at a constant rate of vertical strain of 4.0E-5 s^{-1}.

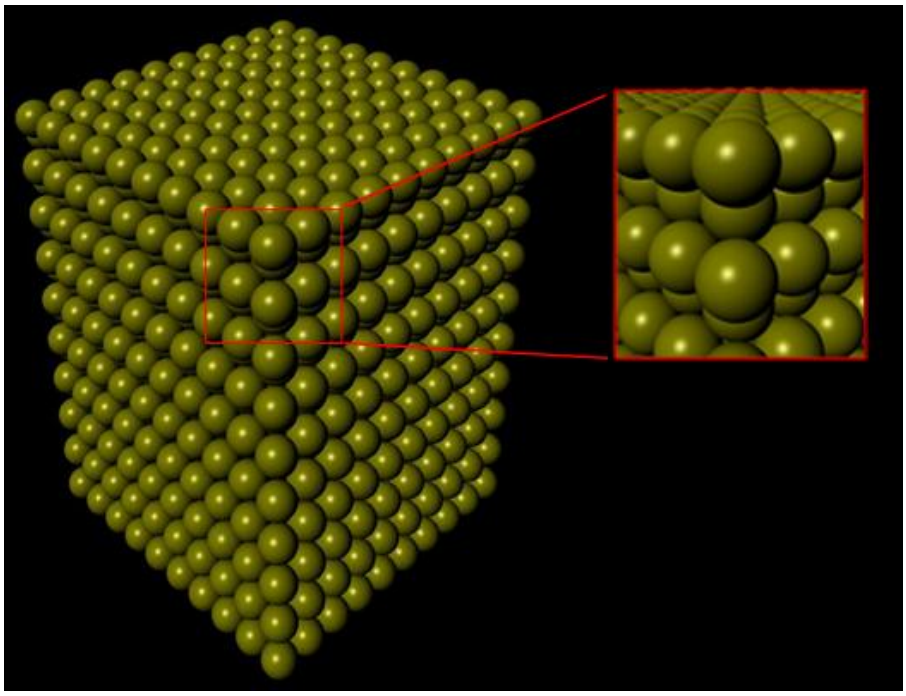

Fig. 5-42. Octahedral assembly formed by 0.25 in diameter spheres.

The macroscopic friction angle estimated using DEM is shown in Fig. 5-43. Fig. 5-43 also includes results from laboratory experiments and theoretical relationships (Rowe 1962). The values of macroscopic friction angle calculated using the three methodologies are very similar.

5.4.2.2 Tetrahedral Packing

Rowe (1962) found that Eq. 61 also applies packs of spheres in a tetrahedral configuration. For a tetrahedral arrangement, the magnitude of angles α and β are 70.6° and 54.7°. Details of their calculation can be found in Rowe (1962). Using those values of α and β, along with a magnitude of ϕ_μ of 7° for steel spheres, Eq. 61 gives a macroscopic friction angle of approximately 43°. Results from laboratory drained triaxial compression tests using samples formed by 0.25 in diameter steel spheres packed forming a tetrahedral arrangement yielded a friction angle of 42°.

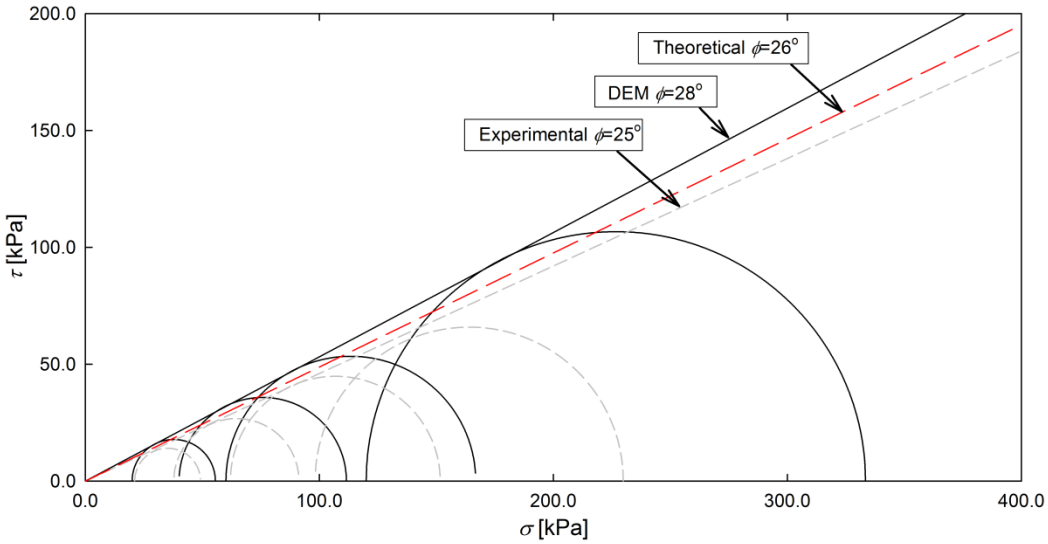

Fig. 5-43. Failure envelopes for steel spheres in an octahedral packing configuration. Results from theoretical, experimental, and DEM simulations.

OVAL was used to run DEM simulations of triaxial tests on a particle assembly formed by 0.25 in diameter spheres packed forming a tetrahedral configuration. The particle assembly is shown in Fig. 5-44. Particle properties are those of steel, with a shear modulus equal to 80 GPa, and friction coefficient of 0.12 (ϕ_μ=7°). A time step of 0.01 s was used for the simulation. The assembly was sheared using a constant rate of strain of 4.0E-5 s^{-1}.

Fig. 5-43 shows the macroscopic friction angles calculated using theoretical relationships, laboratory experiments, and DEM simulations. The values of macroscopic friction angle calculated using the three methodologies are very similar, differing by only 2.5 degrees. DEM simulations estimated higher sample strengths.

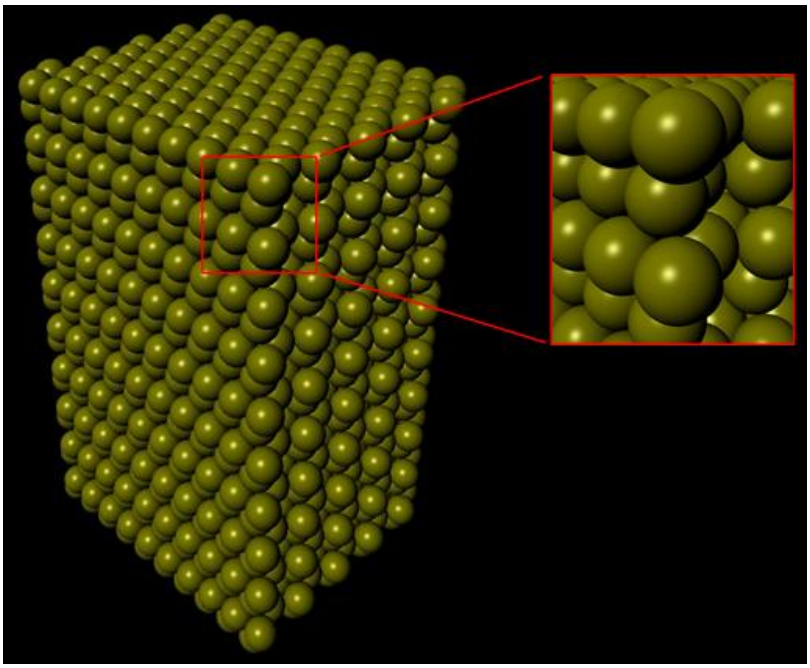

Fig. 5-44. Tetrahedral assembly formed by 0.25 in diameter spheres.

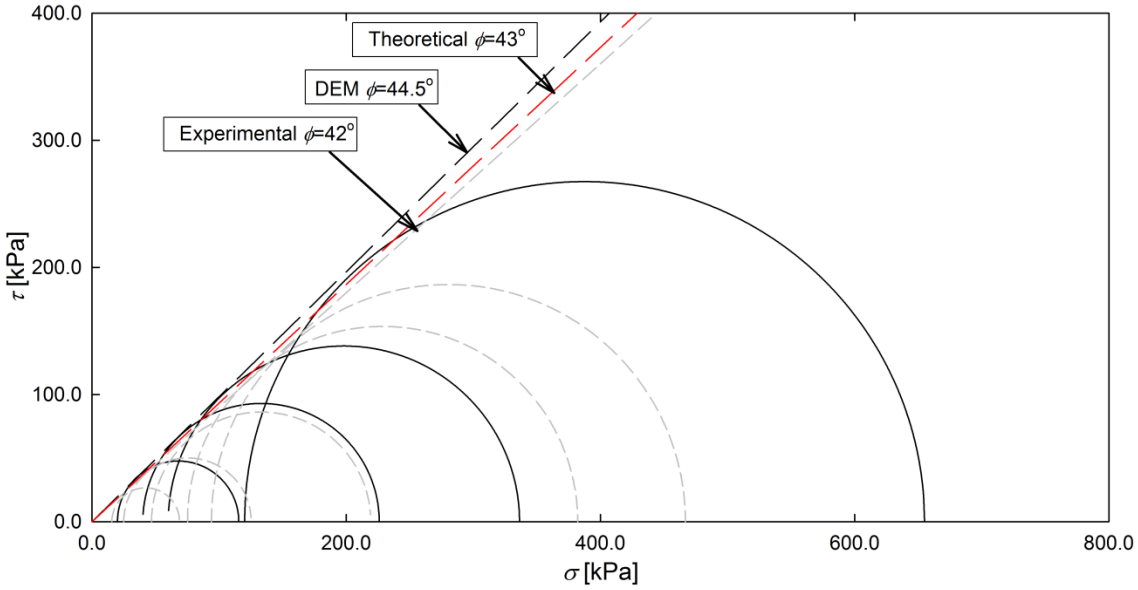

Fig. 5-45. Failure envelopes for steel spheres in a tetrahedral packing configuration. Results from theoretical, experimental, and DEM simulations.

5.5 Conclusions

DEM allows modeling granular assemblies by calculating and tracking the movement of each individual particle, in an attempt to predict macroscopic responses of granular materials based on micromechanical characteristics of the particles and properties of the assemblies. Even though DEM is now being widely used in different fields, there are several problems in its implementation, mainly related to lengthy processing times and difficulties in estimating the parameters needed for the computations. Some of these issues are:

- Even simple DEM simulations require unreasonably long computer run times if real particle and simulation parameters are used. DEM implementation in geotechnical applications is not practical without artificially modifying the magnitude of input parameters such as the particle density, particle stiffness, or the strain rate during shear. Variations in these parameters can cause important changes in the computed macroscopic properties of the assembly.
- Large time steps reduce computation time but can make the analysis unstable. The effects of variations in Δt on the DEM analysis depend on the packing configuration, the number of contacts per particle, the type of analysis (2D or 3D), and even the DEM software used. The selection of the magnitude of Δt is ultimately based on the judgment of the analyst.
- Upward density scaling to enable use of larger time steps adds an additional inertial force opposing the particle movements, reducing the resulting accelerations, and slowing the dynamic response of the arrangement. This procedure affects the dynamic response of the particles to the disturbance.

Assuming increased particle densities may also result in higher apparent macroscopic sample strength.

- Common values of strain rate used in DEM models for geotechnical applications are considerably higher than magnitudes used in practice, which do not regularly exceed 0.01 min-1. Variations in shear strain rate may produce unrealistic changes in the macroscopic strength and dilatancy of the arrangement. Errors in DEM results produced by changes in strain rate are amplified by the local and contact viscosity.
- If the simulation parameters are controlled carefully, DEM simulations can reasonably predict the macroscopic behavior of particle assemblies.

Approximations are required to obtain DEM simulations that describe real soil behavior correctly. Because most of such approximations are based solely on the user's judgment, special attention is critical when using DEM in geotechnical applications, especially during the selection of the simulation parameters.

Consequentially, it is necessary to understand the limitations of the model prior to its implementation. For this investigation DEM will be used to study changes in the structure of the soil occurring during aging. Results from DEM simulations will provide reasonable approximations of the general behavior of granular materials over time. The effect of factors such as the initial void ratio, the particle shape, and the principal stress anisotropy on the aging process in granular soils will also be considered. However, as previously discussed, quantitative DEM results are not often sufficiently reliable to be used directly in geotechnical practice without adequate calibration and experimental verification.

Chapter 6

The Rate Process Theory

6.1 Introduction

This investigation studies the changes in the soil structure occurring during aging and their effect on the engineering properties of granular soils. The main purposes are to validate the proposed driving mechanism of aging, study factors which affect it, and estimate the rate and magnitude of change in in soil properties during aging.

DEM will be used to study the particle-level processes occurring over time and their implications on the macro-scale properties of particle assemblies. Modeling time-dependent properties of granular materials using DEM requires the incorporation of a contact mechanism which simulates particle interactions as rate-dependent processes. DEM simulations often assume pseudo-static conditions, where the out-of-balance forces of the particles are artificially and arbitrarily reduced to avoid instability conditions, as

described in Chapter 5. However, this research implements DEM to model the true dynamic response of a particle assembly.

The only simulation parameter which describes time-dependent particle interactions in DEM is the contact viscosity. The magnitude of viscosity is often selected arbitrarily, because its main purpose in most DEM applications is to dissipate excessive energy in the particle system by artificially reducing the out-of-balance forces, allowing reaching a close to steady-state solution faster. Using arbitrarily selected magnitudes of viscosity can have a significant effect on the results from DEM simulations, particularly affecting the dynamic response of the assembly.

The magnitude of viscosity for DEM simulations, represented by the values of the local damping constant (α) and the coefficient of contact viscosity (β), is difficult to estimate as it does not relate to any specific material property. For this research, the contact viscosity will be estimated using the ratio of the tangential to normal forces acting at a contact, and the relative velocity of the particles. The relationship between these factors is based on the Rate Process Theory (RPT). The contact viscosity will be incorporated as a sinh-type dashpot in series with the stiffness component of the tangential contact mechanism. Previous work in this area was done by Kuhn (1987), who conducted DEM simulations using two dimensional assemblies formed by disks with a linear elastic CM to model creep in clays.

This investigation will use DEM with a contact mechanism which incorporates the RPT to simulate aging in granular materials. The rate process theory will be used in along with the Hertz-Mindlin CM, which reduces the number of approximations required to run DEM simulations and gives better accuracy to DEM models. Two- and three-

dimensional assemblies formed by particles of different shapes will be used for the analysis.

This chapter presents a description of the rate process theory and the methodology used for its incorporation into DEM analysis.

6.2 Theoretical Background

The theory of rate processes was developed by Eyring (1935) to describe the temperature dependence of reaction rates during chemical processes. According to Eyring (1935), chemical reactions continue as long as the reactants surpass a determinate *threshold energy*, or minimum energy which prevents the reaction to occur. This energy threshold, often called the *activation energy*, creates an energy barrier which separates positions of thermodynamic equilibrium. At equilibrium, the rate of reaction is equal to the rate of break down, so the net reaction rate is zero. If energy is supplied to the system, the rate of the reaction increases by a magnitude which depends on factors such as the absolute temperature, the concentration of particles, and the magnitude of the activation energy. The relationships developed by Eyring (1935) for reaction rates can be used to describe the rate of any process in which matter rearranges by surmounting energy barriers (Eyring 1936).

RPT was used to estimate the strain during viscous deformation. Eyring (1936) observed that, in steady state, the rate at which an elemental unit, or *flow unit*, fluctuates between equilibrium positions, called k_1, can be approximated using Eq. 62, where E_0 is the energy of activation of the flow unit. The parameter kT/h represents the thermal vibration frequency at rest, while $\exp(-E_0/kT)$ is the probability of a flow unit to become

activated. The parameter E_0 can be substituted by $\Delta F/N$ in Eq. 62, where N is the Avogadro number (6.022E23) and ΔF is the energy required to move one mole of flow units between adjacent equilibrium positions. The result is shown in Eq. 63.

$$k_1 = \frac{kT}{h}\exp\left(\frac{-E_0}{kT}\right) \tag{62}$$

$$k_1 = \frac{kT}{h}\exp\left(\frac{-\Delta F}{RT}\right) \tag{63}$$

k = Boltzmann's constant (1.38E-23 J/°K)
T = absolute temperature
h = Plank's constant (6.63E-34 J-s)
R = universal gas constant (8.314 J/°K-mol)

Eyring (1936) studied the relative movement of two neighboring layers of molecules. For that case, if a shear force f is applied to a molecule, the number of times per second that the molecule moves in the direction of f, named k_f, can be estimated using Eq. 64, where λ is the distance that separates adjacent equilibrium positions and k_1 is the absolute rate for the transition when no force is applied.

$$k_f = k_1 \exp\left(\frac{f\lambda}{2kT}\right) \tag{64}$$

The shear force (f) reduces the work required to pass over the energy barrier through a distance $\lambda/2$. After the application of f, the magnitude of the energy barrier ($E_0=\Delta F/N$) is reduced by an amount $f\cdot\lambda/2$ in the forward direction (direction of f) and increased by the same amount in the backward direction. The change in the magnitude of the energy barrier caused by the application of a shear force f is shown in Fig. 6-1.

The rate for the transition in the backward direction after the application of the shear force, called k_b, can be expressed as:

$$k_b = k_1 \exp\left(-\frac{f\lambda}{2kT}\right) \tag{65}$$

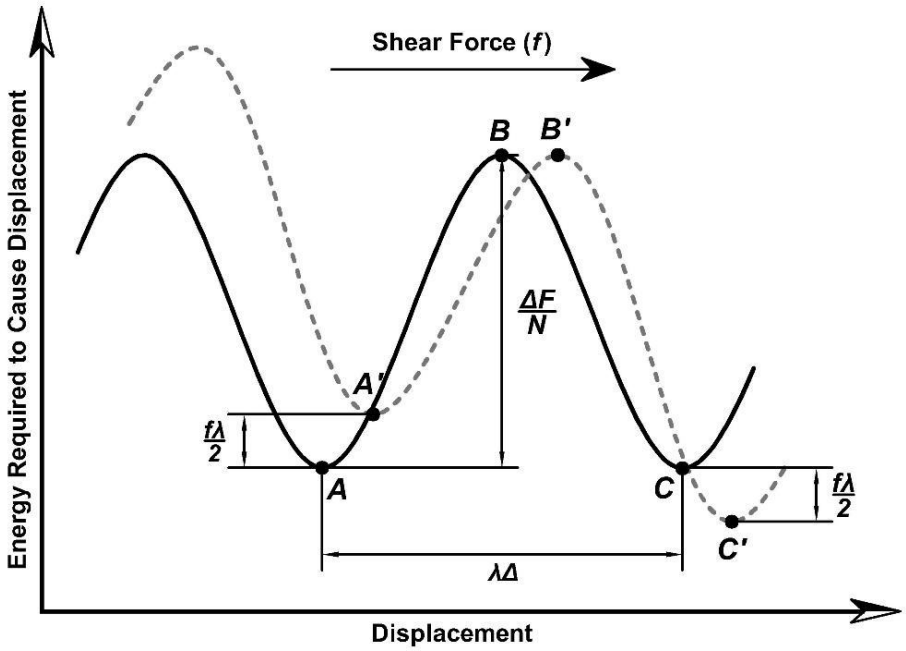

Fig. 6-1. Energy barrier in steady state (continuous line) and after the application of a shear force (dotted line).

The net rate at which a flow unit moves in the direction of the shear force, called k_n, can be calculated by subtracting the rate of fluctuation in the backward direction (k_b) from the rate in the forward direction (k_f), resulting in:

$$k_n = k_f - k_b = k_1\left[\exp\left(\frac{f\lambda}{2kT}\right) - \exp\left(-\frac{f\lambda}{2kT}\right)\right] \tag{66}$$

$$k_n = k_1 2\sinh\left(\frac{f\lambda}{2kT}\right) \tag{67}$$

The parameter k_n is the net number of times per second that a flow unit moves over an energy barrier in the direction of the applied shear force. The relative velocity of two neighboring layers ($\dot{x}$) of molecules can be calculated by multiplying k_n by the distance between equilibrium positions, called λ, as follows:

$$\dot{x} = \lambda k_1 2\sinh\left(\frac{f\lambda}{2kT}\right) \tag{68}$$

Substituting k_1 from Eq. 62 in Eq. 68, gives Eq. 69, which allows calculating the relative velocity between the molecule layers based on the magnitude of the shear force, the distance between the equilibrium positions, the activation energy, and the absolute temperature.

$$\dot{x} = 2\lambda \frac{kT}{h} \exp\left(\frac{-\Delta F}{RT}\right) \sinh\left(\frac{f\lambda}{2kT}\right) \tag{69}$$

Eyring (1936) used the previous relationship to describe the increase in viscosity with shearing stress for gases and liquids. Mitchell et al. (1968) assumed that that the behavior described by Eq. 69 was applicable for solids under plastic deformation, and used it to estimate the stress-strain-time relationship of clays during creep.

6.3 Incorporation of RPT into DEM Analysis

Kuhn (1987) noted the possibility of implementing the relationships developed by Eyring (1936) to describe time-dependent particle interactions during DEM simulations, thus allowing DEM to model rate-dependent macro-scale properties of soils. He assumed that particle interactions could be described as rate processes, controlled by the interaction of molecules on the particles' outer-shells. Consequentially, Eq. 69 could be used to calculate the relative velocity of particles in contact under stress.

Kuhn (1987) considered the flow units as single bonds formed at the contact surface of the particles. The shear or sliding force acting on a flow unit (f) is equal to the total tangential force acting the contact (f_t) divided by the number of bonds at the contact surface (n), this gives:

$$f = \frac{f_t}{n} \tag{70}$$

The number of bonds at the contact surface of two particles was assumed proportional to the normal force which is pushing the particles together (f_n), so that:

$$n = f_n n_1 \tag{71}$$

where n_1 is the proportionality constant between n and f_n.

Substituting f and n from Eqs. 70 and 71 in Eq. 69 gives:

$$\dot{x} = 2\lambda \frac{kT}{h} \exp\left(\frac{-\Delta F}{RT}\right) \sinh\left(\frac{f_t}{f_n} \frac{\lambda}{2n_1 kT}\right) \tag{72}$$

Eq. 72, which relates the relative rate of sliding between two particles to the ratio of the tangential and the normal forces acting at the contact, can be incorporated into the contact mechanism used during DEM simulations. Kuhn (1987) developed a methodology to use Eq. 72 in a linear elastic CM. However, for this investigation, RPT will be used along with the Hertz-Mindlin CM, described in Chapter 5, to reduce the amount of approximations required to run DEM simulations and build DEM models which are closer to physical reality. This requires the application of some modifications to Kuhn's methodology. Both calculation procedures are described next.

6.3.1 Linear Elastic Contact Mechanism

Kuhn (1987) developed a methodology to incorporate the RPT into the linear elastic CM used for DEM simulations to model creep in clays. This was done by using a sinh-type dashpot in series with the stiffness element in the tangential component of the contact mechanism. Fig. 6-2 shows the contact mechanism used by Kuhn (1987).

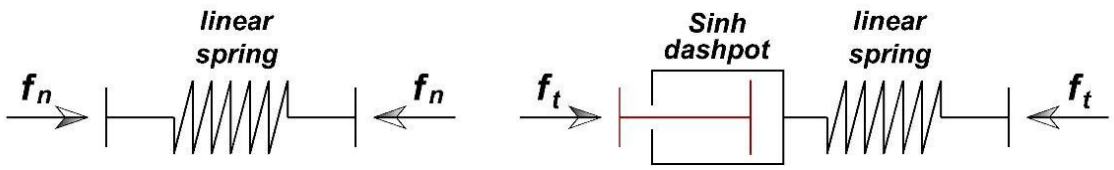

(a) (b)

Fig. 6-2. (a) Normal and (b) Tangential components of the contact mechanism used by Kuhn (1987).

The viscous force and rate of strain at the contact are controlled by the ratio of the tangential to normal forces acting at the particle contact, based on Eq. 72. The sinh-type dashpot controls micro-scale particle interactions including the failure condition, represented by the maximum value or f_t/f_n, and viscous effects during plastic strain. The stiffness element controls the elastic component of the deformation. The sinh-type dashpot replaces both the frictional slider and the viscous dashpot in the contact mechanism.

Calculations performed to estimate the magnitude of the normal and tangential forces at the particle contacts for a linear elastic CM were described in Section 0. For the linear elastic CM the magnitude of the tangential stiffness (k_t) is not affected by the level of deformation or the magnitude of the normal force. This simplifies significantly the complexity of the calculations compared to the Hertz-Mindlin CM.

The tangential force f_t acting on a contact is equal to the viscous force from the sinh-type dashpot, called f_t^v, which also equals the elastic force from the linear spring (f_t^e). This relationship is shown in Eq. 73. The total tangential indentation, named U_t, is the sum of the viscous deformation in the dashpot (U_t^v) and the elastic deformation in the spring (U_t^e), as shown in Fig. 6-3.

$$f_t = f_t^v = f_t^e \tag{73}$$

$$U_t = U_t^v + U_t^e \tag{74}$$

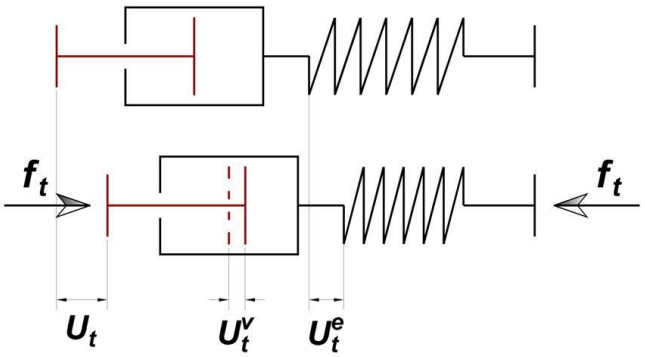

Fig. 6-3. Components of the total tangential indentation at a contact.

For the linear elastic CM, the elastic tangential force (f_t^e) is equal to the contact stiffness (k_t) multiplied by the total deformation in the linear spring (U_t^e), giving:

$$f_t^e = k_t U_t^e \tag{75}$$

Eq. 76, which relates the net tangential force (f_t) to the tangential contact stiffness, the total tangential indentations, and the indentations in the dashpot, is derived using Eqs. 73 to 75, as follows:

$$\begin{aligned} f_t^e &= f_t \\ f_t &= k_t U_t^e \\ U_t^e &= U_t - U_t^v \\ f_t &= k_t \left(U_t - U_t^v\right) \end{aligned} \tag{76}$$

The magnitude of U_t^v is calculated for each time step. Its magnitude during cycle i ($U_{t(i)}^v$) is equal to sum of its value during the previous cycle ($U_{t(i-1)}^v$) and the change in indentation during the current cycle ($\Delta U_{t(i)}^v$). The change in the indentation at the dashpot is estimated based on the magnitude of time step and the average of sliding velocity in the dashpot ($\dot{U}_t^v$) for the previous and current cycles, using the following equation:

$$\Delta U_{t(i)}^v = \frac{\dot{U}_{t(i-1)}^v + \dot{U}_{t(i)}^v}{2} \Delta t \tag{77}$$

Eq. 78, which is used to calculate the magnitude of tangential force at the contact, is derived using Eqs. 76 and 77 as follows:

$$U^{v}_{t(i)} = U^{v}_{t(i-1)} + \frac{\dot{U}^{v}_{t(i-1)} + \dot{U}^{v}_{t(i)}}{2}\Delta t$$
$$f_{t(i)} = k_t\left[U_{t(i)} - \left(U^{v}_{t(i-1)} + \frac{\dot{U}^{v}_{t(i-1)} + \dot{U}^{v}_{t(i)}}{2}\Delta t\right)\right] \quad (78)$$

The sliding velocity in the dashpot ($\dot{U}_t^v$) is controlled by the rate process theory. Eq. 72 defines the magnitude of the total rate of sliding between two particles in contact ($\dot{x}$). Because $\dot{U}_t^v$ is the rate of sliding for a single particle, its magnitude is equal to half of the total sliding rate ($\dot{x}/2$), resulting in:

$$\dot{U}^{v}_{t(i)} = \lambda\frac{kT}{h}\exp\left(\frac{-\Delta F}{RT}\right)\sinh\left(\frac{f_{t(i)}}{f_{n(i)}}\frac{\lambda}{2n_1kT}\right) \quad (79)$$

The magnitude of tangential force for the current calculation cycle ($f_{t(i)}$) is approximated using Eqs. 78 and 79, and the values of the normal force and the total tangential indentation. However, the solution of the system of equations is not implicit, and requires the implementation of iterative methods for its estimation.

6.3.2 Hertz-Mindlin Contact Mechanism

Advantages of the Hertz-Mindlin Cm over the linear elastic CM were discussed in Section 0. In general, the implementation of the Hertz-Mindlin CM allows a better representation of real soils using DEM.

The linear elastic CM assumes a constant value of stiffness regardless of the level of indentation, while Hertz-Mindlin CM assumes a non-linear relationship between contact stiffness and the particle indentation. Additionally, the tangential stiffness of the contact depends also on the magnitude of the normal force pushing the particles together. The relationships used to calculate the magnitude of normal and tangential contact stiffnesses based on the values of shear modulus, Poison's ratio, indentation, and radii of

the particles were given in Section 0. As the magnitude of normal and tangential contact stiffness changes along with the particle indentation, the implementation of the RPT to the Hertz-Mindlin CM requires modifications to the methodology proposed by Kuhn (1987) and discussed in the previous Section.

Eq. 36 indicates that the value of k_t is proportional to the magnitude of the normal force to the power of 1/3. Consequentially, the value of the tangential stiffness is likely to change significantly from on calculation cycle to the next. As a result, f_t needs to be calculated using a step-by-step process, where the value for a calculation cycle i is the sum of its magnitude for the previous cycle ($f_{t\,(i\text{-}1)}$) and the change in tangential force ($\Delta f_{t\,(i)}$) estimated based on the current tangential stiffness ($k_{t\,(i)}$) and the change in tangential indentation ($\Delta U_{t\,(i)}$), giving:

$$f_{t(i)} = f_{t(i-1)} + \Delta f_{t(i)} \tag{80}$$

The incorporation of the RPT in the Hertz-Mindlin CM requires using the magnitude of distinct changes in indentations for each time step (ΔU_t, ΔU_t^e, and ΔU_t^v), instead of the net total values used for the linear elastic CM. Eqs. 81 to 84 are applicable to the Hertz-Mindlin CM.

$$\Delta f_{t(i)} = \Delta f^{e}_{t(i)} = \Delta f^{v}_{t(i)} \tag{81}$$

$$\Delta f^{e}_{t(i)} = k_{t(i)} \Delta U^{e}_{t(i)} \tag{82}$$

$$\Delta U_{t(i)} = \Delta U^{e}_{t(i)} + \Delta U^{v}_{t(i)} \tag{83}$$

$$\Delta f_{t(i)} = k_{t(i)} \left(\Delta U_{t(i)} - \Delta U^{v}_{t(i)} \right) \tag{84}$$

$$\Delta U^{v}_{t(i)} = \frac{\dot{U}^{v}_{t(i-1)} + \dot{U}^{v}_{t(i)}}{2} \Delta t \tag{85}$$

Substituting $\Delta f_{t(i)}$ from Eq. 84 and $\Delta U_{t(i)}{}^{v}$ from Eq. 85 in Eq. 80 results in::

$$f_{t(i)} = f_{t(i-1)} + k_{t(i)} \left(\Delta U_{t(i)} - \frac{\dot{U}^{v}_{t(i-1)} + \dot{U}^{v}_{t(i)}}{2} \Delta t \right) \tag{86}$$

The value of f_t for a calculation cycle is estimated solving the system of equations formed by Eqs. 79 and 86, using the values of the tangential force ($f_{t\ (i\text{-}1)}$), as well as the indentation and velocity in the dashpot ($U^{v}_{t\ (i\text{-}1)}$, $\dot{U}^{v}_{t\ (i\text{-}1)}$) for the previous cycle. The solution of the system of equations is not implicit and requires the implementation of an iterative method.

6.4 Parameters of the RPT Equation

The relationship which describes the rate of sliding of two neighboring layers of molecules developed by Eyring (1936), and later modified by Kuhn (1987) to study creep in clays using DEM, requires the estimation of some input parameters. Some of them are physical constants; i.e., Boltzmann's constant (k), Plank's constant (h), universal gas constant (R); which are known. Other parameters such as the activation energy of a mole of flow units (ΔF), the distance between equilibrium, positions (λ), and the proportionality constant between the normal force and the number of bonds formed at the contact between two particles (n_1), are properties of the constitutive material of the particles, and need to be estimated prior to the application of the RPT in DEM analysis.

The following section describes each of the parameters and estimates reasonable values for DEM simulations.

6.4.1 Distance between Equilibrium Positions [λ]

The parameter λ denotes the distance between adjacent equilibrium positions of a flow unit. Mitchell et al. (1969) assumed that, for two silicate particles in contact, λ is equal to the distance between consecutive atomic valleys in the surface of a silicate mineral, as shown in Fig. 6-4. This distance, which is approximately 2.8 Å, is applicable

to any silicate mineral. Sands and clays should have similar values of λ, because they share a similar chemical composition and crystal structure at the surface. Kwok (2008) also assumed a value of 2.8 Å for λ during DEM simulations of creep in granular materials.

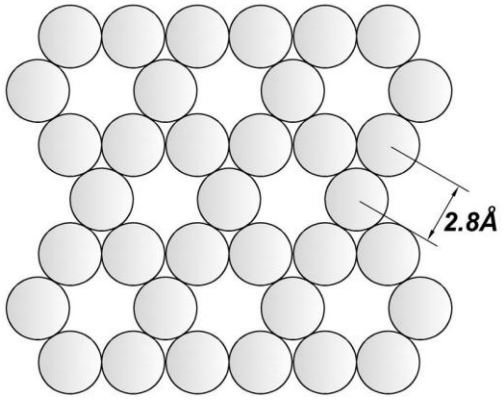

Fig. 6-4. Surface of a silicate mineral. Each circle represents and oxygen molecule (redrawn from Mitchell and Soga, 2005).

6.4.2 Activation Energy [ΔF]

The energy required to move one flow unit from one equilibrium position to the next is called the activation energy (E_0). For practical purpose, the energy of activation of the system is often expresses as ΔF, which the energy required to move a mole of flow units between adjacent equilibrium positions. The value of E_0 can be found based on the magnitude of ΔF as follows:

$$E_0 = \frac{\Delta F}{N} \tag{87}$$

Common values of ΔF for clays range from 80 to 180 kJ/mol (Mitchell and Soga 2005). Some examples are shown in Table 6-1.

Table 6-1. Activation energy of different materials (Mitchell et al. 1997).

Material	Activation Energy (kJ/mol)	Reference
Remolded illite, saturated, water content of 30 to 43%	105-165	Mitchell et al. (1969)
Dried illite: samples air-dried from saturation, then evacuated	155	Mitchell et al. (1969)
San Francisco Bay mud, undisturbed	105-135	Mitchell et al. (1969)
Dry Sacramento River sand	~105	Mitchell et al. (1969)
Water	16-21	Glasstone et al. (1941)
Montmorillonite – water paste, dilute	30-60	Ree and Eyring (1958)
Soil asphalt	84-109	Ripple and Day (1966)
Lake clay, undisturbed and remolded	113	Abdel-Hady and Herrin (1966)
Osaka clay, overconsolidated	96-113	Christensen and Wu (1964)
Concrete	120-134	Murayama and Shibata (1961)
Metals	226	Finnie and Heller (1959)
Frozen Soils	210	Andersland and Akili (1967)
Sault Ste. Marie clay, suspensions, discontinuous structures	Same as water	Andersland and Douglas (1970)
Sault Ste. Marie clay, Li^+, Na^+, K^+, forms, in H_2O and CCl_4, consolidated	117	Andersland and Douglas (1970)

The magnitude of activation energy measured in the laboratory is often the experimental activation energy (E); i.e. ΔF reduced by the application of a shear force f. The relationship between E and ΔF is shown below:

$$E = \Delta F - \frac{\lambda f N}{2} \tag{88}$$

The magnitude of E is often estimated using Dorn's method (Tietz and Dorn 1956). Tietz and Dorn developed a technique to determine the activation energy for creep of copper, by rapidly changing the test temperature during a constant stress creep test. The magnitude of the activation energy was obtained from the relationship shown in Eq. 89, where $\dot{\varepsilon}$ is the strain rate, T is the absolute temperature, and the subscripts refer to the conditions just before and after the sudden temperature change.

$$\dot{\varepsilon}_1 e^{\frac{E}{RT_1}} = \dot{\varepsilon}_2 e^{\frac{E}{RT_{21}}} \tag{89}$$

Mitchell et al. (1968) used Dorn's method to determine the energy of activation for creep in clays. The application of Dorn's method has the advantage of only requiring one sample, thus allowing to measure creep rates at two temperatures under essentially the same sample conditions. Mitchell et al. (1968) conducted constant stress creep tests using a temperature-controlled triaxial apparatus. A detailed description of the equipment used can be found in Mitchell and Campanella (1964). During the tests, the specimens were allowed to creep under a constant deviator stress. The test temperature was then increased, and new creep strains were recorded. Results from tests on San Francisco Bay mud led to the conclusion that, for the temperature increment tests described previously, the experimental energy of activation (E) could be calculated using the following relationship:

$$E = \frac{2.3RT_2T_1}{T_2 - T_1} \log\left(\frac{\dot{\varepsilon}_2 T_1}{\dot{\varepsilon}_1 T_2}\right) \tag{90}$$

Even though rate-dependent soil properties are studied almost exclusively in clays, results of tests conducted on sands suggest that the values of activation energy for clays and sands are of the same order of magnitude (Mitchell and Soga 2005). That is reasonable because sand and clay particles are composed of silicate minerals which share similar surface molecular composition. Additionally, as long as the soil is not suspended in the pore fluid, the magnitude of activation energy does not seem to be affected by the water content, absorbed cations, consolidation pressure, void ratio, or pore fluid (Mitchell and Soga 2005), which can differ significantly for sands and clays.

Kuhn (Kuhn 1987) assigned a value of 105 kJ/mol to ΔF for DEM simulations of creep in clays. Kwok (2008) proposed a value of 140 kJ/mol for ΔF, obtained by matching results from DEM simulations on assemblies of spheres with results from laboratory creep experiments.

6.4.3 Number of Bonds at the Contact [n_1]

In order to use the RPT to describe particle sliding as a rate process, the magnitude of the shear force acting on a single flow unit has to be estimated. Mitchell et al. (1969) proposed that the cohesion, friction, and deformation in soils were related to interparticle bonds formed at the contacts. Each of the bonds formed is assumed to provide the same resistance to shear, so the total strength of the soil is proportional to the total number of bonds formed and not the number of interparticle contacts (Mitchell et al. 1969).

Mitchell et al. (1969) assumed that the number of interparticle bonds per unit area formed was directly proportional to the normal stress acting on the cross-section. Thee exceptions were considered: (1) soils of very high plasticity where interparticle forces are large, (2) soils whose particles are chemically cemented, and (3) over-consolidated clays which retain some of the bonds after unloading.

According to the previous assumptions, the shear force per flow unit (f) can be approximated by dividing the total shear stress (τ) acting on a plane by the number of bonds per unit area on the cross-section (S), just as follows:

$$f = \frac{\tau}{S} \tag{91}$$

During a triaxial test, the maximum shear stress is equal to half the deviator stress (σ_d). Therefore, the average shear force per flow unit in the plane of maximum shear can be expressed as:

$$f = \frac{\sigma_d}{2S} \tag{92}$$

Assuming creep in clays as a rate process, Eq. 69 can be used to describe the rate of creep strain based on the magnitude of the shear force per flow unit, the distance between equilibrium positions, the energy of activation, and the absolute temperate. The value of *f* from Eq. 92 can be substituted in Eq. 69, which gives:

$$\dot{x} = K \exp(\sigma_d \alpha) \tag{93}$$

$$K = \lambda \frac{kT}{h} \exp\left(\frac{-\Delta F}{RT}\right) \tag{94}$$

$$\alpha = \frac{\lambda}{4SkT} \tag{95}$$

According to Mitchell et al. (1969), the parameter *K* in Eq. 93 can change during creep, while α is a constant for the soil. The magnitude of α is the slope of the relationship between the logarithm of strain rate and the stress, and can be calculated using the strain rates measured at the same time after the start of creep tests conducted under different stress levels.

The magnitude of *S* can be determined knowing the value of α and using Eq. 95. Mitchell et al. (1969) found that the number of bonds per unit area for normally-consolidated soils was proportional to the effective consolidation pressure (σ_p), such as:

$$S = S_1 \sigma_p \tag{96}$$

The proportionality constant, named S_1, was calculated as approximately $2.5*10^9$ bonds/m^2-Pa for San Francisco Bay mud.

Mitchell et al. (1969) conducted creep tests on uniform, angular, medium fine micaceous sand (Dry Antioch sand) with a coefficient of uniformity of 1.6. A triaxial apparatus was used to carry out creep tests under deviator stress levels ranging from 60% to 80%. The results indicated that the number of bonds per unit area for sands was about the same than for clays, with a value of S_1 of approximately 1.0E10 bonds/m^2-Pa.

The parameters S and S_1 require the existence of a well-defined failure plane, which is not commonly the case in DEM models. Additionally, running DEM simulations using RPT require an estimated value for the number of bonds per unit force formed at the contact surface between two particles (n_1), which is not affected by the magnitude of the area of contact.

Kuhn (1987) studied the relationship between parameters S_1 and n_1 using an assembly of regularly packed uniform spheres. He concluded that n_1 is approximately 1 to 2 times S_1. He used a value of n_1 of 1.0E9 bonds/N during DEM simulations of creep in clays.

6.5 Previous Research

In addition to Kuhn's investigation, which was described in previous sections, Kwok (2008) used DEM simulations to study creep processes in granular materials. She considered two possible hypotheses to explain creep in sands: (1) interparticle sliding, and (2) progressive particle breakage.

For the first hypothesis, creep was modeled using the RPT in DEM simulations on assemblies formed by spheres. The RPT was incorporated in the form of a rate-dependent frictional slider, which controlled the maximum tangential force at the contact based on

the normal force and the relative tangential velocity of the particles. For the second hypothesis, static fatigue was modeled applying a time dependent decrease in the magnitude of bond strength of clumps formed by multiple spheres. It was found that the macroscopic behavior during creep from DEM simulation with the implementing rate-dependent particle sliding was very similar to that of real soil samples. However, results from simulations run using the progressive particle breakage failed to represent the macroscopic behavior of soils during creep.

Chapter 2 discussed the different hypotheses formulated to explain the occurrence of aging in granular soils. It was found that aging of sands is likely caused by small particle movements and rotations occurring with time under the new in-situ stress conditions following deposition or densification. For this investigation, aging will be modeled using rate-dependent particle interactions applying the methodology described in Section 6.3.2, which incorporates the rate process theory with the Hertz-Mindlin CM using a sinh-type dashpot.

Kwok (2008) modeled particle sliding incorporating a frictional slider in series with the tangential stiffness component of a linear elastic CM. The friction coefficient (μ) was controlled by the magnitude of the relative tangential velocity ($|\dot{U}_t|$) of the particles. Fig. 6-5 shows the tangential the contact mechanism used by Kwok (2008).

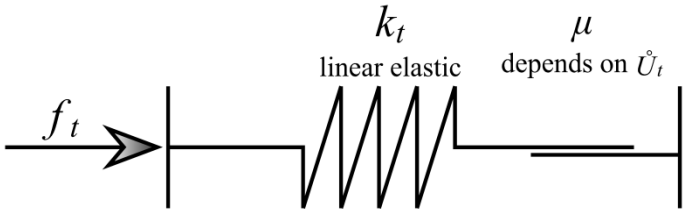

Fig. 6-5. Tangential component of the contact mechanism used by Kwok.

The magnitude of μ controls the maximum attainable tangential force (f_t) based on the normal force acting at the contact (f_n). The relationship for the friction coefficient in

terms of the tangential velocity used by Kwok (2008) was derived from Eq. 79, which was developed by Kuhn (1987) to model creep in clays.

Kwok (2008) replaced $\dot{U}_t^v$ in Eq. 79 with $\dot{U}_t$, which is the relative tangential velocity of the particles, and substituted the ratio f_t/f_n with μ, the friction coefficient of the rate-dependent frictional slider, thus resulting in:

$$\dot{U}_t = \lambda \frac{2kT}{h} \exp\left(\frac{-\Delta F}{RT}\right) \sinh\left(\frac{\lambda}{2n_1 kT}\mu\right) \tag{97}$$

Assuming than value of $\lambda\mu/2kTn_1$ is greater than 1, Eq. 97 can be approximated to:

$$\dot{U}_t = \lambda \frac{2kT}{h} \exp\left(\frac{\lambda}{2n_1 kT}\mu - \frac{\Delta F}{RT}\right) \tag{98}$$

The value of μ can be derived using Eq. 98 as follows:

$$\mu = \frac{2kTn_1}{\lambda}\left[\ln\left(\frac{\dot{U}_t h}{\lambda kT}\right) + \frac{\Delta F}{RT}\right] \tag{99}$$

It is important to note that during DEM simulations, the friction coefficient is only used to find the maximum allowable tangential force based on the normal force acting at the contact ($f_{t\ max}=\mu f_n$). If the magnitude of the tangential force is less than $f_{t\ max}$, the magnitude of the friction coefficient does not affect the simulation.

Kuhn (1987) introduced the relationship shown in Eq. 79 as a velocity dependent viscosity, where the parameter $\dot{U}_t^v$ is the viscous velocity in a sinh-type dashpot. If $\dot{U}_t$ is the net relative tangential velocity between two particles in contact, the total tangential indentation (U_t) for one time step is equal to $\dot{U}_t \Delta t$. The elastic indentation (U_t^e) is equal to the U_t minus the indentation at the viscous dashpot (U_t^v). This was shown in Fig. 6-3. If the elastic indentation is not zero, the magnitudes of U_t and U_t^v, as well as the values of the relative tangential velocity ($\dot{U}_t$) and viscous velocity in the dashpot ($\dot{U}_t^v$), will be

different. As a result, the incorporation of the RPT in DEM simulations using a rate-dependent frictional slider or a velocity-dependent dashpot will produce different results.

An assembly formed by two 2 mm diameter spheres pressed together by a normal force of 10 N was used to compare results from DEM simulations using the two methodologies previously described. The particle assembly is shown in Fig. 6-6. Material properties of the particles are those of silica sand, with a shear modulus of 30GPa and Poisson's ratio equal to 0.18. The relative tangential velocity of the particles was controlled during the simulation.

The relative tangential velocity of the particles was kept constant during displacement increments of 500 μm. After each displacement increment, the magnitude of $\dot{U}_t$ was changed from 1 to 10 μm/s and vice versa to study the effect of variations in sliding velocity on the magnitude of the tangential contact force. The RPT was incorporated in the analysis using the two methodologies previously described: (1) using a rate-dependent frictional slider, and (2) using a sinh-type dashpot.

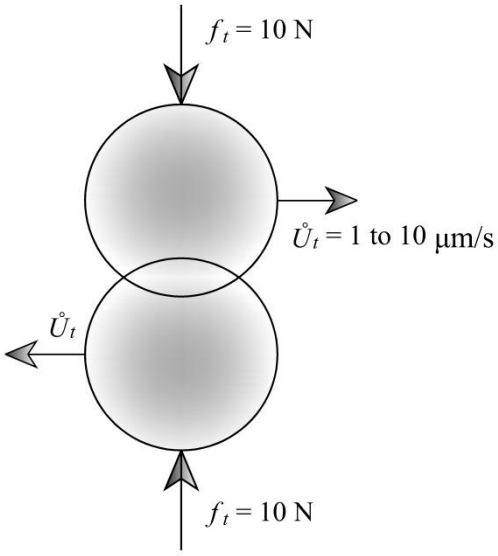

Fig. 6-6. Particle assembly formed by two uniform spheres.

The variation of the ratio f_t/f_n with respect to the tangential indentation (U_t) is shown in Fig. 6-7. Both methodologies seem to reach similar results during the simulation, with values of f_t/f_n ranging from 0.64 to 0.72 for the range of velocities considered. However, the results are quite different once the particles are stopped. Fig. 6-8 gives the variation of ratio f_t/f_n with respect to time for the last 100 seconds of the simulation, when the particles are stopped and the value of $\dot{U}_t$ is kept equal to 0. While results from Eq. 99 (rate-dependent frictional slider) give a sudden decrease in the magnitude of f_t/f_n ($f_t/f_n=0$ for $\dot{U}_t=0$), the methodology described in Section 6.3.1 (sinh-type dashpot) shows a smooth decrease of f_t/f_n over time, which is caused by the time-dependent dissipation of the elastic energy stored in the stiffness component of the contact mechanism.

It is expected that, similar to the behavior observed for the particle assembly shown in Fig. 6-6, DEM models of creep run using more complex particle assemblies would predict different macroscopic behaviors according to the methodology selected to incorporate the RPT in the contact mechanism. Results from DEM simulations will be compared with results presented by Kwok (2008) in Chapter 7.

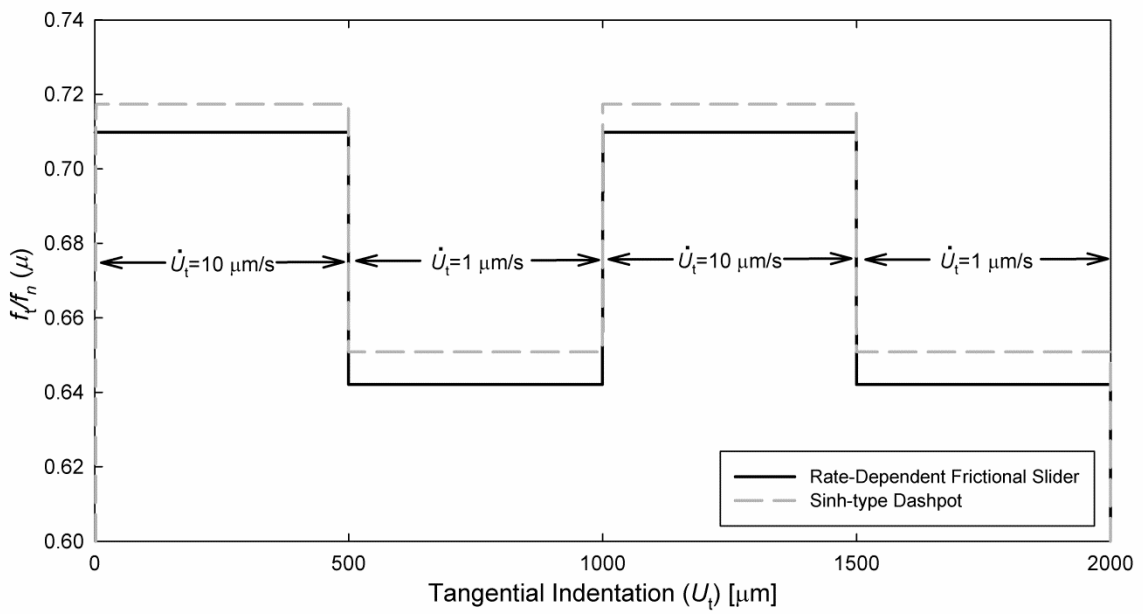

Fig. 6-7. Variation of f_t/f_n with respect to the tangential indentation.

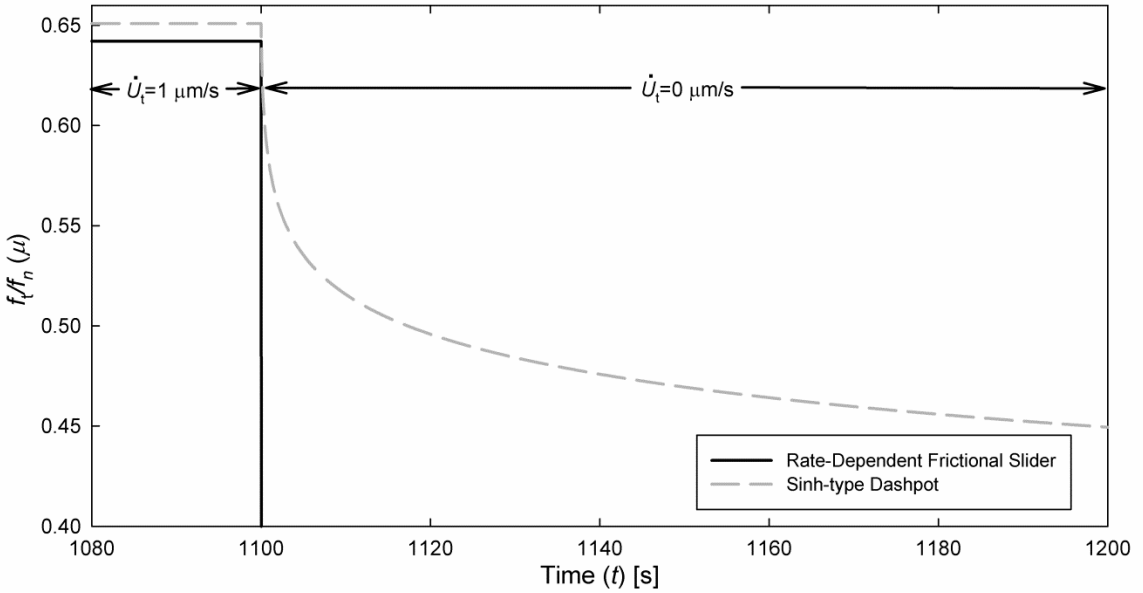

Fig. 6-8. Variation of f_t/f_n with respect to time during the last 100 seconds of the simulation ($\dot{U}_t$=0).

6.6 Conclusions

DEM simulations often assume pseudo static conditions, where the true dynamic response of a granular assembly is neglected. In order to model rate-dependent soil properties, DEM simulations must incorporate a mechanism to simulate time-dependent

particle interactions. That can be achieved by implementing the theory of rate processes, developed by Eyring (1935), to describe the relative displacement of particles in contact.

The rate process theory has been used to estimate the stress-strain-time relationship during creep of clays (Mitchell et al. 1968; Mitchell et al. 1969). The RPT has also been implemented to model time-dependent particle interactions during DEM simulations; e.g., Kuhn (Kuhn 1987), Kwok (2008). Two different methodologies to incorporate the RPT into the contact mechanism during DEM simulations were discussed. Each methodology gives a different description of the particle interactions. Results from DEM simulations conducted using Kuhn's methodology will be compared with results presented by Kwok (2008) in the following sections.

This investigation will incorporate the RPT to model aging in granular materials. DEM simulations will use the Hertz-Mindlin CM and 3D assemblies formed by particles of different geometries. The simulation process and the analysis of the results are presented in the next chapter.

Chapter 7

DEM Analysis of Creep and Aging in Sands

7.1 Introduction

The previous chapters introduced the concept of DEM and its implementation to model granular materials based on the analysis of the interaction between particles. Chapter 6 discussed a methodology developed to model time-dependent processes using DEM by the incorporation of a new contact mechanism which describes rate-dependent particle interactions. This chapter presents the results from DEM simulations of creep and aging in sands conducted using PFC2D and PFC3D and implementing the contact model described.

The first section of the chapter focuses on the calibration of the model, the estimation of the simulation parameters, and the creation of particle assemblies that resemble the granular materials used during the laboratory experiments conducted during

this investigation and described in Chapter 4. Results from DEM simulations, and their implication to the study of aging in granular soils, will be also discussed.

7.2 Preliminary 2D Simulations

Preliminary DEM simulations were conducted using the software PFC2D and assemblies formed of cylindrical rods. The purpose of the 2D models is to provide an initial estimation of the magnitude of parameters required during creep and aging simulations using DEM. Using 2D assemblies for the initial calibration of the model offers several advantages over the implementation of 3D assemblies. In particular, 2D assemblies require fewer calculations per cycle, thus reducing the execution time. However, the packing configuration in assemblies of rods differs from the packing which can be achieved using three-dimensional irregular grains. Therefore, values of void ratio calculated for 2D assemblies are not comparable to magnitudes commonly observed in sands. Additionally, the interaction between rods is different than for grains because the rods can only move in one plane. 3D assemblies will be used later to obtained DEM simulations that can resemble better the behavior of specimens of sand.

7.2.1 2D Particle Assembly

The initial DEM simulations were conducted using an assembly formed by 2094 cylindrical rods with diameters ranging from 3.0 to 5.0 mm, and an initial planar void ratio of 0.14. The particle assembly is shown in Fig. 7-1. Particle properties were selected to resemble Silica sand, and are shown in Table 7-1. The Hertz-Mindlin contact mechanism with the incorporation of the Rate Process Theory equation (Eq. 79) was used to model rate-dependent particle interactions.

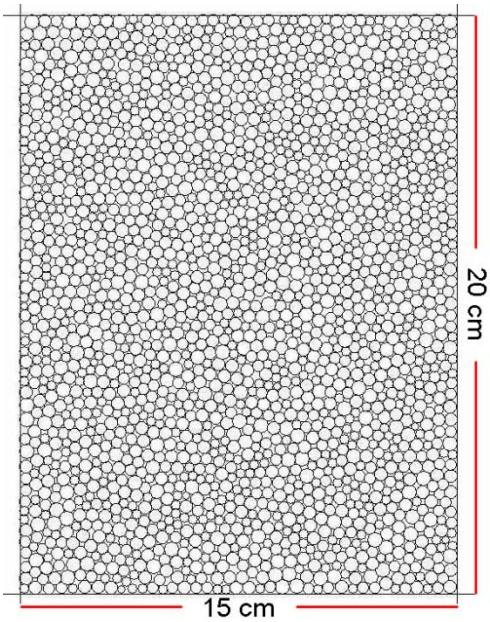

Fig. 7-1. 2D cylindrical rod assembly used during preliminary creep DEM simulations.

Table 7-1. Particle properties and time step for DEM biaxial tests.

Property	**Value**
Shear Modulus (G)	30 GPa
Poisson Ratio (v)	0.18
Specific gravity (G_s)	2.64
Time step (Δt)	1.0E-7 s

7.2.2 Parameters of the RPT Equation

The parameters of the RPT equation were described in Chapter 6. That chapter also presents values for each parameter estimated by different investigators. This section reports the effect that each parameter has on the results from DEM creep simulations during biaxial compression of the assembly shown in Fig. 7-1. A 2D assembly is used instead of a 3D particle arrangement because 2D simulations require a shorter time for execution. Running a parametric study using 3D assemblies would be very time consuming.

Changes in the stress-strain relationship of the assembly during shear caused by variations in the magnitude of the RPT parameters are studied to verify if the new contact mechanism is suitable to model the macroscopic behavior of an assembly during a simple simulation. Results from biaxial test simulations conducted using the RPT contact mechanism are compared with results obtained from simulations run with a contact mechanism which uses the Mohr-Coulomb failure model to determine particle interactions (i.e., standard CM). Even though DEM simulations run using the Mohr-Coulomb failure model do not necessarily give the correct stress-strain relationship, they provide a reasonable estimation of the macroscopic behavior of the assembly during shear.

There are four variables in the RPT equation which need to be estimated: temperature (T), activation energy (ΔF), distance between equilibrium positions (λ), and the number of bonds at the particle contact per unit force (n_1). Each parameter is analyzed next.

7.2.2.1 Distance between Equilibrium Positions [λ]

The parameter λ can be assumed as 2.8 Å, which corresponds to the distance between atomic valleys in a silicate mineral surface (see Section 6.4.1). Because this parameter is not expected to change significantly for the materials under study (natural occurring sands), its effect on the simulation results will not be considered in this analysis.

7.2.2.2 Activation Energy [ΔF]

The value of activation energy has a relatively small range of variation. Magnitudes of ΔF shown in Table 6-1 for clay and sand range from about 105 to 165 kJ·mol^{-1} (25 to 40 kcal·mol^{-1}). The effect of changes in the magnitude of ΔF on results from DEM plane strain biaxial test simulations conducted using the assembly described in Section 7.2.1 is studied next.

DEM biaxial test simulations were conducted using the following procedure: (1) the assembly is created and allowed to reach internal equilibrium; (2) a small isotropic confining stress of 50 kPa is applied to the assembly; (3) the RPT contact mechanism is activated and the isotropic external stress is increased to 400kPa; (4) the assembly is sheared by the application of a deviator stress. The assembly is sheared using a constant rate of strain of 20 s^{-1} to reduce the execution time. Preliminary values for the RPT parameters were based on the magnitudes used by Kuhn (1987) , and are presented in Table 7-2.

Table 7-2. RPT parameters used for preliminary 2D creep simulations.

Property	**Value**
Bonds per unit force (n_1)	5.0E8 bonds/N
Distance between equilibrium positions (λ)	2.8 Å
Temperature (T)	20°C
Activation Energy (ΔF)	25 to 45 kcal·mol^{-1}

Results showing the variation in principal stress ratio and volumetric strain with axial strain during shear are shown in Fig. 7-2. The figure also includes results from a DEM biaxial simulation run without the incorporation of the RPT equation and using a particle-to-particle friction coefficient of 0.4 (ϕ_μ=22°). Results show that the magnitude

of ΔF affects the macroscopic strength of the assembly. The value of PSR_{max} increases with increasing ΔF.

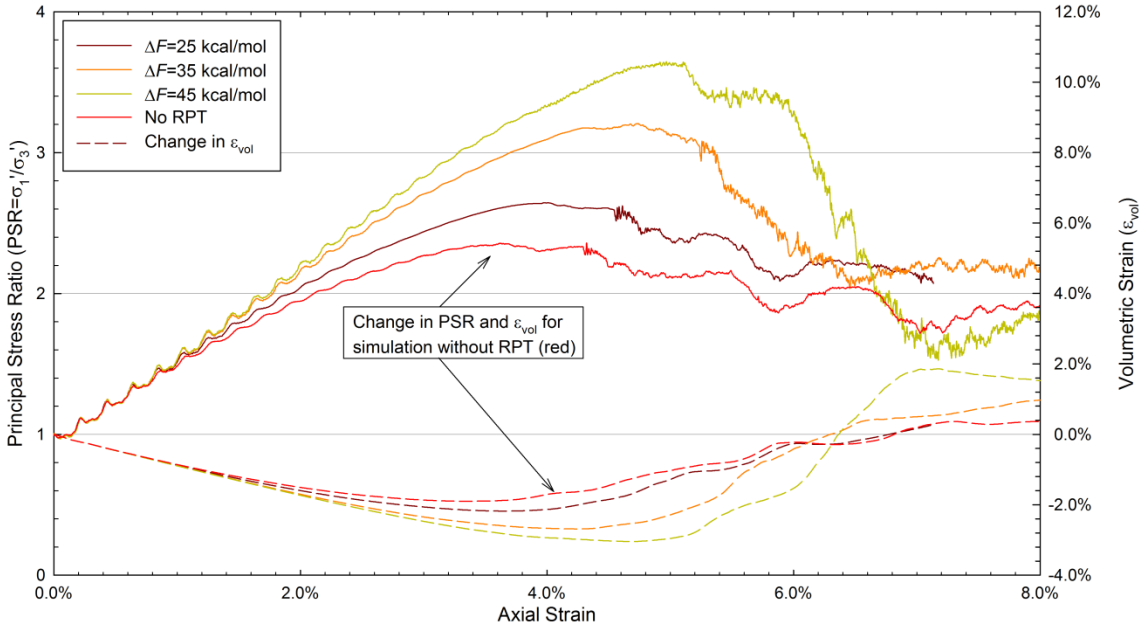

Fig. 7-2. Change in principal stress ratio and volumetric strain with axial strain during DEM simulation of biaxial compression. Effect of changes in the magnitude of ΔF on the principal stress ratio and volumetric strain as a function of axial strain.

The ratio of the normal to tangential contact forces, which is controlled by the frictional slider (i.e., Mohr-Coulomb failure mechanism) in standard DEM simulations, depends on the magnitude selected for the parameters ΔF, λ, and n_1. Hence, the value of the parameters of the RPT equation should produce a similar macroscopic behavior during shear as does a DEM model with the standard CM, which uses a frictional slider rather than a sinh-type dashpot, with the particle-to-particle friction angle of quartz. According to Fig. 7-2, smaller values of ΔF are in better agreement with results obtained using the Hertz-Mindlin contact mechanism with the frictional slider (shown in red in Fig. 7-2).

The value of ΔF also affects the results of DEM creep simulations conducted on the assembly shown in Fig. 7-1 under constant anisotropic confining stress (σ'_1=600kPa, σ'_3=400kPa). The variations in axial strain and axial strain rate with time during creep obtained from DEM simulations conducted using different values of ΔF are shown in Fig. 7-3 and Fig. 7-4. The figures show that the axial strain and axial strain rate increase, and the time to creep failure decreases, with decreasing ΔF.

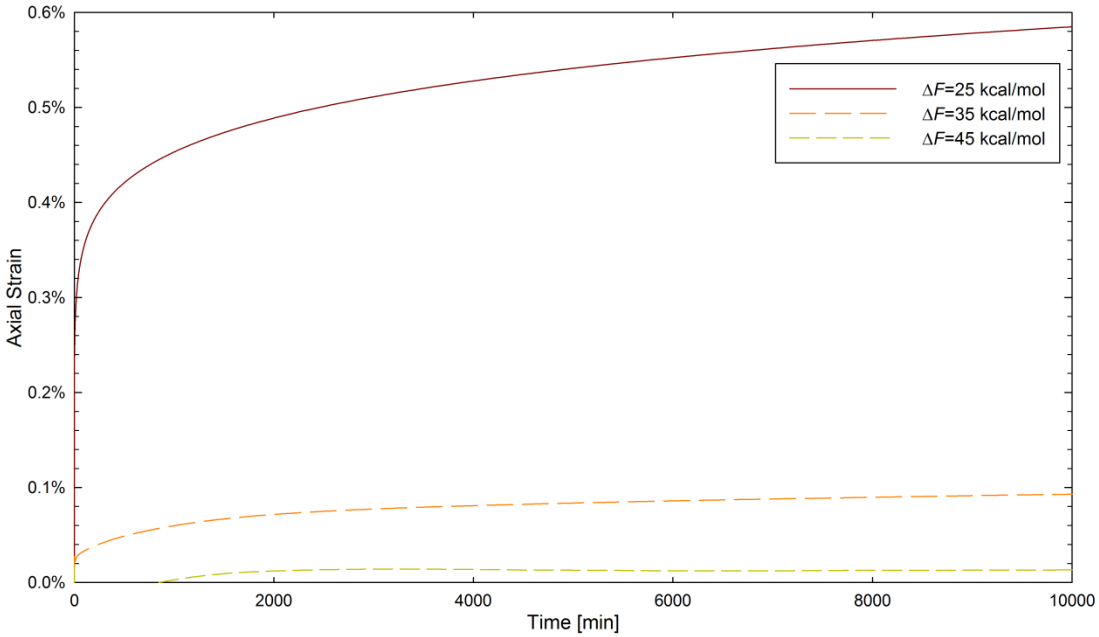

Fig. 7-3. Change in axial strain with time during creep. Effect of changes in the magnitude of ΔF on the axial strain as a function of time.

7.2.2.3 Number of inter-particle contacts [n_1]

The magnitude of the parameter n_1 is perhaps the most complex of the RPT parameters to determine. Kuhn used a value of around 1.0E9 bonds/N to model creep in clays using DEM. According to Mitchell et al. (1969), the value of the parameter S_1, which is related to n_1 (see Section 6.4.3), should be similar for clays and sands.

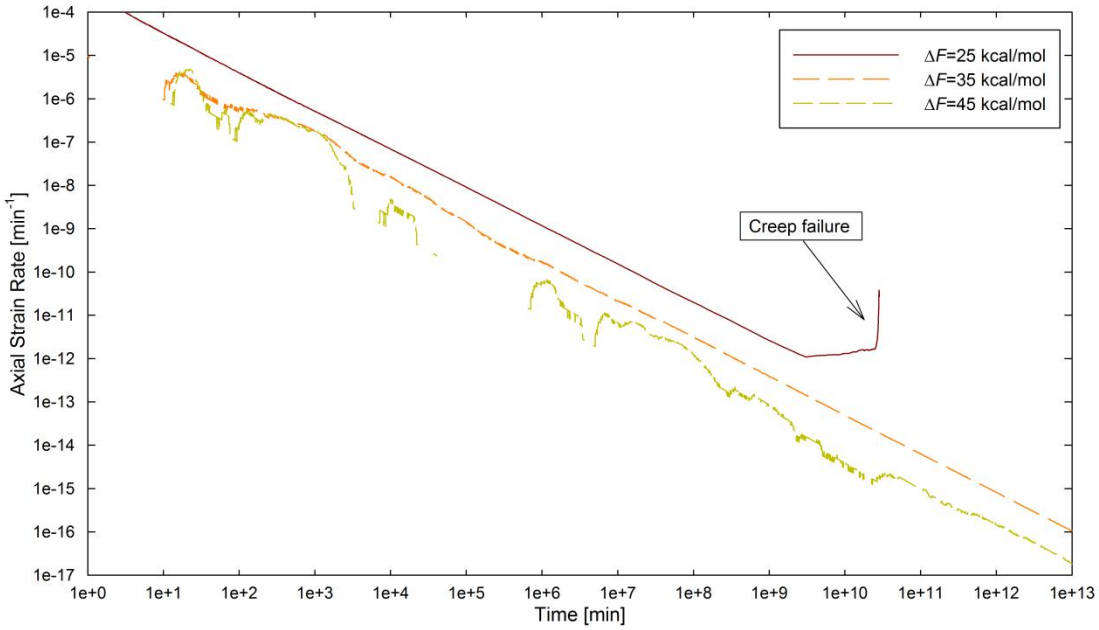

Fig. 7-4. Change in axial strain rate with time during creep. Effect of changes in the magnitude of ΔF on the axial strain rate as a function of time.

For this investigation, values of n_1 ranging from 1.0E8 to 1.0E9 bonds/N were considered. The selection of the magnitude of n_1 was based on the level of agreement between results from DEM biaxial test simulations conducted using the RPT contact mechanism and a standard contact mechanism with a frictional slider and a particle-to-particle friction coefficient similar to quartz sand (about 0.4).

DEM biaxial test simulations were conducted using the same procedure described in Section 7.2.2.2 and different values of n_1. A magnitude of 25 kcal·mol^{-1} for ΔF, which is the same magnitude used by Kuhn (1987), was selected for the model. Results from the simulations, showing the variation in principal stress ratio and volumetric strain during shear, are shown in Fig. 7-5.

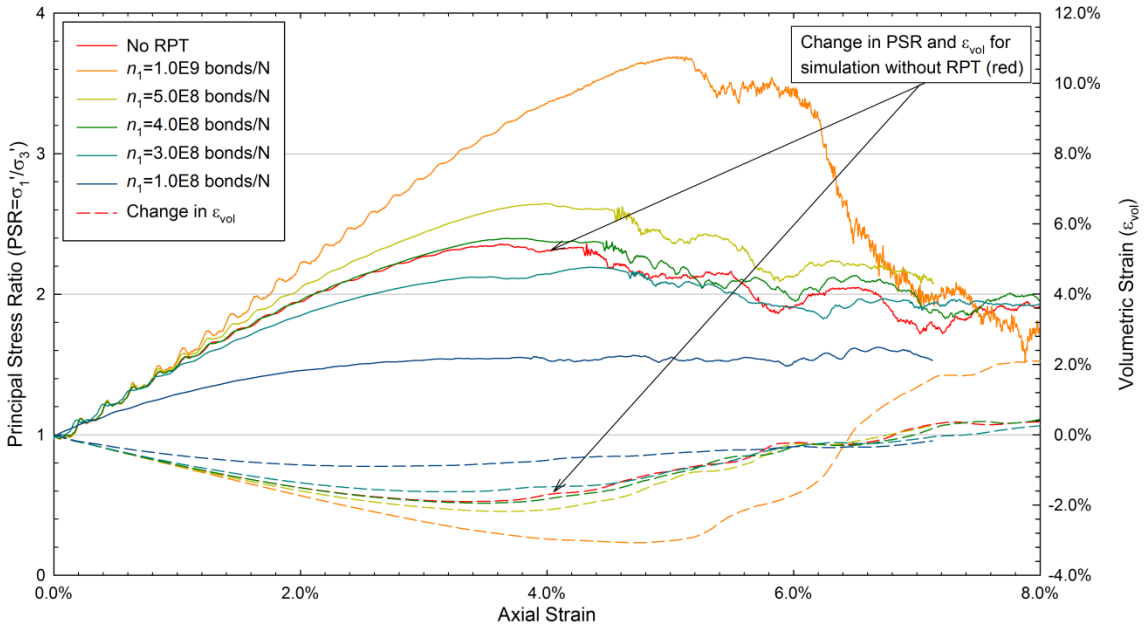

Fig. 7-5. Change in principal stress ratio and volumetric strain with axial strain during DEM simulation of biaxial compression. Effect of changes in the magnitude of n_1 on the principal stress ratio and volumetric strain as a function of axial strain.

According to the figure, the macroscopic strength of the assembly increases with an increasing magnitude of n_1. The figure also indicates that a value of n_1 of 4.0E8 bonds/N combined with a value of ΔF of 25 kcal·mol^{-1} reproduces a similar macroscopic stress-strain relationship during shear as does a simulation conducted without incorporating the RPT equation and using a particle-to-particle friction coefficient of 0.4. These values (n_1=4.0E8 bonds/N and ΔF=25 kcal·mol^{-1}) were selected for the RPT parameters during the 3D simulations described in following sections.

The effect of the magnitude of n_1 on DEM creep models was studied by conducting multiple simulations using values of n_1 ranging from 1.0E8 to 1.0E9 bonds/N. Results showing the variation in axial deformation and axial strain rate with time during creep under constant anisotropic confining stress (σ'_1=600kPa, σ'_3=400kPa) are shown in Fig. 7-6 and Fig. 7-7.

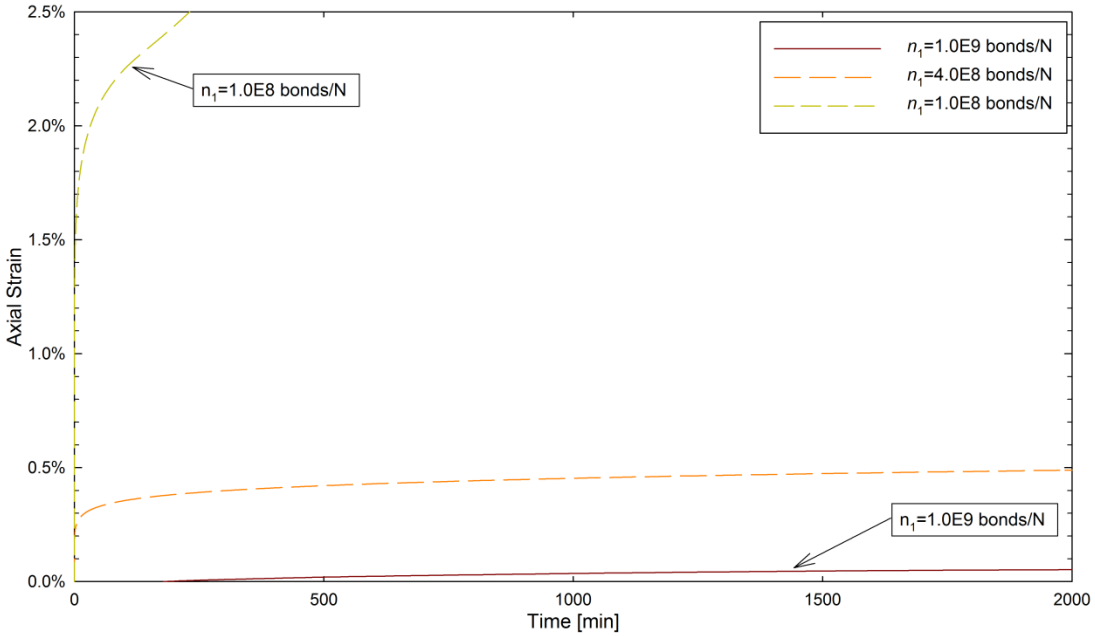

Fig. 7-6. Change in axial strain with time during creep. Effect of changes in the magnitude of n_1 on the axial strain as a function of time.

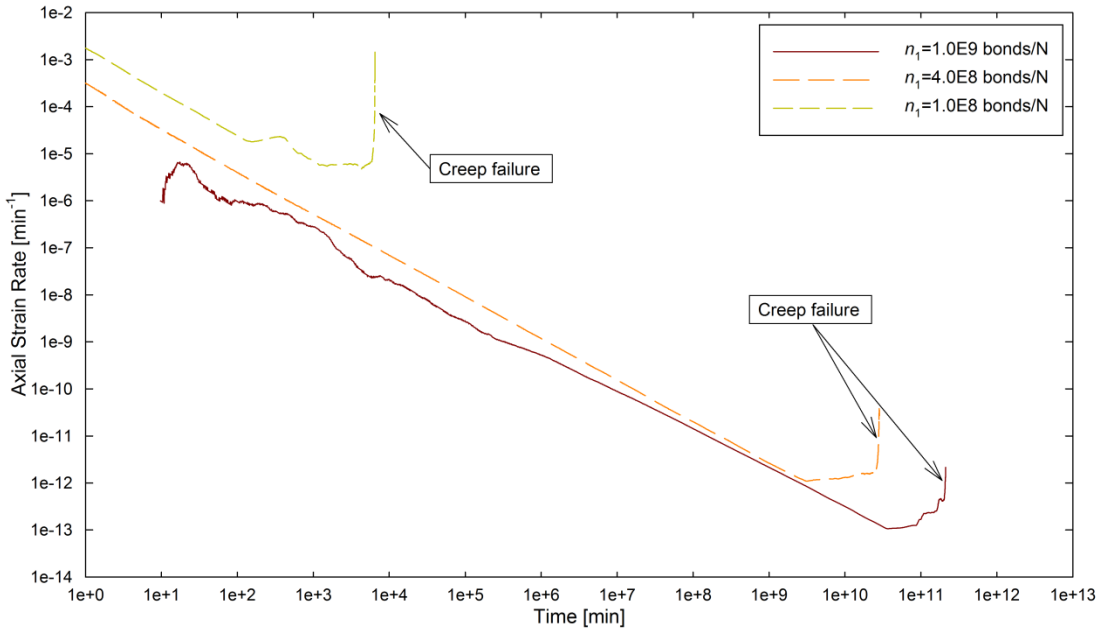

Fig. 7-7. Change in axial strain rate with time during creep. Effect of changes in the magnitude of n_1 on the axial strain rate as a function of time.

The figures show that the axial strain and axial strain rate increase, and the time to creep failure decreases, with decreasing n_1. These changes are similar to the changes observed due to variations in the value of ΔF, described in the previous section.

7.2.2.4 Temperature [*T*]

Even though the magnitude of *T* of temperature is readily determined, the effect that it has on DEM creep simulations conducted using the RPT equation can provide initial evidence of the adequacy of the newly developed contact mechanism to simulate creep processes in granular materials. According to the RPT theory, higher temperatures cause an increase in the thermal vibration of the material, making the particle contacts become more "active."

Results from DEM biaxial test simulation run using values of temperature ranging from 283ºK to 323ºK (i.e., 10ºC to 50ºC) are shown in Fig. 7-8. The figure shows the variation in principal stress ratio and volumetric strain during shear. Note that changes in temperature produce only small variations in the stress-strain relationship, with a small increase in PSR_{max} and macroscopic stiffness with decreasing temperature.

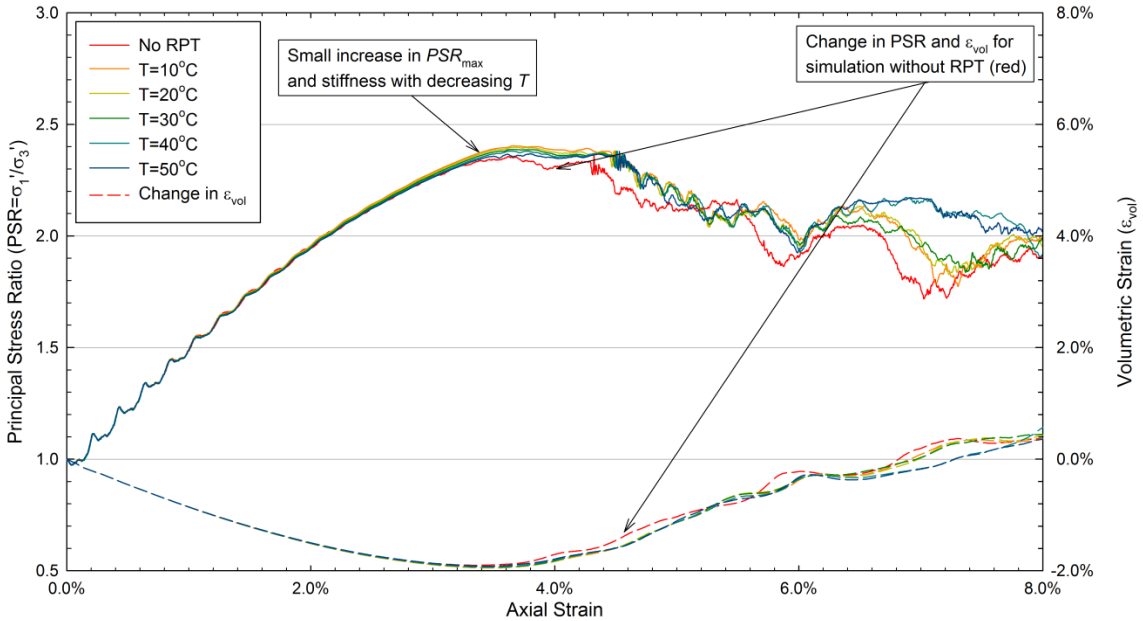

Fig. 7-8. Change in principal stress ratio and volumetric strain with axial strain during DEM simulation of biaxial compression. Effect of changes in the magnitude of *T* on the principal stress ratio and volumetric strain as a function of axial strain.

The effect of the magnitude of T on DEM creep simulations was also studied. DEM simulations of creep under constant anisotropic confining stress (σ'_1=600kPa, σ'_3=400kPa) were conducted using values of T ranging from 10 to 50°C. Magnitudes of 25 kcal·mol^{-1} and 4.0E8 bonds/N were assigned to the parameters ΔF and n_1. The variation in axial deformation and axial strain rate with time during creep calculated based on the results from DEM simulations is shown in Fig. 7-9 and Fig. 7-10.

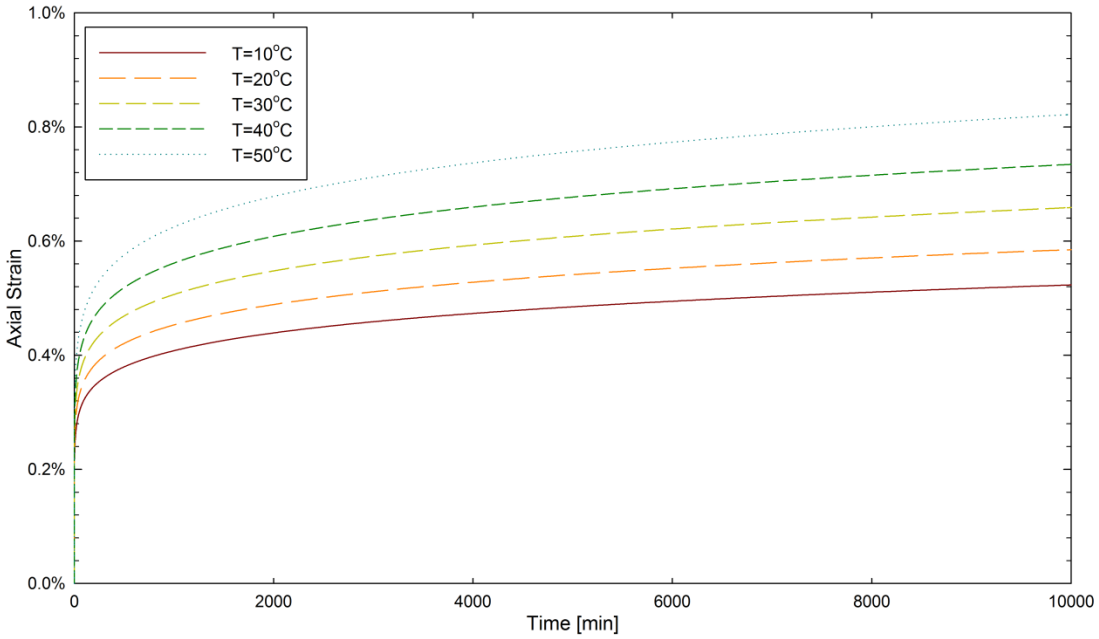

Fig. 7-9. Change in axial strain with time during creep. Effect of changes in the magnitude of T on the axial strain as a function of time.

The figures show that the temperature has a significant effect on the DEM creep simulations. Higher temperatures cause an increase in axial deformation and axial strain rate during creep, and shorter times to creep failure. Note that the magnitude of T seems to have a greater effect on the result of DEM simulations when the particle move at slower velocities (e.g., during the creep stage as opposed to during shear).

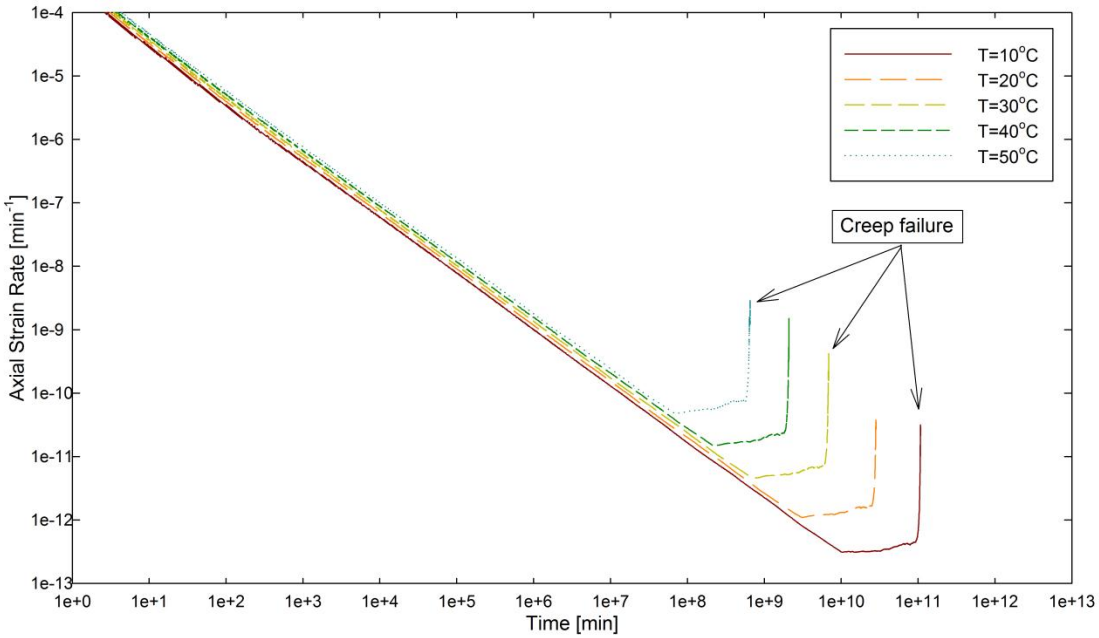

Fig. 7-10. Change in axial strain rate with time during creep. Effect of changes in the magnitude of T on the axial strain rate as a function of time.

The effect of the magnitude of T on the DEM creep simulations conducted using the RPT equation agrees with results from laboratory experiments reported by several investigators. Murayama (1969) (cited by Mitchell and Soga, 2005) reported an increase in creep deformation with increasing temperature during undrained triaxial compression of Osaka clay. Mitchell and Soga (2005) noted that an increase in temperature weakens the soil structure and increases the rate of deformation during creep.

7.2.3 Results from 2D Creep Simulations

Preliminary creep simulations were conducted using the 2D assembly shown in Fig. 7-1. Particle properties used are shown in Table 7-1. The magnitudes assigned to the parameters of the RPT equation are presented in Table 7-3. During the simulation, an anisotropic stress was applied and the assembly was allowed to creep under drained conditions and constant confining stress.

Table 7-3. RPT parameters used for preliminary 2D creep simulations

Property	**Value**
Bonds per unit force (n_1)	4.0E8 bonds/N
Distance between equilibrium positions (λ)	2.8 Å
Temperature (T)	20°C
Activation Energy (ΔF)	25 kcal·mol^{-1}

Four simulations were performed, each using the same horizontal (σ_h=σ_3=400 kPa) and different vertical confining stresses (σ_v=σ_1=600, 720, 800, and 880 kPa). Results showing the variation in axial strain and axial strain rate with time during creep are shown in Fig. 7-11 and Fig. 7-12. The figures show a characteristic relationship between the strain rate and the time during creep. At any stress level, the logarithm of the axial strain rate decreases linearly with respect to the logarithm of time, and the slope of this relationship is independent of the magnitude of stress level during creep. Increasing the stress level causes an increase in the axial strain and axial strain rate during creep, and reduces the time to creep failure. Fig. 7-13 shows the strain rate as a function of the stress level at different times of creep. At low stress levels the rates of deformation are very low, but the rates increase for greater stress levels. These observations agree with behavioral characteristics of clays during creep described by Mitchell and Soga (2005).

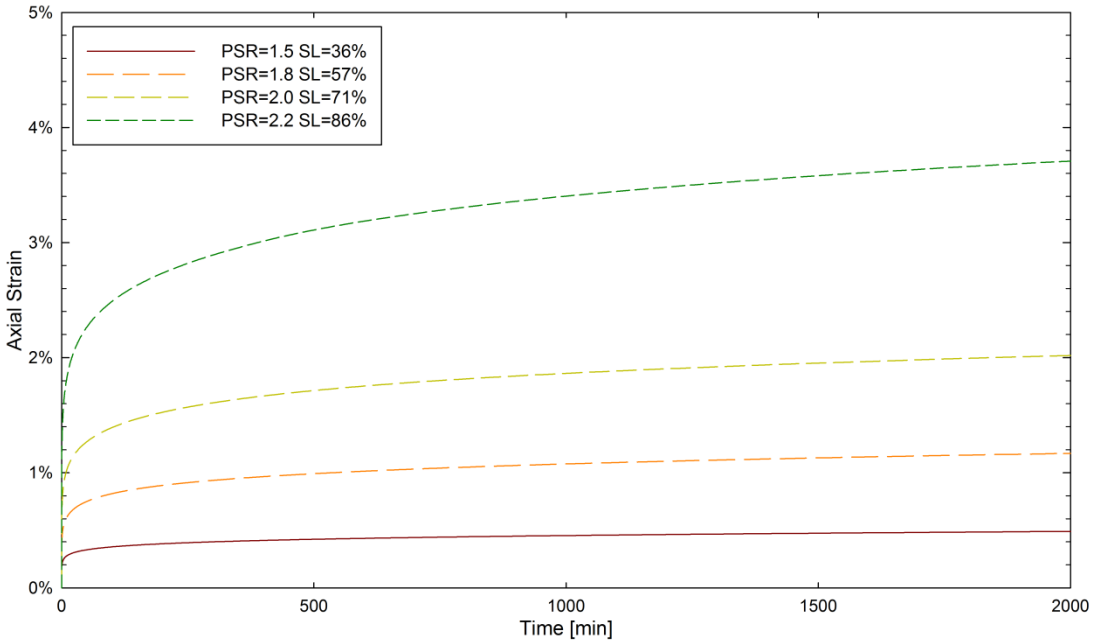

Fig. 7-11. Change in axial strain with time during creep. Effect of the magnitude of principal stress ratio (σ'_1/σ'_3) during creep (σ'_3=400 kPa).

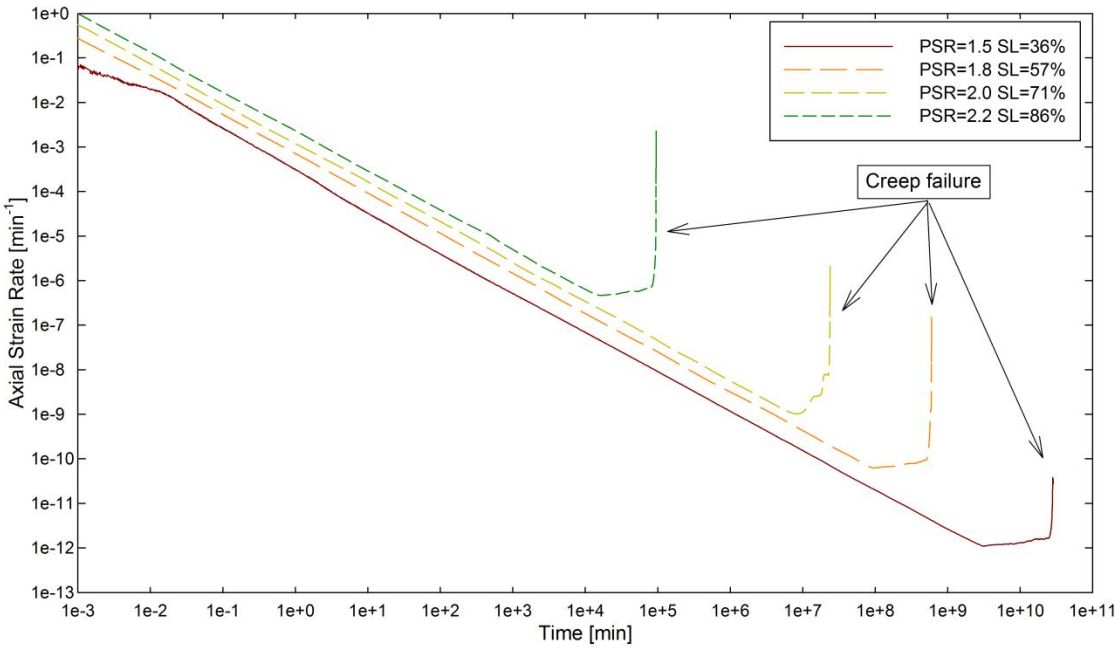

Fig. 7-12. Change in axial strain rate with time during creep. Effect of the magnitude of principal stress ratio (σ'_1/σ'_3) during creep (σ'_3=400 kPa).

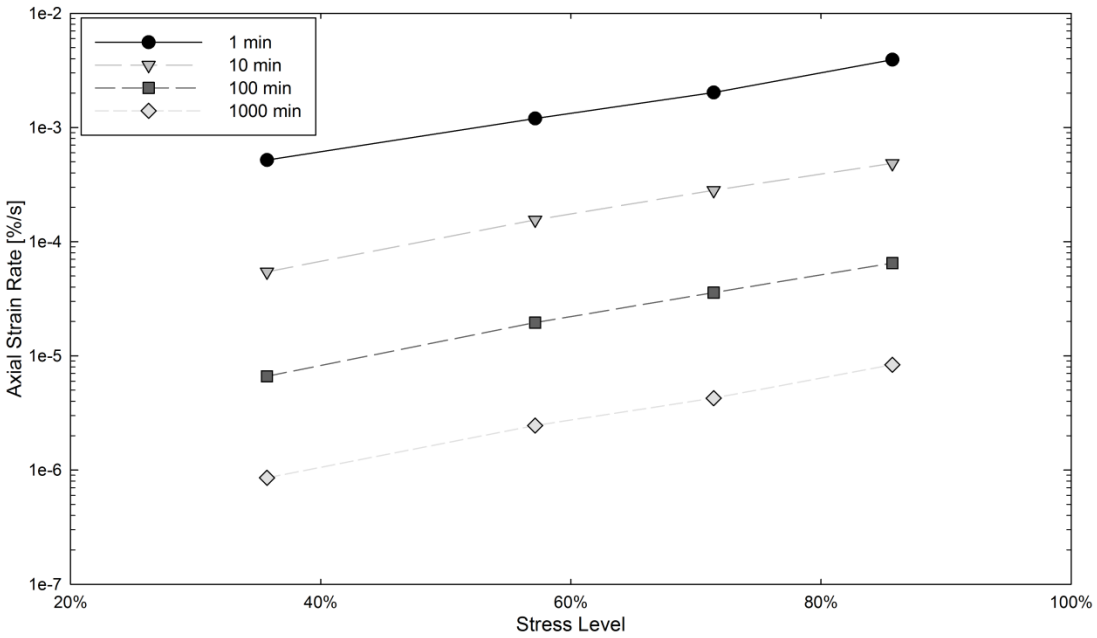

Fig. 7-13. Variation of axial strain rate during creep with stress level.

DEM creep simulations incorporating the RPT equation to describe particle interactions produce a macroscopic assembly behavior that resembles the results from laboratory creep experiments. However, the characteristics of the assembly used in the simulations differ from the characteristics of real sands, particularly in the shape and dimension of the particles. 3D assemblies will be used in the following section to provide a better representation of changes occurring to the internal structure of specimens of sand during creep.

7.3 Analysis of Creep in Granular Materials using 3D DEM

DEM simulations using 3D assemblies were conducted to obtain a better representation of changes to the internal structure of granular materials taking place during aging and creep. A total of five particle assemblies were created. Each assembly intends to represent properties of the specimens used during the laboratory experiments

described in Chapter 4. Some characteristics of the specimens targeted during the creation of DEM assemblies are shown in Table 7-4.

Table 7-4. Properties of specimens targeted during DEM assembly creation.

Material	D_r	$e_{initial}$	d_{90} **[mm]**	d_{10} **[mm]**
Silica sand	80% (Dense)	0.60	1.1	0.41
	30% (Loose)	0.73		
Filter sand	80% (Dense)	0.73	0.90	0.31
	30% (Loose)	0.84		
Glass beads	40%	0.62	0.82	0.41

Additional characteristics of the materials, including the particle sphericity and strength, were also taken into consideration when creating the 3D particle arrangements.

7.3.1 Creation of Particle Assemblies

Particle arrangements were generated using a procedure which involved creating a loose assembly, increasing the diameter of the particles, and later allowing the assembly to reach internal equilibrium. A typical example is shown in Fig. 7-14. This process reduces the time needed create the assemblies because it does not require displacing the boundaries of the particle arrangement.

First, a loose particle configuration formed by spheres with diameters ranging from $0.56 \cdot d_{10}$ to $0.56 \cdot d_{90}$ was created inside an 8.75 mm high and 5 mm diameter cylindrical container. The diameter of the spheres is randomly distributed between the maximum and the minimum values selected; i.e. any particle diameter within the range defined has the same probability of occurrence. The limits of the assembly were defined using rigid boundaries (see Section 5.2.2). The magnitudes of d_{90} and d_{10} depend on the material being modeled, and are shown in Table 7-4. Material properties of the particles

are those of silica sand and are shown in Table 7-5 along with other parameters used during simulation. Note that the assembly was sheared at a fast rate of strain to reduce the execution time of the simulations. A typical example of an initial loose particle configuration is shown in Fig. 7-14(a).

Table 7-5. Particle properties and simulation parameters for 3D DEM simulations.

Property	**Value**
Shear Modulus (G)	30 GPa
Poisson Ratio (v)	0.18
Density (ρ)	2400 g/cm^3
Friction Coefficient (μ)	0.5
Viscosity coefficient (α)	0.9
Vertical Strain Rate ($\dot{\varepsilon}$)	10%/s
Time step (Δt)	1.0E-8 s

Once the initial assembly is generated, particle diameters are increased by 80% (see Fig. 7-14 b). The sudden increase in diameter produces large particle indentations and a corresponding increase in the magnitude of out-of-balance forces. In order to reduce the magnitude of the out-of-balance forces, the assembly is allowed to reach internal equilibrium (i.e., out-of-balance forces tend towards 0) by running numerous calculation cycles with zero boundary movements. The resulting assembly configuration is shown in Fig. 7-14(c).

After the assembly is in equilibrium, the sphericity of the materials is introduced into the model by replacing the spherical particles with particle *clumps*. Particle clumps are formed by multiple particles joined together using rigid bonds. Clumps are allowed to move during the simulations. However, the relative position of the individual particles within the clump with respect to each other does not change as the simulation progresses.

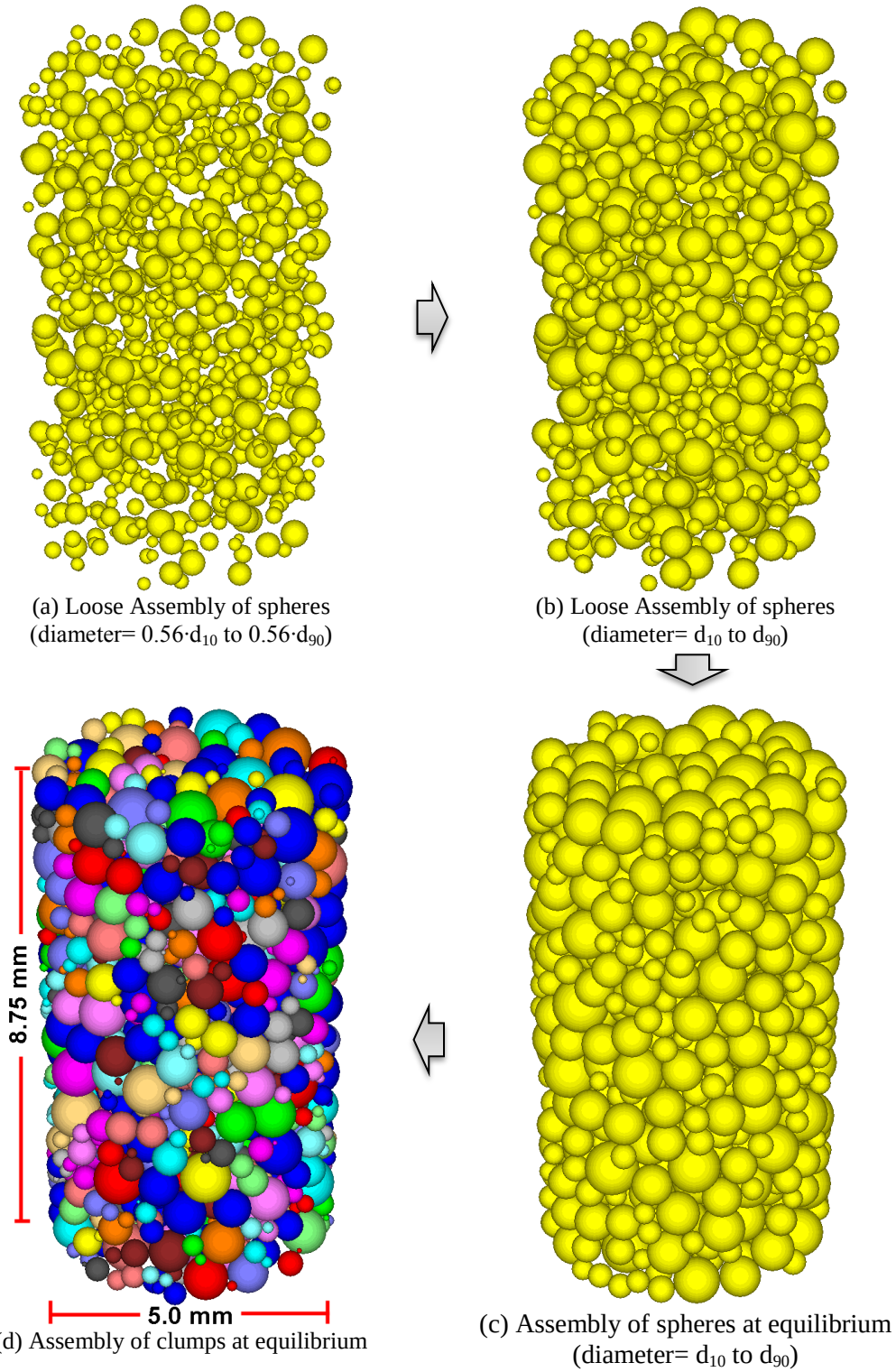

(a) Loose Assembly of spheres (diameter= $0.56 \cdot d_{10}$ to $0.56 \cdot d_{90}$)

(b) Loose Assembly of spheres (diameter= d_{10} to d_{90})

(c) Assembly of spheres at equilibrium (diameter= d_{10} to d_{90})

(d) Assembly of clumps at equilibrium

Fig. 7-14. Process used to generate particle assemblies.

Clumps formed by two particles were used for the simulations presented in this chapter. Even though clumps formed using more particles may describe better the

irregular geometry of sand grains, they also cause an important increase in the time required to run the simulations. Fig. 7-14(d) shows a particle assembly formed by 2-particle clumps. Spheres that belong to the same clump have the same color in the figure.

7.3.1.1 Sphericity

The sphericity (a measure of how round an object is) of the material is introduced into the model by controlling the diameter of the particles forming each of the clumps. Two examples are shown in Fig. 7-15, corresponding to sand grains with maximum to minimum diameter ratio (D_{max}/D_{min}) of 2.0 and 1.2. A grain with maximum to minimum diameter ratio of 2.0 is modeled using a clump formed by two spheres with the same diameter (D), while a sand grain with D_{max}/D_{min} equal to 1.2 is modeled using a clump formed by a sphere of diameter D bonded to another sphere of diameter $0.2 \cdot D$.

Because it is not possible to model the shape of each sand grain of a specimen individually, the sphericity of the material is introduced into the model using the Box-Muller transform, which is a pseudo-random sampling method based on a normal distribution (Box and Muller 1958). Before introducing the sphericity of the material into the model, particle diameters followed a random distribution where all the magnitudes have the same probability of occurrence. The Box-Muller transform allows introducing a normal distribution to the sphericity of the particles, where more particles have maximum-to-minimum diameter ratio closer the average of the material, and fewer particle have a more elongated or spherical shape.

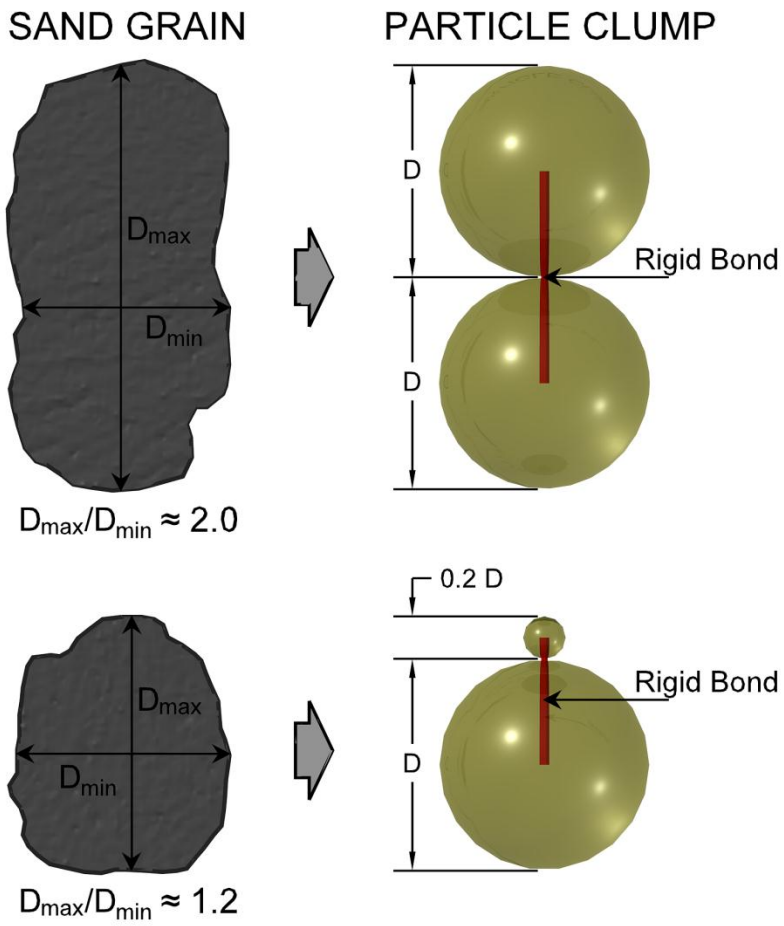

Fig. 7-15. Modeling grain sphericity using particle clumps.

According to the Box-Muller methodology, if U_1 and U_2 are two independent random variables on the interval (0, 1), then X_1 and X_2, which are defined as:

$$X_1 = \sqrt{-2\ln(U_1)}\cos(2\pi U_2) \tag{100}$$

$$X_2 = \sqrt{-2\ln(U_1)}\sin(2\pi U_2) \tag{101}$$

are two independent random variables from a normal distribution with mean zero and unit variance. A more detailed explanation of this methodology can be found in Box and Muller (1958).

The variables X_1 and X_2 can be transformed into two random variables, Y_1 and Y_2, from a normal distribution with mean $\bar{x}$ and standard deviation σ as follows:

$$Y_1 = X_1 \cdot \sigma + \bar{x} \tag{102}$$

$$Y_2 = X_2 \cdot \sigma + \bar{x} \tag{103}$$

The sphericity of the materials is incorporated into the model using Eqs. 100 to 103 and the values of the mean and standard deviation of D_{max}/D_{min} shown in Table 4-7. The result is an assembly formed by particles with a sphericity that follows a normal distribution and resembles the real material. The procedure used is summarized below

- One spherical particle in the assembly is selected. Its volume (V) and location (x, y, z) are calculated.
- The spherical particle is deleted from the assembly.
- A random variable Y_1 from a normal distribution with mean $\bar{x}$ and standard deviation σ (from Table 4-7) is generated using Eqs. 100 to 103.
- A new clump formed by two spherical particles is created. The diameter of the two spheres (D_1 and D_2) is selected such that $(D_1+D_2)/D_1=Y_1$ (where $D_1>D_2$).
- The clump is rotated in the x, y, and z axes by a random amount ranging from 0 to 360°.
- The clump is scaled so its volume matches the volume of the spherical particle deleted.
- The clump is moved such that its centroid (calculated based on the location and mass of its two constituent particles) matches the centroid of the deleted particle.
- The same process is repeated for each spherical particle in the assembly.
- Once all spherical particles are replaced by 2-particle clumps, the assembly is allowed to reach internal equilibrium with zero lateral and vertical macroscopic deformation.

Note that 2-particle clumps can only represent particles with a maximum to minimum diameter ratio less than or equal to 2.0. Note also that as D_{max}/D_{min} tends to 1.0,

D_2, which is the diameter of the smaller sphere, tends towards 0. Chapter 5 explained that the magnitude of the time step (Δt) depends on the size of the smallest particle in the assembly. Consequentially, small values of D_2 require small magnitudes of Δt and a longer execution time. For that reason, it is necessary to truncate the minimum value of D_{max}/D_{min}. For this research the magnitude D_{max}/D_{min} for the 2-particle clumps was allowed to fluctuate between 1.2 and 2.0. The resulting grain size distributions for the particles assemblies generated are shown in Fig. 7-16.

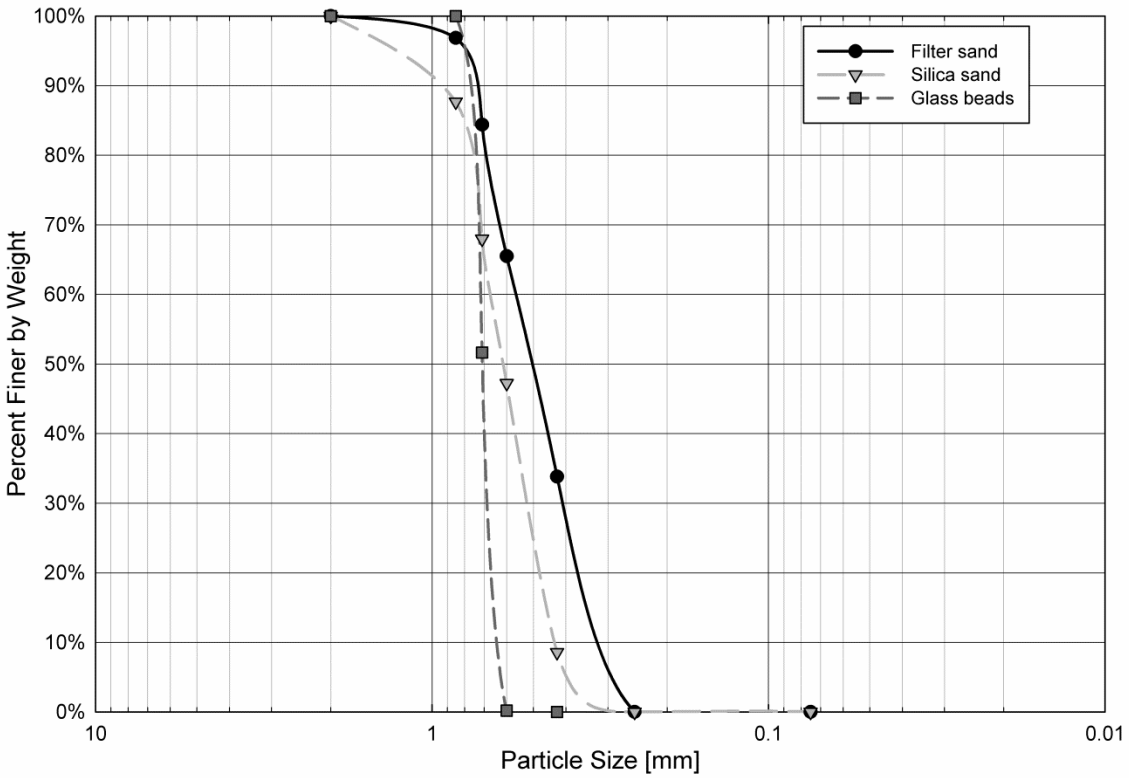

Fig. 7-16. Grain size distribution of particle assemblies used during the simulations.

7.3.1.2 Initial Void Ratio

The initial void ratio of assemblies generated for 3D DEM simulations targeted the values of e_{ini} measured for the specimens used during the macro-scale laboratory experiments presented in Chapter 4 and shown in Table 7-4. Two different procedures were implemented to obtain the desired value of initial void ratio:

- The amount and volume of the spherical particles generated was controlled to achieve the required weight of solids based on the volume of the assembly. This step targeted a value of *e* approximately 30% larger than the desired initial void ratio in order to obtain a looser particle assembly.
- Once the spheres are replaced by 2-particle clumps and the arrangement reaches internal equilibrium, the assembly is "vibrated." Vibrations were generated by fluctuating rapidly the external stress from 150kPa to 300kPa at a frequency of about 800 Hz. A large frequency was implemented to reduce the number of calculation cycles and the execution time of the simulation. The assembly was subjected to continuous vibration until the required initial void ratio was achieved.

7.3.1.3 Particle Crushing

The implementation of 2-particle clumps allows the study of particle crushing during creep and aging. For this analysis, particle crushing is incorporated into the model by assigning an ultimate normal and shear strength to the rigid bond that joins two particles in a clump. The normal (f_n) and shear (f_s) forces at the bond are determined using the out-of-balance forces (**F**) acting on each particle in the. The sum of the out-of-balance forces is subdivided into the forces acting at the bond, which are at equilibrium, and the out-of-balance force of the clump, which is not at equilibrium. An example is shown in Fig. 7-17.

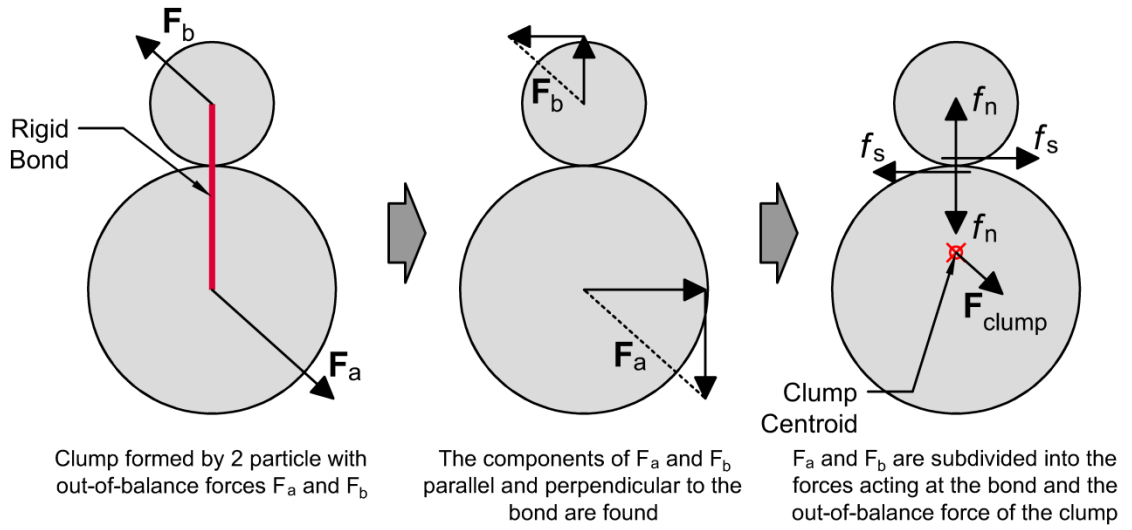

Fig. 7-17. Determination of the normal (f_n) and shear (f_s) force acting at the clump bond

The strength of the grains was estimated using results from crushing tests described in Chapter 4. The crushing load from tests, resembling an unconfined compression experiment, was assigned as the ultimate crushing load for the clumps. The maximum tensile force sustained by the clump before breakage (tensile failure load) was assigned based on observations by Goodman (1989), who compiled values for the ratio of unconfined compressive strength to indirect tensile strength measured for different rocks. Values for rocks such as Dwoeshak Dam gneiss, Baraboo quartzite, Pikes Peak granite, Nevada Test Site granite, Palisades diabase, and John Day basalt that ranged from about 11.3 to 29.1. A value of 20 was selected for this analysis. The values of maximum crushing and tensile failure loads assigned for the clumps during the simulations are shown in Table 7-6.

Table 7-6. Crushing and tensile failure load.

Material	**Crushing load [N]**	**Tensile failure load [N]**
Silica sand	70	3.5
Filter sand	70	3.5
Glass beads	140	7

7.3.1.4 Particle Assemblies

Five particle assemblies were created and used during 3D DEM simulations. Each particle assembly is shown in Table 7-7. The table also includes some of the characteristics of the assemblies and the clumps. Each particle assembly resembles a specimen used during laboratory experiments presented in Chapter 4.

7.3.2 Creep during Triaxial Compression

The initial 3D DEM simulations model creep during a drained triaxial compression experiment. For these simulations creep takes places under constant vertical and horizontal stresses. The procedure used to conduct the creep simulations is described below:

- A small isotropic confining stress of 150 kPa is applied and the assembly is allowed to reach internal equilibrium.
- The contact mechanism which incorporates the RPT equation is activated. This contact model is kept inactive during previous steps to reduce the time required for execution.
- The isotropic confining stress is increased to 300 kPa.
- The assembly is sheared by the application of a vertical deviator stress.
- When a desired principal stress ratio ($PSR=\sigma'_1/\sigma'_3$) is reached, shear is stopped and the vertical (σ'_1) and horizontal (σ'_3) stresses are kept constant. The assembly is allowed to creep under constant stress.
- After creep, the deviator stress is increased and drained triaxial compression continues.

Table 7-7. Particle assemblies used for 3D DEM simulations.

Dense Silica Sand (DSS)	Loose Silica Sand (LSS)	Glass Beads (GB)
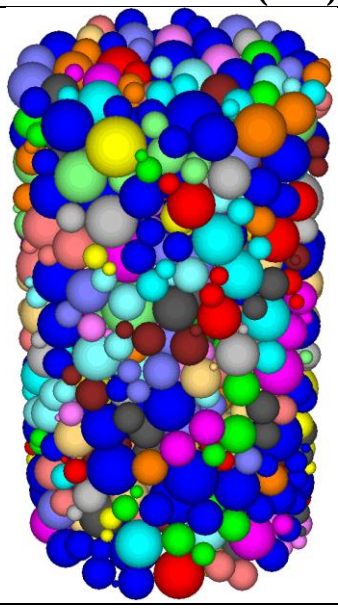	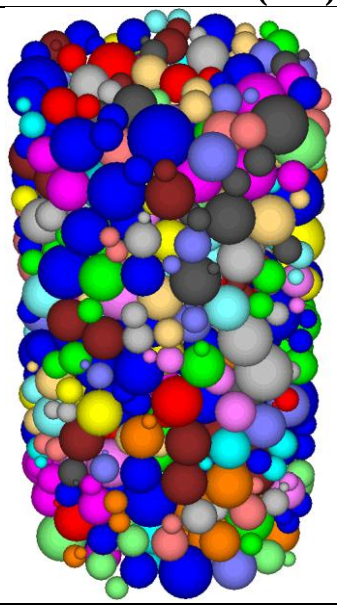	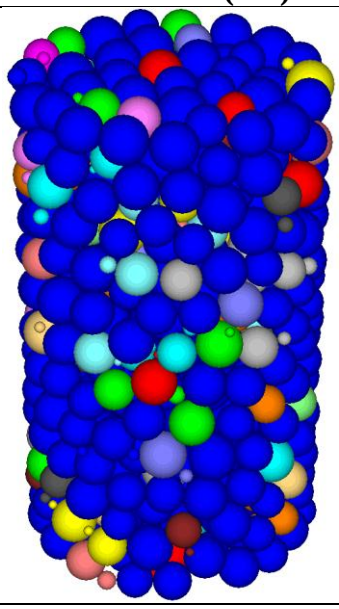
e_{ini} = 0.655 Assembly height = 9.20 mm Assembly diameter = 5.33 mm Part. diameter = 1.10 to 0.41 mm Number of clumps = 705 Mean D_{max}/D_{min} = 1.45	e_{ini} = 0.754 Assembly height = 8.64 mm Assembly diameter = 5.01 mm Part. diameter = 1.10 to 0.41 mm Number of clumps = 539 Mean D_{max}/D_{min} = 1.45	e_{ini} = 0.704 Assembly height = 8.88 mm Assembly diameter = 2.60 mm Part. diameter = 0.82 to 0.41 mm Number of clumps = 577 Mean D_{max}/D_{min} = 1.09

Dense Filter Sand (DFS)	Loose Filter Sand (LFS)
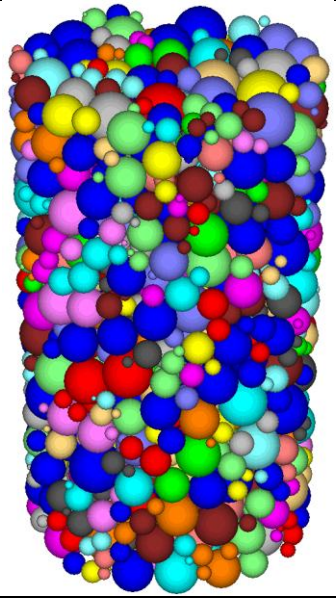	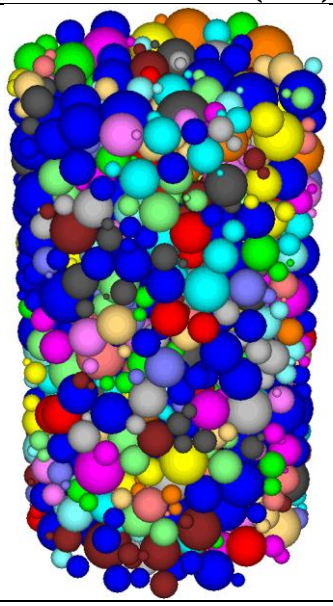
e_{ini} = 0.620 Assembly height = 8.77 mm Assembly diameter = 5.03 mm Particle diameter = 0.90 to 0.31 mm Number of clumps = 947 Mean D_{max}/D_{min} = 1.40	e_{ini} = 0.746 Assembly height = 8.74 mm Assembly diameter = 5.00 mm Particle diameter = 0.90 to 0.31 mm Number of clumps = 869 Mean D_{max}/D_{min} = 1.40

7.3.2.1 Magnitude of RPT Parameters

Before running the simulations it is necessary to define the magnitude of the parameters from the RPT equation. The selection of the magnitude of these parameters for 2D simulations was described in Section 7.2.2. Results from 3D drained triaxial compression simulations run with (i.e., using a sinh-type dashpot) and without (i.e., using a frictional slider) the incorporation of the RPT contact mechanism were compared to assess if the magnitude of the RPT parameters reproduce a reasonable macroscopic assembly behavior during shear. Values assigned during the simulations are shown in Table 7-8. Results from DEM simulations conducted using the dense filter sand (DFS), loose filter sand (LFS), and Glass bead (GB) assemblies are shown in Fig. 7-18, Fig. 7-19, and Fig. 7-20.

Table 7-8. RPT parameters used for 3D creep simulations.

Property	**Value**
Bonds per unit force (n_1)	4.0E8 bonds/N
Distance between equilibrium positions (λ)	2.8 Å
Temperature (T)	20°C
Activation Energy (ΔF)	25 kcal·mol^{-1}

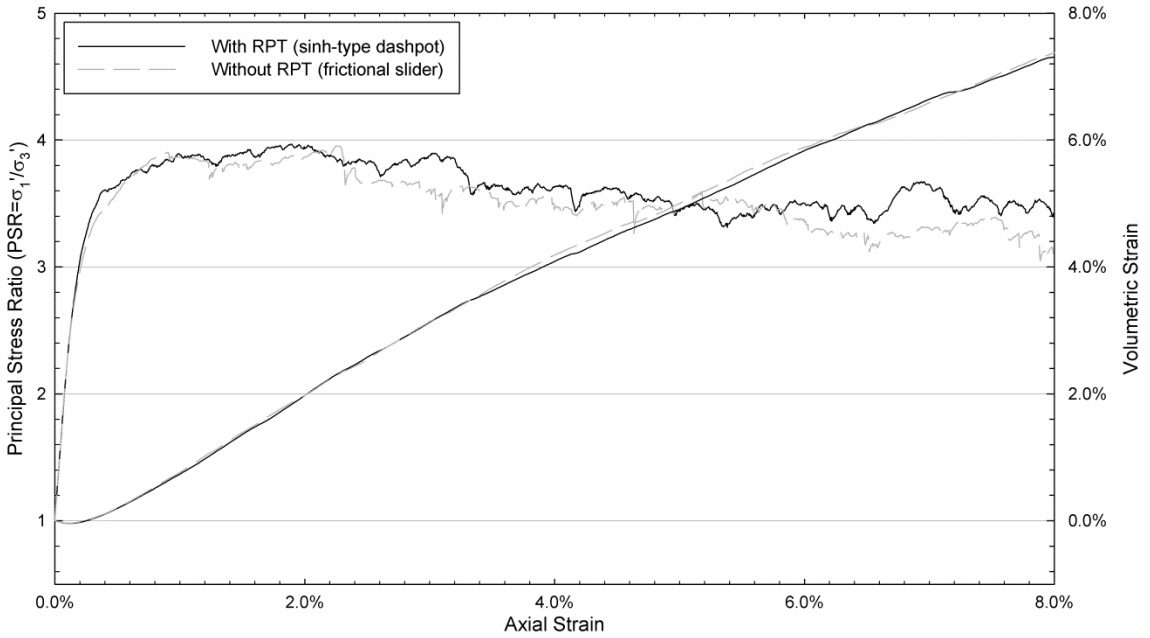

Fig. 7-18. Change in principal stress ratio and volumetric strain with axial strain during triaxial compression. Results from DEM simulations run with and without the incorporation of the RPT equation. Dense filter sand.

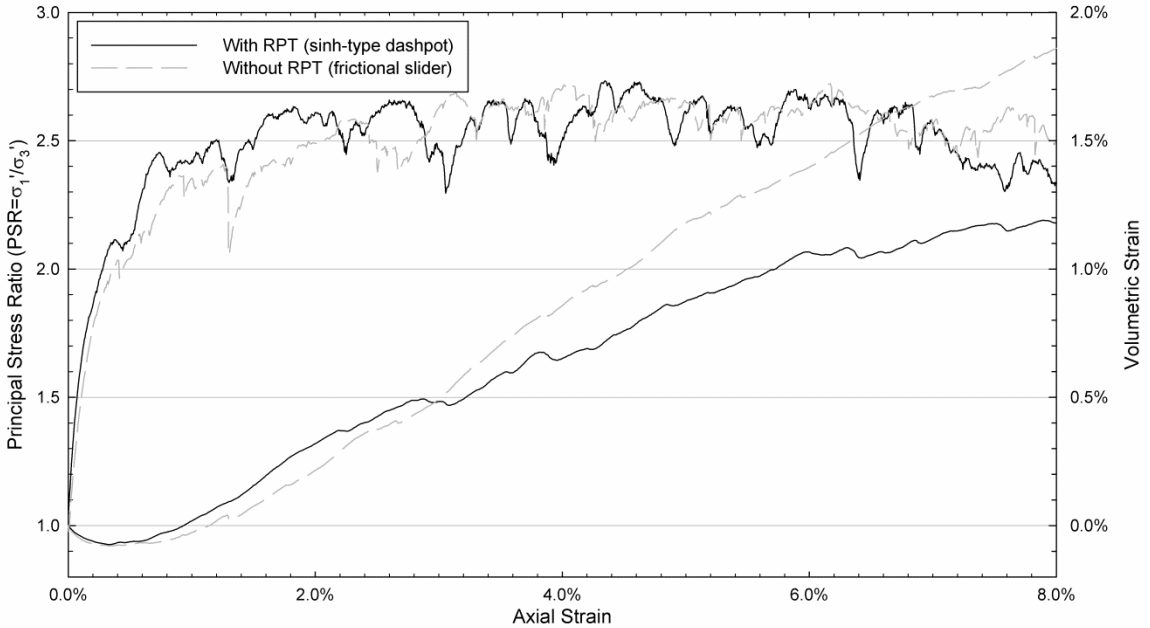

Fig. 7-19. Change in principal stress ratio and volumetric strain with axial strain during triaxial compression. Results from DEM simulations run with and without the incorporation of the RPT equation. Loose filter sand.

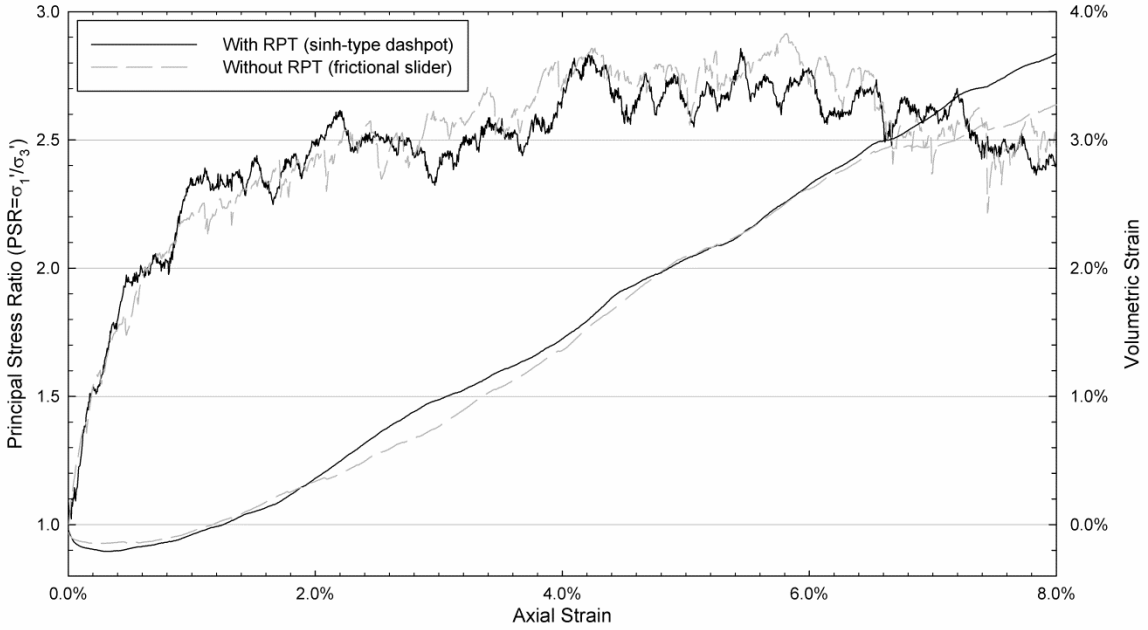

Fig. 7-20. Change in principal stress ratio and volumetric strain with axial strain during triaxial compression. Results from DEM simulations run with and without the incorporation of the RPT equation. Glass beads.

The change in principal stress ratio and volumetric strain during shear determined from simulations run with and without the incorporation of the RPT equation are very similar. Therefore, the sinh-type dashpot with the parameters shown in Table 7-8 provide a representation of tangential particle interactions similar to that described by the Mohr-Coulomb failure mechanism (i.e., frictional slider) with a particle-to-particle friction coefficient of 0.5 (ϕ_μ=26.6°) during triaxial compression. This shows that the implementation of the sinh dashpot with the parameters shown in Table 7-8 reproduces a reasonable macroscopic assembly behavior during the simulation.

Note that the strength of the particle assemblies, as indicated by the maximum value of principal stress ratio, calculated from DEM simulation is less than the strength calculated from laboratory experiments described in Chapter 4. Fig. 7-21, Fig. 7-22, and Fig. 7-23 show a comparison of results from DEM simulations and laboratory experiments. Even though the implementation of 2-particle clumps allows a better

representation of the particle shape of real sands, the results indicate that more effort is required to model the macroscopic sand behavior using DEM. Perhaps using clumps formed by more particles would help to represent in more detail the shape of the particles. However, using clumps formed by more particles requires a longer execution time because it increases the number of particles in the model and the amount of calculations performed during each cycle. Also, note that the strength calculated from DEM simulations on the GB assembly, which is formed primarily by spherical particles, is still less than that measured during laboratory experiments on glass beads. That indicates that DEM fails to describe other important particle characteristics or interactions in addition to the particle shape.

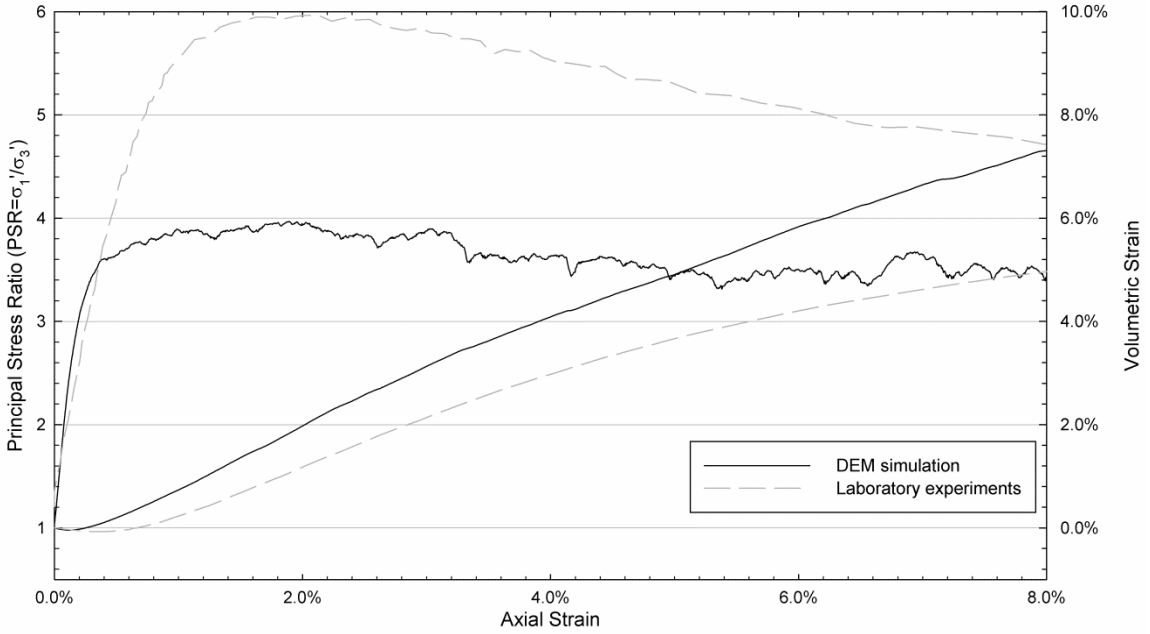

Fig. 7-21. Change in principal stress ratio and volumetric strain with axial strain during triaxial compression. Results from DEM simulations and laboratory experiments. Dense filter sand.

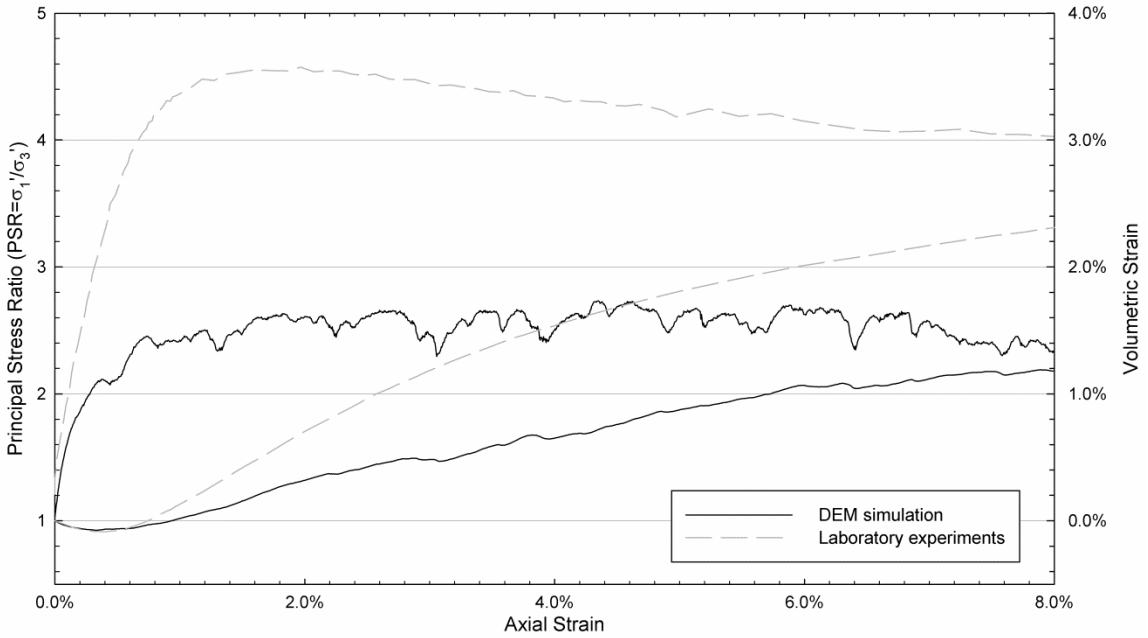

Fig. 7-22. Change in principal stress ratio and volumetric strain with axial strain during triaxial compression. Results from DEM simulations and laboratory experiments. Loose filter sand.

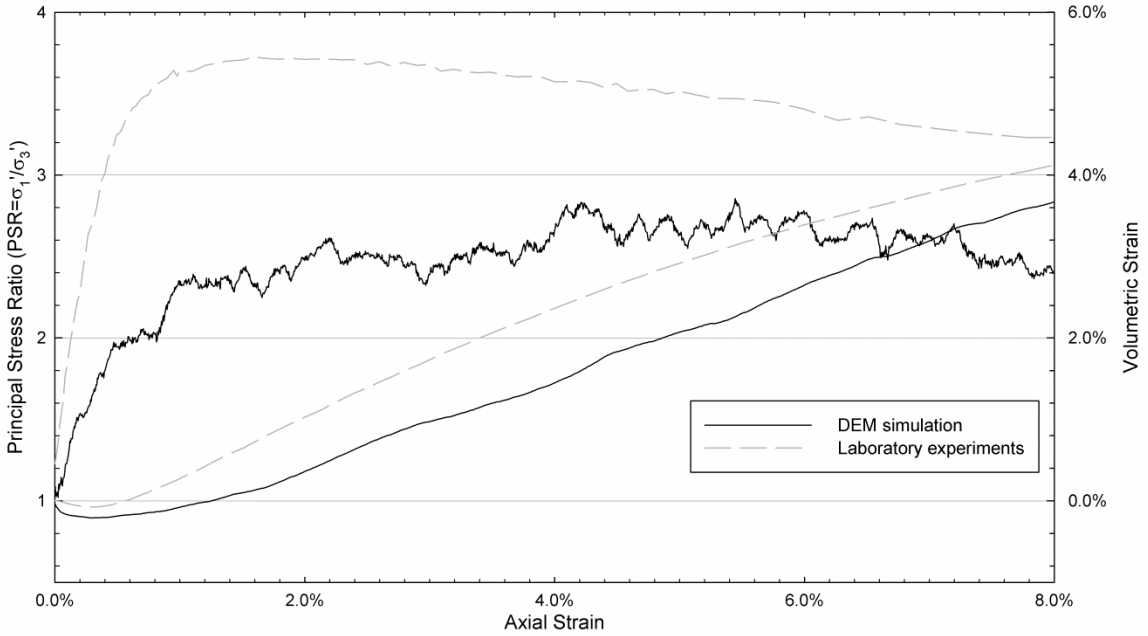

Fig. 7-23. Change in principal stress ratio and volumetric strain with axial strain during triaxial compression. Results from DEM simulations and laboratory experiments. Glass beads.

It is clear that the strengths obtained from the DEM models implemented in this study cannot be directly correlated to results from laboratory experiments conducted on

specimens of sand. However, DEM simulations provide an indication of the effect that changes in the characteristics of the particles and the assemblies have on the macroscopic properties of the arrangement. For this investigation, results from DEM simulations will only be used to provide a general description of changes taking place in the internal structure of particle assemblies during creep and aging, and to estimate the effect of changes in the properties of the particle assemblies, such as grain sphericity and void ratio, on the macroscopic behavior of the arrangement during and after creep.

7.3.2.2 Description of the Simulation

Three creep stages were modeled during each triaxial compression simulation. During each creep stage, the particle assembly was allowed to creep under constant vertical and horizontal stresses for elapsed times up to 1.0E6 s. The magnitude of the vertical stress applied during the creep stages was selected based on the ultimate strength of the assembly. Creep simulations were conducted under values of stress level ($SL=\sigma_d/\sigma_{d\text{-}max}$) of approximately 25%, 50%, and 75%.

The effects of the creep stage on the macroscopic properties of the particle arrangement were evaluated by shearing the assembly after 1.0E2, 1.0E4, and 1.0E6 s of creep. Fig. 7-24 shows the change in principal stress ratio and volumetric strain during shear of DFS assemblies allowed to creep for 1.0E2, 1.0E4, and 1.0E6 s under a stress level (i.e., ratio of stress to computed strength) of approximately 27% (σ_1'=540 kPa, σ_3'=300 kPa). The same procedure was used for DFS, LFS, and GB assemblies at stress levels of approximately 25%, 50%, and 75%.

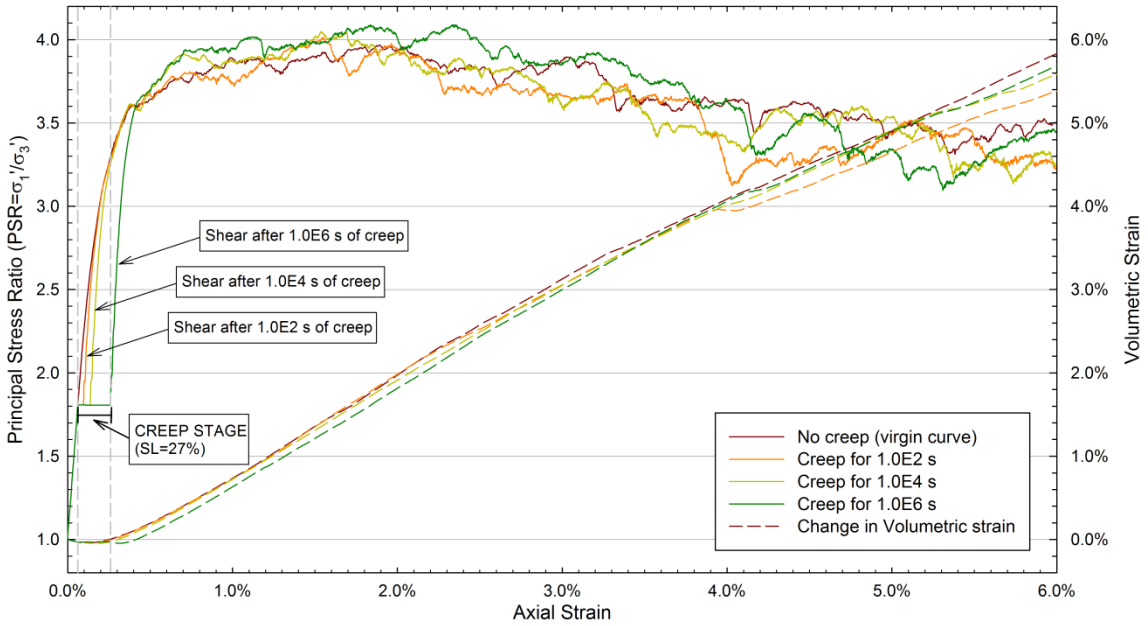

Fig. 7-24. Change in principal stress ratio and volumetric strain with axial strain during triaxial compression. Assembly allowed to creep for 1.0E2, 1.0E4, and 1.0E6 seconds under SL=27%. Dense filter sand.

7.3.2.3 Analysis of Results

The change in axial strain with time during creep under stress levels of approximately 25% and 50% for DFS, LFS, and GB assemblies is shown in Fig. 7-25, Fig. 7-26, and Fig. 7-27. Note that the magnitude of the vertical deformation from DEM simulations is greater than the values recorded from laboratory experiments. The change in volumetric strain with respect to time during creep for DFS, LFS, and GB assemblies is plotted in Fig. 7-31, Fig. 7-32, and Fig. 7-33.

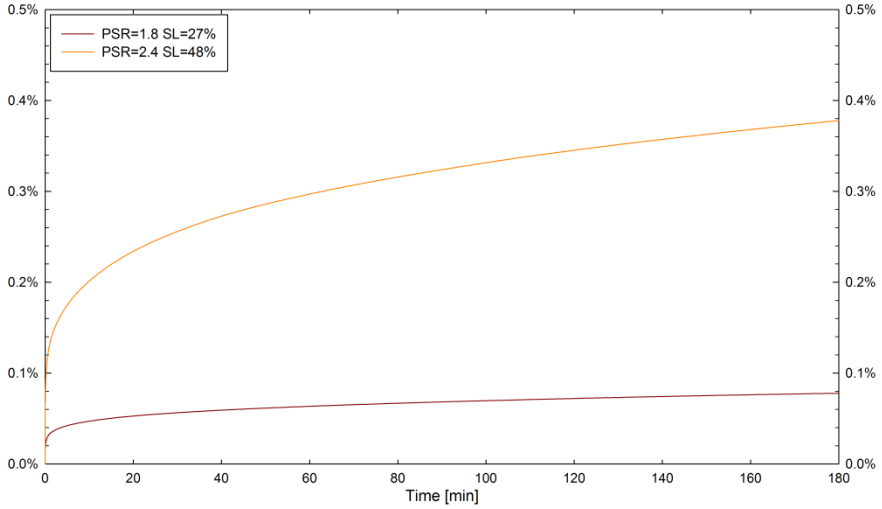

Fig. 7-25. Change in axial strain with time during creep. Dense filter sand.

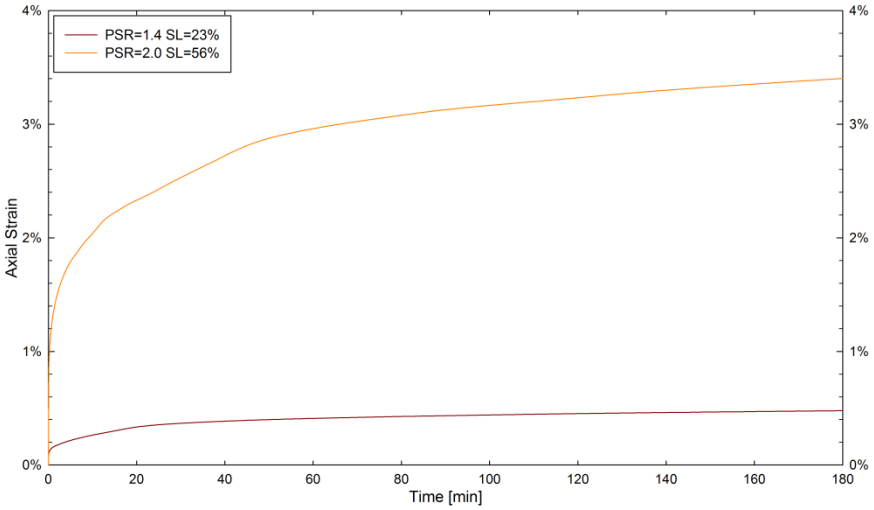

Fig. 7-26. Change in axial strain with time during creep. Loose filter sand.

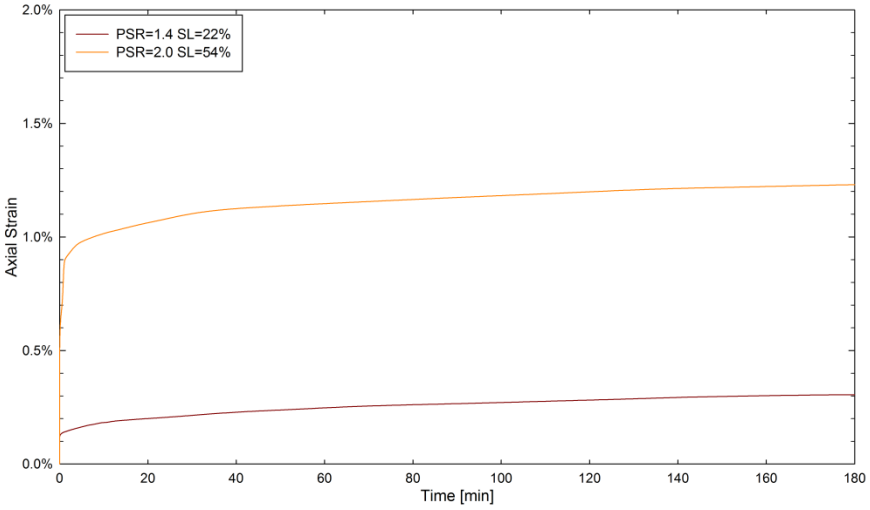

Fig. 7-27. Change in axial strain with time during creep. Glass beads.

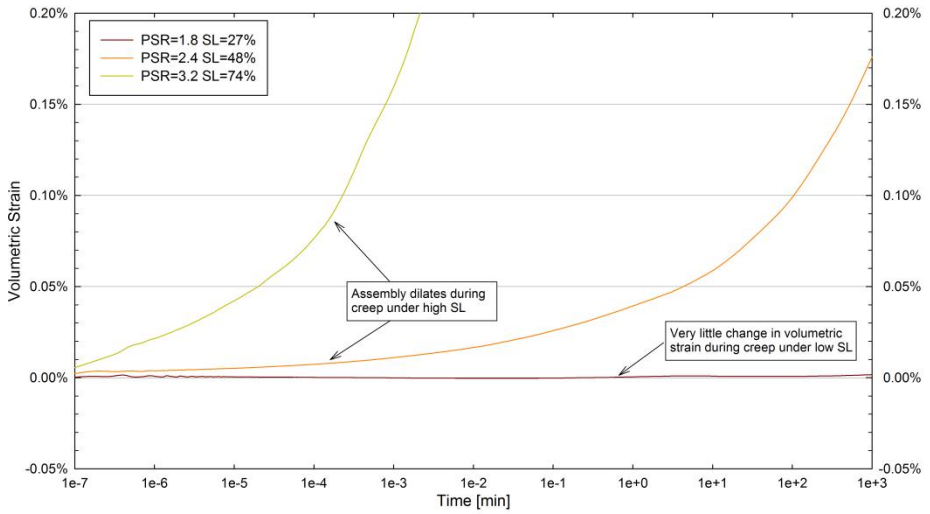

Fig. 7-28. Change in volumetric strain with time during creep. Dense filter sand.

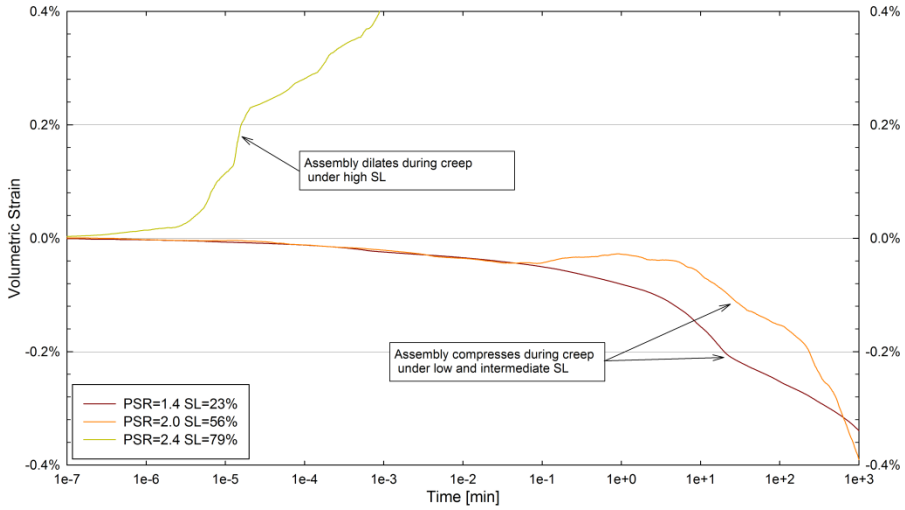

Fig. 7-29. Change in volumetric strain with time during creep. Loose filter sand.

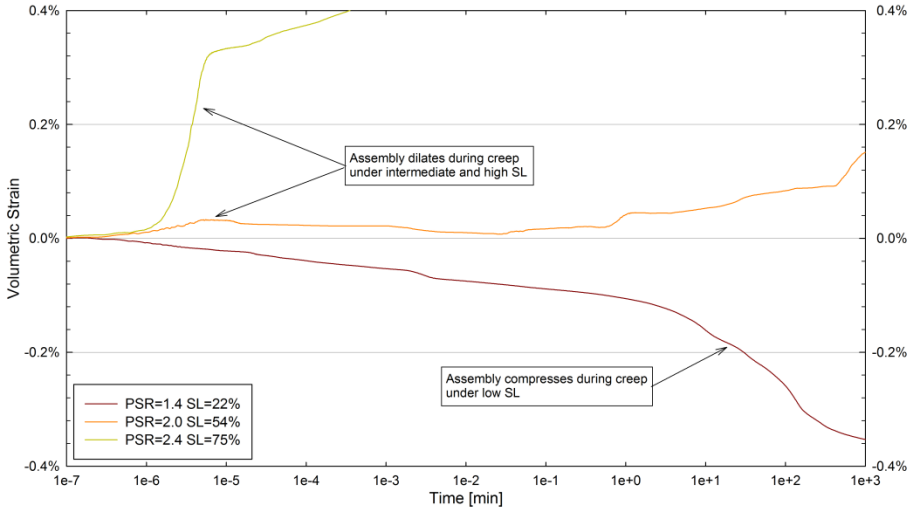

Fig. 7-30. Change in volumetric strain with time during creep. Glass beads.

The magnitude of volumetric deformation calculated from DEM simulations is also greater than values measured during laboratory experiments on specimens of sand. However, DEM results show a similar behavior to that observed during the laboratory experiment, where dense, angular materials tend to dilate during creep, while loose spherical materials tend to compress during creep. The change in volumetric strain during the creep stage follows a similar trend to that exhibited by the virgin curve (i.e., assembly sheared without creep stages). If creep starts when the assembly is compressing during shear (e.g., low stress level), the assembly tends to continue compressing during creep. If, on the other hand creep starts when the assembly is dilating (e.g., high stress level), the particle arrangement tends to continue dilating during creep.

The logarithm of the axial strain rate is plotted against the logarithm of time in Fig. 7-31, Fig. 7-32, and Fig. 7-33. The figures show that the logarithm of the axial strain rate decreases linearly with the logarithm of time during creep, and increases with increasing stress level. Additionally, the slope of the log-strain rate versus log-time relationship is independent of the magnitude of stress level. These observations agree with behavioral characteristics of sands and clays described by Mitchell and Soga (2005). The magnitude of the slope of the log-strain rate versus log-time relationship (m) for the DFS, LFS, and GB assemblies ranged from 0.77 to 0.92. These magnitudes are similar to values reported by Mejia et al. (1988) and Murayama et al. (1984), who measured magnitudes of m of 0.9 and 1.0 during creep tests on Tailings sand and Toyoura sand, respectively.

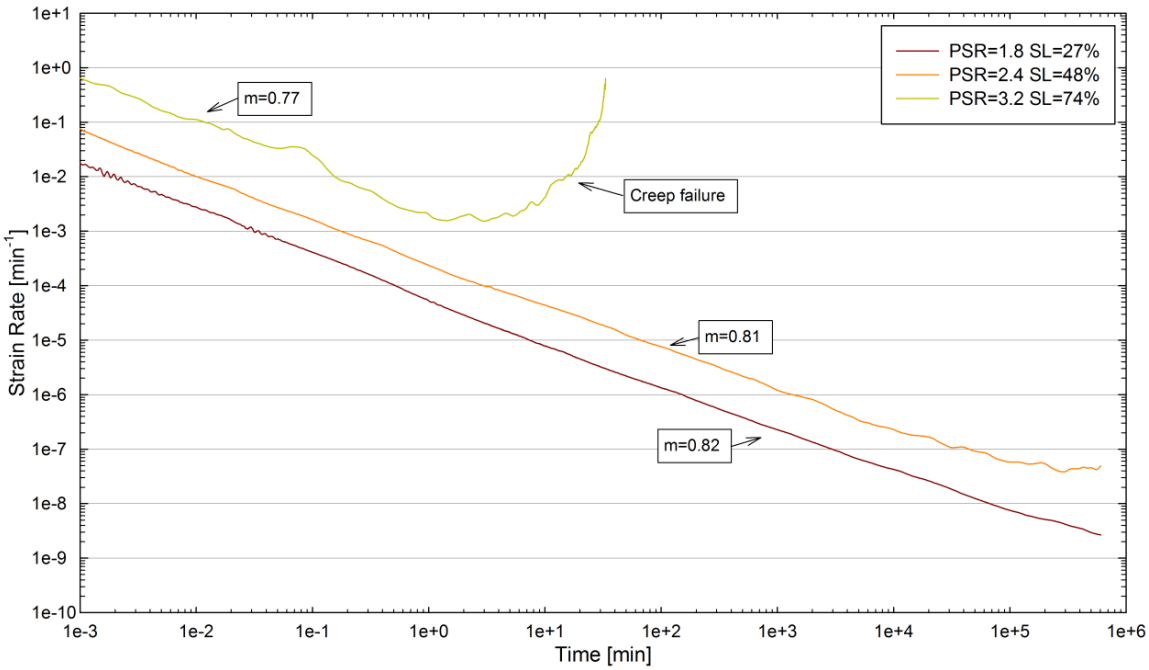

Fig. 7-31. Change in logarithm of vertical strain rate versus the logarithm of time during creep. Dense filter sand.

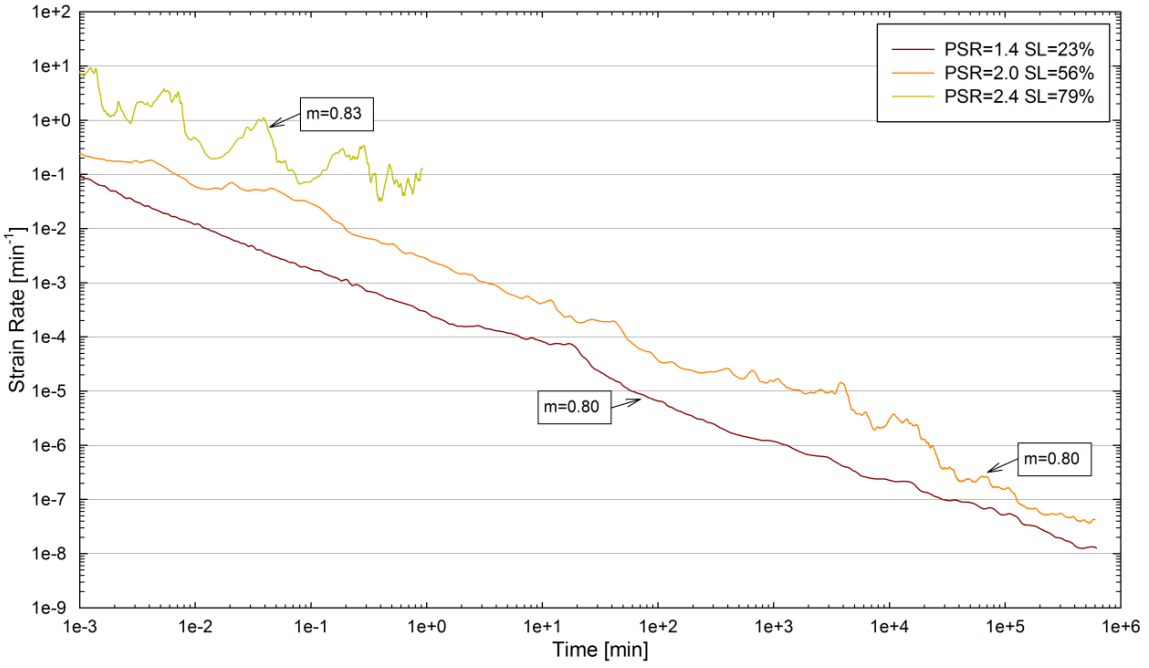

Fig. 7-32. Change in logarithm of vertical strain rate versus the logarithm of time during creep. Loose filter sand.

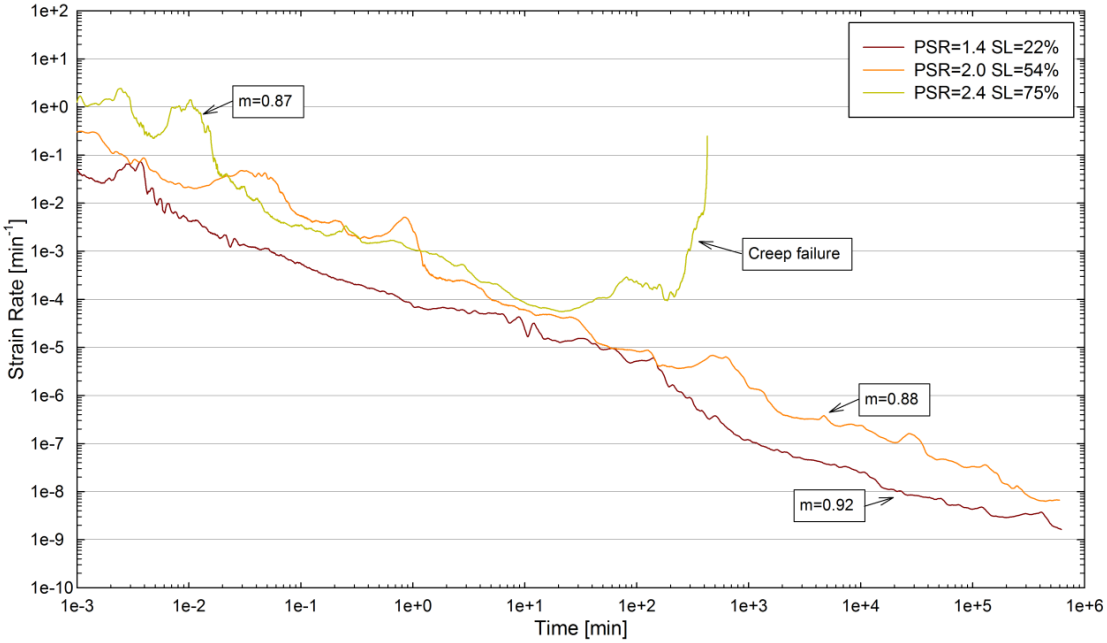

Fig. 7-33. Change in logarithm of vertical strain rate versus the logarithm of time during creep. Glass beads.

Fig. 7-34, Fig. 7-35, and Fig. 7-36 show the strain rate as a function of the stress level at different times of creep. At low magnitudes of stress level the rates of deformation during creep are very low, and they increase with increasing stress level. Creep failure is observed after longer times of creep and greater values of stress level.

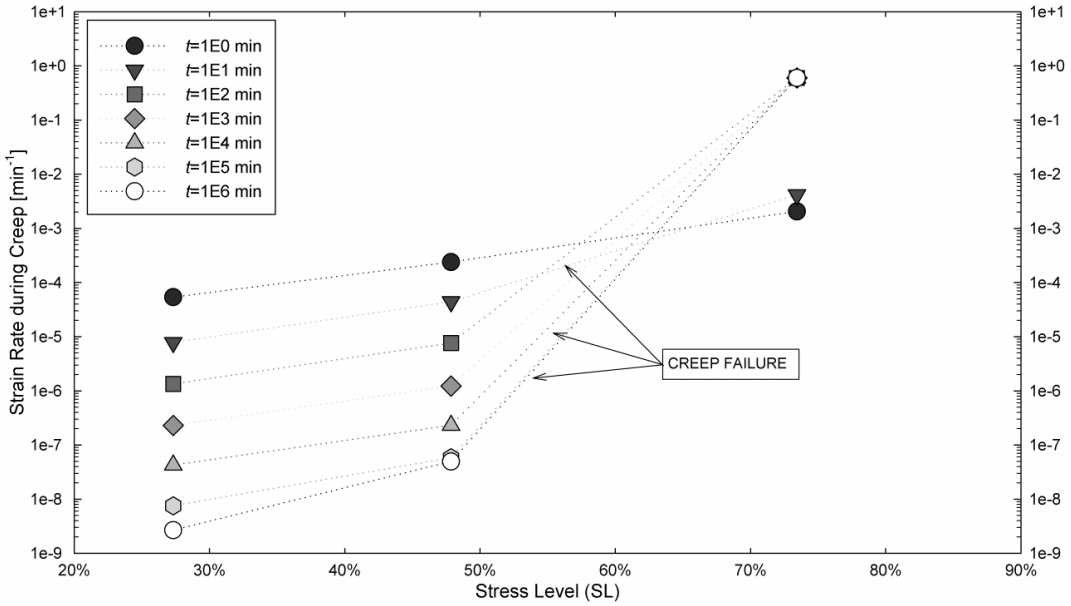

Fig. 7-34. Variation of the axial strain rate with stress level for different times of creep. Dense filter sand.

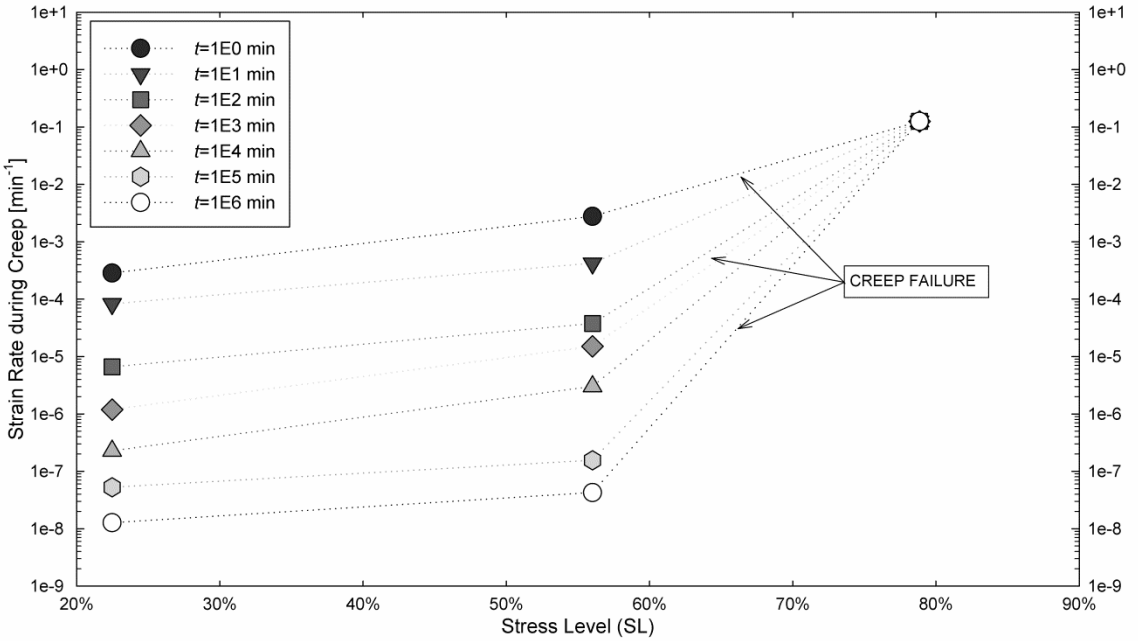

Fig. 7-35. Variation of the axial strain rate with stress level for different times of creep. Loose filter sand.

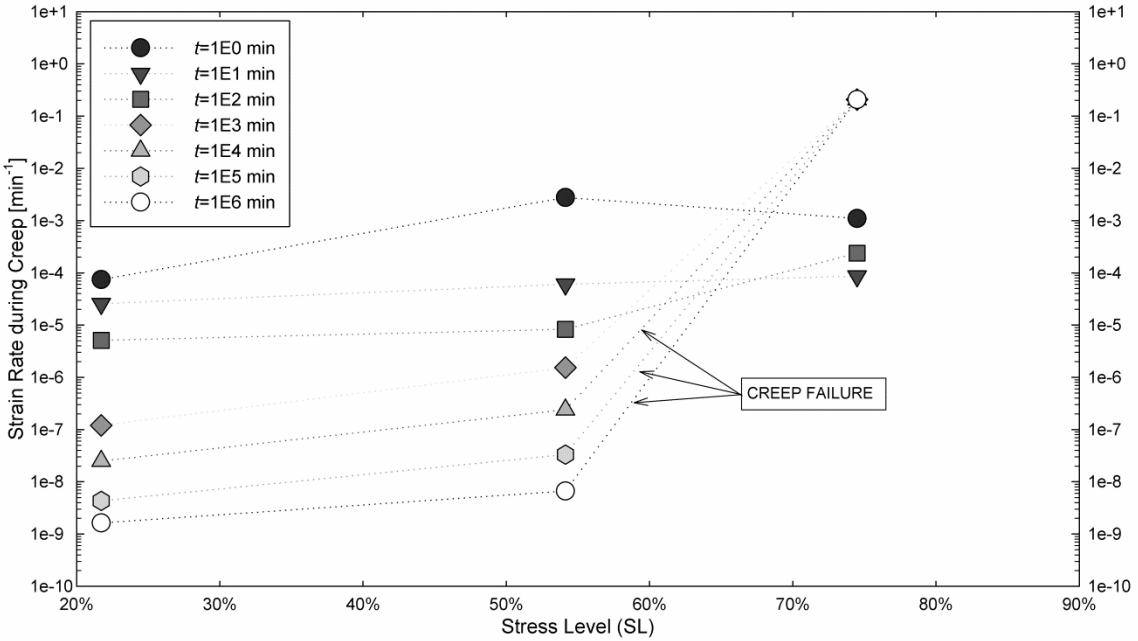

Fig. 7-36. Variation of the axial strain rate with stress level for different times of creep. Glass beads.

The results shown in Fig. 7-34, Fig. 7-35, and Fig. 7-36 were compared with results from laboratory experiments described in Chapter 4. Fig. 7-37 shows the stress level versus log-strain rate relationship after 10 minutes of creep calculated from DEM

simulations compared to values measured from laboratory experiments conducted on specimens of dense filter sand, loose filter sand, and glass beads (see Chapter 4). Note that the magnitude of strain rate from DEM simulations is about one order of magnitude greater than values measured in the laboratory. DEM simulation results are compared to results reported by Mejia et al. (1988), Murayama et al. (1984), Kwok (2008), and Kuhn (1987) in Fig. 7-38. The magnitude of the strain rate determined from DEM simulations conducted on DFS and GB assemblies are similar to those reported by Mejia et al. (1988) for Tailings sand and Murayama et al. (1984) for Toyoura sand, and tend to be less than magnitudes determined by Kwok (2008) from 3D DEM simulations. Values of strain rate calculated from DEM simulations conducted on the LFS assembly are greater than results reported by these investigators.

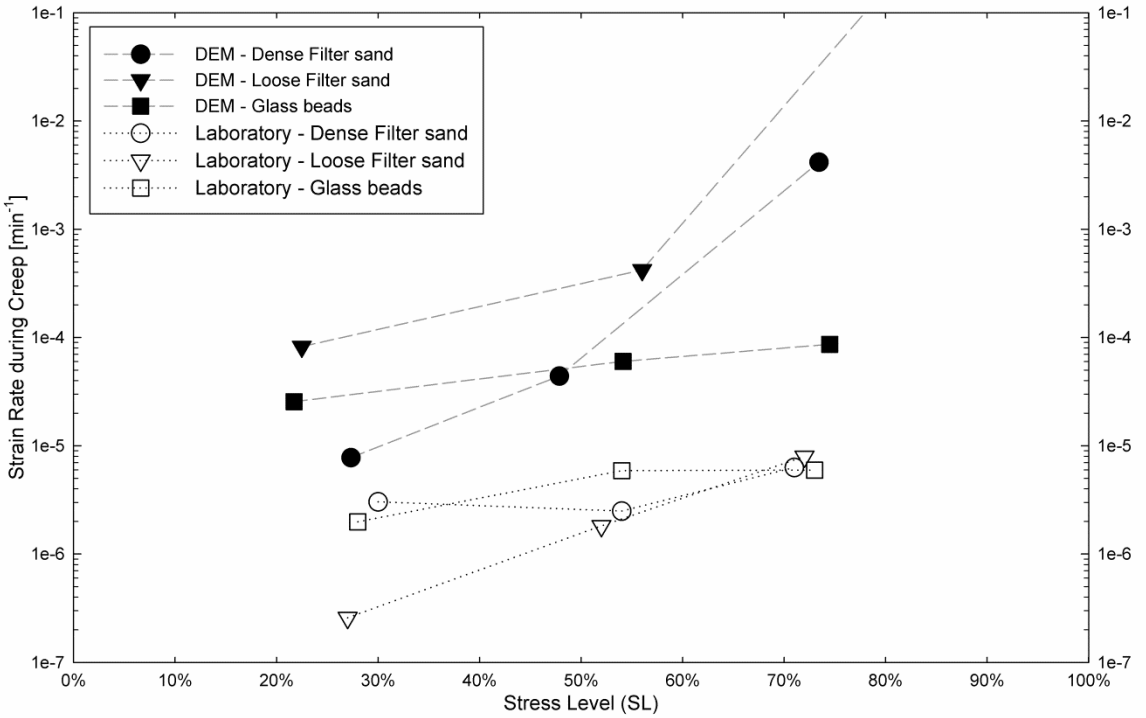

Fig. 7-37. Variation of axial strain rate with stress level after 10 minutes of creep. Results from DEM simulations and laboratory tests.

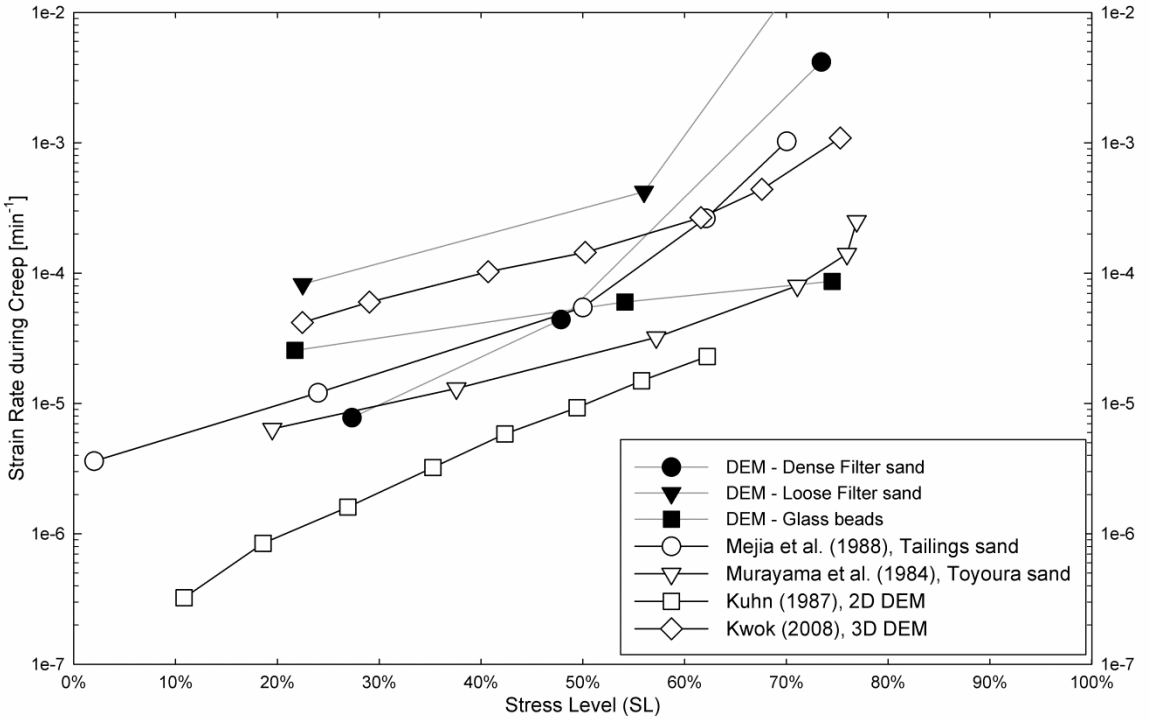

Fig. 7-38. Variation of axial strain rate with stress level after 10 minutes of creep. Results from DEM simulations compared to results reported by various investigators.

Magnitudes of strain rate determined from DEM simulations are often greater than results from laboratory experiments. Differences between DEM and laboratory results may be caused by differences in the sphericity of grains of sand and DEM particles. The method used to introduce the grain sphericity in this investigation (i.e., two-particle clumps) may not be enough to fully represent the shape of sand grains and its effect on the macroscopic properties of the specimen. Future research may consider the implementation of clumps formed by more particles which resemble more closely the shape of sand grains. However, it must be considered that using more particles per clump will increase significantly the execution time of DEM simulations.

Another factor which may influence the results obtained from DEM simulations is the magnitude selected for the RPT parameters. The magnitude of parameters such as the activation energy (ΔF) or the number of interparticle contacts per unit force (n_1) are

difficult to determine. Greater values of ΔF and n_1 reduce the magnitude of the strain rate and may be more adequate to model creep in sands.

7.3.2.4 Aging Effects

The effects of aging on the macroscopic properties of the particle arrangements are estimated by continuing the drained compression simulation after the creep stage is finalized. Changes in macroscopic properties of the assembly, such as the stiffness or the tendency towards volumetric dilation, can be estimated by comparing the respective values with magnitudes determined from a simulation conducted without creep, which will be referred as the virgin curve.

Results from DEM simulations conducted on DFS, LFS, and GB assemblies are shown in Fig. 7-39 through Fig. 7-44. The figures show the stress-axial strain and volumetric strain-axial strain relationships of assemblies allowed to age from 0 to 1.0E6 s under stress levels of approximately 25% and 50%.

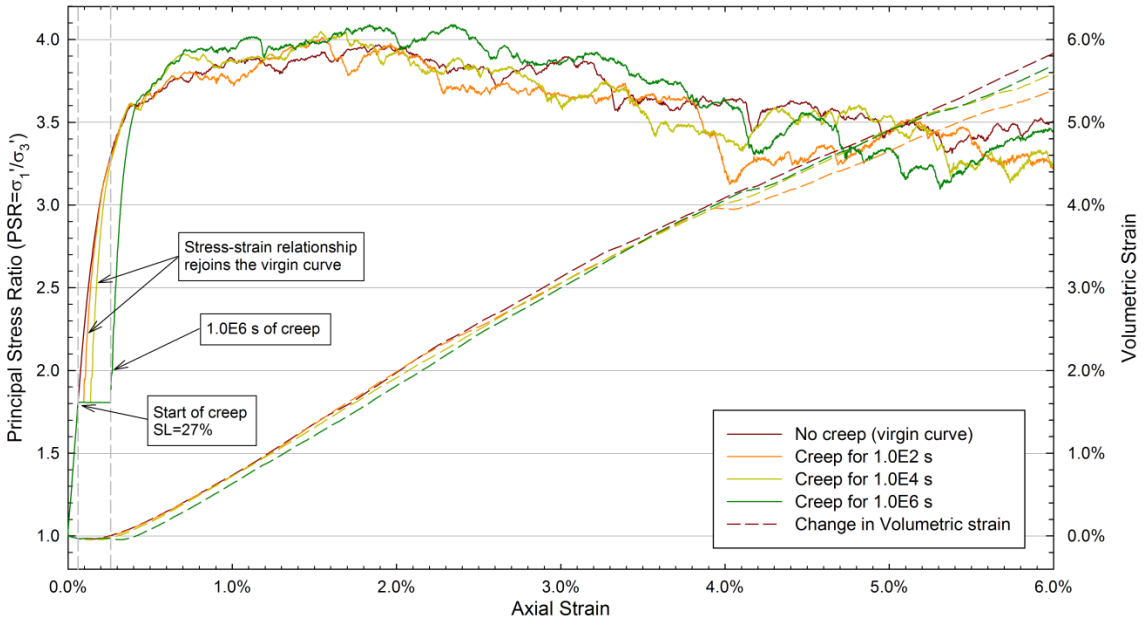

Fig. 7-39. Change in principal stress ratio and volumetric strain during shear for particle arrangements allowed to age from 0 to 1.0E6 s under a stress level of 27%. Dense filter sand.

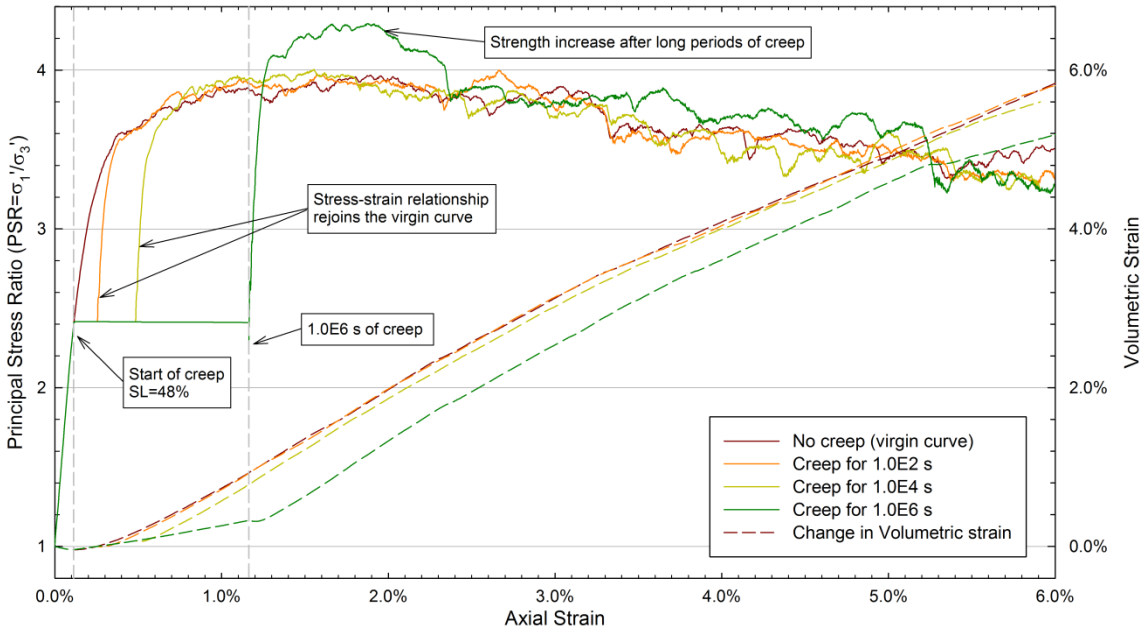

Fig. 7-40. Change in principal stress ratio and volumetric strain during shear for particle arrangements allowed to age from 0 to 1.0E6 s under a stress level of 48%. Dense filter sand.

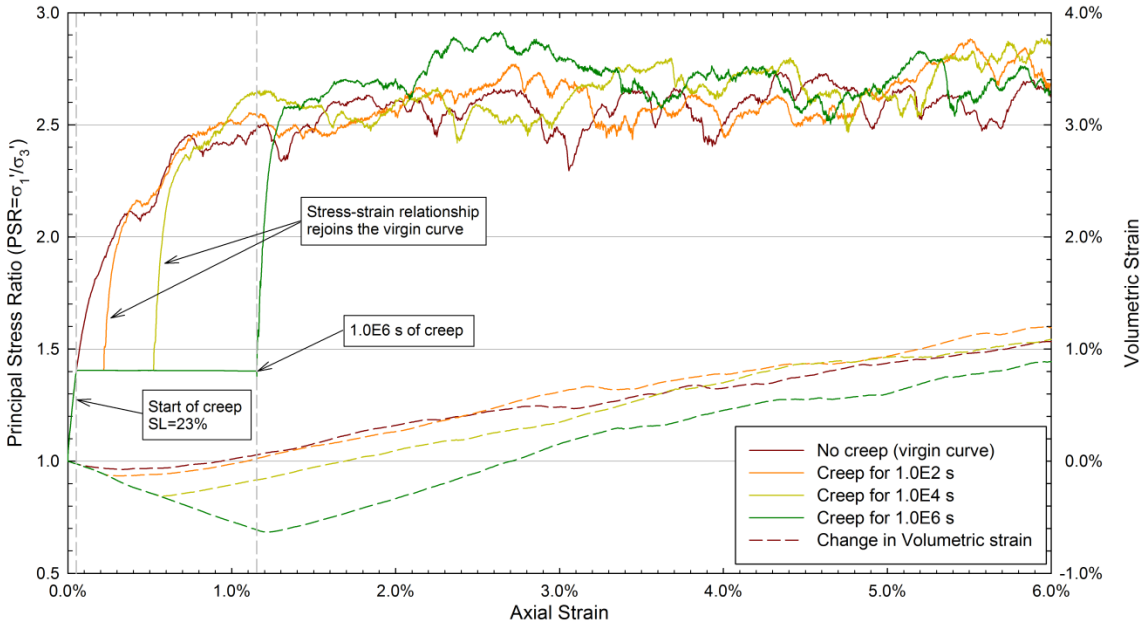

Fig. 7-41. Change in principal stress ratio and volumetric strain during shear for particle arrangements allowed to age from 0 to 1.0E6 s under a stress level of 23%. Loose filter sand.

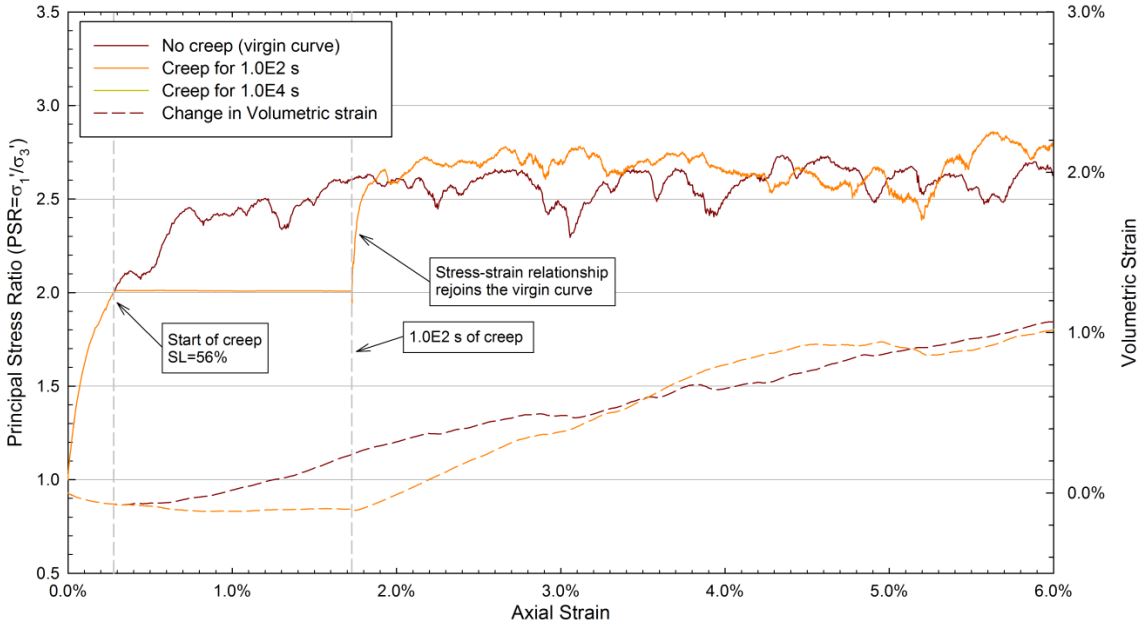

Fig. 7-42. Change in principal stress ratio and volumetric strain during shear for particle arrangements allowed to age from 0 to 1.0E2 s under a stress level of 56%. Loose filter sand.

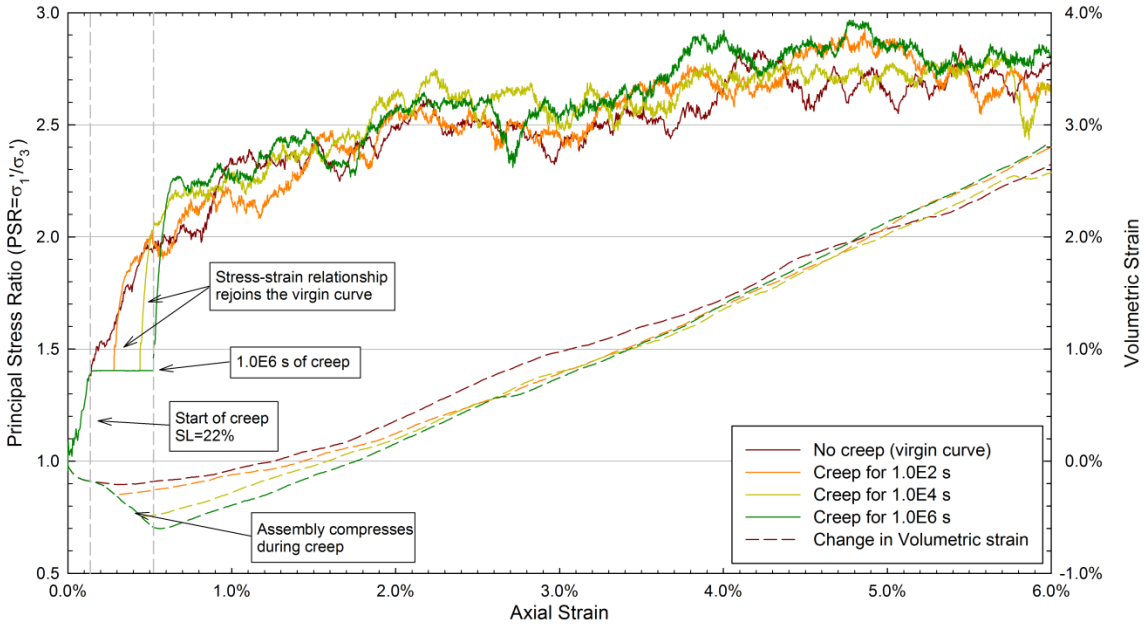

Fig. 7-43. Change in principal stress ratio and volumetric strain during shear for particle arrangements allowed to age from 0 to 1.0E6 s under a stress level of 22%. Glass beads.

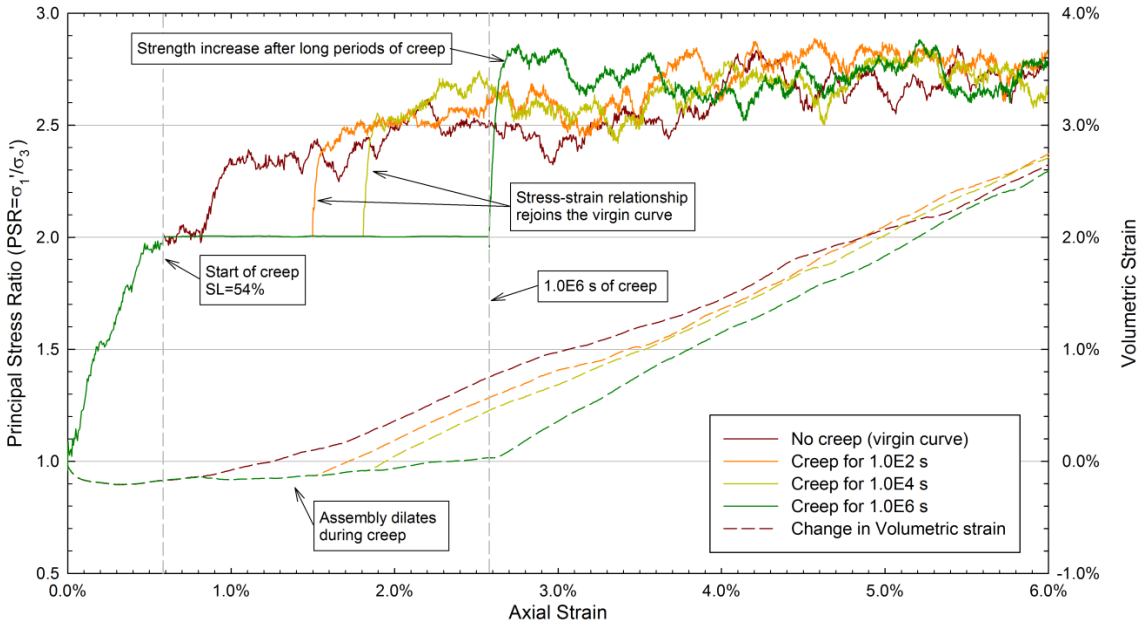

Fig. 7-44. Change in principal stress ratio and volumetric strain during shear for particle arrangements allowed to age from 0 to 1.0E6 s under a stress level of 54%. Glass beads.

The figures show that the creep stage produces an increase in the macroscopic stiffness of the assembly. The stress-strain relationship of assemblies allowed to creep

tends to rejoin the stress-strain relationship of the virgin curve once shear continues following a creep stage.

Additionally, assemblies seem to be more dilative after creep. Note that the volumetric strain-axial strain relationships of assemblies allowed to creep for up to 1.0E6 s rejoin the virgin curve after further shear, a trend which causes the assemblies to become apparently more dilative. This behavior indicates that that the aged structure of the assembly is destroyed when the particle arrangement is deformed. Longer periods of creep produce a greater effect on the volumetric strain-axial strain relationship of the assembly, causing a greater tendency towards dilation. These behavioral trends agree with characteristics exhibited by specimens of sand during laboratory creep experiments which were described in Chapter 4.

Only in some cases where the assembly was allowed to creep for long periods of time under high stress levels (e.g., DFS assembly allowed to creep for 1.0E6 s under a stress level of 48%, DFS assembly allowed to creep for 1.0E6 s under a stress level of 48%, GB assembly allowed to creep for 1.0E6 s under a stress level of 54%), did the creep stage had an effect on the macroscopic strength of the assembly.

The change in magnitude of the secant Young's modulus at 0.005% strain ($E_{0.005\%}$) with respect to the length of the creep stage for different values of stress level during creep is shown in Fig. 7-45, Fig. 7-46, and Fig. 7-47. Fig. 7-48 shows the respective change is $E_{0.005\%}$ as the ratio of the magnitude calculated after creep and the magnitude determined for the virgin curve ($E_{0.005\%\text{-with creep}}/E_{0.005\%\text{-without creep}}$). Note that the stiffness increases with increasing length of creep and increasing magnitude of stress level. In addition, the magnitude of that increase tends to be greater for loose assemblies

formed by angular particles than for dense assemblies with spherical grains. The magnitude of the increase in secant modulus ($E_{0.005\%}$) ranged from about 10% per log-cycle of time for the DFS assembly under a stress level of 27%, to about 100% per log-cycle of time for the LFS assembly under a stress level of 56%.

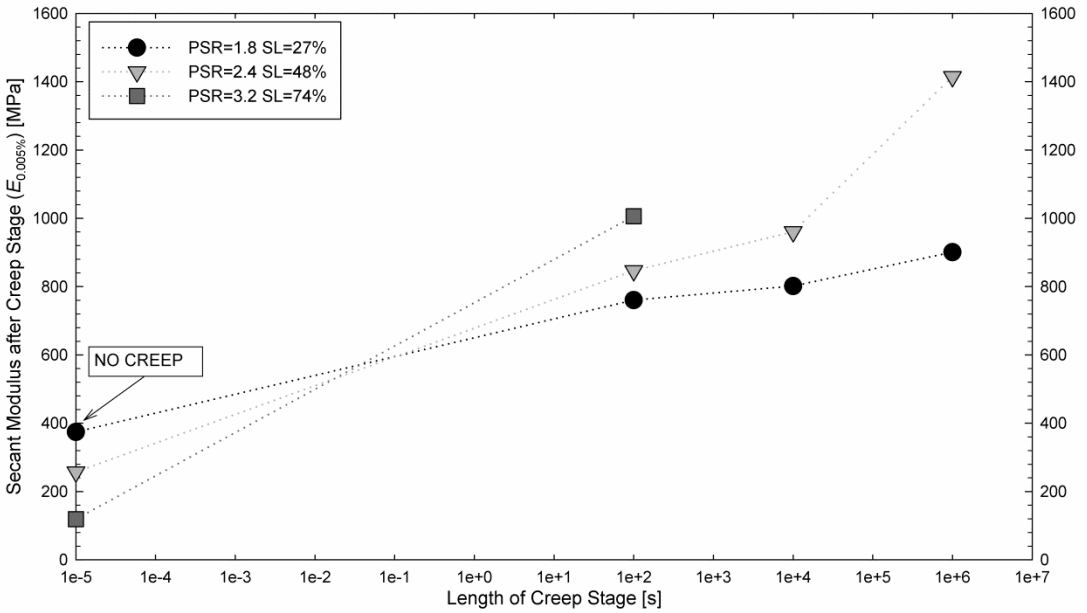

Fig. 7-45. Change in the magnitude of $E_{0.005\%}$ with respect to the length of the creep stage for different stress levels during creep. Dense filter sand.

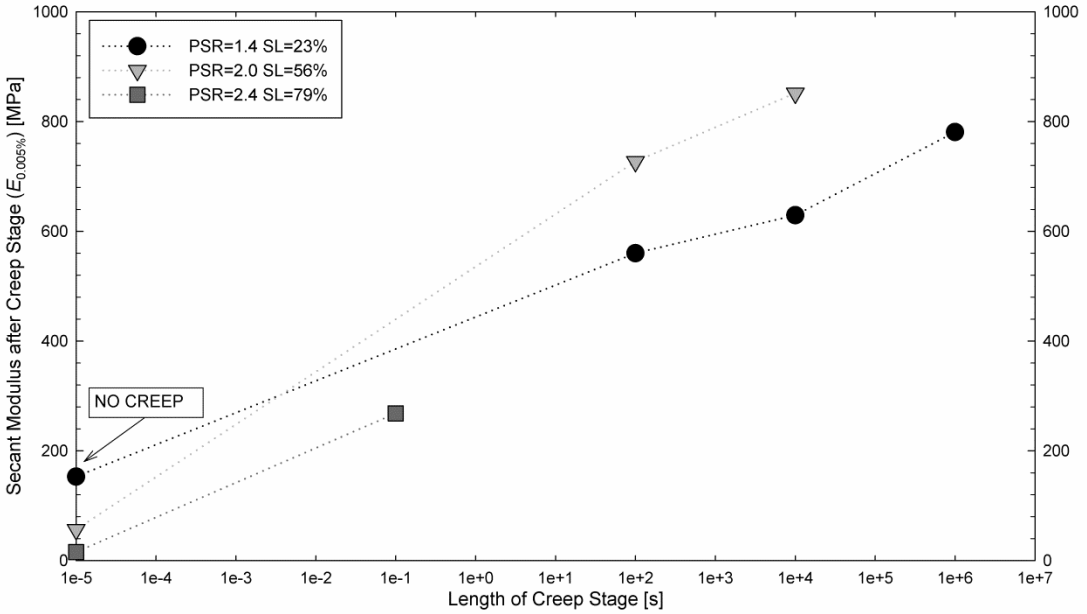

Fig. 7-46. Change in the magnitude of $E_{0.005\%}$ with respect to the length of the creep stage for different stress levels during creep. Loose filter sand.

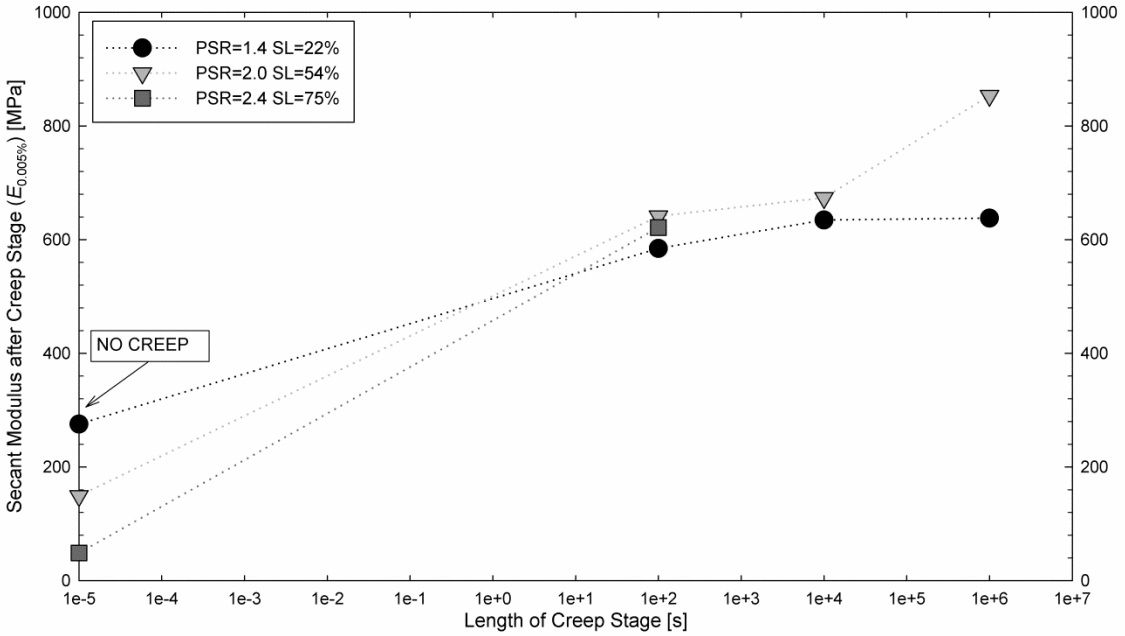

Fig. 7-47. Change in the magnitude of $E_{0.005\%}$ with respect to the length of the creep stage for different stress levels during creep. Glass beads.

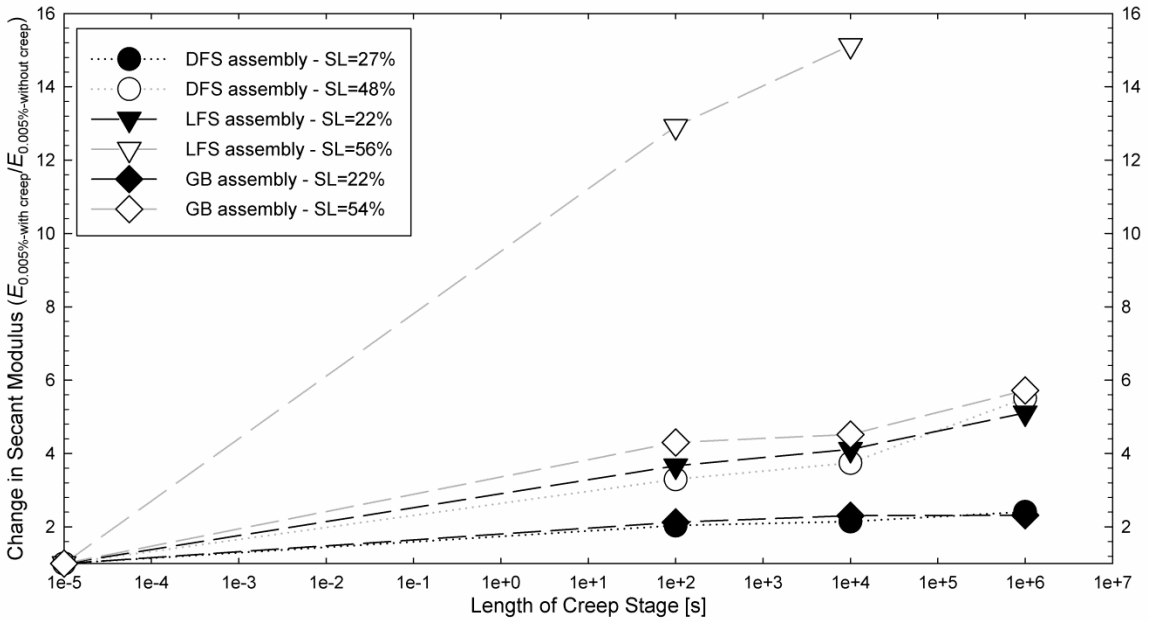

Fig. 7-48. Change in magnitude of Young's modulus ($E_{0.005\%\text{-with creep}}/E_{0.005\%\text{-without creep}}$) with respect to the length of the creep stage.

The rate of change in small-strain Young's modulus shown in the previous figures is similar to data reported by numerous investigators compiled and shown in Fig. 2-21. However, the magnitude of the change in macroscopic stiffness calculated from DEM

simulations should not be correlated directly to variations in granular soils because the strength and deformation of the assemblies determined using DEM models are not in complete agreement with results obtained from laboratory tests. Nevertheless, DEM allows studying plausible causes of the behavior exhibited by particle arrangements after creep; e.g., increase in the assembly stiffness and dilatancy.

For instance, consider the driving mechanism proposed by Lade et al. (2010), which relates aging effects in granular materials to static fatigue of the particles, a form of time-dependent soil grain crushing. It was described in previous sections that the DEM simulations presented in this chapter incorporate the analysis of particle crushing into the model, which is done by calculating the normal and tangential forces acting at the clump bond, which joins spherical particle together, and defines critical values based on crushing tests conducted on individual grains described in Chapter 4. Results from the DEM model indicate that the clumps did not break during any of creep simulations. The variation of the mean normal and shear force at the clump bond (sum of the forces acting at each bond divided by total the number of clumps) with respect to time during creep is shown in Fig. 7-49, Fig. 7-50, and Fig. 7-51 for DFS, LFS, and GB assemblies. Note that the magnitude of the mean normal and shear force is well below the estimated ultimate strength of the grains (see Table 7-6). That leads to conclude that grain crushing cannot account for the changes in macroscopic properties of the assemblies observed after aging in the DEM simulations.

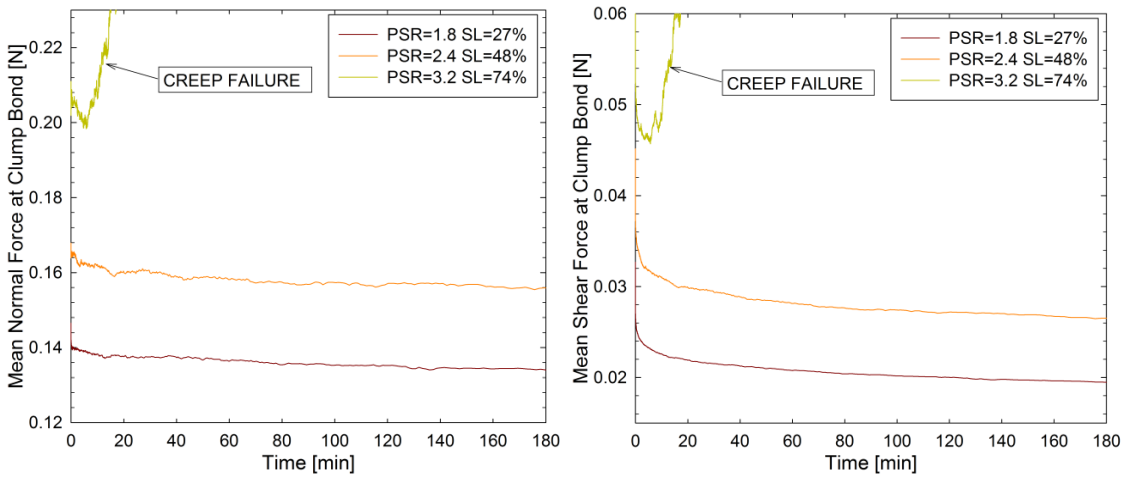

Fig. 7-49. Change in mean normal force (left) and mean shear force (right) at the clump bonds with respect to time during creep. Dense filter sand.

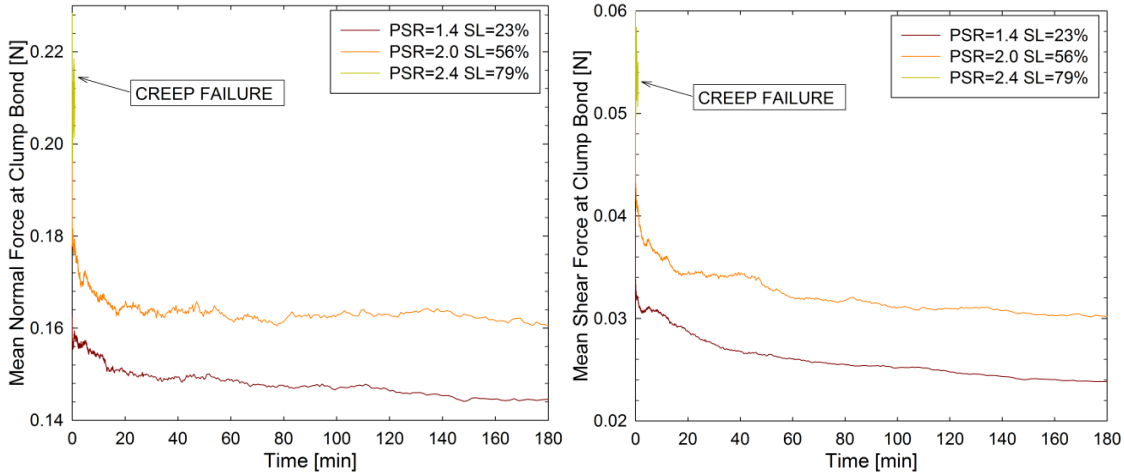

Fig. 7-50. Change in mean normal force (left) and mean shear force (right) at the clump bonds with respect to time during creep. Loose filter sand.

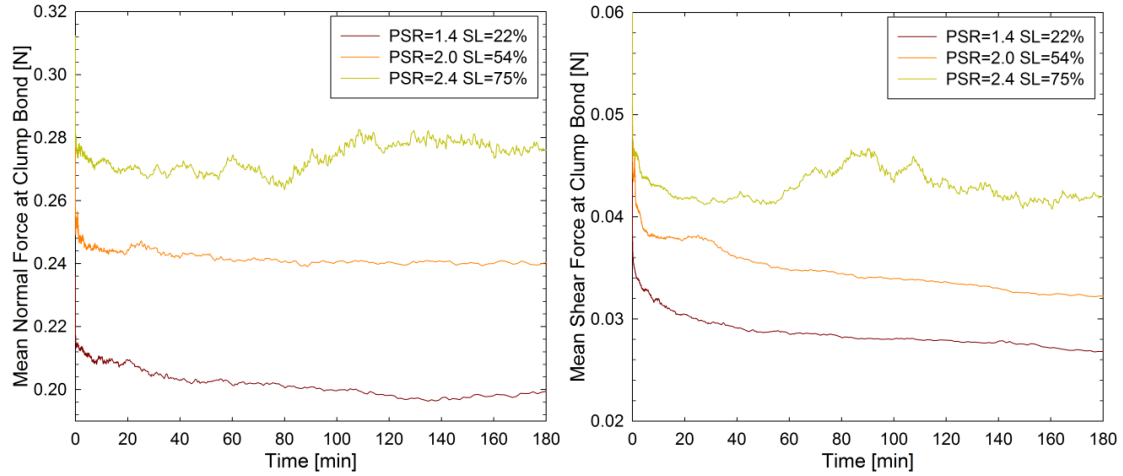

Fig. 7-51. Change in mean normal force (left) and mean shear force (right) at the clump bonds with respect to time during creep. Glass beads.

Fig. 7-49, Fig. 7-50, and Fig. 7-51 show that for all the assemblies, the magnitude of the mean normal and tangential force at the clumps decreases over time. A reduction in the magnitude of the mean shear force can be explained by the transfer of the part of the deviator stress carried by the tangential inter-particle forces to the normal forces acting between the grains.

The variation in the number of particle contacts with time during creep is shown Fig. 7-52, Fig. 7-53, and Fig. 7-54. Note that the number of contacts increases over time during creep for all the DEM simulations conducted. The reduction in the magnitude of the mean normal clump force during creep can be explained by the increase in the number of particle contacts, which reduces the force carried by each particle.

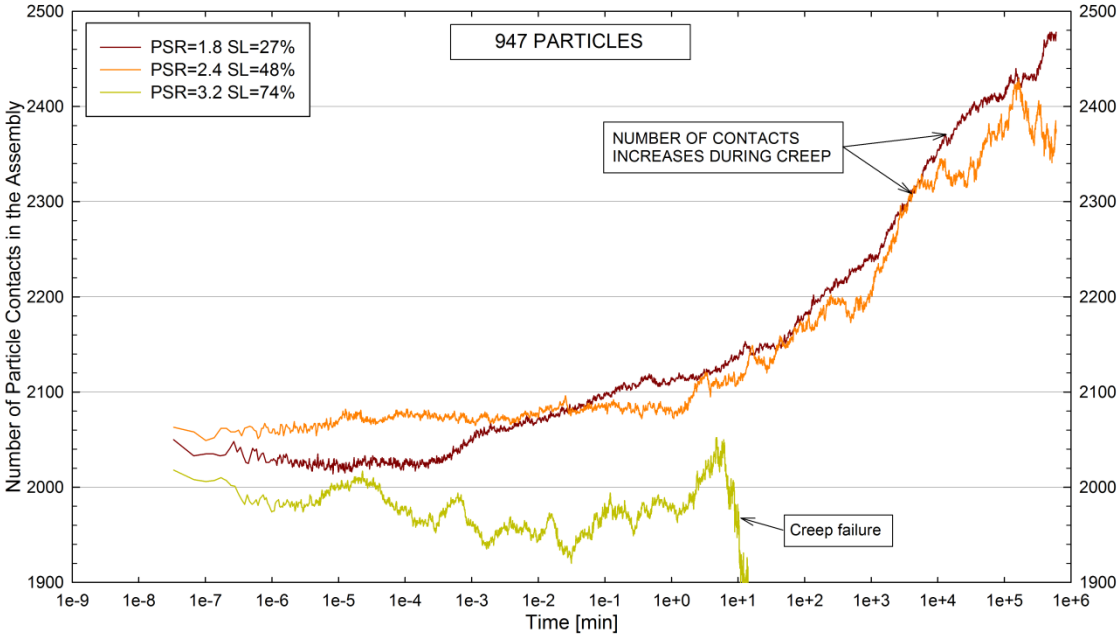

Fig. 7-52. Change in the number of particle contacts with time during creep. Dense filter sand.

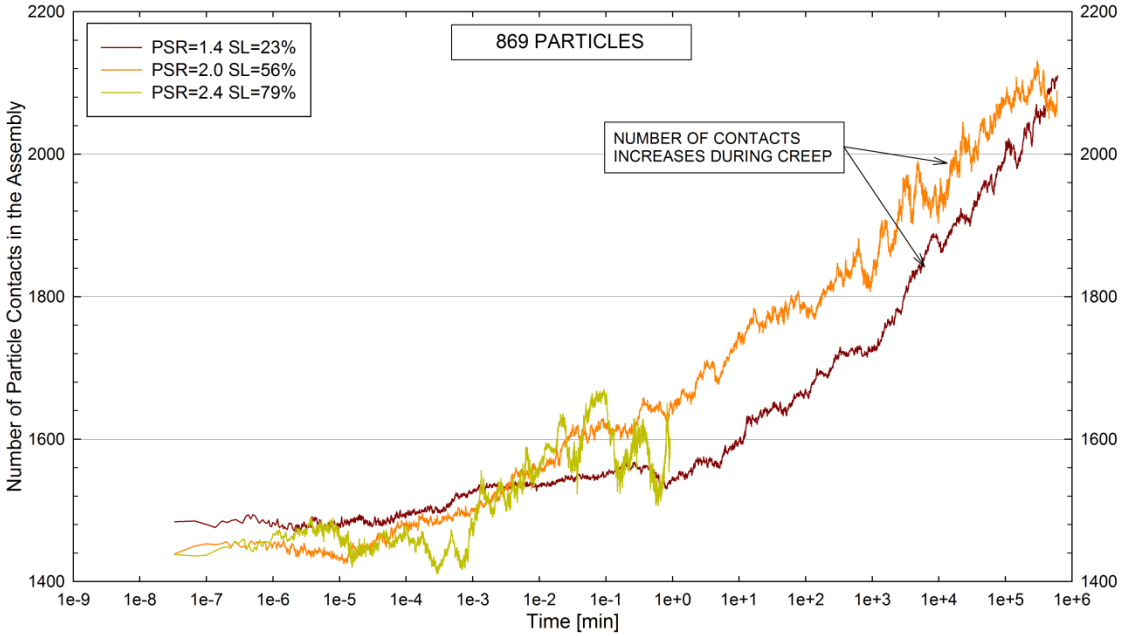

Fig. 7-53. Change in the number of particle contacts with time during creep. Loose filter sand.

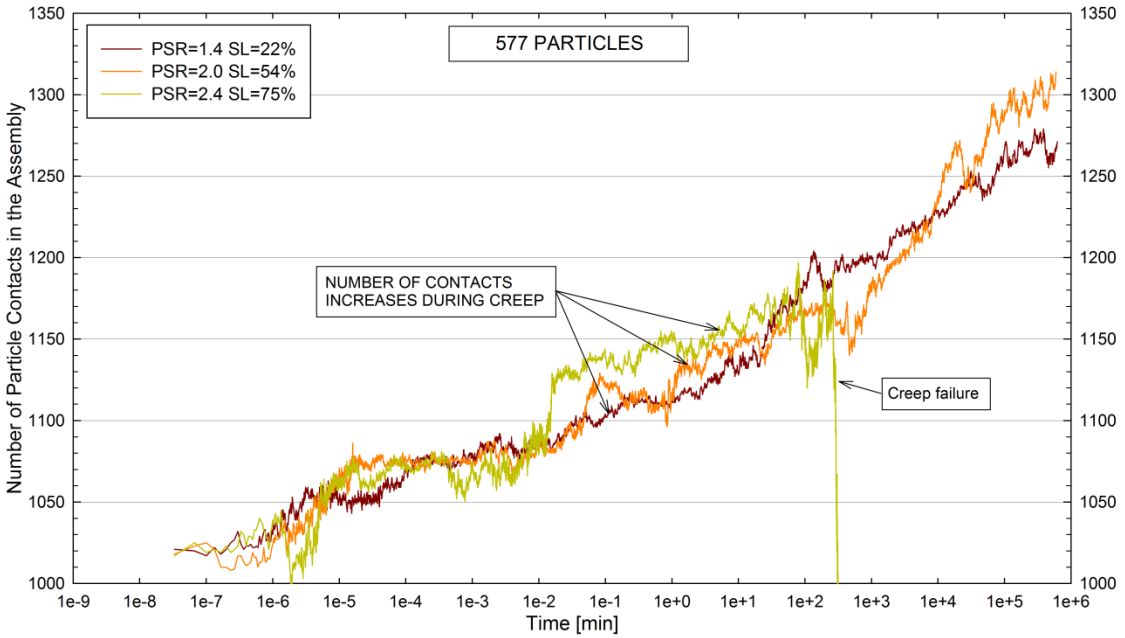

Fig. 7-54. Change in the number of particle contacts with time during creep. Glass beads.

The increase in the number of particle contacts observed in during the DEM simulations infers that the internal structure of the particle arrangement changes during creep. The rearrangement of the particle structure should also affect the way the grains

carry the applied stresses. Fig. 7-55 and Fig. 7-56 show the load distribution within the DFS and GB assemblies before and after 1.0E6 s of creep under a stress level of approximately 50%. The internal stress distribution is illustrated using load chains, where particle-to-particle contact forces are shown as red lines. The thickness of each line represents the magnitude of the respective force.

It is evident that the load chain configuration changes over time. That change ultimately produces a more uniform distribution of the stress within the assembly, which may account for the changes in macroscopic stiffness and dilatancy observed after creep. The homogenization of the stress distribution within the assembly is readily apparent in Fig. 7-56.

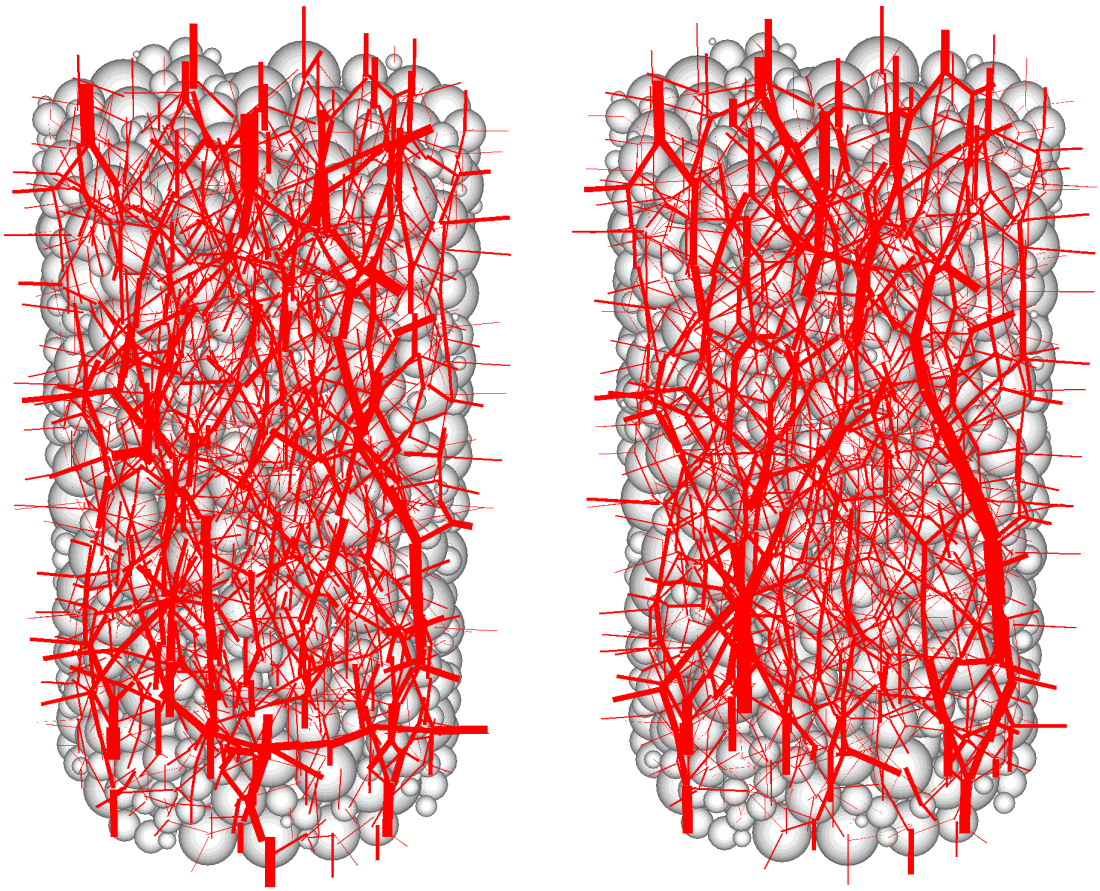

(a) (b)

Fig. 7-55. Load chain distribution for dense filter sand: (a) before, and (b) after 1.0E6 s of creep under a stress level of 48%.

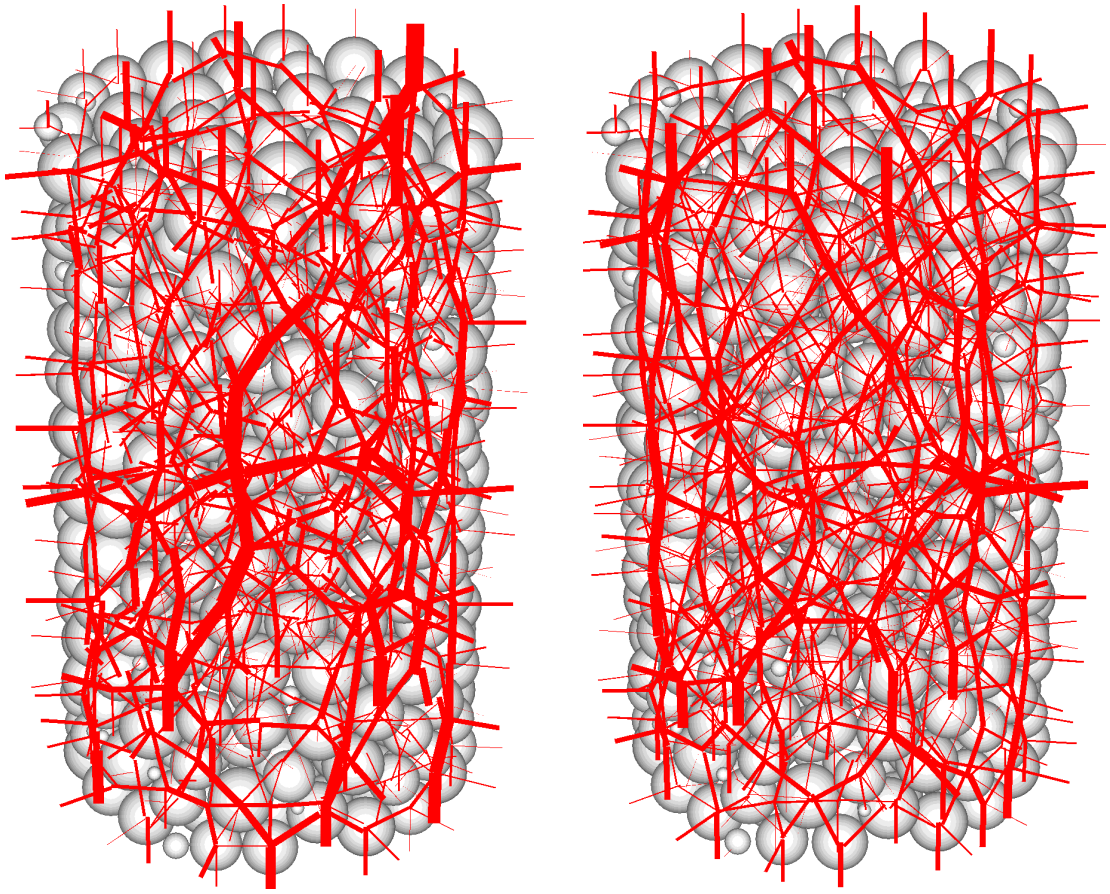

(a) (b)

Fig. 7-56. Load chain distribution for Glass beads: (a) before, and (b) after 1.0E6 s of creep under a stress level of 54%.

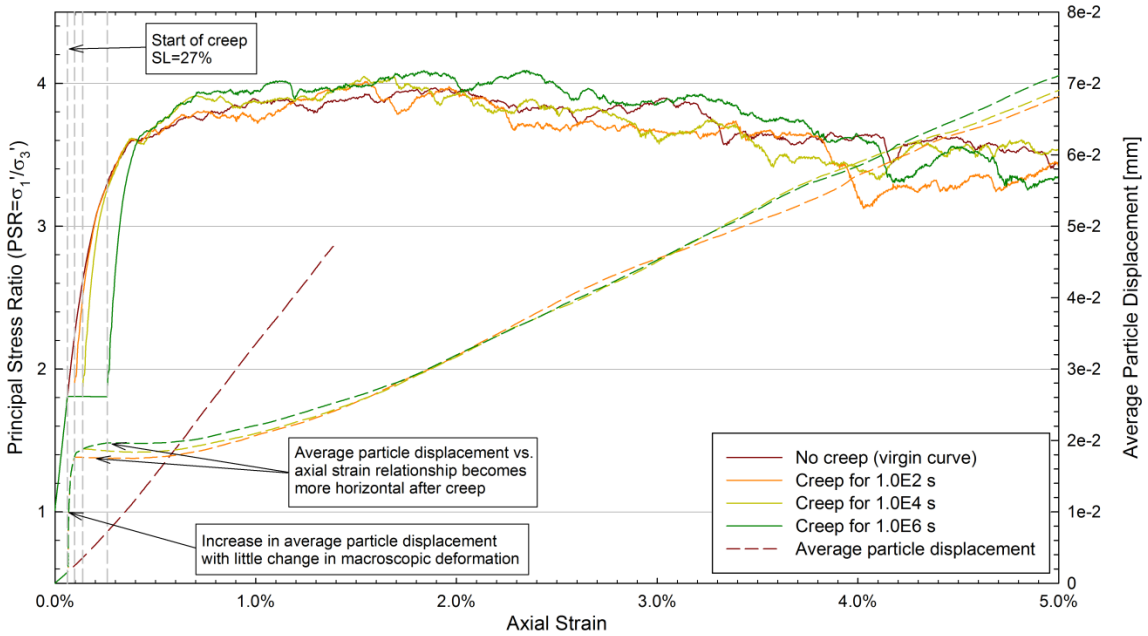

Fig. 7-57. Change in principal stress ratio and average particle displacement during shear for particle arrangements allowed to age from 0 to 1.0E6 s under a stress level of 27%. Dense filter sand.

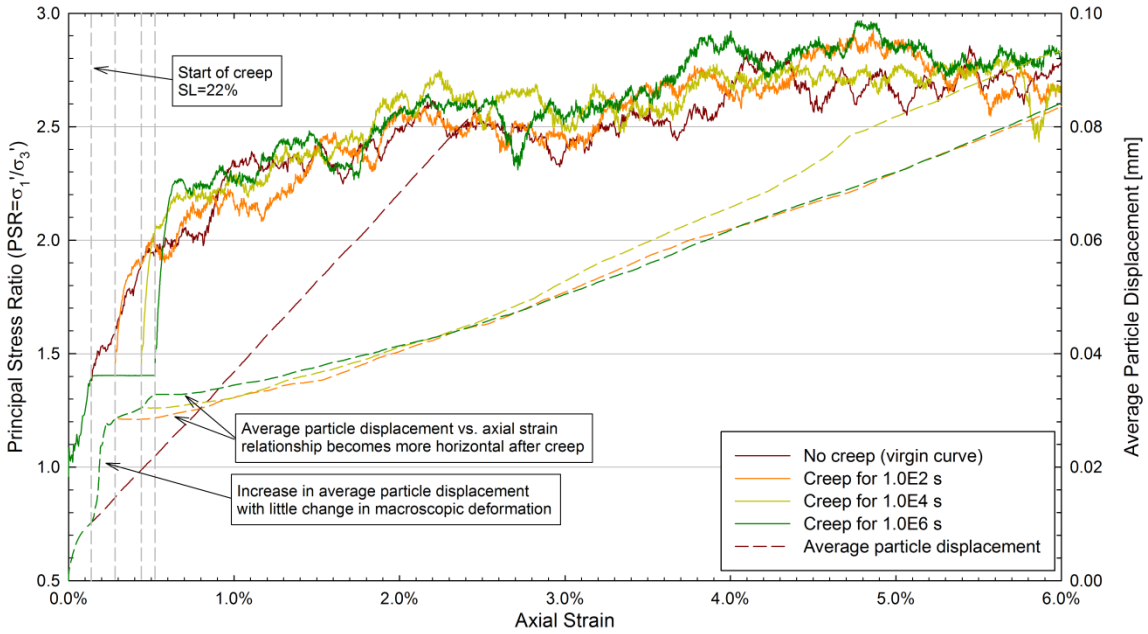

Fig. 7-58. Change in principal stress ratio and average particle displacement during shear for particle arrangements allowed to age from 0 to 1.0E6 s under a stress level of 22%. Glass beads.

The magnitude of the particle displacements taking place during DEM creep simulations can be compared to values measured during the micro-scale laboratory

experiments described in Chapter 3. Particle displacements were calculated using the particle positions just before the start of creep as reference. The change in average particle displacement and principal stress ratio with respect to the axial deformation for DFS and GB assemblies is shown in Fig. 7-57 and Fig. 7-58. The following behavioral trends can be inferred from the figures:

- Particles continue moving during creep, as indicated by the increase in average particle displacement during the creep stage.
- Particle movements during creep cause only small changes in macroscopic strain.
- The average particle displacement-axial deformation relationship becomes practically horizontal (very little particle movement with respect to macroscopic deformation) once shearing continues following the creep stage. The slope increases as shear progresses indicating increased particle displacements with further strain.

Similar observations were described in Chapter 4 based on results from AE analysis of creep during triaxial compression experiments. For that case, the cumulative AE count was being analyzed rather than the particle displacements. However, because particle crushing is not expected to play a significant role in the generation of AEs under the magnitudes of confining stress used (based on the values of B_r determined for the laboratory tests and the magnitude of the contact forces estimated from DEM simulations), the value of the cumulative AE count is primarily related to the particle-to-particle frictional sliding, and consequentially to the particle displacements. Therefore, it can be concluded that the results from DEM simulations described previously agree with

behavioral characteristics of sands measured during the laboratory experiments using AE techniques.

The inclination of the long-axis of the clumps with respect to the vertical axis was evaluated following a similar procedure to that described is Section 3.6.1. The frequency distribution of the long-axis inclination of the clumps calculated just before, and after 1.0E6 s of creep under a stress level of approximately 50% is shown in Fig. 7-59.

Results from micro-scale laboratory experiments presented in Chapter 3 found that the inclination of the long-axis of the particles became more homogeneously distributed in space during creep. A similar behavior was also observed by Bowman and Soga (2003) on samples of dense ($D_r \approx 74\%$) Leighton Buzzard sand aged under oedometric conditions. Results from DEM simulations only show homogenization of the long-axis inclination during creep for the dense filter sand assembly. In the LFS assembly the long-axes of the clumps tend become perpendicular to the direction of major principal stress.

7.3.3 Creep during One-Dimensional Compression

DEM simulations of creep were also conducted under oedometric conditions using the particle assemblies shown in Table 7-7. The procedure followed for creep simulations during 1D compression is similar to the method used to conduct creep simulations during triaxial compression (see Section 7.3.2). Each step is described below:

- A small isotropic confining stress 150 kPa is applied and the assembly is allowed to reach internal equilibrium.

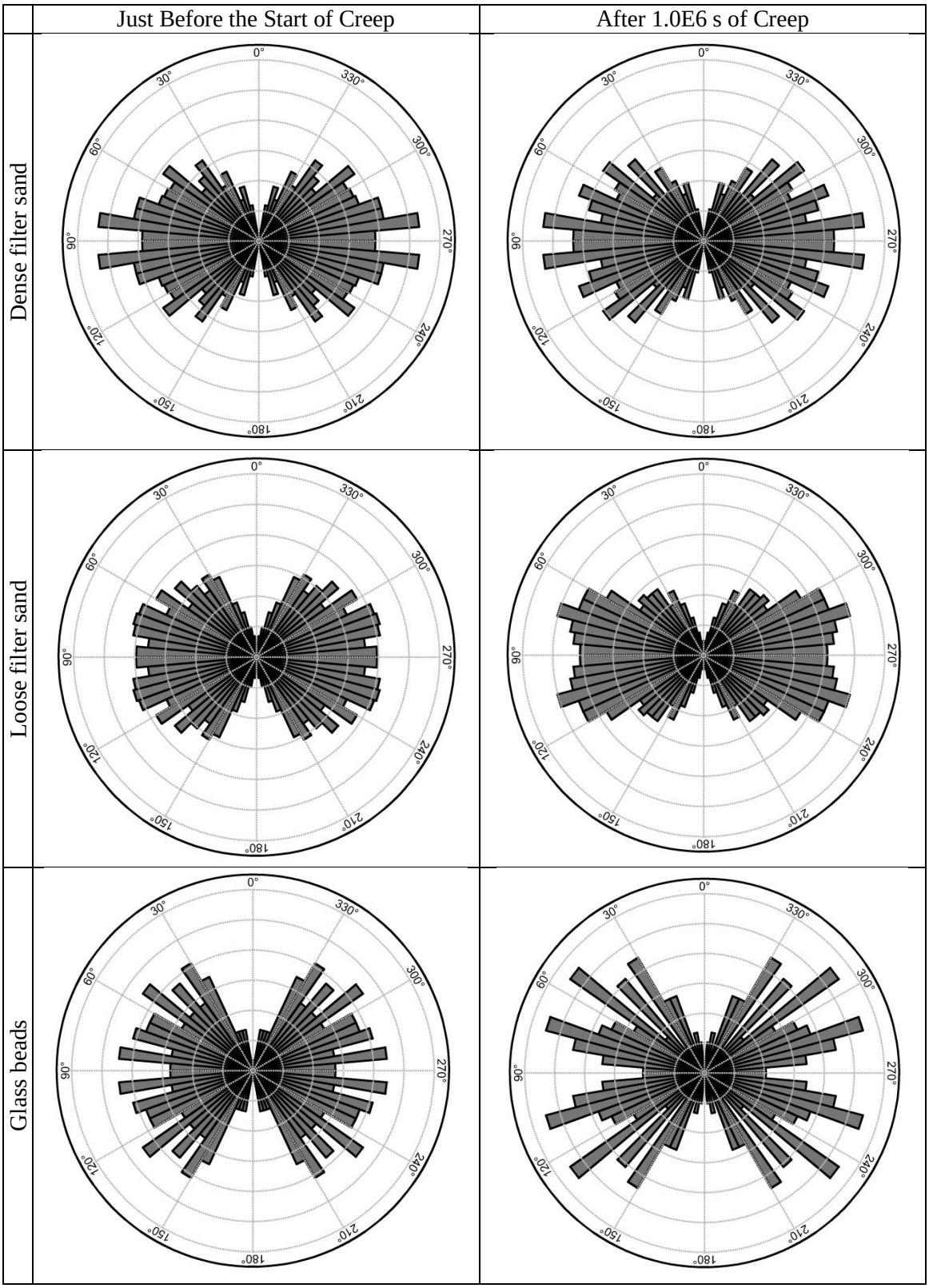

Fig. 7-59. Frequency distribution of long-axis inclination before, and after 1.0E6 s of creep under a stress level of approximately 50%.

- The contact mechanism which incorporates the RPT equation into the DEM model is activated. This contact model is kept inactive during previous steps to reduce the execution time.
- Lateral deformation is restrained; i.e., the velocity of the cylindrical, vertical, rigid wall is kept equal to zero.
- The top and bottom rigid walls are displaced at a constant velocity, deforming the assembly at a constant rate of vertical deformation. The velocity of the walls is assigned to achieve a vertical rate of strain of 1 min^{-1}.
- When a desired value of vertical stress is reached, the constant rate of strain 1D compression simulation is stopped and the assembly is allowed creep under constant vertical stress and zero lateral deformation.
- After creep, the vertical stress in increased and the constant rate of strain 1D compression simulation continues.

7.3.3.1 Magnitude of RPT Parameters

The magnitudes selected for the parameters of the RPT equation were the same as used during triaxial compression simulations. The respective values are shown in Table 7-8.

7.3.3.2 Description of the Simulation

Constant rate of strain 1D compression simulations were conducted using the DFS, LFS, and GB assemblies. During each simulation, the assemblies were allowed to creep under three different magnitudes of vertical stress (σ_v): (1) 340 kPa, (2) 680 kPa, and (3) 1360 kPa. These values of σ_v were selected to match the magnitudes used during

the 1D compression laboratory experiments described in Chapter 4. The assemblies were allowed to creep for up to 1.0E6 s under the corresponding vertical stress.

The variation in void ratio and at-rest pressure coefficient ($K_0=\sigma_h/\sigma_v$) with respect to the change in vertical stress during 1D compression simulations (without creep) conducted on DFS, LFS, and GB assemblies is shown in Fig. 7-60, Fig. 7-61, and Fig. 7-62. Note that the vertical strain calculated from DEM simulations is of the same order of magnitude as the deformations measured during laboratory experiments on specimens of sand under the same magnitudes of vertical stress.

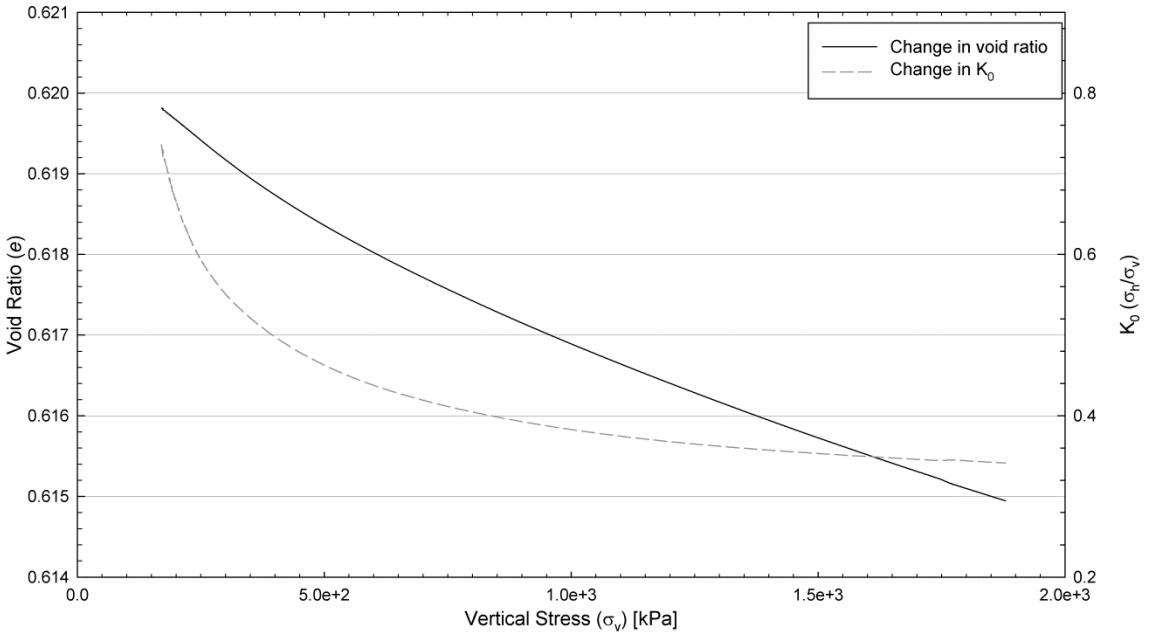

Fig. 7-60. Change in void ratio and at-rest pressure coefficient (K_0) with respect to the variation in vertical stress (σ_v). Dense filter sand.

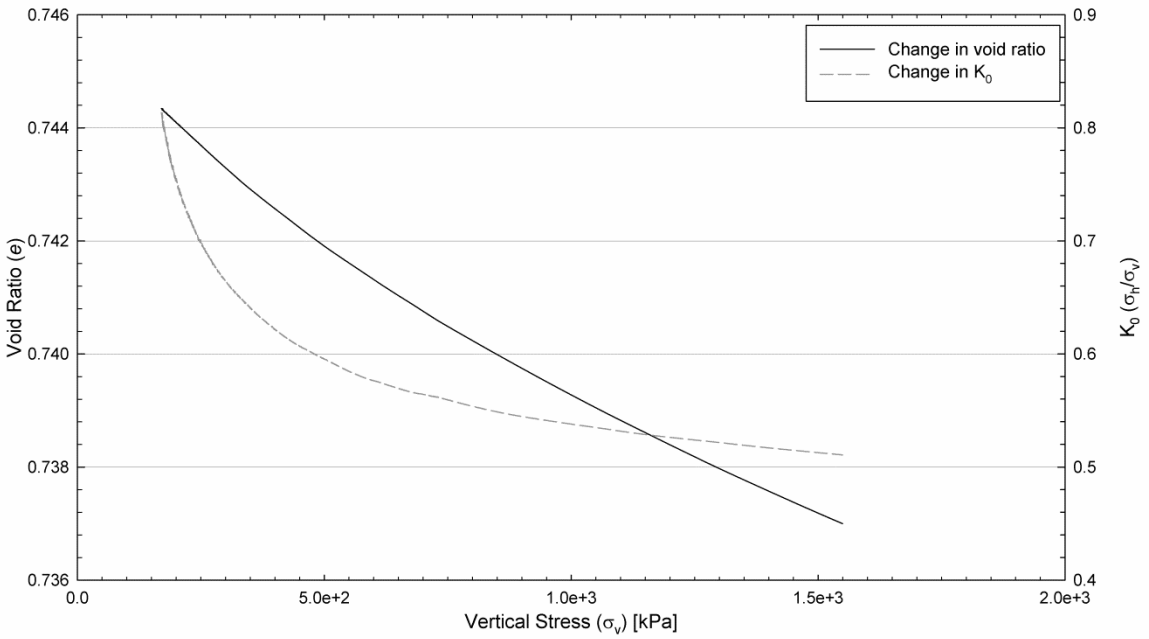

Fig. 7-61. Change in void ratio and at-rest pressure coefficient (K_0) with respect to the variation in vertical stress (σ_v). Loose filter sand.

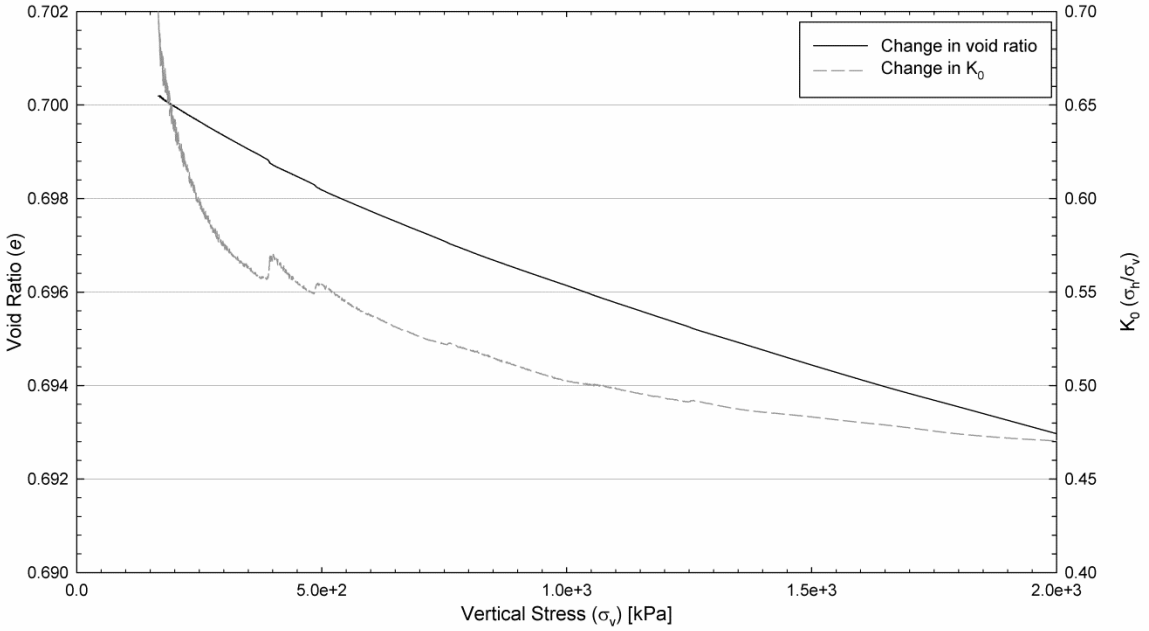

Fig. 7-62. Change in void ratio and at-rest pressure coefficient (K_0) with respect to the variation in vertical stress (σ_v). Glass beads.

Three creep stages were allowed during 1D compression simulations of DFS, LFS, and GB assemblies. For the first stage, the vertical stress was kept constant at 340 kPa, while for the second and third the magnitude of σ_v was kept at 680 and 1360 kPa.

The change in vertical strain calculated during each creep stage for the three different assemblies is shown in Fig. 7-63, Fig. 7-64, and Fig. 7-65.

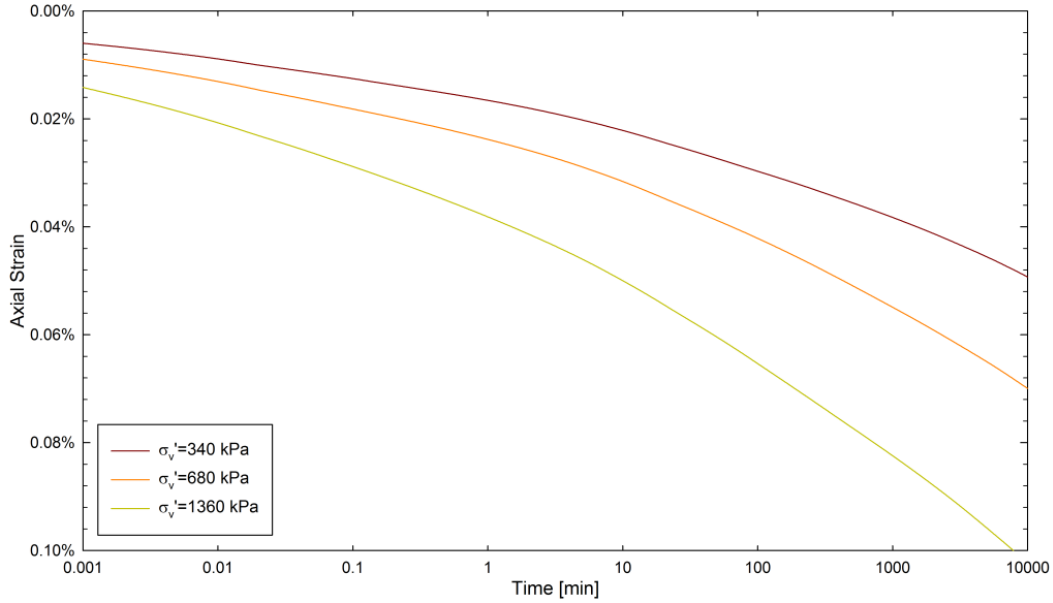

Fig. 7-63. Change in axial strain with time during creep. Dense filter sand.

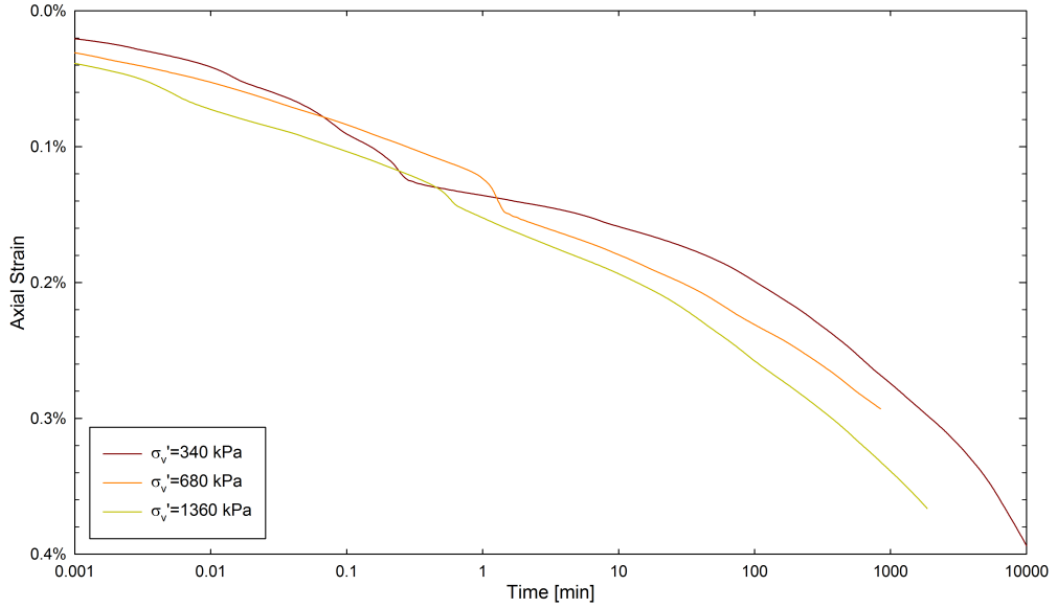

Fig. 7-64. Change in axial strain with time during creep. Loose filter sand.

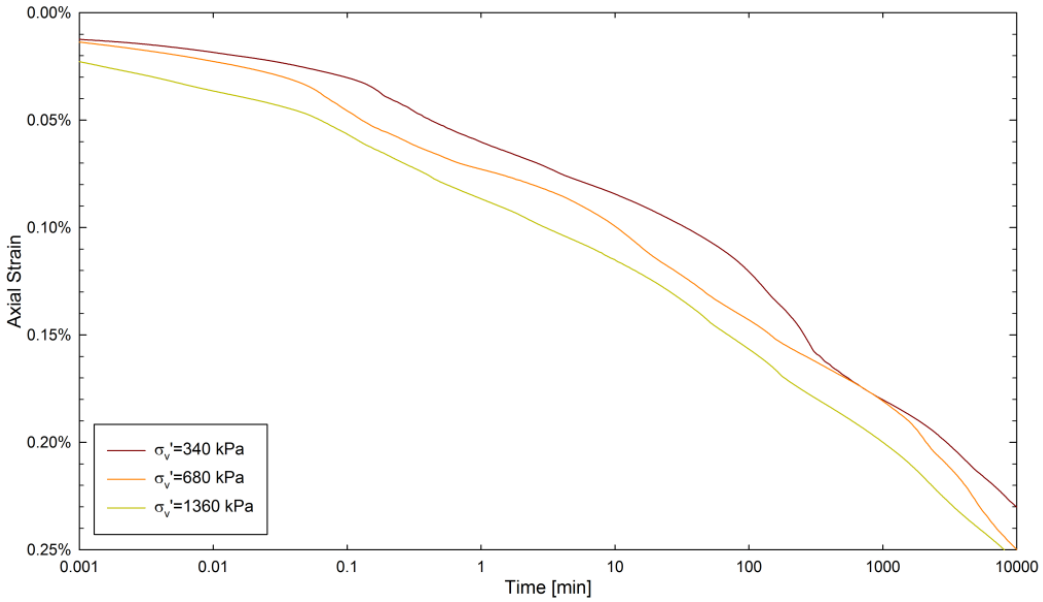

Fig. 7-65. Change in axial strain with time during creep. Glass beads.

7.3.3.3 Analysis of Results

The axial deformation calculated during the creep simulations is similar in magnitude to the deformation measured in the laboratory 1D compression experiments. However, the rate of deformation with respect to the logarithm of time during the DEM simulations was not constant throughout the test, and increased slightly with increasing time of creep for all the assemblies. This differs from laboratory experiment results, where the rate of deformation with respect to the logarithm of time of sand specimens was almost linear. The vertical deformation increased with increasing vertical stress during creep even though clumps did not break during any of the creep simulations.

The magnitude of the average normal and shear forces acting at the clump bonds was less than about 0.17 N during all the creep simulations. The maximum value was calculated during the creep simulation conducted on the LFS assembly under a vertical stress of 1360 kPa. The value of average normal and shear forces acting on the clumps' bonds is significantly less than the value required to achieve failure, which was estimated

based on single-particle crushing test (see Chapter 4). That indicates that particle crushing does not play an important role during creep under the magnitudes of stress being considered (less than 1400 kPa). A similar conclusion was attained from 1D compression laboratory experiments based on the magnitude of the Hardin's breakage factor (B_r). Consequentially, aging effects on the macroscopic properties of the assemblies observed during DEM simulations are related to changes in the internal structure of the assembly due to particle rearrangement and redistribution of the carried stresses rather than to breakage of the grains during creep. Note that the DEM simulation only considers particle failure and does take into account crushing of surface asperities, as described by Michalowski and Nadukuru (2012).

Fig. 7-66, Fig. 7-67, and Fig. 7-68 show the axial strain rate as a function of time for creep simulations under oedometric conditions. The strain rate increases with increasing σ_v, and decreases over time during creep. The change in the logarithm of the axial strain rate is linear with respect to the logarithm of time, and the slope is independent of the magnitude of vertical stress. This behavior is consistent with what is observed in most creep tests.

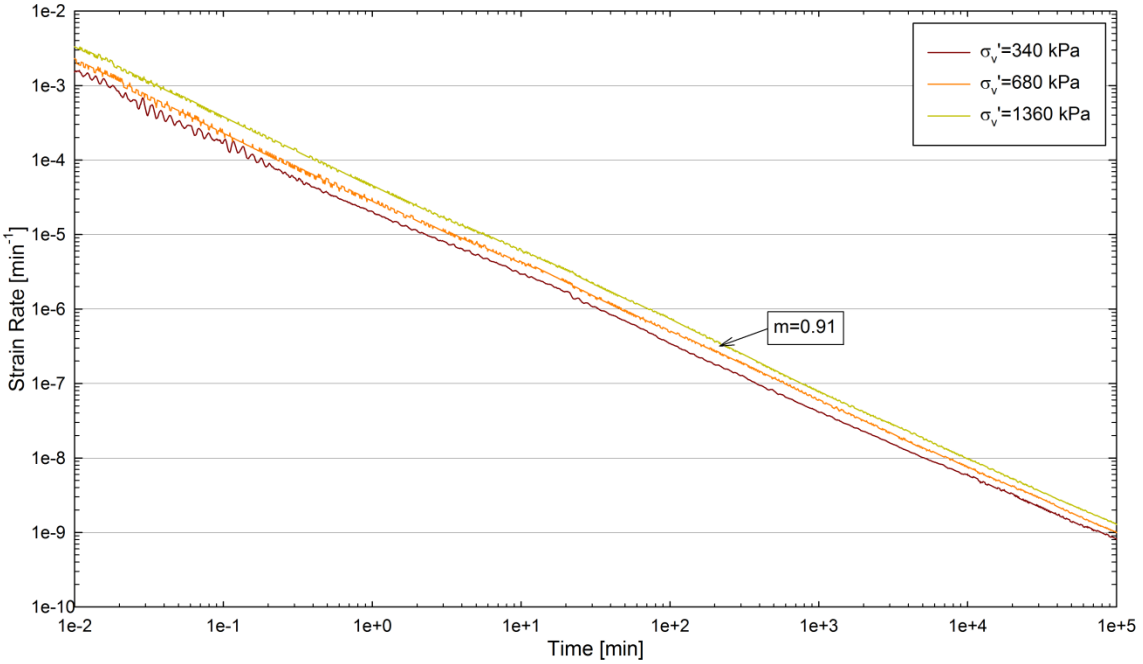

Fig. 7-66. Change in logarithm of axial strain rate against the logarithm of time during creep under oedometric conditions. Dense filter sand.

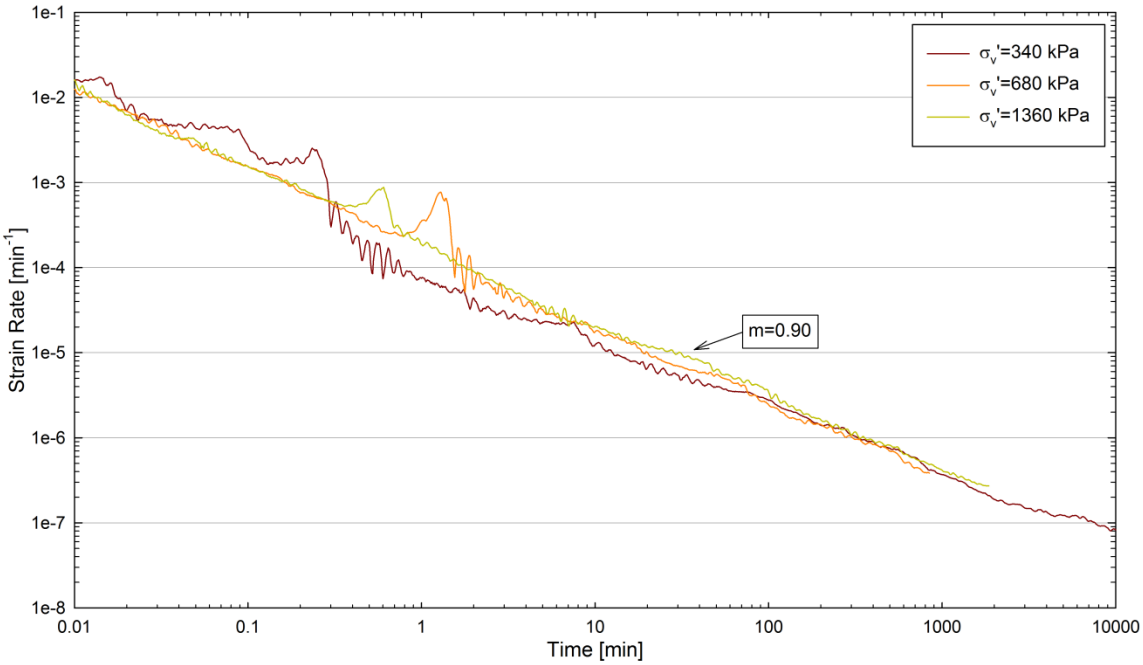

Fig. 7-67. Change in logarithm of axial strain rate against the logarithm of time during creep under oedometric conditions. Loose filter sand.

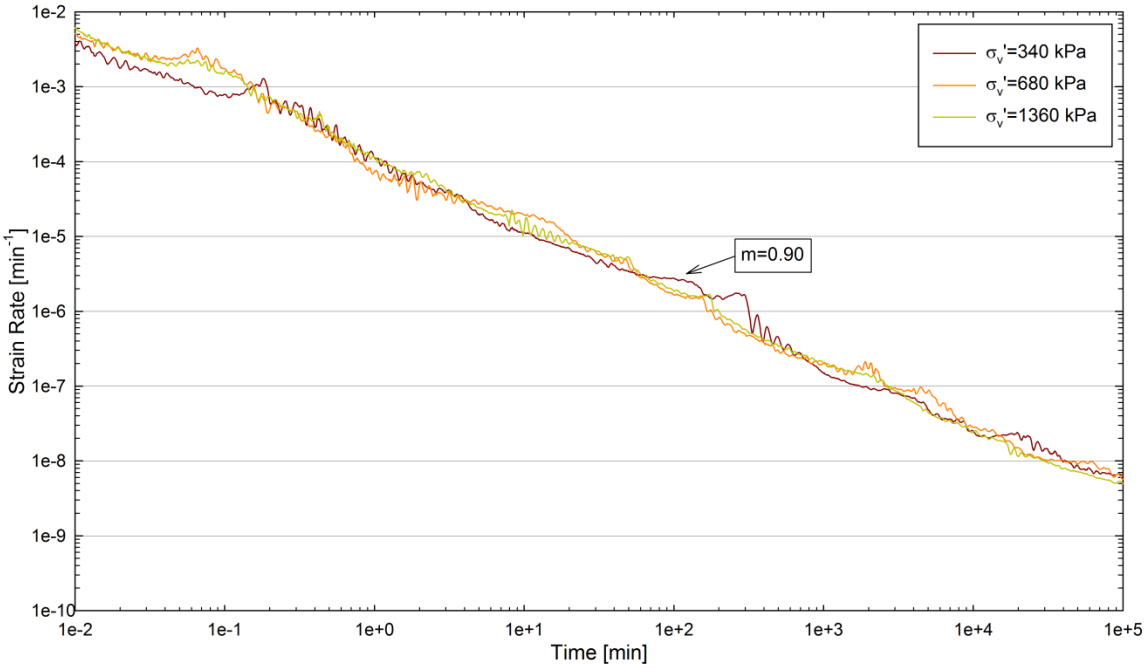

Fig. 7-68. Change in logarithm of axial strain rate against the logarithm of time during creep under oedometric conditions. Glass beads.

7.3.3.4 Aging Effects

Aging effects on the macroscopic properties of the assemblies were evaluated by increasing the magnitude of the vertical stress after creep. The change in void ratio and at-rest pressure coefficient ($K_0=\sigma_h/\sigma_v$) during the aging simulations of assemblies allowed to creep for 1.0E4 s under a vertical stress of 340, 680, and 1360 kPa is shown in Fig. 7-69, Fig. 7-70, and Fig. 7-71. The following characteristics are observed on results from DEM simulations of aging and creep under oedometric conditions:

- The horizontal stress increases over time during creep under constant vertical stress, as indicated by the increase in the magnitude of K_0.
- The constrained modulus of the assembly increases after creep.
- The K_0 versus vertical stress relationship of aged assemblies tends to rejoin the relationship shown by the virgin curve as σ_v increases after creep.

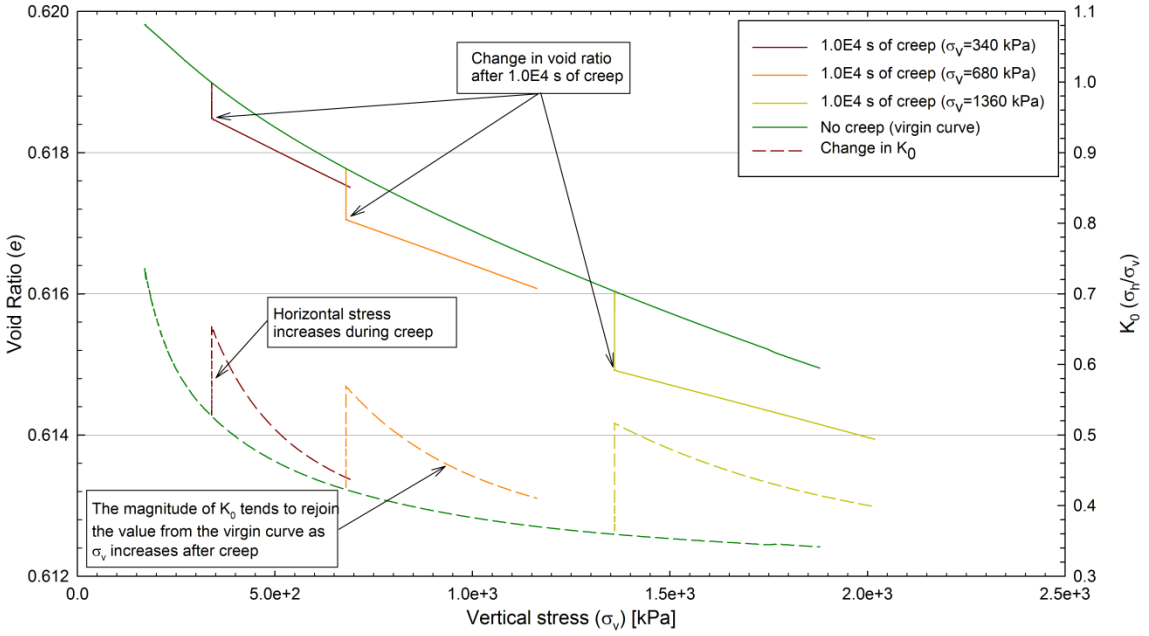

Fig. 7-69. Change in void ratio and K_0 with vertical stress during aging simulations. Dense filter sand.

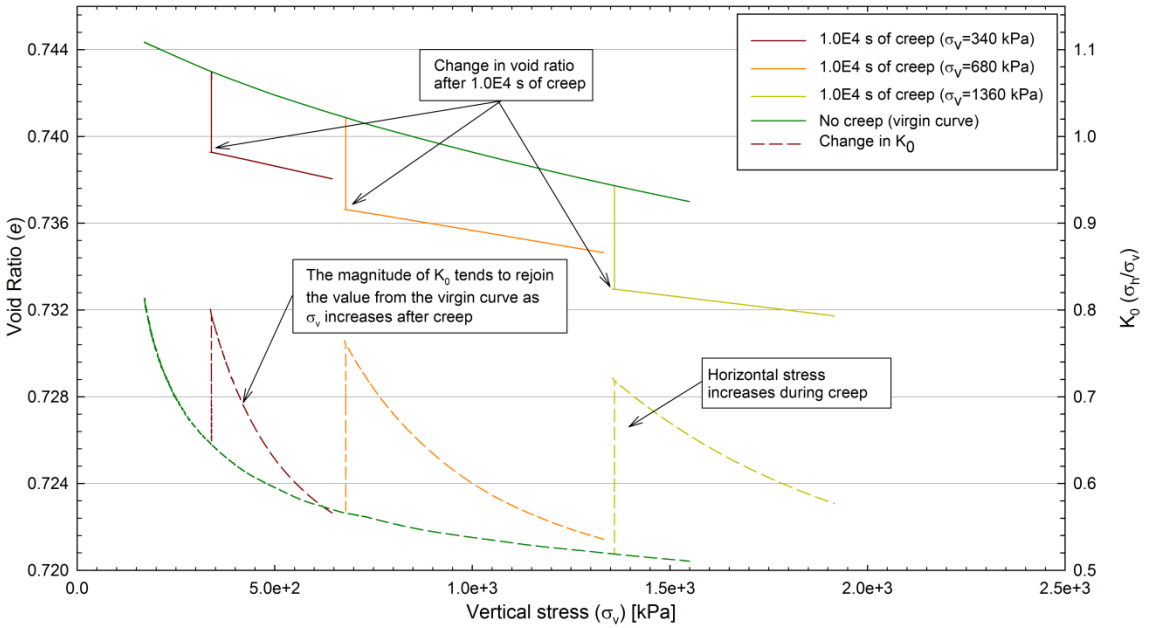

Fig. 7-70. Change in void ratio and K_0 with vertical stress during aging simulations. Loose filter sand.

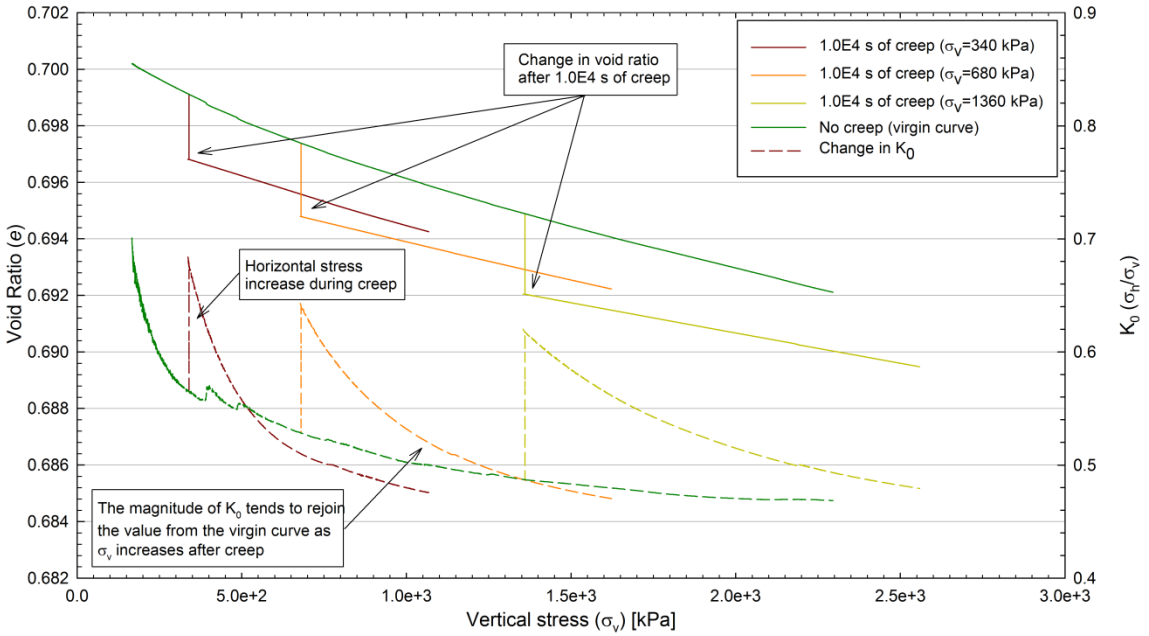

Fig. 7-71. Change in void ratio and K_0 with vertical stress during aging simulations. Glass beads.

Results from DEM creep simulations show very consistent patterns that agree with expected soil behavior. In addition, the figures indicate that continued deformation breaks down the structural changes that develop during creep and aging.

The change in the magnitude of K_0 during creep simulations conducted on DFS, LFS, and GB assemblies is shown in Fig. 7-72, Fig. 7-73, and Fig. 7-74. It is evident that the magnitude of the horizontal stress increases over time during creep, and magnitude of that change seems to be linear with respect to the logarithm of time.

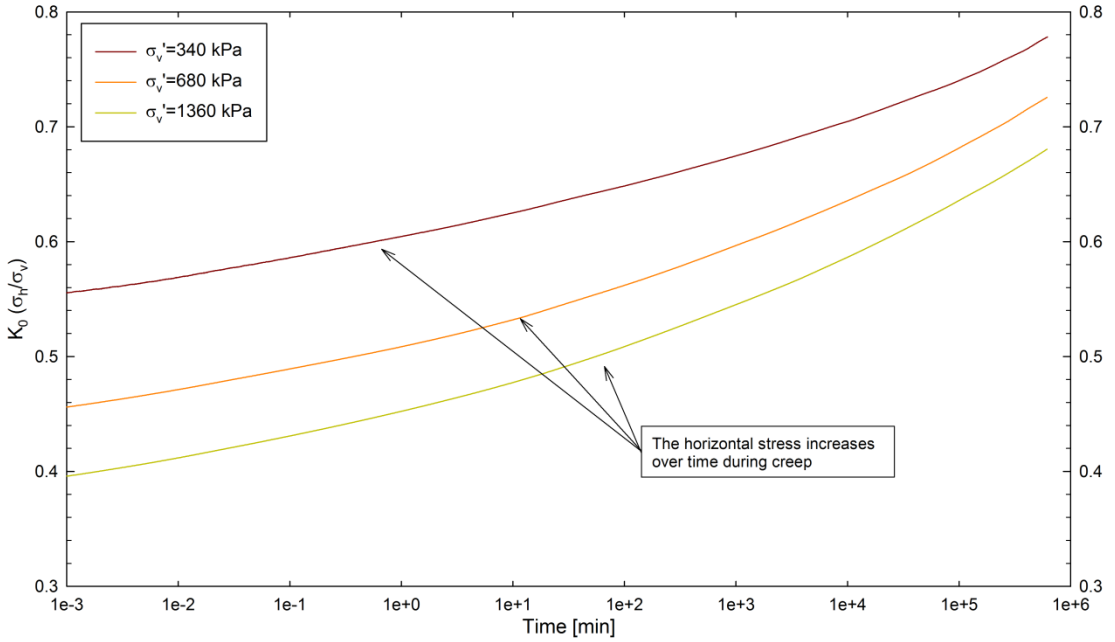

Fig. 7-72. Change in the magnitude of K_0 during creep. Dense filter sand.

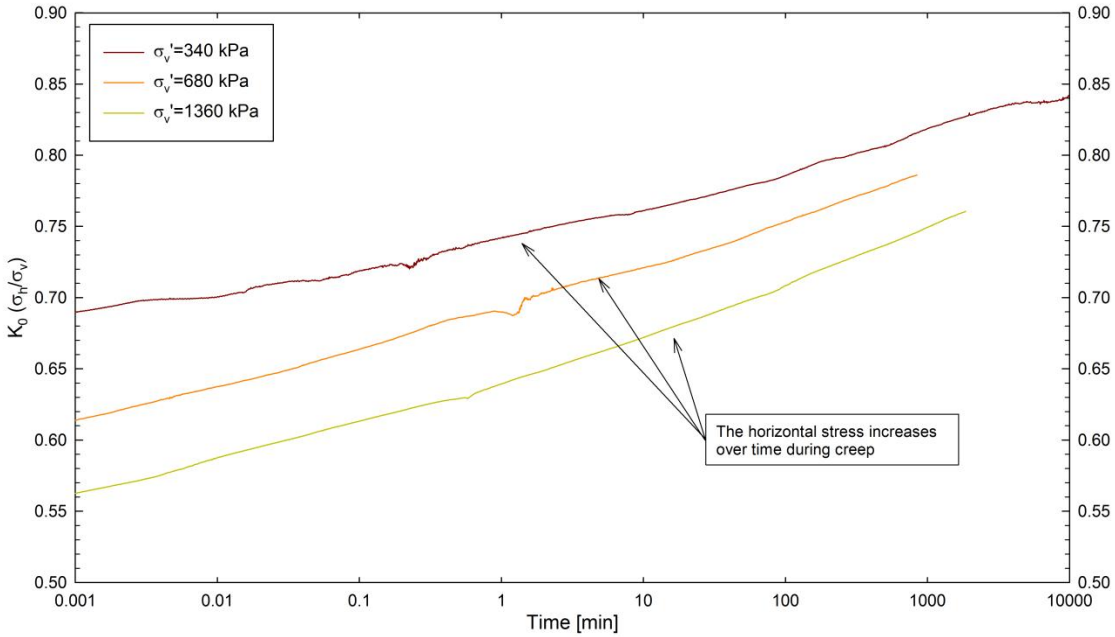

Fig. 7-73. Change in the magnitude of K_0 during creep. Loose filter sand.

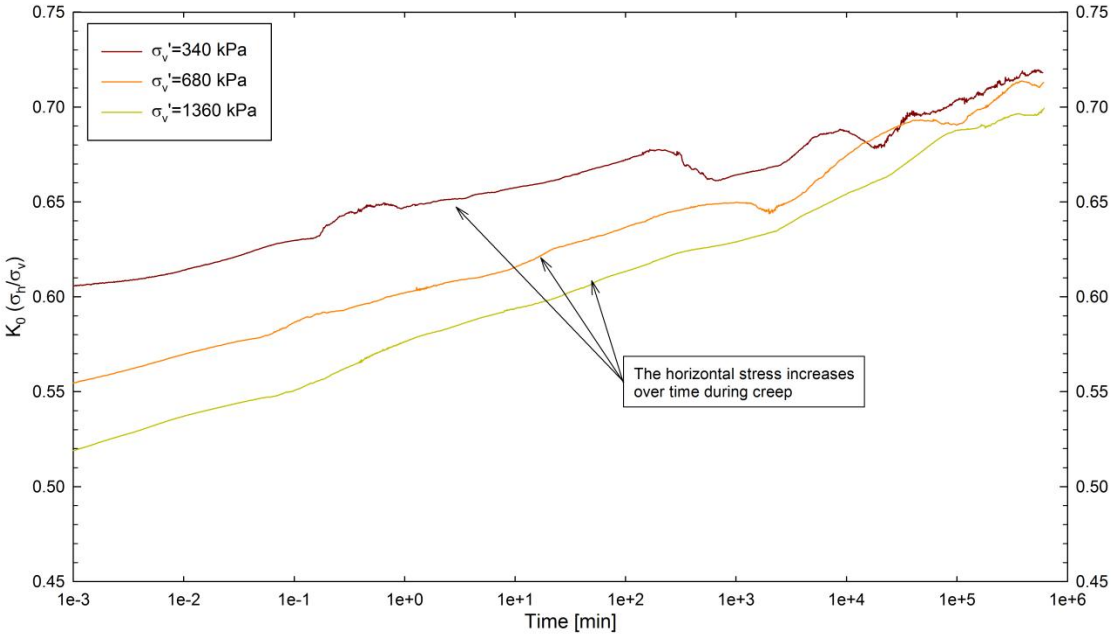

Fig. 7-74. Change in the magnitude of K_0 during creep. Glass beads.

The variation of the magnitude of horizontal stress during creep is presented in Fig. 7-75 as the ratio $\sigma_h/\sigma_{h\text{-}t=0}$, where $\sigma_{h\text{-}t=0}$ is the magnitude of the horizontal stress just before the start of the creep stage. The figure shows that the change in the magnitude of σ_h is greater for the DFS assembly than for the LFS and GB assemblies, and it increases with increasing vertical stress during creep. The change in horizontal stress during creep appears to be greater in assemblies formed by angular particles (e.g. DFS, and LFS assemblies) than in assemblies formed by spherical particles (e.g., GB assembly).

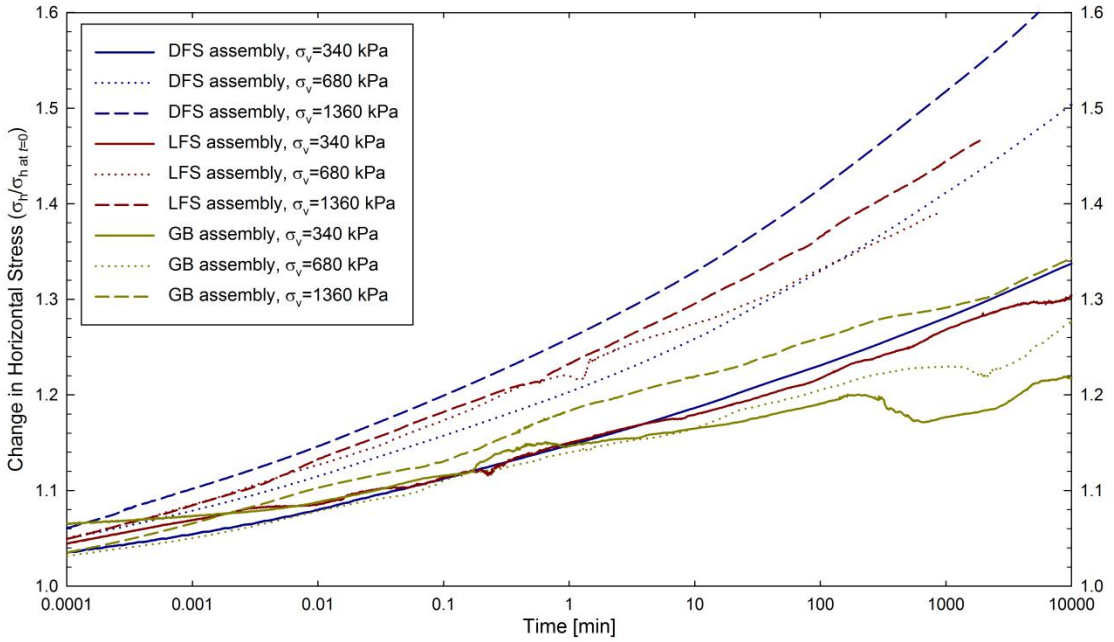

Fig. 7-75. Change in horizontal stress (σ_h) during creep with respect to the horizontal stress before creep ($\sigma_{h\ t=0}$).

The rate of change in horizontal stress during creep shown in Fig. 7-75 ranges from about a 2% increase per log-cycle of time for the GB assembly under low vertical stress (340 kPa), to about 7% per log-cycle of time for the DFS assembly under high vertical stress (1380 kPa).

The change in horizontal stress with time evidenced during the creep simulations would help explain the aging effects on granular soil evidences in the field and the laboratory discussed in Chapter 2. In particular, the increase in penetration resistance in granular soils observed during aging of sands reported by numerous investigators (Mitchell and Solymar 1984; Skempton 1986; Schmertmann 1991) could be a direct result of the increase in horizontal stress in sand beds over time.

In addition, aging simulations showed that the constrained modulus of the particle assembly changes after creep as compared with the magnitude determined for the virgin curve (see Fig. 7-69, Fig. 7-70, and Fig. 7-71). The magnitude of the constrained modulus

at 0.005% strain ($M_{0.005\%}$) determined for assemblies allowed to creep for 0, 100, and 10000 s is shown in Fig. 7-76, Fig. 7-77, and Fig. 7-78. Note that the magnitude of the constrained modulus increases with increasing time of creep.

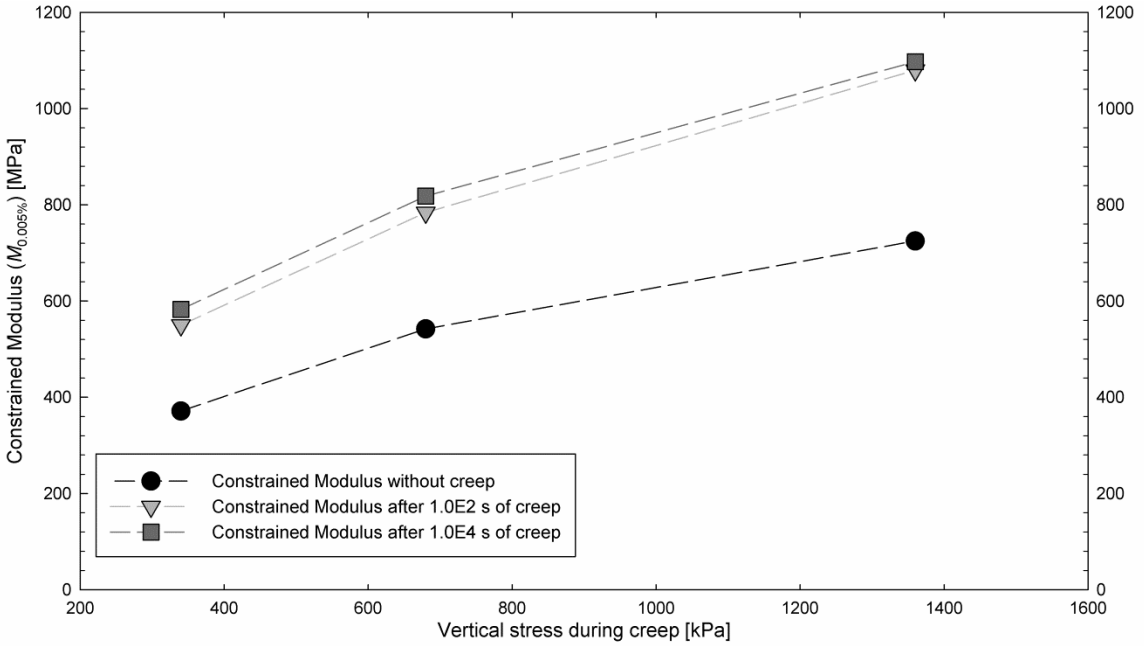

Fig. 7-76. Magnitude of small strain constrained modulus after 0, 100, and 10000 s of creep. Dense filter sand.

The analysis of changes occurring within the particle assembly during the DEM simulations provides indication of plausible causes which may account for the variation in horizontal stress and constrained modulus that take place during creep. The average particle displacement calculated based on the particle positions just before the start of the creep stage are shown in Fig. 7-79, Fig. 7-80, and Fig. 7-81.

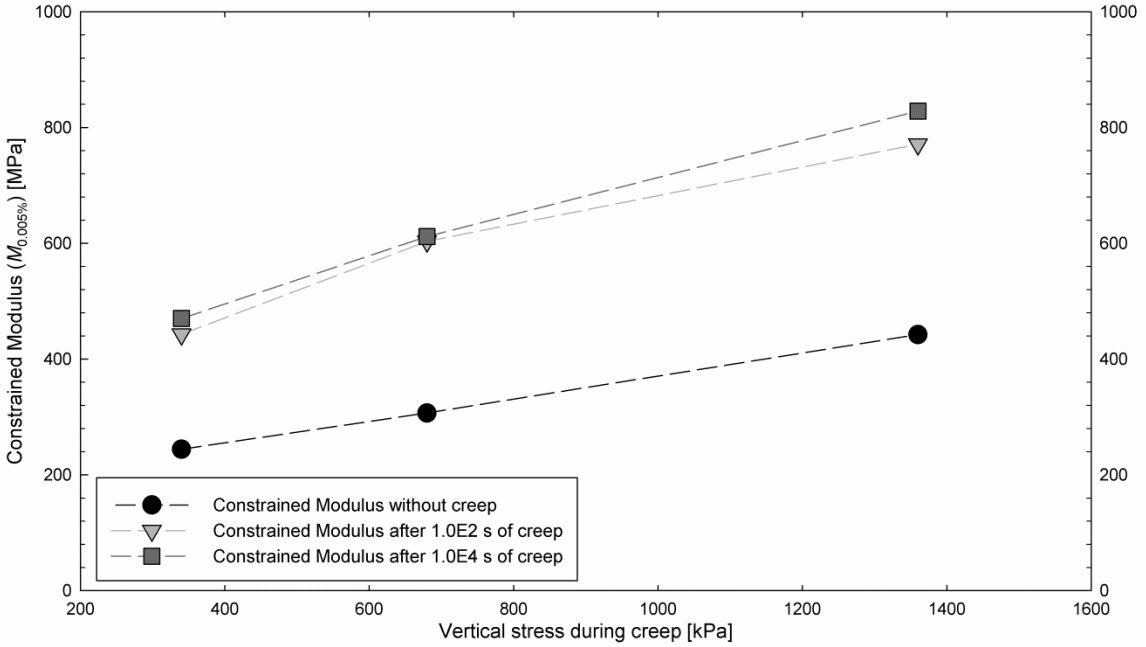

Fig. 7-77. Magnitude of small strain constrained modulus after 0, 100, and 10000 s of creep. Loose filter sand.

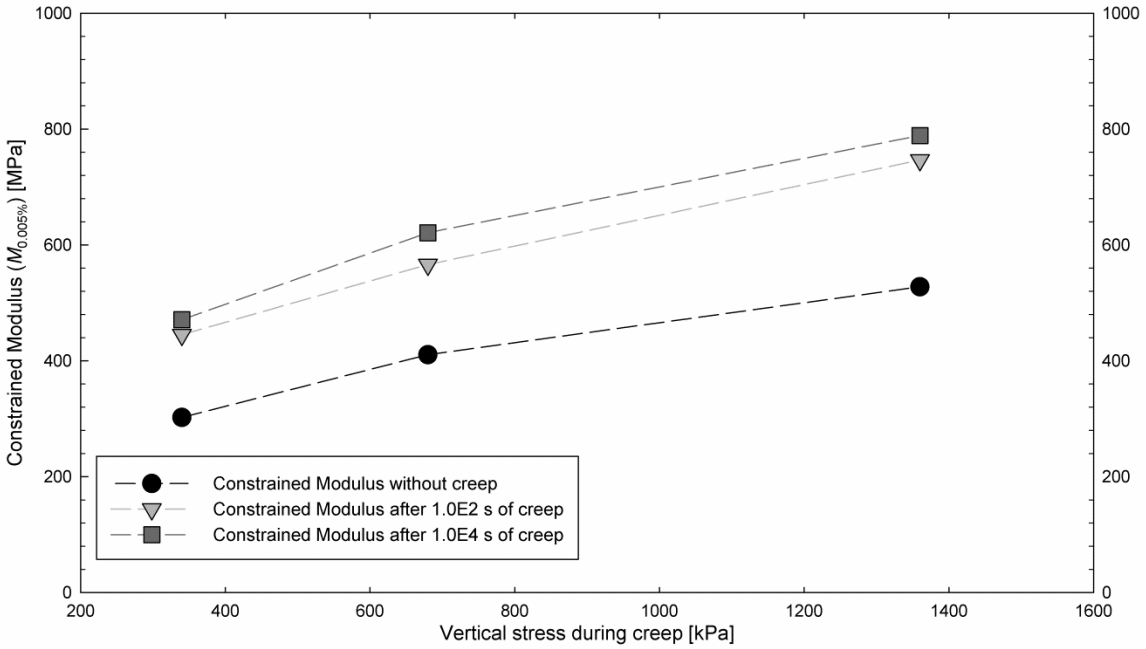

Fig. 7-78. Magnitude of small strain constrained modulus after 0, 100, and 10000 s of creep. Glass beads.

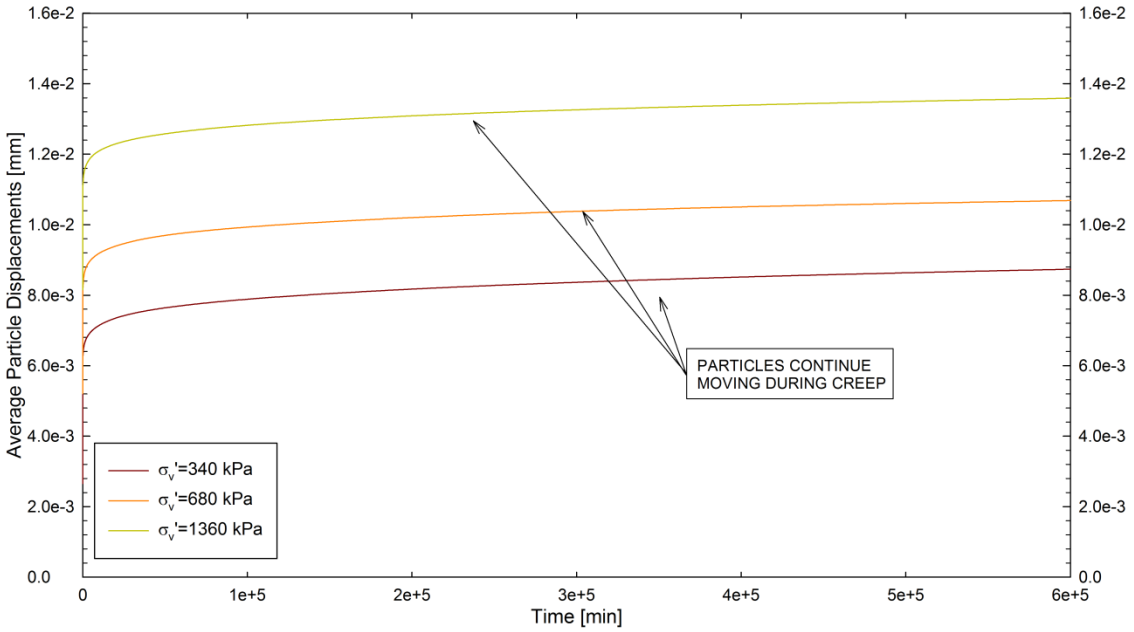

Fig. 7-79. Average particle displacement during creep. Dense filter sand.

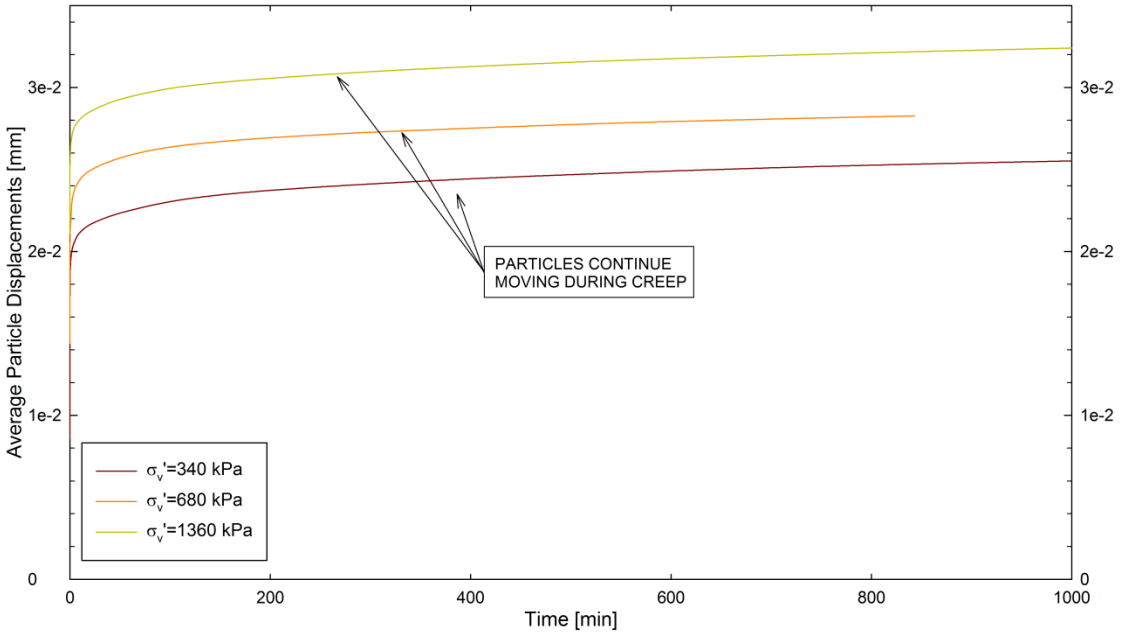

Fig. 7-80. Average particle displacement during creep. Loose filter sand.

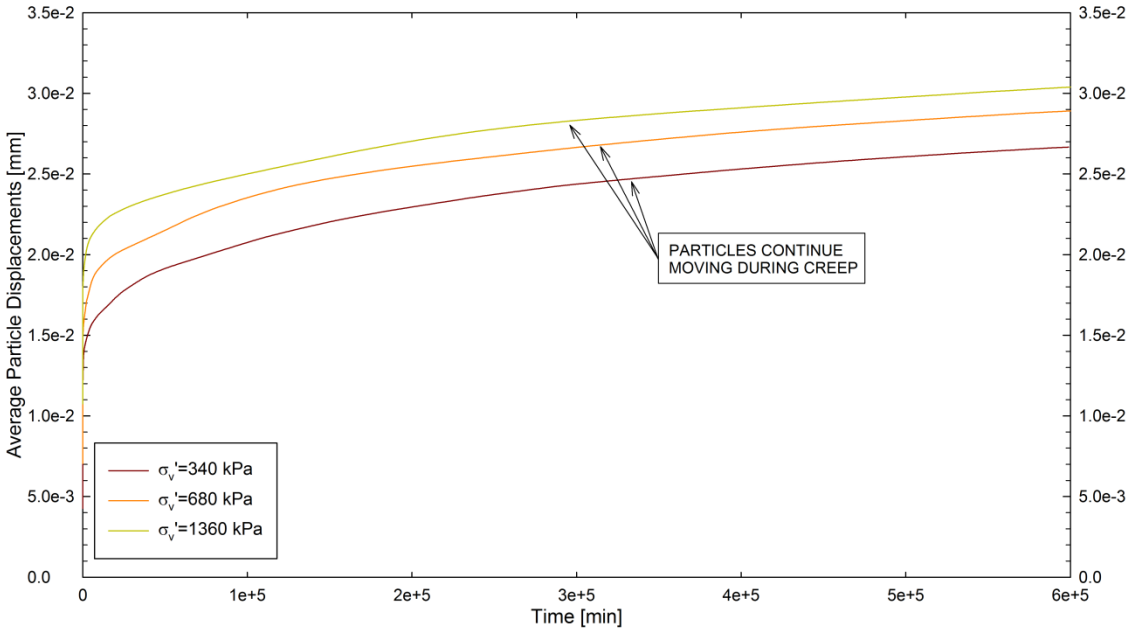

Fig. 7-81. Average particle displacement during creep. Glass beads.

The figures show that the magnitude of the particle displacements calculated during DEM creep simulations are in the same order of magnitude of values measured using X-Ray CT scanning during the 1D compression experiments described in Chapter 3 (see Table 3-3). The magnitude of the average particle displacement increases over time during creep, and particle movements are only reflected as small changes in macroscopic vertical deformation.

The number of particle contacts also changes over time. The change in the number of contacts in the assembly during creep is shown in Fig. 7-82, Fig. 7-83, and Fig. 7-84. The figures show that in the number of contacts increases over time in all of the assemblies. That behavior indicates that the internal structure of the assembly changes over time. More contacts make the assembly more stable and allow a more homogenous distribution of the carried load.

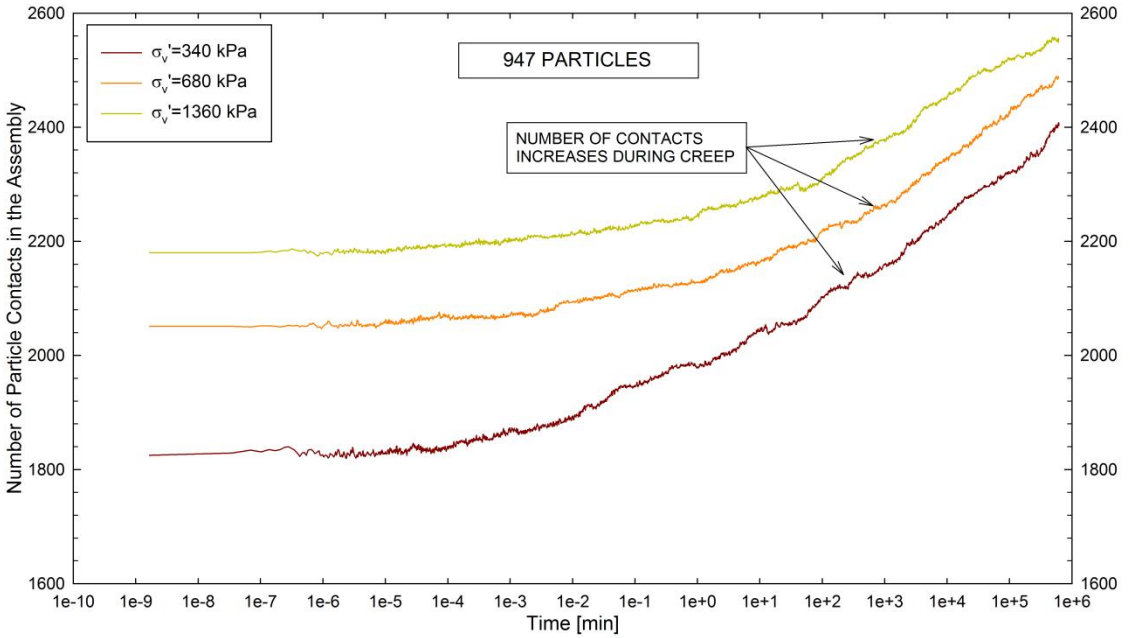

Fig. 7-82. Change in the amount of particle contacts during creep. Dense filter sand.

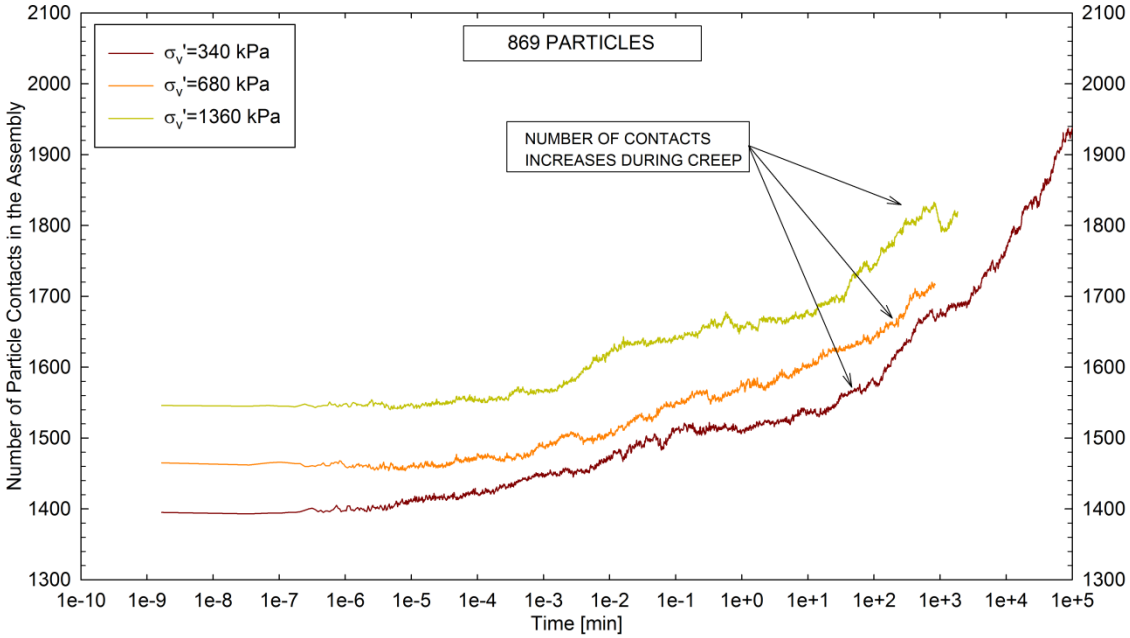

Fig. 7-83. Change in the amount of particle contacts during creep. Loose filter sand.

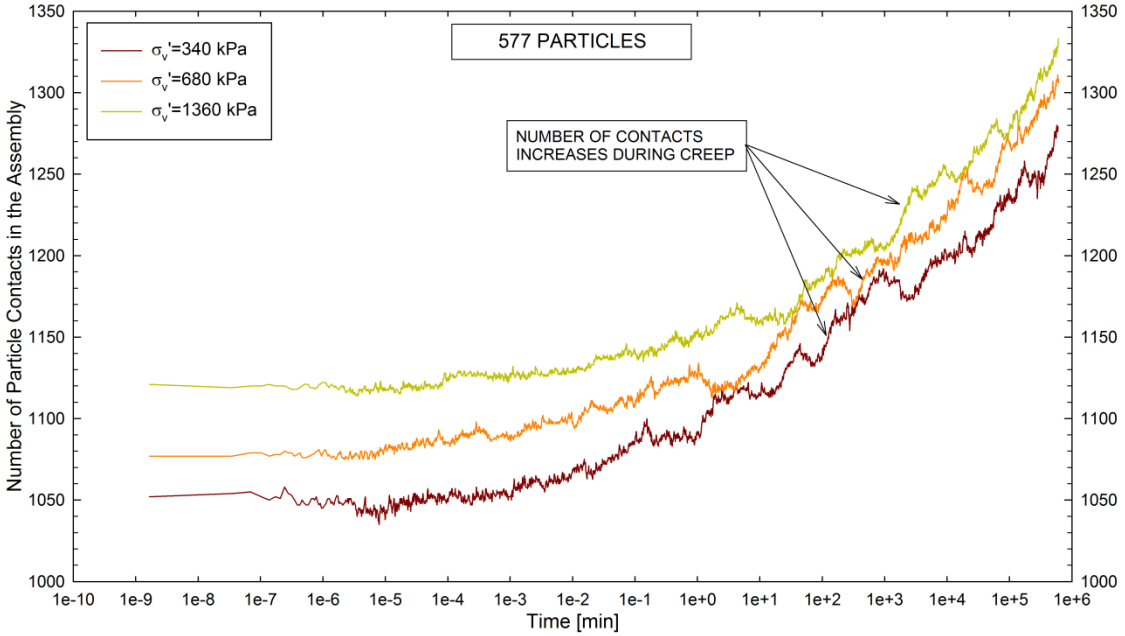

Fig. 7-84. Change in the amount of particle contacts during creep. Glass beads.

The stress distribution within the DFS particle assembly just before, and after 1.0E6 s of creep under oedometric conditions and a vertical stress of 1360 kPa is shown in Fig. 7-85. The figure shows the change in the load chain configuration taking place during creep, where the width of the red lines represents the magnitude of the contact forces. At the start of the creep stage the load is transferred though a close-to-vertical load chain configuration. As creep, progresses the load chain distribution becomes more homogeneous, as shown in Fig. 7-85(b). The homogeneous distribution of the stress within the assembly makes the structure more efficient at carrying the applied stresses, which would help explain the increase in constrained modulus observed after creep.

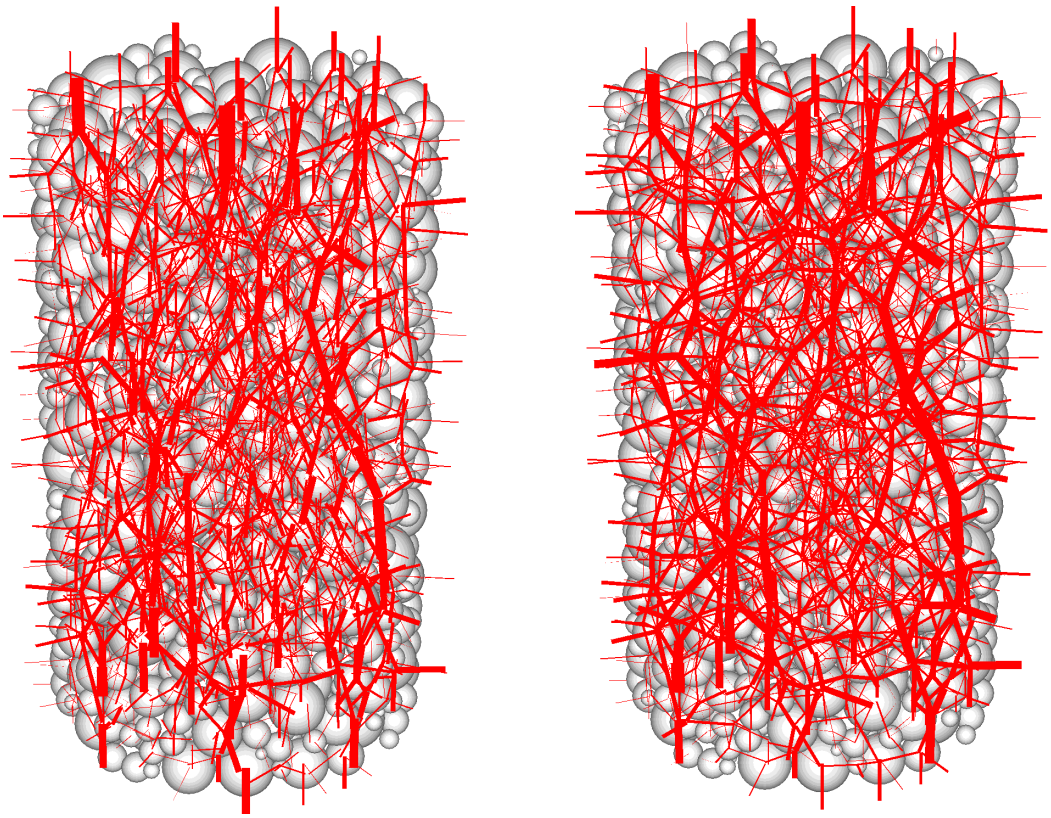

(a) (b)

Fig. 7-85. Load chain distribution for DFS assembly: (a) before, and (b) after 1.0E6 s of creep under oedometric conditions and a vertical stress of 1360 kPa.

The particles also rotate during creep. The frequency distribution of the long-axis inclination with respect to the vertical axis before and after 10000 s of creep is shown in Fig. 7-86. The figure indicates that particles continue moving during creep. For the LFS assembly, creep resulted in a more homogenously distributed long-axis orientation. Clumps did not exhibit a particular reorientation preference during creep simulations conducted using DFS and GB assemblies.

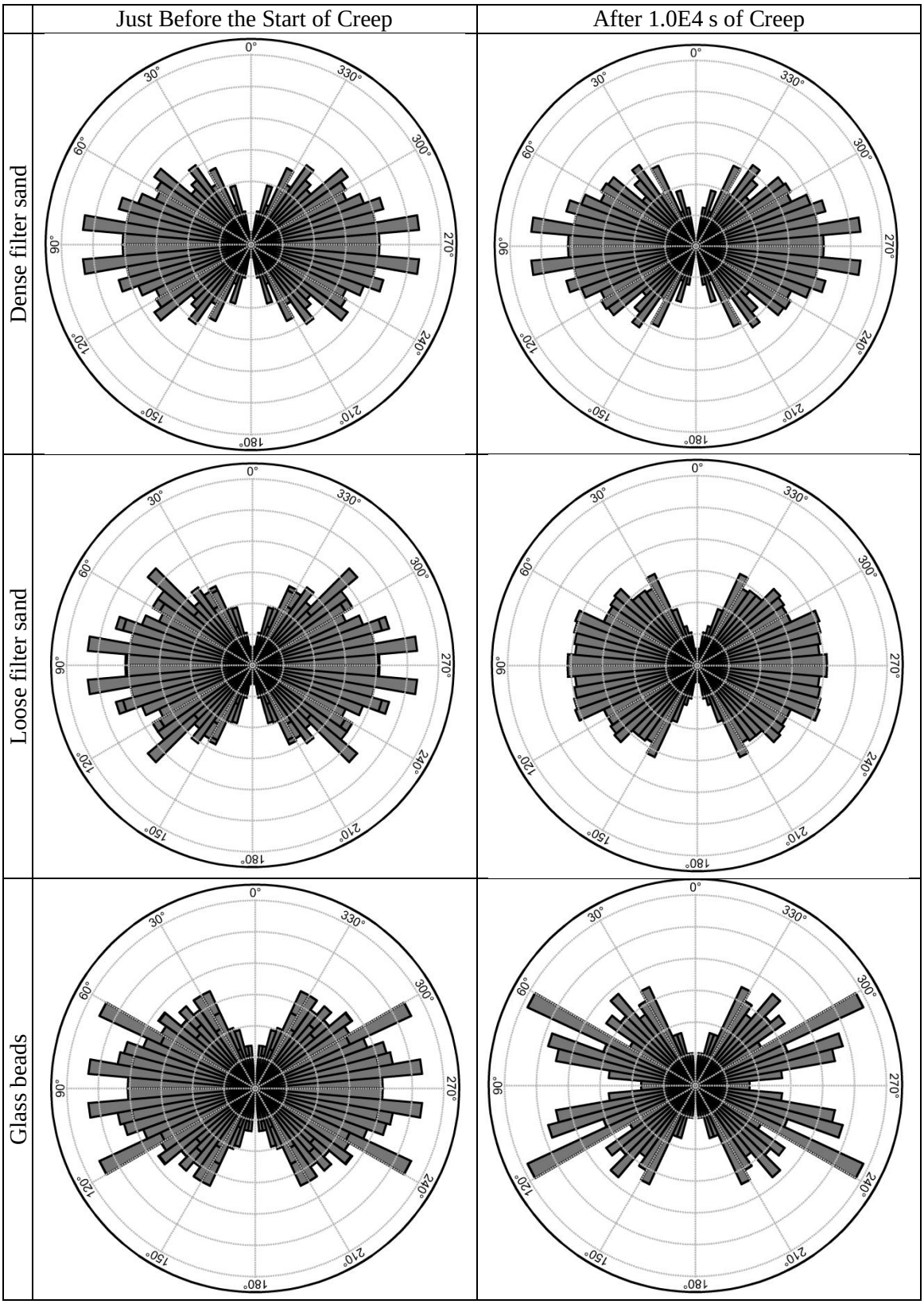

Fig. 7-86. Frequency distribution of long-axis inclination before, and after 1.0E4 s of creep under oedometric conditions and a vertical stress of 1360 kPa.

7.4 Conclusions

Creep and aging in granular materials were modeled with 2D and 3D DEM by the incorporation of a new contact mechanism which uses the RPT equation to model rate-dependent particle interactions. The analysis of the results from DEM creep simulations provides indication of the plausible driving mechanism of aging in sands. Some of the main conclusions are:

- The incorporation of the new contact mechanism, which uses the rate process theory to simulate rate-dependent particle interactions and the Hertz-Mindlin model to estimate inter-particle forces based on particle indentations, provides a macroscopic assembly behavior that resembles the results from laboratory creep experiments.
- The effect of the magnitudes of RPT parameters, such as the temperature, on the DEM creep simulations agrees with results from laboratory experiments reported by several investigators. For instance, higher temperatures cause an increase in axial deformation and axial strain rate during creep simulations, a behavior that was reported by Murayama (1969) (cited by Mitchell and Soga, 2005) during creep experiments on Osaka clay.
- Even though the sphericity of the particles was included in the model, the strength of the particle assemblies determined from DEM simulation was less than the strength measured during the laboratory experiments described in Chapter 4. A better representation of the shape of the sand grains can be achieved by using clumps formed by more particles. However, increasing the number of particles in a clump also increases the execution time of the simulations. Additionally, the

strength calculated from DEM simulations on the GB assembly, which is formed primarily by spherical particles, was less than the strength measured from laboratory experiments on glass beads. This indicates that DEM fails to describe other important particle characteristics or interactions besides the particle shape.

- The change in volumetric strain during DEM simulations of creep under constant vertical and horizontal stresses showed a similar behavior to that observed during laboratory experiments, where dense, angular materials tend to dilate during creep, while loose spherical materials tend to compress during creep. Behavioral characteristics of sands and clays during creep, such as the linear relationship between the logarithm of the axial strain rate and the logarithm of time, were also reproduced using DEM. This leads to conclude that DEM simulations with the incorporation of the RPT equation can be used to represent the general behavior of granular materials during creep and aging.
- DEM simulations of creep during triaxial compression show that aging produces a change in in the macroscopic stiffness of the assembly. The Young's modulus of the assembly increases with increasing time of creep and increasing stress level during creep. In addition, the stress-strain relationship of aged assemblies tends to rejoin the stress-strain relationship of the virgin curve once shear continues following a creep stage. These observations agree with the behavior of specimens of sand during the laboratory experiments described in Chapter 4. The magnitude of the increase in secant Young's modulus at 0.005% strain ($E_{0.005\%}$) ranged from about 10% per log-cycle of time for the DFS assembly under a stress level of

27%, to about 100% per log-cycle of time for the LFS assembly under a stress level of 56%.

- Results from creep simulations during 1D compression showed that the horizontal stress and the constrained modulus of the assembly increase over time during creep. The increase in the magnitude of the horizontal stress is almost linear with respect to the logarithm of time and is greater in dense assemblies formed by angular particles under a high vertical stress. The increase in σ_h during the DEM creep simulations ranged from about 2% to 7% per log-cycle of time.
- Particle crushing does not seem to play a significant role during creep under the magnitudes of stress being considered (less than 1400 kPa). It appears that particle rotations and rearrangement of the soil structure during creep is a more suitable driving mechanism of aging. This investigation only considered crushing of the grains, similar to driving mechanism of aging proposed by Lade et al. (2010). Recently, the author became aware of a new driving mechanism of aging proposed by Michalowski and Nadukuru (2012), involving crushing of surface asperities during creep. The DEM models developed during this investigation do not account for this mechanism, and the results from the simulations cannot support or reject this theory. However, DEM simulations do show that particle rearrangement may cause some of the changes in macroscopic properties of sands evidenced under laboratory and field conditions.
- The variation in macroscopic properties of the assembly observed after creep is likely caused by the rearrangement of particles and the redistribution of the stress within the arrangement. DEM simulations showed that the magnitude of the

normal and tangential contact forces decreases over time. This behavior is explained by the increase in the number of particle contacts observed during creep. As the number of contacts increases, the load carried by each particle decreases. A more homogeneous distribution of the load and a greater number of particle contacts produces a more structurally stable fabric, which accounts for the increase in macroscopic stiffness.

- The reduction of the slope of the average particle displacement versus axial strain relationship observed once the assembly is sheared after the creep stage is evidence of the structuration taking place within the particle arrangement during creep. A reduction of the particle displacement-axial strain slope indicates that the particles have to move less to support the same load. Low magnitudes for the average particle displacement-axial strain slope are observed during the initial stages of shear, where the assembly has only been subjected to a small axial deformation and exhibits a greater macroscopic stiffness. A similar behavior was observed using AE techniques during creep laboratory experiments.
- The calculation of the long-axis inclination of the clumps before and after creep indicates that some particles rotate over time. It is not clear if particles have a particular reorientation preference during creep.

Chapter 8

Summary and Conclusions

The main objective of this research is to determine the causes of aging in granular materials and to study factors that influence its effect on macroscopic properties of granular soils. Driving mechanisms proposed by numerous investigators were evaluated. It was found that mechanical processes at the particle level were the most plausible cause of the changes in engineering soil properties of sands evidenced in the field and in the laboratory. Changes in the internal structure and macroscopic properties of granular materials during creep were evaluated using laboratory experiments and computer simulations. The effects of factors such as the grain sphericity, initial relative density, the magnitude of external stresses, stress anisotropy, and time of creep were analyzed. The main conclusions from this investigation are summarized in this chapter.

8.1 Summary of Work Accomplished

A summary of the work accomplished during this investigation is given below:

1. A literature review was conducted to establish theories postulated to account for aging in granular soils.
2. Available data on changes in macroscopic properties of sands reported during field studies or laboratory experiments were compiled and analyzed. General trends of variation in engineering soil properties (e.g., penetration resistance, stiffness, liquefaction resistance) with time during aging were generated.
3. Micro-scale laboratory experiments including X-Ray computed tomography (CT scanning) scanning and acoustic emission (AE) analysis were implemented to study changes in the internal structure of specimens of sand during creep.
4. Macro-scale laboratory experiments were conducted on specimens of sand and glass beads to study changes in macroscopic properties, such as small-strain stiffness, dilatancy, and constrained modulus, during aging. The effect of factors, including the stress anisotropy, initial relative density, and time of creep, were evaluated.
5. Advantages and limitations of the discrete element method (DEM) were analyzed. The applicability of DEM as an aid for solving geotechnical engineering problems was assessed.
6. A new contact mechanism was developed to model creep and aging using DEM. This model uses the rate process theory (RPT) to simulate time-dependent particle interactions and the Hertz-Mindlin model to estimate inter-particle contact forces based on particle indentations.

7. A literature review was conducted to collect and summarize values for the RPT parameters reported by numerous investigators.
8. A parametric study was performed to study the effect of variations in the magnitude of the RPT parameters on the results from DEM simulations.
9. A method for generating three-dimensional particle assemblies that resemble the particle shapes and initial void ratio of sand specimens was developed.
10. DEM creep simulations during triaxial and one-dimensional compression were conducted using three-dimensional particle assemblies. Results were compared with data obtained from laboratory experiments.
11. The proposed driving mechanisms of aging were assessed based on the results from DEM simulations.
12. The proposed driving mechanisms of aging were assessed based on the results from DEM simulations General trends of variation in macroscopic properties (e.g., small-strain Young's modulus and constrained modulus) were determined.

8.2 Conclusions

8.2.1 Characteristics of Aging in Granular Soils

Evidence of aging has been reported by numerous investigators. Available data on aging in sands were compiled and analyzed. Some of the conclusions from this analysis are summarized below:

1. Aging produces changes in engineering properties of granular soils. These changes are generally beneficial and may occur in a period of time that ranges from days to months after deposition or densification of the material.

2. Engineering properties reported to change during aging include the small–strain shear modulus, dilatancy, penetration resistance, and liquefaction resistance. Aging does not seem to have a significant effect on the shear strength of sands.
3. The cone penetration resistance of granular soils may as much as double during the first year following densification. The small strain shear modulus of clean silica sand increases about 1% to 3% per ten-fold increase in time.
4. Aging effects in granular soils are significantly diminished when the material is deformed. This behavior helps explain why properties measured after large strains, such as the shear strength, may appear to be unaffected by aging.
5. Aging seems to be affected by temperature. Changes in soil properties appear to occur more rapidly at higher temperatures.

8.2.2 Analysis of Results from Laboratory Experiments

An extensive laboratory testing program including micro- and macro-scale experiments was conducted to study changes in the internal structure and macroscopic properties of specimens of sand during aging. Results from laboratory tests are summarized below:

8.2.2.1 Changes in the Internal Structure

1. Small particle movements and rotations were measured using X-Ray CT during creep of specimens of sand subjected to constant vertical stress and restrained lateral deformation.
2. Particles keep moving and rotating over time. Particle movements of the grains were measured directly using X-Ray CT and detected indirectly using AE

techniques during the extent of laboratory creep experiments that lasted up to six days.

3. Particle movements occurring during creep may be reflected in minor macroscopic specimen deformation.
4. Particle movements and rotations lead towards a more uniform and stable soil structure. This was evidenced by a more even distribution of the long axis orientation of the grains and a reduction in the magnitude of the particle movements, rotations, and AEs emitted.

8.2.2.2 Changes in Macroscopic Properties

1. Creep produces an increase in the macroscopic stiffness of the material. The increase in stiffness caused by creep disappears when the specimen is subsequently deformed.
2. Creep causes the material to become more dilative during shear. Specimens allowed to creep during triaxial compression are more dilative than specimens where no creep is allowed.
3. The values of the Hardin's breakage factor (B_r) determined after the creep experiments indicate that particle breakage/crushing does not seem to be important during creep under the magnitudes of confining stress being considered (i.e., less than 1400 kPa).

8.2.3 DEM Analysis

This investigation focused on the analysis and implementation of the discrete element method as an aid to solve geotechnical engineering problems, particularly

regarding time-dependent processes such as creep and aging. Advantages and limitations of the application DEM in geotechnical practice were determined. In addition, a new contact mechanism was developed to allow modeling time-dependent particle interactions. Results from DEM simulations were compared with results obtained during the laboratory testing program. The main conclusions of this analysis are:

8.2.3.1 Implementation of DEM in Geotechnical Engineering

1. Implementing DEM in geotechnical engineering problems requires using strategies to increase the magnitude of the time step and reduce the execution time. These strategies include artificially increasing the magnitude of particle density, decreasing the particle stiffness, or increasing the rate of macroscopic deformation. However, variations in these parameters can cause important changes in the computed macroscopic properties of the assembly.
2. If the simulation parameters are controlled carefully, DEM simulations provide a reasonable estimation of the known macroscopic behavior of granular assemblies.
3. The incorporation of the new contact mechanism, which uses the rate process theory to estimate time-dependent particle interactions and the Hertz-Mindlin model to determine inter-particle forces based on the magnitude of particle indentation at contacts, produces a macroscopic assembly behavior that agrees with expected behavior of granular soils.
4. The effect of changes in the magnitude of RPT parameters on the results from DEM creep simulations agrees with results from laboratory experiments reported by numerous investigators; e.g., increase in rate of strain during creep at higher temperatures.

5. Several approximations are required to obtain DEM simulations that describe real soil behavior correctly, most of which are based solely on the user's judgment. As DEM results are greatly influenced by decisions made by the analyst during simulation, and accurate tools to confirm their validity are not available, the results of analyses using DEM in geotechnical engineering are not always completely reliable. For these reasons DEM has value for studying mechanisms, but is presently not very useful to perform engineering predictions.

8.2.3.2 Analysis of DEM Creep Simulations

1. The implementation of the new contact mechanism based on the rate process theory provides a macroscopic assembly behavior that resembles the results from laboratory creep experiments.
2. Particle movements and rotations produced by time-dependent particle interactions during creep cause changes to the internal structure of the assemblies. The analysis of DEM simulations showed that particle movements cause an increase in the number of particle contacts within the assembly and a reduction in the magnitude of the average load carried by each particle. These changes produce a more uniform distribution of the stresses and a more stable and stiffer soil fabric.
3. The study of the load chain configuration of particle arrangements before and after creep showed that the distribution of the stress within the material changes over time. During the initial stages of creep the load chains tend to be parallel to the direction of the major principal stress, and most of the load is carried fewer particles. As creep progresses, part of the this load is transferred to weakly loaded

chains, decreasing the load carried by each particle, and producing a more uniform distribution of the stress inside the assembly.

4. Changes in the internal structure of the assemblies during creep are evidenced by an increase in the Young's modulus, dilatancy, constrained modulus, and at-rest lateral earth pressure coefficient. Continued deformation breaks down the structural changes that develop during creep and aging. These behavioral trends agree with aging effects in granular soils reported by numerous investigators.
5. The rate of change in small-strain Young's modulus ($E_{0.005\%}$) ranged from about 10% to 100% per log-cycle of time. The rate of change in the magnitude of $E_{0.005\%}$ was greater in loose assemblies formed by angular particles and increased with increasing stress level during creep. Aging effects determined from DEM simulations appear to be greater than those evidenced in the laboratory and in the field. This may be caused by the large creep strains obtained during DEM simulations.
6. The horizontal stress increased linearly with respect to the logarithm of time during creep simulations with constant vertical stress and restrained lateral deformation. The rate of increase in σ_h ranged from about 2% to 7% per log-cycle of time, and was greater in dense assemblies formed by angular particles under a high vertical stress.

8.2.4 Aging Driving Mechanism in Granular Soils

Results from laboratory experiments support the hypothesis that points towards physical processes, involving particle movements and rotations causing restructuration of the material during creep, as the main driving mechanism during aging. Particle

rearrangement during aging causes a more uniform distribution of the stress within the assembly and a stiffer soil fabric. Results from DEM simulations conducted using a new contact mechanism which models time-dependent particle interactions agree with behavioral trends observed during laboratory experiments.

DEM models developed help understand the changes occurring within granular materials during aging. The study of the load chain configuration before and after creep shows that the number of contacts increases and the magnitude of the contact forces decreases with time during aging. Particles continue moving and rotating during creep, and are reflected in minor changes in macroscopic strain.

The aged soil structure is brittle, and aging effects observed during DEM simulations, such as the increase in Young's modulus and at-rest pressure coefficient, decrease rapidly when the assembly is deformed. It appears that the new contact mechanism allows modeling aging effects satisfactorily, thus providing additional evidence of the driving mechanism being controlled by rearrangement of particles during aging.

Recently the author became aware of a new hypothesis proposed by Michalowski and Nadukuru (2012) to explain aging effects in granular soils. According to these investigators, aging is caused by fracturing of superficial asperities of the grains, causing an increase in the particles' stiffness. This hypothesis was not taken into consideration during the DEM simulation program developed for this investigation. Consequentially, DEM results presented previously cannot disprove nor support this new hypothesis. However, it is expected that crushing of asperities should also increase the rate of sliding between particles, thus increasing the rate at which the particles rearrange during creep.

In other words, if asperities are fractured during creep, as suggested by Michalowski and Nadukuru (2012), the rearrangement of the grains and the internal redistribution of the stress should still account for a significant part of the aging effects observed in granular soils.

8.3 Recommendations for Future Research

During the development of this research it became apparent that further study of some aspects of the investigation may prove useful in geotechnical engineering practice. Some recommendations for future research are listed below:

1. X-Ray CT scanning was used in this research to measure the movement of individual particles within a specimen of sand during creep. However, some limitations were encountered due to the limited capability of the equipment. Future research may implement a higher energy X-Ray emitter to study larger specimens formed by smaller grains, thus reducing the extent of the errors due to boundary effects. In addition, different types of X-Ray CT scanners allow adjusting the equipment to scan specimens while being tested in a conventional triaxial apparatus, eliminating restrictions to the magnitude of the applied stress encountered during this investigation. Implementing X-Ray CT scanning on typical-size specimens during standard geotechnical tests (e.g., triaxial compression, one-dimensional compression) would be useful to understand the particle-scale behavior of a granular material not only during creep, but also under conditions such as shear and plastic deformation.

2. It is recommended that laboratory creep experiments conducted for future research use dead weight loading as opposed to servo-controlled loading. This is particularly important due to the small-magnitude strains measured during creep in sands. Laboratory tests conducted during this investigation using servo-mechanical load actuators showed a fluctuation in the magnitude of the applied stress that may have affected the results. In addition, it is recommended that other methodologies be developed, or bigger samples be used in future research to achieve more accurate values of initial void ratio during sample preparation for creep experiments during one-dimensional compression.
3. The implementation of AE techniques was useful to study and quantify changes in the internal structure of specimens of sand taking place during creep. In Section 4.5.1.2 it is shown that AEs emitted during creep have a characteristic frequency content (see Fig. 4-41). The study of the frequency of acoustic events may provide an indication of their source (e.g., crushing versus sliding), which would help to understand better the aging mechanism in granular soils.
4. Results from DEM simulations provide a reasonable approximation of the general behavior of granular materials. However, the magnitude of macroscopic properties of assemblies, such as shear strength, estimated from DEM models often differs from values determined from laboratory experiments. Some examples were introduced in Section 7.3.2.1. Future research may implement DEM assemblies that resemble more the material being modeled, which can be achieved by using clumps formed by multiple particles. However, using that strategy would significantly increase the execution time of the simulations.

Consequentially, that type of analysis is only recommended if faster computers are available to conduct the simulations.

Chapter 9

References

Afifi, S. S. and Richart, F.E..J. (1973). "Stress History Effects on Shear Modulus of Soils." *Soils and Foundations*, 13(1), 77-95.

Al-Sanad, H. A. and Ismael, N. F. (1996). "Effects of aging on freshly deposited or densified calcareous sands." *Transportation Research Record*, 1547, 76-81.

Anderson, D. G. and Stokoe, K. H. (1978). "Shear Modulus: a Time-Dependent Soil Property." *ASTM Special Technical Publications 654*, 66-90.

Andrus, R. D., Hayati, H., and Mahanan, N. P. (2009). "Correcting Liquection Resistance for Aged Sands Using Measured to Estimated Velocity Ratio." *Journal of Geotechnical and Geoenvironmental Engineering*, 135(6), 735-744.

Antony, S. J., Kuhn, M. R., and Bland, R. (2005). "Strength and signature of force networks in axially compacted sphere and non-sphere granular media: micromechanical investigations." *Journal of Physics D (Applied Physics)*, 38(21), 3944-3952.

Arango, I., Lewis, M. R., and Kramer, C. (2000). "Updated liquefaction potential analysis eliminates foundation retrofitting of two critical structures." *Soil Dynamics and Earthquake Engineering*, 20(1-4), 17-25.

Ashford, S. A., Rollins, K. M., and Lane, J. D. (2004). "Blast-induced liquefaction for full-scale foundation testing." *Journal of Geotechnical and Geoenvironmental Engineering*, 130(8), 798-806.

Baranov, V., Kudryavtsev, E., and Schavelin, V. (2007). "Acoustic Emission in Friction." 1st ed., Elsevier, Amasterdam.

Baxter, C. D.P. and Mitchell, J. K. (2004). "Experimental Study on the Aging of Sands." *Journal of Geotechnical and Geoenvironmental Engineering*, 130(10), 1051-1062.

Belheine, N., Plassiard, J.-P., Donze, F.-V., Darve, F., and Seridi, A. (2009). "Numerical simulation of drained triaxial test using 3D discrete element modeling." *Computers and Geotechnics*, 36(1-2), 320-31.

Bharadwaj, R., Khambekar, J., Orlando, A., Gao, Z., Shen, H., Helenbrook, B., Royal, T.A., and Weitzman, P. (2008). "A comparison of discrete element modeling, finite element analysis, and physical experiment of granular material systems in a direct shear cell." *AIP Conference Proceedings*, AIP, Albuquerque, NM, USA, 221-8.

Bowman, E. T. and Soga, K. (2003). "Creep, Ageing and Microstructural Change in Dense Granular Material." *Soils and Foundations*, 43(4), 107-117.

Bowman, E. T. and Soga, K. (2005). "Mechanisms of Setup of Displacement Piles in Sand: Laboratory Creep Tests." *Canadian Geotechnical Journal*, 42(5), 1391-1407.

Box, G.E.P. and Muller, M.E. (1958). "A Note on the Generation of Random Normal Deviates." *The Annals of Mathematical Statistics*, 29(2), 610-611.

Bradshaw, A. S. (2006). "Liquefaction Potential of Non-Plastic Silts." PhD Thesis, University of Rhode Island, Kingston, RI.

Byerlee, J. D. and Lockner, D. (1977). "Acoustic Emission During Fluid Injection." *Proceedings of the First Conference on Acoustic Emission/Microseismic Activity in Geologic Structures and Materials*, Trans Tech Publications, Pennsylvania State University, 87-98.

Cambou, B., Jean, M., and Radjai, F. (2009). "Micromechanics of Granular Materials." ISTE Ltd and John Wiley & Sons, Inc., London, UK.

Cavarretta, I., Coop, M., and O'Sullivan, C. (2010). "The influence of particle characteristics on the behaviour of coarse grained soils." *Geotechnique*, 60(6), 413-423.

Charlie, W. A., Rwebyogo, M. F., and Doehring, D. O. (1992). "Time-Dependent Cone Penetration Resistance Due to Blasting." *Journal of Geotechnical Engineering*, 118(8), 1200-1215.

Chow, F. C., Jardine, R. J., Brucy, F., and Nauroy, J. F. (1998). "Effects of Time on Capacity of Pipe Piles in Dense Marine Sand." *Journal of Geotechnical and Geoenvironmental Engineering*, 124(3), 254-264.

Cundall, P.A. and Strack, O.D.L. (1979). "Discrete Numerical Model For Granular Assemblies." *Geotechnique*, 29(1), 47-65.

Dai, Q. and You, Z. (2007). "Prediction of creep stiffness of asphalt mixture with micromechanical finite-element and discrete-element models." *Journal of Engineering Mechanics*, 133(2), 163-173.

Daramola, O. (1980). "Effect of Consolidation age on Stiffness of Sand." *Geotechnique*, 30(20), 213-216.

DeJong, J. T., Fritzges, M. B., and Nüsslein, K. (2006). "Microbially induced cementation to control sand response to undrained shear." *Journal of Geotechnical and Geoenvironmental Engineering*, 132(11), 1381-1392.

Denisov, N.Y. and Reltov, B.F. (1961). "The Influence of Certain Processes on the Strength of Soils." *Proc. 5th Int. Conf. Soil Mech. and Found. Engr.*, Paris, 75-78.

Desrues, J., Chambon, R., Mokni, M., and Mazerolle, F. (1996). "Void ratio evolution inside shear bands in triaxial sand specimens studied by computed tomography." *Geotechnique*, 46(3), 529-546.

Dieterich, J. H. and Kilgore, B. D. (1994). "Direct Observation of Frictional Contacts: New Insights for Sate-dependent Properties." *Pure and Applied Geophysics*, 143(1-3), 283-302.

Dinesh, S.V., Sitharam, T.G., and Vinod, J.S. (2004). "Dynamic properties and liquefaction behaviour of granular materials using discrete element method." *Current Science*, 87(10), 1379-87.

Dove, P.M. and Elston, S.F. (1992). "Dissolution kinetics of quartz in sodium chloride solutions: Analysis of existing data and a rate model for 25°C." *Geochimica et Cosmochimica Acta*, 56(12), 4147-4156.

Dowding, C. H. and Hryciw, R. D. (1986). "A Laboratory Study of Blast Densification of Saturated Sand." *Journal of Geotechnical Engineering*, 112(2), 187-199.

Drnevich, V. P., Hardin, B. O., and Shippy, D. J. (1978). "Modulus and Damping of Soils by Resonant-Column Method." *Dynamic Geotechnical Testing, ASTM STP 654*, 91-125.

Dumas, J. C. and Beaton, N. F. (1986). "Discussion of "Practical Problems from Surprising Soil Behavior" by James K. Mitchell (March, 1986, Vol. 112, No. 3)." *Journal of Geotechnical Engineering*, 114(3), 367-368.

Duran, J. (2000). "Sands, Powders, and Grains." Springer-Verlag, New York.

Eyring, H. (1935). "The Activated Complex in Chemical Reactions." *Journal of Chemical Physics*, 3, 107-115.

Eyring, H. (1936). "Viscosity, plasticity and diffusion as examples of absolute reaction rates." *Journal of Chemical Physics*, 4, 283-291.

Feng, J., Chuhan, Z., Gang, W., and Guanglun, W. (2003). "Creep modeling in excavation analysis of a high rock slope." *Journal of Geotechnical and Geoenvironmental Engineering*, 129(9), 849-857.

Fernandes, F., Syahrial, A.I., and Valdes, J.R. (2010). "Monitoring the Oedometric Compression of Sands with Acoustic Emissions." *Geotechnical Testing Journal*, 33(5), 1-5.

Fu, Y. (2005). "Experimental Quantification and DEM Simulation of Micro-Macro Behaviors of Granular Materials Using X-Ray Tomography Imaging." PhD Dissertation, Louisiana State University and Agricultural and Mechanical College, Baton Rouge, LA.

Fu, Y., Wang, L., Tumay, M. T., and Li, Q. (2008). "Quantification and simulation of particle kinematics and local strains in granular materials using X-ray tomography imaging and discrete-element method." *Journal of Engineering Mechanics*, 134(2), 143-154.

Gohl, W. B., Howie, J. A., Hawson, H. H., and Diggle, D. (1994). "Field Experience with Blast Densification in an Urban Setting." *Proceedings of teh 5th U.S. National Conf. on Earthquake Engineering*, Chicago, IL, 221-230.

Goodman, R. E. (1989). "Introduction to Rock Mechanics." 2nd ed., John Wiley and Sons, New York.

Hardin, B. O. (1985). "Crushing of Soil Particles." *Journal of geotechnical engineering*, 111(10), 1177-1192.

Hardy, H. R.J. (2003). "Acoustic Emission/Microseismic Activity." A.A. Balkema Publishers, Lisse, The Netherlands.

Hayati, H. and Andrus, R. D. (2009). "Updated Liquefaction Resistance Correction Factors for Aged Sands." *Journal of Geotechnical and Geoenvironmental Engineering*, 135(11), 1686-1692.

Howie, J. A., Shozen, T., and Vaid, Y. P. (2002). "Effect of Ageing on stiffness of Very Loose Sand." *Canadian Geotechnical Journal*, 39(1), 149-156.

Huang, Z.-Y., Yang, Z.-X., and Wang, Z.-Y. (2008). "Discrete element modeling of sand behavior in a biaxial shear test." *Journal of Zhejiang University: Science A*, 9(9), 1176-1183.

Human, C. A. (1992). "Time-Dependent Property Changes of Freshly Deposited or Densified Sands, Ph.D. Dissertation." University of California, Berkeley.

Itasca Consulting Group Inc. (2008). "PDF2D - Particle Flow Code in 2 Dimensions - Version 3.0." ICG, Minneapolis.

Jamiolkowski, M. and Manassero, M. (1995). "The Role of the In-Situ Testing in Goetechnical Engineering - Thoughts About the Future." *Proceedings of the International Conference on Advances in Site Investigation Practice*, Thomas Telford, London, U.K., 929-951.

Jardine, R. J., Standing, J. R., and Chow, F. C. (2006). "Some observations of the effects of time on the capacity of piles driven in sand." *Geotechnique*, 56(4), 227-244.

Jefferies, M. G. and Rogers, B. T. (1993). "Discussion of "Time-Dependent Cone Penetration Resistance due to Blasting" by Wayne A. Charlie, Mutabihirwa F. J. Rwebyogo, and Donald O. Doehring (August, 1992, Vol. 118, No. 8)." *Journal of Geotechnical Engineering*, 119(12), 2008-2012.

Jefferies, M.G., Rogers, B.T., Stewart, H.R., Shinde, S., James, D., and Williams-Fitzpatrick, S. (1988). "Island construction in the Canadian Beaufort sea." *Hydraulic Fill Structures*, ASCE, Fort Collins, CO, 816-883.

Jiang, M. J., Yu, H.-S., and Harris, D. (2006). "Discrete element modelling of deep penetration in granular soils." *International Journal for Numerical and Analytical Methods in Geomechanics*, 30(4), 335-361.

Joshi, R. C., Achari, G., Kaniraj, S. R., and Wijeweera, H. (1995). "Effect of Aging on the Penetration Resistance of Sands." *Canadian Geotechnical Journal*, 32(5), 767-782.

Kaiser, J. (1953). "Recognition and Behavior of Noise Measurements in Metal Materials under Various Stresses." *Arkiv fur Eisenhuttenwesen*, 25(43).

Karrech, A., Duhamel, D., Bonnet, G., Chevoir, F., Roux, J.-N., Canou, J., and Dupla, J.-C. (2008). "A discrete element study of settlement in vibrated granular layers: Role of contact loss and acceleration." *Granular Matter*, 10(5), 369-375.

Ketcham, R. A. and Carlson, W. D. (2001). "Acquisition, optimization and interpretation of x-ray computed tomographic imagery: Applications to the geosciences." *Computers and Geosciences*, 27(4), 381-400.

Khair, A. W. (1972). "Failure Criteria Applicable to Pressurized Cavities in Geologic Materials Under In-Situ Stress Conditions." Ph.D. Thesis, Geomechanics Section, Department of Mineral Engineering, The Pennsylvania State University.

Koerner, R. M., Lord Jr., A. E., and Deutsch, W. L. (1984). "Determination of Prestress in Granular Soils using AE." *Journal of Geotechnical Engineering*, 110(3), 346-358.

Koerner, R. M., Lord Jr., A. E., McCabe, W.M., and Curran, J. W. (1976). "Acoustic Emission Behavior of Granular Soils." *Journal of the Geotechnical Engineering Division*, 102(7), 761-773.

Kosoglu, L. (2011). "Modeling Macro-scale Clay Behavior at Micro-scale Clay Particle Interfaces." PhD Dissertation, Virginia Polytechnic Institute and State University, Blacksburg, VA.

Kuhn, M. R. (1987). "Micromechanical aspects of soil creep." Ph.D. Dissertation, University of California Berkeley, Berkeley, CA., U.S.

Kuhn, M. R. (1999). "Structured deformation in granular materials." *Mechanics of Materials*, 31(6), 407-429.

Kuhn, M. R. and Mitchell, J. K. (1993). "New perspectives on soil creep." *Journal of Geotechnical Engineering*, 119(3), 507-524.

Kulhawy, F.H. and Mayne, P.W. (1990). "Manual on Estimating Soil Properties for Foundation Design (EL-6800)." Electric Power Research Institute, Palo Alto, CA.

Kuwano, R. and Jardine, R. J. (2002). "On measuring creep behaviour in granular materials through triaxial testing." *Canadian Geotechnical Journal*, 39(5), 1061-1074.

Kwok, C. Y. (2008). "Micromechanical Investigation of Soil Creep." PhD Dissertation, University of Cambridge, Cambridge, United Kingdom.

Ladd, R. S. (1978). "Preparing Test Specimens Using Undercompactionn." *Geotechnical Testing Journal*, 1(1), 16-23.

Lade, P. V., Nam, J., and Liggio, C. D. (2010). "Effects of particle crushing in stress drop-relaxation experiments on crushed coral sand." *Journal of Geotechnical and Geoenvironmental Engineering*, 136(3), 500-509.

Latière, H.J. and Mazerolle, F. (1987). "The X-ray scanner. A tool for the examination of the intravoluminal crystalline state of aluminium." *Engineering Fracture Mechanics*, 27(4), 413-463.

Leon, E., Gassman, S. L., and Talwani, P. (2006). "Accounting for Soil Aging When Assessing Liquefaction Potential." *Journal of Geotechnical and Geoenvironmental Engineering*, 132(3), 363-377.

Liao, T. and Mayne, P. W. (2005). "Cone penetrometer measurements during Mississippi embankment seismic excitation experiment." *Geotechnical Special Publications, n.130-142*, Geo-Frontiers, , 1353-1364.

Li, J., Langston, P.A., Webb, C., and Dyakowski, T. (2004). "Flow of sphero-disc particles in rectangular hoppers-a DEM and experimental comparison in 3D." *Chemical Engineering Science*, 59(24), 5917-29.

Lin, X. and Ng, T.-T. (1997). "A three-dimensional discrete element model using arrays of ellipsoids." *Geotechnique*, 47(2), 319-329.

Li, Y., Xu, Y., and Thornton, C. (2005). "A comparison of discrete element simulations and experiments for 'sandpiles' composed of spherical particles." *Powder Technology*, 160(3), 219-228.

Lobo-Guerrero, S. and Vallejo, L. E. (2005). "Discrete element method evaluation of granular crushing under direct shear test conditions." *Journal of Geotechnical and Geoenvironmental Engineering*, 131(10), 1295-1300.

Malone, K. F. and Xu, B. H. (2008). "Determination of contact parameters for discrete element method simulations of granular systems." *Particuology*, 6(6), 521-528.

Matsushita, M., Tatsuoka, F., Koseki, J., Cazacliu, B., Bennedetto, H., and Yasin, S. J.M. (1999). "Time effect on the pre-peak deformation properties of sands." *Proceedings of the International Conference on Pre-failure Deformation Characteristics of Geomaterials*, M. Jamiolkowski, R. Lancellotta, and D. Lo Presti, eds., Torino, Balkema, 681-689.

McBride, A., Govender, I., Powell, M., and Cloete, T. (2004). "Contributions to the experimental validation of the discrete element method applied to tumbling mills." *Engineering Computations*, 21(2-4), 119-136.

Mejia, C. A., Vaid, Y. P., and Negussey, D. (1988). "Time dependent behavior of sand." *International Conference on Rheology and Soil Mechanics*, M. J. Keedwell, ed., Elsevier, London, 312-326.

Mesri, G., Feng, T. W., and Benak, J. M. (1990). "Postdensification Penetration Resistance of Clean Sands." *Journal of Geotechnical and Geoenvironmental Engineering*, 116(7), 1095-1115.

Michalowski, R. L. and Nadukuru, S. S. (2012). "Static Fatigue, Time Effects, and Delayed Increase in Penetration Resistance after Dynamic Compaction of Sands." *Journal of Geotechnical and Geoenvironmental Engineering*, 138(5), 564-574.

Mindlin, R.D. (1949). "Compliance of elastic bodies in contact." *American Society of Mechanical Engineers -- Transactions -- Journal of Applied Mechanics*, 16(3), 259-268.

Mindlin, R.D. and Deresiewicz, H. (1953). "Elastic spheres in contact under varying oblique forces." *Journal of applied mechanics.*, 20(3), 327-344.

Mitchell, J. K. (2008). "Aging of Sand - A Continuing Enigma?" *6th International Conference on Case Histories in Geotechnical Engineering*, Arlington, VA

Mitchell, J.K., and Baxter, C.D.P., and and Soga, K. (1997). "Time effects on the stress-deformation behavior of soils." *Proceedinga of Professor Sakuro Murayama Memorial Symposium*, Kyoto, Japan, 1-64.

Mitchell, J.K. and Campanella, R.G. (1964). "Creep studies on saturated clays." *American Society for Testing and Materials -- Special Technical Publications*, (361), 90-110.

Mitchell, J.K., Campanella, R.G., and Singh, A. (1968). "Soil creep as rate process." *American Society of Civil Engineers Proceedings, Journal of the Soil Mechanics and Foundations Division*, 94(SM1), 231-253.

Mitchell, J. K. and Santamarina, J. C. (2005). "Biological Considerations in Geotechnical Engineering." *Journal of Geotechnical and Geoenvironmental Engineering*, 131(10), 1222-1233.

Mitchell, J.K., Singh, A., and Campanella, R.G. (1969). "Bonding, Effective Stress, and Strength of Soils." *Journal of the Soil Mechanics and Foundations Division*, 95(SM5), 1219-1246.

Mitchell, J. K. and Soga, K. (2005). "Fundamentals of Soil Behavior." Third Edition ed., John Wiley & Sons, New Jersey.

Mitchell, J. K. and Solymar, Z. V. (1984). "Time-Dependent Strength Gain in Freshly Deposited or Densified Sand." *Journal of Geotechnical Engineering*, 110(10), 1559-1576.

Murayama, S. (1969). "Effect of temperature on elasticity of clays." *Highway Research Board Special Report 103*, a2194–202.

Murayama, S., Michihiro, K., and Sakagami, T. (1984). "Creep Characteristics of Sands." *Soils and Foundations*, 24(2), 1-15.

Muthuswamy, M., Peters, J., and Tordesillas, A. (2005). "Uncovering the secrets to relieving stress: discrete element analysis of force chains in particulate media." *ANZIAM Journal*, 47, c355-c372.

Nakata, Y., Hyde, A. F.L., Hyodo, M., and Murata, H. (1999). "A probabilistic approach to sand particle crushing in the triaxial test." *Geotechnique*, 49(5), 567-583.

Ng, T.-T. (1994). "Numerical simulations of granular soil using elliptical particles." *Computers and Geotechnics*, 16(2), 153-169.

Ng, T.-T. (2006). "Input parameters of discrete element methods." *Journal of Engineering Mechanics*, 132(7), 723-729.

Ng, T.-T. (2009). "Discrete Element Method Simulations of the Critical State of a Granular Material." *International Journal of Geomechanics*, 9(5), 209-216.

Obert, L. (1977). "The Microseismic Method: Discovery and Early History." *Proceedings: First Conference on Acoustic Emission/Microseismic Activity in Geologic Structures and Materials*, H.R. Hardy, ed., Trans Tech Publications, Pennsylvania State University, University Park, Pennsylvania, 11-12.

Obert, L. and Duvall, W.I. (1942). "Use of Subaudible Noises for the Prediction of Rock Bursts, Part II." Report of Investigation R.I. 3654, U.S. Bureau of mines.

Oda, M., Iwashita, K., and Kakiuchi, T. (1997). "Importance of particle rotation in the mechanics of granular materials." *Proceedings of the Third International Conference on Powders and Grains*, R. P. Behringer and J. T. Jenkins, eds., A.A. Balkema, Durham, NC, 207-210.

O'Sullivan, C. and Bray, J. D. (2004). "Selecting a suitable time step for discrete element simulations that use the central difference time integration scheme." *Engineering Computations*, 21(2), 278-303.

Owen, J.P., Cleary, P.W., and Meriaux, C. (2009). "Quasi-static fall of planar granular columns: comparison of 2D and 3D discrete element modelling with laboratory experiments." *Geomechanics and Geoengineering: An International Journal*, 4(1), 55-78.

Pham Van Bang, D., Di Benedetto, H., Duttine, A., and Ezaoui, A. (2007). "Viscous behaviour of dry sand." *International Journal for Numerical and Analytical Methods in Geomechanics*, 31(15), 1631-58.

Raynaud, S., Fabre, D., Mazerolle, F., Geraud, Y., and Latiere, H.J. (1989). "Analysis of the internal structure of rocks and characterization of mechanical deformation by a non-destructive method: X-ray tomodensitometry." *Tectonophysics*, 159(1-2), 149-159.

Rimstidt, J. D. (1997). "Quartz solubility at low temperatures." *Geochimica et Cosmochimica Acta*, 61(13), a22553–2558.

Rogers, B.T., Graham, C.A., and Jefferies, M.G. (1990). "Compaction of hydraulic fill sand in Molikpaq core." *Proceedings of the 43rd Canadian Geotechnical*

Conference. Part 2, Canadian Geotechnical Soc, Montreal, Canada, Chateau, Que, Can, 567-575.

Rowe, P. W. (1962). "The stress-dilatancy relation for static equilibrium of an assembly of particles in contact." *Proceedings of the Royal Society of London. Series A, Mathematical and Physical*, 269(1339), 500-527.

Schmertmann, J. H. (1964). "Generalizing and measuring the Hvorslev effective components of shear resistance." *Symp. on Laboratory Shear Stregnth Testing of Soils*, ASTM, Philadelphia, PA, 147-162.

Schmertmann, J. H. (1987). "Discussion of "Time Dependent Stregnth Gain in Freshly Deposited or Densified Sand" by J. K. Mitchell and Z. V. Solymar." *Journal of Geotechnical Engineering*, 113(2), 173-175.

Schmertmann, J. H. (1991). "The Mechanical Aging of Soils." *Journal of Geotechnical Engineering*, 117(9), 1288-1330.

Schwarz, O.J., Horie, Y., and Shearer, M. (1998). "Discrete element investigation of stress fluctuation in granular flow at high strain rates." *Physical Review E (Statistical Physics, Plasmas, Fluids, and Related Interdisciplinary Topics)*, 57(2), 2053-61.

Seed, H.B. (1979). "Soil Liquefaction and Cyclic Mobility Evaluation for Level Ground During Earthquakes." *Journal of the Geotechnical Division*, 105(GT 2), 201-235.

Sheng, Y., Lawrence, C. J., Briscoe, B. J., and Thornton, C. (2004). "Numerical studies of uniaxial powder compaction process by 3D DEM." *Engineering Computations*, 21(2), 304-317.

Sitharam, T. G. (2003). "Discrete element modelling of cyclic behaviour of granular materials." *Geotechnical and Geological Engineering*, 21(4), 297-329.

Skempton, A. W. (1986). "Standard Penetration Test Procedures and the Effects in Sands of Overburden Pressure, Relavite Density, Particle Size, Ageing and Overconsolodation." *Geotechnique*, 36(3), 425-447.

Solymar, Z. V. (1984). "Compaction of Alluvial Sands by Deep Blasting." *Canadian Geotechnical Journal*, 21(2), 305-321.

Sorensen, K.K., Baudet, B.A., and Simpson, B. (2007). "Influence of structure on the time-dependent behaviour of a stiff sedimentary clay." *Geotechnique*, 57(1), 113-24.

Stocks-Fischer, S., Galinat, J. K., and Bang, S. S. (1999). "Microbiological precipitation of CaCO3." *Soil Biology and Biochemistry*, 31(11), 1563-1571.

Strack, O. D.L. and Cundall, P. A. (1984). "Fundamental studies of fabric in granular materials." Report to NSF, University of Minnesota, Minneapolis, MN.

Tatsuoka, F., Santucci de Magistris, F., Hayano, K., Momoya, Y., and J., K. (2000). "Some new aspects of time effects on the stress-strain behaviour of stiff geomaterials." *The geotechnics of hard soils--soft rocks : proceedings of the Second International Symposium on Hard Soils, Soft Rocks*, Naples, Italy, 1285-1353.

Thornton, C. and Randall, W. (1988). "Applications of Theoretical Contact Mechanics to Soild Particle System Simulation." *Micromechanics of Granular Materials - Proceedings of the US/Japan Seminar on Micromechanics of Granular Materials*, Elsevier, Sendai-Zao, Japan, 133-142.

Thornton, C. and Zhang, L. (2006). "A numerical examination of shear banding and simple shear non-coaxial flow rules." *Philosophical Magazine*, 86(21-22), 3425-52.

Tietz, T.E. and Dorn, J.E. (1956). "Creep of copper at intermediate temperatures." *Journal of Metals*, 8(2, Sec2), 156-162.

Tordesillas, A. (2007). "Force chain buckling, unjamming transitions and shear banding in dense granular assemblies." *Philosophical Magazine*, 87(31-33), 31-33.

Troncoso, J.H. and Garcés, E. (2000). "Ageing effects in the shear modulus of soils." *Soil Dynamics and Earthquake Engineering*, 19(8), 595-601.

Vinogradov, O. (2004). "Equivalent normal stiffness of the ball in granular dynamics simulations." *Granular Matter*, 5(3), 153-158.

Vu-Quoc, L., Zhang, X., and Walton, O.R. (2000). "A 3D discrete-element method for dry granular flows of ellipsoidal particles." *Computer Methods in Applied Mechanics and Engineering*, 187(3-4), 483-528.

Wang, J., Gutierrez, M.S., and Dove, J.E. (2007). "Numerical studies of shear banding in interface shear tests using a new strain calculation method." *International Journal for Numerical and Analytical Methods in Geomechanics*, 31(12), 1349-1366.

Wang, Y.-H. and Leung, S.-C. (2008). "A particulate-scale investigation of cemented sand behavior." *Canadian Geotechnical Journal*, 45(1), 29-44.

Wang, Y.-H. and Tsui, K.-Y. (2009). "Experimental characterization of dynamic property changes in aged sands." *Journal of Geotechnical and Geoenvironmental Engineering*, 135(2), 259-270.

Wang, Y.-H., Xu, D., and Tsui, K. Y. (2008). "Discrete element modeling of contact creep and aging in sand." *Journal of Geotechnical and Geoenvironmental Engineering*, 134(9), 1407-1411.

Wang, D. and Zhou, Y. (2008). "Discrete element simulation of localized deformation in stochastic distributed granular materials." *Science in China, Series G: Physics, Mechanics and Astronomy*, 51(9), 1403-1415.

Yuu, S., Abe, T., Saitoh, T., and Umekage, T. (1995). "Three-dimensional numerical simulation of the motion of particles discharging from a rectangular hopper using distinct element method and comparison with experimental data (effects of time steps and material properties)." *Advanced Powder Technology*, 6(4), 259-269.